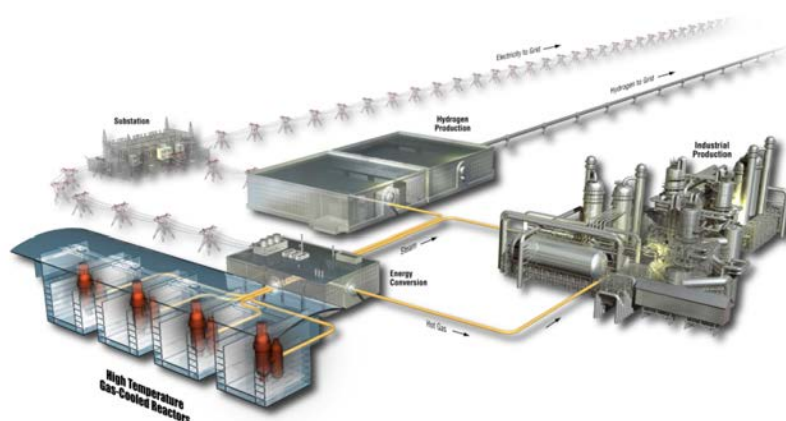


# Advanced Electron Microscopy and Micro-Analytical Technique Development and Application on Irradiated TRISO-Coated Particles from the AGR-1 Experiment

I. J. van Rooyen, T. M. Lillo, H. Wen,  
K. E. Wright, J. Madden, and J. A. Aguiar

January 2017

The INL is a  
U.S. Department of Energy  
National Laboratory  
operated by  
Battelle Energy Alliance



#### **DISCLAIMER**

This information was prepared as an account of work sponsored by an agency of the U.S. Government. Neither the U.S. Government nor any agency thereof, nor any of their employees, makes any warranty, expressed or implied, or assumes any legal liability or responsibility for the accuracy, completeness, or usefulness, of any information, apparatus, product, or process disclosed, or represents that its use would not infringe privately owned rights. References herein to any specific commercial product, process, or service by trade name, trade mark, manufacturer, or otherwise, does not necessarily constitute or imply its endorsement, recommendation, or favoring by the U.S. Government or any agency thereof. The views and opinions of authors expressed herein do not necessarily state or reflect those of the U.S. Government or any agency thereof.



# **Advanced Electron Microscopy and Micro-Analytical Technique Development and Application on Irradiated TRISO-Coated Particles from the AGR-1 Experiment**

**I. J. van Rooyen, T. M. Lillo, H. Wen, K. E. Wright, J. Madden, and J. A. Aguiar**

**January 2017**

**Idaho National Laboratory  
INL ART TDO Program  
Idaho Falls, Idaho 83415**

**<http://www.inl.gov>**

**Prepared for the  
U.S. Department of Energy  
Office of Nuclear Energy  
Under DOE Idaho Operations Office  
Contract DE-AC07-05ID14517**



## INL ART TDO Program


# Advanced Electron Microscopy and Micro-Analytical Technique Development and Application on Irradiated TRISO-Coated Particles from the AGR-1 Experiment

INL/EXT-15-36281

Revision 0

January 2017

### Author:



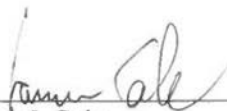
Isabella J. van Rooyen

ART TRISO Fuel Electron Microscopic and Micro-analysis Technical Lead

1/12/17

Date

### Independent Technical Reviewer:



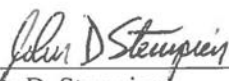
James I. Cole

Fuel Development Pillar Deputy National Technical Lead,  
US High Performance Reserch Reactor Program

1/12/17

Date

### Approved by:



John D. Stempien

ART TRISO Fuel Post-Irradiation Examination Technical Lead

1/17/2017

Date



Paul A. Demkowicz

ART TRISO Fuel Director

1/17/17

Date

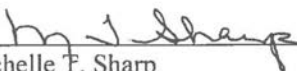


Hans D. Gougar

ART Technology Development Office Director

1/12/2017

Date



Michelle F. Sharp

ART Quality Assurance Lead

1/12/17

Date



## ACKNOWLEDGEMENTS

This work was sponsored by the U.S. Department of Energy's Office of Nuclear Energy, under U.S. Department of Energy Idaho Operations Office Contract DE-AC07-05ID14517, as part of the Advanced Reactor Technologies Program (ART) and the National Science User Facility Rapid Turnaround Experiment (NSUF-RTE) Program.

The experimental work and data analysis presented here were performed by the Idaho National Laboratory (INL) ART fuels electron microscopy team and collaborators:

- Scott Ploger and Jason Harp: Mount and decontamination preparation for electron microscopy examination and micro-analysis
- Dawn Janney: Basic transmission electron microscopy (TEM) microscopy (Compact 6-3-2, Compact 4-1-1)
- Jim Madden: Focused ion beam (FIB)-TEM and atom probe tomography (APT) sample preparation; electron backscatter diffraction (EBSD) sample preparation improvement
- Tammy Trowbridge: EBSD data collection and input to sample preparation techniques
- Thomas O'Holleran: Preliminary EBSD microscopy on JEOL 7000 SEM
- Yaqiao Wu (Boise State University): APT, scanning transmission electron microscopy (STEM), energy filtered transmission electron microscopy (EFTEM), and electron energy loss spectroscopy (EELS) microscopy
- Tom Lillo: Basic TEM, EBSD, APT, STEM, EFTEM, and EELS microscopy
- Bin Leng (University of Wisconsin-Madison): Contribution towards APT measurements, STEM Compact 6-3-2
- Daniel Goran (Brucker-Nano): transmission Kikuchi diffraction (TKD) of unirradiated SiC
- Jan Neethling, Mike Lee, Jaco Olivier, and William Goossen (Nelson Mandela Metropolitan University): TKD and high-resolution transmission electron microscopy (HRTEM) of irradiated SiC (Compact 4-1-1)
- Karen Wright: Electron probe micro-analysis (EPMA)
- Haiming Wen: STEM, HRTEM, and precession electron diffraction (PED)
- Terry Holesinger (Los Alamos National Laboratory [LANL]): HRTEM Compacts 1-3-1 and 4-3-3
- Jhonathan Rosales (University of Florida; INL intern summer 2016): Chemical composition trend graphical presentation, partial tabulation of energy dispersive x-ray spectroscopy (EDS) results
- Jeffery Aguiar: HRTEM Compact 4-3-3, partial tabulation of EDS results, contribute to Compact 4-3-3 PED
- John Hunn, Tyler Gerczak (ORNL): IPyC breached particle collaboration (Compact 5-2-3)
- Connie Hill (Idaho State University, INL intern): scanning electron microscopy (SEM) montage and interlayer thickness
- Isabella van Rooyen: ART tristructural isotropic (TRISO) fuels advanced electron microscopy and micro-analysis lead, design of experiments, trend analysis, interpretation, and first author of report
- The staff contributions at several key Materials and Fuels Complex (MFC) facilities (Hot Fuels Examination Facility, Analytical Laboratory, and Electron Microscopy Laboratory) and Center for Advanced Energy Studies (CAES) in completing this work are also gratefully acknowledged.

- Paul Demkowicz, John Stempien, Michele Sharp, Jim Cole, Hans Gougar and Diana Croson are thanked for their review of this report. Andrea L Stringham, LauraLee Gourley, Heather Rohrbaugh, Jodi Vollmer, and Judy Mount are acknowledged for their editing and administrative support in completing this report.
- Madeline Feltus is acknowledged for her supportive discussions and motivation to enhance the understanding and science base of our work.

## SUMMARY

Advanced Gas Reactor (AGR) experiments AGR-1, AGR-2, and AGR-3/4 have been conducted in the Advanced Test Reactor at Idaho National Laboratory. The first experiment (AGR-1) was completed in November 2009 at an effective 620 full-power days. Objectives of the AGR-1 experiment were primarily to provide lessons learned on the multi-capsule test train design, provide early data on fuel performance for use in further development of the fuel fabrication process, and to provide fuel specimens for post-irradiation examination and safety testing at high temperatures. Fuel performance assessment focuses on the behavior of the kernel and tristructural isotropic (TRISO) coating layers and retention of fission products by coated particles and fuel compacts. Knowledge and understanding of fission product transport mechanisms are fundamental objectives for facilitating potential improvements that contribute to extension of the performance envelope of modern TRISO-coated particle fuel. This report describes the advanced microscopy and micro-analysis results on selected AGR-1 coated particles from Compacts 6-3-2, 5-3-1, 5-2-3, 1-3-1, 4-1-1, and 4-3-3, which represent compacts from four capsules irradiated to burnups of 11.4 to 19.4% fissions per initial metal atom (FIMA).

The objective of the electron microscopic examination of fuel particles is to characterize the effects of radiation upon the microstructure, particularly with respect to fuel kernel porosity, layer degradation or corrosion, fission product precipitation, layer debonding, and grain characteristics. Another objective is to determine if there are microstructural differences between particles that exhibited high and low releases of Ag-110m to aid in understanding of transport mechanisms. Because silicon carbide (SiC) is the main fission product barrier and resolving the nano-sized fission product precipitates within the SiC layer is complex, determining which fission products were present and the distributions of those fission products within the SiC layer and characterizing SiC grain boundaries were prioritized during the AGR-1 campaign. Multiple publications (e.g., reports, journal papers, conference papers, and presentations) previously reported on these results from the AGR-1 post-irradiation activities (2011 to current); therefore, the aim of this report is to present the details of the large body of recent unpublished work, while referencing the main findings of the previous published work.

A number of advanced microscopy and micro-analytical techniques (described within) were explored and deployed to construct an informative picture of the behavior of the particle microstructure, focusing on the SiC layer and SiC-inner pyrolytic carbon (IPyC) interface. This exploration and associated method developments and analyses led to numerous first-of-a-kind achievements. Scanning transmission electron microscopy, transmission electron microscopy, high resolution transmission electron microscopy for microstructural effects, qualitative chemical composition using energy dispersive X-ray spectroscopy (EDS) techniques, and TRISO-specific analysis approaches were successfully employed during AGR-1 post irradiation examinations (PIE) and are recommended for subsequent AGR experiments. The quantification of chemical composition was explored using electron probe micro-analysis (EPMA), electron energy loss spectroscopy (EELS), energy filtered transmission electron microscopy, atom probe tomography (APT), and high-resolution transmission electron microscopy with a new generation high-resolution EDS detector.

Although success was recently achieved using APT to quantify chemical composition in nano-sized fission product precipitates, further optimization is needed before APT can be utilized as a standard tool for TRISO fuel examination. Additionally, EELS may provide a more effective analysis technique for quantification, but further exploration is recommended. EPMA and HRTEM examinations provided significant results, and their use is recommended in future PIE.

It is significant that silver (Ag) was found at both intra- and intergranular sites within the SiC microstructure, although it was predominantly in grain boundaries and triple points. It was further found that palladium (Pd) dominated most of the fission product precipitates examined and is often found throughout the SiC layer, either separately or co-existing with other elements. Qualitatively, the general Pd concentration in the SiC layer is greater than that of Ag, although no specific trend was found relating the Pd-to-Ag ratios of the precipitates to the location in the SiC layer. This is consistent with the relative amount of Pd and Ag generated during fission (the total Pd inventory is much higher than Ag).

In addition, the combinations of elements in more than 700 precipitates that were examined from a number of different particles are complex and varying in nature, and often other elements (e.g., europium, cerium, plutonium, and cesium) can be present in precipitates that predominantly contain Pd, Si, Ag, and uranium (U). This complicates the interpretation for determining possible trends with fuel type (i.e. Baseline, Variant 1, Variant 2, and Variant 3), level of Ag retention within the particle, and SiC layer location. Generally, more elemental combinations exist for precipitates from particles with relatively low Ag-retention compared to particles with relatively high Ag-retention irrespective of fuel type. Uranium is predominantly found in combination with other elements and is only found alone in precipitates from Compact 1-3-1, which is a Variant 3 fuel compact. Uranium and Ag are only found as a combination in the low Ag retention safety-tested Particle AGR1-433-001. Cesium was identified in the SiC layer of particles from all compacts evaluated.

Recent HRTEM examination on the safety-tested Variant 3 fuel-type particles from Compact 4-3-3 showed that all evaluated nano-sized precipitates have a cubic structure, while the micron-sized precipitates from Compact 6-3-2 (Baseline fuel) showed a tetragonal  $\text{UPd}_2\text{Si}_2$  structure. Micron-sized precipitates were identified as both single and multiphase; no obvious trend could be established in relation to location, size, and phase. Success in characterizing a precipitate was achieved using atom probe tomography, where a multi-phased Ag-Pd-U precipitate (nano-sized) was quantified on a grain boundary. The three-dimensional re-construction of this precipitate showed that elements are localized and not evenly distributed, which is significant for the understanding of transport mechanisms because it suggests a multi-phased precipitate even at grain boundaries. This finding may further suggest movement of these elements independent of each other or that, at the time of precipitation during a decrease in temperature, compounds preferentially precipitated.

Although this work did not predominantly focus on fission product mechanistic studies, most of the results and observations contributed toward knowledge on transport mechanisms. From this work, no single mechanism hypothesis can be reported. The complexity of mechanisms is further highlighted by the multiple variations of elemental combinations found in the fission product



precipitates. This may indicate that various transport mechanisms are present, depending on specific irradiation conditions. In addition, it seems that movement of Ag is not assisted by a specific element in all cases due to the fact that various element combinations were identified and that Ag was also found separately from any other fission products as well as uranium. Therefore, it is not necessarily true that a chemical-assisted Ag transport mechanism is dominant.

The presence of Ag predominantly on grain boundaries suggests that the grain boundary transport mechanism may be prominent. With that said, it appears the changing SiC grain boundary distribution from the inner to outer regions for the Variant 1 and Baseline particles (i.e., AGR1-531-038, AGR1-531-031, and AGR1-632-035) has created a SiC layer center region that controls, or, at least, correlates well with the retention of Ag-110m. (Additional analyses of irradiated Variant 1 and Baseline particles with similar irradiation histories are needed to verify a trend and find the correlation in this work). The Variant 3 particles (AGR1-131-066, AGR1-131-099, AGR1-433-001, and AGR1-433-004) do not seem to exhibit a consistent change in the SiC grain boundary distribution from the inner to outer regions, which may be due to the changed SiC layer fabrication conditions compared to those of the other fuel variants.

The TRISO fabrication parameters can potentially be optimized to produce layer grain boundary characteristics that improve fission product retention, if additional studies over a large population of particles could confirm the following observations: (1) a negative correlation between Ag-110m retention and random, high-angle grain boundary fraction, (2) a positive correlation between Ag-110m retention and coincident site lattice-related grain boundary fraction; (3) a positive correlation between Ag-110m retention, twin boundary fraction; and (4) a positive correlation between Ag-110m retention and the low-angle grain boundary fraction. Future TRISO fuels development could potentially engineer the SiC layer microstructure to include features correlated with higher Ag retention.

Neutron damage and its effects on fission product transport were not examined during post-irradiation examination due to prioritization on fission product distribution, chemical composition, and grain boundary characteristics. However, this is a very important microstructural effect that needs to be considered in transport mechanistic studies. The alignment of voids on grain boundaries in the vicinity of Pd-containing precipitates within the SiC grains and at the triple point precipitates on irradiated AGR-1 TRISO-coated Particle AGR1-632-035 shows a potential effect on transport mechanisms. Recently, this was further demonstrated in out-of-pile research. It is recommended that further work be performed on irradiated TRISO particles from the AGR-1 and AGR-2 experiments on this topic.

The evidence provided in this report and associated references show significant new results describing the behavior of TRISO fuel particles during irradiation testing, as well as provide information contributing toward understanding fission product transport mechanisms. Suitable techniques, facilities, and methods were identified and developed during the AGR-1 advanced microscopy and micro-analysis campaign that were necessary to identify fission product chemical compositions and distributions within the TRISO coatings and determine SiC grain boundary characteristics.



# CONTENTS

ACKNOWLEDGEMENTS .....	vi
SUMMARY .....	viii
ACRONYMS .....	xliv
1. INTRODUCTION .....	1
1.1 AGR-1 Experiment Design .....	1
1.2 AGR-1 Experiment Fission Product Release .....	3
1.3 Advanced Microscopy and Micro-Analysis Objectives .....	4
1.4 Selection of AGR-1 Coated Particles for Advanced Microscopy and Micro-Analysis .....	5
1.5 Irradiation Conditions for the Selected AGR-1 Compacts .....	5
2. ADVANCED ELECTRON MICROSCOPY TECHNIQUES .....	6
2.1 Advanced Microscopy and Micro-Analytical Technique Description and Development .....	8
2.1.1 Focused Ion Beam Sample Preparation .....	11
2.1.2 Fission Product Identification and Distribution .....	11
2.1.3 Energy-Filtered Transmission Electron Microscopy and Electron Energy Loss Spectroscopy .....	18
2.1.4 Quantitative Chemical Composition of Fission Product Precipitates using Atom Probe Tomography .....	19
2.2 Techniques to Determine Crystallographic Information .....	20
2.3 Phases and Crystal Structure of Fission Products .....	21
3. ADVANCED CHARACTERIZATION RESULTS ON IRRADIATED COATED PARTICLES .....	22
3.1 Irradiated Baseline Fuel Examination: Compact 6-3-2 .....	22
3.1.1 Particle Selection and Analysis Performed .....	22
3.1.2 Identification, Confirmation, and Quantification of Silver .....	24
3.1.3 Chemical Composition and Distribution of Minor Elements on Particle AGR1-632-035 .....	30
3.1.4 Crystallographic Information Obtained on Particle AGR1-632-035 .....	44
3.1.5 Fission Product Phase Identification Structural Information and Irradiation Effects .....	57
3.1.6 Inter- and Intragranular Identification of Palladium and Uranium .....	59
3.1.7 Summary and Main Findings on Compact 6-3-2 Particles .....	64
3.2 Irradiated Variant 1 Fuel Examination: Compact 5-3-1 .....	65
3.2.1 Particle Selection and Analysis Performed .....	65
3.2.2 Particle AGR1-531-031 .....	68
3.2.3 Particle AGR1-531-038 .....	80
3.2.4 Crystallographic Characteristics of Particle AGR1-531-038 .....	95
3.2.5 Crystallographic Characteristic Comparison and Main Findings on Compact 5-3-1 Particles .....	107
3.3 Irradiated Variant 1 Fuel Examination: Compact 5-2-3 .....	110
3.3.1 Particle Selection and Lamellae .....	110

3.3.2	Microstructural Examination .....	112
3.3.3	Electron Probe Micro-Analysis.....	117
3.3.4	Conclusions and Main Findings.....	127
3.4	Irradiated Variant 3 Fuel Examination: Compact 1-3-1.....	128
3.4.1	Particle Selection and Analysis Performed .....	128
3.4.2	Chemical Composition and Distribution of Fission Products in Precipitates from Particle AGR1-131-066.....	130
3.4.3	Chemical Composition and Distribution of Fission Products in Precipitates from Particle AGR1-131-099.....	163
3.4.4	Crystallographic Information Obtained on Particle AGR1-131-099 .....	178
3.4.5	Precipitate Phase and Structure Evaluation (High-Resolution Transmission Electron Microscopy Performed at Los Alamos National Laboratory) .....	184
3.4.6	Precipitate Chemical Composition Quantification Using Energy-Filtered Transmission Electron Microscopy Performed at Los Alamos National Laboratory .....	190
3.4.7	Summary and Main Findings on Coated Particles from Compact 1-3-1 .....	193
3.5	Irradiated Variant 3 Fuel Examination: Compact 4-1-1.....	196
3.5.1	Particle Selection and Analysis Performed .....	196
3.5.2	Microstructural Examination .....	198
3.5.3	Summary and Main Findings on Compact 4-1-1 Particles .....	205
3.6	Irradiated and Safety-Tested Variant 3 Fuel Examination: Compact 4-3-3.....	206
3.6.1	Particle Selection and Lamellae Locations .....	206
3.6.2	Coated Particle AGR1-433-001 (Low [66%] Ag Retention).....	209
3.6.3	Coated Particle AGR1-433-004 (High [98%] Ag Retention) .....	249
3.6.4	Coated Particles AGR1-433-003 and AGR1-433-007.....	290
4.	DISCUSSION AND CONCLUSIONS OF ADVANCED MICROSCOPY AND MICRO-ANALYTIC EXAMINATION OF AGR-1 COMPACTS.....	298
4.1	Fission Product Identification and Distribution .....	298
4.1.1	Silver Found at Inter- and Intragranular Locations.....	298
4.1.2	Palladium Found at Inter- and Intragranular Locations .....	299
4.1.3	Fission Product Precipitate Composition .....	299
4.2	Fission Product Precipitate Phase and Structure.....	302
4.3	Quantification and Distribution of Fission Products Using Electron Probe Micro- analysis and Atom Probe Tomography .....	303
4.4	Crystallographic Characteristic Discussion.....	304
4.4.1	General Grain Boundary Distributions.....	304
4.4.2	Inner Areas .....	305
4.4.3	Center Areas.....	306
4.4.4	Outer Areas.....	307
4.4.5	Combined Regions .....	308
4.4.6	Conclusions .....	309
4.4.7	Grain Boundary/Fission Product Precipitate Correlations .....	310
4.4.8	Recommendations .....	311
4.5	Fission Product Transport .....	318
4.6	Maturity Level of Techniques and Method Development .....	319
4.7	Publications and Scientific Achievements .....	321

5.	CONCLUSIONS SUMMARY .....	321
6.	REFERENCES .....	323
	Appendix A Leverage of Additional Funding .....	330
	Appendix B AGR-1 Advanced Microscopy and Micro-Analysis Publications and Presentations.....	336
	Appendix C Diffraction Spot Differences .....	344

## FIGURES

Figure 1.	An example of the numbering scheme for AGR-1 compacts demonstrated for Compact 6-3-2. ....	1
Figure 2.	Fraction of retained Ag-110m inventory in 56 of the 72 AGR-1 fuel compacts after irradiation. Data are plotted as a function of vertical position in the experiment (top of the experiment at the left) and by stack number (Demkowicz et al., 2015a).....	4
Figure 3.	Schematic presentation of the electron microscopy and micro-analytical technique envelope explored for the AGR-1 experiment.....	7
Figure 4.	Schematic overview of the crystallographic work done as part of AGR-1 PIE with complimentary projects and other funding sources (stars indicating the most successful results obtained at present). ....	21
Figure 5.	Distribution of the measured-to-calculated Ag-110m activity ratio for the irradiated Compact 6-3-2 particles (adapted from Demkowicz et al., 2012).....	23
Figure 6.	(a) SEM image of the polished cross section of AGR1-632-035, indicating the location of STEM lamellae, extracted by FIB methods, for advanced microstructural characterization. (b) The FIB Lamella Positions 6a and 6b. (c) FIB-prepared TEM samples were taken from the locations indicated for the inner (IE), center (Ctr), and outer (OE) lamellae. The center sample significantly overlaps the inner and outer samples. ....	24
Figure 7.	Image showing the HAADF STEM image of Ag-containing grain boundaries and triple junction at the outmost edge of the SiC adjacent to IPyC (van Rooyen et al., 2014b).....	25
Figure 8.	Image showing (a) the EDS spectrum that identifies the Ag $K\alpha_{\text{Ave}}$ peak at 22.104 keV, the Ag $K\beta_{\text{Ave}}$ at 24.987 keV and the presence of Cd in the center of the triple junction shown in Figure 7, and (b) the EDS linescan profile through the triple junction, indicating the presence of Ag. Although no Pd is observed in the triple junction, Pd and U are identified in the SiC matrix adjacent to this triple junction (Cu is an artifact from the FIB grid holder) (van Rooyen et al., 2014b).....	26
Figure 9.	STEM HAADF image of (a) an unirradiated surrogate TRISO APT sample tip and (b) corresponding reconstructed 3D APT maps of C and Si in a volume size of $48 \times 49 \times 293 \text{ nm}^3$ (Wu et al., 2016). ....	27
Figure 10.	STEM HAADF image of (a) an irradiated TRISO APT sample tip, (b) corresponding reconstructed 3D APT maps showing a Ag-Pd-U-rich phase in a volume size of	

32 × 31 × 12 nm <sup>3</sup> , and (c) mass spectrum showing detected isotopes of Ag, Pd, and U (Wu et al., 2016).....	28
Figure 11. Proxigram with respect to a 3 at.% Pd iso-concentration surface, clearly indicating a Pd (blue), Ag (red), and U (green)-enriched phase. This phase also contains Si (grey), some C (brown), and oxygen (turquoise) is noticed as well (Wu et al., 2016).....	29
Figure 12. 3D elemental map of Pd (blue), Ag (red), and U (green) in a selected small volume of 6 × 6 × 6 nm <sup>3</sup> (Wu et al., 2016). .....	29
Figure 13. Qualitative trend analysis of precipitate composition (Pd, Ag, and U only) as a function of the approximate distance from the SiC-IPyC interface of Particle AGR1-632-035. ....	30
Figure 14. Large field of view STEM dark field image taken from the Lamella fabricated from the inner area (marked “IE” in Figure 6[b]) of the SiC layer from TRISO Particle AGR1-632-035. ....	32
Figure 15. STEM HAADF image combined with EDS labeling to track the chemical composition of fission product precipitates from the inner area of the SiC layer from TRISO Particle AGR1-632-035 within (a) Area 1 and (b) Area 2 highlighted in Figure 14. Note the reported chemical compositions are in Table 10. ....	32
Figure 16. STEM HAADF image combined with EDS labeling to track the chemical composition of fission product precipitates from the inner area of the SiC layer from TRISO Particle AGR1-632-035 within Area 3 highlighted in Figure 14. Note the reported chemical compositions are in Table 11. ....	33
Figure 17. STEM HAADF image combined with EDS labeling to track the chemical composition of fission product precipitates from the inner area of the SiC layer from TRISO Particle AGR1-632-035 within the subtended (a) Area 4 and (b) Area 5 highlighted in Figure 14. Note the reported chemical compositions are in Table 12. ....	34
Figure 18. Large field of view STEM dark field image taken from the center area (the “ctr” Lamella in Figure 6[c]) of the SiC layer from TRISO Particle AGR1-632-035. Area 3 is divided into two sections called 3a and 3b due to the relatively larger area examined. ....	36
Figure 19. STEM HAADF image combined with EDS labeling to track the chemical composition of fission product precipitates from the center area of the SiC layer from TRISO Particle AGR1-632-035 within the subtended Areas (a) 1 and (b) 2 that are highlighted in Figure 18. Note the reported chemical compositions are in Table 13. ....	36
Figure 20. STEM HAADF image combined with EDS labeling to track the chemical composition of fission product precipitates from the center area of the SiC layer from TRISO Particle AGR1-632-035 within the subtended Areas (a) 3a and (b) 3b that are highlighted in Figure 18. Note the reported chemical compositions are in Table 14. ....	37
Figure 21. STEM HAADF image combined with EDS labeling to track the chemical composition of fission product precipitates from the center area of TRISO Particle AGR1-632-035 within subtended Areas (a) 4 and (b) 5 that are highlighted in Figure 18. Note the reported chemical compositions are in Table 15. ....	38
Figure 22. STEM HAADF image combined with EDS labeling to track the chemical composition of fission product precipitates from the center area of the SiC layer from TRISO Particle AGR1-632-035 within the subtended Areas (a) 6 and (b) 7 that are highlighted in Figure 18. Note the reported chemical compositions are in Table 16. ....	39

Figure 23. Large field of view STEM dark field image taken from the outer area of the SiC layer (marked “OE” in Figure 6[c]) from TRISO Particle AGR1-632-035. ....	40
Figure 24. STEM HAADF image combined with EDS labeling to track the chemical composition of fission product precipitates from the outer area of the SiC layer from TRISO Particle AGR1-632-035 within the subtended Areas (a) 1 and (b) 2. Note the reported chemical compositions are in Table 17. ....	40
Figure 25. STEM HAADF image combined with EDS labeling to track the chemical composition of fission product precipitates from the outer area of the SiC layer from TRISO Particle AGR1-632-035 within the subtended Areas (a) 3 and (b) 4 that are highlighted in Figure 23. Note the reported chemical compositions are in Table 18. ....	41
Figure 26. STEM HAADF image combined with EDS labeling to track the chemical composition of fission product precipitates from the outer area of the SiC layer from TRISO Particle AGR1-632-035 within the subtended Areas (a) 5 and (b) 6 that are highlighted in Figure 23. Note the reported chemical compositions are in Table 19. ....	42
Figure 27. STEM HAADF image combined with EDS labeling to track the chemical composition of fission product precipitates from the outer area of the SiC layer from TRISO Particle AGR1-632-035 within the subtended Areas (a) 7 and (b) 8 that are highlighted in Figure 23. Note the reported chemical compositions are in Table 20. ....	43
Figure 28. HAADF images of the (a) inner, (b) center, and (c) outer TEM samples taken from three locations within the SiC layer, indicated in Figure 6(c) from Particle AGR1-632-035, with the specific areas highlighted where fission product precipitates were analyzed. ....	44
Figure 29. Orientation maps of (a) Area A, (b) Area B, (c) Area C, (d) Area D, and (e) Area E in Figure 28(a). ....	45
Figure 30. Distributions of (a) grain boundary misorientation angles, (b) CSL-related grain boundary fractions, and (c) grain boundary types in each area analyzed on the inner Lamella (Figure 28[a]) and average distribution with the accompanying error bars determined using standard error. ....	46
Figure 31. Distributions averaged over all areas analyzed for each Lamella of (a) grain boundary misorientation angles, (b) CSL-related grain boundary fractions, and (c) grain boundary types with the accompanying error bars determined using standard error. ....	47
Figure 32. Example area (center sample, Area B of Figure 28[b]) showing precipitates on the grain boundaries that were analyzed for composition and grain boundary character. (a) TEM image, (b) STEM image using the HAADF, and (c) the corresponding orientation image. The arrow in each image denotes the same reference point. ....	50
Figure 33. Summary of the grain boundary types associated with fission products. ....	51
Figure 34. Composition distribution of the grain boundary precipitates from the combined results on the inner, center and outer regions. ....	54
Figure 35. Distribution of the fission product precipitates on the various boundary types as a percentage, generated by combining the results from the inner, center, and outer samples. ....	55
Figure 36. Distributions of fission product precipitates, as a percentage, by grain boundary type for Pd only, Ag only, Pd+Ag, and Pd+ U. ....	56

Figure 37. TEM micrographs of Particle AGR1-632-034. TEM sample 2a shown in (a) a micron-sized Pd-U-Si precipitate in the SiC layer, with (b) a higher magnification image of the grain boundary marked with an orange circle in image (a).The spherical-shaped gas bubbles concentrated alongside grain boundaries near the Pd-rich precipitate (image [b] is adapted from van Rooyen et al., 2012c, van Rooyen et al., 2013).....	58
Figure 38. STEM HAADF images showing nanometer-sized Pd precipitates (about 10 to 20-nm diameter) inside SiC grains (a) at the SiC-IPyC interface and (b) approximately 4 $\mu\text{m}$ inside the SiC layer (images adapted from van Rooyen, Wu, and Lillo 2014b). ....	59
Figure 39. Examples of intragranular precipitates – (a) round and (c) rod-like, showing only significant amounts of Pd – (b) and (d), respectively. ....	60
Figure 40. STEM images of (a) fission-product distribution networks at the SiC-IPyC interlayer of Particle AGR1-632-035, (b) higher-magnification image showing intragranular precipitates labeled P1 and P2 and the triple points T1 through T3, which all contain mainly Pd, (c) higher magnification of the Pd-rich nodules, and (d) a honeycomb network of mainly U (adapted from Leng et al., 2016). ....	60
Figure 41. Summary of the distribution of elements in fission product precipitates found on SiC grain boundaries in AGR1-632-035. ....	61
Figure 42. Examples of triple junctions containing (a) only Pd, (b) Pd and U, (c) Pd and Ag, and (d) Ag.....	63
Figure 43. Summary of the distribution of the fission product elements and uranium in triple junctions in the SiC layer of Particle AGR1-632-035. ....	64
Figure 44. Distribution of the measured-to-calculated Ag-110m activity ratio for the irradiated Compact 5-3-1 particles (adapted from Demkowicz et al., 2016a). The M/C values for particles AGR1-531-059 and 038 are based on the minimum detectable activity for Ag-110m in the gamma spectra, because no Ag-110m was detected.....	66
Figure 45. Polished metallographic cross sections through TRISO particles (a) AGR1-531-038 and (b) AGR1-531-031 (Demkowicz 2016a). ....	67
Figure 46. (a) Locations of the TEM samples extracted from Particle AGR1-531-031, (b) larger magnification of the SiC layer with the lamellae locations schematically presented, and (c) (d) their locations on the SiC layer at higher magnification ([d] shows the locations of Lamellae 1 through 3 after FIB extraction).....	67
Figure 47. (a) Locations of the TEM samples extracted from Particle AGR1-531-038, (b) larger magnification SEM image showing the area of where the TEM samples will be fabricated from, and (c) their locations after FIB extraction. ....	68
Figure 48. Qualitative trend analysis of precipitate composition (Pd, Ag, and U only) as a function of the approximate distance from the SiC-IPyC interface of Particle AGR1-531-031. ....	69
Figure 49. Qualitative trend analysis of precipitate composition for U as a function of the approximate distance from the SiC-IPyC interface of Particle AGR1-531-031.....	70
Figure 50. Low magnification HAADF images of the TEM samples of the SiC layer in AGR1-531-031 showing no precipitates except very near the IPyC/SiC interface. (a) Inner area (Lamella 1), (b) inner area (Lamella 1b), (c) outer area (Lamella 2), (d) center (Lamella 3), and (e) inner area (Lamella 4). ....	71



Figure 51. STEM HAADF image combined with EDS labeling to track the chemical composition of fission product precipitates from the inner area of TRISO Particle AGR1-531-031 within the subtended areas (a) 1, (b) 2, (c) 3, (d) 4, and (e) 5 of Lamella 1 highlighted in Figure 50(a). Note the reported chemical compositions are in Table 28.....	72
Figure 52. (a) STEM HAADF image combined with EDS labeling to track the chemical composition of fission product precipitates from the inner area (Lamella 1b, Area 1), and (b) STEM HAADF image combined with EDS labeling to track the chemical composition of fission product precipitates from the inner area (Lamella 4, Area 1) of TRISO Particle AGR1-531-031 highlighted in Figure 50. Note the reported chemical compositions are in Table 29.....	73
Figure 53. Orientation maps of randomly selected areas (a) 1 and (b) 2 generated from PED data.....	75
Figure 54. Distributions of (a) grain boundary misorientation angles, (b) value of CSL-related grain boundaries, and (c) grain boundary types for two randomly selected areas on the inner Lamella (Figure 50[a]) and averaged distributions with accompanying standard error bars.....	76
Figure 55. Distributions averaged over all areas analyzed for each sample: (a) misorientation angle, (b) CSL designation, and (c) grain boundary type for the SiC grain boundaries of samples taken from AGR1-531-031.....	78
Figure 56. Low magnification overviews of (a) Lamella 2 (AGR1-531-031-2) showing a lack of fission product precipitates. Pores in the SiC appear as dark features. (b) Lamella 3 (AGR1-531-031-3) showing a lack of fission product precipitates. Pores in the SiC appear as dark features.....	79
Figure 57. Qualitative trend analysis of precipitate composition (Pd, Ag, and U only) as a function of the approximate distance into the SiC layer from the SiC-IPyC interface of Particle AGR1-531-038.....	81
Figure 58. Qualitative trend analysis of the average Ag content found in precipitates as a function of the approximate distance into the SiC layer from the SiC-IPyC interface of Particle AGR1-531-038.....	82
Figure 59. Large field of view STEM dark field image taken from the (a) inner area (Lamella 1) of TRISO Particle AGR1-531-038. (b) Large field of view STEM dark field image taken from the center area (Lamella 2) of TRISO Particle AGR1-531-038 taken within the SiC layer. (c) Large field of view STEM dark field image taken from the outer area (Lamella 3) of TRISO Particle AGR1-531-038 (lamellae locations are indicated in Figure 47). .....	82
Figure 60. STEM HAADF image combined with EDS labeling to track the chemical composition of fission product precipitates from the inner area of TRISO Particle AGR1-531-038 within the subtended Area 1 from Figure 59(a). Note the reported chemical compositions are in Table 33.....	83
Figure 61. STEM HAADF image combined with EDS labeling to track chemical composition of fission product precipitates from the inner area of TRISO Particle AGR1-531-038 within the subtended Area 2 from Figure 59(a), (a) low, (b) medium, and (c) higher magnification of the intragranular Pd-Cs, spherical precipitate (Number 4). Note the reported chemical compositions are in Table 34. ....	84
Figure 62. STEM HAADF image combined with EDS labeling to track the chemical composition of fission product precipitates from the inner area of TRISO Particle AGR1-531-038	

within the subtended Area 3 that is highlighted in Figure 59(a). Note the reported chemical compositions are in Table 35.....	85
Figure 63. STEM HAADF image combined with EDS labeling to track the chemical composition of fission product precipitates from the inner area of TRISO Particle AGR1-531-038 within the subtended Area 4 from Figure 59(a). Note the reported chemical compositions are in Table 36.....	86
Figure 64. STEM HAADF image combined with EDS labeling to track the chemical composition of fission product precipitates from the inner area of TRISO Particle AGR1-531-038 within the subtended Area 5 from Figure 59(a). Note the reported chemical compositions are in Table 37.....	86
Figure 65. STEM HAADF image combined with EDS labeling to track the chemical composition of fission product precipitates from the center area of TRISO Particle AGR1-531-038 within two sub-areas, referred to as Area 1a and Area 1b of Area 1 from Figure 59(b). Note the reported chemical compositions are in Table 38.....	87
Figure 66. STEM HAADF image combined with EDS labeling to track the chemical composition of fission product precipitates from the center area of TRISO Particle AGR1-531-038 within the subtended Area 2 from Figure 59(b). Note the reported chemical compositions are in Table 39.....	88
Figure 67. STEM HAADF image combined with EDS labeling to track the chemical composition of fission product precipitates from the center area of TRISO Particle AGR1-531-038 within two sub-areas, referred to as Area 3a and Area 3b, of Area 3 within Figure 59(b). Note the reported chemical compositions are in Table 40.....	89
Figure 68. STEM HAADF image combined with EDS labeling to track the chemical composition of fission product precipitates from the center area of TRISO Particle AGR1-531-038 within the subtended Area 4 from Figure 59(b). Note the reported chemical compositions are in Table 41.....	90
Figure 69. STEM HAADF image combined with EDS labeling to track the chemical composition of fission product precipitates from the center area of TRISO Particle AGR1-531-038 within the subtended Area 5 from Figure 59(b). Note the reported chemical compositions are in Table 42.....	91
Figure 70. STEM HAADF image combined with EDS labeling to track the chemical composition of fission product precipitates from the center area of TRISO Particle AGR1-531-038 within the subtended Area 6 from Figure 59(b). Note the reported chemical compositions are in Table 43.....	92
Figure 71. STEM HAADF image combined with EDS labeling to track the chemical composition of fission product precipitates from the outer area of TRISO Particle AGR1-531-038 within the subtended Areas (a) 1 and (b) 2 from Figure 59(c). Note the reported chemical compositions are in Table 44.....	93
Figure 72. STEM HAADF image combined with EDS labeling to track the chemical composition of fission product precipitates from the outer area of TRISO Particle AGR1-531-038 within the subtended Area 3 highlighted in Figure 59(c). Note the reported chemical compositions are in Table 45.....	94
Figure 73. STEM HAADF image combined with EDS labeling to track the chemical composition of fission product precipitates from the outer area of TRISO Particle AGR1-531-038 within the subtended Areas (a) 4 and (b) 5 highlighted in Figure 59(c). Note the reported chemical compositions are in Table 46. ....	94

Figure 74. Orientation maps of (a) Area 1, (b) Area 2, (c) Area 3, (d) Area 4, and (e) Area 5 in Lamella 1 (from Figure 59[a]).	96
Figure 75. Distributions of (a) grain boundary misorientation angles, (b) value of CSL-related grain boundaries, and (c) grain boundary types in each area analyzed on the inner Lamella (Lamella 1, Figure 47[c] and Figure 59[a]), as well as the averaged distributions with the accompanying standard error bars.	97
Figure 76. Distributions averaged over all areas analyzed for each sample: (a) misorientation angle, (b) CSL designation, and (c) grain boundary type for the SiC grain boundaries of samples taken from AGR1-531-038.	100
Figure 77. Comparison of the distribution of grain boundary types that contained any fission product precipitates.	105
Figure 78. Composition distribution of the grain boundary precipitates.	106
Figure 79. Distribution of fission product precipitates on various boundary types as a percentage.	106
Figure 80. Distributions of fission product elements, as a percentage, by grain boundary type.	107
Figure 81. Comparison of the (a) misorientation angle distributions, (b) CSL boundary distributions, and (c) grain boundary-type distributions between AGR1-531-031 and AGR1-531-038.	109
Figure 82. X-ray tomographs and a reference optical micrograph of TRISO Particle AGR1-523-SP01: (a) near-mid plane showing indication of a localized defect through SiC layer thickness; (b) close-up view of the SiC layer defect in (a), indicating that fission product build-up at the IPyC-SiC interface and that the SiC defect traverses the whole SiC layer; (c) optical micrograph of particle cross section produced by metallographic preparation of the particle from the plane orthogonal to that shown in (a); (d) matching tomographic slice to that shown in (c), showing correlation of layer construction with that of the analyzed particle cross-section; (e) plane approximately 25 $\mu\text{m}$ above (d) in the same orientation; and (f) plane approximately 25 $\mu\text{m}$ below (d) in the same orientation. The progression of images from (e) to (d) to (f) show the nature of crack termination at the IPyC-SiC interface and indicate that the SiC defect/degradation is localized to one location along the exposed SiC surface that is greater than 50 $\mu\text{m}$ (Wen et al., 2016).	111
Figure 83. SEM images of the cross section of the studied AGR1-523-SP01 TRISO-coated particle. (a), (b) and (d) are secondary electron images and (c) is a back-scattered electron image. In (a), (b), and (c), the numbers indicate the locations where TEM lamellae were sectioned. The bright spots/areas in (c) are fission product precipitates.	112
Figure 84. Low-magnification STEM images of TEM Lamellae 4 (a), 5 (b), 6 (c), 7 (d), 8 (e), and 9 (f), showing the general distribution of fission products.	113
Figure 85. STEM image showing aligned nano voids (dark) and Pd nano precipitates (light features) in a SiC grain of Lamella 10.	114
Figure 86. An Ag-Pd-Cd precipitate at stacking fault inside a SiC grain from Lamella 10. (a) and (b) STEM images show the location of the Ag-Pd-Cd precipitate, whose composition was determined by EDS; (c) TEM image corresponding to (b); (d) a magnification of the red rectangle in (c); (e) a magnification of the red rectangle in (d) where the Ag-Pd-Cd precipitate is located; (f) a magnification of the red rectangle in (d) where stacking faults are present; (g) inverse fast Fourier transform of the white square in (f),	

where the continuous lattice fringes indicate absence of grain boundary and confirm the presence of stacking faults.....	114
Figure 87. Selected area electron diffraction on precipitates from Lamella 10 from Particle AGR1-523-SP01. (a) A low-magnification TEM image; (b) a magnification of the red rectangle in (a), with diffraction performed on the blue circle and the corresponding diffraction pattern presented in the inset; (c) a magnification of the green rectangle in (a), with diffraction performed on the blue circle and the corresponding diffraction pattern presented in the inset; (d) TEM image of another precipitate, with diffraction performed on the blue, white, and red circles and the corresponding diffraction patterns presented in (d1), (d2), and (d3), respectively. Precipitate in (b) and (d) are Pd-U with small Ce concentrations and precipitate in (c) is Pd-Si, as determined by EDS in STEM. From the diffraction patterns, precipitate in (b) is amorphous, and precipitate in (c) is semi-crystalline; for the precipitate in (d), the lower-left part is amorphous, whereas the upper-right part is semi-crystalline. ....	115
Figure 88. Backscattered electron image of the TRISO particle showing the path of the radial traverse measurement. ....	117
Figure 89. Elemental concentrations along the radial traverse for U, Si, Cs, Ba, Xe, I, Sr, and Te. ....	118
Figure 90. Elemental concentrations along the radial traverse for La, Ce, Pr, Nd, Eu, and Sm. ....	119
Figure 91. Elemental concentrations along the radial traverse for Pd, Ag, Cd, Sn, Ru, Mo, and Zr. ....	120
Figure 92. Backscattered electron image of irradiated TRISO particle (a) and quantitative X-ray maps of U, Pu, O, Ru, C, Mo, Si, and Zr (b–i). Recoil zone is shown with the white arrow in (b). ....	121
Figure 93. Quantitative X-ray maps of Cs, La, Ba, Ce, Xe, Nd, Sr, Pd, Te, and Ag (j–s).....	122
Figure 94. Shows a backscattered electron image of the kernel (a) and X-ray maps of Ru, Mo, and Zr (b-d) in the area outlined by the red square. ....	123
Figure 95. Backscattered electron image of precipitates in the IPyC crack (a) and X-ray maps of (b) Pd, (c) Cd, (d) Sn, and (e) Ag. X-ray maps were corrected for peak overlaps. ....	124
Figure 96. Locations of analyzed precipitates in the crack in the IPyC (a) and between the IPyC and SiC layer (b). Analyses are shown in Table 52.....	125
Figure 97. Distribution of the measured-to-calculated Ag-110m activity ratio for the irradiated Compact 1-3-1 particles (Demkowicz et al., 2016b). ....	129
Figure 98. Figure showing (a) cross section from Particle AGR1-131-066 with (b) the corresponding SiC layer FIB lamellae (4 to 7) and fuel kernel FIB lamellae (1 to 3) for AGR1-131-066. ....	130
Figure 99. Figure showing (a) cross section from Particle AGR1-131-099 with (b) the corresponding SiC layer FIB- lamellae (1 to 5).....	130
Figure 100. Images of (a) Lamella 4 (b) Lamella 5, (c) Lamella 6, and (d) Lamella 7, where microstructural analyses were carried out on the SiC layer of AGR1-131-066. ....	131
Figure 101. (a)(b) STEM images and (c) TEM image of TEM Lamella 4, showing a relatively low number density of precipitates at the IPyC-SiC interface. Precipitates are relatively small. Porosity is present at the IPyC-SiC interface. ....	132
Figure 102. STEM images of precipitates in the SiC layer very close to the IPyC-SiC interface (Areas 1 and 2 on Lamella 4 [shown in Figure 98 and Figure 100]), where precipitates	

indicated by arrows or circles were subjected to EDS composition analyses. Chemical composition is reported in Table 54. ....	133
Figure 103. STEM images of (a) precipitates in the IPyC layer close to the IPyC-SiC interface (Area 3 on Lamella 4 [shown in Figure 98 and Figure 100]), (b) where precipitates indicated by arrows or circles, and (c–d) larger magnification images of precipitate numbers 6 through 8 were subjected to EDS composition analyses. Majority of precipitates are Pd-Si-U, with a small fraction of Pd-Si. Chemical composition is reported in Table 55.....	134
Figure 104. STEM images of precipitates in the IPyC layer away from the IPyC-SiC interface (a) (Area 4, Lamella 4), where precipitates indicated by arrows or circles were subjected to EDS composition analyses (b) with larger magnification images of precipitate Number 4 to 6 (c and d). Precipitates are small with a low number density. Chemical composition is reported in Table 56. ....	135
Figure 105. STEM images of precipitates in the SiC layer within about 2 $\mu\text{m}$ from the IPyC-SiC interface (Area 1, Lamella 5), where precipitates indicated by arrows or circles were subjected to EDS composition analyses. Chemical composition is reported in Table 57. Most precipitates within about 300 nm from the IPyC-SiC interface (Precipitates 1, 2, 3, and 5) contain U. ....	136
Figure 106. STEM images of precipitates in the SiC layer about 6 to 7 $\mu\text{m}$ from the IPyC-SiC interface (Area 2, Lamella 5), where precipitates indicated by arrows or circles were subjected to EDS composition analyses. Chemical composition of precipitates is reported in Table 58.....	138
Figure 107. STEM images of precipitates in the SiC layer about 9 to 10 $\mu\text{m}$ from the IPyC-SiC interface (Area 3, Lamella 5), where precipitates indicated by arrows or circles were subjected to EDS composition analyses. Chemical composition is reported in Table 59. ....	139
Figure 108. STEM images of (a) Area 1 of AGR1-131-066 Lamella 6 (Figure 100), where precipitates indicated by arrows (b through f) were subjected to EDS composition analyses. Qualitative chemical composition is reported in Table 60.....	141
Figure 109. STEM images of Area 2 of AGR1-131-066 Lamella 6 (Figure 100), where precipitates indicated by arrows were subjected to EDS. Composition analyses are reported in Table 61.....	143
Figure 110. STEM images of Area 3 of AGR1-131-066 Lamella 6 (Figure 100), where precipitates are indicated by arrows, were subjected to EDS composition analyses. Chemical composition of precipitates is reported in Table 62. ....	145
Figure 111. (a) STEM HAADF image combined with EDS labeling to track the chemical composition of fission product precipitates from the outer area (Lamella 7, Area 1 shown previously in Figure 100) of TRISO Particle AGR1-131-066. Within Area 1, five subtended areas (b) 1a, (c) 1b, (d) 1c, (e) 1d, and (f) 1e were studied with point-resolved EDS. Note the reported chemical compositions are in Table 63. ....	147
Figure 112. (a) STEM HAADF image combined with EDS labeling to track the chemical composition of fission product precipitates from the outer area (Lamella 7) of TRISO Particle AGR1-131-066 within subtended Area 2 (see Figure 100). Within Area 2, two subtended Areas (b) 2a and (c) 2c were studied with point-resolved EDS. Note the reported chemical compositions are in Table 64. ....	149
Figure 113. STEM HAADF image combined with EDS labeling to track the chemical composition of fission product precipitates from the outer area (Lamella 7) of TRISO	

Particle AGR1-131-066 within subtended Area 3 (see Figure 100). Note the reported chemical compositions are in Table 65.....	150
Figure 114. SiC grain orientation maps from the areas analyzed in Figure 100[b]: (a) Area 1, (b) Area 2, and (c) Area 3.....	152
Figure 115. Distributions of the (a) grain boundary misorientation angle, (b) CSL distribution, and (c) grain boundary type for the areas in Lamella 5. The average distribution for Lamella 5 is included and consists of all data from the three areas.....	153
Figure 116. Distributions averaged over all areas analyzed for each sample, (a) misorientation angle, (b) CSL designation, and (c) grain boundary type for the SiC grain boundaries for samples taken from AGR1-131-066. ....	155
Figure 117. Comparison of the distribution of grain boundary types that contained any fission product precipitates.....	156
Figure 118. Composition distribution of the grain boundary precipitates in Particle AGR1-131-066. ....	158
Figure 119. Distribution of fission product precipitates on the various grain boundary types in Particle AGR1-131-066.....	158
Figure 120. Distributions of fission product elements by grain boundary type for Particle AGR1-131-066. ....	159
Figure 121. Images showing (a) the location of Lamella 2 of Particle AGR1-131-066 (Figure 98) examined in this study; with higher magnification and STEM Z-contrast images (b) and (c) showing where further STEM examination of the irradiation effects and EDS chemical composition were obtained.....	160
Figure 122. STEM Z contrast image of the fuel kernel from Particle AGR1-131-066 Lamella 2, showing the overall structure after neutron irradiation. Two phases are identified in the uranium-containing material in a core shell type of arrangement. The outer or shell material is U-rich, contains some Zr, Mo, and Ru, and is nearly metallic in nature. The core material is a U-(O,C) of approximate composition of 1:2. ....	161
Figure 123. STEM BF image and EDS spectral images from the indicated region (Figure 121[c]) of the fuel kernel from Particle AGR1-131-066 Lamella 2.....	162
Figure 124. HRTEM images of some U (Zr, Mo, Ru)(C, O) nanoparticles found within the map region of the fuel kernel from Particle AGR1-131-066 Lamella 2 described above in Figure 123.....	162
Figure 125. Images of the TEM Lamella from Particle AGR1-131-099 showing (a) SEM image showing the Lamella locations in the SiC layer (b) Lamella 4 with PED areas marked (EDS analysis completed on precipitates located in Area 2), (c) Lamella 2 with PED areas marked (EDS locations indicated in Section 3.4.3.1.3), (d) Lamella 1 with EDS precipitate analysis areas marked, (e) Lamella 3 with EDS precipitate analysis areas marked, and (f) Lamella 5 with EDS precipitate analysis areas marked. ....	163
Figure 126. (a) (b) STEM images and (c) TEM image of AGR1-131-099 Lamella 1 that was sectioned from the IPyC-SiC interface (Lamella is parallel to the interface).....	164
Figure 127. STEM images of precipitates in Lamella 1 (at the IPyC-SiC interface), where precipitates indicated by arrows were subjected to EDS point scan. The qualitative compositions corresponding to the EDS point scans are displayed in Table 69. The	

majority of the precipitates are Pd-U or Pd-Si-U, with a small fraction of U and U-Si. All precipitates contain U. ....	165
Figure 128. (a) (b) (c) STEM images of TEM Lamella 5 (across the IPyC-SiC interface), showing the whole sample (a), the IPyC layer (b), and the IPyC-SiC interface (c), and (d) TEM image of an area close to the IPyC-SiC interface. ....	167
Figure 129. Images (a) through (f) are STEM images of precipitates in TEM Lamella 5 (across the IPyC-SiC interface), where precipitates indicated by arrows and numbers were subjected to an EDS point scan. The qualitative compositions corresponding to the EDS point scans are displayed in Table 70. Images (a), (c), and (e) are of low-magnification and show the locations of the investigated precipitates relative to the IPyC-SiC interface, and (b), (d), and (f) are higher magnification images showing the exact precipitates on which EDS point scans were performed. Precipitates 1 through 6 are in the SiC layer and Precipitates 7 through 12 are in the IPyC layer. The majority of the precipitates in the SiC layer are Pd-Si-U, Pd-U, or U, with a small fraction of Pd-Si and Pd (not shown in the figure). Precipitates in the IPyC layer are Pd-Si-U, Pd-Si, U-Si, or U. ....	168
Figure 130. (a) and (b) STEM images of TEM Lamella 2 (from the inner region of the SiC layer), with different magnifications, showing the whole sample (a) and part of the sample (b). (c) TEM image of a selected area. ....	170
Figure 131. STEM images of precipitates in TEM Lamella 2 (from the inner region of the SiC layer), where precipitates indicated by arrows and numbers were subjected to EDS point scan. The quantified compositions corresponding to the EDS point scans are displayed in Table 71. Precipitates are Pd-Si-U, Pd-Si, Pd-U, Pd, U, or U-Si. ....	171
Figure 132. (a) (b) STEM images and (c) TEM image of AGR1-131-099 Lamella 4 that was sectioned from the middle region of the SiC layer. ....	173
Figure 133. STEM images of precipitates in TEM Lamella 4 (in the middle region of the SiC layer), where precipitates indicated by arrows were subjected to EDS composition analyses. The quantified compositions correspond to the EDS point scans are displayed in Table 72. Precipitates are Pd or Pd-U. A small fraction of Pd-Si-U precipitates is also present in the TEM lamella, but is not shown in this figure. ....	174
Figure 134. (a) STEM image of TEM Lamella 3 (from the outer region of the SiC layer) and showing the whole sample; (b) TEM image of a selected area. ....	176
Figure 135. STEM images of precipitates in TEM Lamella 3 (from the outer region of the SiC layer), where precipitates indicated by arrows and numbers were subjected to EDS point scan. The quantified compositions corresponding to the EDS point scans are displayed in Table 73. Precipitates are Pd-Si-U or Pd-Si. A small fraction of Pd precipitates is also present in the TEM lamella, but is not shown in this figure. ....	177
Figure 136. SiC grain orientation maps for (a) Area 1, (b) Area 2, (c) Area 3, and (d) Area 4 from Lamella 4 (center), Figure 125(b), of AGR1-131-099. ....	178
Figure 137. Distributions of the (a) grain boundary misorientation angle, (b) CSL distribution, and (c) grain boundary type for the areas in Lamella 4. The averaged distributions for Lamella 4 are included and are a combination of all data from all four areas. ....	179
Figure 138. Distributions averaged over all areas analyzed for each sample: (a) misorientation angle, (b) CSL designation, and (c) grain boundary type for the SiC grain boundaries for samples taken from AGR1-131-099. ....	181

Figure 139. Distribution of grain boundary types that contained any fission product precipitate for Lamella 4 (center) AGR1-131-099, Figure 125(b).....	182
Figure 140. Composition distribution of the grain boundary precipitates for Lamella 4 (center) AGR1-131-099, Figure 125(b). ....	182
Figure 141. Distribution of fission product elements, as a percentage, by grain boundary type AGR1-131-099. ....	183
Figure 142. A precipitate at the SiC grain boundary. ....	184
Figure 143. Interface between the precipitate in Figure 142 and the SiC matrix. (a) HRTEM showing the interface between the precipitate and the SiC matrix (a magnification of the white square in Figure 142); (b) FFT of the black square area in (a); (c) inverse FFT of (b); (d) FFT of the white square area in (a); and (e) inverse FFT of (d). ....	185
Figure 144. (a) HRTEM image of the precipitate in Figure 142 (a magnification of the red square in Figure 142); (b)(c)(d)(e) FFT of the areas 1, 2, 3, and 4 in (a), respectively. From (b) through (d), the top part of the precipitate has a slight misorientation (within a few degrees) with the bottom part of the precipitate; however, the crystal structure is identical. The small misorientation may be due to a difference in dislocation density between the top and bottom parts of the precipitate. ....	186
Figure 145. HRSTEM image and EDS mapping of a small area containing precipitates in the IPyC layer of Particle AGR1-131-099 close to the IPyC-SiC interface. Maximum and minimum concentration values for the elements with the maps are listed. The EDS spectra are extracted from the spectral maps. ....	187
Figure 146. HRSTEM image and EDS mapping of a small area containing precipitates in the IPyC layer of Particle AGR1-131-099) close to the IPyC-SiC interface.....	188
Figure 147. HRSTEM image and EDS mapping of an area containing precipitates in the SiC layer of Particle AGR1-131-099 close to the IPyC-SiC interface. ....	188
Figure 148. HRTEM images of the interface between a particle and the SiC matrix of Particle AGR1-131-099 Lamella 1. ....	189
Figure 149. HRTEM image of a grain boundary phase in the SiC layer. The inset is a FFT of the area outlined by the box. Indicated lattice spacings are also shown and are consistent with Pd <sub>2</sub> Si, although it is not confirmed by chemical analysis.....	189
Figure 150. HRTEM image of a precipitate along the grain boundary between SiC grains. The bands rising from the mass contrast suggest a more complex structure to this precipitate. ....	190
Figure 151. EFTEM images take at (left) zero loss and at an energy loss of 71 eV (right). A layered structure nestled between SiC grains is suggested by the zero-loss image and the different sets of Moire fringes shown in the 71-eV loss image. ....	191
Figure 152. EFTEM maps derived from the jump ratio method to show the relative distributions of (a) Pd, (b) Ag, and (c) U in the particle. The EFTEM image in (d) shows some of the damage to the area from the imaging process, which is primarily occurring in the nearby SiC matrix. ....	192
Figure 153. Atomic resolution image of the edge of the precipitate (right) and a corresponding diffractogram (left) from a precipitate in Particle AGR1-131-099.....	193



Figure 154. Comparison of the (a) misorientation angle distributions; (b) CSL boundary distributions, and (c) grain boundary-type distributions between AGR1-131-066 and AGR1-131-099. ....	194
Figure 155. Comparison of (a) the fission product element distribution and (b) the distribution of fission product precipitates as a function of grain boundary type for AGR1-131-066 and AGR1-131-099. ....	195
Figure 156. Summary of precipitate compositions in different TEM lamellae from AGR1-131-099. ....	196
Figure 157. Distribution of measured-to-calculated Ag-110m activity ratios, normalized by the Cs-137 activity to account for variations in fissile content and burnup (Demkowicz et al 2016c). ....	197
Figure 158. SEM image showing the AGR1-411-030 FIB SEM lamellae sectioned at Positions 1b, 1c, and 2 as indicated on the cross section of the coated particle. ....	198
Figure 159. Localized areas at the IPyC-SiC interface showing intact interfaces at (a) Lamella 1a; (b) Lamella 1b; and (c) slight localized indications of debonding observed at the IPyC-SiC interface at Lamella 2 as shown by the red arrows. Indications of debonding were not observed previously on specimens from Compact 6-3-2. ....	199
Figure 160. Image showing the presence and morphology of Cs in the buffer layer of the AGR1-411-030 particle (FIB Position 3 in Figure 159). ....	199
Figure 161. HAADF STEM images showing (a) accumulation of Pd at the IPyC-SiC interface, (b) no significant corrosion except for a few approximate 1-nm diameter corrosion pits only visible at this magnification, and (c) and (d) the presence of Pd in two spectra of associated areas in (a). ....	200
Figure 162. BF (a) and dark field (b) STEM images of fission product networks at grain boundaries and triple points of specimen AGR-411-030 Position 1b. (c) High-resolution BF STEM image Pd-Ag-Cd accumulations co-existing at Location 1 at a SiC grain boundary of specimen AGR1-411-030 Position 1b. Only Pd was found at Locations 2 and 3. (Adapted from van Rooyen et al., 2014a). ....	201
Figure 163. EDS spectra showing (a) co-existence of Pd, Ag, and Cd at Location 1 of specimen AGR1-411-030 Position 1b. The peaks for Ag and Cd passed the 2-sigma test as determined by the Oxford software. Therefore, the peaks are deemed to be statistically relevant and show that only Pd was found at Locations 2 and 3 (shown in [b] and [c]). ....	202
Figure 164. BF STEM image (a) of a Pd-Ag-Cd containing triple point with the corresponding high-resolution BF STEM image (b). ....	203
Figure 165. BF STEM image in (a) showing the position of the Pd accumulation at a stacking fault in a SiC grain with a high-resolution BF STEM image in (b) with the corresponding EDS spectrum in (c). ....	203
Figure 166. Selected HRSTEM image showing the six locations where EDS analysis was completed using the new higher-resolution EDS detector. ....	204
Figure 167. HRSTEM-EDS spectra at points 1(a) and 5(b) showing the presence of P (as indicated by the arrow) at the grain boundary but not in the SiC grain, respectively. ....	204
Figure 168. Selected HRSTEM image (a) showing the four locations where EDS analysis was completed using the new higher-resolution EDS detector. HRSTEM-EDS spectra at	

Points 1(b) and 2(c) showing the presence of P (as indicated by the arrow) at the grain boundary triple points. ....	205
Figure 169. Distribution of the measured-to-calculated Ag-110m activity ratio for the irradiated Compact 4-3-3 particles (Demkowicz et al., 2016d). ....	206
Figure 170. Optical microscope image of AGR1-433-003 (left) and AGR1-433-007 (right). Paths of radial traverses EPMA elemental composition measurements are shown with white lines. The arrow in the left image highlights kernel extrusion (deformation) into a fractured region of the buffer layer. ....	207
Figure 171. Images from Particle AGR1-433-001 showing the (a) cross section of the particle, (b) all FIB preparation locations labeled 1 through 10, (c) actual locations marked on the SiC layer ready for FIB lamellae preparation on the areas used for HRTEM, and (d) through (f) actual Lamellae 5 to 7, respectively, used for HRTEM examination. ....	208
Figure 172. Images from Particle AGR1-433-004 showing (a) the cross section of the particle, (b) all FIB preparation locations labeled 1 through 7, (c) actual FIB locations ready for lift-out of the lamellae, and (d) through (f) actual Lamellae 4 to 7, respectively, used for HRTEM examination. ....	208
Figure 173. Qualitative trend analysis of precipitate composition (Pd, Ag, and U only) as a function of the approximate distance from the SiC-IPyC interface of Particle AGR1-433-001 with (a) a plot of the individual concentrations and averages, and (b) only the average concentration trend analysis for better clarity. ....	210
Figure 174. Qualitative trend analysis of precipitate composition for U as a function of the approximate distance from the SiC-IPyC interface of Particle AGR1-433-001. ....	211
Figure 175. Large field of view STEM dark field image taken from the inner area (Lamella 4, Figure 171[b]) of TRISO Particle AGR1-433-001 at the IPyC/SiC interface showing three analysis areas (labeled 1 to 3) in the SiC layer. ....	212
Figure 176. STEM HAADF image combined with EDS labeling to track the chemical composition of fission product precipitates from the inner area (Lamella 4) of TRISO Particle AGR1-433-001 within the subtended Area 1, which was subdivided into two Areas (a) 1a and (b) 1b. Note the reported chemical compositions are in Table 80. ....	213
Figure 177. STEM HAADF image combined with EDS labeling to track the chemical composition of fission product precipitates from the inner area (Lamella 4) of TRISO Particle AGR1-433-001 within the subtended Areas (a) 2 and (b) 3. Note the reported chemical compositions are in Table 81. ....	213
Figure 178. Large field of view STEM dark field image taken from the inner area of TRISO Particle AGR1-433-001 (Lamella 5) showing three areas (labeled 1 to 3) in the SiC layer. ....	214
Figure 179. STEM HAADF image combined with EDS labeling to track the chemical composition of fission product precipitates from the inner area (Lamella 5 in Figure 178) of TRISO Particle AGR1-433-001 within subtended area 1. Note the reported chemical compositions are in Table 82. ....	215
Figure 180. (a) STEM HAADF image combined with EDS labeling to track the chemical composition of fission product precipitates from the inner area (Lamella 5) of TRISO Particle AGR1-433-001 within subtended Area 2. Note the reported chemical compositions are in Table 82. (b) STEM HAADF image combined with EDS labeling to track the chemical composition of fission product precipitates from the inner area	

(Lamella 5) of TRISO Particle AGR1-433-001 within subtended Area 3. Note the reported chemical compositions are in Table 83. ....	216
Figure 181. Large field of view STEM dark field image taken from the inner area (Lamella 10) of TRISO Particle AGR1-433-001 at the IPyC/SiC interface showing three areas of analysis in the SiC layer (Areas 1-3) and one (Area 4) in the IPyC/SiC interface. ....	217
Figure 182. (a) STEM HAADF image combined with EDS labeling to track the chemical composition of fission product precipitates from the inner area at the IPyC-SiC interface (Lamella 10) of TRISO Particle AGR1-433-001 within subtended Area 1. Note the reported chemical compositions are in Table 84. (b) STEM HAADF image combined with EDS labeling to track the chemical composition of fission product precipitates from the inner area (Lamella 10) of TRISO Particle AGR1-433-001 within subtended Area 2. Note the reported chemical compositions are in Table 84. ....	217
Figure 183. (a) STEM HAADF image combined with EDS labeling to track the chemical composition of fission product precipitates from the IPyC-SiC interface (Lamella 10) of TRISO Particle AGR1-433-001 within subtended Area 3 (from the inner area of the SiC layer). Note the reported chemical compositions are in Table 85. (b) STEM HAADF image combined with EDS labeling to track the chemical composition of fission product precipitates from the IPyC-SiC interface (Lamella 10) of TRISO Particle AGR1-433-001 within the subtended Area 4 that is within the IPyC layer. Note the reported chemical compositions are in Table 85. ....	219
Figure 184. Large field of view STEM dark field image taken from the center area (Lamella 6) of TRISO Particle AGR1-433-001. ....	220
Figure 185. STEM HAADF image combined with EDS labeling to track the chemical composition of fission product precipitates from the center area (Lamella 6) of TRISO Particle AGR1-433-001 within subtended Areas (a) 1a and (b) 1b. Note the reported chemical compositions are in Table 86 (note that Figure 185(a) consists of a combination of 2 images that overlap). ....	221
Figure 186. STEM HAADF image combined with EDS labeling to track the chemical composition of fission product precipitates from the center area (Lamella 6) of TRISO Particle AGR1-433-001 within subtended area 2. Note the reported chemical compositions are in Table 87. ....	222
Figure 187. Large field of view STEM dark field image taken from the outer area (Lamella 7) of TRISO Particle AGR1-433-001. ....	223
Figure 188. STEM HAADF image combined with EDS labeling to track the chemical composition of fission product precipitates from, (a) the outer area (Lamella 7) of TRISO Particle AGR1-433-001, within subtended area 1. Note the reported chemical compositions are in Table 88; (b) STEM HAADF image combined with EDS labeling to track the chemical composition of fission product precipitates from the outer area (Lamella 7) of TRISO Particle AGR1-433-001 within subtended Area 2. Note the reported chemical compositions are in Table 88. ....	224
Figure 189. STEM HAADF image combined with EDS labeling to track the chemical composition of fission product precipitates from the outer area (Lamella 7) of TRISO Particle AGR1-433-001, within subtended Areas (a) 3a and (b) 3b. Note the reported chemical compositions are in Table 89. ....	225

Figure 190. SiC grain orientation maps of the areas analyzed in Lamella 5 (Figure 171[c], Figure 178): (a) Area 1, (b) Area 2, and (c) Area 3. The black areas in (a) represent large fission product precipitates. ....	228
Figure 191. Distributions of (a) grain boundary misorientation angle, (b) value of CSL-related grain boundaries, and (c) grain boundary types in each area analyzed on the inner Lamella (Lamella 5, Figure 171[c]) and the averaged distribution with error bars calculated from the standard error. ....	229
Figure 192. Distributions averaged over all areas analyzed for each lamella: (a) misorientation angle, (b) CSL designation, and (c) grain boundary type for the SiC grain boundaries in samples taken from AGR1-433-001. ....	230
Figure 193. Comparison of the distribution of grain boundary precipitates on the various grain boundary types in various regions of the SiC layer of AGR1-433-001. ....	231
Figure 194. Composition distribution of the grain boundary precipitates AGR1-433-001. ....	233
Figure 195. Distribution of fission product precipitates on the various boundary types as a percentage AGR1-433-001. ....	234
Figure 196. Distributions of fission product elements, as a percentage, by grain boundary type AGR1-433-001. ....	234
Figure 197. (a) Large field of view atomic contrast HAADF image from the inner area of TRISO Particle AGR1-433-001, where Areas 1 and 2 containing precipitates were analyzed using STEM and HRTEM imaging away from the SiC-IPyC interface contained within Lamella 5. (b) Atomic contrast dark field imaging centered over each of the two areas reveals a network of fission product precipitates, which migrate under neutron irradiation along SiC grain boundary interiors and nucleate in large concentrations at triple point junctions. (c) STEM HAADF, and (d) low-angle annular BF centered over the first area reveal Pd-Ag fission product precipitates concentrated at triple point junctions reported in Table 93. Similarly, centered over the second area (e) STEM-HAADF and (f) annular BF reveal similarly sized fission product precipitates, with a large concentration located at triple-point junctions. Note the composition of precipitates contained in each of these areas is reported in Table 93. ....	235
Figure 198. (a) Large field of view centered covered the subtended Area 1, from the inner area of TRISO Particle AGR1-433-001. Three individual fission product precipitates are located and labeled, and two precipitates (1, 2) were subsequently imaged with HRTEM from Lamella 5. The third precipitate could not be resolved with HRTEM lattice imaging due to significant SiC grain overlap. For fission product Precipitate (b) 1 and (c) 2, both contain Pd and Ag and are located at triple point junctions within the SiC lattice. To address overlapping SiC grains and raw image signal to noise, a filtered inverse FFT was also performed for each of these areas, including Precipitate (d) 1 and (e) 2. To identify the structural and crystallographic details, FFTs were calculated for Precipitate (f) 1 and (g) 2. Each of the respective FFTs reveal the cubic SiC and Pd-Ag lattice points labeled by white and blue circles, respectively. Note the composition of precipitates contained in this area is reported in Table 93. ....	236
Figure 199. (a) STEM dark field imaging centered over area 2 from the inner area of TRISO Particle AGR1-433-001 exposes individual fission product precipitates that have been later identified and analyzed using both STEM and HRTEM from Lamella 5. (b) Over the same area, TEM was performed and each area containing a precipitate is labeled. For each of these precipitates, HRTEM and EDS was utilized to image and determine	

intact fission product precipitate structure and chemistry. Note the chemical compositions of the fission product precipitates contained within Area 2 are reported in Table 93. ....	237
Figure 200. Atomic scale HRTEM imaging and FFTs of individual fission product precipitates contained within the subtended area 2 from the inner area of TRISO Particle AGR1-433-001, including (a–b) 1, (c–d) 2, and (e–f) 3 from Lamella 5. For each of the respective FFTs, white circles label the cubic SiC and blue circles highlight the Pd and Pd-Ag lattice points. ....	238
Figure 201. Atomic scale HRTEM imaging and FFTs of individual fission product precipitates contained within the subtended area 2 from the inner silicon carbide area of TRISO Particle AGR1-433-001, including (a–b) 4, (c–d) 5, and (e–f) 6 from Lamella 5. For each of the respective FFTs, white circles label the cubic SiC and blue circles highlight the Pd and Pd-Ag lattice points. For a closer examination of the fission product precipitation chemistry along each of the specific grain boundaries, point-resolved STEM EDS chemical profiling was used to identify elements, contained within each fission product precipitate. Table 93 reports the most and least abundant fission product elements, measuring less than 1 at.% for some. ....	239
Figure 202. (a) STEM HAADF large field of view image taken over the center of the SiC layer of the TRISO coated Particle AGR1-433-001, where two areas containing precipitates were analyzed using STEM imaging within the SiC layer contained within Lamella 6 (the arrows indicating the presence of other precipitates although not measured in this study). Atomic contrast (b) dark field and (c) BF imaging centered over each of these two areas, reveals a network of fission product precipitates that migrate under neutron irradiation and are found in this middle cross section of the SiC layer. A closer examination of the area containing these two areas, (d) STEM dark and (e) BF, reveal Pd-Ag fission product precipitates concentrated within these two areas. Subsequently, over these two areas STEM, EDS, and HRTEM was performed. Note the chemical composition of fission product precipitates contained in these areas is reported in Table 94. ....	241
Figure 203. (a) STEM dark and (b) BF imaging centered over subtended Area 1 from the center area of TRISO Particle AGR1-433-001, reveals each of individual fission product precipitates within Lamella 6 that have been later identified and analyzed using HRTEM and EDS. Note the report chemical compositions for each of these fission product precipitates are reported in Table 94. ....	242
Figure 204. Atomic-scale, high-resolution TEM imaging and FFTs of individual fission product precipitates contained within Area 1 from the center of the silicon carbide layer of TRISO Particle AGR1-433-001, including (a–b) 1, (c–d) 2, and (e–f) 3 from Lamella 6. For each of the respective FFTs, white circles label the cubic SiC and blue circles highlight the Pd and Pd-Ag lattice points. Over Area 2, fission product precipitates were imaged with dark field STEM and HRTEM to reveal both their structural and chemical details. ....	242
Figure 205. (a) STEM dark and (b) BF imaging centered over Area 2 from the center of the silicon carbide layer of TRISO Particle AGR1-433-001, reveals the individual fission product precipitates that have been later identified and analyzed using both STEM and HRTEM contained within Lamella 6. Over the same Area 2, HRTEM was performed for each of these three fission product precipitates labeled. Note the report chemical compositions are reported in Table 94. ....	243

Figure 206. Atomic-scale, high-resolution TEM imaging and FFTs of individual fission product precipitates, including (a–b) 1, (c–d) 2, and (e–f) 3 with from area 2 of the center of the silicon carbide layer of TRISO Particle AGR1-433-001 contained within Lamella 6. For each of the respective FFTs, white circles label the cubic SiC and blue circles Pd-Ag lattice points. ....	244
Figure 207. (a) Large field of view from the outer area of TRISO Particle AGR1-433-001, where one area containing precipitates was analyzed using STEM imaging within the SiC layer contained within Lamella 7. Atomic contrast (b) dark field and (c) BF imaging centered over the area, reveals a network of fission product precipitates within the SiC layer that migrate under neutron irradiation. A closer examination of the area, (d) STEM dark and (e) BF reveal Pd-Ag fission product precipitates concentrated within the area of interest. Note the chemical composition of the fission product precipitates contained within this one area is provided in Table 95. ....	246
Figure 208. (a) STEM dark and (b) BF imaging centered over area 1 reveals the individual fission product precipitates contained with Area 1 from the outer area of TRISO Particle AGR1-433-001 of Lamella 7 that have been later identified and analyzed using both STEM and HRTEM. Over the same Area 1, HRTEM was performed for fission product Precipitates 3 and 4. Note the report chemical compositions for each of these labeled fission product precipitates are reported in Table 95. ....	246
Figure 209. Atomic-scale HRTEM imaging and FFTs of individual fission product precipitates, including (a and b) 3 and (d through f) 4, taken from Area 1 within the outer area of TRISO Particle AGR1-433-001 contained within Lamella 7. From (a) low to (b) higher magnification, fission product Precipitate 3 is resolved with HRTEM. (c) The accompanying FFT reveals both the Pd-Ag and SiC lattice spots for fission product Precipitate 3. Similarly, for fission product Precipitate 4, (d) low to (e) higher magnification HRTEM was used to image the atomic structure of the precipitate and accompanying FFT pattern. For each of the respective FFTs, white and blue circles label the cubic SiC and blue circles label the Pd and Pd-Ag lattice points. ....	247
Figure 210. (a) STEM dark and (b) BF imaging centered over Area 2 from the outer area of TRISO Particle AGR1-433-001, reveals the individual fission product precipitates that have been later identified and analyzed using both STEM and EDS contained within Lamella 7. Note the report chemical compositions are reported in Table 95. ....	248
Figure 211. Overview of the TEM Lamella from AGR1-433-004 showing the analysis areas for (a) inner, Lamella 4, (b) inner, Lamella 5, (c) center, Lamella 6, and (d) outer, Lamella 7. ....	249
Figure 212. Qualitative trend analysis of precipitate composition (Pd, Ag, and U only) as a function of the approximate distance from the SiC-IPyC interface of Particle AGR1-433-004. ....	251
Figure 213. Large field of view STEM dark field image taken from the inner area (Lamella 4) of TRISO Particle AGR1-433-004. ....	252
Figure 214. STEM HAADF image combined with EDS labeling to track the chemical composition of fission product precipitates from the inner area (Lamella 4) of TRISO Particle AGR1-433-04 within subtended Area 1. Note the reported chemical compositions are in Table 97. ....	252
Figure 215. STEM HAADF image combined with EDS labeling to track the chemical composition of fission product precipitates from the inner area (Lamella 4) of TRISO	

Particle AGR1-433-004, within subtended Area 2. Note the reported chemical compositions are in Table 98. ....	253
Figure 216. Large field of view STEM dark field image taken from the inner area (Lamella 5) of TRISO Particle AGR1-433-004. ....	255
Figure 217. (a) STEM HAADF image combined with EDS labeling to track the chemical composition of fission product precipitates from the center area (Lamella 5) of TRISO Particle AGR1-433-004 within subtended Area 1. Note the reported chemical compositions are in Table 99(b), The STEM HAADF image combined with EDS labeling to track the chemical composition of fission product precipitates from the center area (Lamella 5) of TRISO Particle AGR1-433-004 within subtended Area 2. Note the reported chemical compositions are in Table 99. ....	255
Figure 218. Large field of view STEM dark field image taken from the center area (Lamella 6) of TRISO Particle AGR1-433-004. ....	257
Figure 219. STEM HAADF image combined with EDS labeling to track the chemical composition of fission product precipitates from the center area (Lamella 6) of TRISO Particle AGR1-433-004, within subtended Area 1. Note the reported chemical compositions are in Table 100. ....	257
Figure 220. STEM HAADF image combined with EDS labeling to track the chemical composition of fission product precipitates from the center area (Lamella 6) of TRISO Particle AGR1-433-004 within subtended Area 2. Note the reported chemical compositions are in Table 101. ....	258
Figure 221. Large field of view STEM dark field image taken from the outer area (Lamella 7) of TRISO Particle AGR1-433-004. ....	259
Figure 222. STEM HAADF image combined with EDS labeling to track the chemical composition of fission product precipitates from the outer area (Lamella 7) of TRISO Particle AGR1-433-004 within subtended Area 1. Note the reported chemical compositions are in Table 102. ....	260
Figure 223. STEM HAADF image combined with EDS labeling to track the chemical composition of fission product precipitates from the outer area (Lamella 7) of TRISO Particle AGR1-433-004 within subtended Area 2. Note the reported chemical compositions are in Table 103. ....	261
Figure 224. Orientation maps of (a) Area 1 and (b) Area 2 on the inner sample, Lamella 4, AGR1-433-004. ....	263
Figure 225. Distributions of (a) grain boundary misorientation angles, (b) value of CSL-related grain boundaries, and (c) grain boundary types in each area analyzed on the inner sample (Lamella 4, Figure 211[a]) AGR1-433-004. Averaged distributions are included. ....	264
Figure 226. Grain boundary distributions averaged over all areas analyzed on each sample, (a) misorientation angle, (b) CSL value, and (c) grain boundary type for the SiC samples taken from AGR1-433-004. ....	266
Figure 227. Comparison of the distribution of grain boundary types that contain any fission product precipitates in different regions of the SiC layer in TRISO particle, AGR1-433-004. ....	268
Figure 228. Composition distribution of the various fission product-containing grain boundary precipitates in the SiC layer of AGR1-433-004. ....	269

Figure 229. Distribution of the fission product-containing precipitates on the various boundary types, as a percentage, in the SiC layer of AGR1-433-004. ....	270
Figure 230. Distributions of precipitates containing specific fission product elements or their combination, as a percentage, by grain boundary type in the SiC layer of AGR1-433-004. ....	270
Figure 231. Comparison of the (a) misorientation angle, (b) CSL-related, and (c) grain boundary-type distributions in the SiC layers of AGR1-433-001 and AGR1-433-004. ....	272
Figure 232. Comparison of (a) the precipitate distribution for grain boundary precipitates containing various fission product elements, and (b) the distribution of fission product precipitates as a function of grain boundary type for the safety-tested TRISO particles (AGR1-433-001 and AGR1-433-004). ....	273
Figure 233. (a) STEM dark field large field of view taken over the inner area from TRISO Particle AGR1-433-004, where two areas containing fission product precipitates were analyzed using STEM imaging near the SiC/IPyC interface contained within Lamella 4. Atomic contrast (b) dark field and (c) BF imaging centered over the area found within the SiC layer, near the SiC/IPyC interface. A closer examination of the area, (d) STEM dark and (e) BF reveal Pd-Ag fission product precipitates concentrated within the area of interest. Note the chemical composition for the fission product precipitates contained within Area 1 is reported in Table 107. ....	274
Figure 234. (a) STEM dark field (from Figure 233[b]) and (b) BF centered over the first subtended Area 1a (from Figure 233c) reveal Pd-Ag fission product precipitates concentrated along grain boundaries and triple point junctions from the inner area of TRISO Particle AGR1-433-004 contained within Lamellae 4. Similarly, centered over the second subtended Area 1b STEM (c) dark (from Figure 233[d]) and (d) BF (from Figure 233[e]) from the inner area of TRISO Particle AGR1-433-004 with subtended Area 1b reveals similarly sized fission product precipitates, with a large concentration of precipitates nucleated at triple-point junctions. ....	275
Figure 235. (a) SAED was collected from a larger field of view containing Areas 1a and 1b within the inner area of TRISO Particle AGR1-433-004, Lamella 4. Based on the SAED pattern, the {022} fundamental reflection spot for the cubic face center cubic (FCC) structure corresponding to Pd, Pd-Ag, Pd-U, and Pd-Pu was selected (i.e., circled in a white outline) for dynamic dark field TEM imaging. (b) From subtended Area 1a, Precipitate 1, a BF and (c) dark field image centered over a large precipitate reveals scattered intensities, consistent with a spatially varying distribution contained within the fission product precipitate. Similarly, for Area 1b, (d) BF and (e) dark field TEM reveal similarly sized points within the fission product precipitate. Note Areas 1a and 1b were highlighted in Figure 234. ....	276
Figure 236. STEM dark field image taken over the larger field of view containing subtended Area 1b from the inner area of TRISO Particle AGR1-433-004, where a series of point-resolved EDS scans were acquired over fission product precipitates and their respective chemical composition is tabulated and reported in Table 108 contained within Lamella 4. ....	278
Figure 237. (a) Large field of view taken from the outer area of TRISO Particle AGR1-433-004, where a single area containing precipitates was analyzed using STEM and HRTEM imaging near the outer SiC/OPyC interface contained in Lamella 5. Atomic contrast (b) dark field and (c) BF imaging centered over the area, reveals a network of fission product precipitates that migrate under neutron irradiation and are found within the SiC	



layer. A closer examination of the area, STEM (d) dark and (e) BF reveal Pd-Ag fission product precipitates concentrated within the area of interest.....	280
Figure 238. From the outer silicon carbide layer of TRISO Particle AGR1-433-004 (a) STEM dark field and (b) BF imaging centered over the area of interest, revealing a Pd fission product precipitate contained within Lamella 5. Note the chemistry at each of these points along a single fission product precipitate circled in white is reported in Table 109. ....	281
Figure 239. (a) TEM and (b) high-resolution imaging centered over fission product Precipitate 2 from the outer silicon carbide layer of TRISO Particle AGR1-433-004 reveals lattice fringes pertaining to the Pd precipitate contained within Lamella 5. (c) The observed lattice was confirmed with FFT analyses centered over the precipitate showing cubic Pd lattice spots. ....	281
Figure 240. (a) Large field of view taken over the outer silicon carbide layer from TRISO particle of Lamella AGR1-433-004-06, where a single area was analyzed using STEM and HRTEM imaging within the outer SiC layer. Atomic contrast (b) dark field and (c) BF imaging centered over the area reveals the vicinity of precipitates from one another. At higher magnification, STEM (d) dark and (e) BF imaging reveals the individual fission product precipitates concentrated within the area of interest that were analyzed with HRTEM. ....	282
Figure 241. Over the outer silicon carbide layer from TRISO Particle AGR1-433-004, Lamella 6, (a) STEM dark field and (b) BF imaging, reveal fission product precipitates that were analyzed in detail with both HRTEM and point-resolved EDS. STEM EDS was collected from five fission product precipitates and three of which were adequate for HRTEM. Note the reported chemical composition for each of these fission product precipitates is provided in Table 110. ....	283
Figure 242. Atomic-scale, high-resolution TEM imaging and FFTs of individual fission product precipitates, including (a–b) 1, (c–d) 2, and (e–f) 3 within the outer silicon carbide layer identified for Particle AGR1-433-004 contained within Lamella 6. ....	284
Figure 243. (a) Large field of view taken over the outer area of the silicon carbide layer from TRISO Particle AGR1-433-004, Lamella 7, where a single area was analyzed using STEM and HRTEM imaging within the SiC layer. Atomic contrast (b) dark field and (c) BF imaging centered over the area reveals the vicinity of precipitates from one another. At higher magnification, STEM (d) dark and (e) BF imaging reveals the individual fission product precipitates concentrated within the area of interest that were analyzed with HRTEM. ....	286
Figure 244. (a) STEM dark field and (b) BF imaging centered over Area 1 from TRISO Particle AGR1-433-004, revealing three fission product precipitates contained within Lamella 7 lifted out from outer silicon carbide layer that were analyzed in detail with point-resolved STEM EDS and two of which were adequate for HRTEM. Note the report chemical compositions are reported in Table 111. ....	286
Figure 245. Atomic-scale HRTEM imaging and FFTs of individual fission product precipitates, including (a, b) 1 and (c, d) 3 within the outer silicon carbide layer identified for TRISO Particle AGR1-433-004, contained within Lamella 7. The precipitate labeled shown in (c) is overlapped with the surrounding SiC lattice, where Moire fringes are resolved.....	287

Figure 246. Predicted quaternary phase diagram for U-Si-Pd, based on ab-initio first principles-based calculations using materials project (Jain et al., 2011, 2013). The stable compounds and formation energies (eV/atom) are shown for U-Si-Pd stable containing compounds. ....	289
Figure 247. Optical microscope image of AGR1-433-003 (left) and AGR1-433-007 (right). Paths of measured radial traverses are shown with white lines. The arrow in the left image highlights kernel extrusion (deformation) into a fractured region of the buffer layer. ....	290
Figure 248. Eu concentration (A), Sr concentration (B), and Te concentration (C) in AGR1-433-003 and AGR1-433-007. Squares represent the radial traverse on the side with the deformed kernel of AGR1-433-003 and diamonds represent the radial traverse on the intact side. Triangles represent AGR1-433-007. If no error bars are visible, the error is smaller than the symbol. ....	291
Figure 249. Concentration (A), Xe concentration (B), and Cs concentration (C) in AGR1-433-003 and AGR1 433-007. Squares represent the radial traverse on the side with the deformed kernel of AGR1-433-003 and diamonds represent the radial traverse on the intact side. Triangles represent AGR1-433-007. If no error bars are visible, the error is smaller than the symbol. ....	292
Figure 250. Backscattered electron images of AGR1-433-007 showing the 110-degree arc of precipitates (between the arrows) along the SiC-IPyC interface. The line indicates the path of the measured analytical traverse. ....	293
Figure 251. (A through D): Ce, Pd, Ag, and Cs wt%, respectively, across the IPyC-SiC interface. Squares represent the radial traverse on the side with the deformed kernel of AGR1-433-003; diamonds represent the radial traverse on the intact side. Triangles represent AGR1-433-007. Where no error bars are visible, the error is smaller than the symbol. ....	295
Figure 252. Pd concentration (A), Cd concentration (B), Sn concentration (C), and Ag concentration (D) in AGR1-433-003 and AGR1-433-007. Squares represent the radial traverse on the side with the deformed kernel of AGR1-433-003; diamonds represent the radial traverse on the intact side. Triangles represent AGR1-433-007. Where no error bars are visible, the error is smaller than the symbol. ....	296
Figure 253. Comparison of the distributions of grain boundary types: (a) inner regions, (b) center regions, (c) outer regions, and (d) the combined regions are compared. Baseline in black, Variant 1 in red, and Variant 3 in green. ....	312
Figure 254. Correlations between the Ag-110m retention and (a) random, high-angle grain boundary fraction, (b) CSL-related grain boundary fraction, (c) twin boundary fraction, and (d) low-angle grain boundary fraction for inner regions of the SiC layer. ....	313
Figure 255. Correlations between the Ag-110m retention and (a) random, high-angle grain boundary fraction, (b) CSL-related grain boundary fraction, (c) twin boundary fraction, and (d) low-angle grain boundary fraction for central regions of the SiC layer. ....	314
Figure 256. Correlations between the Ag-110m retention and (a) random, high-angle grain boundary fraction, (b) CSL-related grain boundary fraction, (c) twin boundary fraction, and (d) low-angle grain boundary fraction for outer regions of the SiC layer. ....	315
Figure 257. Correlations between the Ag-110m retention and (a) random, high-angle grain boundary fraction, (b) CSL-related grain boundary fraction, (c) twin boundary fraction, and (d) low-angle grain boundary fraction for all regions of the SiC layer combined to yield correlations representative of the entire SiC layer. ....	316

Figure 258. (a) Plot showing the types of grain boundaries on which fission product precipitates were found and (b) the distribution of fission product elements in the grain boundary precipitates. Variants are in different colors (i.e., Baseline in black, Variant 1 in red, and Variant 3 in green). .....	317
--	-----

## TABLES

Table 1. Variation in baseline process parameter conditions for three TRISO particle types (adapted from Hunn et al. 2008).....	2
Table 2. Irradiation conditions for AGR-1 experiment selected compacts (adapted from Demkowicz et al., 2015a).....	6
Table 3. Advanced microscopy and micro-analytical analysis matrix for the selected particles from the AGR-1 experiment.....	7
Table 4. Electron microscopic and micro-analytical techniques explored to achieve objectives. ....	8
Table 5. Standards, crystals, and interferences corrected for each X-ray line. ....	14
Table 6. Detailed experimental microscope parameters used in the study of each compact using STEM EDS.....	16
Table 7. The most effective LEAP parameters determined to date. ....	20
Table 8. Advanced microscopy and micro-analysis examination performed on Compact 6-3-2 particles.....	24
Table 9. Identification of minor elements present in fission product precipitates in the SiC layer of Particle AGR1-632-035.....	31
Table 10. Reported qualitative EDS compositions from the inner area of the SiC layer from TRISO Particle AGR1-632-035, taken from Areas 1 and 2 that are highlighted in Figure 14.....	33
Table 11. Reported qualitative EDS compositions from the inner area of the SiC layer from TRISO Particle AGR1-632-035, taken from the subtended Area 3 highlighted in Figure 14.....	34
Table 12. Reported qualitative EDS compositions from the inner area of the SiC layer from TRISO Particle AGR1-632-035 that are taken from subtended Areas 4 and 5 highlighted in Figure 14. ....	35
Table 13. Reported qualitative EDS compositions from the center area of the SiC layer from TRISO Particle AGR1-632-035, taken from subtended Areas 1 and 2 that are highlighted in Figure 18. ....	37
Table 14. Reported qualitative EDS compositions from the center area of the SiC layer from TRISO Particle AGR1-632-035, taken from subtended Areas 3a and 3b that are highlighted in Figure 18. ....	38
Table 15. Reported qualitative EDS compositions from the center area of TRISO Particle AGR1-632-035, taken from subtended Areas 4 and 5 that are highlighted in Figure 18. ....	39

Table 16. Reported qualitative EDS compositions from the center area of the SiC layer from TRISO Particle AGR1-632-035, taken from subtended Areas 6 and 7 that are highlighted in Figure 18. ....	39
Table 17. Reported qualitative EDS compositions from the outer area of the SiC layer from TRISO Particle AGR1-632-035, taken from subtended Areas 1 and 2 that are highlighted in Figure 23. ....	41
Table 18. Reported qualitative EDS compositions from the outer area of the SiC layer from TRISO Particle AGR1-632-035, taken from subtended Areas 3 and 4 that are highlighted in Figure 23. ....	42
Table 19. Reported qualitative EDS compositions from the outer area of the SiC layer from TRISO Particle AGR1-632-035, taken from subtended Areas 5 and 6 that are highlighted in Figure 23. ....	43
Table 20. Reported qualitative EDS compositions from the outer area of the SiC layer from TRISO Particle AGR1-632-035, taken from subtended Areas 7 and 8 that are highlighted in Figure 23. ....	43
Table 21. Average fraction of twin-related grain boundaries in SiC layer from Particle AGR1-632-035. ....	48
Table 22. Average fraction of grain boundary types in the SiC layer from Particle AGR1-632-035. ....	49
Table 23. Summary of fission product precipitate information and associated grain boundary information from the center sample in Area B of Figure 28(b). ....	50
Table 24. Summary of the distribution of fission product elements. ....	51
Table 25. Summary of CSL-related boundaries with precipitates. ....	54
Table 26. Advanced microscopy and micro-analysis examination performed on Compact 5-3-1 particles. ....	66
Table 27. Identification of minor elements present in fission product precipitates in the SiC layer of Particle AGR1-531-031 (locations of lamellae and corresponding analyzed areas are shown in Figure 46 and Figure 50, respectively). ....	69
Table 28. Reported qualitative EDS at.% compositions from the inner area of TRISO Particle AGR1-531-031, taken from subtended Areas 1 through 5 of Lamella 1 as highlighted in Figure 50(a) and precipitates labeled in Figure 51. ....	73
Table 29. Reported qualitative EDS at.% compositions from the inner area (Grid 1, Sample 1b) of TRISO Particle AGR1-531-31, taken from subtended Area 1 from Lamellae 1b and 4 as highlighted in Figure 50. ....	74
Table 30. Average fraction of twin-related grain boundaries in the SiC layer from Particle AGR1-531-031. ....	77
Table 31. Average fraction of grain boundary types in the SiC layer from Particle AGR1-531-031. ....	78
Table 32. Identification of minor elements present in fission product precipitates in the SiC layer of Particle AGR1-531-038. ....	80
Table 33. Reported qualitative EDS compositions from the inner area of TRISO Particle AGR1-531-038, taken from subtended Area 1. ....	83

Table 34. Qualitative EDS composition of precipitates from Particle AGR1-531-038, Lamella 1 Area 2. ....	84
Table 35. Reported qualitative EDS compositions (in at.%) from the inner area of TRISO Particle AGR1-531-038, taken from subtended Area 3.....	85
Table 36. Reported qualitative EDS compositions (in at.%) from the inner area of TRISO Particle AGR1-531-038, taken from subtended Area 4.....	86
Table 37. Reported qualitative EDS compositions (in at.%) from the inner area of TRISO Particle AGR1-531-038, taken from subtended Area 5.....	87
Table 38. Reported qualitative EDS compositions (in at.%) from the center area of TRISO Particle AGR1-531-038, taken from subtended Area 1 (a and b) from Figure 59(b).....	88
Table 39. Reported qualitative EDS compositions (in at.%) from the center area of TRISO Particle AGR1-531-038, taken from subtended Area 2 from Figure 59(b).....	88
Table 40. Reported qualitative EDS compositions (in at.%) from the center area of TRISO Particle AGR1-531-038, taken from subtended Areas 3a and 3b from Figure 59(b).....	89
Table 41. Reported qualitative EDS compositions (in at.%) from the center area of TRISO Particle AGR1-531-038, taken from subtended Area 4 from Figure 59(b).....	90
Table 42. Reported qualitative EDS compositions (in at.%) from the center area of TRISO Particle AGR1-531-038, taken from subtended Area 5 from Figure 59(b).....	91
Table 43. Reported qualitative EDS compositions (in at.%) from the center area of TRISO Particle AGR1-531-038, taken from subtended Area 6 in Figure 59(b).....	92
Table 44. Reported qualitative EDS compositions (in at.%) from the outer area of TRISO Particle AGR1-531-038, taken from subtended Areas 1 and 2 from Figure 59(c).....	93
Table 45. Reported qualitative EDS compositions (in at.%) from the outer area of TRISO Particle AGR1-531-038, taken from subtended Area 3 in Figure 59(c).....	94
Table 46. Reported qualitative EDS compositions (in at.%) from the outer area of TRISO Particle AGR1-531-038, taken from subtended Areas 4 and 5 that are highlighted in Figure 59(c). ....	95
Table 47. Average fraction of twin-related grain boundaries in the SiC layer from Particle AGR1-531-038. ....	98
Table 48. Average fraction of grain boundary types in the SiC layer from Particle AGR1-531-038. ....	99
Table 49. Summary of fission product precipitate analysis for the inner sample (AGR1-531-038-01). ....	102
Table 50. Summary of fission product precipitate analysis for the center sample (AGR1-531-038-02). ....	103
Table 51. Summary of the distribution of fission product elements. ....	104
Table 52. Analyses of spots (in weight percent) whose location is shown in Figure 96. ....	126
Table 53. Advanced microscopy and micro-analysis examination performed on Compact 1-3-1 particles.....	129

Table 54. EDS compositions correspond to precipitates indicated in Figure 102 from Areas 1 and 2 from Lamella 4. The majority of the precipitates are Pd-Si-U or Pd-U. Most precipitates contain U, but U concentration is typically low. ....	133
Table 55. EDS compositions corresponding to the precipitates indicated in Figure 103. The majority of the precipitates are Pd-Si-U, with a small fraction of Pd-Si. ....	135
Table 56. EDS compositions correspond to precipitates indicated in Figure 104 from Area 4 on Lamella 4 from Particle AGR1-131-066. Most precipitates are U and U-Si. ....	136
Table 57. EDS compositions correspond to precipitates indicated in Figure 105 from Area 1 on Lamella 5 from Particle AGR1-131-066. Precipitates are Pd, Pd-Si, Pd-U, and Pd-Si-U. Most precipitates within about 300 nm from the IPyC-SiC interface contain U. ....	137
Table 58. Qualitative EDS compositions corresponding to precipitates indicated in Figure 106 from Area 2 on Lamella 5 from Particle AGR1-131-066. Majority of precipitates are Pd, with a small fraction of Pd-Si and Pd-U. ....	138
Table 59. Qualitative EDS compositions correspond to precipitates indicated in Figure 107 from Area 3 on Lamella 5 from Particle AGR1-131-066. The majority of the precipitates are Pd and Pd-Si, with a small fraction of Pd-Si-U. ....	140
Table 60. Qualitative EDS compositions correspond to precipitates (indicated in Figure 108) of Area 1 of AGR1-131-066 Lamella 6. Most precipitates are Pd, with a small fraction of Pd-Si precipitates. ....	142
Table 61. Qualitative EDS compositions correspond to precipitates indicated in Figure 109. The majority of the precipitates are Pd, with a small fraction of Pd-Si and Pd-U precipitates. ....	144
Table 62. Qualitative EDS compositions correspond to precipitates indicated in Figure 110 from Area 3 of AGR1-131-066 Lamella 6. The majority of the precipitates are Pd, with a noticeable fraction of Pd-Si precipitates and a small fraction of Pd-Si-U precipitates. ....	146
Table 63. Reported qualitative EDS compositions from the outer area (Lamella 7) of TRISO Particle AGR1-131-066, taken from subtended Areas 1a, 1b, 1c, 1d, and 1e from Figure 111. ....	148
Table 64. Reported qualitative EDS compositions from the precipitates (Figure 112) from the outer area (Lamella 7) of TRISO Particle AGR1-131-066 (Figure 100), taken from subtended Areas 2a and 2b. ....	150
Table 65. Reported qualitative EDS compositions from the precipitates (Figure 113) from the outer area (Lamella 7) of TRISO Particle AGR1-131-066 (Figure 100), taken from Area 3. ....	151
Table 66. Average fraction of twin-related grain boundaries in the SiC layer from Particle AGR1-131-066. ....	154
Table 67. Average fraction of grain boundary types in the SiC layer from Particle AGR1-131-066. ....	156
Table 68. Summary of the distribution of fission product elements. ....	157
Table 69. Representative composition of precipitates in TEM Lamella 1 (at the IPyC-SiC interface). These compositions correspond to precipitates indicated in Figure 127. 0.2 at.% is taken as the detection limit for Pd, Ag, Cs and Ce, and 0.1 at.% for U. Any element with concentration below the detection limit is considered not to be present. ....	166

Table 70. Representative composition of precipitates in TEM Lamella 5 (across the IPyC-SiC interface). These compositions correspond to precipitates indicated in Figure 129. The 0.2 at.% is taken as the detection limit for Pd, Ag, Cs, and Ce and 0.1 at.% for U. Any element with a concentration below the detection limit is considered to not be present.....	169
Table 71. Representative compositions of precipitates in TEM Lamella 2 (from the inner region of the SiC layer). These compositions correspond to precipitates indicated in Figure 131. A 0.2 at.% is taken as the detection limit for Pd, Ag, Cs, and Ce and 0.1 at.% for U. Any element with a concentration below the detection limit is considered to not be present.....	172
Table 72. Representative qualitative compositions of precipitates in TEM Lamella 4 (from the middle region of the SiC layer). These compositions correspond to precipitates indicated in Figure 133. A 0.2 at.% is taken as the detection limit for Pd, Ag, Cs, and Ce and 0.1 at.% for U. Any element with a concentration below the detection limit is considered to not be present. ....	175
Table 73. Representative compositions of precipitates in TEM Lamella 3 (from the outer region of the SiC layer). These compositions correspond to precipitates indicated in Figure 135. A 0.2 at.% is taken as the detection limit for Pd, Ag, Cs, and Ce and 0.1 at.% for U. Any element with a concentration below the detection limit is considered to not be present.....	176
Table 74. Average fraction of twin-related grain boundaries in the SiC layer of Particle AGR1-131-099.....	180
Table 75. Average fraction of grain boundary types in the SiC layer of Particle AGR1-131-099. ....	180
Table 76. Summary of the distribution of fission product elements.....	183
Table 77. Advanced microscopy and micro-analysis examination performed on Compact 4-1-1 particles.....	197
Table 78. Advanced microscopy and micro-analysis examination performed on Compact 4-3-3 particles.....	207
Table 79. Identification of minor elements present in fission product precipitates in the SiC layer of Particle AGR1-433-001.....	209
Table 80. Reported qualitative EDS compositions (at.%) from the outer area (Lamella 4) of TRISO Particle AGR1-433-001, taken from subtended Areas 1a and 1b that are shown in Figure 176.....	212
Table 81. Reported qualitative EDS compositions (at.%) from precipitates (Figure 177) from the outer area (Lamella 4) of TRISO Particle AGR1-433-001, taken from subtended Areas 2 and 3 (Figure 175). ....	214
Table 82. Reported qualitative EDS compositions (at.%) from precipitates (Figure 179) from the inner area (Lamella 5) of TRISO Particle AGR1-433-001, taken from subtended Area 1 (Figure 178). ....	215
Table 83. Reported qualitative EDS compositions (at.%) from the inner area (Lamella 5) of TRISO Particle AGR1-433-001, taken from subtended Areas 2 and 3 (Figure 178). ....	216
Table 84. Reported qualitative EDS compositions (at.%) from precipitates (Figure 182) from the inner area (Lamella 10) of TRISO Particle AGR1-433-001, taken from subtended Areas 1 and 2 (Figure 181). ....	218

Table 85. Reported qualitative EDS compositions (at.%) from precipitates (Figure 183) from the inner area (Lamella 10) of the SiC layer of TRISO Particle AGR1-433-001, taken from subtended Areas 3 and 4 (Figure 181).	219
Table 86. Reported qualitative EDS compositions (at.%) from the precipitates (Figure 185) from the center area (Lamella 6) of TRISO Particle AGR1-433-001, taken from subtended Areas 1a and 1b (Figure 184).	221
Table 87. Reported qualitative EDS compositions (at.%) from precipitates (Figure 186) from the center area (Lamella 6) of TRISO Particle AGR1-433-001, taken from subtended Area 2 (Figure 184).	222
Table 88. Reported qualitative EDS compositions (at.%) from precipitates (showing in Figure 188) from the outer area (Lamella 7) of TRISO Particle AGR1-433-001, taken from subtended Area 1 and 2 (Figure 187).	224
Table 89. Reported qualitative EDS compositions (at.%) from precipitates (Figure 189) from the outer area (Lamella 7) of TRISO Particle AGR1-433-001, taken from subtended Areas 3a and 3b (Figure 187).	225
Table 90. Average fraction of twin-related grain boundaries in the SiC layer from Particle AGR1-433-001.	227
Table 91. Average fraction of grain boundary types in the SiC layer from Particle AGR1-433-001.	227
Table 92. Summary of the distribution of fission product elements.	232
Table 93. Qualitative fission product precipitate chemistry reported in atomic % from the inner area of the silicon carbide layer of TRISO Particle AGR1-433-001 taken from subtended Area 1 and 2 of Lamella 5 as highlighted in Figure 197 and labeled in Figure 198 and Figure 199.	240
Table 94. Qualitative fission product precipitate chemistry reported in atomic % from the center area of the silicon carbide layer of TRISO Particle AGR1-433-001 taken from subtended Areas 1 and 2 of Lamella 6 as highlighted in Figure 202 and labeled in Figure 203 and Figure 205.	245
Table 95. Qualitative fission product precipitate chemistry reported in atomic % from the outer area of the silicon carbide layer of TRISO Particle AGR1-433-001 taken from subtended Areas 1 and 2 of Lamella 7 as highlighted in Figure 207 and labeled in Figure 208 and Figure 210.	248
Table 96. Identification of minor elements present in fission product precipitates in the SiC layer of Particle AGR1-433-004.	250
Table 97. Reported qualitative EDS compositions from precipitates (Figure 214) from the inner area of TRISO Particle AGR1-433-004, measured in subtended Area 1 (Figure 213).	253
Table 98. Reported qualitative EDS compositions from precipitates (Figure 215) from the inner area of TRISO Particle AGR1-433-004, taken from subtended Area 2 (Figure 213).	254
Table 99. Reported qualitative EDS compositions from precipitates (Figure 217) from the center area (Lamella 5) of TRISO Particle AGR1-433-004, taken from subtended Areas 1 and 2 (Figure 216).	256
Table 100. Reported qualitative EDS compositions from precipitates (Figure 219) from the center area (Lamella 6) of TRISO Particle AGR1-433-004, taken from subtended Area 1 (Figure 218).	258



Table 101. Reported qualitative EDS compositions from the center area (Lamella 6) of TRISO Particle AGR1-433-004, taken from subtended Area 2.....	259
Table 102. Reported qualitative EDS compositions from precipitates (Figure 222) from the outer area (Lamella 7) of TRISO Particle AGR1-433-004, measured in subtended Area 1 (Figure 221). ....	260
Table 103. Reported qualitative EDS compositions from precipitates (Figure 223) from the outer area (Lamella 7) of TRISO Particle AGR1-433-004, taken from subtended Area 2 (Figure 221). ....	262
Table 104. Average fraction of twin-related grain boundaries in the SiC layer from Particle AGR1-433-004. ....	265
Table 105. Average fraction of grain boundary types in the SiC layer from Particle AGR1-433-004. ....	267
Table 106. Summary of the distribution of fission product elements in the SiC layer of AGR1-433-004. ....	268
Table 107. Qualitative fission product precipitate chemistry reported in at. % from the inner area of TRISO Particle AGR1-433-004 taken from subtended Areas 1a and 1b of Lamellae 4 as highlighted in and labeled in Figure 235. ....	277
Table 108. Qualitative fission product precipitate chemistry, reported in atomic %, for precipitates from the subtended inner Area 1b of TRISO Particle AGR1-433-004, Lamella 4 taken as highlighted and labeled in Figure 236. Shading indicates overlapping points considered to be contained within the same fission product precipitate. ....	279
Table 109. Qualitative fission product precipitate chemistry, reported in atomic % from outer silicon carbide layer of TRISO Particle AGR1-433-004 taken from subtended Area 1 of Lamella 5 as highlighted in Figure 237 and labeled in Figure 238. ....	282
Table 110. Qualitative fission product precipitate chemistry reported in atomic % from outer silicon carbide layer of TRISO Particle AGR1-433-004 taken from subtended Area 1 of Lamella 6 as highlighted in Figure 240 and labeled in Figure 241. ....	285
Table 111. Qualitative fission product precipitate chemistry, reported in atomic % from outer silicon carbide layer of TRISO Particle AGR1-433-004 taken from subtended Area 1 of Lamella 7 as highlighted in Figure 243 and labeled in Figure 244.....	288
Table 112. Penetration of analyzed elements into the SiC layer.....	294
Table 113. Precipitate element combination summary (a detection limit of 0.2 at.% was used to determine if an element is present, as measured by STEM EDS analysis). For each particle, results are grouped by the specific area of the SiC layer (inner, center, or outer layer) and by the number of elements observed in the precipitates (one element, two elements, and three or more elements). ....	301
Table 114. Maturity level and applicability for future AGR advanced microscopy and micro-analytical techniques. Only the techniques identified to be further explored or applied are indicated in this table. (The grading system used is as follows: “Good” means acceptable for PIE application, “Medium-Good” means it is successfully demonstrated, but it still needs optimization, and “Low” means low maturity and cannot be applied without significant effort and development).....	320
Table B-1. AGR-1 advanced microscopy and micro-analysis publications and presentations.....	337



## ACRONYMS

3D	three-dimensional
AGR	advanced gas reactor
APT	atom probe tomography
at. %	Atomic %
ART	Advanced Reactor Technologies
ATR	Advanced Test Reactor
BF	bright field
CAES	Center for Advanced Energy Studies
CEOS	Corrected Electron Optical Systems
CSL	coincident site lattice
CVD	chemical vapor deposition
EBSD	electron backscatter diffraction
EDS	energy dispersive x-ray spectroscopy
EELS	electron energy loss spectroscopy
EFTEM	energy filtered transmission electron microscopy
EML	electron microscopy laboratory
EPMA	electron probe micro-analysis
FCC	face center cubic
FEG	field emission gun
FFT	fast Fourier transformation
FIB	focused ion beam
FIMA	fissions per initial metal atom
FY	fiscal year
HAADF	high-angle annular dark field
HRSTEM	high-resolution scanning transmission electron microscopy
HRTEM	high-resolution transmission electron microscopy
HTR	high-temperature reactor
IFFT	inverse fast Fourier transformation
INL	Idaho National Laboratory
IPyC	inner pyrolytic carbon
LANL	Los Alamos National Laboratory
LEAP	local electron atom probe
MaCS	microscopy and characterization suite

MFC	Materials and Fuels Complex
NMMU	Nelson Mandela Metropolitan University
NSUF	Nuclear Science User Facilities
ORNL	Oak Ridge National Laboratory
PED	precession electron diffraction
PIE	post-irradiation examination
RTE	Rapid Turn Around Experiment
SAD	selected area diffraction
SAED	selected area electron diffraction
SEM	scanning electron microscopy
SiC	silicon carbide
STEM	scanning transmission electron microscopy
TAP	Thallium acid phthalate
TAVA	temperature average volume average
TEM	transmission electron microscopy
TKD	transmission Kikuchi diffraction
TRISO	tristructural isotropic
UCO	uranium oxide, uranium –carbide mixture
VHTR	very high-temperature reactor
WDS	wavelength dispersive X-ray spectroscopy

# Advanced Electron Microscopy and Micro-Analytical Technique Development and Application on Irradiated TRISO-Coated Particles from the AGR-1 Experiment

## 1. INTRODUCTION

A series of seven irradiation experiments are planned for the Advanced Gas Reactor (AGR)-fuel development and quantification program, with irradiation completed at the Advanced Test Reactor (ATR) at Idaho National Laboratory (INL) for experiments AGR-1, AGR-2, and AGR-3/4. The first experiment (AGR-1) was completed in November 2009 at an effective 620 full-power days. The objective of the AGR-1 experiment was primarily to provide lessons learned on the multi-capsule test train design, to provide early data on fuel performance for use in fuel fabrication process development, and to provide irradiated fuel samples for post-irradiation safety testing data at high temperatures. This report describes the advanced microscopy and micro-analysis results on selected AGR-1 coated particles.

### 1.1 AGR-1 Experiment Design

The capsule design and details of the AGR-1 experiment are described by Grover et al. (2010) and Maki (2009). The AGR-1 experiment consisted of six capsules, each filled with 12 fuel compacts of similar fuel type that were stacked in a  $3 \times 4$  array for a total of 72 compacts, each containing approximately 4,100 tristructural isotropic (TRISO)-coated particles with kernels composed of a heterogeneous mixture of uranium oxide ( $\text{UO}_2$ ) and uranium carbide (UC) termed UCO (details of the experiments are discussed by Demkowicz 2010, Collins 2012). Each compact was given a unique identifier, reflecting the specific capsule, level, and stack number for each compact. For example, Figure 1 identifies the stack and position (or level) within the stack of a specific compact within a particular capsule. Compact 6-3-2 refers to the compact in Capsule 6 at Level 3 of Stack 2.

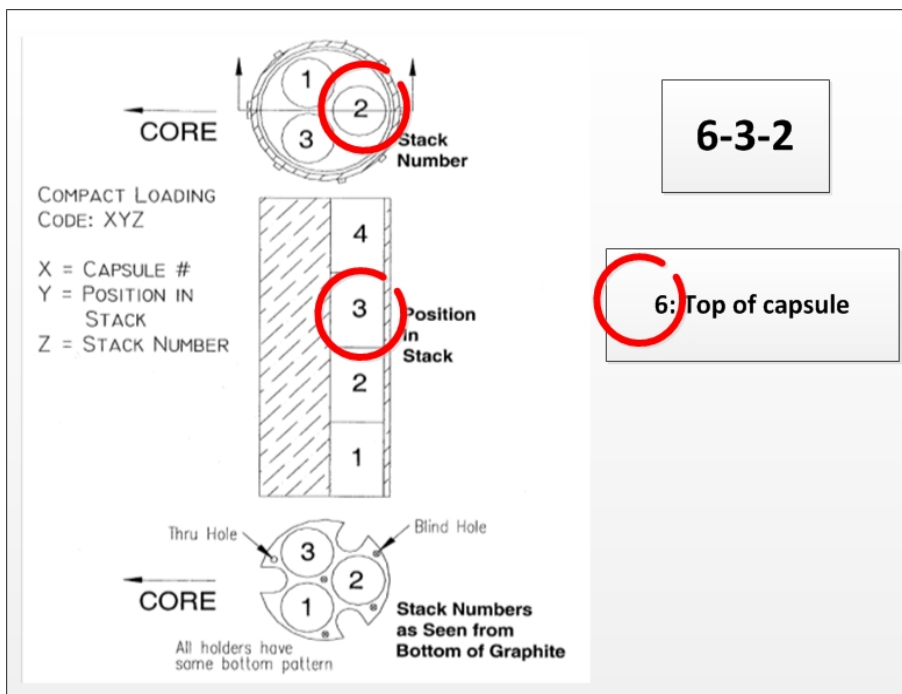


Figure 1. An example of the numbering scheme for AGR-1 compacts demonstrated for Compact 6-3-2.

The AGR-1 experiment contained four types of TRISO-coated particles (called Baseline and Variant 1 through Variant 3) fabricated with different conditions. In this report, microstructural comparisons are made between three fuel types: Baseline, Variant 1, and Variant 3. Examination of Variant 2 was lowest priority and not performed due to strain on budget and schedule because it had properties very similar to the Baseline fuel type (unlike the other IPyC variant, Variant 1, for which there were significant differences in IPyC density and anisotropy) (Demkowicz et al., 2015). Fabrication parameter conditions and the purpose of varying these parameter conditions are summarized for the different fuel types in Table 1. The AGR-1 TRISO-coated fuel particles were fabricated at Oak Ridge National Laboratory (ORNL) using about 350- $\mu\text{m}$ -diameter UCO kernels at 19.74 wt% U-235 enrichment, produced by BWX Technologies, Inc., Nuclear Operations Group.

Table 1. Variation in baseline process parameter conditions for three TRISO particle types (adapted from Hunn et al. 2008).

<b>Fuel Type</b>	<b>Inner Pyrolytic Carbon (IPyC) Deposition Temperature (<math>^{\circ}\text{C}</math>)</b>	<b>IPyC Coating Gas Fraction</b>	<b>Silicon Carbide (SiC) Deposition Temperature (<math>^{\circ}\text{C}</math>)</b>	<b>Description</b>
Baseline	1265	0.30	1500	Fabricated to closely match historically proven German fuel containing $\text{UO}_2$ particles.
Variant 1	1290	0.30	1500	Enhanced irradiation stability of the pyrocarbon, although permeability is expected to increase and, consequently, uranium dispersion (IPyC layer less dense than in Baseline fuel) by changing IPyC deposition temperature.
Variant 3 <sup>a</sup>	1265	0.30	1425	Reduce the potential for SiC-layer defects resulting from uranium dispersion and provide a change in polycrystalline microstructure that may be less permeable to metallic fission products. Changed SiC deposition temperature and introduced argon into the fluidization gas mix.
a. Variant 3 SiC was deposited using 50:50 mix of Ar:H for the fluidization gas.				

Post-irradiation examination (PIE) of the AGR-1 experiment commenced in 2010 at INL and ORNL, which include electron microscopy of irradiated particles, as described in PLN-2828 (Demkowicz 2010). Fuel performance assessment focuses on the behavior of the kernel and coating layers and the retention of fission products by the particles and fuel compacts. Knowledge and understanding of fission product transport mechanisms are fundamental objectives for facilitating improvements that contribute to the extension of the performance envelope of modern TRISO-coated particle fuel.

## 1.2 AGR-1 Experiment Fission Product Release

The fission product element palladium (Pd) isotopes (i.e., Pd-105, Pd-106, Pd-107, Pd-108, and Pd-109) and the activation product Ag-110m have been identified as key elements to fission product retention in the TRISO-coated particle. The release of Ag-110m has been observed in the primary circuit of early experimental high-temperature reactors (HTRs) (Engelhard et al., 1975, Hick et al., 1970, Nabielek et al., 1977), and Pd has been implicated in corrosion of the SiC layer (IAEA-TECDOC-CD-1674, 2012). Radio-cesium isotopes (i.e., Cs-134 and Cs-137) are important fission products due to their offsite dose consequence in the event of an accident in gas-cooled reactors. Cesium (Cs) release is indicative of a failed SiC layer. Strontium (i.e., Sr-90) has high biological significance and is also released primarily in the event of SiC layer failures. Europium (i.e., Eu-154 and Eu-155) is generally well-retained by intact SiC layers (although very small diffusive releases may occur at accident temperatures) and is a consideration for reactor plant maintenance and reactor designs. Krypton (e.g., Kr-85), xenon (e.g., Xe-133), and iodine (e.g., I-131) are well retained by any dense TRISO coating layer and measured releases of these fission products would indicate complete TRISO coating failure. In this report, the term “fission product” is used in a general sense to refer to all isotopes generated from fission processes. These include direct fission products and those generated by neutron activation of direct fission products, as well as the relevant daughter isotopes. Note that U was often observed concurrently with various fission products in the coating layers and is often grouped in this term in this report. Different TRISO coating layers are effective for retaining different fission products. In addition, advanced microscopy techniques were applied to characterize performance of the TRISO coating layers and distribution of key fission products within these layers.

Because no TRISO failures occurred during irradiation in ATR and only four SiC layer failures were determined to have occurred during irradiation, releases of Cs, Eu, Kr, Pd, Xe, and I were very small (Demkowicz et al., 2015[a]). In contrast, the fraction of Ag-110m retained in individual particles often varied considerably within a single compact. Particles with disparate Ag-110m retentions were targeted for comparison during advanced microscopy. Fifty-six of the 72 AGR-1 compacts were individually gamma scanned at INL with sufficiently long counting times to quantify the Ag-110m inventory (Harp 2014). The estimated fraction of Ag-110m retained in these 56 compacts is displayed in Figure 2 (Demkowicz et al., 2015[a]). This was determined from fuel compact gamma scanning data, with the total measured inventory for each compact compared to the predicted inventory from physics simulations. The individual fractions for each particle investigated using advanced microscopy techniques will be discussed in Section 2.

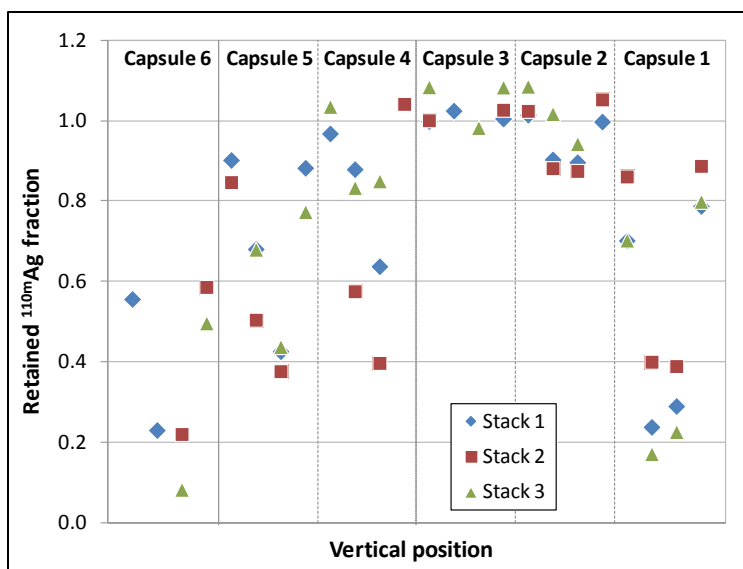


Figure 2. Fraction of retained Ag-110m inventory in 56 of the 72 AGR-1 fuel compacts after irradiation. Data are plotted as a function of vertical position in the experiment (top of the experiment at the left) and by stack number (Demkowicz et al., 2015a).

### 1.3 Advanced Microscopy and Micro-Analysis Objectives

The main objective of the electron microscopic examination of fuel particles is to characterize the effects of radiation upon the microstructure and microchemistry, particularly with respect to fuel kernel porosity, layer degradation or corrosion, fission product precipitation, layer debonding, and grain characteristics. Because the silicon carbide (SiC) layer is the main fission product barrier, fission product identification, and distribution within the SiC layer, and SiC grain boundary characteristics were prioritized during the AGR-1 campaign due to the complex nature of resolving the nano-sized fission product precipitates within the SiC layer. The migration of fission products from the kernels across the TRISO layers is also examined. In particular, corrosion of the SiC layers by fission products (such as Pd), resulting in localized layer thinning, is investigated. Another objective is to determine if there are microstructural differences between particles that exhibited high and low releases of Ag-110m. The interpretation and discussion of results presented in this report focus on the microstructure and fission products found at the IPyC/SiC interlayer and the SiC layers with only brief reporting on buffer layer and fuel kernel observations. A detailed technical discussion of the fuel kernels will be presented in a separate report at a later stage.

As mentioned, a key component of AGR-1 PIE has been to examine various particles based on their observed Ag-110m retention (as determined by comparing gamma-counting data to physics calculations) in an attempt to correlate Ag-retention behavior with specific SiC layer characteristics, irradiation effects, and fabrication features. This will be fundamentally important for establishing an understanding of the transport mechanisms of various fission products, especially Ag-110m. Although numerous mechanisms for Ag transport were derived (e.g. from irradiation data, out-of-pile experimentation under simulated conditions, and empirical studies), over the past four decades, no definitive conclusion on the mechanism(s) responsible for Ag transport in the SiC layer of TRISO fuel under very high temperature reactor (VHTR) conditions has been reached. The experimental test conditions and test samples varied significantly when comparing experimental results resulting that individual experimental results supported a variety of possible Ag transport mechanisms. Various Ag-110m transport mechanisms (e.g., grain boundary diffusion, surface diffusion, or vapor transport through interconnected nano-pores or nano-cracks, Pd-assisted transport



alongside grain boundaries) have been identified in these out-of-pile experiments and must be considered as potentially viable Ag-110m transport mechanisms in the SiC layer of TRISO fuel under neutron irradiation.

As analysis and interpretation of results were performed during the earlier years of the AGR-1 PIE campaign, additional advanced techniques were explored to provide data to fill in the knowledge gaps. Because most of these advanced microscopy and micro-analysis techniques were first-of-a-kind for irradiated TRISO-coated particles and irradiated SiC, the level of effort to establish facilities, and develop methods for performing the advanced analysis was high during the earlier part of the AGR-1 campaign. This report provides a compilation of data obtained and a summary of the impact it had on the comparative knowledge base, and it makes recommendations for analysis of the second irradiation experiment (i.e., AGR-2). Because multiple publications (e.g., journal papers, conference papers, and presentations) were prepared during the lifetime of the AGR-1 PIE activities (2011 to the time of report writing) on the advanced microscopy and micro-analytical results, the aim of this report is to provide a summary of the main findings, referencing these publications. However, a large body of work recently performed has not yet been published. Therefore, certain sections of this report will contain more data, representing the recent work. Additionally, this report will provide a summary on the maturity level of the technique development and measurements performed. In addition to AGR-1 fuel performance data; these tests have also yielded important operational experience and data on these analytical methods and additional support activities necessary to perform this work.

This report describes particle selection in Section 1.4, followed by rationale for methods or techniques applied in Section 2. Results obtained using advanced microscopy and micro-analytical techniques for each compact are provided in Section 3. The report concludes with a discussion and conclusions in Section 4 and a conclusion summary provided in Section 5.

## **1.4 Selection of AGR-1 Coated Particles for Advanced Microscopy and Micro-Analysis**

For these studies, coated particles from one Baseline fuel compact, two Variant 1 fuel compacts, and three Variant 3 fuel compacts were chosen. An expanded dataset from TRISO-coated particles from Compacts 6-3-2, 5-3-1, 5-2-3, 4-1-1, 1-3-1, and 4-3-3 are reported and compared. Generally, particles from each compact were selected to represent a low and high-Ag-retention particle (details of the selection criteria are described by Demkowicz et al., 2015a). Unfortunately, in the case of Compact 6-3-2 (i.e., the Baseline fuel-type compact), the low-retention particle (AGR1-632-030) was over-polished during sample preparation and important SiC-IPyC interface features were lost. Therefore, only the high-retention particles (i.e., AGR1-632-034 and AGR1-632-035) were examined. Particles from the two Variant 1 compacts include (a) high and low Ag-110m retention particles from Compact 5-3-1 for comparative microstructural analysis and (b) one particle from Compact 5-2-3 that was identified after an interesting IPyC fracture was observed during three-dimensional (3D) X-ray tomography studies conducted by ORNL (Hunn et al., 2015). The three Variant 3 compacts include (a) Compact 4-3-3, (which was safety tested at 1600°C for 300 hours) to examine the effect that high-temperature post-irradiation heating may have on microstructure in correspondence with Ag-110m retention; (b) Compact 1-3-1 from which high and low Ag-110m retention particles were chosen, and (c) a particle with relatively high Ag-110m retention (i.e., 90% retention) from Compact 4-1-1 that was submitted for atomic resolution examination using a double spherical aberration corrected JEOL ARM200F high-resolution transmission electron microscope (HRTEM) operated at 200 kV to develop an understanding of the structure and crystallography associated with fission products measuring less than 40 nm and as small as 2 nm.

## **1.5 Irradiation Conditions for the Selected AGR-1 Compacts**

The irradiation conditions for the selected AGR-1 compacts are shown in Table 2. It should be noted that these values are compact averages and the specific parameters for each coated particle are not known for the AGR-1 experiment. This complicates the final conclusions of this report because temperature

gradients within the compacts may be on the order of 300°C (Hawkes and Murray 2014), and burnup gradients will also exist.

Table 2. Irradiation conditions for AGR-1 experiment selected compacts (adapted from Demkowicz et al., 2015a).

<b>Compact</b>	<b>Fuel Type</b>	<b>Burnup (%FIMA<sup>a</sup>)</b>	<b>Fast Neutron Fluence<sup>b</sup></b>	<b>Time-Average Volume-Average Temperature (°C)</b>	<b>Time-Average Peak Temperature (°C)</b>
6-3-2	Baseline	11.4	2.55	1070	1144
5-3-1	Variant 1	16.7	3.60	1040	1122
5-2-3	Variant 1	17.4	3.77	1059	1141
1-3-1	Variant 3	15.3	3.22	1092	1166
4-1-1	Variant 3	19.4	4.13	1072	1182
4-3-3	Variant 3	18.6	4.16	1094	1179
a. Fissions of initial metal atoms (FIMA).					
b. $10^{25}$ n/m <sup>2</sup> E > 0.18 MeV					

## 2. ADVANCED ELECTRON MICROSCOPY TECHNIQUES

Microstructural work in early 2012 focused on the analysis of particles from Compact 6-3-2, a Baseline fuel type. This earlier work was exploratory to establish knowledge on fission product location within the fuel and features to refine the scanning electron microscope (SEM) analysis techniques necessary to achieve the microstructural characterization objectives and to identify specific areas of interest. The initial electron microscopy techniques used in the AGR-1 PIE campaign included only basic SEM examination and electron backscatter diffraction (EBSD) of selected, mounted, cross-sectioned TRISO-coated particles (Demkowicz 2010). The basic SEM examination also included elemental analysis, namely energy dispersive x-ray spectroscopy (EDS) and wavelength dispersive X-ray spectroscopy (WDS) to provide information on elemental compositions, especially at particle layer boundaries. Basic electron microscopic examination of Compact 6-3-2 coated particles using SEM EDS, SEM WDS, and transmission electron microscopy (TEM)-EDS provided some information on micro-level distribution of fission products (van Rooyen et al., 2012, van Rooyen et al., 2012a). However, this work could neither provide positive identification of Ag in fission product precipitates nor an accurate quantification of chemical elemental compositions and distributions. This led to exploration of other more advanced analytical and microscopic techniques (van Rooyen et al., 2013). An overview of the entire electron microscopic examination technique envelope explored for AGR-1 particles is schematically shown in Figure 3. Prior to the first advanced microscopy activity step (i.e., first box in Figure 3; the mount preparation and decontamination step), the samples would have been irradiated in ATR, the sample train shipped to the Materials and Fuels Complex (MFC) for disassembly, individual compacts would have been selected for deconsolidation leach-burn-leach, and individual particles would have been selected from the deconsolidated compact for advanced microscopic analysis. As indicated in Section 3, not all techniques are necessarily applied to each particle. Table 3 shows an overview of the techniques applied on the selected particles. The analysis techniques indicated in Table 3 resulted from measurement technique methods development. Other techniques were also explored that yielded limited results, which aided in the decision-making process to determine the usefulness of the technique for obtaining the required level of scientific data.

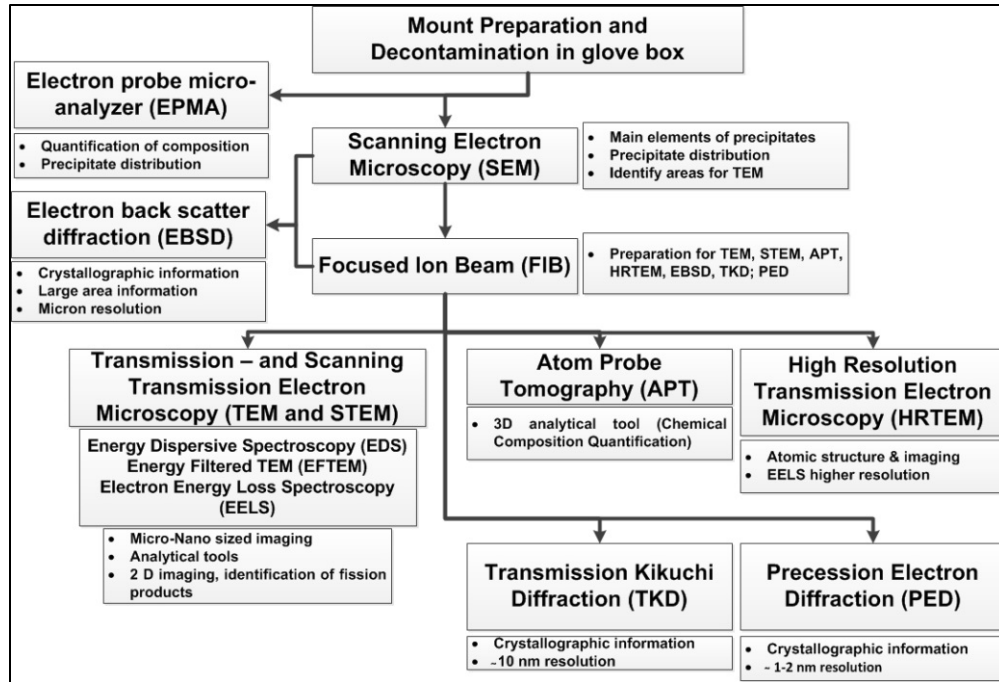


Figure 3. Schematic presentation of the electron microscopy and micro-analytical technique envelope explored for the AGR-1 experiment.

Table 3. Advanced microscopy and micro-analytical analysis matrix for the selected particles from the AGR-1 experiment.

Technique <sup>a</sup>	SEM <sup>b</sup> EDS/WDS	EELS/ EFTEM	STEM	EPMA	PED	APT	HRTEM
<b>Compact 6-3-2 (Baseline)</b>							
AGR1-632-030 (Low (21% ) Ag retention) <sup>c</sup>	X	—	—	—	—	—	—
AGR1-632-034 (High (65%) Ag retention) <sup>c</sup>	X	—	X	—	—	X	—
AGR1-632-035 (High (79%) Ag retention) <sup>c</sup>	X	X	X	—	X	X	—
<b>Compact 5-3-1 (Variant 1)</b>							
AGR1-531-038 (Low (< 19%) Ag retention) <sup>c</sup>	X	—	X	—	X	—	—
AGR1-531-031 (High (105%) Ag retention) <sup>c</sup>	X	—	X	—	X	—	—
<b>Compact 5-2-3 (Variant 1)</b>							
AGR-523-SP01 (16% Ag retention) <sup>c</sup>	—	—	X	—	X	—	—
<b>Compact 1-3-1 (Variant 3)</b>							
AGR1-131-099 (Low (<6%) Ag retention) <sup>c</sup>	X	X	X	—	X	—	X
AGR1-131-066 (High (39%) Ag retention) <sup>c</sup>	X	—	X	—	X	—	X

Table 3. (continued).

Technique <sup>a</sup>	SEM <sup>b</sup> EDS/WDS	EELS/ EFTEM	STEM	EPMA	PED	APT	HRTEM
<b>Compact 4-1-1 (Variant 3)</b>							
AGR-411-030 (Average (90%) Ag retention)	X	—	—	—	—	—	X
<b>Compact 4-3-3 (Variant 3; 1600°C safety tested)</b>							
AGR1-433-003 (Low (< 22%) Ag retention) <sup>c</sup>	—	—	—	X	—	—	—
AGR1-433-007 (High (100%) Ag retention) <sup>c</sup>	—	—	—	X	—	—	—
AGR1-433-001 (Low (66%) Ag retention) <sup>c</sup>	X	—	X	—	X	—	X
AGR1-433-004 (High (98%) Ag retention) <sup>c</sup>	X	—	X	—	X	—	X
<p>a. APT – atom probe tomography EELS – electron energy loss spectroscopy EFTEM – energy-filtered transmission electron microscopy EPMA – electron probe micro-analysis PED – precession electron diffraction STEM – scanning transmission electron microscopy</p> <p>b. Reported in separate report by van Rooyen et al., 2017.</p> <p>c. See Section 3 for more details on Ag retention values for each compact. Note that retention values are relatively high and low for the specific compact collection of particles. Estimated Ag retention values are determined by comparing the measured Ag-110m activity in each particle to the predicted inventory from physics calculations. Values in excess of 100% are possible if Ag retention in the particle was high, and the calculated inventory was biased low (Demkowicz et al., 2015a)</p>							

## 2.1 Advanced Microscopy and Micro-Analytical Technique Description and Development

As mentioned earlier, the initial SEM and basic TEM with WDS and EDS analysis could neither provide positive identification of Ag in the fission product precipitates; nor an accurate quantification of elemental compositions and distributions, which led to the exploration of other more advanced analytical and microscopic techniques.

Table 4 provides a summarized description of the initial electron microscope work (Phase 1), with advanced microscopy and micro-analytical techniques (Phase 2) explored to achieve the objectives (listed in the first column) and to overcome the gaps identified during Phase 1 work (not described in this report). Earlier advanced microscopy and micro-analytical exploratory work are also described in a previous milestone report by van Rooyen (2013).

Table 4. Electron microscopic and micro-analytical techniques explored to achieve objectives.

Objective	Electron Microscopic Technique: Basic Examination (Phase 1)	Electron Microscopic Technique: Advanced Examination (Phase 2)
Observe microstructure to establish irradiation effects	Not applicable.	<p>TEM/STEM: Micro and nanostructures studied to measure diffraction patterns to identify phase and irradiation damage if any.</p> <p>The quantification of irradiation damage and its effects on transport mechanisms could not have been studied because priority was given to the identification and distribution of fission products.</p>

Table 4. (continued).

Objective	Electron Microscopic Technique: Basic Examination (Phase 1)	Electron Microscopic Technique: Advanced Examination (Phase 2)
Observe layer degradation or corrosion and layer debonding	<p><u>SEM</u>: Basic examination to identify the location of any corrosion or thinning visible on the micro-level.</p> <p><u>SEM</u>: Identification of macro and micro-debonding of layers.</p>	<p><u>TEM/STEM/HRTEM</u>: Localized corrosion or degradation specifically at the SiC/IPyC interface is studied for each particle.</p>
Fission product identification and distribution	<p><u>SEM</u>: Basic examination to identify the location of fission product precipitates.</p> <p><u>SEM-EDS and SEM-WDS</u>: Detection thresholds are typically at the level of one atom per thousand; therefore, these instruments can quantify concentrations of the primary elemental constituents and can map relative abundance of fission products. However, measurements performed in this study are qualitative only, because only standardless calibration was used.</p>	<p><u>EPMA/TEM/TEM-EDS/STEM/HRTEM/APT/EELS/EFTEM</u>: This examination will reveal more detail about the nature and location of the precipitate (e.g., if the precipitate consists of multiple phases, the main elemental constituents, and if it is located intra- or inter-granularly). (Note EDS measurements used only standardless elemental quantification analysis.)</p> <p><u>Advanced microscopy techniques</u>: Only selected samples were analyzed for quantitative results at the atomic level to resolve small quantities of Ag in the precipitates</p>
Grain size and grain boundary character	<p><u>SEM-EBSD</u>: Provide data on crystallographic orientation of SiC grains and grain boundary character to aid interpretation of observed fission product behavior.</p>	<p><u>TKD</u>: SEM-based technique with resolution of about 10 nm.</p> <p><u>PED</u>: TEM-based technique with resolution of less than 5 nm and as low as 1 nm, depending on electron probe size, typically 1 to 2 nm.</p> <p>It was determined that grain size is not the only criterion for determining the effects on fission transport. Grain boundary characteristics at the nano-level were necessary to resolve the characteristics at the locations of nano-size fission product precipitates found during STEM/TEM examination.</p>
Fuel kernel porosity	<p><u>SEM</u>: No quantitative analysis will be done using SEM; only comparative micrographs will be produced. Optical microscopy measurements will be conducted to compare the relative porosity among different kernels (not part of this work).</p>	<p><u>TEM/STEM/HRTEM</u>: Because of a priority on identification and distribution of fission products, quantification of kernel porosity could not have been studied. Work on this is performed separately as part of a new work package that started in Fiscal Year (FY) 2016 to be continued in FY 2017. This includes the fission product and microstructural effects of the fuel kernel.</p>
Fission product transport mechanism		<p>Although the objectives of the AGR-1 experiment did not include separate effects research on fission product transport, all microscopy results were analyzed to provide knowledge toward understanding transport mechanisms. Specifically, the grain boundary characteristics and the fission product identification, location, and distribution are used for some preliminary conclusions reached in this regard. This report should not be seen as a full body of work on this topic.</p>

### 2.1.1 Focused Ion Beam Sample Preparation

Electron transparent focused ion beam (FIB) lamellae were prepared using a FEI Quanta 3D field emission gun (FEG) FIB instrument located at INL. A final cleaning of the FIB Lamella was performed using a 5-keV gallium beam and operated with a beam current of 12 pA to remove material deposited during FIB preparation and reduce damage from the initial milling and lift-out process. Care was taken to minimize ion beam interaction with the exposed surface throughout the TEM sample preparation. This was done by first depositing a thin layer of electron beam-deposited platinum, followed by a gradient of fine-to-coarse-grained ion beam platinum deposited at 30 keV within a typical size of 20–22  $\mu\text{m}$  in length by 2–3  $\mu\text{m}$  in width and 1–2  $\mu\text{m}$  in thickness. The initial standard lift-out was done using a typical sample size of about 20 by 15  $\mu\text{m}$  and a thickness of approximately 2  $\mu\text{m}$  prior to further thinning to electron transparency. The electron transparent region observed in TEM was only about 17 by 13  $\mu\text{m}$ .

### 2.1.2 Fission Product Identification and Distribution

**2.1.2.1 Scanning Electron Microscopy, Basic Transmission Electron Microscopy, and Montages.** Analysis of particles from Compact 6-3-2 (the first particles examined at INL in 2011) focused on refining the SEM analysis techniques necessary to achieve microstructural characterization objectives and to identify specific areas or features of interest. SEM examination typically included fission product identification, evaluation of any chemical attack of the SiC layer, SiC microstructural characteristics focusing on the IPyC-SiC interlayer, and fuel kernel microstructure. Numerous clusters of fission product precipitates were observed in the coating layers during initial SEM characterization of the cross sections, but compositional quantification was problematic using SEM analytical tools (standardless EDS and WDS) due to the relatively small size of the precipitates and X-ray energy overlaps of constituents in the clusters. The SEM used for examination at INL is a JEOL-7000F equipped with WDS detectors. The SEM was operated between 10 and 30 kV. Earlier SEM and TEM results are reported by van Rooyen et al., 2012, van Rooyen et al., 2012a, van Rooyen 2013, and van Rooyen et al., 2014c. The result of these studies was the exploration of other techniques to bridge the gap in chemical composition quantification, identification of Ag, and structure and location of nano-precipitates.

SEM image montages of the IPyC-SiC interface around the entire circumference of several particle cross sections were acquired to examine the fission product feature distributions along the interface, as well as the local interfacial microstructure. This work was initiated as insights on variations of feature distribution as a function of Ag retention behavior; (e.g. possible variations in the IPyC-SiC interface integrity and thickness) may provide a better understanding of fission product release. Montages were prepared for five coated particles from two Variant 3 compacts (i.e., 4-1-1 and 1-3-1), three coated particles from a Baseline compact (i.e., 6-3-2), two coated particles from a Variant 1 compact (i.e., 5-3-1), and two coated particles from a 1600°C safety-tested Variant 3 compact (i.e., 4-3-3). Details of how these montages were produced and the specific results are described in van Rooyen et al., 2012b, van Rooyen et al., 2014c, and van Rooyen et al., 2017. Although slight correlation could be made with respect to kernel distance from the SiC-IPyC interface and the concentration of fission product precipitates, these measurements did not provide significant quantitative data for studying fission product transport mechanisms or fuel behavior. However, this tool is a good comparative tool for studying micro and macro-features and their effects on fission product distribution patterns. These studies yielded quantitative results on the SiC-IPyC interface thickness, showing a thicker interface layer for the Variant 3 particles compared with the other fuel variants.

**2.1.2.2 Electron Probe Micro-Analysis.** This section details the developmental efforts for preparing irradiated TRISO samples, loading them into the Cameca SX100-R electron probe micro-analysis (EPMA), and successfully analyzing them for parameters such as kernel chemistry and precipitate composition. Initial work on unirradiated TRISO-coated particles was performed at the EPMA facility in the Analytical Laboratory at MFC. This EPMA facility was not approved for handling irradiated fuel until September 2013. As a result, only Particle AGR1-523-SP01, mounted by ORNL in a

mini-met-mount, was used for EPMA method development prior to the first EPMA measurements of irradiated TRISO particles at INL in FY 2014 (see Section 3.3.3 for results). The EPMA instrument was transferred to the Irradiated Materials Characterization Laboratory facility at MFC in July 2014 and was briefly operational from May 2015 until June 2016 when work stoppages were necessary due to construction for facility upgrades to allow highly irradiated fuel components for characterization. During this period, EPMA analyses were completed on two particles from Compact 4-3-3 and results are discussed in Section 3.6.

**2.1.2.2.1 Sample Preparation and Handling.** Sample geometry for EPMA is quite restrictive. The manufacturer-provided sample holder requires the sample to be mounted into a 1-in. diameter, commercially designed metallography mount. This metallography mount is typically about 0.99 in. in diameter and will fit into the sample holder. Larger diameter samples cannot be accommodated.

Because commercial mounts are typically constructed of plastic and are difficult to decontaminate, efforts were centered on fabricating a steel metallography mount. A cylindrically shaped mount that has an outer diameter of 0.99 in. and from 0.5 to 0.75 in. in height will fit into the sample holder.

In addition, to facilitate collaboration with ORNL, a sample adapter was designed to accommodate the uniquely shaped samples produced by ORNL and polished in their MiniMet™. Briefly, the adapter consists of a cylinder that will fit into the EPMA sample holder, but that has an adjustable platform onto which the MiniMet sample can be adhered with double-sided carbon tape. The platform can be raised or lowered to provide the correct height for the sample to be in-focus under the beam.

While fabrication efforts were underway, sample handling and preliminary analysis techniques were investigated using a non-irradiated (as-fabricated) TRISO particle. Sample handling techniques were devised under the assumption that, at least in the short term, irradiated specimens would be coated and loaded into the EPMA absent of any significant shielding or remote handling tools. To that end, an acrylic block was fashioned to allow loading of the irradiated sample into the sample holder, while the operator was shielded from radiation; primarily beta radiation. In addition, various types of tongs were procured and tested to ensure that the sample could be reliably handled with minimal risk of dropping the sample. Finally, several different beta-shielded boxes and lead-lined acrylic boxes were procured to permit moving and storing the sample while minimizing dose to the researcher.

**2.1.2.2.2 Analysis of Unirradiated Tristructural Isotropic-Coated Particle.** Preliminary analysis techniques of an unirradiated TRISO-coated particle focused on analyzing the kernel for U, O, and C, and analysis of the SiC layer using both quantitative spot acquisition and X-ray map acquisition. For both maps and quantitative spots, standards chosen included SiC for Si, depleted U for U, and ThO<sub>2</sub> for O. Crystals chosen using Siegbahn notation to indicate particular X-ray transitions include PC1 for O  $\alpha$ , Thallium acid phthalate (TAP) for Si  $k$ , PC2 for C  $\alpha$  and PET for U  $m\alpha$ .

Quantitative spots used a 20-second peak count time with a 10-second background count time. Accelerating voltage was set to 8 kV, while the current used was 50 nA for spots and 20 nA for X-ray maps. This low accelerating voltage was chosen to minimize the absorption component in the phi-rho-z correction, which for light elements in a heavy metal matrix can be quite large. When measuring C in the kernel, the C peak was measured using a peak integration method due to shifts in the carbon position between different carbon-containing phases. In addition, quantification of data was accomplished with the software package—Probe for EPMA v. 8.65. When measuring C in the PyC or SiC layer, C was measured using a traditional peak-to-background method.

Because analysis of the unirradiated TRISO particle was intended to test loading techniques, sample preparation, and analysis, there were several noteworthy observations that could be applied to future work, including the following:

- The tools, sample mounting jigs, and shielded containers provide a practical and simple way for handling the sample and should work well for irradiated specimens.
- Accurate analysis of light elements would be improved through use of matrixed-matched standards such as  $\text{UO}_2$  and UC. At a minimum, use of these as check standards would allow one to ascertain whether the present standards are or are not adequate.
- While use of an 8-kV accelerating voltage is reasonable for light elements, Monte Carlo modeling shows that U has an inadequate interaction volume using that voltage. A 20 kV accelerating voltage is adequate for U, but results in very large absorption corrections for the light elements. Using the high voltage for U and low voltage for C and O, and combining the datasets with appropriate Phi-Rho-Z correction (which will help correct for matrix effects on apparent concentration) may improve this analysis.

#### **2.1.2.2.3 Methods and Analysis of Irradiated Tristructural Isotropic-Coated**

**Particles.** A particle that experience in-pile SiC failure from Compact 5-2-3 (prepared by ORNL) was analyzed to gather micrometer-scale quantitative chemical analyses of a number of features, including compositional changes that occur across a radial traverse and composition of precipitates formed between the SiC and IPyC layer. In addition, X-ray maps of those same features were collected. Software used for quantitative spot analysis was Probe for EPMA Version 10.2.5. Software used for X-ray mapping was PeakSight Version 5.0. This particle had been irradiated in ATR to a calculated compact-average burnup of 17.4% fissions per initial metal atoms (FIMA) and a time-average, volume-average temperature of 1059°C.

Upon removal from the reactor, it was mounted in a mount specifically designed by ORNL for use with the MiniMet polisher. The sample was fixed in place with epoxy and polished to a less than a 1- $\mu\text{m}$  finish. It was then coated with approximately 20 nm of aluminum to mitigate the charging effects.

Measurement conditions employed include a 20-kV beam with 30-second peak integrations and 20-second background counting times. Silicon  $\text{K}\alpha$  was measured using a 20-nA current while all other X-ray lines were measured using a 200-nA current. Phi-Rho-Z corrections employed were those of Pouchou and Pichoir (1991). Mass absorbance coefficients were those of Heinrich, modified by Farthing and Walker (1990). Additional measurement and calibration information is shown in Table 5.



Table 5. Standards, crystals, and interferences corrected for each X-ray line.

Standard	X-Ray Line	Crystal	Interferences
Pollucite	Cs $l\alpha$	PET	U $l\beta 1$ , Ce $L1$
Tl (Br,I)	I $l\alpha$	PET	Cd $lg3$ , Sn $l\beta 2$
Ag <sub>2</sub> Te	Te $l\alpha$	PET	Sn $l\beta 3$
<sup>a</sup> Interpolated	Xe $l\alpha$	PET	
ThO <sub>2</sub>	Ok $\alpha$	PC1	Zr $l\beta 1$
SiC	Ck $\alpha$	PC1	U, Zrm3
Pd	Pd $l\alpha$	QTZ	Ru $l\beta 2$ , Um3-n1
Ag <sub>2</sub> Te	Ag $l\beta$	QTZ	Cd $la1$ , Um $\alpha$ 1,2
Cd	Cd $l\alpha$	QTZ	
U	U m $\alpha$	QTZ	Pd $l\beta 2$
Pu	Pu m $\beta$	QTZ	Cd $l\beta 2$ , Umg, Pd $lg3$
Barite	Ba $l\alpha$	QTZ	Pr $L1$
Nd <sub>5</sub> O <sub>14</sub>	Nd $l\alpha$	LiF	—
Pr <sub>5</sub> O <sub>14</sub>	Pr $l\alpha$	LiF	La $l\beta 1$
Sm <sub>5</sub> O <sub>14</sub>	Sm $l\alpha$	LiF	Ce $l\beta 2$
Ce <sub>5</sub> O <sub>14</sub>	Ce $l\alpha$	LiF	Ba $l\beta 1$
Eu <sub>5</sub> O <sub>14</sub>	Eu $l\alpha$	LiF	Pr $l\beta 2$ , Nd $l\beta 3$
La <sub>5</sub> O <sub>14</sub>	La $l\alpha$	LiF	Cs $L1$
Zr	Zr $l\alpha$	PET	—
Mo	Mo $l\alpha$	PET	—
Ru	Ru $l\alpha$	PET	—
Sn	Sn $l\alpha$	PET	Cd
SiC	Si k $\alpha$	TAP	Nd $la1$
SrTiO <sub>3</sub>	Sr $l\alpha$	TAP	Si k $\beta 1$

a. Because there is no calibration standard for Xe, the intensities of I  $l\alpha$  and Cs  $l\alpha$  are measured under the same conditions; a linear fit is assumed to predict Xe  $l\alpha$  intensity for use as a standard.

**2.1.2.3 Transmission Electron Microscopy and Scanning Transmission Electron Microscopy.** Initially, basic TEM examination was performed on selected samples to provide information on microstructure and chemical composition of the precipitates identified during SEM examination. It was found during FY 2013, that these analyses could not provide the specific chemical composition detail of precipitates that is needed to fully characterize fission products precipitates leading to an understanding of fission product transport mechanisms. However, this earlier work did provide an initial indication of micron-sized precipitates compositions and some knowledge about microstructural changes due to irradiation damage (van Rooyen 2013).

The scanning transmission electron microscopy (STEM) instrument is an FEI Tecnai G2 F30 FEG located at the Microscopy and Characterization Suite in the Center for Advanced Energy Studies (CAES). This STEM operates at 300 kV and features an FEG that provides superb resolution (better coherent electron beam) and allows for thicker samples (or samples containing heavy elements) to be examined, compared to those commonly possible on a 200 kV LaB<sub>6</sub> STEM systems. This STEM is also an analytical model equipped with a high-angle annular dark-field (HAADF) detector for atomic (Z)-contrast imaging, EDS, and electron energy loss spectroscopy (EELS) for qualitative/quantitative chemical analysis. The above-mentioned Z-contrast imaging, EDS, and EELS techniques were employed during the microstructural investigations of TRISO samples.

The bulk of the STEM EDS data (AGR1-131, AGR1-523, AGR1-531, AGR1-411, AGR1-433, and AGR1-632) was collected on a super-twin FEI Tecnai operated at 300 kV with a probe size of 1.0 nm. Similarly, for HRTEM analysis, an FEI Titan operated at 300 kV at LANL and an analytical probe size of 1.4 nm was used. For Compact AGR1-411, a JEOL ARM 200F fitted with an ultra-high resolution probe pole piece and next generation JEOL Centurio EDS silicon drift detector with a 100-mm<sup>2</sup> area with a 0.82 steradians collection angle was used to study compacts with high-resolution aberration corrected atomic contrast STEM imaging. The setup allows for 1,000 spectra/second to be collected, which results in shorter periods of dwell time on the order of seconds (less than 30 seconds) with total counts exceeding 1,000. Based on the higher count rates, individual peaks are quantified based on two standard deviations ( $2\sigma$ ) over background. For the bulk of the EDS analysis on the FEI Tecnai, linescans and points were collected to qualitatively measure fission product precipitate chemistry. EDS data from these linescans and points were captured with the Si-windowed EDS spectrometer with a 10-eV/channel, 10- $\mu$ s time constant, and 0.13-steradians collection angle. Each sample was tilted toward the EDS detector using a double-tilt, low-background sample holder to overcome shadowing and mitigate effects of electron channelling. The FEI Titan has an ultra-twin pole-piece where the geometry for the EDS detector differs from the super twin FEI Tecnai. To overcome shadowing on both instruments, on the FEI Titan the specimen was tilted to 12.5 degrees rather than 15 degrees on the super-twin FEI Tecnai. The effect on count rate is the same, where the optimum angle for collection for both instruments is these preferred values. The detailed instrument parameters per compact are reported in Table 6.

EDS point and linescan spectra were quantified after subtracting a fitted polynomial background for the X-ray lines identified in Table 6. The reported qualitative chemical composition for the particles examined focused for this study mainly on Pd, Ag, Cs, Ce, Eu, U, and Pu although other elements were also present and will be considered in future studies. Elemental x-ray emission overlaps between Eu/Fe and I/Ag/Pd/U were considered on a case-by-case basis, including comparing acquired EDS data to independent EPMA results for a limited number of particles examined. EDS spectra were collected at a minimum of 10 points for linescans and EDS analysis points in the linescan were separated by 2 to 2.5 nm. Each of the elements was quantified based on a standardless k-factor quantification using 300 kV and a modeled sample thickness correction inside the FEI commercial TEM imaging and analysis software. Based on the provided threshold intensity criterion over background, peak intensities were subsequently integrated, quantified, and reported. For the case of linescans, the EDS spectrum associated with each point in the linescan was analyzed. The point in the linescan exhibiting peaks in the EDS spectrum with the highest number of X-ray counts for the various fission product elements corresponded to the electron beam being most directly situated on the fission product precipitate, providing the largest contribution from the fission product precipitate to the EDS spectrum. (The small size of many of the fission product precipitates made it difficult to manually position the electron beam directly on the precipitate. Therefore, a linescan with a small step size was setup across the precipitate of interest to obtain the largest contribution of the precipitate to the EDS spectrum as possible.) Therefore, the composition provided by the EDS software for this point was considered to be the most representative of the fission product precipitate and only this composition has been reported in the tables of precipitate compositions that follow. For point EDS analyses, the composition obtained from analysis of the EDS spectrum at a point is directly reported in the tables of fission product precipitate compositions that follow. It has been noted that

the accurate determination of detection limits for the different elements requires standards close to composition of the sample and spectra collected under identical conditions, which are extremely challenging to achieve. In a typical energy dispersive x-ray analysis, it was noted that detection limits are typically about 0.1 to 0.5 atomic% (at.%) based on the element; this is an estimate provided by the EDS manufacturer, EDAX. Fission product elements with measured concentrations above the detection limits are taken to be present, and those with measured concentrations below the detection limits are taken to be absent. Fission product elements with measured concentrations above 0.20 at. % are taken as present and adhered to at least a 95% confidence limit. (It is noted that some of the earlier publications used 0.5 at.% as the detection limit; however, for trend and comparative analyses completed in this report, 0.2 at.% is used as stated above). The study is only intended to establish if the elements are present in the fission product precipitates, rather than determine the exact concentration of the elements.

Table 6. Detailed experimental microscope parameters used in the study of each compact using STEM EDS.

Compact	1-3-1	5-2-3	5-3-1	4-1-1	4-3-3	4-3-3 (HRTEM)	6-3-2
STEM Operating Voltage (kV)	300	300	300	200	300	300	300
Linescan or Pointscan	Both	Both	Line	Point	Line	Both	Line
Probe Size (units are nm unless otherwise stated)	1.00	1.00	1.00	<1 Å	1.0	1.40	1.00
Dwell Time (secs)	50 (Point) 10 (Linescan)	50 (Point) 10 (Linescan)	20 (Linescan)	<30	20 (Linescan)	240 (Point) 30 (Linescan)	20 (Linescan)
Uncertainty (at.%)	0.20 (0.10 for U)	0.20 (0.10 for U)	0.20	<0.10	0.20	0.20	0.20
Threshold Intensity	6:1 <sup>a</sup>	6:1 <sup>a</sup>	3:1 <sup>a</sup>	2σ counts over background	3:1 <sup>a</sup>	3:1 <sup>a</sup>	3:1 <sup>a</sup>
Channel Dispersion (eV/pixel)	10.00	10.00	10.00	10.00	10.00	10.00	10.00
Specimen Tilt (deg)	15.00	15.00	15.00	0.0	15.00	12.50	15.00
<b>X-Ray Lines Quantified</b>							
C-K	✓	✓	✓	✓	✓	✓	✓
P-K	—	—	—	✓	—	—	—
O-K	—	—	—	✓	—	—	—
Si-K	✓	✓	✓	✓	✓	✓	✓
Pd-K	—	—	✓	✓	✓	✓	✓
Pd-L	✓	✓	—	✓	—	—	—
Cd-K	—	—	—	✓	—	—	—
Ag-K	✓	✓	✓	✓	✓	✓	✓
Ag-L	—	—	—	✓	—	—	—
Ce-L	✓	✓	✓	—	✓	✓	✓
Eu-L	—	—	—	—	—	✓	—
Cs-L	✓	✓	✓	—	✓	✓	✓

Table 6. (continued).

Compact	1-3-1	5-2-3	5-3-1	4-1-1	4-3-3	4-3-3 (HRTEM)	6-3-2
U-L	✓	✓	✓	✓	✓	✓	✓
Pu-L	✓	✓	✓		✓	✓	✓
a. The integrated peak-to-background ratio							

It should also be noted that the SiC matrix is likely to contribute significantly to the measured EDS spectra of fission product precipitates in the SiC layer (especially for nano-sized precipitates which are approaching or smaller than analytical probe size). These SiC matrix contributions exist, even with the extremely small electron probe size that was used in this study because many of the precipitates are smaller than the thickness of the TEM lamellae, while the electron beam passes through the entire thickness of the lamellae (Lugg 2015). Consequently, the measured fission product elemental concentrations are likely underestimated compared to the actual concentrations (i.e., fission product elemental concentrations are weighted further by the Si and C concentrations from the SiC matrix). Fission product precipitate compositions are reported; however, they are qualitative or semi-quantitative in nature. These reported compositions may enable qualitative comparisons, potential trend analysis, and, when combined with precession electron diffraction (PED), identification of the presence of fission product precipitates at grain boundaries of a specific type or character, e.g., random high-angle, low angle or coincident site lattice (CSL)-related.

#### **2.1.2.4 High-Resolution Transmission Electroscopy and High-Resolution Scanning Transmission Electroscopy.**

**2.1.2.4.1 Particle AGR1-411-030.** Examination of Particle AGR1-411-030 was initiated in 2012 to achieve our objective of identifying and quantifying the nano-sized precipitates, specifically identification of Ag and Cd (van Rooyen 2013, van Rooyen et al., 2014a, van Rooyen et al., 2016). HRTEM and high-resolution STEM (HRSTEM) investigations were performed at the Nelson Mandela Metropolitan University in South Africa on Particle AGR1-411-030 using a double-corrected (i.e., image corrected and probe corrected) JEOL ARM 200F operated at 200 kV. This microscope is equipped with two Corrected Electron Optical Systems (CEOS) spherical aberration correctors for correction in TEM and STEM modes and with an Oxford Instruments XMAX 80 EDS detector and Gatan quantum image filter with dual EELS capabilities. Use of aberration-corrected STEM in analysis of specimens arises from a relative increase in probe current density achieved when compared to uncorrected microscopes. A greater signal can be generated from a comparatively smaller area, which results in analysis of more localized areas in a shorter time period.

Subsequent EDS analyses were performed with a JEOL Centurio EDS detector, which is a next-generation-type silicon drift detector that has a chip area of 100 mm<sup>2</sup> and an enhanced detector design that allows for significant improvement (about 300%) in collection efficiency compared to previous detectors (such as the Oxford XMax 80). In the case of the JEOL Centurio, a collection angle of about 0.82 steradian is specified when using the JEOL ARM 200F fitted with an ultra-high resolution pole piece. The Oxford XMax 80 fitted on the same configuration has an estimated collection angle of 0.21 steradians. The improved collection efficiency leads to better counting statistics over a shorter time period, which allows detection of low concentrations of elements during the shorter analysis time before sample modification or contamination issues by the electron beam arise. A smaller probe size typically means a higher current density because less area of the sample is damaged and it takes less time to collect data; however, the number of electrons impinging on the sample/unit area is increased.

Imaging and analysis of the sample were done using a sub-Ångström-sized probe with a probe current of approximately 68 pA, which was found to give the best balance of resolution, count rate, and sample stability. EDS was mainly used for compositional analysis due to the relative accessibility of the higher energy K-lines

for Ag and Pd, which enabled easy identification due to sufficient separation between the respective x-ray peaks. Another distinct advantage of the microscope is simultaneous acquisition of both bright field (BF) and HAADF STEM images. This aided in identification of grain boundaries in conjunction with elemental atomic number contrast imaging. The main objective of this investigation was to detect very low concentrations of Ag, Pd, and other fission products by using HRTEM/HRSTEM and an EDS system with a high-collection efficiency.

**2.1.2.4.2 AGR1-131-066, AGR1-131-099, AGR1-433-001, and AGR1-433-004.** The LANL microscope used for STEM work on the AGR-1 samples is an image-corrected FEI Titan operated at 300 kV. Fully corrected, it has a point-to-point resolution of 0.7 Å in image (TEM) mode. HRSTEM imaging resolution is 1.3 Å and offers analytical probe size of 2.0 Å formed using 2 nanoamperes of beam current. Features of the microscope and accessories include constant power lenses for beam stability, monochromator, image spherical aberration corrector, 80 and 300-kV alignments, 4k × 4k CCD camera for highest resolution imaging, Lorentz lens (magnetic domain imaging), TEM tomography capabilities, EDS capabilities for point analysis and spectral imaging, and a Gatan imaging filter (Tridiem) for full EELS, spectral imaging, and energy filtered transmission electron microscopy (EFTEM) imaging capabilities. With the monochromator, an energy resolution of 0.18 eV based on the full-width half maximum of zero loss peak is achievable with EELS.

### **2.1.3 Energy-Filtered Transmission Electron Microscopy and Electron Energy Loss Spectroscopy**

**2.1.3.1 Particle AGR1-632-035.** In the strategy to identify and confirm the presence of Ag, another analytical tool, EELS, was also considered and applied to precipitates of Particle AGR1-632-035 as reported by van Rooyen (2013) and van Rooyen et al., (2013). The results presented in these references highlight the requirement of very thin samples for the execution of EELS measurements. Under the electron beam, incoming electrons lose energy when they travel through the specimen due to inelastic interactions with the specimen. EELS analyzes the energy distribution of these scattered electrons and provides quantitative compositional information based on the unoccupied partial density of states. EELS measurements resolve energetically allowed electronic transitions per the atom type under illumination by the electron beam. The transmitted electrons can be filtered with respect to energy loss and only those electrons with a specific energy loss (e.g., those associated with Ag) are chosen for imaging. In essence, these filtered electrons within a selected electron energy loss form an EFTEM image. In EELS analysis, the chemical sensitivity and size of the resolvable feature could be at 1% and smaller than 1 nm, respectively. Moreover, Pd, Ag, and U have close, but separable ionization edge energies in an EELS spectrum, which suggests that trace amounts of Ag samples should be detectable using EELS.

Ag, Pd, and U can be distinguished by using EELS because their edge energies are separated from each other (i.e., Pd M<sub>4,5</sub> 335 eV, Ag M<sub>4,5</sub> 367 eV, U N<sub>7</sub> 381 eV). (Edge energies obtained from Gatan's Chart of inner shell loss edge types and energies for EELS).

Although in 2013 EELS and EFTEM maps were successfully used to identify and confirm Ag at a triple point from Particle AGR1-632-035, where an Ag-rich precipitate was found by EDS, this technique was not routinely applied on all particles. This is mainly because the quantification of each precipitate is time consuming and not always successful due to sample thickness variances in the lamellae using standard practices. Further work on EELS and EFTEM continued under Nuclear Science User Facilities (NSUF)-funded projects in FY 2014 and FY 2016.

**2.1.3.2 Particle AGR1-131-099.** In 2016, spectral images were collected in EFTEM mode using the Gatan (Tridiem) imaging filter at LANL on Particle AGR1-131-099 to quantitatively measure Pd, Ag, and U. Although elemental maps were obtained, quantification could not be fully determined, mainly due to the thickness limitations of the lamellae (results are shown in Section 3.4). EFTEM refers to a set of imaging techniques that use the energy loss spectrum that is present in the transmitted beam to create images with increased contrast and reduced chromatic aberration, and/or contain chemical information

about the material under study. The method for collection is to first move the specimen out of the field of view within the microscope and align the Gatan imaging filter at the magnification of interest. This process uses a standard Gatan routine that adjusts the magnetic lenses within the Gatan imaging filter to minimize the dispersion of the transmitted beam at the energy loss of interest that is selected by the user. In the present work, EFTEM maps for Pd, Ag, and U were collected at 300 kV using the jump ratio method for energy loss signals (ionization edges) at 335 eV (Pd), 367 eV (Ag), and 381 eV (U). In the jump-ratio approach, pre-edge and post-edge images are collected at energies within a pre-determined window width. In the present case, each of these windows was set to a final width of 15 eV. In the jump-ratio approach, the post-edge image is divided by the corresponding pre-edge image to create an image that indicates relative distribution of the element of interest in the field of view.

#### **2.1.4 Quantitative Chemical Composition of Fission Product Precipitates using Atom Probe Tomography**

The atom probe tomography (APT) technique uniquely provides both an atom's position and elemental identity in real 3D space at near-atomic resolution. The technique detects all elements and quantitative analysis that can be done accurately down to the 1-ppm level. The first APT probe tips were prepared using the dual-beam FEI Quanta 3D FIB with a lift-out technique at the electron microscopy laboratory (EML) from specimen AGR1-632-035 during July 2013. A typical APT tip is needle-like—about 2 to 3  $\mu\text{m}$  in length. The diameter of the tip's apex is about 20 to 100 nm, and three tips are typically mounted onto the A, C, and E posts of one standard five-finger Cu grid for a FIB sample. A Hummingbird Tomography holder was used to characterize the APT tips in the STEM. APT data were analyzed by using CAMECA Interactive Visualization and Analysis Software package Version 3.6.12. This Interactive Visualization and Analysis Software is an all-in-one software package that can do quantitative data analysis of data collected by the local electrode atom probe (LEAP) instrument.

Particles AGR1-632-035 and AGR1-632-034 were chosen for this first APT analysis because Ag was identified in the SiC structure during the earlier STEM examination in March 2013. The APT experiments were primarily funded by NSUF Rapid Turn Around Experiment (NSUF-RTE) awards 3 years as a collaborative effort with the University of Wisconsin-Madison and Boise State University (see Appendix A). APT measurements were carried out by using a CAMECA LEAP 4000X HR 3D atom probe. The earlier lessons-learned results were reported in the 2013 milestone report by van Rooyen (2013) with the latest successful results (December 2015) on APT tips prepared from Particle AGR1-632-034 reported in Section 3.1 (van Rooyen et al., 2017, Wu et al., 2016).

These first-of-a-kind APT analyses on irradiated SiC provided numerous valuable lessons, and challenges were addressed and minimized. During the first few APT runs, useful data were not obtained due to frequent tip fractures. Contributing toward these fractures were the presence of a surface oxidation layer of about 2-nm thick, flexible copper grids, inherent properties of irradiated SiC, formation of an amorphous surface layer during FIB sample preparation, and the inconsistent profile contours of the tips. In addition, one of the biggest challenges is to prepare tips with fission product features in the top center of the tip to a depth of less than 100 nm from the tip apex. This requires a highly skilled FIB operator because many precipitates are not visible at the SEM resolution. Additionally, the distance between the FIB and APT facilities contributed to oxidation of the tips. This was later partially resolved by the sample packaging method and transport logistics.

One of the largest challenges was to obtain a large enough volume to encounter features of interest due to the extremely brittle irradiated SiC sample, which has low electric and thermal conductivities and big differences in the evaporation field needed in LEAP runs between C (142 V/nm C+, 103 V/nm C++) and Si (45 V/nm Si+ and 33 V/nm Si++). By tailoring LEAP running parameters, the mode, sample-setting temperature, laser energy, and pulse frequency for optimized SiC APT, data were obtained for unirradiated surrogate and irradiated TRISO samples. The most effective LEAP parameters for the unirradiated surrogate and irradiated TRISO samples are shown in Table 7. A Pd-Ag-U precipitate was

successfully quantified using these laser parameters for the irradiated sample and is reported in Section 3.1.2.

Table 7. The most effective LEAP parameters determined to date.

	Unirradiated SiC	Neutron Irradiated SiC
Specimen temperature (K)	90	95
Laser pulse energy (pJ)	100	300
Pulse frequency (kHz)	200	125

## 2.2 Techniques to Determine Crystallographic Information

The technology road undertaken for establishing the required resolution needed to determine the crystallographic information at the location of the nano-precipitates was reported previously (Demkowicz et al., 2015a; van Rooyen et al., 2012b, van Rooyen 2013). To elucidate the influence of grain boundary character on fission product migration in individual grain boundaries, it is necessary to employ techniques that can determine the misorientation across individual grain boundaries that contain fission products and across grain boundaries that do not contain fission products. Although EBSD and transmission Kikuchi diffraction (TKD) are well-established methods and suitable for determining larger area grain characteristics, it was found that only the PED technique provided the necessary resolution needed to link the STEM-based data (location and composition) on precipitates with the same area's crystallographic information. PED (ASTAR) from NanoMEGAS is a TEM-based technique (FEI Tecnai F30 STEM FEG) at CAES, which fully utilizes the high-spatial resolution potential of TEM (e.g., less than 2 nm with FEG TEM) to automatically do crystal orientation and phase mapping on nanometer-size grains.

PED is capable of providing crystallographic orientation and phase mapping, grain boundary/precipitation orientation relationships, grain boundary character identification, and dislocation substructure. These are valuable pieces of information for understanding fission product transport processes at grain boundaries during irradiation. Unlike the EBSD-SEM, which relies on Kikuchi lines obtained from the sample surface, in TEM-based grain orientation mapping, controlled by the NanoMEGAS DigiSTAR unit, the electron beam is stepped across the sample area of interest. Electron diffraction (spot) patterns are obtained at each step and individual patterns are compared with pre-calculated electron diffraction patterns via cross-correlation matching techniques for orientation and phase mapping. Particularly, when combined with electron beam precession diffraction mode, the technique provides ultra-precise orientation and phase maps. The orientation resolution is less than 5 nm and as low as 1 nm, depending on electron probe size. Precession mode improves electron diffraction quality by increasing the number of diffraction spots (almost double) and avoiding Kikuchi lines, which is also the only possible way for distinguishing multiple phases in one sample. The ASTAR technique also provides an ultra-fast data acquisition with external/internal charge-coupled device (e.g., approximately 25 minutes for an area of  $5 \times 5 \mu\text{m}^2$ , 20 nm step size [62,500 points]).

Figure 4 provides a schematic overview of the three crystallographic methods explored as part of AGR-1 PIE (complemented by NSUF-RTE funds). The red stars indicate the most successful method used to directly correlate fission product behavior with grain boundary characteristics. PED crystallographic measurements were first successfully proven on unirradiated samples (Lillo, van Rooyen, and Wu 2016) and concluded that the standard FIB preparation technique currently used for STEM analysis is suitable to provide quality data. Thereafter, PED measurements were deployed on lamellae from most irradiated particles examined and are reported in Section 3. More specific details on the process applied for PED measurements on the SiC layer of the TRISO-coated particle are provided in Lillo, van Rooyen, and Wu (2016), and Lillo and van Rooyen (2016).

Although the number of precipitates interrogated in this work is relatively large, the results still only represent a rather small fraction of the SiC layer in a single TRISO particle. The volume of SiC interrogated in this study is extremely small in comparison to the total volume of the SiC layer surrounding the fuel kernel (approximately  $1 \times 10^{-6} V_{tot}^{SiC}$ ), leaving open the possibility that not all types of fission-product-containing precipitates have been found. The microstructure and distribution of fission products may vary significantly on a local level. Furthermore, each fuel compact typically contains over 4,100 TRISO fuel particles; therefore, each TRISO fuel particle experiences slightly different operating conditions, including thermal gradients and irradiation conditions. This may contribute to the relatively large release of Ag from some TRISO-coated fuel particles while other particles from the same compact exhibit a high degree of retention after irradiation.

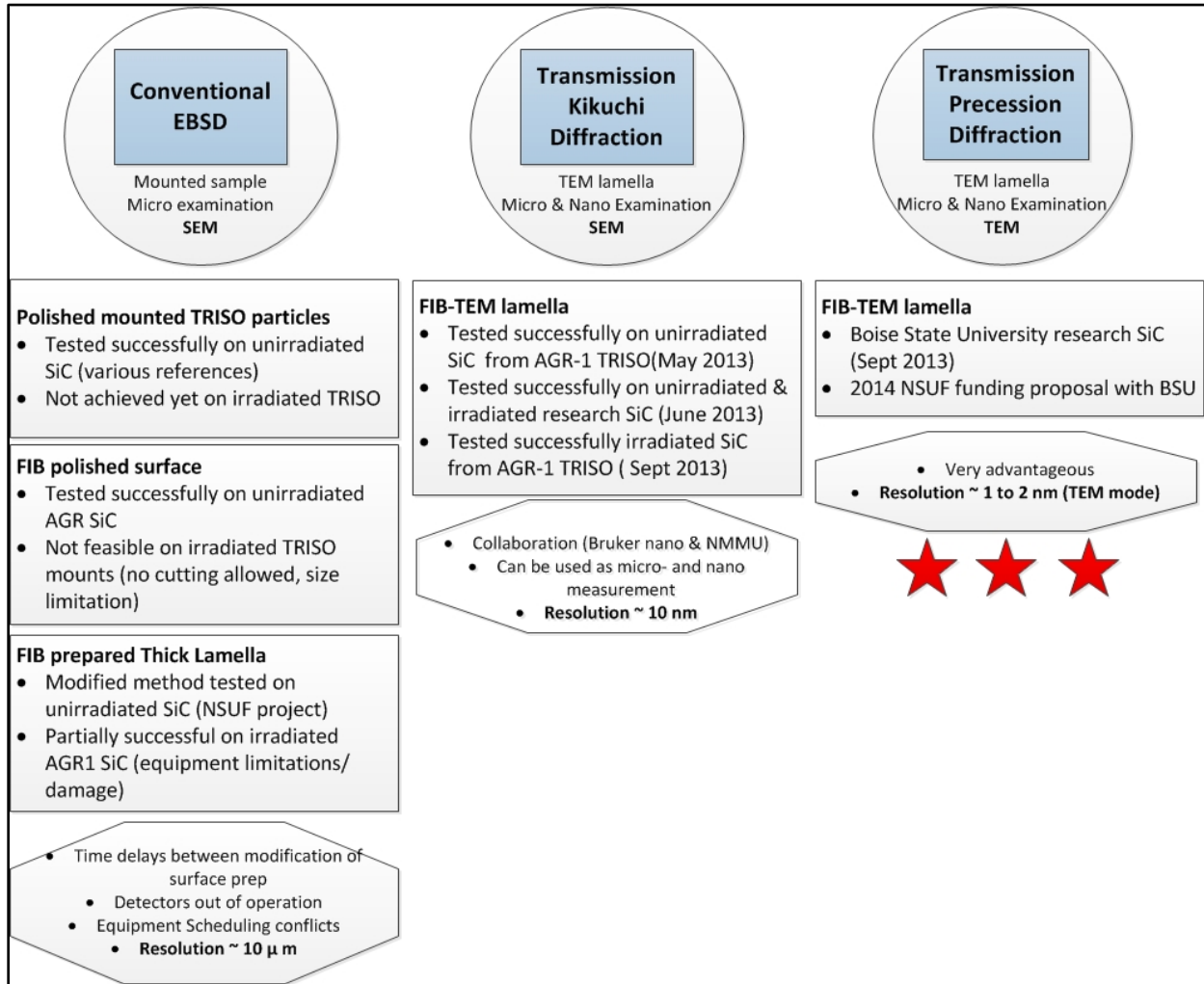


Figure 4. Schematic overview of the crystallographic work done as part of AGR-1 PIE with complimentary projects and other funding sources (stars indicating the most successful results obtained at present).

## 2.3 Phases and Crystal Structure of Fission Products

During the first TEM analysis in 2012, data about individual precipitates were collected using a JEOL 2010 TEM operating at a nominal voltage of 200 kV. Images and diffraction patterns were digitally collected using a Gatan Ultrascan camera and Gatan Digital Micrograph software. EDS spectra were collected using an Oxford Link Petafet EDS detector with a SiLi crystal, nominal 20-eV channel width,



nominal energy range from 0 to 20 keV, and nominal 136-eV resolution. The spectra were collected and qualitatively analyzed using Link ISIS software, ISIS Suite Revision 3.2. This represents ongoing work aimed at a detailed characterization of precipitates within the SiC and IPyC layers.

Diffraction patterns were acquired using a nominal camera length of 30 cm and a selected area aperture with an effective diameter of approximately 155 nm. Because the precipitates are small, tilting an individual precipitate to record diffraction patterns from different zone axes was difficult. Instead, precipitates in strongly diffracting orientations were identified in images and their diffraction patterns were recorded. Phase identification for precipitates in the SiC layer were based on data in the International Centre for Diffraction Data's PDF4+ 2010 database, which contains over 300,000 entries with detailed information that can be used to identify specific phases. Qualitative chemical analyses were used to reduce the number of possible identifications to materials containing some combination of C, Si, Zr, Pd, and U. Elimination of all SiC structures except 3C, 4H, and 6H reduced the number of possible entries to about 550. The International Centre for Diffraction Data's Sieve+ software was used to further limit the number of possible identifications based on characteristics of individual diffraction patterns. However, typically about 125 possible records were consistent with both the qualitative chemical analyses and the diffraction data for each diffraction pattern.

To obtain additional clarification on the structure of the precipitates and phases present, especially on the smaller and nano-sized precipitates, HRTEM examination was performed on specific lamella. The techniques are described under Section 2.1.2.4. HRTEM examination was performed on selected Lamella from particles namely AGR1-411-030, AGR1-131-066, AGR1-131-099, AGR1-433-001 and AGR1-433-004. The main objective of this examination was to obtain atomic high-resolution images of individual fission product precipitates with corresponding EDS or EELS analysis to provide information on the structure and composition of the fission product precipitates.

### **3. ADVANCED CHARACTERIZATION RESULTS ON IRRADIATED COATED PARTICLES**

Multiple journal articles, conference papers, and reports were issued to-date based on these examinations. However, in this section, only a summary of the main findings published previously are presented, which includes fission products identification and location, grain boundary characteristic, and fission product structural results. Unpublished chemical compositional trend analyses and new grain boundary characteristic data are provided for most particles examined.

#### **3.1 Irradiated Baseline Fuel Examination: Compact 6-3-2**

Particles AGR1-632-030, AGR1-632-034, and AGR1-632-035 were the first irradiated TRISO-coated particles examined. Therefore, many of the advanced microscopy techniques and methodologies were developed from examining these three particles. Lessons learned from these results were then applied to particles from the subsequent compacts that were examined. Although basic TEM analysis on the Compact 6-3-2-coated particles was completed in FY 2012 by van Rooyen et al., (2012), some microstructural questions remained to be addressed, namely, accurate quantification of fission product elemental composition, accurate distributions of elements in a specific precipitate, the phases of precipitates, fission product (specifically Ag, Pd) transport mechanisms through "intact" layers, and precipitate crystallographic properties.

The results in this section list the main findings reported in the various referenced journal articles and reports. Although examinations were performed on particles AGR1-632-030, AGR1-632-034, and AGR1-632-035, mainly recent results from Particle AGR1-632-035 are provided here.

##### **3.1.1 Particle Selection and Analysis Performed**

Compact 6-3-2 particles were selected based on the ratio of the measured Ag-110m activity to the predicted Ag-110m activity (shown in Figure 5) to investigate microstructural characteristics related to

Ag retention (Demkowicz et al., 2012). From these distributions, three particles were chosen to represent particles having a low measured-to-predicted Ag-110m ratio (Particle AGR1-632-030 ratio is 0.21) and high ratio (AGR1-632-034 ratio is 0.65 and AGR1-632-035 is 0.79 ratio). Figure 5 indicates that particles exhibit Ag retention ranging from about 1 to 90% of the predicted inventory.

**3.1.1.1 Lamella Locations for Particle AGR1-632-035.** Compact 6-3-2, consisting of TRISO-coated particles made with baseline conditions, from the AGR-1 experiment was electrolytically deconsolidated and Particle AGR1-632-035 was selected for further microstructural analysis. This particle exhibited a Ag-110m retention fraction of about 80% in post-irradiation gamma spectroscopy scans after a nominal burnup of 11.4% FIMA, neutron fluence of  $2.6 \times 10^{25}$  n/m<sup>2</sup>, and a time-averaged, volume-averaged irradiation temperature of 1070°C (Hawkes 2014; Sterbentz 2013). (Note: the burnup, neutron fluence, and time-averaged, volume-averaged temperature are an average values for the compact. The actual values of these parameters experienced by this particular particle in this compact may have been significantly different depending on the location of this particle in the compact, which is not known.) Samples for TEM and STEM were selected from a polished cross section of the particle, and TEM samples (lamellae) were extracted and prepared by FIB techniques from the specific areas of the SiC layer shown in Figure 6, with the specific advanced microscopy and micro-analytical analyses performed for each particle indicated in Table 8.

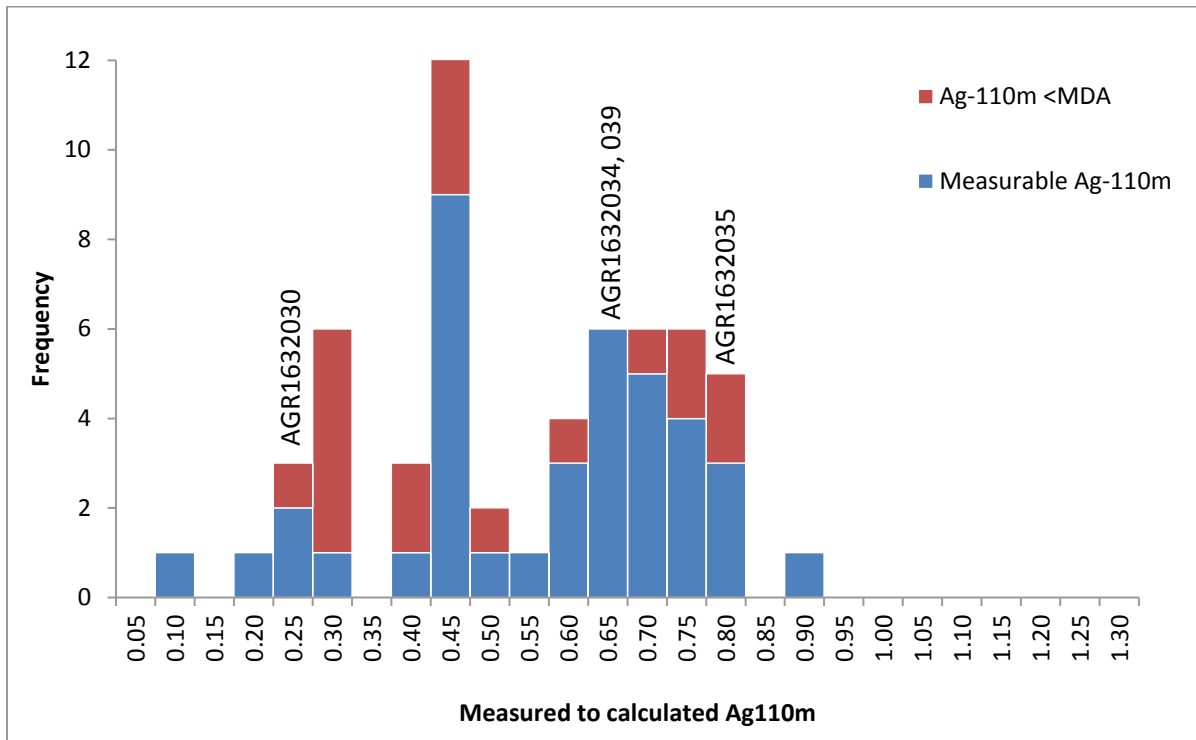


Figure 5. Distribution of the measured-to-calculated Ag-110m activity ratio for the irradiated Compact 6-3-2 particles (adapted from Demkowicz et al., 2012).

Table 8. Advanced microscopy and micro-analysis examination performed on Compact 6-3-2 particles.

Techniques	SEM <sup>a</sup> EDS/WDS	EELS/ EFTEM	STEM	EPMA	PED	APT	HRTEM
<b>Compact 6-3-2 (Baseline)</b>							
AGR1-632-030 (Low (21% ) Ag retention)	X <sup>a</sup>	—	Basic TEM <sup>b</sup>	—	—	—	—
AGR1-632-034 (High (65%) Ag retention)	X <sup>a</sup>	—	X	—	—	X	—
AGR1-632-035 (High (79%) Ag retention)	X <sup>a</sup>	X	X	—	X	X	—
<sup>a.</sup> Reported in separate report by van Rooyen et al., 2017. <sup>b.</sup> Reported in separate report by van Rooyen et al., 2012c.							

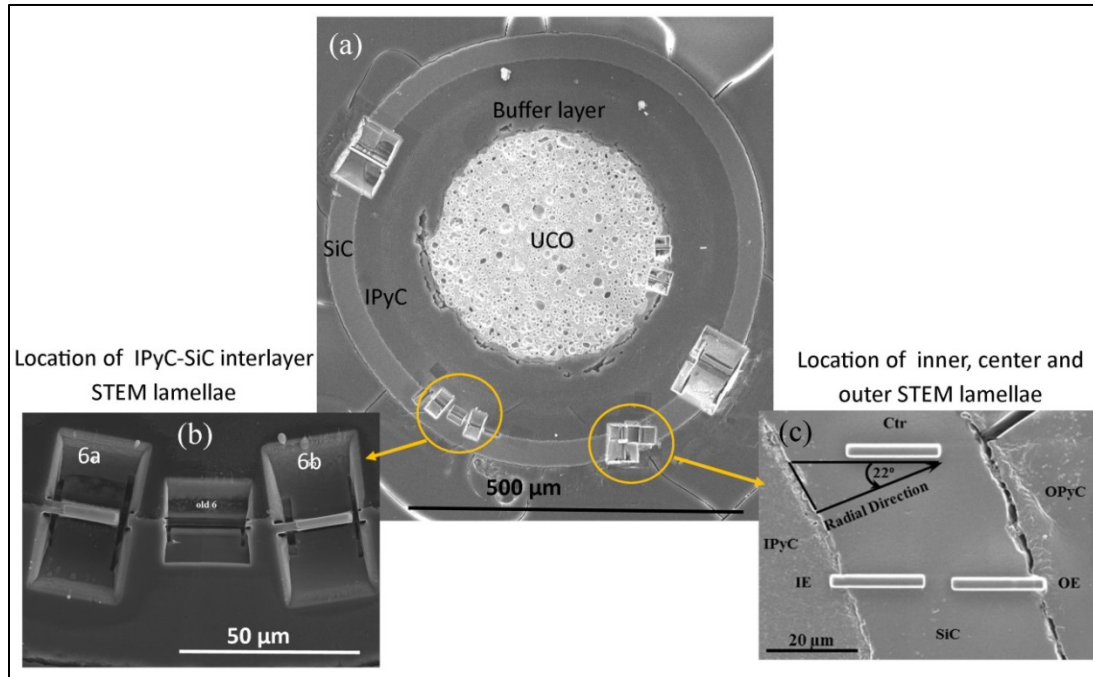


Figure 6. (a) SEM image of the polished cross section of AGR1-632-035, indicating the location of STEM lamellae, extracted by FIB methods, for advanced microstructural characterization. (b) The FIB Lamella Positions 6a and 6b. (c) FIB-prepared TEM samples were taken from the locations indicated for the inner (IE), center (Ctr), and outer (OE) lamellae. The center sample significantly overlaps the inner and outer samples.

### 3.1.2 Identification, Confirmation, and Quantification of Silver

As indicated in earlier sections, SEM and initial TEM investigations on particles from Compact 6-3-2 in 2012 could not identify Ag in the fission product network, mainly due to the resolution of the instruments available at that time and the overlap with Pd and U. Exploration of alternative methods and equipment in other facilities led to the first finding of Ag in 2013 (van Rooyen et al., 2013). Although this finding of Ag on triple points and grain boundaries catalyzed detailed research for the subsequent compacts with regards to location pathways, quantification was still an elusive challenge. Because EELS was used as a validation technique for the presence of Ag, the quantification by APT was then evaluated. Successful results in quantification of Ag (as shown in Section 3.1.2.2) were only recently attained due to

various challenges such as the brittle nature and small size and location of these precipitates (discussed in Section 2.1.4).

**3.1.2.1 First Identification of Silver.** STEM examinations of lamellae from Particle AGR1-632-035, provided the first evidence of nano-sized Ag precipitates at triple-points (Figure 7) and grain boundaries in the SiC on the edge of the SiC-IPyC interface. Cadmium was also found to be present in the triple junctions (Figure 8).

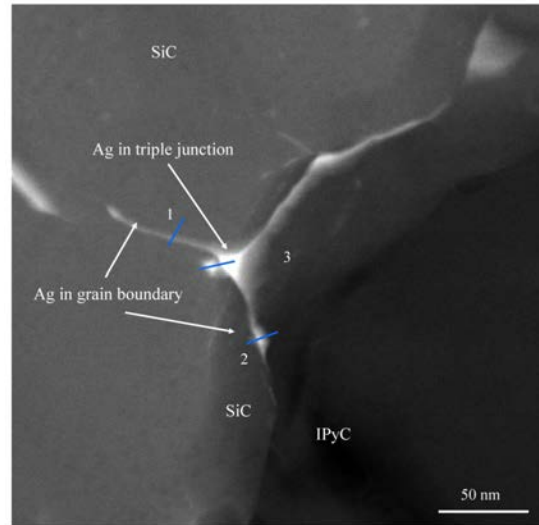


Figure 7. Image showing the HAADF STEM image of Ag-containing grain boundaries and triple junction at the outmost edge of the SiC adjacent to IPyC (van Rooyen et al., 2014b).

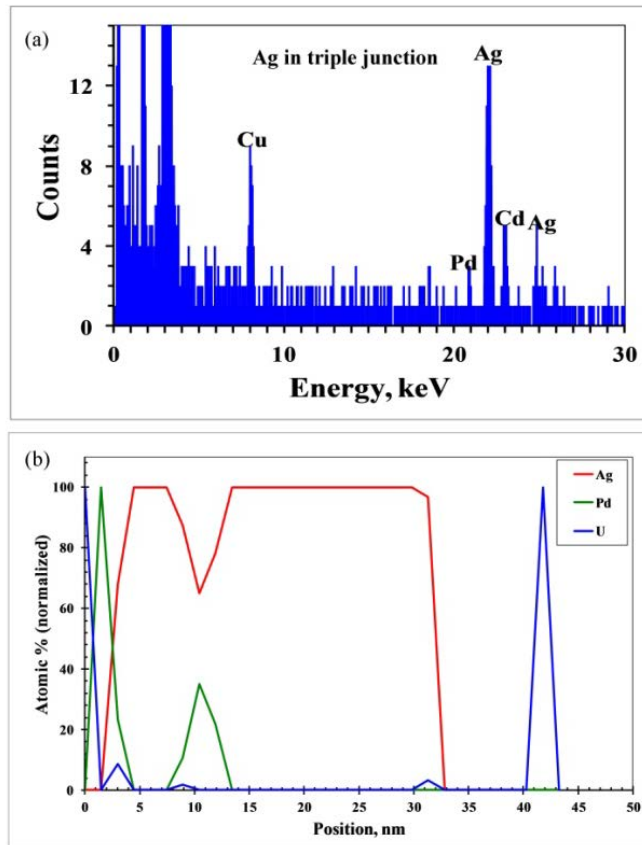


Figure 8. Image showing (a) the EDS spectrum that identifies the Ag  $K\alpha_{\text{Ave}}$  peak at 22.104 keV, the Ag  $K\beta_{\text{Ave}}$  at 24.987 keV and the presence of Cd in the center of the triple junction shown in Figure 7, and (b) the EDS linescan profile through the triple junction, indicating the presence of Ag. Although no Pd is observed in the triple junction, Pd and U are identified in the SiC matrix adjacent to this triple junction (Cu is an artifact from the FIB grid holder) (van Rooyen et al., 2014b).

### 3.1.2.2 Quantification of Chemical Composition Using Atom Probe Tomography.

Representative scanning TEM HAADF images of an atom probe sample tip from unirradiated surrogate TRISO fuel and corresponding reconstructed 3D elemental maps of C and Si are shown in Figure 9. The diameter of the sample tip apex is about 50 nm. C and Si atoms are uniformly distributed in the volume ( $48 \times 49 \times 293$  nm). Quantitative analysis shows that the concentrations of C and Si within this volume are 44.81 at.% (error 0.01 at.%) and 53.96 at.% (error 0.01 at.%), respectively. About 1.2 at.% O was also detected within this volume, which could be mostly attributed to the air. More APT data were also obtained from the unirradiated surrogate TRISO fuel samples and they show similar concentrations of C and Si of about 45 at.% and 54 at.%, respectively, while the remainder is likely O. This may indicate localized non-stoichiometry of the SiC and the results needs to be explored in more depth.

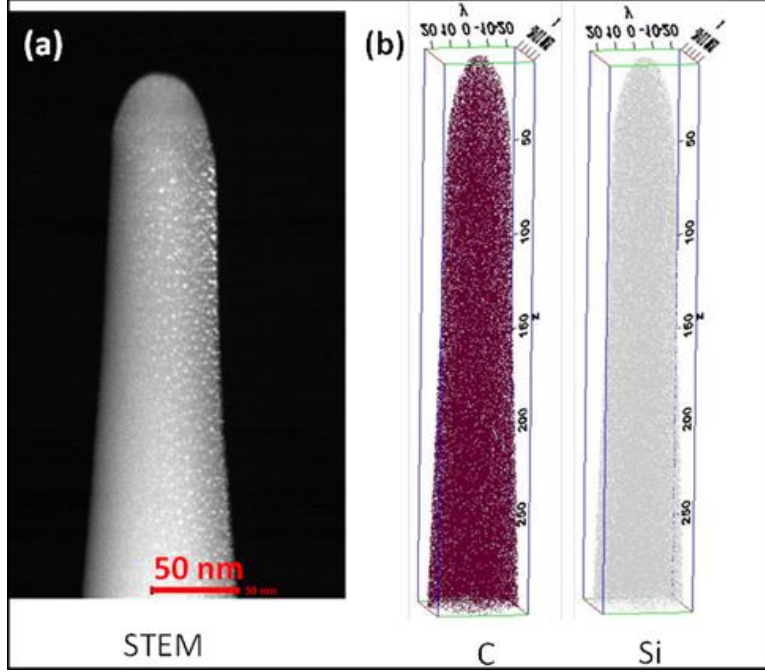


Figure 9. STEM HAADF image of (a) an unirradiated surrogate TRISO APT sample tip and (b) corresponding reconstructed 3D APT maps of C and Si in a volume size of  $48 \times 49 \times 293 \text{ nm}^3$  (Wu et al., 2016).

Figure 10(a) shows a STEM image of an irradiated TRISO APT tip and corresponding LEAP data (Figure 10[b] and [c]). An Ag-Pd-U phase is identified at one side of the reconstructed volume (Figure 10[b]), which corresponds to the dashed-red-line circled region in Figure 10(a). The mass spectrum (Figure 10[c]) clearly indicates an isotope of Ag-109+ among Pd isotopes, as well as U-235+2 and U-238+2 isotopes.

By selecting 3 at.% Pd as an interface, a proxigram calculated across the interface (Figure 11) clearly indicates a Pd, Ag, and U-enriched phase. This phase also contains Si and some C.

A 3D elemental map of a smaller volume (i.e.,  $6 \times 6 \times 6 \text{ nm}^3$ ) selected to exemplify this Pd-Ag-U-rich phase is shown in Figure 12. Quantitative analysis within the Pd-Ag-U-rich phase shows the normalized concentrations of Pd, Ag, U, Si, and C are 12.1 at.% (error 0.3 at.%), 3.5 at.% (error 0.2 at.%), 3.3 at.% (error 0.1 at.%), 60.0 at.% (error 0.3 at.%), and 21.2 at.% (error 0.2 at.%), respectively.

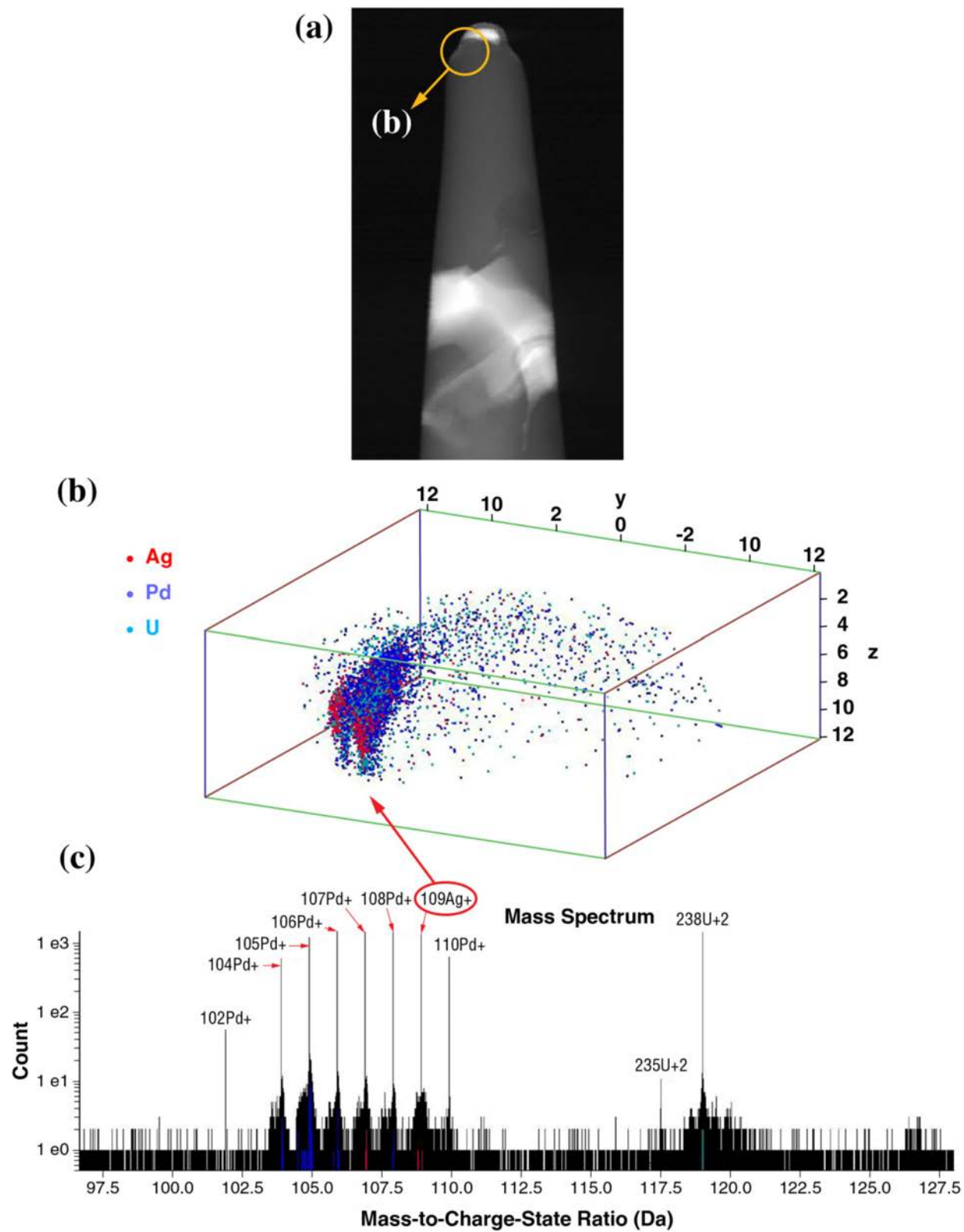


Figure 10. STEM HAADF image of (a) an irradiated TRISO APT sample tip, (b) corresponding reconstructed 3D APT maps showing a Ag-Pd-U-rich phase in a volume size of  $32 \times 31 \times 12 \text{ nm}^3$ , and (c) mass spectrum showing detected isotopes of Ag, Pd, and U (Wu et al., 2016).



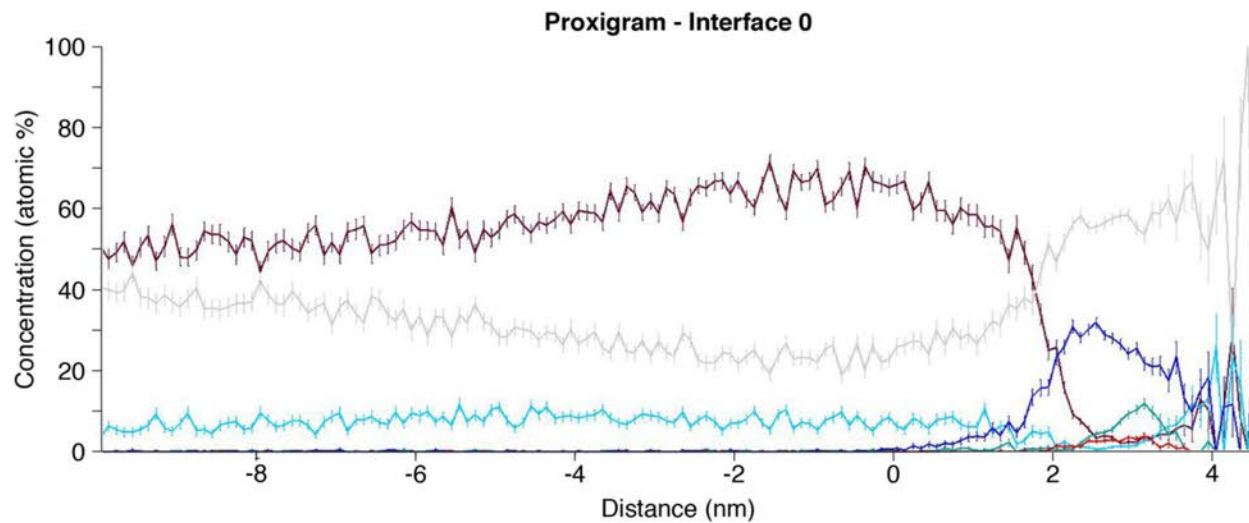


Figure 11. Proxigram with respect to a 3 at.% Pd iso-concentration surface, clearly indicating a Pd (blue), Ag (red), and U (green)-enriched phase. This phase also contains Si (grey), some C (brown), and oxygen (turquoise) is noticed as well (Wu et al., 2016).

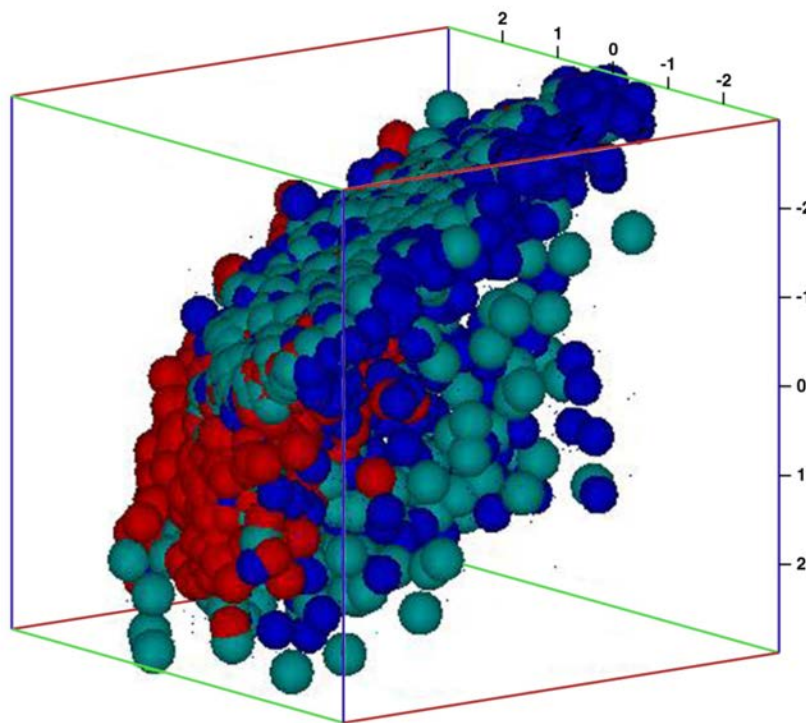


Figure 12. 3D elemental map of Pd (blue), Ag (red), and U (green) in a selected small volume of  $6 \times 6 \times 6 \text{ nm}^3$  (Wu et al., 2016).



### 3.1.3 Chemical Composition and Distribution of Minor Elements on Particle AGR1-632-035

This section reports the qualitative chemical composition of minor elements on Particle AGR1-632-035 to first determine the type of fission products present; second, determine the location of these particles in relation to the SiC layer thickness; and, last, determine fission product elemental composition. The reported fission product precipitate compositions (atomic %) are qualitative or semi-quantitative in nature. Fission product elements with measured concentrations above 0.20 at. % are taken as present and adhered to at least a 95% confidence limit (as described in Section 2.1.2.3).

A summary of the minor elements present in these three lamellae are shown in Table 9 with Sections 3.1.3.1 to 3.1.3.3 describing the precipitates found in the inner, center, and outer area of the SiC layer. From this summary, it is determined that Pd, Ag, Ce, Eu, U, and Pu were found in the SiC layer. It is also determined that no U is present in the outer area of the SiC layer, Pu is found only in the inner area, and no Cs was found in the SiC layer. Figure 13 shows a qualitative trend analysis of precipitate composition (for Pd, Ag, and U only) as a function of the approximate distance from the SiC-IPyC interface of Particle AGR1-632-035. This schematic presentation also shows the movement of Pd and Ag through the full thickness of the SiC layer with U only up to approximately 22  $\mu\text{m}$ . No specific trend of the concentration versus distance correlation is determined. Further, the trend analysis of Pd/U and Pd/Ag ratios in relation to distance also do not exhibit a correlation. (Earlier TEM work on other areas [lamellae] from AGR1-632-034 and AGR1-632-035 show also elements like Pu, Sr, Cs, Cd, and Zr present in precipitates analyzed [van Rooyen et al., 2012, 2012b, 2014, 2016, and Leng et al., 2016]. These elements are not included in Table 9 to keep consistency for chemical composition comparison purposes on the program significant elements with all the other compact lamellae discussed in this report).

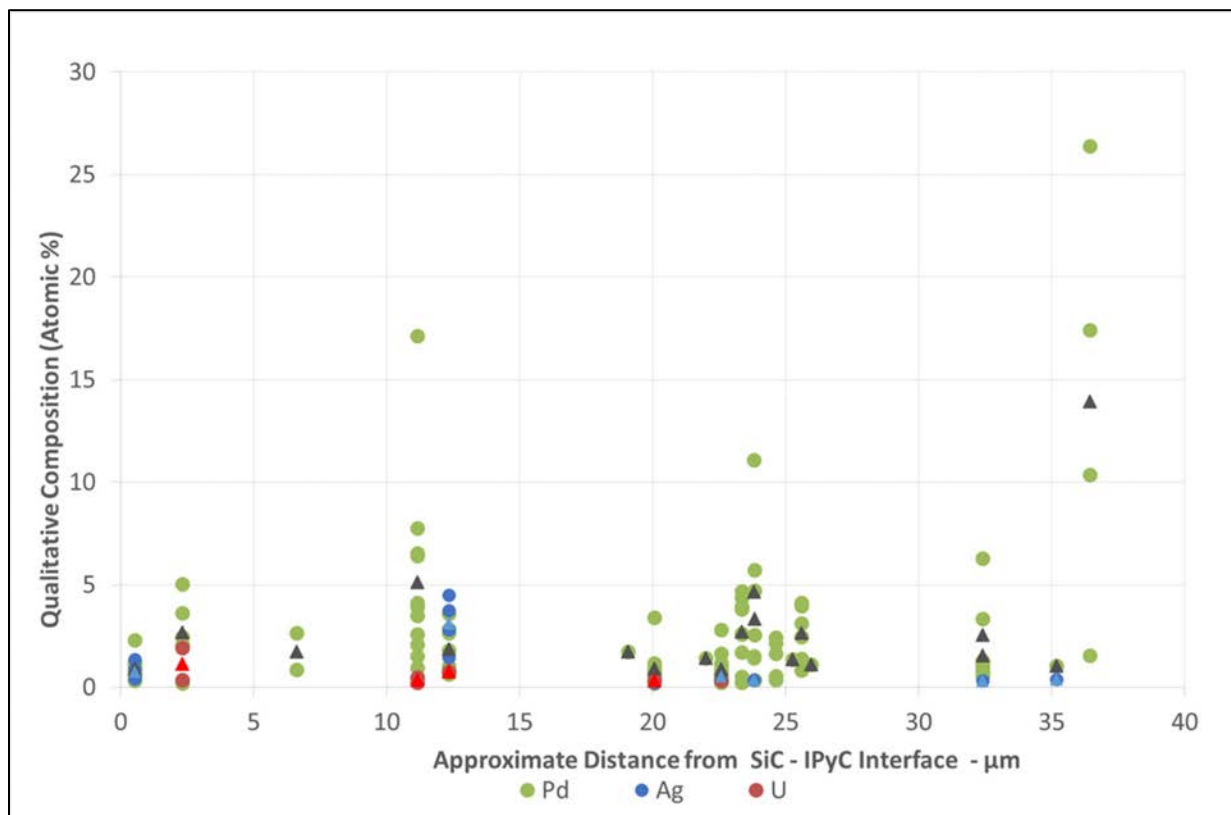


Figure 13. Qualitative trend analysis of precipitate composition (Pd, Ag, and U only) as a function of the approximate distance from the SiC-IPyC interface of Particle AGR1-632-035.

Table 9. Identification of minor elements present in fission product precipitates in the SiC layer of Particle AGR1-632-035.

Lamella	Area	Elements Present									Precipitate Identification
		C	Si	Pd	Ag	Cs	Ce	Eu	U	Pu	
Inner Figure 14	Area 1	X	X	X	X		X				Pd, Ag, Pd-Ag, Pd-Ce
	Area 2	X	X	X					X		Pd, Pd-U
	Area 3	X	X	X							Pd
	Area 4	X	X	X			X		X		Pd, Pd-U, Pd-Ce
	Area 5	X	X	X	X				X	X	Pd, Ag, Pd-Ag, Pd-Pu, Pd-U-Pu
Inner Summary		X	X	X	X		X		X	X	
Center Figure 18	Area 1	X	X	X			X				Pd, Ce,
	Area 2	X	X	X	X				X		Pd, Ag, Pd-U
	Area 3	X	X	X	X				X		Pd, Pd-Ag, Pd-U
	Area 4	X	X	X							Pd
	Area 5	X	X	X	X		X				Pd, Pd-Ag
	Area 6	X	X	X			X				Pd, Pd-Ce
	Area 7	X	X	X							Pd
Center Summary		X	X	X	X		X		X		
Outer Figure 23	Area 1	X	X	X			X	X			Pd, Pd-Ce, Pd-Ce-Eu
	Area 2	X	X	X							Pd
	Area 3	X	X	X							Pd
	Area 4	X	X	X							Pd
	Area 5	X	X	X							Pd
	Area 6	X	X	X	X						Pd, Pd-Ag
	Area 7	X	X	X	X		X				Pd, Pd-Ag-Ce
	Area 8	X	X	X				X			Pd, Pd-Eu
Outer Summary		X	X	X	X		X	X			
Summary SiC Layer		X	X	X	X		X	X	X	X	

**3.1.3.1 Chemical Composition in the Inner Area of the SiC Layer.** The inner area of the SiC layer is defined as the STEM Lamella containing the IPyC/SiC interface and corresponds to the Lamella labeled “IE” in Figure 6(c). Figure 14 shows the Lamella fabricated from the inner area of Particle AGR1-632-035 with five areas marked in yellow (labeled 1 through 5), where precipitates were examined and the composition determined by qualitative EDS analysis (presented in Tables 9 through 11 and Figure 15 through Figure 17). From these qualitative analyses it was determined that precipitates contain mainly Pd, with Ag, Ce, U, Eu, and Pu present. No Cs or Eu was found to be present in the precipitates examined.

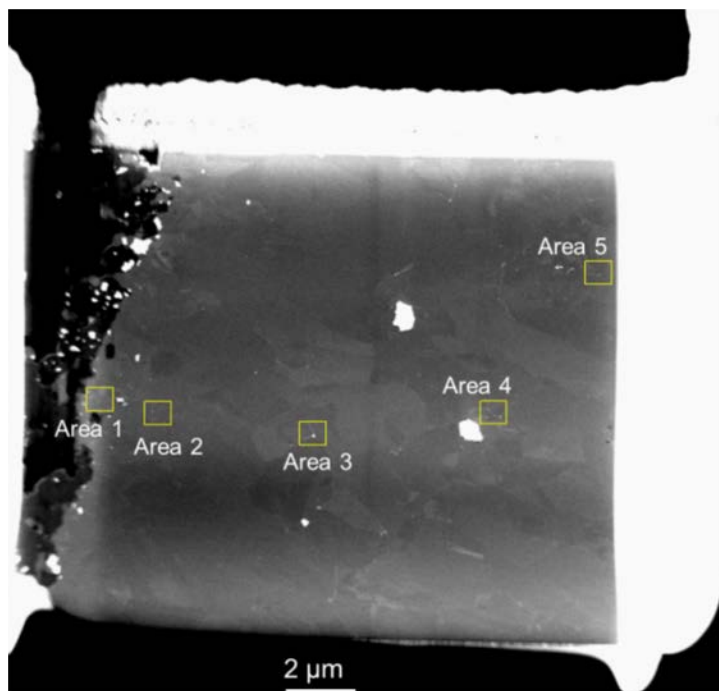


Figure 14. Large field of view STEM dark field image taken from the Lamella fabricated from the inner area (marked “IE” in Figure 6[b]) of the SiC layer from TRISO Particle AGR1-632-035.

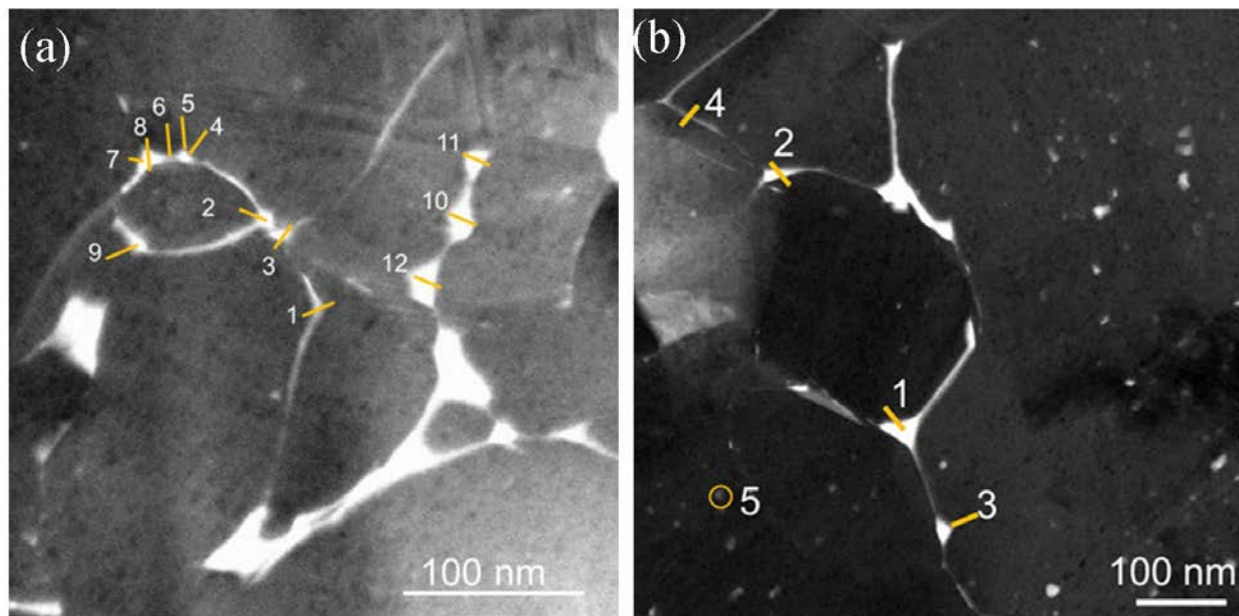


Figure 15. STEM HAADF image combined with EDS labeling to track the chemical composition of fission product precipitates from the inner area of the SiC layer from TRISO Particle AGR1-632-035 within (a) Area 1 and (b) Area 2 highlighted in Figure 14. Note the reported chemical compositions are in Table 10.

Table 10. Reported qualitative EDS compositions from the inner area of the SiC layer from TRISO Particle AGR1-632-035, taken from Areas 1 and 2 that are highlighted in Figure 14.

Precipitate Number	Concentration (at.%)									Precipitate Identification
	C	Si	Pd	Ag	Cs	Ce	Eu	U	Pu	
Area 1										
1	44.08	54.63	1.25	0.00	0.00	0.00	0.00	0.00	0.04	Pd
2	34.68	64.84	0.48	0.00	0.00	0.00	0.00	0.00	0.00	Pd
3	44.09	54.81	1.10	0.00	0.00	0.00	0.00	0.00	0.00	Pd
4	46.06	52.28	0.76	0.90	0.00	0.00	0.00	0.00	0.00	Pd-Ag
5	48.27	50.99	0.32	0.42	0.00	0.00	0.00	0.00	0.00	Pd-Ag
6	44.55	55.33	0.12	0.00	0.00	0.00	0.00	0.00	0.00	
7	45.05	53.80	0.68	0.47	0.00	0.00	0.00	0.00	0.00	Pd-Ag
8	51.46	48.42	0.13	0.00	0.00	0.00	0.00	0.00	0.00	
9	49.90	48.65	0.58	0.00	0.00	0.85	0.00	0.02	0.00	Pd-Ce
10	44.65	54.23	0.94	0.00	0.00	0.00	0.00	0.15	0.04	Pd
11	46.13	51.57	2.31	0.00	0.00	0.00	0.00	0.00	0.00	Pd
12	41.92	56.58	0.15	1.36	0.00	0.00	0.00	0.00	0.00	Ag
Area 2										
1	46.56	47.87	3.63	0.00	0.00	0.00	0.00	1.94	0.00	Pd-U
2	52.64	42.29	5.03	0.00	0.00	0.00	0.00	0.04	0.00	Pd
3	50.85	46.27	2.46	0.00	0.00	0.00	0.00	0.36	0.07	Pd-U
4	52.88	44.88	2.07	0.12	0.00	0.00	0.00	0.05	0.00	Pd
5	52.78	46.94	0.20	0.00	0.00	0.00	0.00	0.06	0.02	Pd

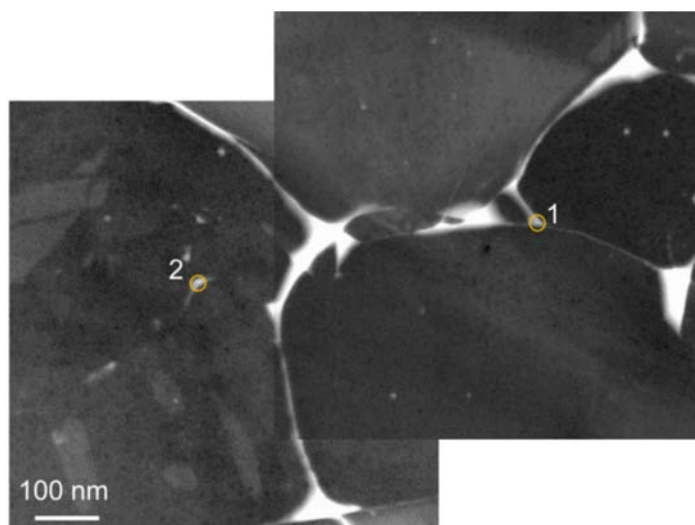


Figure 16. STEM HAADF image combined with EDS labeling to track the chemical composition of fission product precipitates from the inner area of the SiC layer from TRISO Particle AGR1-632-035 within Area 3 highlighted in Figure 14. Note the reported chemical compositions are in Table 11.

Table 11. Reported qualitative EDS compositions from the inner area of the SiC layer from TRISO Particle AGR1-632-035, taken from the subtended Area 3 highlighted in Figure 14.

Precipitate Number	Concentration (at.%)									Precipitate Identification
	C	Si	Pd	Ag	Cs	Ce	Eu	U	Pu	
1	48.81	48.39	2.64	0.11	0.00	0.00	0.00	0.00	0.05	Pd
2	46.02	53.10	0.87	0.00	0.00	0.00	0.00	0.00	0.00	Pd

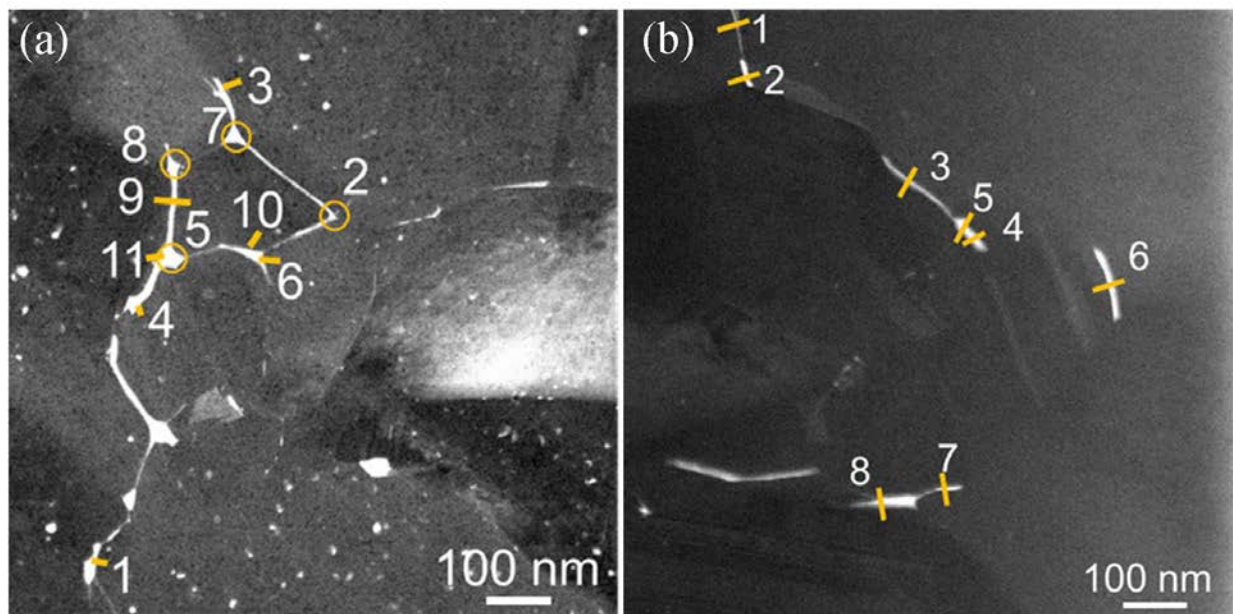


Figure 17. STEM HAADF image combined with EDS labeling to track the chemical composition of fission product precipitates from the inner area of the SiC layer from TRISO Particle AGR1-632-035 within the subtended (a) Area 4 and (b) Area 5 highlighted in Figure 14. Note the reported chemical compositions are in Table 12.

Table 12. Reported qualitative EDS compositions from the inner area of the SiC layer from TRISO Particle AGR1-632-035 that are taken from subtended Areas 4 and 5 highlighted in Figure 14.

Precipitate Number	Concentration (at.%)									Precipitate Identification
	C	Si	Pd	Ag	Cs	Ce	Eu	U	Pu	
Area 4										
1	51.01	46.83	0.96	0.00	0.00	1.03	0.00	0.15	0.03	Pd-Ce
2	57.06	41.39	1.52	0.00	0.00	0.00	0.00	0.03	0.00	Pd
3	52.56	44.59	2.60	0.00	0.00	0.00	0.00	0.24	0.00	Pd-U
4	52.69	40.89	6.42	0.00	0.00	0.00	0.00	0.00	0.00	Pd
5	45.62	37.22	17.15	0.00	0.00	0.00	0.00	0.00	0.01	Pd
6	49.40	46.54	3.93	0.00	0.00	0.00	0.00	0.00	0.13	Pd
7	50.50	44.83	4.13	0.00	0.00	0.00	0.00	0.49	0.05	Pd-U
8	48.84	44.62	6.55	0.00	0.00	0.00	0.00	0.00	0.00	Pd
9	52.75	45.05	2.08	0.00	0.00	0.00	0.00	0.10	0.03	Pd
10	54.48	41.99	3.51	0.00	0.00	0.00	0.00	0.03	0.00	Pd
11	57.33	34.92	7.75	0.00	0.00	0.00	0.00	0.00	0.00	Pd
Area 5										
1	48.31	49.87	1.81	0.00	0.00	0.00	0.01	0.00	0.00	Pd
2	40.21	55.10	0.66	3.75	0.00	0.07	0.21 (possible overlap)	0.00	0.00	Pd-Ag
3	49.45	46.89	3.59	0.00	0.00	0.07		0.00	0.00	0.00
4	44.36	52.65	2.64	0.00	0.00	0.00	0.00	0.15	0.20	Pd-Pu
5	46.20	49.79	2.84	0.00	0.00	0.00	0.07	0.78	0.33	Pd-U-Pu
6	43.72	53.64	1.01	1.46	0.00	0.00	0.05	0.12	0.00	Pd-Ag
7	44.02	52.52	0.64	2.81	0.00	0.00	0.00	0.00	0.02	Pd-Ag
8	49.49	45.66	0.17	4.50	0.00	0.10	0.09	0.00	0.00	Ag

### 3.1.3.2 Chemical Composition in the Center Area of the Silicon Carbide Layer.

Figure 18 shows the Lamella fabricated from the center area (marked “Ctr” in Figure 6[b]) of the SiC layer from Particle AGR1-632-035, with seven areas marked in yellow (labeled 1 through 7) where precipitates were examined and the composition determined by qualitative EDS analysis (presented in Tables 13 through 16 and Figures 19 through 22). From these qualitative analyses it was determined that precipitates contain mainly Pd, with Ag, Ce, and U present. No Cs, Pu, or Eu were found to be present in the precipitates examined.

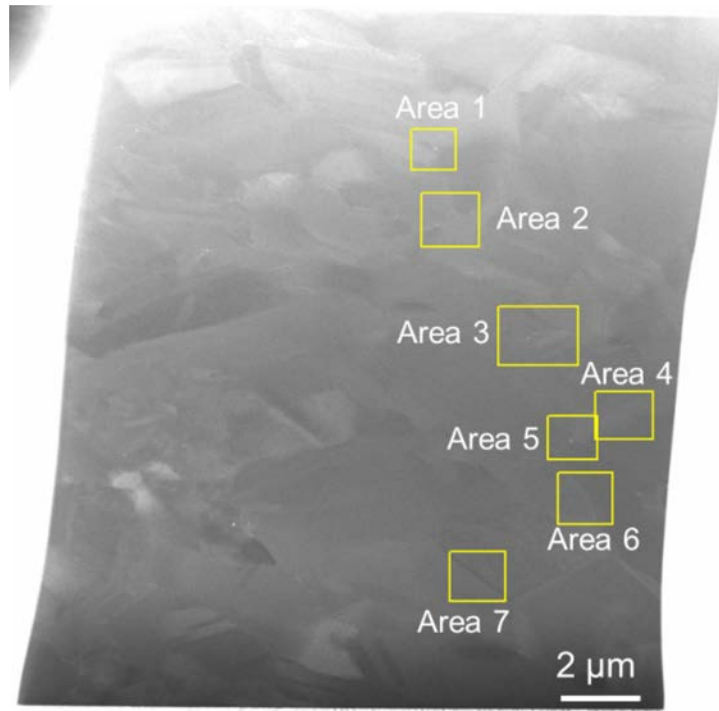


Figure 18. Large field of view STEM dark field image taken from the center area (the “ctr” Lamella in Figure 6[c]) of the SiC layer from TRISO Particle AGR1-632-035. Area 3 is divided into two sections called 3a and 3b due to the relatively larger area examined.

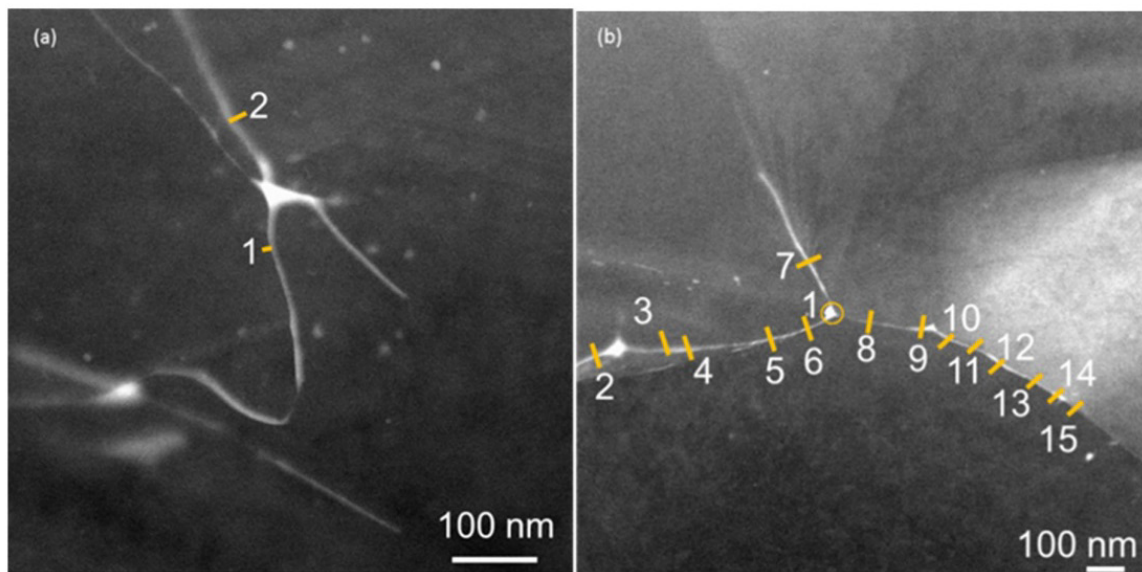


Figure 19. STEM HAADF image combined with EDS labeling to track the chemical composition of fission product precipitates from the center area of the SiC layer from TRISO Particle AGR1-632-035 within the subtended Areas (a) 1 and (b) 2 that are highlighted in Figure 18. Note the reported chemical compositions are in Table 13.



Table 13. Reported qualitative EDS compositions from the center area of the SiC layer from TRISO Particle AGR1-632-035, taken from subtended Areas 1 and 2 that are highlighted in Figure 18.

Precipitate Number	Concentration (at.%)									Precipitate Identification
	C	Si	Pd	Ag	Cs	Ce	Eu	U	Pu	
Area 1										
1	22.04	77.51	1.73	0.00	0.00	0.00	0.00	0.00	0.00	Pd
2	23.68	73.55	0.10	0.00	0.00	1.96	0.00	0.00	0.03	Ce
Area 2										
1	22.88	73.40	3.39	0.00	0.00	0.00	0.00	0.33	0.00	Pd-U
2	26.59	72.92	0.36	0.00	0.00	0.00	0.00	0.13	0.00	Pd
3	25.86	73.94	0.00	0.20	0.00	0.00	0.00	0.00	0.00	Ag
4	25.59	73.88	0.04	0.49	0.00	0.00	0.00	0.00	0.00	Ag
5	26.31	73.65	0.04	0.00	0.00	0.00	0.00	0.00	0.00	
6	26.54	73.22	0.21	0.03	0.00	0.00	0.00	0.00	0.00	Pd
7	27.76	71.23	1.01	0.00	0.00	0.00	0.00	0.00	0.00	Pd
8	25.98	74.01	0.01	0.00	0.00	0.00	0.00	0.00	0.00	
9	26.57	72.27	1.16	0.00	0.00	0.00	0.00	0.00	0.00	Pd
10	24.55	74.59	0.86	0.00	0.00	0.00	0.00	0.00	0.00	Pd
11	25.07	74.35	0.58	0.00	0.00	0.00	0.00	0.00	0.00	Pd
12	21.12	77.92	0.72	0.00	0.00	0.00	0.00	0.11	0.13	Pd
13	18.80	80.47	0.56	0.15	0.00	0.00	0.00	0.00	0.02	Pd
14	25.98	73.96	0.06	0.00	0.00	0.00	0.00	0.00	0.00	
15	24.60	74.96	0.31	0.00	0.00	0.00	0.00	0.01	0.12	Pd

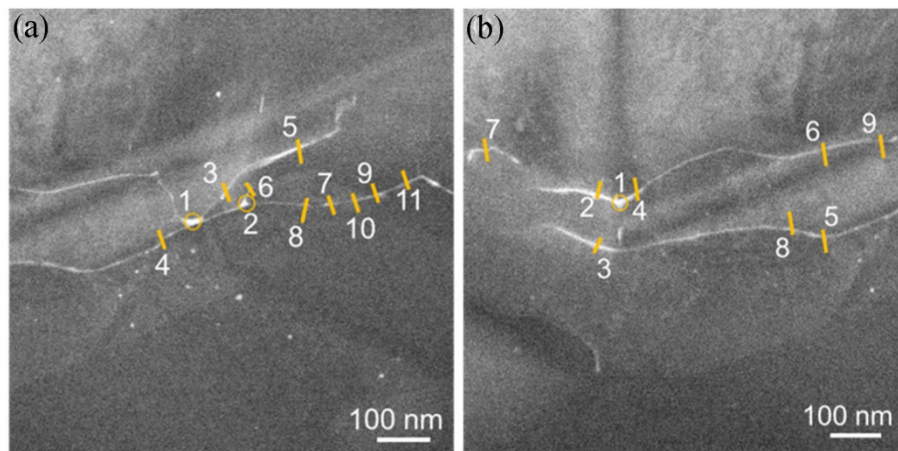


Figure 20. STEM HAADF image combined with EDS labeling to track the chemical composition of fission product precipitates from the center area of the SiC layer from TRISO Particle AGR1-632-035 within the subtended Areas (a) 3a and (b) 3b that are highlighted in Figure 18. Note the reported chemical compositions are in Table 14.



Table 14. Reported qualitative EDS compositions from the center area of the SiC layer from TRISO Particle AGR1-632-035, taken from subtended Areas 3a and 3b that are highlighted in Figure 18.

Precipitate Number	Concentration (at.%)									Precipitate Identification
	C	Si	Pd	Ag	Cs	Ce	Eu	U	Pu	
Area 3a										
1	27.50	69.65	2.81	0.04	0.00	0.00	0.00	0.00	0.00	Pd
2	24.34	74.37	1.16	0.00	0.00	0.00	0.00	0.14	0.00	Pd
3	24.28	75.35	0.23	0.00	0.00	0.00	0.00	0.13	0.00	Pd
4	33.77	65.64	0.59	0.00	0.00	0.00	0.00	0.00	0.00	Pd
5	26.99	71.36	1.65	0.00	0.00	0.00	0.00	0.00	0.00	Pd
6	25.92	73.42	0.32	0.00	0.00	0.00	0.00	0.34	0.00	Pd-U
7	27.47	72.40	0.14	0.00	0.00	0.00	0.00	0.00	0.00	
8	24.97	74.69	0.34	0.00	0.00	0.00	0.00	0.00	0.00	Pd
9	24.06	74.81	1.12	0.00	0.00	0.00	0.00	0.00	0.00	Pd
10	24.06	75.42	0.52	0.00	0.00	0.00	0.00	0.00	0.00	Pd
11	29.04	70.70	0.26	0.00	0.00	0.00	0.00	0.00	0.00	Pd
Area 3b										
1	31.00	68.70	0.15	0.00	0.00	0.00	0.00	0.15	0.00	
2	28.51	70.27	1.19	0.02	0.00	0.00	0.00	0.00	0.00	Pd
3	22.14	76.51	0.68	0.54	0.00	0.00	0.00	0.13	0.00	Pd-Ag
4	32.40	67.22	0.30	0.00	0.00	0.00	0.00	0.08	0.00	Pd
5	23.94	75.69	0.23	0.07	0.00	0.00	0.00	0.07	0.00	Pd
6	26.74	72.89	0.37	0.00	0.00	0.00	0.00	0.00	0.00	Pd
7	23.92	75.22	0.86	0.00	0.00	0.00	0.00	0.00	0.00	Pd
8	25.46	73.96	0.43	0.00	0.00	0.00	0.00	0.15	0.00	Pd
9	27.47	72.24	0.16	0.13	0.00	0.00	0.00	0.00	0.00	

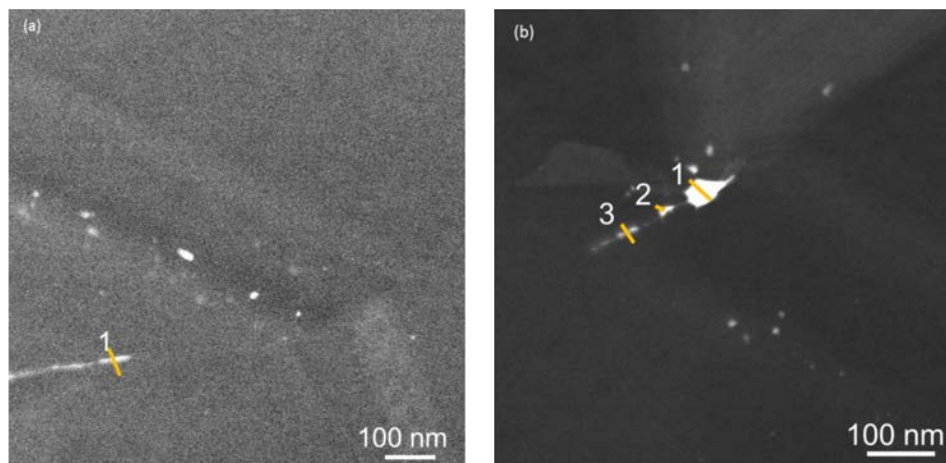


Figure 21. STEM HAADF image combined with EDS labeling to track the chemical composition of fission product precipitates from the center area of TRISO Particle AGR1-632-035 within subtended Areas (a) 4 and (b) 5 that are highlighted in Figure 18. Note the reported chemical compositions are in Table 15.

Table 15. Reported qualitative EDS compositions from the center area of TRISO Particle AGR1-632-035, taken from subtended Areas 4 and 5 that are highlighted in Figure 18.

Precipitate Number	Concentration (at.%)									Precipitate Identification
	C	Si	Pd	Ag	Cs	Ce	Eu	U	Pu	
Area 4										
1	31.91	66.72	1.37	0.00	0.00	0.00	0.00	0.00	0.00	Pd
Area 5										
1	12.45	76.09	11.07	0.35	0.00	0.00	0.00	0.03	0.00	Pd-Ag
2	20.45	78.04	1.51	0.00	0.00	0.00	0.00	0.00	0.00	Pd
3	22.68	75.88	1.44	0.00	0.00	0.00	0.00	0.00	0.00	Pd

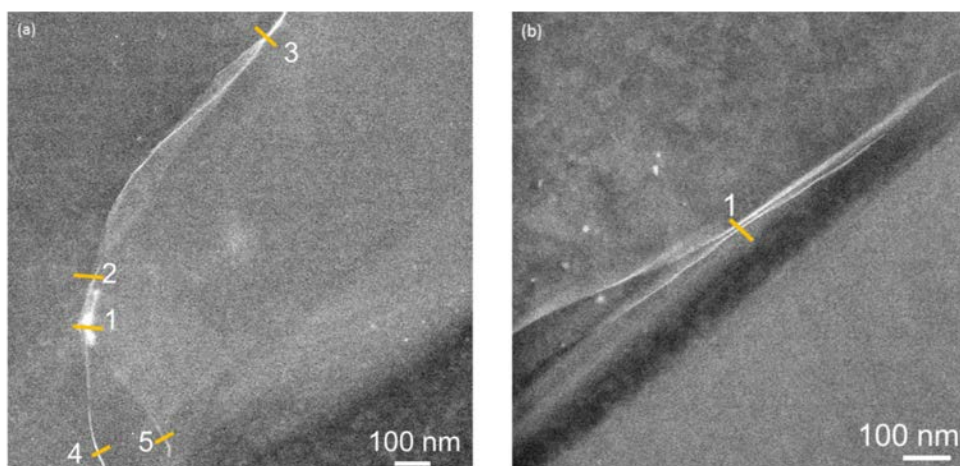


Figure 22. STEM HAADF image combined with EDS labeling to track the chemical composition of fission product precipitates from the center area of the SiC layer from TRISO Particle AGR1-632-035 within the subtended Areas (a) 6 and (b) 7 that are highlighted in Figure 18. Note the reported chemical compositions are in Table 16.

Table 16. Reported qualitative EDS compositions from the center area of the SiC layer from TRISO Particle AGR1-632-035, taken from subtended Areas 6 and 7 that are highlighted in Figure 18.

Precipitate Number	Concentration (at.%)									Precipitate Identification
	C	Si	Pd	Ag	Cs	Ce	Eu	U	Pu	
Area 6										
1	32.59	64.91	2.44	0.05	0.00	0.00	0.00	0.00	0.00	Pd
2	29.65	66.09	0.54	0.00	0.00	3.72	0.00	0.00	0.00	Pd-Ce
3	26.25	71.48	2.14	0.00	0.00	0.00	0.00	0.00	0.13	Pd
4	32.95	65.41	1.65	0.00	0.00	0.00	0.00	0.00	0.00	Pd
5	23.14	76.39	0.36	0.00	0.00	0.00	0.00	0.11	0.00	Pd
Area 7										
1	30.16	68.41	1.43	0.00	0.00	0.00	0.00	0.00	0.00	Pd

**3.1.3.3 Chemical Composition in the Outer Area of the SiC Layer.** Figure 23 shows the Lamella fabricated from the outer area of the SiC layer (marked “OE” in Figure 6[c]) from Particle AGR1-632-035, with eight areas marked in yellow (labeled 1 through 8) where precipitates were examined and the composition determined by qualitative EDS analysis (presented in Tables 17 through 20

and Figures 24 through 27). From these qualitative analyses, it was determined that precipitates contain mainly Pd, Ag, Ce, and Eu. No Cs, Pu, or U were found to be present in the precipitates examined. It was found that five precipitates in this outer section of the SiC layer contain Eu and/or Ce, which is about three times more than the only two precipitates in each of the inner and center areas of the SiC layer.

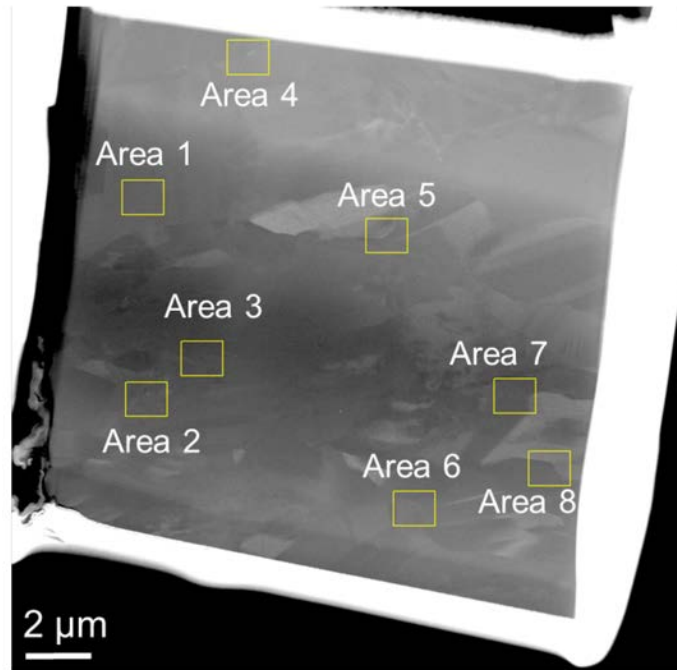


Figure 23. Large field of view STEM dark field image taken from the outer area of the SiC layer (marked “OE” in Figure 6[c]) from TRISO Particle AGR1-632-035.

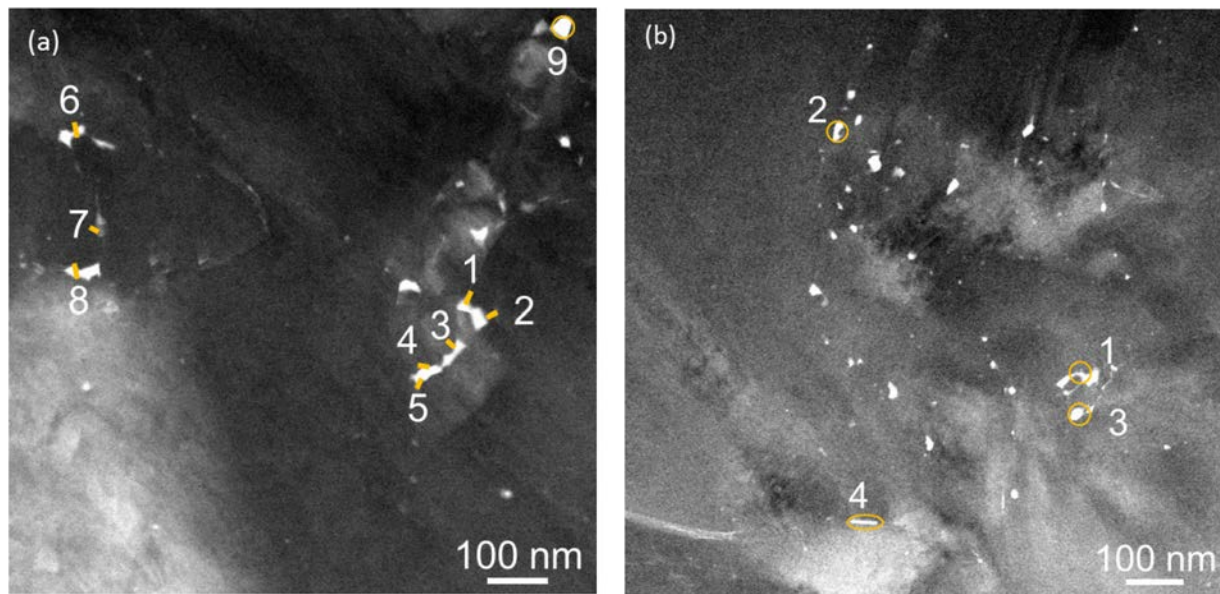


Figure 24. STEM HAADF image combined with EDS labeling to track the chemical composition of fission product precipitates from the outer area of the SiC layer from TRISO Particle AGR1-632-035 within the subtended Areas (a) 1 and (b) 2. Note the reported chemical compositions are in Table 17.

Table 17. Reported qualitative EDS compositions from the outer area of the SiC layer from TRISO Particle AGR1-632-035, taken from subtended Areas 1 and 2 that are highlighted in Figure 23.

article 1581 652-655, taken from suspended Areas 1 and 2 that are highlighted in Figure 25.

Precipitate Number	Concentration (at.%)									Precipitate Identification
	C	Si	Pd	Ag	Cs	Ce	Eu	U	Pu	
Area 1										
1	30.41	68.23	0.22	0.00	0.00	0.52	0.61	0.00	0.00	Pd-Ce-Eu
2	34.99	61.79	2.63	0.00	0.00	0.08	0.51	0.00	0.00	Pd-Eu
3	32.71	64.13	2.60	0.00	0.00	0.05	0.51	0.00	0.00	Pd-Eu
4	34.51	63.35	1.72	0.00	0.00	0.15	0.26 <sup>a</sup>	0.03	0.00	Pd
5	25.33	70.23	3.93	0.00	0.00	0.24	0.27 <sup>a</sup>	0.00	0.00	Pd-Ce
6	38.49	57.32	3.81	0.00	0.00	0.08	0.29	0.00	0.00	Pd-Eu
7	38.11	61.15	0.51	0.00	0.00	0.01	0.21 <sup>a</sup>	0.00	0.00	Pd
8	37.18	58.14	4.68	0.00	0.00	0.00	0.00	0.00	0.00	Pd
9	29.86	65.71	4.37	0.00	0.00	0.00	0.07	0.00	0.00	Pd
Area 2										
1	32.24	61.81	5.72	0.00	0.00	0.00	0.00	0.00	0.00	Pd
2	49.51	49.41	0.37	0.00	0.00	0.00	0.00	0.00	0.00	Pd
3	39.53	54.47	4.73	0.00	0.00	0.00	0.00	0.00	0.00	Pd
4	33.33	64.01	2.54	0.00	0.00	0.00	0.00	0.00	0.00	Pd

a. Cannot differentiate between Eu and Fe

a. Cannot differentiate between Eu and Fe

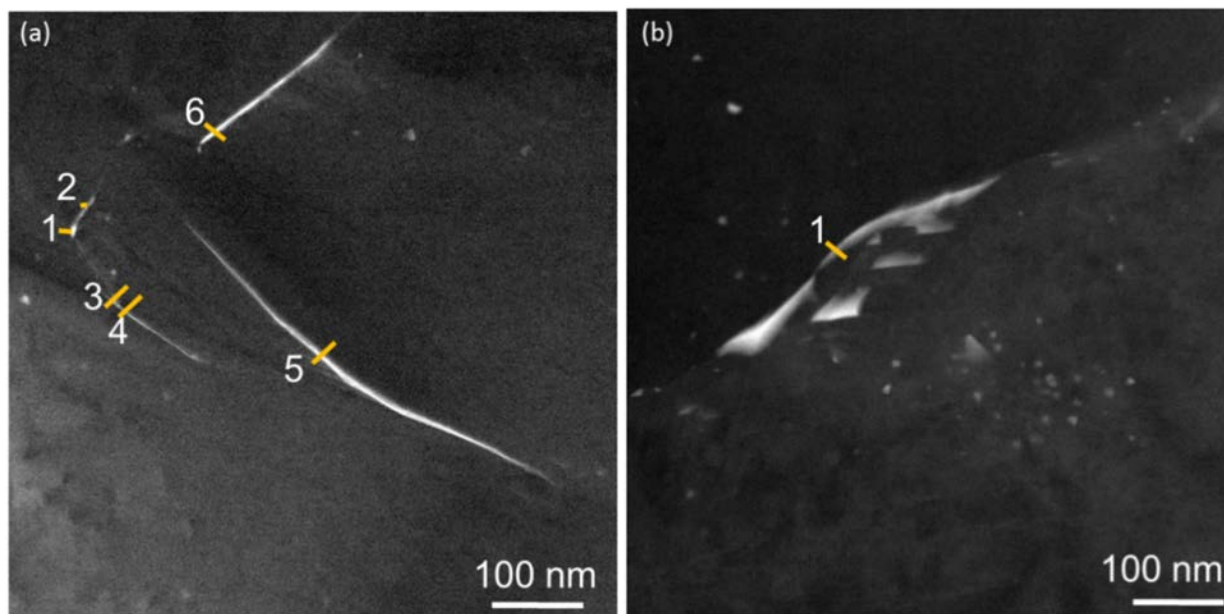


Figure 25. STEM HAADF image combined with EDS labeling to track the chemical composition of fission product precipitates from the outer area of the SiC layer from TRISO Particle AGR1-632-035 within the subtended Areas (a) 3 and (b) 4 that are highlighted in Figure 23. Note the reported chemical compositions are in Table 18.



Table 18. Reported qualitative EDS compositions from the outer area of the SiC layer from TRISO Particle AGR1-632-035, taken from subtended Areas 3 and 4 that are highlighted in Figure 23.

Precipitate Number	Concentration (at.%)									Precipitate Identification
	C	Si	Pd	Ag	Cs	Ce	Eu	U	Pu	
Area 3										
1	47.69	48.18	4.13	0.00	0.00	0.00	0.00	0.00	0.00	Pd
2	48.14	50.44	1.41	0.00	0.00	0.00	0.00	0.00	0.00	Pd
3	43.15	55.90	0.84	0.00	0.00	0.00	0.00	0.00	0.12	Pd
4	38.59	58.19	3.13	0.00	0.00	0.00	0.00	0.09	0.00	Pd
5	44.89	52.65	2.46	0.00	0.00	0.00	0.00	0.00	0.00	Pd
6	45.50	50.53	3.96	0.00	0.00	0.00	0.00	0.00	0.01	Pd
Area 4										
1	32.54	66.34	1.12	0.00	0.00	0.00	0.00	0.00	0.00	Pd

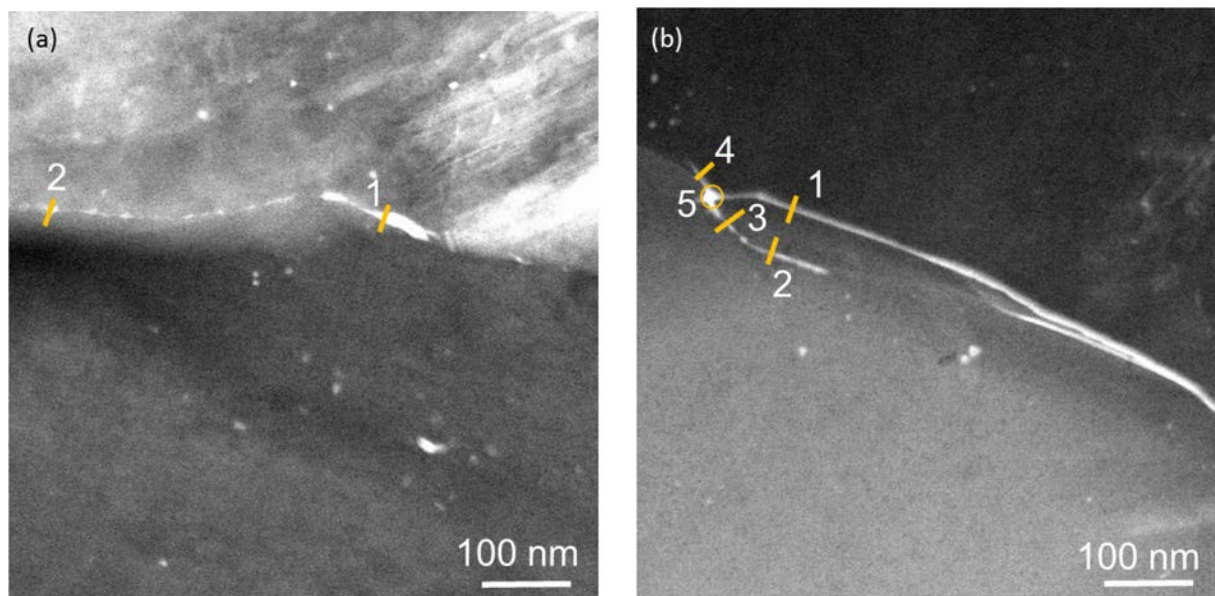


Figure 26. STEM HAADF image combined with EDS labeling to track the chemical composition of fission product precipitates from the outer area of the SiC layer from TRISO Particle AGR1-632-035 within the subtended Areas (a) 5 and (b) 6 that are highlighted in Figure 23. Note the reported chemical compositions are in Table 19.

Table 19. Reported qualitative EDS compositions from the outer area of the SiC layer from TRISO Particle AGR1-632-035, taken from subtended Areas 5 and 6 that are highlighted in Figure 23.

Precipitate Number	Concentration (at.%)									Precipitate Identification
	C	Si	Pd	Ag	Cs	Ce	Eu	U	Pu	
Area 5										
1	37.28	56.45	6.28	0.00	0.00	0.00	0.00	0.00	0.00	Pd
2	39.89	59.33	0.77	0.00	0.00	0.00	0.00	0.00	0.00	Pd
3	35.81	63.56	0.57	0.06	0.00	0.00	0.00	0.00	0.00	Pd
Area 6										
1	38.30	60.79	0.91	0.00	0.00	0.00	0.00	0.00	0.00	Pd
2	37.87	61.09	1.04	0.00	0.00	0.00	0.00	0.00	0.00	Pd
3	39.42	59.40	1.18	0.00	0.00	0.00	0.00	0.00	0.00	Pd
4	40.72	57.47	1.30	0.32	0.00	0.00	0.00	0.19	0.00	Pd-Ag
5	37.10	59.57	3.33	0.00	0.00	0.00	0.00	0.00	0.00	Pd

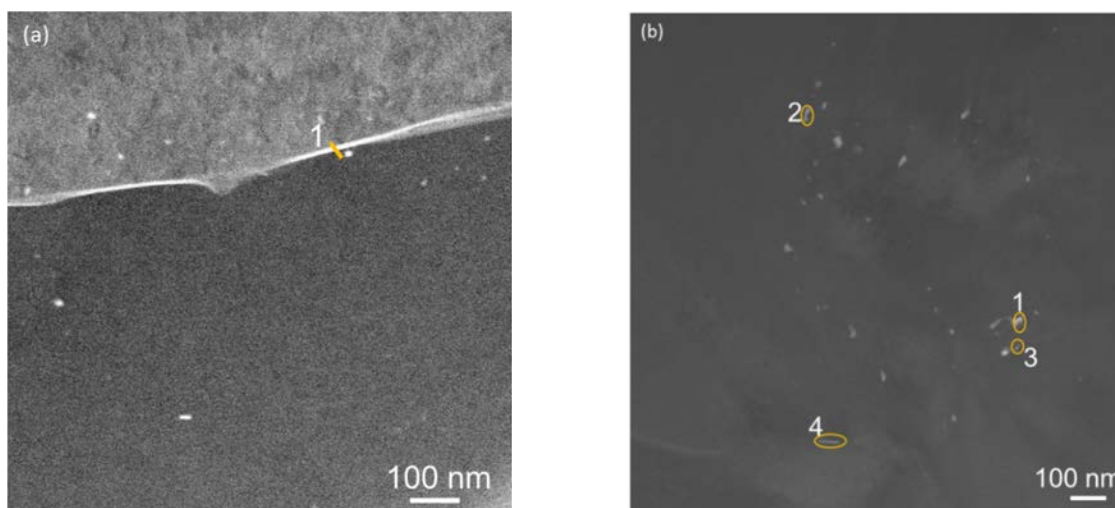


Figure 27. STEM HAADF image combined with EDS labeling to track the chemical composition of fission product precipitates from the outer area of the SiC layer from TRISO Particle AGR1-632-035 within the subtended Areas (a) 7 and (b) 8 that are highlighted in Figure 23. Note the reported chemical compositions are in Table 20.

Table 20. Reported qualitative EDS compositions from the outer area of the SiC layer from TRISO Particle AGR1-632-035, taken from subtended Areas 7 and 8 that are highlighted in Figure 23.

Precipitate Number	Concentration (at.%)									Precipitate Identification
	C	Si	Pd	Ag	Cs	Ce	Eu	U	Pu	
Area 7										
1	34.24	59.13	1.05	0.40	0.00	4.29	0.00	0.00	0.00	Pd-Ag-Ce
Area 8										
1	19.10	63.17	17.43	0.00	0.00	0.00	0.28 <sup>a</sup>	0.00	0.00	Pd
2	24.97	73.04	1.55	0.00	0.00	0.06	0.27 <sup>a</sup>	0.07	0.00	Pd
3	13.46	60.13	26.39	0.00	0.00	0.00	0.00	0.00	0.00	Pd
4	22.04	67.60	10.35	0.00	0.00	0.00	0.00	0.00	0.00	Pd
a. Cannot differentiate between Eu and Fe										

a. Cannot differentiate between Eu and Fe

### 3.1.4 Crystallographic Information Obtained on Particle AGR1-632-035

Areas containing fission product precipitates were selected on each of the TEM samples (Figure 28). The chemical composition of the fission product precipitates and crystallographic information pertaining to the grain boundary on which they resided were analyzed. Additionally, PED was performed in each of the areas indicated in Figure 28.

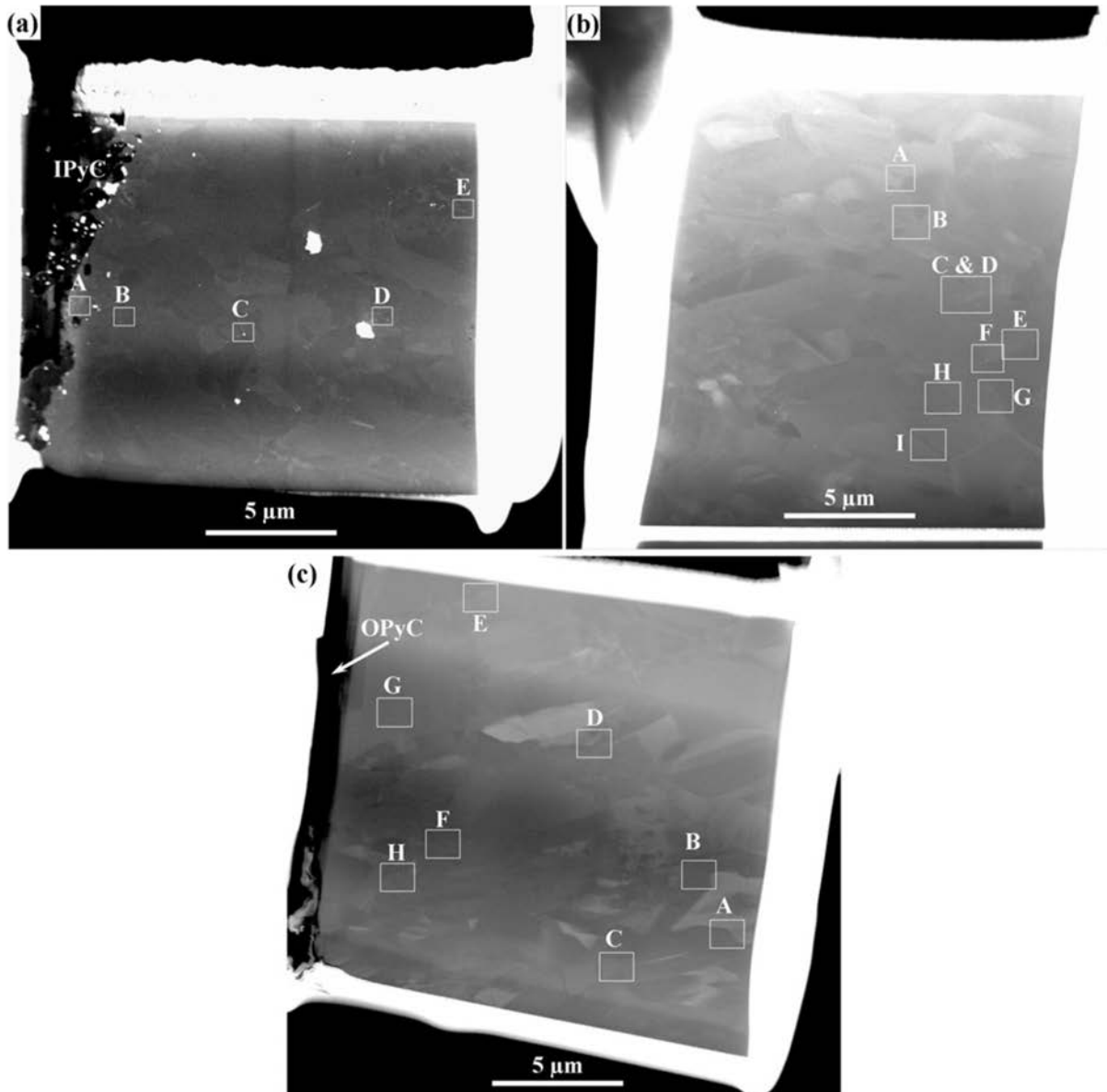


Figure 28. HAADF images of the (a) inner, (b) center, and (c) outer TEM samples taken from three locations within the SiC layer, indicated in Figure 6(c) from Particle AGR1-632-035, with the specific areas highlighted where fission product precipitates were analyzed.

**3.1.4.1 General Boundary Distributions across the Silicon Carbide Layer.** The grain orientation maps of the areas analyzed on the inner sample, Figure 28(a), are shown in Figure 29 as an example of the orientation information obtained. Grain orientation maps for each of the areas analyzed on the center (Figure 28[b]) and outer (Figure 28[c]) Lamella can be found in an INL internal report (Lillo et al., 2017).

Determination of the SiC grain orientations afforded the determination of the grain boundary distribution in each area analyzed. The distributions of grain boundary misorientation angles found in each area and the average distribution are given in Figure 30(a). Similarly, distributions of coincident site lattice (CSL)-related grain boundaries and grain boundary fractions by type for areas on the inner Lamella are given in Figure 30(b) and Figure 30(c), respectively. Distributions in Figure 30 show considerable variability. However, the areas, in general, do not contain a large number of grain boundaries and significant variation is expected. Therefore, the areas were combined to yield an average distribution for each plot and error bars based on the standard error. The standard error was determined by dividing the standard deviation for each measured value by the square root of the number of regions analyzed (i.e., number of observations). Orientation data obtained from various areas on the other Lamella (i.e., the center and outer samples) were similarly analyzed and plotted.

Figure 31 shows distributions when all areas on each sample are used to produce an average distribution for each lamella. Differences in the sample distributions taken from the inner, center, and outer regions are discussed in the following subsections.

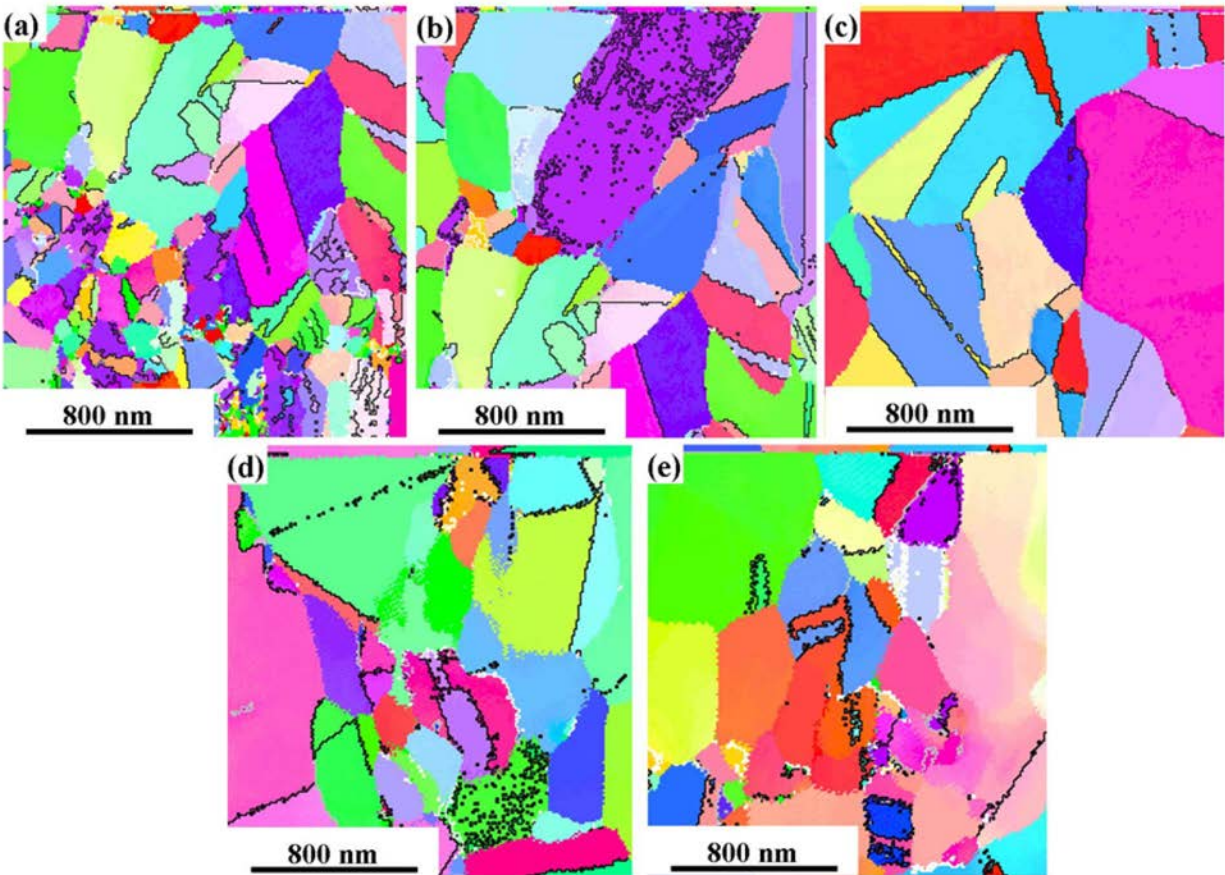


Figure 29. Orientation maps of (a) Area A, (b) Area B, (c) Area C, (d) Area D, and (e) Area E in Figure 28(a).



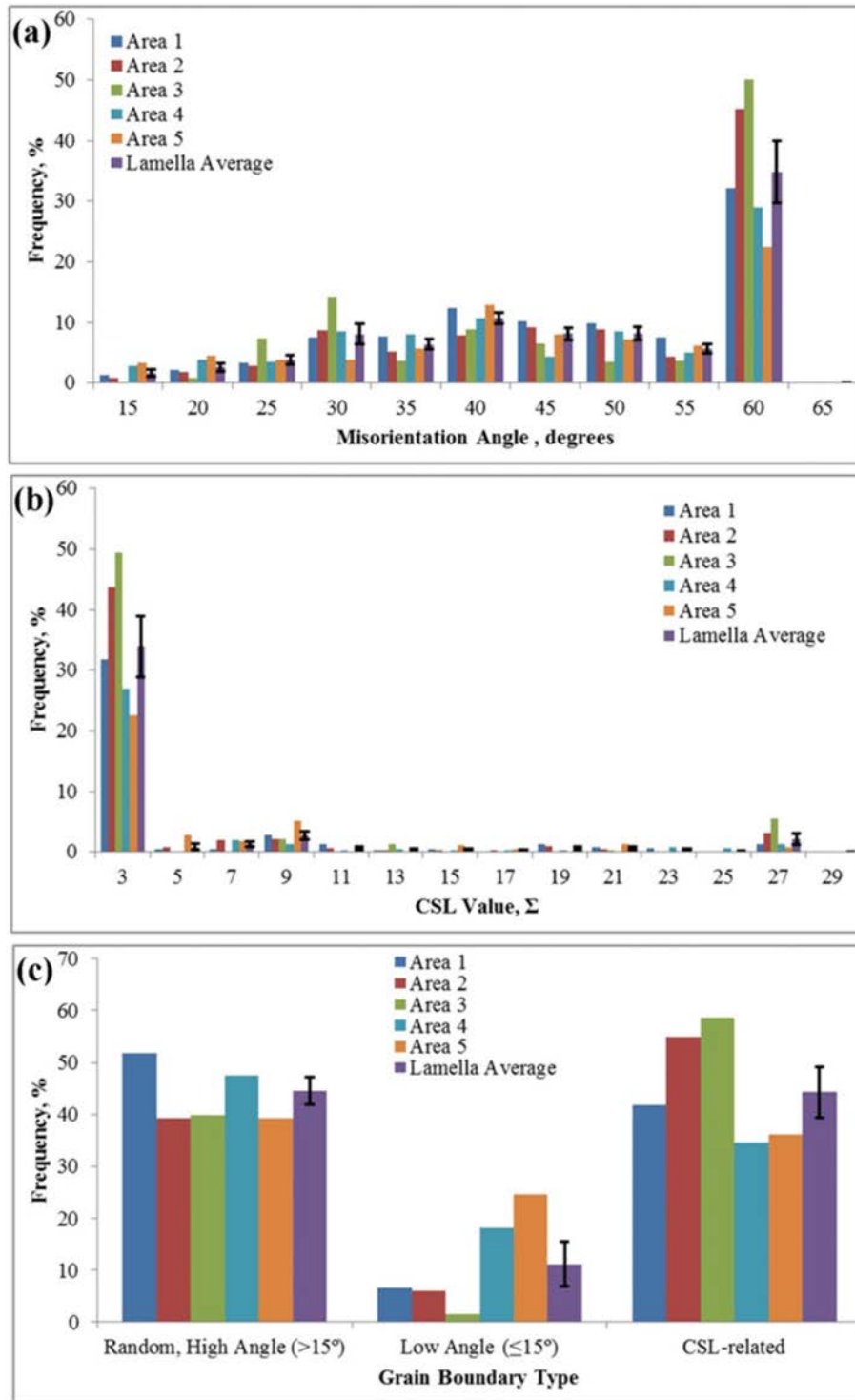


Figure 30. Distributions of (a) grain boundary misorientation angles, (b) CSL-related grain boundary fractions, and (c) grain boundary types in each area analyzed on the inner Lamella (Figure 28[a]) and average distribution with the accompanying error bars determined using standard error.

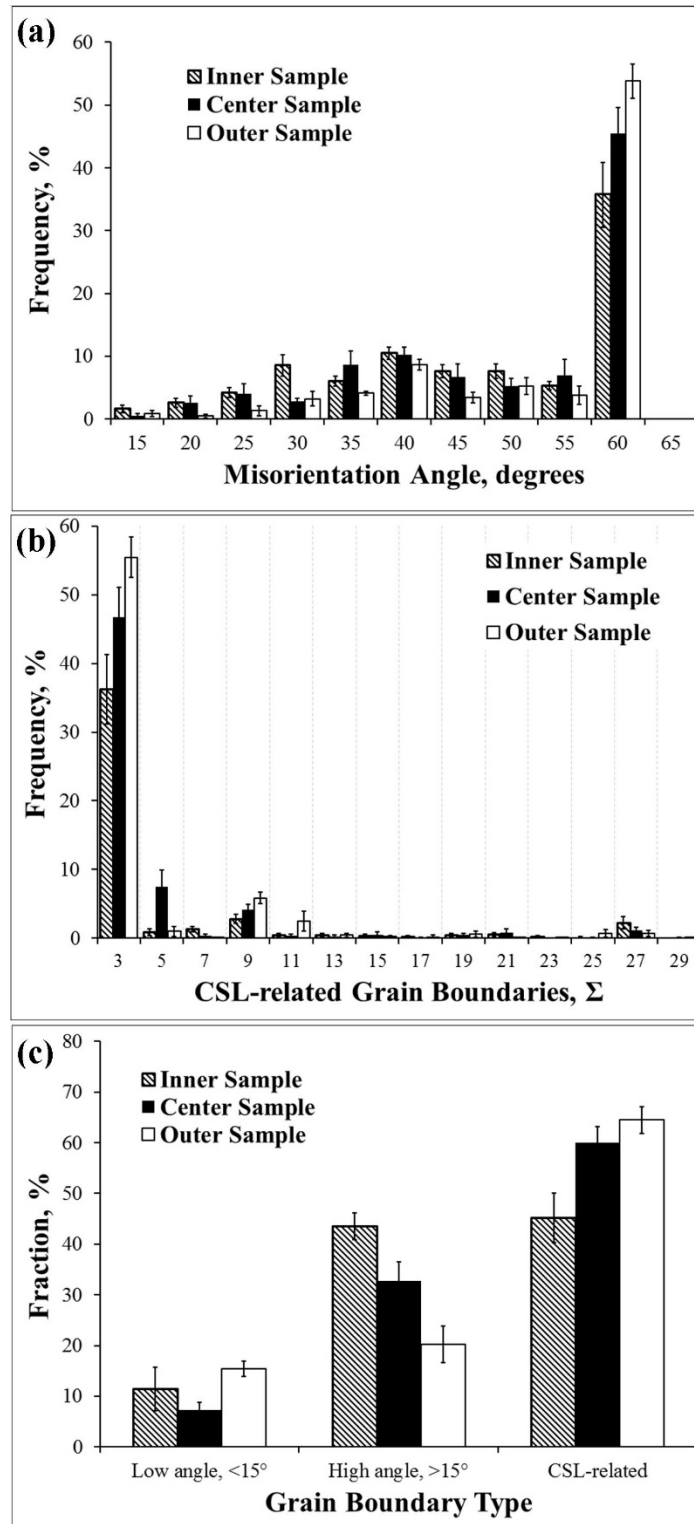


Figure 31. Distributions averaged over all areas analyzed for each Lamella of (a) grain boundary misorientation angles, (b) CSL-related grain boundary fractions, and (c) grain boundary types with the accompanying error bars determined using standard error.

**3.1.4.1.1 Misorientation Angle Distribution.** Figure 31(a) shows the grain boundary misorientation angle frequency distribution found in the inner, center, and outer samples. The error bars represent the standard error in each misorientation angle category. It should be kept in mind that the center sample contains significant overlap with both the inner and outer (see Figure 6[c]).

The distribution in Figure 31(a) is based on the number fraction of grain boundaries (i.e., the number of grain boundaries with a given misorientation angle divided by the total number of grain boundaries in the analyzed area). In general, the inner, center, and outer distributions are quite similar. Low-angle grain boundaries make up approximately 10% of the analyzed boundaries in each sample. Twin boundaries, with a 60-degree misorientation angle, represent a majority of the grain boundaries in the SiC layer. A smaller peak in the distribution occurs around 40 degrees. The only major difference among the three distributions lies in the frequency of the twin boundaries. Significantly fewer twins are in the inner sample, where growth of the SiC layer began compared to the outer sample, where competitive growth during the chemical vapor deposition (CVD) process has downselected grains with favorably oriented fast growth directions.

**3.1.4.1.2 Distribution of Coincident Site Lattice-Related Grain Boundaries.** As mentioned, the twin boundary fraction appears to dominate in the misorientation angle distribution in Figure 31(a). This is confirmed in the distribution by CSL boundary type (indicated by the  $\Sigma$  value) in Figure 31(b). The  $\Sigma 3$  boundary type, which corresponds to the twin boundary, is the most prevalent of the CSL-related grain boundaries in all three samples. The higher order twins (i.e.,  $\Sigma 9$  and  $\Sigma 27$ ) make up the majority of the remaining CSL-related grain boundaries. The fraction of grain boundaries that are twin-related boundaries (i.e.,  $\Sigma 3$  in Figure 31[b]) increases from inner to outer areas (the fractions of non-twin related CSL boundaries remains relatively constant across the thickness of the SiC layer).

The fraction of  $\Sigma 3$  grain boundaries, which correspond to twin boundaries, in these irradiated SiC samples is not consistent with those reported by Kirchhofer et al., (2013) obtained by SEM-based EBSD analysis on the SiC layer from an unirradiated, Baseline AGR-1 TRISO particles. The  $\Sigma 3$  boundary fraction found here (averaging about 44% across the entire SiC layer, Table 21) is substantially higher than that reported for unirradiated SiC, which is reported to be about 29% (Kirchhofer et al., 2013). The fractions of the  $\Sigma 9$  and  $\Sigma 27$  boundaries in this work at about 4% and 1%, respectively, are identical to those reported by Kirchhofer et al., (2013). The reason for the difference in the  $\Sigma 3$  boundary fractions between the two studies is not clear, but could be a statistical variation in the analyses, particle-to-particle variation that might arise during TRISO particle fabrication or because of neutron irradiation effects.

Table 21. Average fraction of twin-related grain boundaries in SiC layer from Particle AGR1-632-035.

CSL Value	Fraction %	Std. Error
3	44.2	1.4
9	4.3	0.7
27	1.4	0.5

**3.1.4.1.3 Distribution by Grain Boundary Type.** The grain boundary information may be further analyzed to determine the relative fractions of the different types of grain boundaries—low angle, random high angle, and CSL-related grain boundaries (only  $\Sigma 3$  through  $\Sigma 29$  are considered). The distribution found in each sample is summarized in Figure 31(c). The fraction of  $\Sigma 3$  and  $\Sigma 9$  grain boundaries increases from the inner sample to the outer sample as pointed out in the discussion of the distributions in Figure 31(a) and Figure 31(b). Figure 31(c) shows the increasing fraction of twin boundaries is offset by a diminishing fraction of random high-angle grain boundaries from the inner to the outer sample. The fraction of low-angle grain boundaries is relatively constant across the thickness of the SiC layer.

The trends in the grain boundary character distribution found here follow those obtained by Kirchhofer et al., (2013) from SEM-based EBSD analysis of the SiC layer in an unirradiated, AGR-1 TRISO fuel particle fabricated under baseline conditions. Similar to that work, CSL-related boundaries were found to be most prevalent here, averaging 56.5% across the entire SiC layer; random, high-angle grain boundaries were the next most common at an average of 32.1%, and low angle grain boundaries were least common at an average of 11.3% (Table 22). (However, Kirchhofer et al., (2013) reports a considerably higher fraction of low-angle grain boundaries at about 24% and values of 40% and 36% for CSL-related and random, high-angle grain boundaries, respectively, although the statistical error associated with these grain boundary types is not reported. The main difference between the two studies is unirradiated SiC for the Kirchhofer study versus high-temperature (i.e., about 1100°C and about 14,900 hours) irradiated SiC for this study. Additionally, the SiC orientation data collection step size in the Kirchhofer study grain orientation information was collected at 50-nm intervals and was approximately five times larger than in this study, where grain orientation information was collected at 10-nm intervals. Differences in grain boundary character distributions may be attributable to either neutron irradiation effects or the difference in data acquisition step size. Lattice dislocation rearrangement requires diffusion. It is generally accepted that self-diffusion becomes significant above about half the melting point (Ralls et al., 1976) in the absence of irradiation damage, and neutron irradiation produces additional vacancies that aid in diffusion. While the time-average, volume-average (TAVA) irradiation temperature (1070°C) represents approximately less than half of the melting point of SiC (2700°C), enhanced diffusion due to irradiation-induced vacancies, in combination with a long-exposure duration, may allow significant rearrangement of lattice dislocations and alter the relative fraction of low-angle grain boundaries compared to as-fabricated SiC. Conversely, if lattice dislocations, potentially arising from CVD fabrication of the SiC layer, are distributed relatively uniformly throughout grain interiors, a larger data acquisition step size could result in an apparent low-angle grain boundary if enough dislocations exist between adjacent data collection points to exceed the minimum misorientation angle defined in the EBSD analysis software (set to 2 degrees in both studies). Additionally, each study is based on the analysis of a single TRISO particle, and the particle-to-particle variation in microstructure is not known for this experiment. Therefore, grain boundary character distribution studies on additional particles in the as-fabricated and irradiated conditions, using the same data collection technique and step size, will be required to determine the cause of the differences discussed here, if the differences are statistically significant.

Table 22. Average fraction of grain boundary types in the SiC layer from Particle AGR1-632-035.

Grain Boundary Type	Fraction %	Std. Error
Low angle, <15°	11.3	2.3
High angle, >15°	32.1	6.7
CSL-Related	56.5	5.8

**3.1.4.1.4 Grain Boundary Data for Grain Boundaries Containing Fission Product Precipitates.** Figure 32 shows one example from the center sample, Area B, Figure 28(b), where fission product precipitates were analyzed for both composition and the associated grain boundary information. In this particular area, seven grain boundary segments exhibited fission product precipitates. Even though all segments were connected, the fission products present in each grain boundary segment were not necessarily the same (Table 23). Most segments contain Pd with the exception of Boundary Segments 2 and 3, which contain only Ag. In this example, it appears that the grain boundary parameters, which determine grain boundary energy and grain boundary atomic structure, affect the fission products that may be present on a particular grain boundary segment. This is somewhat surprising because Boundary Segments 1, 2, 3, and 4 in Table 23 are all considered to be random, high-angle grain boundaries and all are expected to be of relatively high energy and with no expected specific repeating atomic structure because they are random grain boundaries. However, they exhibit elevated levels of different fission

product elements. Therefore, since they are all connected, they must possess unique characteristics, energy, or atomic structures, which allow preferential segregation of certain fission product elements to them. Because Boundaries 1 through 4 are linearly connected, one would expect to find the fission products on all four grain boundaries to be the same with approximately the same concentration if all random, high-angle boundaries were equivalent, which is clearly not the situation in this example. At the very least, specific boundary parameters strongly influence diffusion of the various fission products.

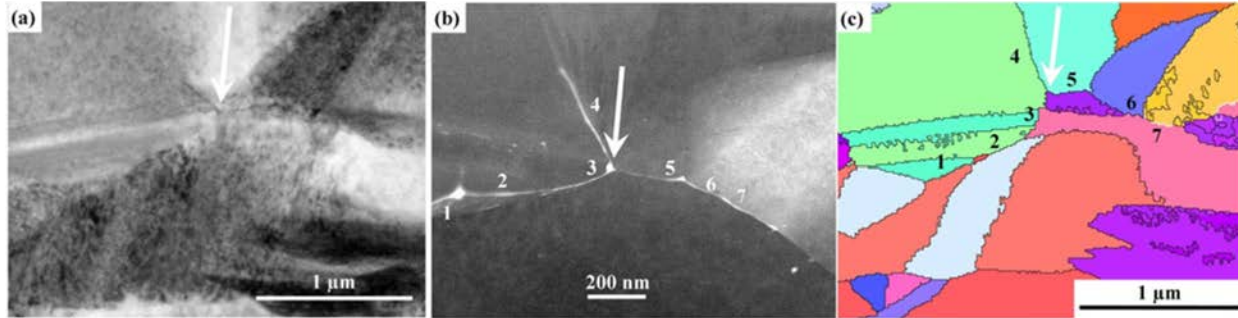


Figure 32. Example area (center sample, Area B of Figure 28[b]) showing precipitates on the grain boundaries that were analyzed for composition and grain boundary character. (a) TEM image, (b) STEM image using the HAADF, and (c) the corresponding orientation image. The arrow in each image denotes the same reference point.

Table 23. Summary of fission product precipitate information and associated grain boundary information from the center sample in Area B of Figure 28(b).

Grain Boundary	Misorientation Angle (degrees)	Misorientation Axis			CSL Designation, $\Sigma$	Fission Product Element		
		x	y	z		Pd	Ag	U
1	33.6	20	13	-13	—	●		●
2	45.7	5	13	15	—		●	
3	54.2	18	2	-15	—		●	
4	43.6	4	16	-19	—	●		
5	38.7	1	0	1	9	●		
6	56.8	20	-1	23	—	●		
7	13.8	-7	23	-18	—	●		

Analyses similar to this example were carried out on the various areas of each sample taken from the SiC layer. The following summarizes the combined results of the areas analyzed in each sample. It should be noted that not all the locations of fission product precipitates that were analyzed for composition by EDS, and presented in Section 3.1.3, could be found in the corresponding orientation maps (i.e. locations in the HAADF images could not always be found in the orientation maps from the same areas – most likely due to overlapping SiC grains). Therefore, only fission product precipitates with locations that could be identified in the orientation maps are included in the discussion that follows.

**Area Nearest IPyC (Inner Sample):** Grain boundary precipitates were most prevalent in the SiC layer near the IPyC layer (Figure 33), which is expected because this location is nearest the source of the fission products (i.e., the central fuel kernel.) Sixty-three boundaries were analyzed that exhibited fission product precipitates in this sample. As summarized in Table 24, the majority of the fission product precipitates had detectable levels of only Pd (about 58%) or Pd in conjunction with U (about 22%). Fission product precipitates exhibiting only Ag were present in significant quantities (about 13%), as

were fission product precipitates that contained both Pd and Ag (about 8%). Figure 33 also shows that fission product precipitates in the inner sample had the highest probability of occurring at random, high-angle-type grain boundaries, regardless of the fission product element(s) present, but were also found on CSL-related and low-angle grain boundary types. Table 24 shows precipitates consisting of only Ag that were found only on random, high-angle type grain boundaries, whereas Pd only, Pd+Ag, and Pd+U were found occasionally on CSL-related grain boundaries, but were predominantly found on random, high-angle grain boundaries. The fission product precipitate on the single low-angle grain boundary in Area C and D (Figure 28[b]) contained Pd exclusively.

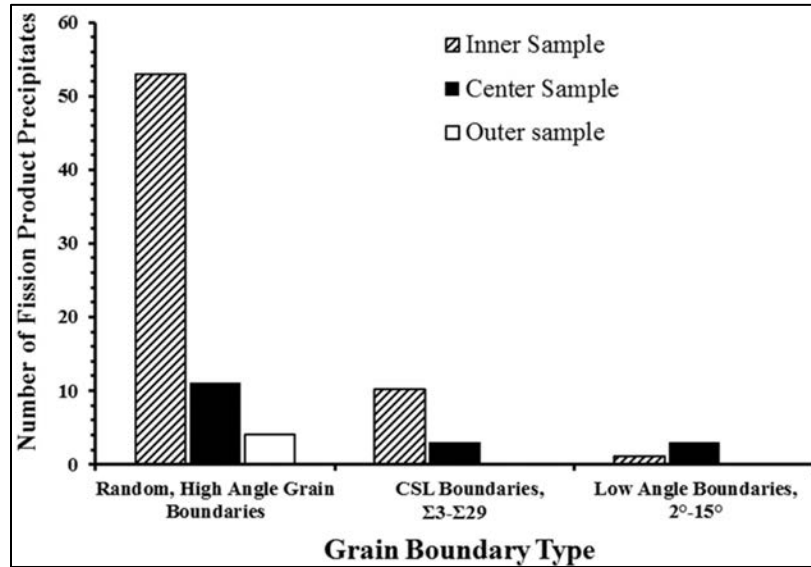


Figure 33. Summary of the grain boundary types associated with fission products.

Table 24. Summary of the distribution of fission product elements.

	Pd only	Ag only	U only	Pd and Ag	Pd and U	Ag and U
<b>Inner Sample</b>						
Number of grain boundaries	37	8	0	5	14	0
Fraction of all boundaries with fission products, %	57.8	12.5	0.0	7.8	21.9	0.0
Low angle, %	2.8	0.0	— <sup>a</sup>	0.0	0.0	—
Random, high angle, %	80.6	100.0	—	80.0	85.7	—
CSL, %	19.4	0.0	—	20.0	14.3	—
<b>Center Sample</b>						
Number of grain boundaries	12	4	0	0	1	0
Fraction of all boundaries with fission products, %	70.6	23.5	0.0	0.0	5.9	0.0
Low angle, %	25.0	0.0	—	—	0.0	—
Random, high angle, %	50.0	100.0	—	—	100.0	—
CSL, %	25.0	0.0	—	—	0.0	—
<b>Outer Sample</b>						
Number of grain boundaries	4	0	0	0	0	0
Fraction of all boundaries with fission products, %	100.0	0.0	0.0	0.0	0.0	0.0
Low angle, %	0.0	—	—	—	—	—
Random, high angle, %	100.0	—	—	—	—	—
CSL, %	0.0	—	—	—	—	—

a. Dashes indicate no precipitates of this type were found on any type of grain boundary.

**Middle of the SiC Layer (Center Sample):** The number of precipitates in the center sample was much lower when compared to the inner sample. As a result, only 17 fission product precipitates and their associated grain boundary types were analyzed in this sample. However, the trends observed for the inner sample appear to be followed in the center sample (Figure 33). Again, most of the fission product precipitates contain Pd and are associated with random, high-angle grain boundaries. However, small numbers of Pd-containing precipitates are associated with either CSL-related or low-angle grain boundaries. As in the inner sample, precipitates containing only Ag were found exclusively on random, high-angle grain boundaries and were never observed on either CSL-related or low-angle grain boundaries. In this sample, only one precipitate containing Pd in conjunction with U was found on a random, high-angle grain boundary while observations in the inner sample found similar Pd/U-containing precipitates occur, to a small degree, on CSL-related grain boundaries. It is possible that Pd/U-containing grain boundary precipitates would be found on CSL-related grain boundaries in the middle of the SiC layer if analyses on additional precipitates in additional samples taken from the center of the SiC layer were performed. No Pd/Ag-containing precipitates were found in this sample, and may again be due to the small number of precipitates found in the center sample.

**Outer Edge:** Only four fission product precipitates and their associated grain boundary information could be determined for the fission product precipitates that were analyzed in the outer sample. The number of fission product precipitates was very low, possibly due to the relatively large grain size in this part of the SiC layer, the relatively long diffusion distances involved, and/or potentially low fission product concentrations that were insufficient to form a precipitate. In this sample, all fission product precipitates were found to contain Pd exclusively and only found on random, high-angle-type grain boundaries (Table 24 and Figure 33, respectively). Precipitates with other elements may be present in other outer areas of the SiC layer that were not analyzed in this study. However, an impractical number of TEM samples would be required to determine these occurrences with any reasonable certainty. The combination of increasing grain size, increasing diffusion distance, and changing grain boundary distribution (see Figure 31[c]) are thought to contribute to the decreasing precipitate density in this region.

**3.1.4.1.5 Associations of Fission Products with Grain Boundary Types – Low Angle, High Angle,  $\Sigma$ .** Pd-containing precipitates (i.e., Pd only and Pd with U) were the most common throughout the SiC layer (Table 24 and Figure 34). Ag-containing precipitates (i.e., Ag only and Pd with Ag) were the next most common precipitate type. This is expected based on the higher Pd generation rate compared to that of Ag during irradiation of the TRISO fuel particle (Sterbentz and Gougar 2011). The source of U most likely originated from the UCO fuel kernel either due to contamination during the CVD fabrication of the SiC layer (Hunn et al., 2015) or as a result of reducing conditions in the kernel imposed by the adjacent carbon buffer and IPyC layers during irradiation that enabled U to migrate into the SiC layer. However, U-containing precipitates were not observed in examinations of the as-fabricated SiC layer of unirradiated TRISO fuel (Lillo, van Rooyen, and Wu 2016). Therefore, it is likely that the U migrated into the SiC layer during irradiation. Because U precipitates are not found in the interior of the SiC grains, but are always found associated with Pd on grain boundaries (Table 24), U is likely moving with the assistance of Pd. Both Pd and U form silicides and U has considerable solubility in metallic Pd (Kleykamp and Kang 1996); therefore, it is reasonable to assume significant interaction between Pd and U under irradiation conditions, with U being in a solid solution with metallic Pd or a Pd-based compound (van Rooyen et al., 2014c). Further understanding of precipitation behavior will require definitive identification of the precipitates as to whether they are metallic or silicides.

From the results presented, it appears Pd more readily moves through the SiC grain boundary network than either Ag or U (Table 24), because very few Ag and U-containing precipitates were found beyond the region nearest the IPyC. Ag and U could be detected only part way through the SiC layer during irradiation in the AGR-1 experiment, whereas Pd precipitates were found throughout the entire SiC layer. Additionally, it is interesting to note that in the outer sample, Pd precipitates were only found on random, high-angle grain boundaries and not on low-angle or CSL-related grain boundaries. Pd precipitates did

occur in small numbers on these types of grain boundaries in the inner and center samples (Table 24). One possible explanation is that, although Pd can migrate along these types of grain boundaries, the migration rate on low-angle and CSL-related grain boundaries is significantly lower than on random, high-angle grain boundaries. The Pd+U and the Pd+Ag precipitate distributions tend to also support this explanation. These precipitate types were present on CSL-related grain boundaries in the inner sample but not in the center sample. Table 24 shows that both Ag-only and Pd+U type precipitates were present in the analyzed regions of the center sample on random, high-angle grain boundaries. If the migration rate along CSL-related grain boundaries were on the same order as the random boundaries, then these instances had a reasonable chance of being detected. However, it is likely that the migration rate along CSL-related boundaries is dependent on the CSL value through grain boundary energy. Lower energy grain boundaries have been demonstrated to have lower diffusivity (Priester 1989, Peterson 1983) and, generally, CSL-related grain boundaries have lower energy than random, high-angle grain boundaries, although the grain boundary plane can have a considerable influence on the grain boundary energy (Wolf 1989, Wolf 1990, Randle 1997). Table 25 summarizes the CSL-related boundaries with precipitates on them by fission product element. In the case of Pd+Ag and Pd+U, the CSL-related boundaries exhibit high values of  $\Sigma$  and are not found on the lower  $\Sigma$  value grain boundaries (e.g.,  $\Sigma 3$ ), which tend to exhibit the lower grain boundary energies although the grain boundary plane is an important factor in defining the grain boundary energy of CSL-related boundaries. Palladium, with an atomic radius smaller than either Ag or U, seems to be less affected by the  $\Sigma$  value and was even observed to reside on a  $\Sigma 3$  twin boundary and a higher order  $\Sigma 9$  twin boundary. This is not overly surprising because Pd precipitates have been found in the interior of the SiC grains (Lillo and van Rooyen 2015), where the local atomic registry is perfect and the interaction energy to accommodate the mismatch of atomic radii between Pd, Si, and C would be expected to be higher than in a grain boundary that has associated excess free volume and more readily accommodate the mismatch in atomic radii.

Of course, the other explanation for a lack of Pd precipitates on low-angle and CSL-related grain boundaries in the outer sample is that simply not enough precipitates were analyzed in the outer sample to reveal occurrences on either of these two other types of grain boundaries. The low generation rates of Ag and low concentrations of U, in combination with long diffusion distances, also may have prevented the concentrations of these elements from reaching the critical levels needed to form a fission product precipitate. Additional areas and precipitates will need to be analyzed to resolve this observed behavior. However, observations in this work would seem to justify a reconsideration of which  $\Sigma$  values should actually be considered to possess “special” properties, at least for the precipitation of fission products. Furthermore, additional consideration of the grain boundary plane is needed because it can significantly affect the resulting grain boundary energy (Wolf 1990; Lojkowski, Gleiter and Mauer 1988; Herrmann, Gleiter and Baro 1976) and grain boundary diffusivity (Priester 1989). Therefore, a low CSL value alone may not be sufficient to inhibit precipitate formation and, ultimately, the grain boundary structure, as determined by both misorientation and the grain boundary plane, which may be more relevant to fission product migration and precipitation behavior.



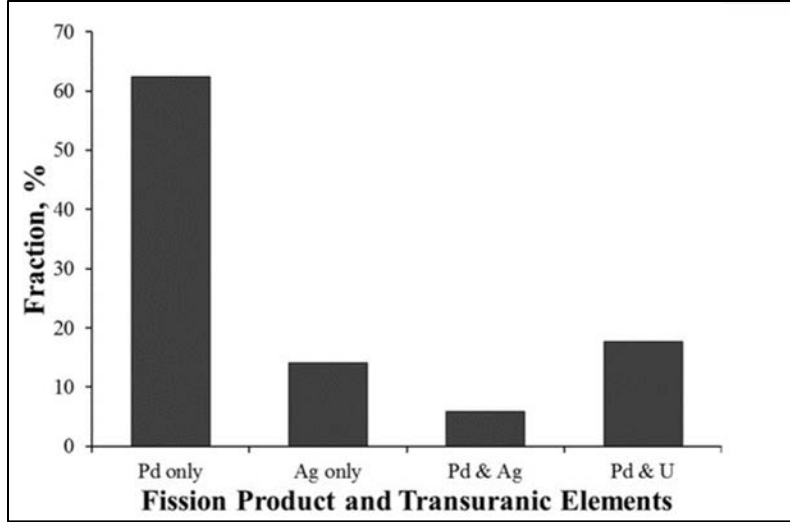


Figure 34. Composition distribution of the grain boundary precipitates from the combined results on the inner, center and outer regions.

Table 25. Summary of CSL-related boundaries with precipitates.

	Elements in Fission Product					
	Pd Only		Pd+Ag		Pd+U	
	$\Sigma$ Value	Number of Grain Boundaries	$\Sigma$ Value	Number of Grain Boundaries	$\Sigma$ Value	Number of Grain Boundaries
Inner Sample	7	2	25b	1	19a	1
	17a	2			25b	1
	19a	1				
	25b	1				
	29b	1				
Center	3	1	—	—	—	—
	9	1				
	19b	1				
Outer	—	—	—	—	—	—

Because comparison of the distributions of grain boundary precipitates is not statistically relevant between inner, center, and outer samples in this study, it makes sense to combine data from the three samples and discuss the results as they pertain to the entire SiC layer. Specifically, fission product precipitates are most likely to occur on random, high-angle grain boundaries (Figure 35). As noted above, random, high-angle grain boundaries typically have higher grain boundary energies than low  $\Sigma$ , CSL-related grain boundaries, regardless of grain boundary plane (Goodhew 1979). It has been demonstrated that a linear relationship exists between grain boundary energy and grain boundary excess volume (Wolf 1989, Wolf 1990); therefore, a larger excess volume is expected for random, high-angle grain boundaries compared to either low-angle or low  $\Sigma$ , CSL-related grain boundaries. The fission product elements and U have significantly larger atomic radii compared to either Si or C. Strains caused by these elements would be minimized if located in grain boundaries with larger values of excess volume (e.g., random, high-angle grain boundaries). The diffusivity of a grain boundary is significantly affected by the excess grain boundary volume (Randle 1993, Randle 2004, Shewmon 1969). Thus, random, high-angle grain boundaries, with relatively large values of grain boundary energy (and larger values of excess volumes) are considered to be the high diffusivity paths for impurity atoms (Peterson 1983). The fraction of CSL-related grain boundaries containing fission products in Figure 35 is composed mostly of

boundaries with a high  $\Sigma$  value (Table 25) that tend to exhibit larger grain boundary energy than boundaries associated with low values of  $\Sigma$  (e.g.,  $\Sigma 3$ ). Finally, diffusion of fission product elements in low-angle grain boundaries is limited to slower dislocation pipe diffusion because these boundaries are composed of one or more arrays of discrete dislocations.

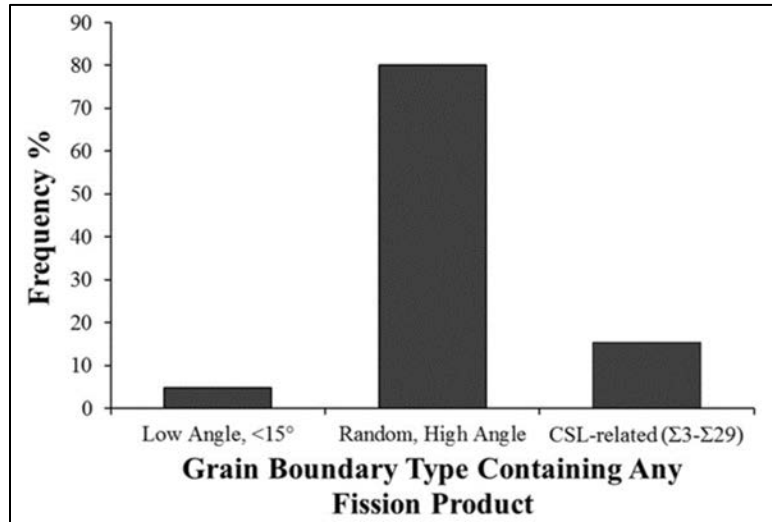


Figure 35. Distribution of the fission product precipitates on the various boundary types as a percentage, generated by combining the results from the inner, center, and outer samples.

**3.1.4.1.6 Relationship between Specific Fission Product Elements and Grain Boundary Types.** Further analysis of the occurrence of specific fission product elements and combinations of them revealed some interesting trends related to grain boundary type, which are summarized in Figure 36. Specifically, as mentioned above, precipitates that contain only Pd seem to occur on all types of grain boundaries (Figure 36[a]) with preference for random, high-angle grain boundaries. Again, Pd is found in precipitates at interior locations in SiC grains (Lillo and van Rooyen 2015); therefore, it is not surprising that precipitates with only Pd can be found on all three types of grain boundaries. However, when Pd was found in conjunction with either Ag or U, low-angle grain boundaries no longer appear to be viable defects for formation of fission product precipitates (Figure 36). The lack of precipitation on low-angle grain boundaries when either Ag or U are associated with Pd can be rationalized by noting the larger atomic radii of these two fission product elements, which could increase the strain energy of such precipitates on low-energy boundaries (therefore low excess volume) to the point where they are no longer energetically favorable. Finally, Ag was found to only occur on random, high-angle grain boundaries (Figure 36) and never on low-angle or CSL-related grain boundaries. The presence of precipitates containing only Ag on only random, high-angle grain boundaries can be rationalized by both the larger atomic radius and the almost complete lack of solubility of Ag in SiC (i.e., a thermodynamic consideration). However, it is difficult to rationalize the presence of Ag-only precipitates when Pd is present in the surroundings.

Another study (Lopez-Honorato et al., 2011) also shows that Ag is capable of diffusing through SiC, even when Pd is not present. However, if Pd were available, as is the case in the present study, then one would expect to find only Pd+Ag precipitates due to the complete solubility of Ag in Pd (Morioka and Hasebe 1990) if the precipitates are metallic, solid solutions. If a particular boundary possesses a grain boundary energy and structure amenable for Ag-only precipitates (i.e., Figure 36 implies that this will be a random, high-angle grain boundary), then Pd would not be expected to be excluded from also being present on this boundary, based on its apparent ability to precipitate on grain boundaries of all energies and types. Figure 36 shows Pd-only and Pd+Ag precipitates are prevalent on random, high-angle grain boundaries. Thus, it is not clear what combination of grain boundary energy and structure could allow

precipitation of Ag and prevent Pd from precipitating also. The possibility exists that Pd is actually present in the Ag-only precipitates found in this study but at levels below the limits of detection of the characterization methods (estimated to be on the order of 0.2 at.%). The same may be said of the Pd-only precipitates that Ag may actually be present but below the limits of detection. If so, then the grain boundary structure and/or energy of random, high-angle grain boundaries somehow determines the ratio of Ag to Pd in the fission product precipitate, again implying that not all random, high-angle grain boundaries should be considered equivalent or even similar when it comes to segregation and transport of fission product elements.

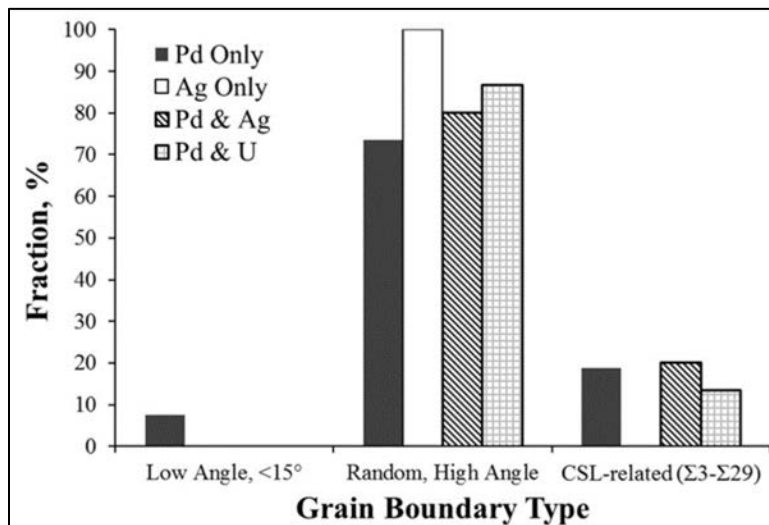


Figure 36. Distributions of fission product precipitates, as a percentage, by grain boundary type for Pd only, Ag only, Pd+Ag, and Pd+ U.

Alternatively, if the fission product precipitates are in the form of silicides, then it might be possible to have Ag in solid solution in a Pd-silicide to produce the Pd+Ag precipitates, and yet not have Pd in solid solution in an Ag-silicide to produce the Ag-only precipitates. However, Ag-silicides do not seem to occur (Hassam 2006). Olivier and Neethling (2013) found that only very small amounts of Pd were necessary to assist Ag migration through SiC, and the Pd concentrations may be below the limits of detection used in this study. Therefore, the existence of Ag-only precipitates found in this study is unexplained at this time and will require determination of not only the crystal structure of the Ag-only precipitates but also that of the Pd and Pd+U precipitates to fully understand the segregation of the fission product elements during (and after) irradiation. A more detailed understanding of the grain boundary energy and grain boundary structure also will be required.

It also must be kept in mind that the results reported here may or may not have implications on the dominant transport mechanism(s) in the release of fission products from irradiated TRISO fuel. One must consider that dominant transport mechanism(s) may be sufficiently fast and, when coupled with low fission product production rates, especially in the case of Ag (Sterbenz and Gougar 2011), fission products may never accumulate to the extent that they exceed the minimum levels of detection for EDS analyses. Thus, fission products are not detected in this analysis and/or the concentration levels may never achieve that necessary for the formation of precipitate on the grain boundary. Therefore, the grain boundaries and triple junctions that exhibit precipitates containing fission products and uranium may simply represent slower transport paths that allow for accumulation of the fission products to levels exceeding the limits of detection and/or that necessary for the formation of a precipitate. However, both scenarios suggest fission product transport (and uranium transport) appears to be dependent on the specific properties of individual grain boundaries and triple junctions. Crystallographic information on grain boundaries and triple junctions with and without precipitates containing fission products, along with

modeling and simulation studies on transport in these two types of grain boundaries and triple junctions, will be required to fully elucidate the dominant transport mechanism through SiC. Some work has seemed to indicate that grain boundary character has a strong influence on at least Ag migration in SiC (Khalil et al., 2011). Experimental efforts to explore the influence of grain boundary character have been presented above and will be discussed more below.

Finally, it needs to be mentioned that the results presented here seemingly contradict those reported by O'Connell and Neethling (2014) on Ag migration in neutron-irradiated SiC, where they saw very little migration at similar temperatures and irradiation conditions. However, a number of experimental differences exist between that work and the results presented here. Silver migration in O'Connell and Neethling's (2014) study was characterized following a 24-hour anneal at 1000°C on samples that were created by depositing thin layers of Pd and Ag on *previously* neutron irradiated CVD-SiC. The source of Pd and Ag in this study, though much lower in concentration, was present at the SiC layer throughout the duration of the neutron irradiation, which was over 600 times longer than in the O'Connell work. Additionally, the time-averaged, volume-averaged temperature at which Ag migration took place in this work was also slightly higher (i.e., about 1070°C versus 1000°C for the O'Connell work), where Ag-110m transport appears to dramatically increase (Hunn et al., 2015a). Additionally, the TAVA temperature of the particle compact (~1100°C) may not accurately reflect the actual temperature of the particle in this study since particle temperature is a function of its location within the compact (Hawkes and Murray 2014). The differences in behavior observed here can reasonably be attributed to differences in experimental conditions and are in no-way contradictory to those obtained by O'Connell and Neethling (2014). There is no reason to believe their conclusions regarding the strong influence of neutron irradiation fluence and irradiation temperature on Ag migration behavior do not apply.

### **3.1.5 Fission Product Phase Identification Structural Information and Irradiation Effects**

Although the focus of the work performed was on fission product identification and location, limited observations were made on the cavities formed due to irradiation and structure of the precipitates. Figure 37 shows spherical-shaped gas bubbles concentrated alongside grain boundaries near a Pd-rich precipitate. Numerous results suggest that neutron damage may also have an impact on the transport mechanism. O'Connell and Neethling (2014) recently reported that the transport of a Pd-Ag mixture along grain boundaries in neutron-irradiated commercial polycrystalline SiC annealed at a 1000°C in contact with the Pd-Ag mixture was significantly enhanced compared to Pd-Ag transport in unirradiated SiC. In this out-of-reactor study, the penetration of Pd in neutron-irradiated commercial SiC was investigated by annealing the irradiated ( $9.4 \times 10^{21}$  n/cm<sup>2</sup> at 1460°C,  $E > 0.1$  MeV) 3C-SiC in contact with a vapor-deposited Pd layer for 24 hours at 1000°C. A TEM investigation of the neutron-irradiated SiC revealed the presence of a high concentration of voids aligned in rows along the (111) planes of SiC along with Pd inclusions. The rows of neutron irradiation-induced voids in SiC were found to enhance the penetration of Pd in the SiC grains. The clustering of voids in bands parallel to the (111) planes is consistent with the suggestion that void nucleation is aided by impurities segregated at lattice faults (such as stacking faults), which readily form on (111) planes in 3C-SiC due to its very low stacking fault energy (Price 1973).

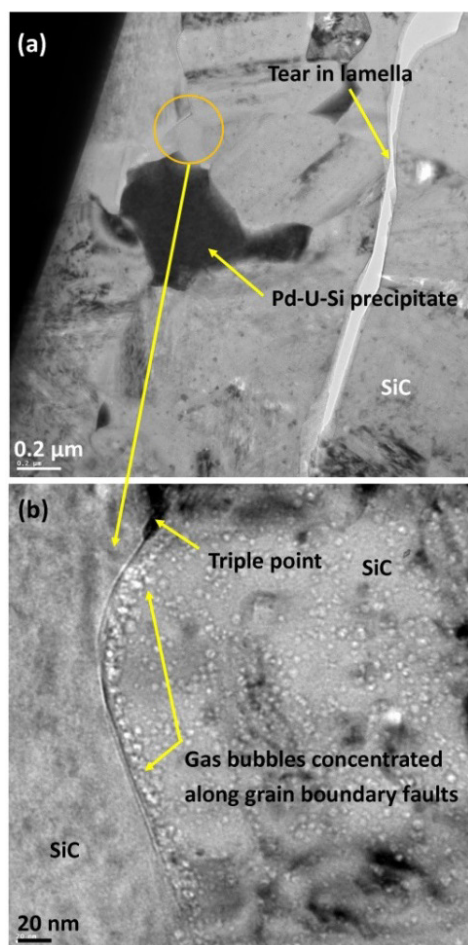


Figure 37. TEM micrographs of Particle AGR1-632-034. TEM sample 2a shown in (a) a micron-sized Pd-U-Si precipitate in the SiC layer, with (b) a higher magnification image of the grain boundary marked with an orange circle in image (a). The spherical-shaped gas bubbles concentrated alongside grain boundaries near the Pd-rich precipitate (image [b] is adapted from van Rooyen et al., 2012c, van Rooyen et al., 2013).

Several of the TEM-EDS spectra from micron-sized precipitates in SiC layers in particles AGR1-632-034 and AGR1-632-035 show qualitatively detectable concentrations of Ag, Zr, and Pu or Sr. A number of ternary silicides with the general formula  $RX_2Si_2$ , where R is U, Th, or Gd and X is a 4d transition metal (Cr, Mn, Fe, Co, Ni, Cu, Ru, Rh, Pd, Ir, Pt, or Au) have been synthesized and determined to have  $ThCu_2Si_2$ -type structures (Shemirani et al., 1993, Leciejewicz et al., 1979, Ptasiwicz et al., 1981, Marazza et al., 1977, Buschow and Mooij 1986). Specific examples include  $UPd_2Si_2$  and  $GdAg_2Si_2$ . Although the Advanced microscopy and micro-analysis team are not aware of any reported syntheses of  $UAg_2Si_2$ , it seems likely that it would also have a  $ThCu_2Si_2$ -type structure. Given the identical atomic radii of Ag and Pd (both 0.144 nm for the pure elements) (Brandes and Brook 1992), it seems reasonable to speculate that Ag atoms would substitute for Pd atoms in  $UPd_2Si_2$ . Although there is less evidence to support the speculation, it also seems reasonable to expect that any Pu that may be present could substitute for U. Although Zr is a 4d transition metal, no reports of  $UZr_2Si_2$  or any phase containing U, Pd, Si, and Zr, were found. However, Zr does form a variety of phases with U, Pd, and Si. It seems likely that the Zr in the precipitates in particles AGR1-632-034 and AGR1-632-035 is in one of these phases. Sr is not a transition metal and we are not aware of any reason to expect that it would substitute into  $UPd_2Si_2$ , assuming that it is actually present in the sample (van Rooyen et al., 2012).

### 3.1.6 Inter- and Intragranular Identification of Palladium and Uranium

STEM examination of additional lamellae from AGR1-632-035 revealed that only Pd was found in all 16 triple points analyzed on the outermost region of SiC. Ag was located mostly with Pd in the inner and center sections of the SiC layers. U was never found with Ag, but often found with Pd. Only a small number of intragranular particles were analyzed on each sample (Lillo and Van Rooyen 2014).

**3.1.6.1 Intragranular Precipitates.** Although more prevalent in the inner sample (Figure 6) from the SiC layer, intragranular precipitates were found throughout all three samples (i.e., inner, center, and outer in Figure 6[c]). Figure 38 and Figure 39 show examples of these mostly round and one rod-like precipitates. In all compositional profiles obtained from intragranular precipitates, the only element present in significant quantities (other than Si or C) was Pd (Lillo and Van Rooyen 2014).

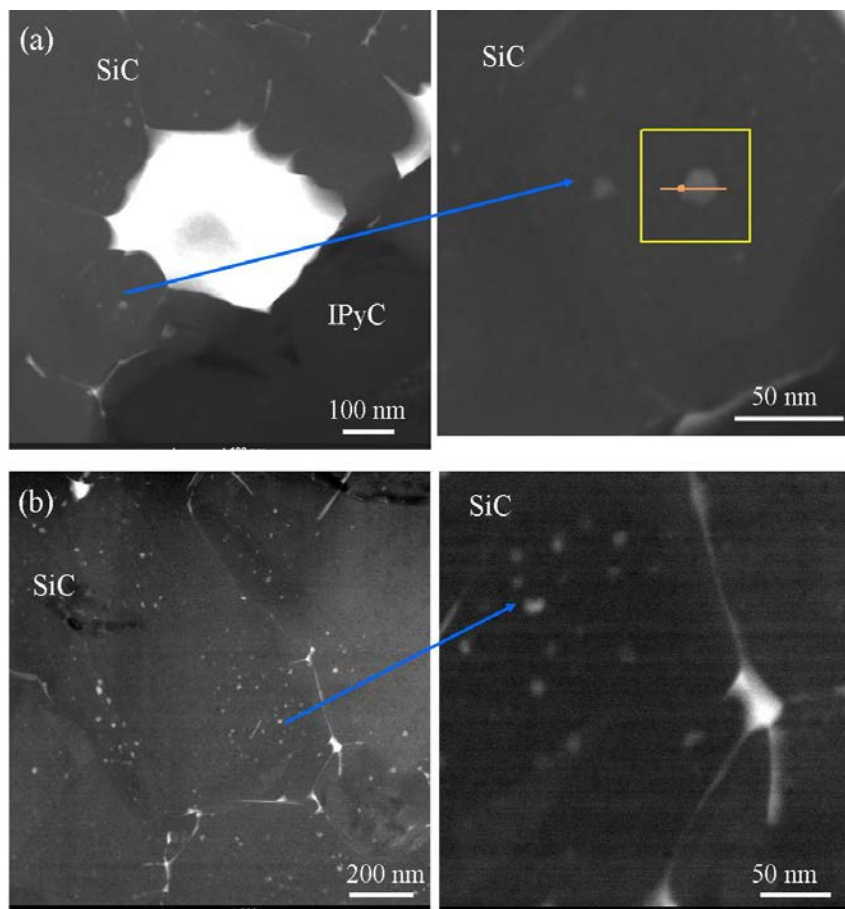


Figure 38. STEM HAADF images showing nanometer-sized Pd precipitates (about 10 to 20-nm diameter) inside SiC grains (a) at the SiC-IPyC interface and (b) approximately 4  $\mu\text{m}$  inside the SiC layer (images adapted from van Rooyen, Wu, and Lillo 2014b).

The different types of Pd-containing precipitates observed in Particle AGR1-632-035-6b (where 6b is the Lamella number) are exemplified further in Figure 40. Figure 40(a) shows the examination area and Figure 40(b) shows the intragranular Pd-rich precipitates labeled as P1 and P2, while Pd-rich triple points are indicated with T1 to T3. Additional precipitates identified in Figure 40(c) are also Pd rich, and a U-rich honeycomb-like network is shown in Figure 40(d).

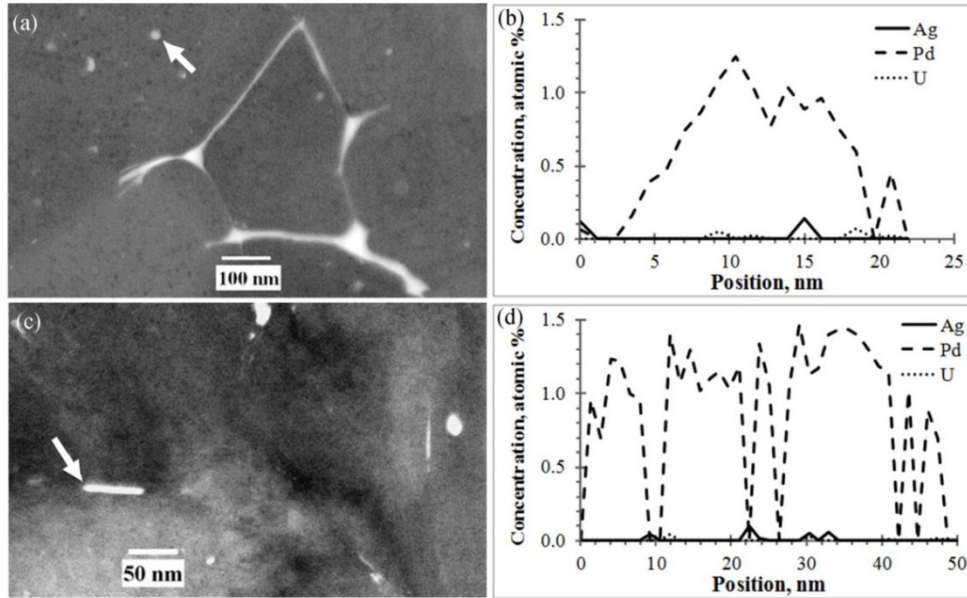


Figure 39. Examples of intragranular precipitates – (a) round and (c) rod-like, showing only significant amounts of Pd – (b) and (d), respectively.

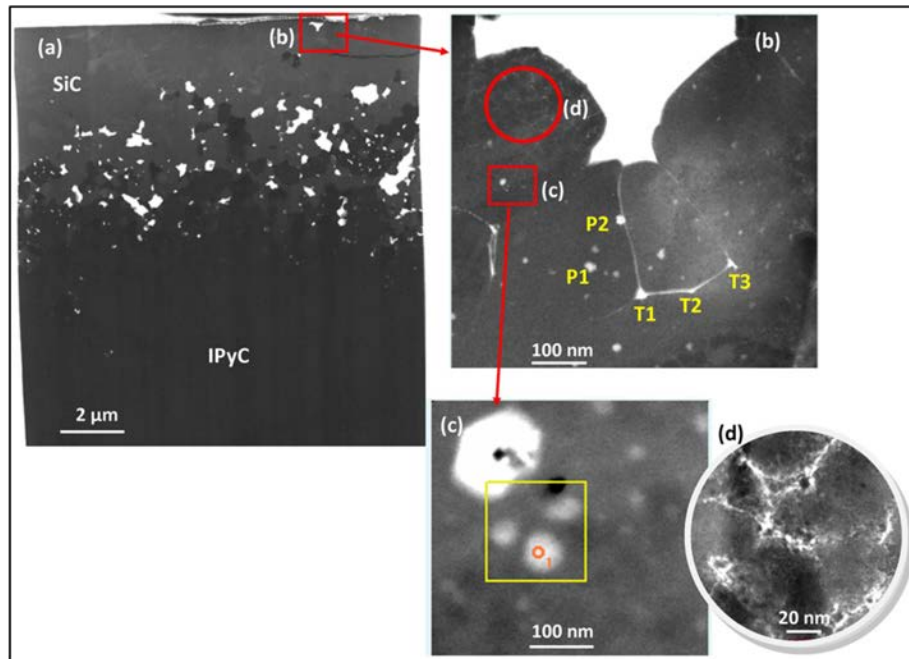


Figure 40. STEM images of (a) fission-product distribution networks at the SiC-IPyC interlayer of Particle AGR1-632-035, (b) higher-magnification image showing intragranular precipitates labeled P1 and P2 and the triple points T1 through T3, which all contain mainly Pd, (c) higher magnification of the Pd-rich nodules, and (d) a honeycomb network of mainly U (adapted from Leng et al., 2016).



**3.1.6.2 Grain Boundaries.** Intergranular precipitates on grain boundaries only showed significant levels of Pd, U, and/or Ag. Grain boundary precipitates with exclusive concentrations of Pd were quite prevalent. A significant number of grain boundaries that exhibited concentrations of only Ag were found in the inner and center samples. Ag and U, whether alone or in combination with other elements, were not found in any grain boundaries analyzed in the outer sample. Also, no grain boundaries with measurable concentrations of co-located Pd, U, and Ag were found in any grain boundary in the three samples (inner, center, and outer) of AGR1-632-035.

These observations on distribution of Pd, U, Ag, and the combinations of these elements in grain boundaries across the irradiated SiC layer are summarized quantitatively in Figure 41. In all three samples, grain boundary precipitates exhibiting only Pd were most prevalent. Grain boundary precipitates with Pd and Ag associated together were found in the inner Lamella (i.e., the “IE” sample in Figure 6[c]) but not in the center or outer Lamella (i.e., the “Ctr” or “OE” samples in Figure 6[c], respectively). However, grain boundary precipitates exhibiting only the presence of Ag were found in both inner and center lamellae, but not in grain boundaries of the outer lamella. U was found with Pd in grain boundary precipitates of the inner and center samples, but never found alone or associated with Ag in any of the samples.

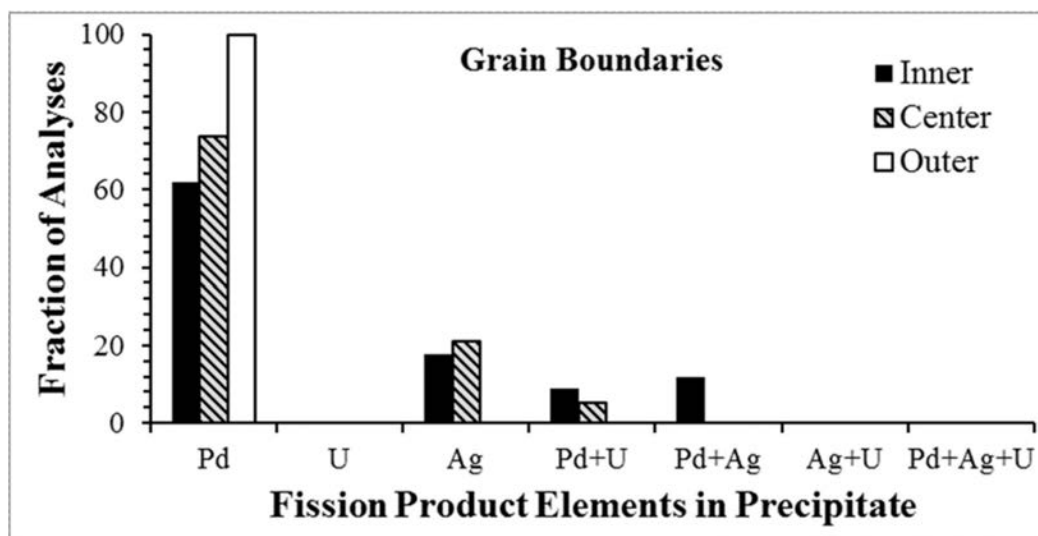


Figure 41. Summary of the distribution of elements in fission product precipitates found on SiC grain boundaries in AGR1-632-035.

**3.1.6.3 Triple Junctions.** Fission product precipitates were also prevalent at triple junctions; however, as with grain boundaries, not all triple junctions had fission products and transuranic elements associated with them. Triple junctions with precipitates exhibited segregation behavior of fission products and U similar to that of grain boundaries. As in the observations on grain boundaries, triple junctions also exhibited significant concentrations of either Pd, Pd + U, Pd + Ag, or Ag. Typical compositional line profiles observed for each type of segregation behavior are given in Figure 42. The relative fraction of each type of segregation is summarized in Figure 43. A relatively high fraction of triple junction precipitates in all three samples (inner, center, and outer) exhibit the presence of only Pd with no indication of either U or Ag (see Figure 42[a] and Figure 43). A somewhat smaller fraction of triple junction precipitates in the inner and center lamellae showed elevated concentrations of both Pd and U (see Figure 42[b] and Figure 43). Also, a significant fraction of triple junction precipitates in the inner and center lamellae were found to contain both Pd and Ag (see Figure 42[c] and Figure 43). Only two triple junctions in the inner Lamella were found that exhibited only Ag without significant concentrations of either Pd or U (see Figure 42[d]). Triple junction precipitates containing only U, Ag+U or Ag+U+Pd were not found in any of the areas analyzed on the three samples.



Line profiles showing significant amounts of both Pd and U or both Pd and Ag across triple junctions are consistent with an alloy or compound, where these elements are intimately mixed, rather than overlapping pure (or nearly pure) phases (elemental or silicides) of Pd, Ag, and U. The U and Ag concentration profiles (as in Figure 42[b] and Figure 42[c]) tend to follow the Pd concentration profile closely with the maximum concentration of each element occurring at the same location along the analysis line. Precipitates in triple junctions that contain only Pd, U, or Ag could overlap due to stereological effects and both would be illuminated by the electron beam in the TEM, giving rise to concentration line profiles containing both Pd and U or Pd and Ag. However, if such overlapping phases existed, the concentration profiles of either U or Ag would likely be shifted to the right or left with respect to the concentration profile of Pd, and the location of maximum concentration of U or Ag would not coincide with the location of the maximum Pd concentration in the line profiles, at least to some degree. (The precipitates would have to be the same size and exactly align to produce the concentration profiles in Figure 42[b] and Figure 42[c]). This “out-of-phase” behavior was not observed in any of the concentration line profiles of triple junctions exhibiting the presence of both Pd and U or both Pd and Ag. Furthermore, no line profiles across triple junctions were found to contain solely U, U in combination with Ag, or U in combination with Ag and Pd (see Figure 43), which would be expected from the overlap of U or Pd+U precipitate with Ag or Pd+Ag precipitates. These observations tend to indicate that precipitates are not overlapping phases, but rather a single phase, compound, or intermetallic where the elements are intimately mixed.

The distribution of Pd, U, Ag, and the combinations of these elements in triple junctions across the irradiated SiC layer are summarized in Figure 43. This bar chart shows that triple junctions in the inner sample (closest to the fuel kernel) contained precipitates with only Pd, Pd+U, Pd+Ag, or only Ag. However, no triple junction precipitates with just U, U+Ag, or Pd+U+Ag were found in this sample or in the center and outer samples. In the center sample, triple junction precipitates with Pd, Pd+U, and Pd+Ag were found, while precipitates with just Ag, just U, U+Ag, or U+Ag+Pd were not. Finally, in the outer sample (furthest from the fuel kernel), all 16 triple junctions analyzed contained only Pd. No amount of Ag or U, alone or in combination with other elements, was observed above the level-of-detection in any of these triple junction precipitates.

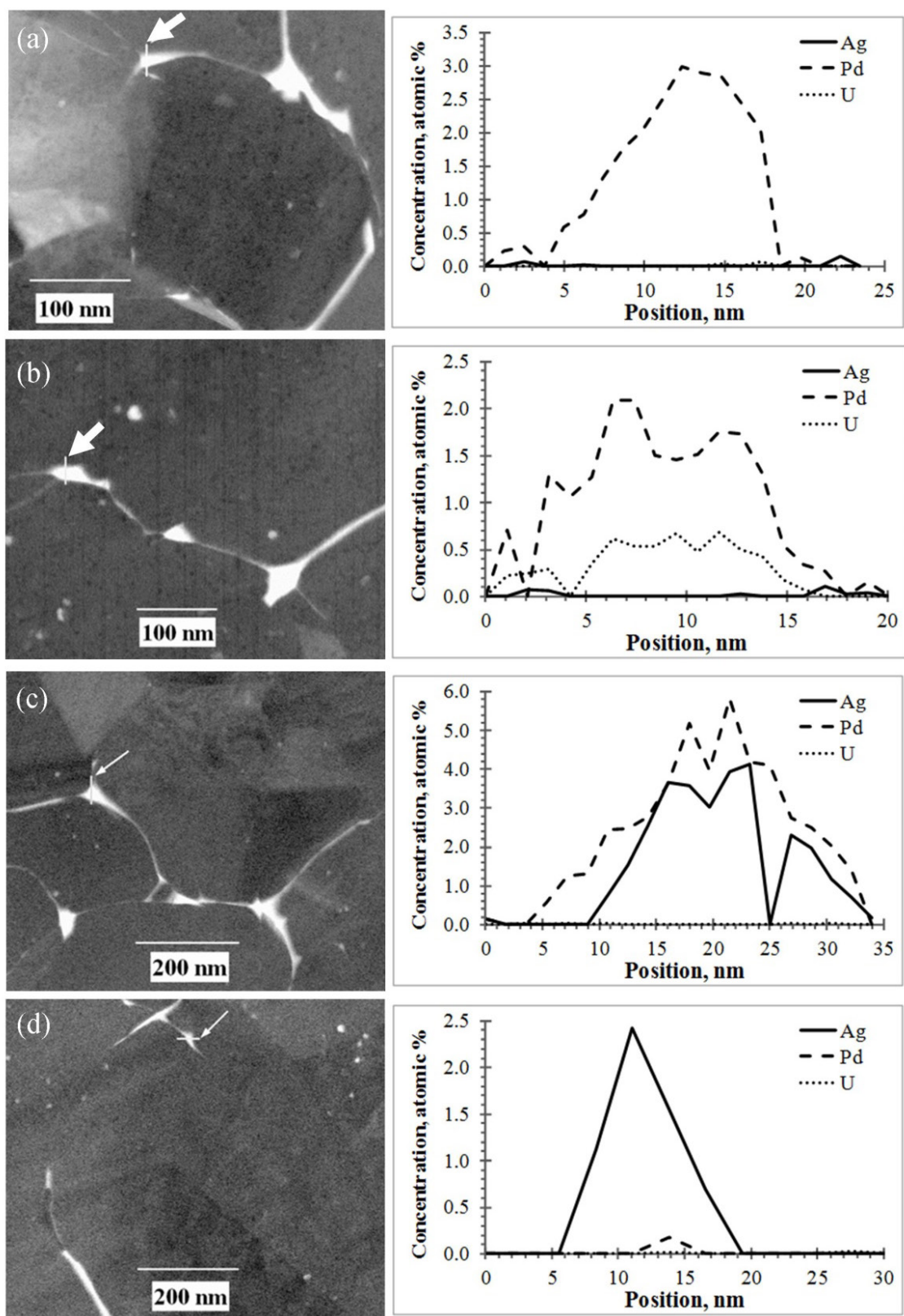


Figure 42. Examples of triple junctions containing (a) only Pd, (b) Pd and U, (c) Pd and Ag, and (d) Ag.

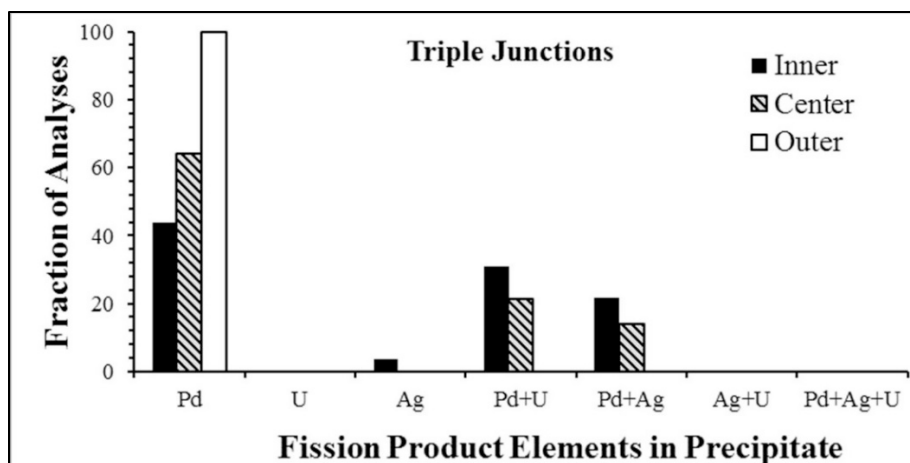


Figure 43. Summary of the distribution of the fission product elements and uranium in triple junctions in the SiC layer of Particle AGR1-632-035.

### 3.1.7 Summary and Main Findings on Compact 6-3-2 Particles

- STEM examination on Particle AGR1-632-035 (Lamella 6b) provided the first evidence of nano-sized Ag precipitates at triple points and grain boundaries in the SiC on the edge of the SiC-IPyC interface. Cadmium was also found to be present in the triple junctions.
- Detailed examination of the low- and high-Ag-retention particles showed very similar structural results on micron-sized precipitates, namely a structure similar to  $UPd_2Si_2$ . The EDS data suggest significant compositional variations and none of the EDS analyses indicate stoichiometric  $UPd_2Si_2$ .
- Cs was not identified in the SiC layer, although a Cs-rich precipitate was observed in a crack in the IPyC from Particle AGR1-632-035. No Cs was observed in the SiC grain structure itself during basic TEM examination.
- Polytype 2H SiC was also identified in Particle AGR1-632-030 (low Ag retention); however, no conclusion could be reached if it was due to temperature exposure during irradiation.
- Spherical-shaped cavities concentrated along grain boundaries near a Pd-rich precipitate.
- Spherical nano-sized palladium-rich precipitates were found inside the SiC grains.
- Pd and U were identified both inter- and intragranularly in the SiC layer from intact TRISO-coated particles. The intragranular Pd-rich precipitates were generally nano-sized and nodular and could also contain small concentrations of Cd and U. Pd-rich precipitates also are present at triple-points and grain boundaries, either alone or co-existing with Ag and Cd or with U.
- It is also important to note that no significant Pd corrosion at the SiC-IPyC interface was observed for all intact AGR-1 particles examined. Analysis of the composition and distribution of these precipitates found on grain boundaries, triple junctions, intragranular precipitates, and intergranular precipitates allowed the following conclusions to be made for Particle AGR1-632-035:
  - The intergranular precipitates were found to contain mainly Pd, Ag, and/or U
  - Palladium was the most common element found in these intergranular precipitates
  - Often either Ag or U was found, along with Pd in these intergranular precipitates
  - Grain boundaries were more likely to contain precipitates exhibiting only significant amounts of Ag compared to triple junctions

- U was never detected when Ag was present and vice versa. Also, U was never found alone, it was always associated with Pd
- Pd was found throughout the 35- $\mu\text{m}$  thick SiC layer
- U and Ag were detected only 23 and 24  $\mu\text{m}$ , respectively, along the radial direction into the SiC layer.
- Not all grain boundaries and triple junctions contained precipitates, suggesting the crystallographic relationships associated with these microstructural features may be important.
- Intragranular, nano-precipitates (about 10 nm in diameter) were found to be Pd-rich without evidence for either Ag or U.
- The grain structure of the SiC layer in an irradiated TRISO fuel particle from the AGR-1 experiment is composed mainly of CSL-related grain boundaries (~59%, of which most are twin boundaries) with a significant fraction of random, high angle grain boundaries (~29%) and a small fraction of low-angle grain boundaries (i.e., on the order of 11%).
- The CSL-related grain boundary fraction increased from the IPyC/SiC interface to the SiC/OPyC interface, mainly due to the increase of the twin boundary fraction, while the fraction of random, high-angle grain boundaries decreased from the IPyC to the OPyC.
- Fission product precipitates were commonly found on random, high-angle grain boundaries and to a lesser degree at low-angle and CSL-related grain boundaries.
- Pd was found at all types of grain boundaries, but most prominently on random, high-angle grain boundaries.
- Pd-U and Pd-Ag precipitates were found on CSL-related and random, high-angle grain boundaries, but not on low-angle grain boundaries.
- Precipitates containing only Ag were only found on random, high-angle grain boundaries (i.e., not on either low-angle or CSL-related grain boundaries). The reason for Ag-only precipitates is not known.

### **3.2 Irradiated Variant 1 Fuel Examination: Compact 5-3-1**

Various STEM lamellae were prepared from selected precipitate-rich areas in the coatings of particles from AGR-1 Compact 5-3-1 (Variant 1 TRISO fuel) that exhibited both low (Particle AGR1-531-038) and high (Particle AGR1-531-031) Ag-110m retention. Fission product precipitates in a number of different areas on each sample (inner, center, and outer) from each particle were identified in the TEM using a HAADF while operating the TEM in STEM mode. The qualitative composition of each precipitate in these areas was determined using EDS, while the parameters of the grain boundaries in each area analyzed were determined from precession electron diffraction data collected using the ASTAR system on TEM. The fuel kernel lamellae were not examined at this stage due to budget constraints.

#### **3.2.1 Particle Selection and Analysis Performed**

The Compact 5-3-1 particles were selected based on the ratio of the measured Ag-110m activity to the predicted activity as shown in Figure 44 to investigate microstructural characteristics related to Ag retention (Demkowicz et al., 2016a). From these distributions, particles were chosen to represent particles having a low (Particle AGR1-531-038: less than 0.19 ratio) and high (AGR1-531-031: 1.05 ratio) Ag-110m measured-to-calculated ratio. Figure 44 indicates that particles exhibit Ag-110m retention ranging from about 0.15 to 105% of the predicted inventory (the particle with a value of 120% in Figure 44 is excluded due to its abnormal distribution of fission product inventories, as discussed in Demkowicz 2016a). The presence of particles with measured-to-predicted ratios greater than 1 is believed to be related to the sizeable variation in the inventory of Ag-110m generated in particles depending on

their original location within the fuel compact (Demkowicz et al., 2015a). The specific advanced microscopy and micro-analytical analyses performed for each particle are indicated in Table 26.

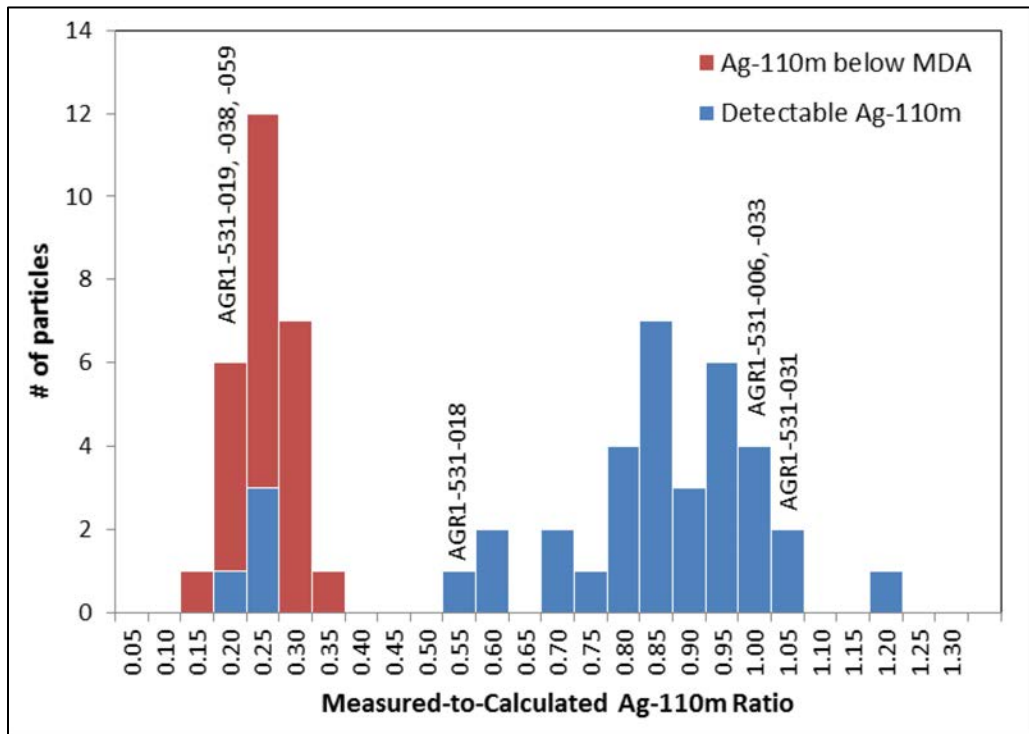


Figure 44. Distribution of the measured-to-calculated Ag-110m activity ratio for the irradiated Compact 5-3-1 particles (adapted from Demkowicz et al., 2016a). The M/C values for particles AGR1-531-059 and 038 are based on the minimum detectable activity for Ag-110m in the gamma spectra, because no Ag-110m was detected.

Table 26. Advanced microscopy and micro-analysis examination performed on Compact 5-3-1 particles.

Techniques	SEM <sup>a</sup> EDS/WDS	EELS/ EFTEM	STEM	EPMA	PED	APT	HRTEM
Compact 5-3-1 (Variant 1)							
AGR1-531-038 (Low (< 19%) Ag retention)	X <sup>a</sup>	—	X	—	X	—	—
AGR1-531-031 (High (105%) Ag retention)	X <sup>a</sup>	—	X	—	X	—	—

a. Reported in separate report by van Rooyen et al., 2017.

**3.2.1.1 Lamellae Locations for Particles AGR1-531-031 and AGR1-531-038.** TEM samples were extracted from these polished cross sections (Figure 45) using conventional FIB techniques. The buffer layer cracked in Particle AGR1-531-038 and the fuel kernel protruded into gaps produced by the radial buffer cracks (Figure 45[a]). Particle AGR1-531-031 (Figure 45[b]) exhibited an intact buffer layer except for a hairline crack, surmised to have formed late in irradiation (Demkowicz 2016a). The plane of the TEM samples was perpendicular to the polished surface in the radial direction. The FIB specimens are shown in Figure 46 and Figure 47 for particles AGR1-531-031 and AGR1-531-038, respectively. These SiC and IPyC-SiC lamellae were transported to CAES during December 2013.



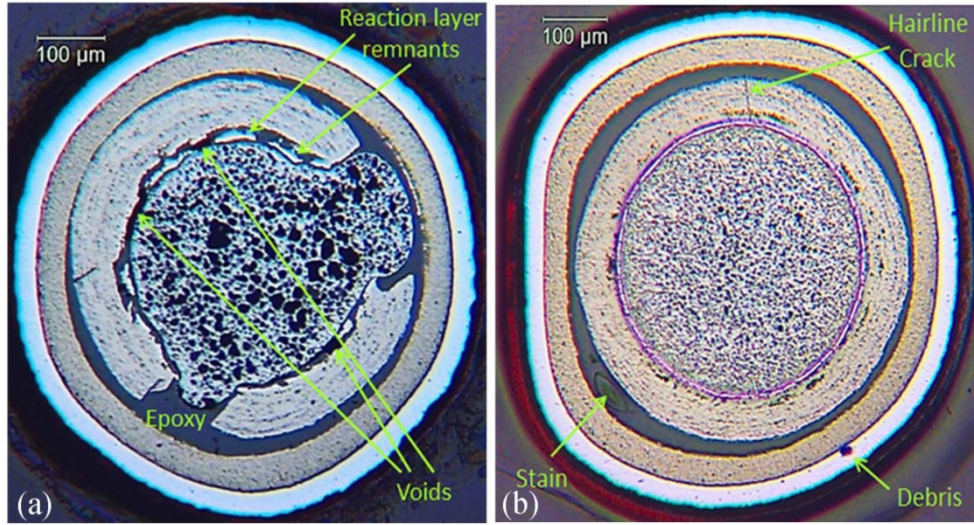


Figure 45. Polished metallographic cross sections through TRISO particles (a) AGR1-531-038 and (b) AGR1-531-031 (Demkowicz 2016a).

The locations in the SiC layer on the polished sample and on the FIB locations for Particle AGR1-531-031 are shown in Figure 46 (subsequently referred to as AGR1-531-031-1, AGR1-531-031-1b, AGR1-531-031-2, AGR1-531-031-3, and AGR1-531-031-4). Similarly, the specific locations of the samples taken from the SiC layer of Particle AGR1-531-038 are shown in Figure 47 as Sample 1, 2, 3, and 4 (subsequently referred to as AGR1-531-038-1, AGR1-531-038-2, AGR1-531-038-3, and AGR1-531-038-4, respectively).

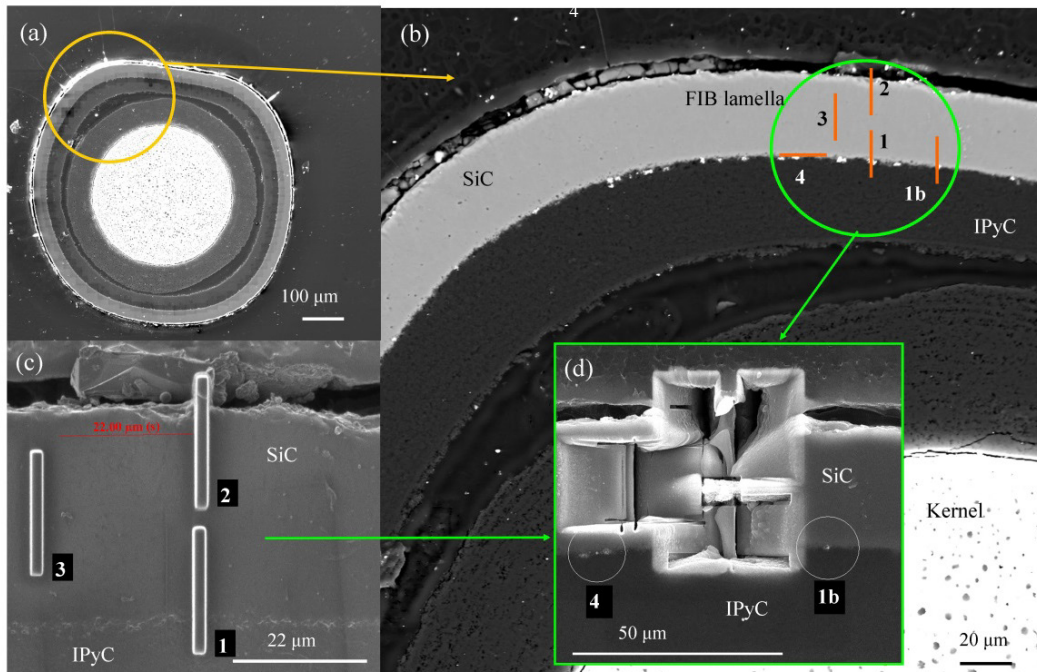


Figure 46. (a) Locations of the TEM samples extracted from Particle AGR1-531-031, (b) larger magnification of the SiC layer with the lamellae locations schematically presented, and (c) (d) their locations on the SiC layer at higher magnification ([d] shows the locations of Lamellae 1 through 3 after FIB extraction).

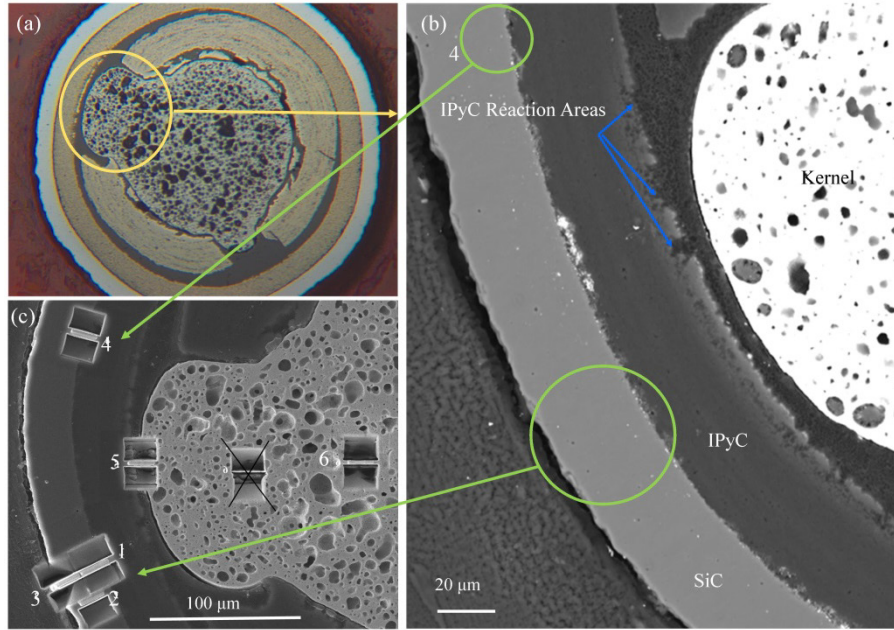


Figure 47. (a) Locations of the TEM samples extracted from Particle AGR1-531-038, (b) larger magnification SEM image showing the area of where the TEM samples will be fabricated from, and (c) their locations after FIB extraction.

### 3.2.2 Particle AGR1-531-031

In this section, qualitative chemical composition, fission product identification, and crystallographic characteristics are provided for Particle AGR1-531-031.

**3.2.2.1 Chemical Composition of Minor Elements of Particle AGR1-531-031.** This section reports the qualitative chemical composition of minor elements on Particle AGR1-531-031 to determine, first, the type of fission products present; second, the location of these particles in relation to the SiC layer thickness; and last, the fission product elemental composition. The reported fission product precipitate compositions (atomic %) are qualitative or semi-quantitative in nature as described in Section 2.1.2.3. A summary of the minor elements present in these three lamellae is given in Table 27, with Sections **Error! Reference source not found.** to 3.2.2.1.2 describing the precipitates found in the inner, center, and outer areas as indicated in Figure 46. From this summary, it was determined that precipitates contain Pd, Ag, Ce, Eu, Cs, U, and Pu that were found in the inner area of the SiC layer, close at the IPyC-SiC interlayer, and no precipitates were found in the center and outer areas of the SiC layer. From this observation, it has been suggested that retention behavior may be attributed to the inner layer microstructural properties, although a temperature effect cannot be ruled out.

Figure 48 shows a qualitative trend analysis of precipitate composition (Pd, Ag, and U only) as a function of the approximate distance from the SiC-IPyC interface of Particle AGR1-531-031. This schematic presentation shows the movement of Pd, Ag, and U to an approximate distance from the IPyC-SiC interface of 0.9, 1.7, and 8.7 µm, respectively. Although there was a slight trend of decreasing precipitate U concentration with increasing distance from the IPyC-SiC interface observed as shown in Figure 49, it should be tested with a larger data set for confirmation (it should also be recognized that the effect of precipitate size are not yet considered in these trend analyses and is recommended for the future). Because of the limited dataset, no specific trend of the concentration and Pd/U and Pd/Ag ratios versus distance correlation is determined.

Figure 50 shows the lamellae fabricated from the inner (Lamellae 1, 1b, and 4, respectively), center (Lamella 3), and outer (Lamella 2) areas of Particle AGR1-531-031.

Table 27. Identification of minor elements present in fission product precipitates in the SiC layer of Particle AGR1-531-031 (locations of lamellae and corresponding analyzed areas are shown in Figure 46 and Figure 50, respectively).

Lamella	Area	Elements Present									Precipitate Identification
		C	Si	Pd	Ag	Cs	Ce	Eu	U	Pu	
Inner Lamella 1	Area 1	X	X				X	X	X		U, Ce-U
	Area 2	X	X						X	X	U, Pu
	Area 3	X	X						X	X	U-Pu
	Area 4	X	X		X	X			X		Cs, Ag-U, Cs-U
	Area 5	X	X	X	X	X			X		Cs, Pd, Ag-U
Inner Lamella 1b	Area 1	X	X	X		X			X		Pd, Cs, U
Inner Lamella 4	Area 1	X	X						X		U
Summary		X	X	X	X	X	X	X	X	X	

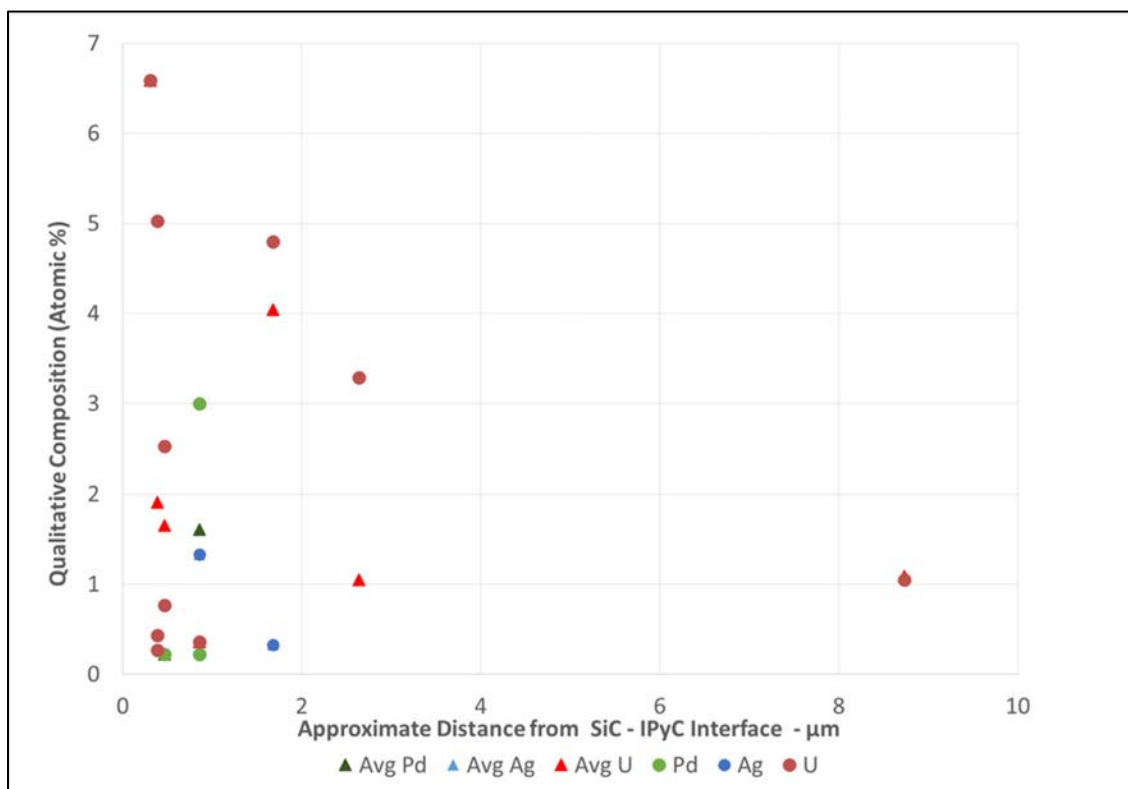


Figure 48. Qualitative trend analysis of precipitate composition (Pd, Ag, and U only) as a function of the approximate distance from the SiC-IPyC interface of Particle AGR1-531-031.



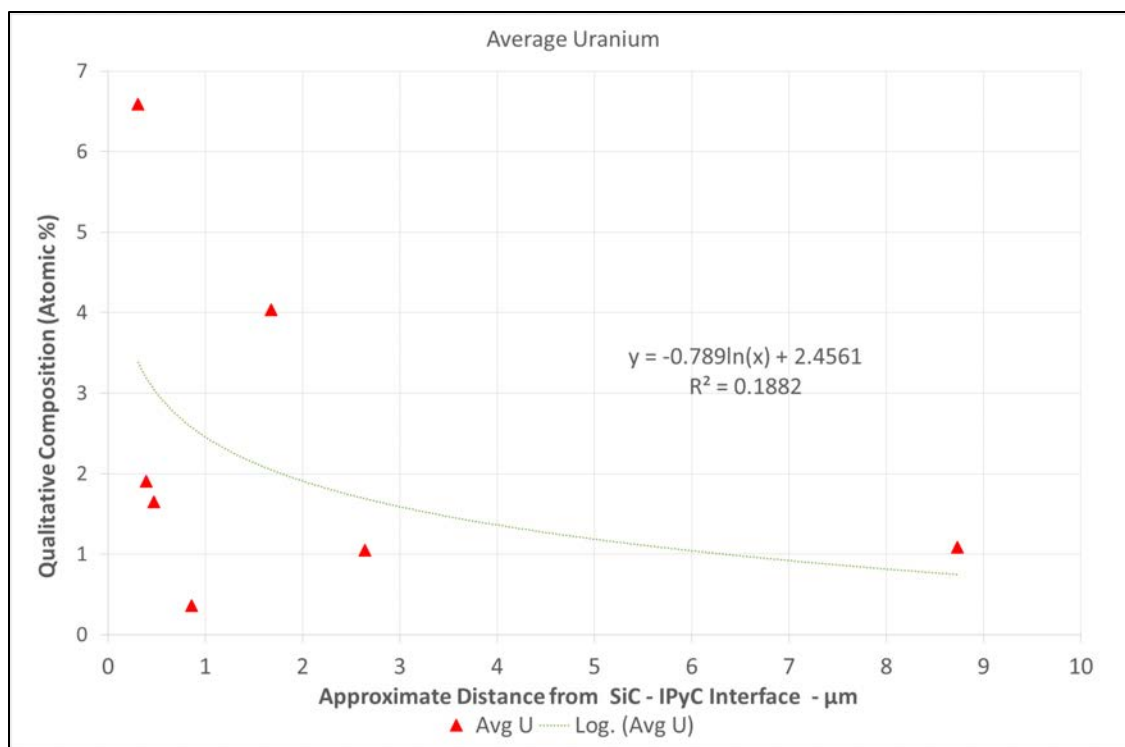


Figure 49. Qualitative trend analysis of precipitate composition for U as a function of the approximate distance from the SiC-IPyC interface of Particle AGR1-531-031.

**3.2.2.1.1 Chemical Composition in the Inner Area of the Silicon Carbide Layer (Lamellae 1, 1b, and 4).** Figure 50(a), (b), and (e) show the lamellae fabricated from the inner areas (Lamellae 1, 1b, and 4, respectively) of Particle AGR1-531-031. Precipitates were examined and the compositions determined by qualitative EDS analysis for seven areas (highlighted in yellow) within the three lamellae. From these quantitative analyses it was determined that precipitates contain Pd, Ag, Ce, Eu, Cs, U, and Pu. It is interesting to note that Cs was found in three precipitates in the inner area of the SiC layer, contrasting the finding from precipitates from Compact 6-3-2 particles where no Cs was found in all precipitates examined. The examined precipitates, with corresponding qualitative composition, are indicated in Figure 51, Figure 52, Table 28, and Table 29.

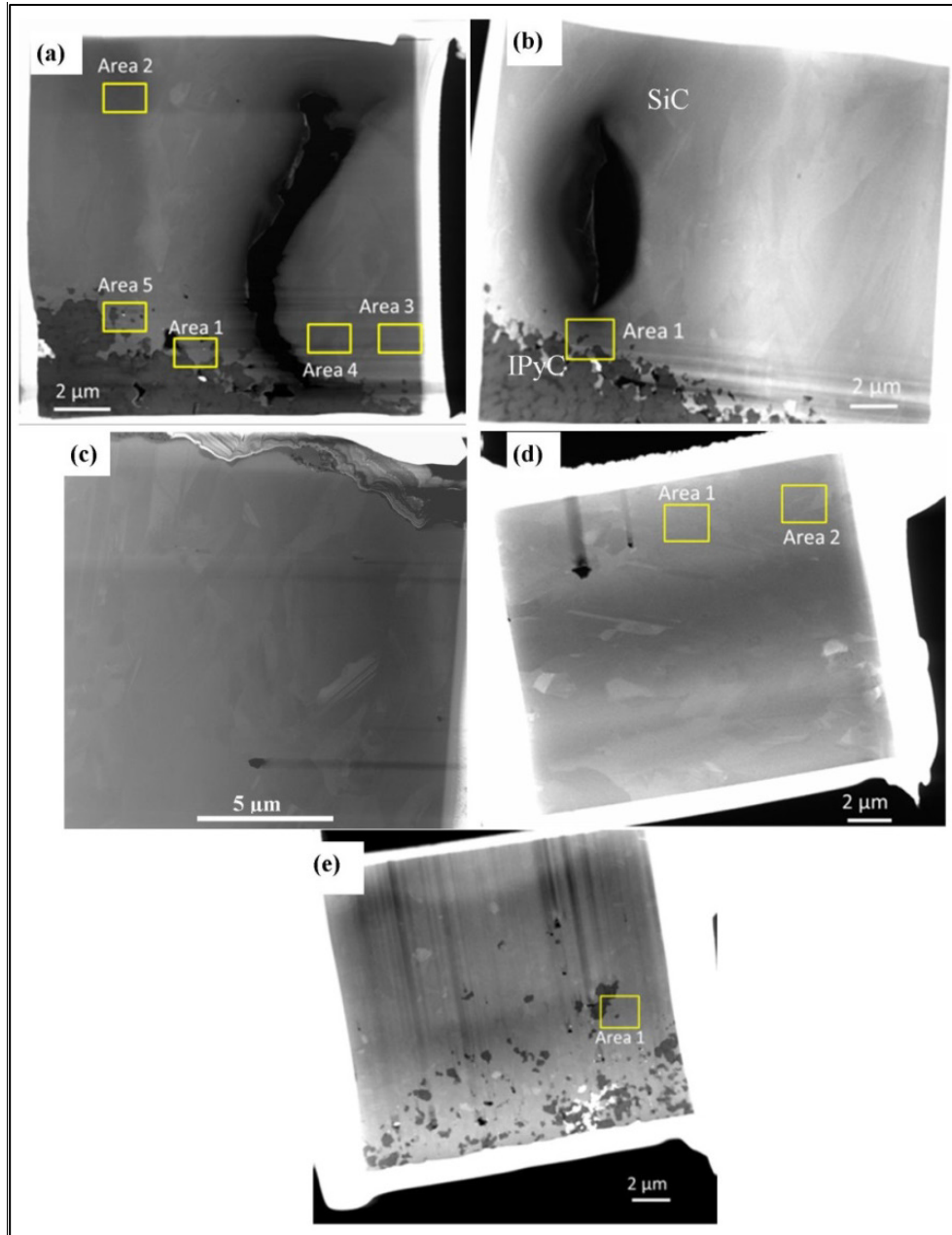


Figure 50. Low magnification HAADF images of the TEM samples of the SiC layer in AGR1-531-031 showing no precipitates except very near the IPyC/SiC interface. (a) Inner area (Lamella 1), (b) inner area (Lamella 1b), (c) outer area (Lamella 2), (d) center (Lamella 3), and (e) inner area (Lamella 4).

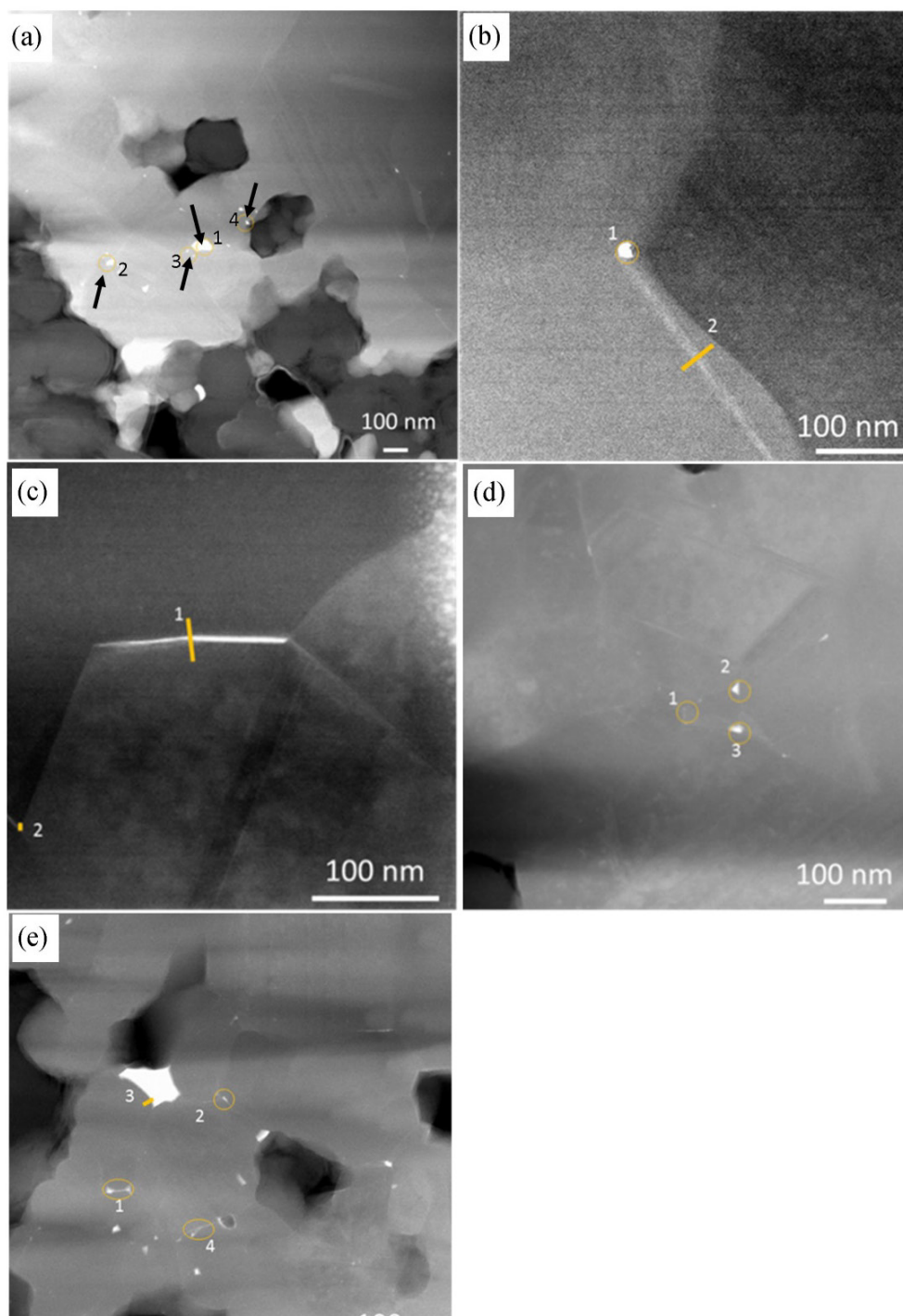


Figure 51. STEM HAADF image combined with EDS labeling to track the chemical composition of fission product precipitates from the inner area of TRISO Particle AGR1-531-031 within the subtended areas (a) 1, (b) 2, (c) 3, (d) 4, and (e) 5 of Lamella 1 highlighted in Figure 50(a). Note the reported chemical compositions are in Table 28.

Table 28. Reported qualitative EDS at.% compositions from the inner area of TRISO Particle AGR1-531-031, taken from subtended Areas 1 through 5 of Lamella 1 as highlighted in Figure 50(a) and precipitates labeled in Figure 51.

Precipitate Number	Concentration (at.%)									Precipitate Identification
	C	Si	Pd	Ag	Cs	Ce	Eu	U	Pu	
Lamella 1, Area 1										
1	48.62	45.01	0.02	0.00	0.00	1.11	0.20 <sup>a</sup>	5.03	0.01	Ce-U
2	49.55	50.24	0.00	0.00	0.00	0.04	0.16	0.00	0.00	
3	61.29	38.28	0.00	0.00	0.00	0.00	0.00	0.43	0.00	U
4	54.23	45.46	0.00	0.00	0.00	0.00	0.00	0.27	0.04	U
Lamella 1, Area 2										
1	65.55	33.20	0.01	0.15	0.00	0.00	0.00	1.09	0.00	U
2	51.00	48.58	0.16	0.00	0.00	0.00	0.00	0.00	0.26	Pu
Lamella 1, Area 3										
1	42.89	49.08	0.00	0.00	0.00	0.00	0.00	6.59	1.43	U-Pu
2	49.19	50.81	0.00	0.00	0.00	0.00	0.00	0.00	0.00	
Lamella 1, Area 4										
1	42.11	46.71	0.15	0.00	11.03	0.00	0.00	0.00	0.00	Cs
2	39.38	55.41	0.00	0.33	0.00	0.09	0.00	4.80	0.00	Ag-U
3	49.65	44.66	0.14	0.00	2.25	0.00	0.00	3.29	0.00	Cs-U
Lamella 1, Area 5										
1	47.55	51.53	0.00	0.00	0.56	0.00	0.15	0.17	0.04	Cs
2	49.79	49.91	0.22	0.00	0.00	0.00	0.00	0.08	0.00	Pd
3	60.12	36.54	3.00	0.04	0.18	0.01	0.10	0.00	0.00	Pd
4	45.71	52.46	0.00	1.33	0.00	0.00	0.00	0.36	0.14	Ag-U
a. Cannot differentiate between Eu and Fe.										

a. Cannot differentiate between Eu and Fe.

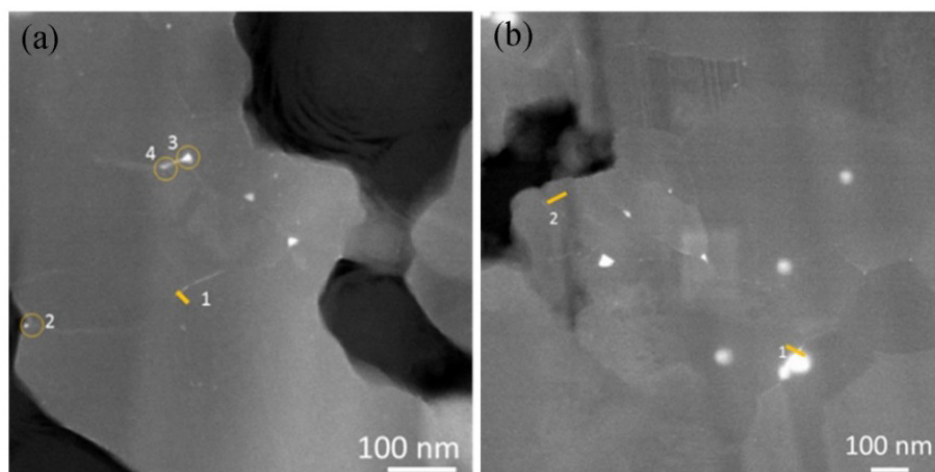


Figure 52. (a) STEM HAADF image combined with EDS labeling to track the chemical composition of fission product precipitates from the inner area (Lamella 1b, Area 1), and (b) STEM HAADF image combined with EDS labeling to track the chemical composition of fission product precipitates from the inner area (Lamella 4, Area 1) of TRISO Particle AGR1-531-031 highlighted in Figure 50. Note the reported chemical compositions are in Table 29.

Table 29. Reported qualitative EDS at.% compositions from the inner area (Grid 1, Sample 1b) of TRISO Particle AGR1-531-31, taken from subtended Area 1 from Lamellae 1b and 4 as highlighted in Figure 50.

Precipitate Number	Concentration (at.%)									Precipitate Identification
	C	Si	Pd	Ag	Cs	Ce	Eu	U	Pu	
Lamella 1b, Area 1										
1	61.42	37.76	0.00	0.00	0.69	0.07	0.06	0.00	0.00	Cs
2	62.12	37.52	0.22	0.00	0.00	0.02	0.13	0.00	0.00	Pd
3	68.74	30.39	0.04	0.00	0.00	0.04	0.02	0.77	0.00	U
4	66.12	32.60	0.11	0.11	0.00	0.00	0.00	2.53	0.00	U
Lamella 4, Area 1										
1	85.69	14.11	0.09	0.01	0.00	0.07	0.00	0.04	0.00	
2	72.77	26.17	0.00	0.00	0.00	0.00	0.00	1.05	0.01	U

**3.2.2.1.2 Chemical Composition in the Center and Outer Areas of the SiC Layer (Lamellae 2 and 3, respectively).** Particle AGR1-531-031 contains no fission product precipitates in Lamellae 2 and 3 as shown in Figure 50(c) and (d).

**3.2.2.2 Crystallographic Information Obtained on Particle AGR1-531-031.** Overall, very few fission product precipitates were found in the TEM samples from the SiC layer (see Figure 50) even though the SEM image (Figure 46[b]) shows numerous precipitates on the IPyC side of the IPyC/SiC interface. Therefore, significant amounts of fission product elements were readily available for transport from the IPyC/SiC interface through the SiC layer during irradiation. However, for some reason it does not appear that the fission products entered the SiC layer in sufficient quantities to result in wide-spread precipitation of fission products in the SiC layer. Because only a few fission product precipitates were present on the SiC side of the IPyC/SiC interface (see Figure 51 and Figure 52), PED orientation data were not collected in the areas analyzed for fission product precipitates. (Correlation of the few available fission product precipitates with grain boundary parameters would yield a very small dataset and identification of trends would be suspect due to poor statistics. These samples are still available and the orientation data for precipitate correlation could be obtained later.) Instead, PED was performed on various areas (not associated with the EDS analysis of fission product precipitates) at random across the SiC layer to obtain general grain boundary distribution across the SiC layer and potentially reveal microstructural-based reasons for low fission product precipitate populations in the SiC layer of this particular irradiated TRISO particle.

**3.2.2.2.1 Distributions in the General Grain Boundary Population.** Two areas, approximately  $3\ \mu\text{m} \times 4\ \mu\text{m}$ , on the inner, center, and outer SiC layer samples were randomly selected, and PED information was collected to map the crystallographic orientation across the SiC layer. The orientation maps for the two randomly selected areas on the inner sample are shown in Figure 53. Figure 54 shows the misorientation angle, CSL value, and grain boundary-type distributions for the inner sample shown in Figure 50(a) as an example of the information obtained in analysis of the PED data. Details of PED analyses for the center and outer samples can be found in Lillo et al., (2017).

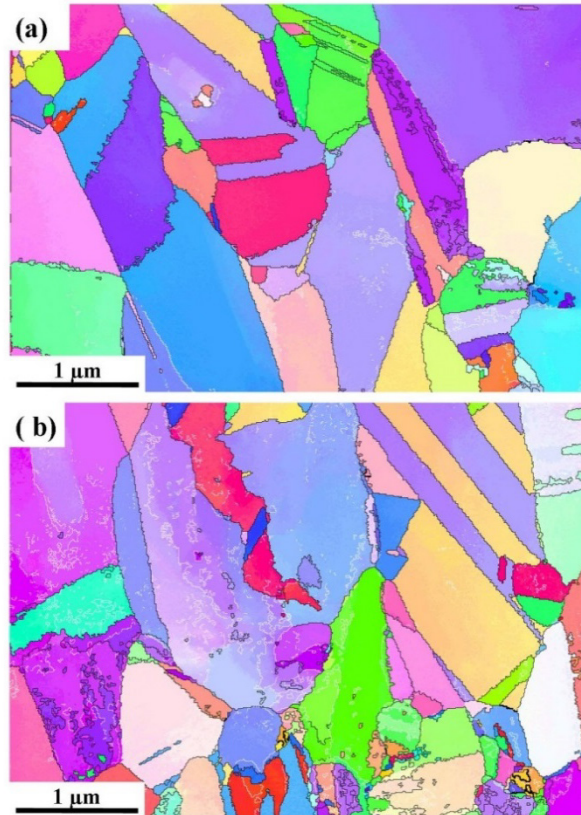


Figure 53. Orientation maps of randomly selected areas (a) 1 and (b) 2 generated from PED data.

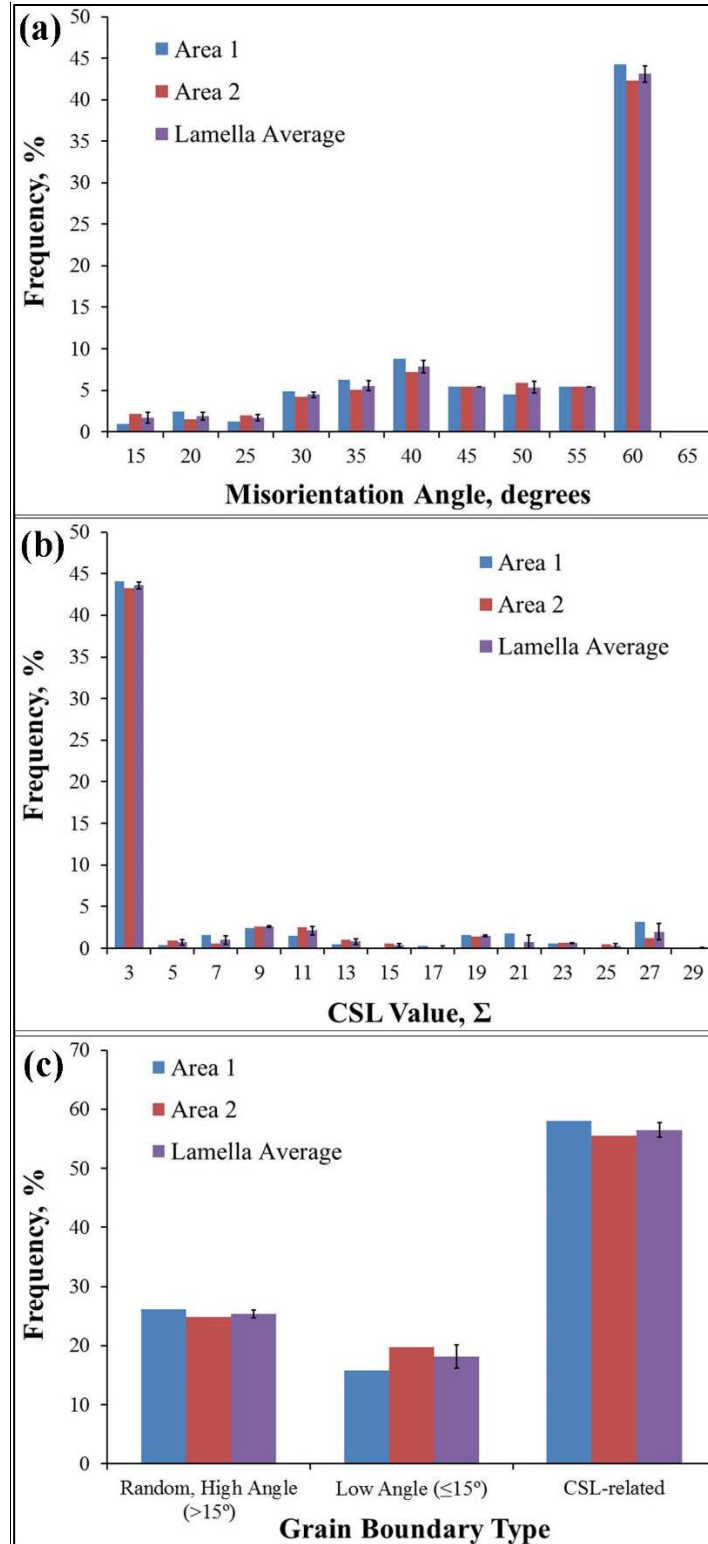


Figure 54. Distributions of (a) grain boundary misorientation angles, (b) value of CSL-related grain boundaries, and (c) grain boundary types for two randomly selected areas on the inner Lamella (Figure 50[a]) and averaged distributions with accompanying standard error bars.



The averaged distributions for the inner, center, and outer sample are plotted in Figure 55. Standard error bars, based on two areas that were analyzed in each lamella, were used in the plots of Figure 55 and are discussed in the following subsections.

**3.2.2.2.2 Misorientation Angle Distribution.** The major fraction of grain boundaries in the inner, center, and outer regions of AGR1-531-031 exhibits a 60-degree misorientation angle (see Figure 55[a]), which corresponds to the twin boundaries. Again, a secondary peak is observed around 40 degrees. Based on the error bars, there are no significant differences between the three samples in the plots of Figure 55(a). The twin fraction is relatively high (i.e., about 50%) across the SiC layer. No obvious differences are evident in the misorientation angle distributions of the three samples.

**3.2.2.2.3 Distribution of CSL-Related Grain Boundaries.** As expected, the twin-related grain boundaries (i.e.,  $\Sigma 3$  fractions in Figure 55[b]) dominate the CSL-related grain boundary distributions. The higher order twin grain boundaries (i.e.,  $\Sigma 9$  and  $\Sigma 27$ ) make up a majority of the remaining CSL-related grain boundaries. In general, there are no statistically significant differences between the CSL distributions for the inner, center, and outer samples and no specific trends from inner to outer regions are observed.

CSL-related grain boundary distribution data can be compared with that provided by Kirchhofer et al., (2013) for the SiC layer of an unirradiated, Variant 1 TRISO particle from their SEM-based EBSD investigation. Data for all areas analyzed on AGR1-531-031 in this study were combined and used to determine CSL-related grain boundary fractions representative of the entire SiC layer for a direct comparison to the Kirchhofer data, which was also based on the entire SiC layer of the unirradiated particle (Kirchhofer et al., 2013). The values for the twin fraction, including higher order twins, for this study are given in Table 30. The values reported by Kirchhofer et al., (2013) were 39% for  $\Sigma 3$ , 6% for  $\Sigma 9$ , and 1% for  $\Sigma 27$  twin boundaries. The values in Table 30 are consistent with their work, although the  $\Sigma 9$  fraction for this particle may be slightly higher than the Kirchhofer work. However, no indication of the error in their work is given; therefore, it cannot be determined whether this difference is statistically significant.

Table 30. Average fraction of twin-related grain boundaries in the SiC layer from Particle AGR1-531-031.

CSL Value, $\Sigma$	Fraction, %	Std. Error
3	45.6	2.9
9	3.1	0.6
27	1.4	0.5

**3.2.2.2.4 Distribution by Grain Boundary Type.** Distribution by grain boundary type is shown in Figure 55(c). The CSL-related grain boundaries are the major grain boundary type that represent 50 to 64% of the grain boundaries in the SiC layer and are consistent with the results of all the other particles analyzed in this work. Random, high-angle grain boundaries, which are expected to have the highest grain boundary diffusivity and the largest influence on fission product transport, make up 20 to 25% of the general grain boundary population (Figure 55[c] and Table 31). Kirchhofer et al., (2013) reports a high-angle grain boundary fraction of 42% in their study of an unirradiated, Variant 1 TRISO by SEM-based EBSD which is considerably higher than found for this particle. They also report values of 54% for the CSL-related grain boundary fraction and 4% for the low-angle grain boundary fraction. It would appear that the low-angle grain boundary fraction in this particle is significantly higher than in the Kirchhofer et al., (2013) study while the CSL-related grain boundary fraction is approximately the same (Table 31).



Table 31. Average fraction of grain boundary types in the SiC layer from Particle AGR1-531-031.

Grain Boundary Type	Fraction, %	Std. Error
Low angle, <15 degree	18.8	1.1
High angle, >15 degree	22.5	2.0
CSL-related	58.7	2.6

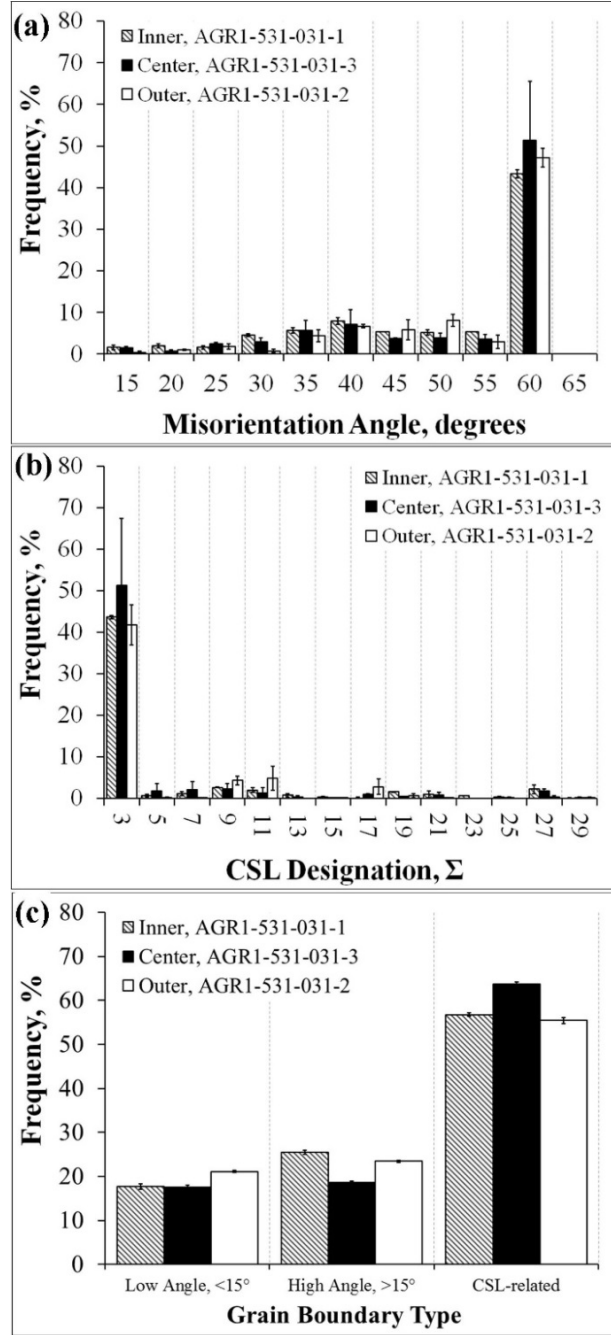


Figure 55. Distributions averaged over all areas analyzed for each sample: (a) misorientation angle, (b) CSL designation, and (c) grain boundary type for the SiC grain boundaries of samples taken from AGR1-531-031.

**3.2.2.3 Fission Product Precipitates.** As mentioned in Section 3.2.2.2, very few fission product precipitates were found in the samples taken from the SiC layer even though the SEM image (Figure 46[a]) shows fission product elements at the IPyC/SiC interface that should be readily available for transport through the SiC layer during irradiation. Fission product precipitates were found only in the inner sample very near the IPyC/SiC interface (Figure 50[a], [b], [e]). No fission product precipitates were found in either the center or outer samples. Because of the low number of fission product precipitates even in the inner sample, PED orientation data collection was not performed in areas analyzed for fission product precipitates. However, fission products in the precipitates near the IPyC/SiC interface of the inner samples of Figure 50(a), (b), (e), have been determined and are discussed elsewhere in this report (see Section **Error! Reference source not found.**). These samples are still available and orientation data can be obtained later if this information is deemed to be of value.

**3.2.2.4 Microstructure Characterization.** During characterization of the microstructure of AGR1-531-031, it was not only noted that the center and outer sample were essentially devoid of fission product precipitates, but pores in the SiC layer were also noted (as shown in Figure 56). This raises the possibility of other transport mechanisms, such as vapor phase transport through potentially interconnected pore structures, at least in this particle variant. However, it remains to be determined whether these features extend completely through the SiC layer or exist as isolated pores. Also, it must be determined whether they are prevalent enough to account for the observed releases of the various fission products. In the case of this particle (i.e., AGR1-531-031), it is unlikely that the pores are interconnected because this particle did not exhibit any release of Ag or Cs (Demkowicz, et al., 2016a). (Cesium is above its boiling point at the irradiation temperature and significant release of Cs would have been detected if interconnected porosity was present in the SiC layer.)”. However, the potential exists for Ag release through interconnected porosity in other particles that also exhibit significant release of Cs which was exceedingly rare in Compact 5-3-1 (only Particle AGR1-531-018 exhibited significant releases of both Ag and Cs, Demkowicz, et al., 2016a). If Ag is released but Cs is not (which is commonly observed in irradiated AGR-1 TRISO particles of Compact 5-3-1, Demkowicz, et al., 2016a) then a mechanism other than Ag release via interconnected porosity through the SiC layer must be responsible for the observed Ag release.

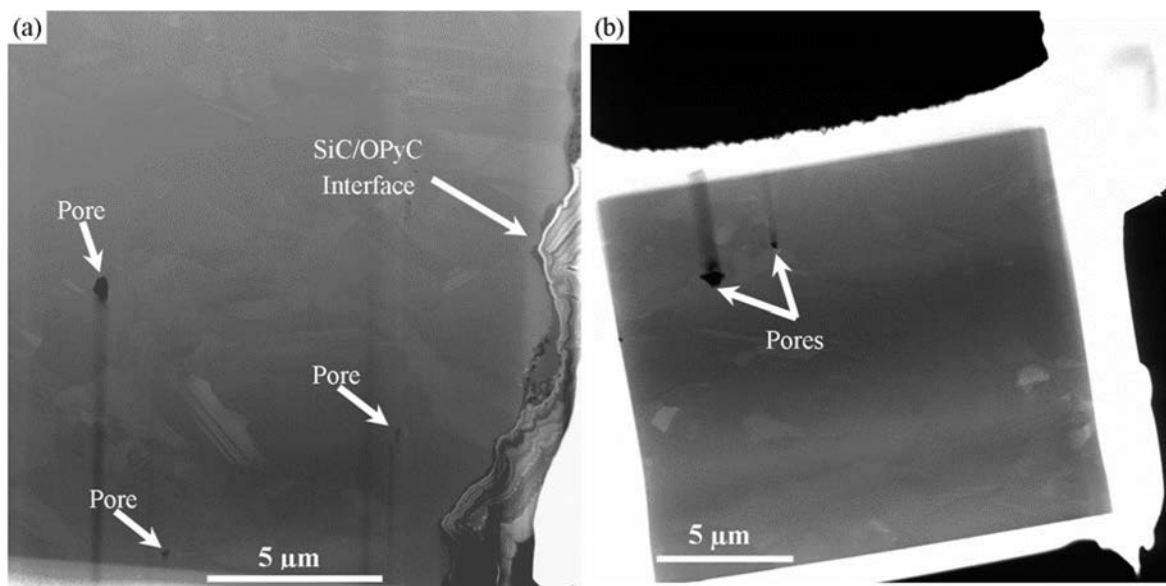


Figure 56. Low magnification overviews of (a) Lamella 2 (AGR1-531-031-2) showing a lack of fission product precipitates. Pores in the SiC appear as dark features. (b) Lamella 3 (AGR1-531-031-3) showing a lack of fission product precipitates. Pores in the SiC appear as dark features.

### 3.2.3 Particle AGR1-531-038

In this section, qualitative chemical composition, fission product identification, and crystallographic characteristics are provided for Particle AGR1-531-038.

**3.2.3.1 Chemical Composition of Minor Elements of Particle AGR1-531-038.** This section reports the qualitative chemical composition of minor elements on Particle AGR1-531-038 to determine the type of fission products present, the location of these particles in relation to the SiC layer thickness, and the fission product elemental composition. The reported fission product precipitate compositions (atomic %) are qualitative or semi-quantitative in nature as described in Section 2.1.2.3.

The SiC Lamella locations are indicated in Figure 47 with a summary of the minor elements present in these four lamellae given in Table 32. Sections 3.2.3.1.1 to 3.2.3.1.3 describe the precipitates found in the inner (Lamella 1), center (Lamella 2), and outer (Lamella 3) areas. Precipitates containing Pd, Ag, Ce, Eu, Cs, U, and Pu were found in the inner area of the SiC layer, close to the IPyC-SiC interlayer, and no Cs precipitates were found in the center and outer areas of the SiC layer. In the outer area, only Pd, U, and Pu were present.

Figure 57 shows a qualitative trend analysis of precipitate composition (Pd, Ag, and U only) as a function of the approximate distance from the SiC-IPyC interface of Particle AGR1-531-038. This figure also shows the movement of Pd, Ag, and U to an approximate thickness of 34, 11, and 30  $\mu\text{m}$ , respectively. No specific concentration trends or Pd/U and Pd/Ag ratios versus distance were evident. The average Ag content found in precipitates exhibits a weak negative slope linear trend, with distance away from the SiC-IPyC interface (shown in Figure 58).

Table 32. Identification of minor elements present in fission product precipitates in the SiC layer of Particle AGR1-531-038.

Lamellae	Elements Present										Precipitate Identification
	Area	C	Si	Pd	Ag	Cs	Ce	Eu	U	Pu	
Inner, Lamella 1	Area 1	X	X	X					X		Pd, Pd-U
	Area 2	X	X	X	X	X		X			Pd, Pd-Ag-Cs, Pd-Cs-Eu
	Area 3	X	X	X	X		X	X			Pd, Pd-Ce-Eu, Pd-Ag
	Area 4	X	X	X						X	Pd, Pd-U, Pd-U-Pu
	Area 5	X	X	X	X			X	X		Pd, Pd-Pu, Pd-Ag-Eu
Inner Summary		X	X	X	X	X	X	X	X	X	
Center, Lamella 2	Area 1a	X	X	X							Pd
	Area 1b	X	X	X	X					X	Pd, Pd-Ag-U
	Area 2	X	X	X	X				X		Pd, Pd-Ag-U
	Area 3a	X	X	X					X		Pd, Pd-U,
	Area 3b	X	X	X			X				Pd, Pd-Ce
	Area 4	X	X	X	X					X	Pd, Pd-U, Pd-Ag
	Area 5	X	X	X	X				X	X	Pd, Pd-U-Pu, Pd-Ag, Pd-U
	Area 6	X	X	X	X						Pd, Ag

Table 32. (continued).

Lamellae	Elements Present										Precipitate Identification
	Area	C	Si	Pd	Ag	Cs	Ce	Eu	U	Pu	
Center Summary		X	X	X	X		X		X	X	
Outer, Lamella 3	Area 1	X	X	X					X	X	Pd, Pd-U-Pu
	Area 2	X	X	X					X	X	Pd, Pd-U-Pu
	Area 3	X	X	X							Pd
	Area 4	X	X	X							Pd
	Area 5	X	X	X							Pd
Outer Summary		X	X	X					X	X	
Final Summary		X	X	X	X	X	X	X	X	X	

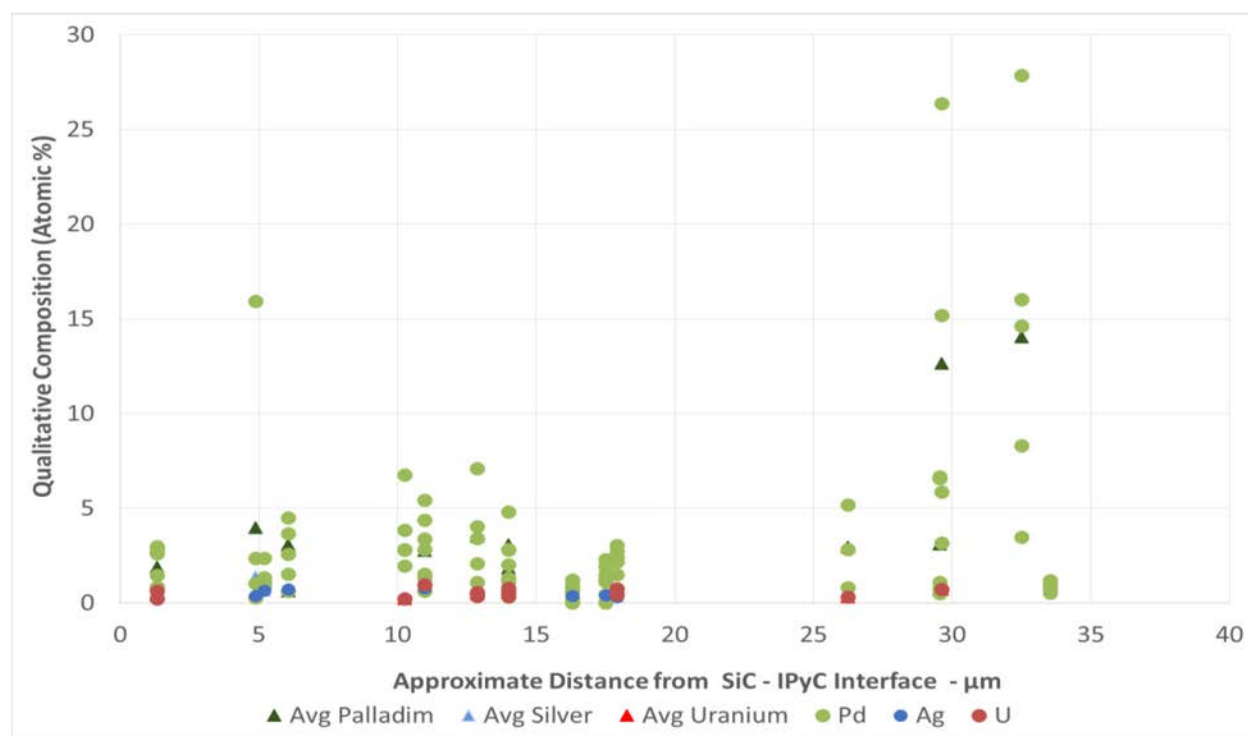


Figure 57. Qualitative trend analysis of precipitate composition (Pd, Ag, and U only) as a function of the approximate distance into the SiC layer from the SiC-IPyC interface of Particle AGR1-531-038.

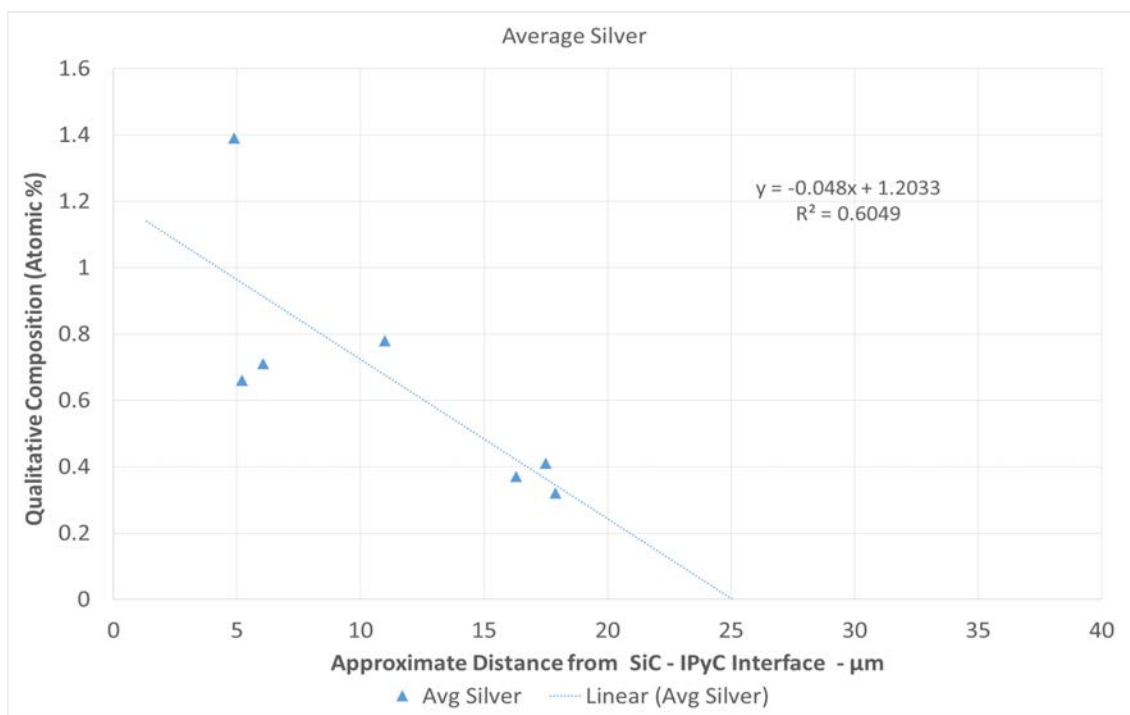


Figure 58. Qualitative trend analysis of the average Ag content found in precipitates as a function of the approximate distance into the SiC layer from the SiC-IPyC interface of Particle AGR1-531-038.

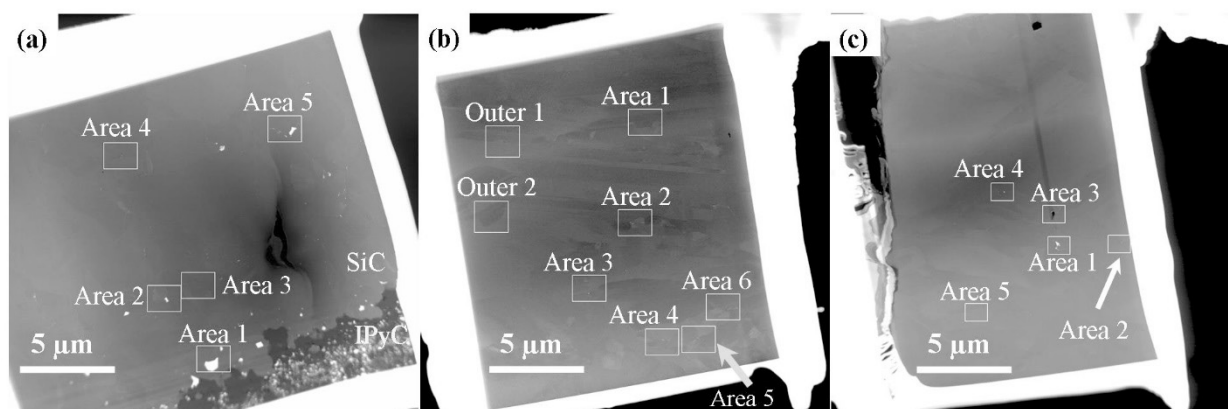


Figure 59. Large field of view STEM dark field image taken from the (a) inner area (Lamella 1) of TRISO Particle AGR1-531-038. (b) Large field of view STEM dark field image taken from the center area (Lamella 2) of TRISO Particle AGR1-531-038 taken within the SiC layer. (c) Large field of view STEM dark field image taken from the outer area (Lamella 3) of TRISO Particle AGR1-531-038 (lamellae locations are indicated in Figure 47).

**3.2.3.1.1 Chemical Composition in the Inner Area of the SiC Layer (Lamella 1).** The inner area of the SiC layer is defined as the STEM Lamella containing the IPyC/SiC interface and corresponds to Lamella 1 in Figure 47(c). Figure 59 shows Lamella 1 from Particle AGR1-531-038 with five areas marked in white (labeled 1 through 5) where precipitates were examined and the composition determined by qualitative EDS analysis (presented in Table 33 to Table 37 and Figure 60 to Figure 64). From these qualitative analyses, it was determined that precipitates contain mainly Pd, with Ag, Ce, Cs, U, Eu, and Pu present.

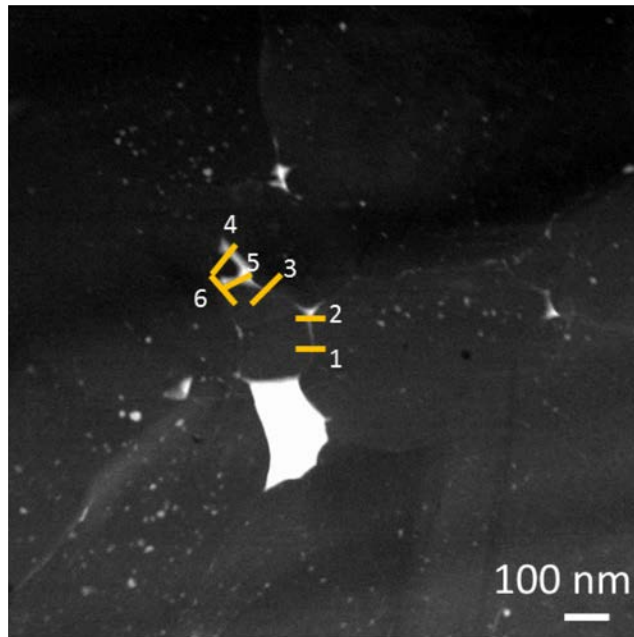


Figure 60. STEM HAADF image combined with EDS labeling to track the chemical composition of fission product precipitates from the inner area of TRISO Particle AGR1-531-038 within the subtended Area 1 from Figure 59(a). Note the reported chemical compositions are in Table 33.

Table 33. Reported qualitative EDS compositions from the inner area of TRISO Particle AGR1-531-038, taken from subtended Area 1.

Precipitate Number	Concentration (at.%)									Precipitate Identification
	C	Si	Pd	Ag	Cs	Ce	Eu	U	Pu	
1	49.74	46.77	2.99	0.00	0.00	0.13	0.09	0.21	0.07	Pd-U
2	51.03	48.04	0.84	0.00	0.00	0.00	0.00	0.10	0.00	Pd
3	58.07	40.39	1.45	0.00	0.00	0.02	0.07	0.00	0.00	Pd
4	61.46	37.67	0.73	0.00	0.00	0.03	0.11	0.00	0.00	Pd
5	61.54	34.75	2.76	0.09	0.00	0.07	0.14	0.62	0.03	Pd-U
6	61.36	35.68	2.62	0.08	0.00	0.06	0.10	0.11	0.00	Pd

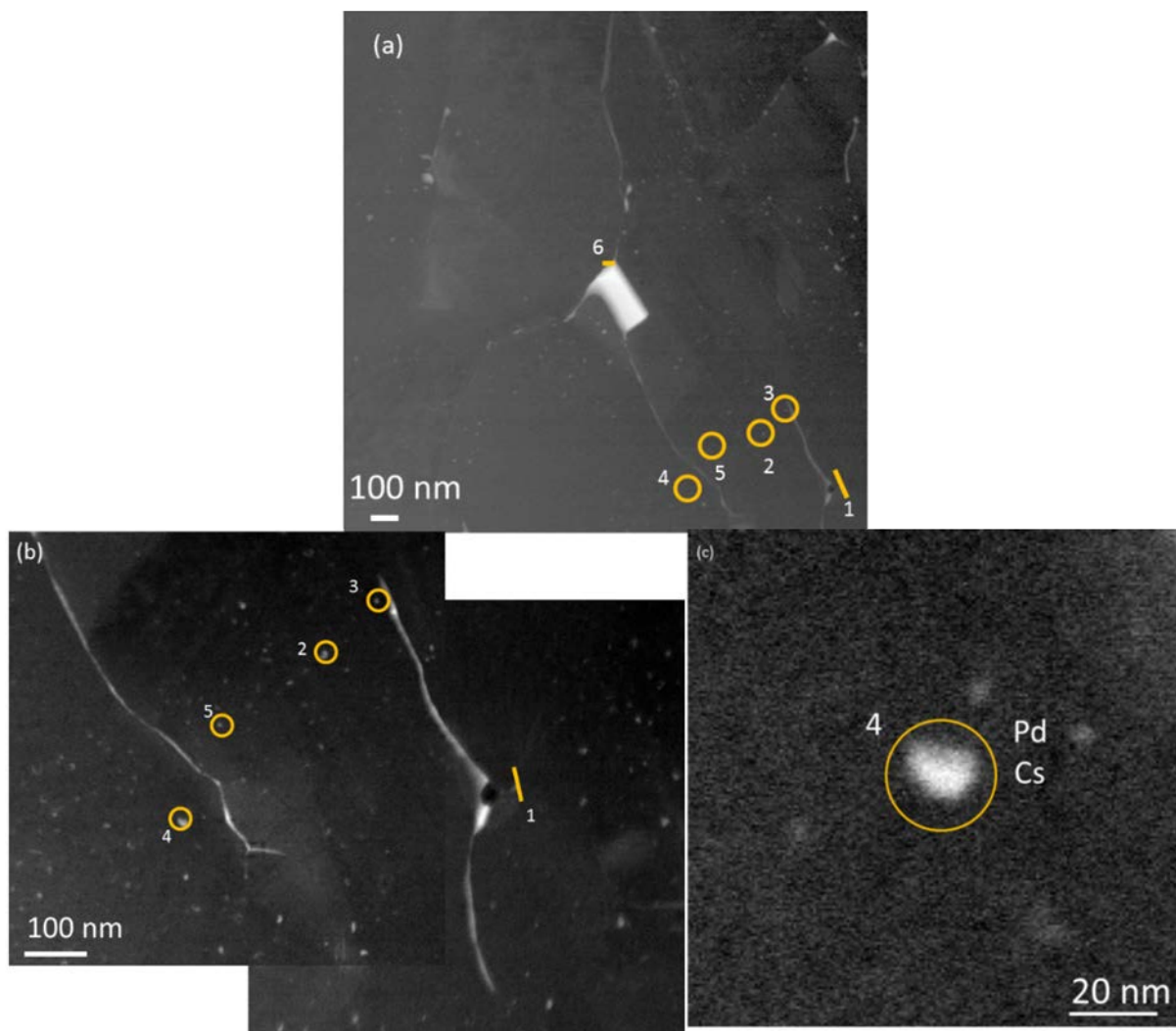


Figure 61. STEM HAADF image combined with EDS labeling to track chemical composition of fission product precipitates from the inner area of TRISO Particle AGR1-531-038 within the subtended Area 2 from Figure 59(a), (a) low, (b) medium, and (c) higher magnification of the intragranular Pd-Cs, spherical precipitate (Number 4). Note the reported chemical compositions are in Table 34.

Table 34. Qualitative EDS composition of precipitates from Particle AGR1-531-038, Lamella 1 Area 2.

Precipitate Number	Concentration (at.%)									Precipitate Identification
	C	Si	Pd	Ag	Cs	Ce	Eu	U	Pu	
1	47.71	49.12	1.08	0.66	1.16	0.01	0.08	0.15	0.03	Pd-Ag-Cs
2	55.07	43.48	1.29	0.03	0.00	0.05	0.07	0.00	0.00	Pd
3	51.11	47.23	1.34	0.08	0.00	0.13	0.11	0.00	0.00	Pd
4	52.49	44.51	2.35	0.00	0.22	0.12	0.22	0.02	0.08	Pd-Cs-Eu
5	52.73	45.94	1.14	0.00	0.00	0.05	0.11	0.02	0.00	Pd
6	62.62	36.44	0.89	0.00	0.00	0.01	0.05	0.00	0.00	Pd

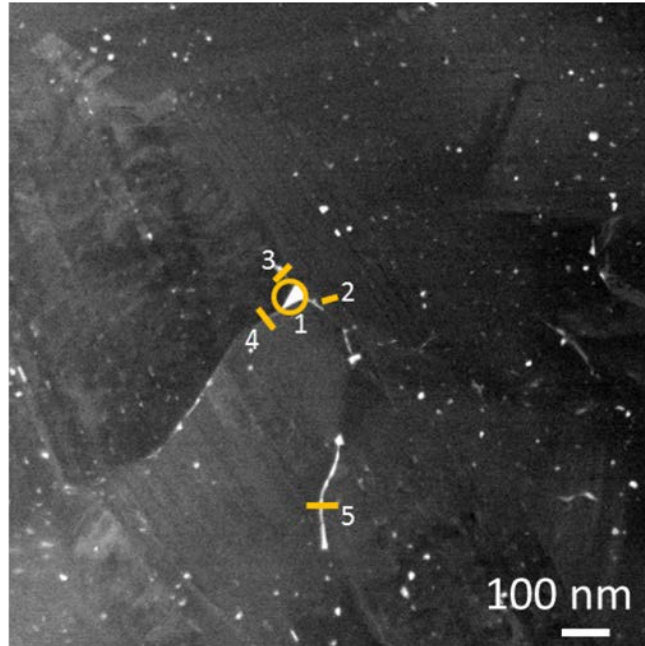


Figure 62. STEM HAADF image combined with EDS labeling to track the chemical composition of fission product precipitates from the inner area of TRISO Particle AGR1-531-038 within the subtended Area 3 that is highlighted in Figure 59(a). Note the reported chemical compositions are in Table 35.

Table 35. Reported qualitative EDS compositions (in at.%) from the inner area of TRISO Particle AGR1-531-038, taken from subtended Area 3.

Precipitate Number	Concentration (at.%)									Precipitate Identification
	C	Si	Pd	Ag	Cs	Ce	Eu	U	Pu	
1	53.28	30.10	15.92	0.00	0.00	0.28	0.39	0.03	0.00	Pd-Ce-Eu
2	57.58	41.17	1.03	0.00	0.00	0.00	0.14	0.08	0.00	Od
3	53.06	46.52	0.29	0.00	0.00	0.03	0.10	0.00	0.00	Pd
4	53.43	45.86	0.28	0.39	0.00	0.00	0.00	0.04	0.00	Pd-Ce
5	54.80	42.81	2.37	0.00	0.00	0.00	0.02	0.00	0.00	Pd



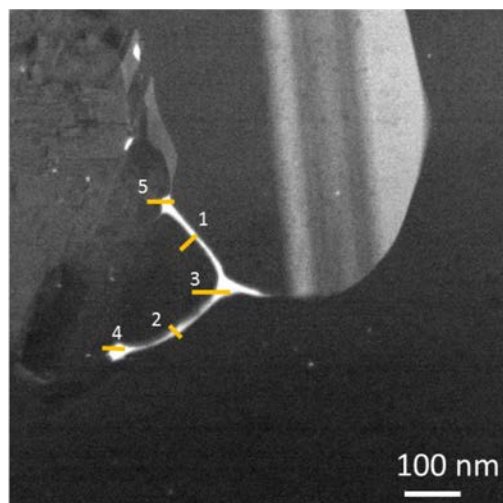


Figure 63. STEM HAADF image combined with EDS labeling to track the chemical composition of fission product precipitates from the inner area of TRISO Particle AGR1-531-038 within the subtended Area 4 from Figure 59(a). Note the reported chemical compositions are in Table 36.

Table 36. Reported qualitative EDS compositions (in at.%) from the inner area of TRISO Particle AGR1-531-038, taken from subtended Area 4.

Precipitate Number	Concentration (at.%)									Precipitate Identification
	C	Si	Pd	Ag	Cs	Ce	Eu	U	Pu	
1	53.99	44.78	1.09	0.00	0.00	0.02	0.07	0.05	0.00	Pd
2	51.63	46.19	2.09	0.00	0.00	0.00	0.00	0.09	0.00	Pd
3	48.65	47.44	3.40	0.00	0.00	0.00	0.00	0.35	0.16	Pd-U
4	42.53	49.85	7.10	0.00	0.00	0.00	0.00	0.50	0.03	Pd-U-Pu
5	49.52	45.47	4.02	0.00	0.00	0.10	0.12	0.58	0.18	Pd-U

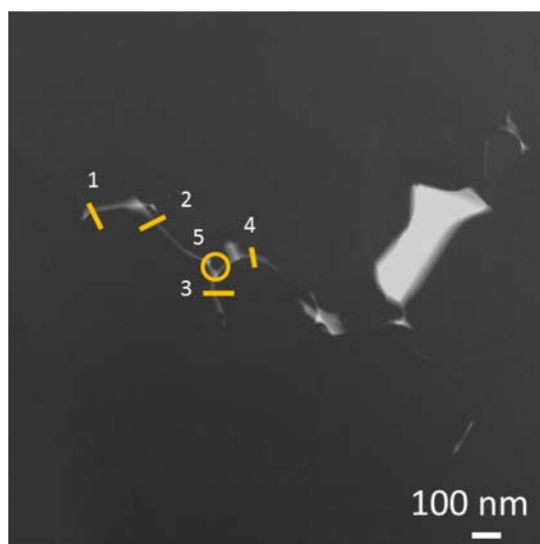


Figure 64. STEM HAADF image combined with EDS labeling to track the chemical composition of fission product precipitates from the inner area of TRISO Particle AGR1-531-038 within the subtended Area 5 from Figure 59(a). Note the reported chemical compositions are in Table 37.

Table 37. Reported qualitative EDS compositions (in at.%) from the inner area of TRISO Particle AGR1-531-038, taken from subtended Area 5.

Precipitate Number	Concentration (at.%)									Precipitate Identification
	C	Si	Pd	Ag	Cs	Ce	Eu	U	Pu	
1	37.91	55.28	6.77	0.00	0.00	0.00	0.04	0.00	0.00	Pd
2	43.80	53.40	2.79	0.00	0.00	0.01	0.00	0.00	0.00	Pd
3	48.88	47.23	3.86	0.00	0.00	0.01	0.02	0.00	0.00	Pd
4	45.83	50.67	2.84	0.26	0.00	0.17	0.22 <sup>a</sup>	0.00	0.00	Pd-Ag
5	46.86	50.58	1.95	0.00	0.00	0.04	0.18	0.23	0.15	Pd-U

a. Cannot differentiate between peaks of Eu and Fe.

**3.2.3.1.2 Chemical Composition in the Center Area of the SiC Layer (Lamella 2).** The center area of the SiC layer is defined as Lamella 2 in Figure 47 and Figure 59 from Particle AGR1-531-038, with six areas marked in white (labeled 1 through 6) where precipitates were examined and the composition determined by qualitative EDS analysis (presented in Tables 38 to 43 and Figures 65 to 70). The two areas marked “Outer 1” and “Outer 2” are relevant to PED (Section 3.2.4). From these qualitative analyses, it was determined that precipitates contain mainly Pd, with Ag, Ce, U, and Pu present. No Cs and Eu were found in the precipitates investigated in the center area of the SiC layer.

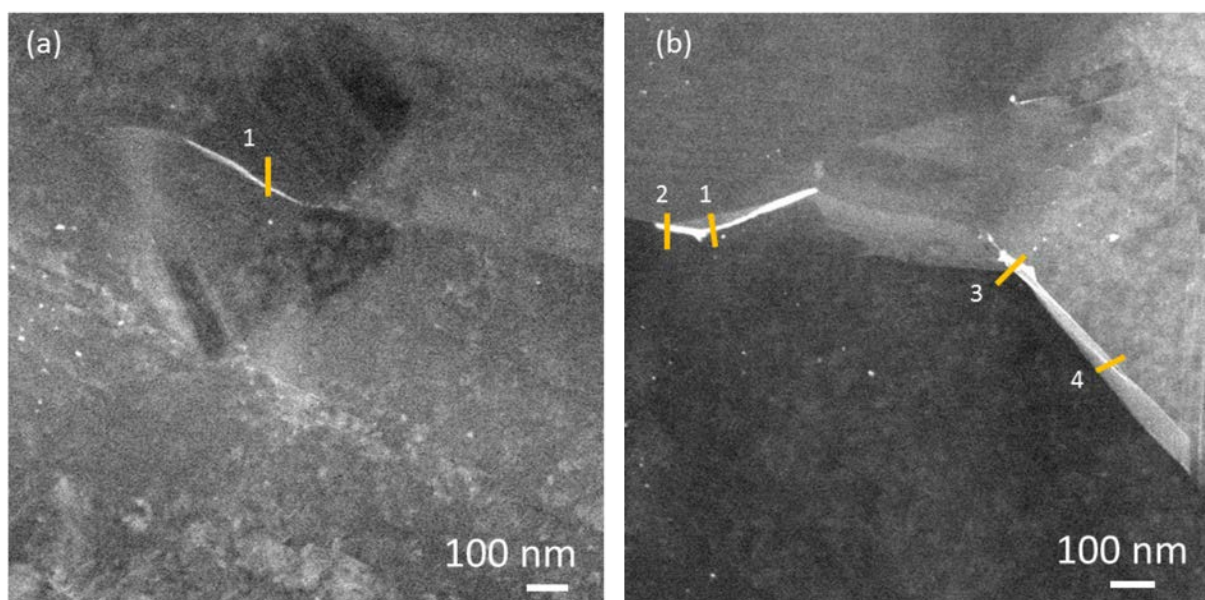


Figure 65. STEM HAADF image combined with EDS labeling to track the chemical composition of fission product precipitates from the center area of TRISO Particle AGR1-531-038 within two sub-areas, referred to as Area 1a and Area 1b of Area 1 from Figure 59(b). Note the reported chemical compositions are in Table 38.

Table 38. Reported qualitative EDS compositions (in at.%) from the center area of TRISO Particle AGR1-531-038, taken from subtended Area 1 (a and b) from Figure 59(b).

Precipitate Number	Concentration (at.%)									Precipitate Identification
	C	Si	Pd	Ag	Cs	Ce	Eu	U	Pu	
Area 1a										
1	50.01	49.35	0.64	0.00	0.00	0.00	0.00	0.00	0.00	Pd
Area 1b										
1	44.82	51.99	2.59	0.09	0.00	0.00	0.00	0.00	0.00	Pd
2	30.71	64.09	4.51	0.00	0.00	0.00	0.00	0.00	0.00	Pd
3	34.96	58.94	3.65	0.71	0.00	0.00	0.00	0.00	0.44	Pd-Ag-Pu
4	37.61	60.84	1.53	0.00	0.00	0.00	0.00	0.00	0.00	Pd

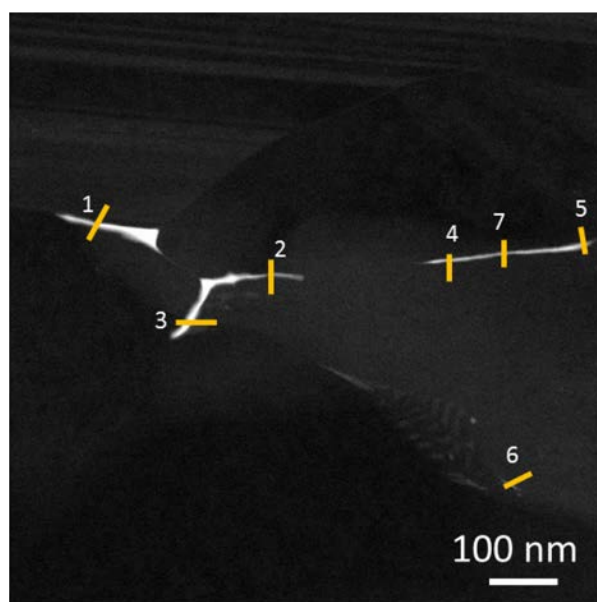


Figure 66. STEM HAADF image combined with EDS labeling to track the chemical composition of fission product precipitates from the center area of TRISO Particle AGR1-531-038 within the subtended Area 2 from Figure 59(b). Note the reported chemical compositions are in Table 39.

Table 39. Reported qualitative EDS compositions (in at.%) from the center area of TRISO Particle AGR1-531-038, taken from subtended Area 2 from Figure 59(b).

Precipitate Number	Concentration (at.%)									Precipitate Identification
	C	Si	Pd	Ag	Cs	Ce	Eu	U	Pu	
1	44.19	51.30	4.37	0.10	0.00	0.00	0.00	0.04	0.00	Pd
2	50.22	46.94	2.83	0.00	0.00	0.00	0.00	0.00	0.00	Pd
3	50.78	43.79	5.44	0.00	0.00	0.00	0.00	0.00	0.00	Pd
4	34.89	59.98	3.38	0.78	0.00	0.00	0.00	0.98	0.00	Pd-Ag-U
5	49.39	49.77	0.63	0.00	0.00	0.00	0.00	0.10	0.11	Pd
6	48.00	50.63	1.35	0.00	0.00	0.00	0.00	0.02	0.00	Pd
7	48.07	50.41	1.52	0.00	0.00	0.00	0.00	0.00	0.00	Pd

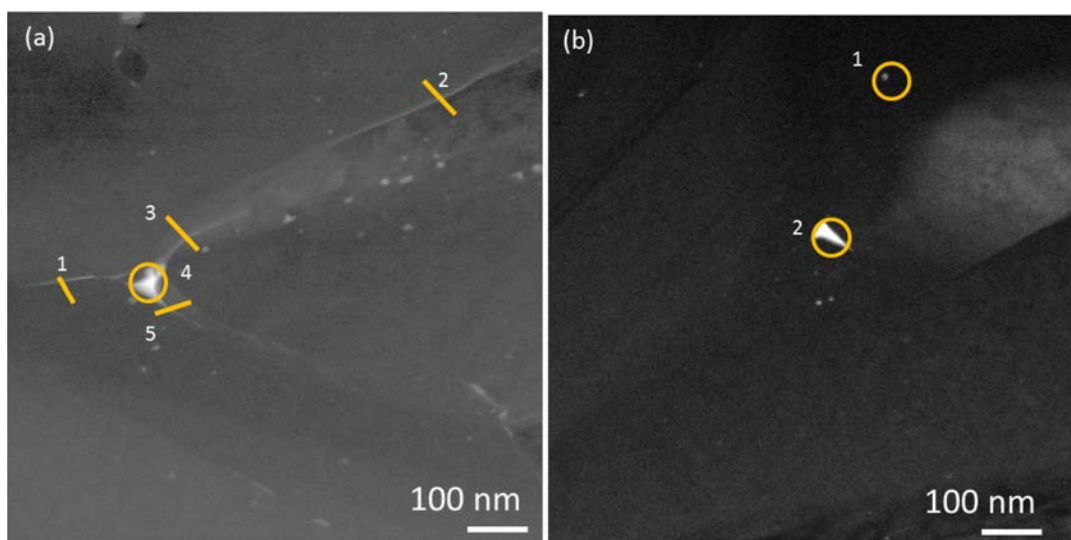


Figure 67. STEM HAADF image combined with EDS labeling to track the chemical composition of fission product precipitates from the center area of TRISO Particle AGR1-531-038 within two sub-areas, referred to as Area 3a and Area 3b, of Area 3 within Figure 59(b). Note the reported chemical compositions are in Table 40.

Table 40. Reported qualitative EDS compositions (in at.%) from the center area of TRISO Particle AGR1-531-038, taken from subtended Areas 3a and 3b from Figure 59(b).

Precipitate Number	Concentration (at.%)									Precipitate Identification
	C	Si	Pd	Ag	Cs	Ce	Eu	U	Pu	
Area 3a										
1	27.50	69.65	2.81	0.04	0.00	0.00	0.00	0.00	0.00	Pd
2	24.34	74.37	1.16	0.00	0.00	0.00	0.00	0.14	0.00	Pd
3	25.92	73.42	0.32	0.00	0.00	0.00	0.00	0.34	0.00	Pd-U
4	46.20	49.79	2.84	0.00	0.00	0.00	0.07	0.78	0.18	Pd-U
5	49.52	45.47	2.02	0.00	0.00	0.10	0.00	0.58	0.13	Pd-U
Area 3b										
1	46.04	51.39	1.30	0.00	0.00	0.49	0.00	0.00	0.00	Pd-Ce
2	45.36	48.41	4.82	0.09	0.00	0.00	0.00	0.00	0.00	Pd

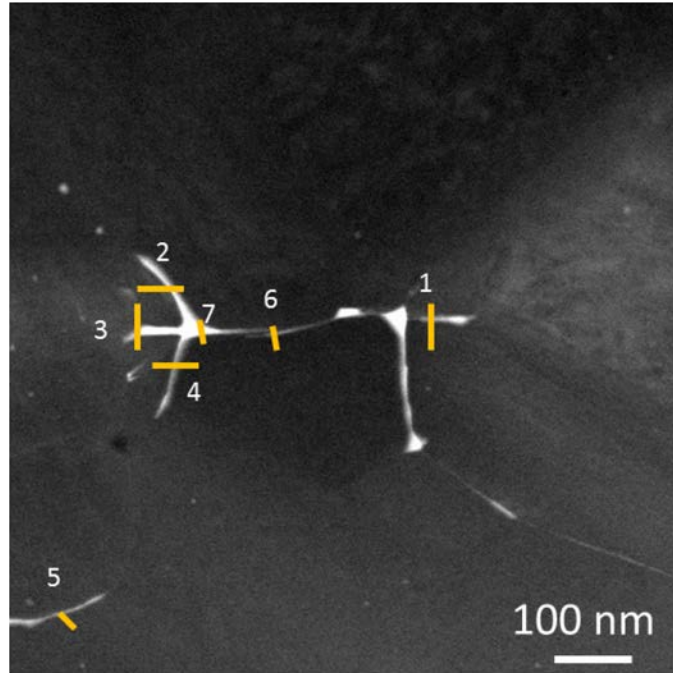


Figure 68. STEM HAADF image combined with EDS labeling to track the chemical composition of fission product precipitates from the center area of TRISO Particle AGR1-531-038 within the subtended Area 4 from Figure 59(b). Note the reported chemical compositions are in Table 41.

Table 41. Reported qualitative EDS compositions (in at.%) from the center area of TRISO Particle AGR1-531-038, taken from subtended Area 4 from Figure 59(b).

Precipitate Number	Concentration (at.%)									Precipitate Identification
	C	Si	Pd	Ag	Cs	Ce	Eu	U	Pu	
1	41.02	57.72	0.18	0.00	0.00	0.00	0.00	0.00	0.00	Pd
2	41.32	56.26	2.29	0.00	0.00	0.00	0.00	0.00	0.00	Pd
3	33.82	63.23	1.94	0.00	0.00	0.00	0.00	0.00	0.39	Pd-Pu
4	41.57	56.99	1.23	0.00	0.00	0.00	0.00	0.00	0.00	Pd
5	39.74	59.13	0.44	0.14	0.00	0.00	0.00	0.00	0.00	Pd
6	35.28	62.68	1.12	0.41	0.00	0.00	0.00	0.08	0.00	Pd-Ag
7	41.52	56.66	1.50	0.00	0.00	0.00	0.00	0.00	0.00	Pd

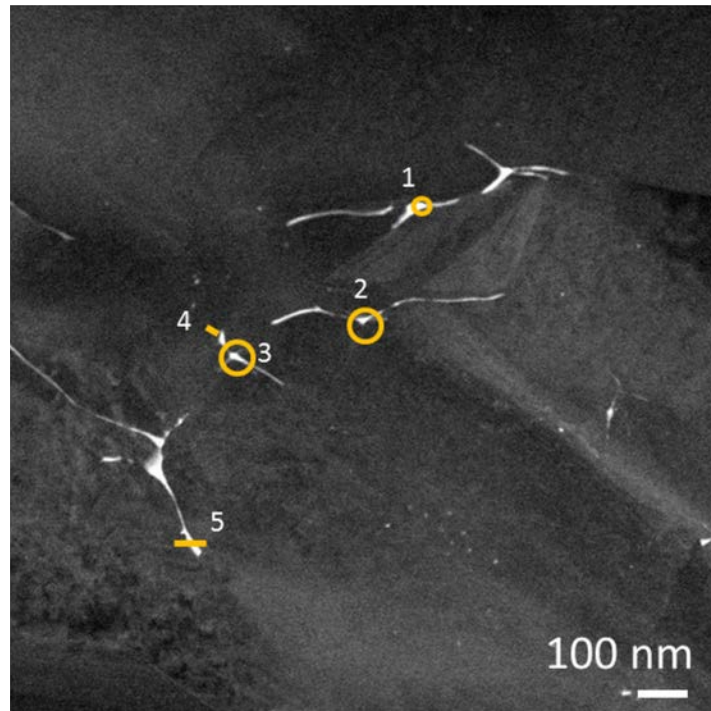


Figure 69. STEM HAADF image combined with EDS labeling to track the chemical composition of fission product precipitates from the center area of TRISO Particle AGR1-531-038 within the subtended Area 5 from Figure 59(b). Note the reported chemical compositions are in Table 42.

Table 42. Reported qualitative EDS compositions (in at.%) from the center area of TRISO Particle AGR1-531-038, taken from subtended Area 5 from Figure 59(b).

Precipitate Number	Concentration (at.%)									Precipitate Identification
	C	Si	Pd	Ag	Cs	Ce	Eu	U	Pu	
1	37.12	59.15	3.05	0.00	0.00	0.00	0.00	0.44	0.22	Pd-U-Pu
2	31.60	65.07	2.71	0.32	0.00	0.00	0.00	0.07	0.00	Pd-Ag
3	37.00	58.95	2.18	0.00	0.00	0.00	0.00	0.76	0.18	Pd-U
4	37.19	61.09	1.49	0.00	0.00	0.00	0.00	0.13	0.00	Pd
5	41.01	55.31	2.43	0.00	0.00	0.00	0.00	0.02	0.00	Pd



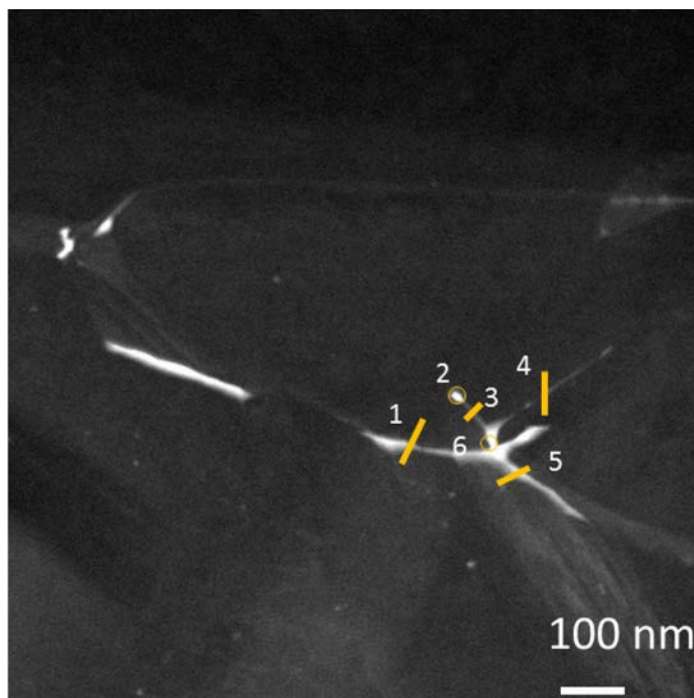


Figure 70. STEM HAADF image combined with EDS labeling to track the chemical composition of fission product precipitates from the center area of TRISO Particle AGR1-531-038 within the subtended Area 6 from Figure 59(b). Note the reported chemical compositions are in Table 43.

Table 43. Reported qualitative EDS compositions (in at.%) from the center area of TRISO Particle AGR1-531-038, taken from subtended Area 6 in Figure 59(b).

Precipitate Number	Concentration (at.%)									Precipitate Identification
	C	Si	Pd	Ag	Cs	Ce	Eu	U	Pu	
1	40.68	58.46	0.86	0.00	0.00	0.00	0.00	0.00	0.00	Pd
	43.38	55.72	0.88	0.00	0.00	0.00	0.00	0.02	0.00	Pd
2	35.50	63.94	0.07	0.37	0.00	0.00	0.00	0.11	0.00	Ag
3	41.55	58.16	0.27	0.00	0.00	0.00	0.00	0.02	0.00	Pd
4	40.17	59.13	0.70	0.00	0.00	0.00	0.00	0.01	0.00	Pd
5	40.42	58.31	1.21	0.00	0.00	0.00	0.00	0.06	0.00	Pd

**3.2.3.1.3 Chemical Composition in the Outer Area of the SiC Layer (Lamella 3).** The outer area of the SiC layer is defined as the STEM Lamella the furthest away from the IPyC/SiC interface and corresponds to Lamella 3 in Figure 47(c) and Figure 59(c). Figure 59(c) shows the five areas marked in white (labeled 1 through 5) where precipitates were examined and the composition determined by qualitative EDS analysis (presented in Table 38 to Table 46 and Figure 71 to Figure 73). From these qualitative analyses, it was determined that precipitates contain mainly Pd, U, and Pu with no Ag, Cs, Ce, and Eu present.

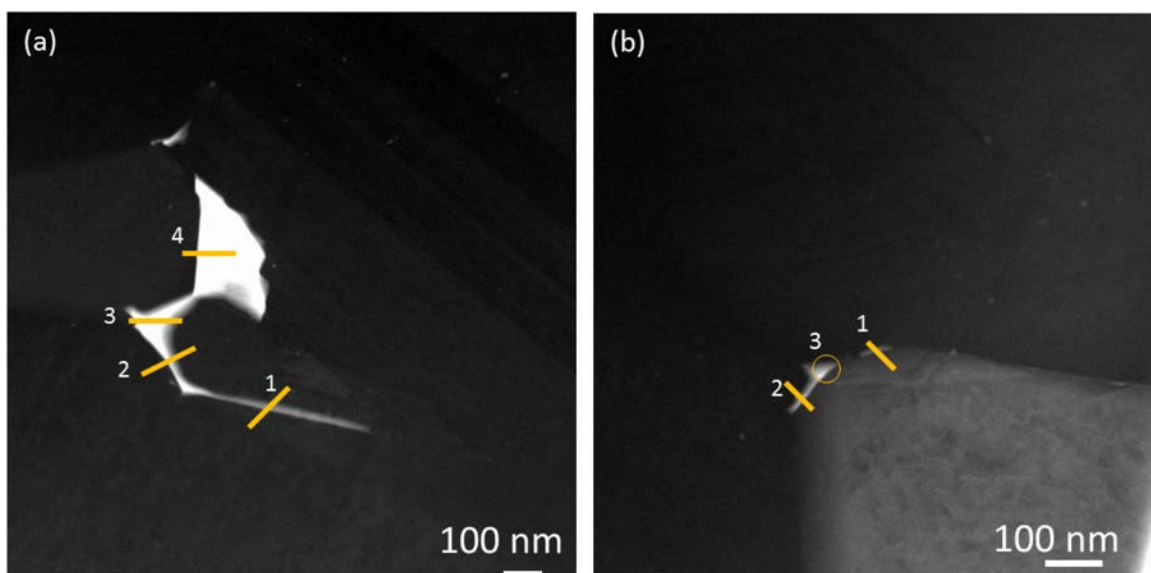


Figure 71. STEM HAADF image combined with EDS labeling to track the chemical composition of fission product precipitates from the outer area of TRISO Particle AGR1-531-038 within the subtended Areas (a) 1 and (b) 2 from Figure 59(c). Note the reported chemical compositions are in Table 44.

Table 44. Reported qualitative EDS compositions (in at.%) from the outer area of TRISO Particle AGR1-531-038, taken from subtended Areas 1 and 2 from Figure 59(c).

Precipitate Number	Concentration (at.%)									Precipitate Identification
	C	Si	Pd	Ag	Cs	Ce	Eu	U	Pu	
Area 1										
1	47.94	48.88	3.18	0.00	0.00	0.00	0.00	0.00	0.00	Pd
2	47.90	46.12	5.85	0.13	0.00	0.00	0.00	0.00	0.00	Pd
3	35.80	47.91	15.20	0.00	0.00	0.00	0.00	0.73	0.35	Pd-U-Pu
4	42.80	30.83	26.37	0.00	0.00	0.00	0.00	0.00	0.00	Pd
Area 2										
1	37.26	61.27	0.82	0.00	0.00	0.00	0.00	0.31	0.35	Pd-U-Pu
2	40.13	54.69	5.18	0.00	0.00	0.00	0.00	0.00	0.00	Pd
3	45.12	52.04	2.84	0.00	0.00	0.00	0.00	0.00	0.00	Pd



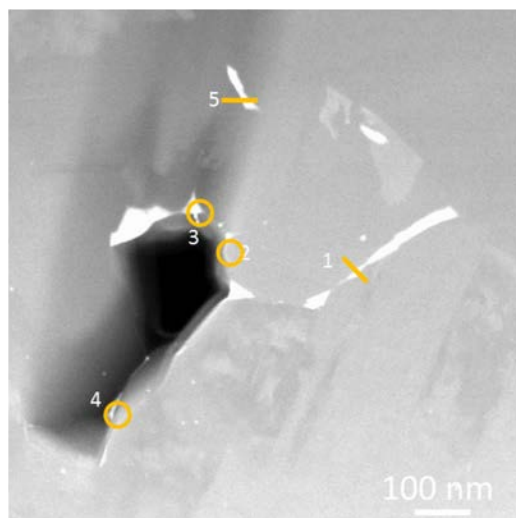


Figure 72. STEM HAADF image combined with EDS labeling to track the chemical composition of fission product precipitates from the outer area of TRISO Particle AGR1-531-038 within the subtended Area 3 highlighted in Figure 59(c). Note the reported chemical compositions are in Table 45.

Table 45. Reported qualitative EDS compositions (in at.%) from the outer area of TRISO Particle AGR1-531-038, taken from subtended Area 3 in Figure 59(c).

Precipitate Number	Concentration (at.%)									Precipitate Identification
	C	Si	Pd	Ag	Cs	Ce	Eu	U	Pu	
1	57.51	41.38	1.10	0.00	0.00	0.00	0.00	0.01	0.00	Pd
2	60.49	39.02	0.49	0.00	0.00	0.00	0.00	0.00	0.00	Pd
3	99.12	0.00	0.76	0.00	0.12	0.00	0.00	0.00	0.00	Pd
4	74.85	18.41	6.57	0.00	0.00	0.00	0.00	0.17	0.00	Pd
5	55.88	37.44	6.67	0.00	0.00	0.00	0.00	0.02	0.00	Pd

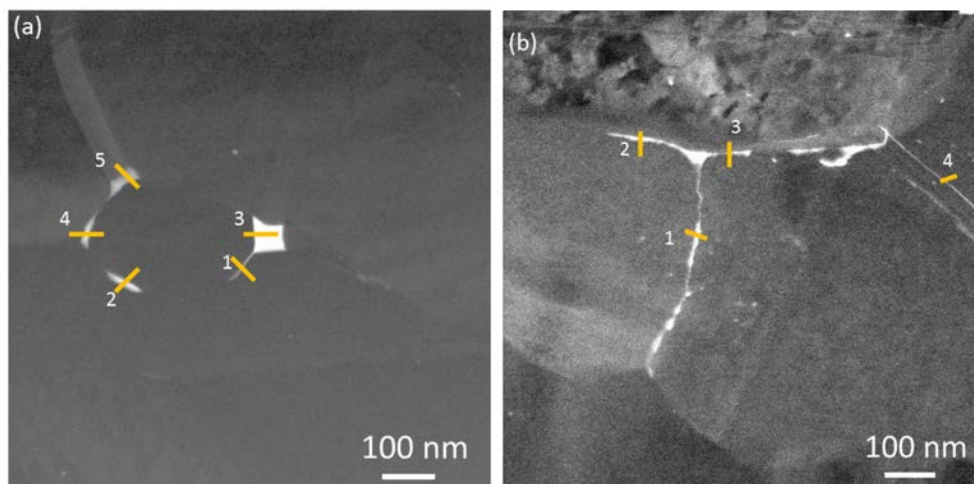


Figure 73. STEM HAADF image combined with EDS labeling to track the chemical composition of fission product precipitates from the outer area of TRISO Particle AGR1-531-038 within the subtended Areas (a) 4 and (b) 5 highlighted in Figure 59(c). Note the reported chemical compositions are in Table 46.

Table 46. Reported qualitative EDS compositions (in at.%) from the outer area of TRISO Particle AGR1-531-038, taken from subtended Areas 4 and 5 that are highlighted in Figure 59(c).

Precipitate Number	Concentration (at.%)									Precipitate Identification
	C	Si	Pd	Ag	Cs	Ce	Eu	U	Pu	
Area 4										
1	44.42	52.10	3.48	0.00	0.00	0.00	0.00	0.00	0.00	Pd
2	55.32	28.66	16.01	0.00	0.00	0.00	0.00	0.00	0.00	Pd
3	54.94	17.22	27.85	0.00	0.00	0.00	0.00	0.00	0.00	Pd
4	55.93	29.44	14.62	0.00	0.00	0.00	0.00	0.00	0.00	Pd
5	59.52	32.17	8.31	0.00	0.00	0.00	0.00	0.00	0.00	Pd
Area 5										
1	46.89	52.01	1.10	0.01	0.00	0.00	0.00	0.00	0.00	Pd
2	47.73	51.10	1.17	0.00	0.00	0.00	0.00	0.00	0.00	Pd
3	46.79	52.39	0.82	0.00	0.00	0.00	0.00	0.00	0.00	Pd
4	47.00	52.45	0.54	0.00	0.00	0.00	0.00	0.00	0.01	Pd

### 3.2.4 Crystallographic Characteristics of Particle AGR1-531-038

In the areas analyzed for fission product precipitates, PED data were collected using the ASTAR system to determine the characteristics of all grain boundaries in the vicinity (i.e., those with and those without fission product precipitates on them). Data were collected from areas approximately  $2\ \mu\text{m} \times 2\ \mu\text{m}$ . Figure 59 shows the areas on each of the TEM samples that were analyzed for fission product precipitates and PED grain orientation data. Unfortunately, the outer sample (Lamella 3, Figure 47[c] and Figure 59[c]) was lost prior to performing PED analysis on the areas where fission product precipitates were analyzed (see Section 3.2.3.1.3 for EDS results). Therefore, two areas on the center sample closest to the OPyC, labeled Outer 1 and Outer 2 in Figure 59(b) were analyzed with PED to represent the grain boundary distribution information in the outer region of the SiC layer. (Figure 47[c] shows that the outer edge of the center sample (Lamella 2 in Figure 47[c]) lies quite close to the SiC/OPyC interface and, thus, should provide a reasonable representation of the grain boundary distribution in the outer regions of the SiC layer.) Unfortunately, because the outer sample (Lamella 3) was lost, the fission product precipitates that were analyzed on the outer sample and presented in Section 3.2.3.1.3 could not be correlated with grain boundary information.

**3.2.4.1 General Grain Boundary Distributions Across the Silicon Carbide Layer.** The grain orientation maps of the areas analyzed on the inner sample (Lamella 1, Figure 59[a]) are shown as an example in Figure 74. Grain orientation maps for each of the areas analyzed on the center (labeled Outer 1 and Outer 2 on Figure 59[b]) and outer (Figure 59[c]) Lamella can be found in Lillo et al., (2017).

Determination of the SiC grain orientation allowed the determination of the grain boundary distribution in each of the analyzed areas. Distributions of grain boundary misorientation angles, CSL values, and grain boundary types found in each area analyzed on the inner sample (Figure 59[a]) are shown in Figure 75(a), (b), and (c), respectively. The relatively small analysis areas produce considerable variability in all distributions and highlight the need to perform PED analyses on multiple areas to yield statistically relevant distributions of grain boundary characteristics. The areas analyzed using PED were considerably smaller than those used in analysis of AGR1-531-031 (see Section 3.2.2.2.1), and the variability is considerably reduced for Particle AGR1-531-031 (see Figure 54). However, the “Averaged Distributions” are virtually identical for the inner regions of the two particles; comparing Figure 75 and Figure 54 illustrates that analysis of a few large areas is equivalent to analysis of a greater number of

small areas. Also, it would appear that particle-to-particle variation, at least for inner regions of the SiC layer for these two Variant 1 TRISO particles, is not large.

The areas on the inner sample were combined to yield an average distribution for each plot in Figure 75 with error bars based on the standard error. (The standard error was determined by dividing the standard deviation for each measured value by the square root of the number of regions analyzed, [i.e., number of observations].) The orientation data obtained from the various areas on the other lamellae, (i.e., the center and outer samples) were similarly analyzed and plotted.

Plots of the grain boundary distributions that have been averaged over all areas analyzed for inner, center, and outer samples are shown in Figure 76. Differences in the distributions in samples taken from the inner, center, and outer regions are discussed in the following subsections.

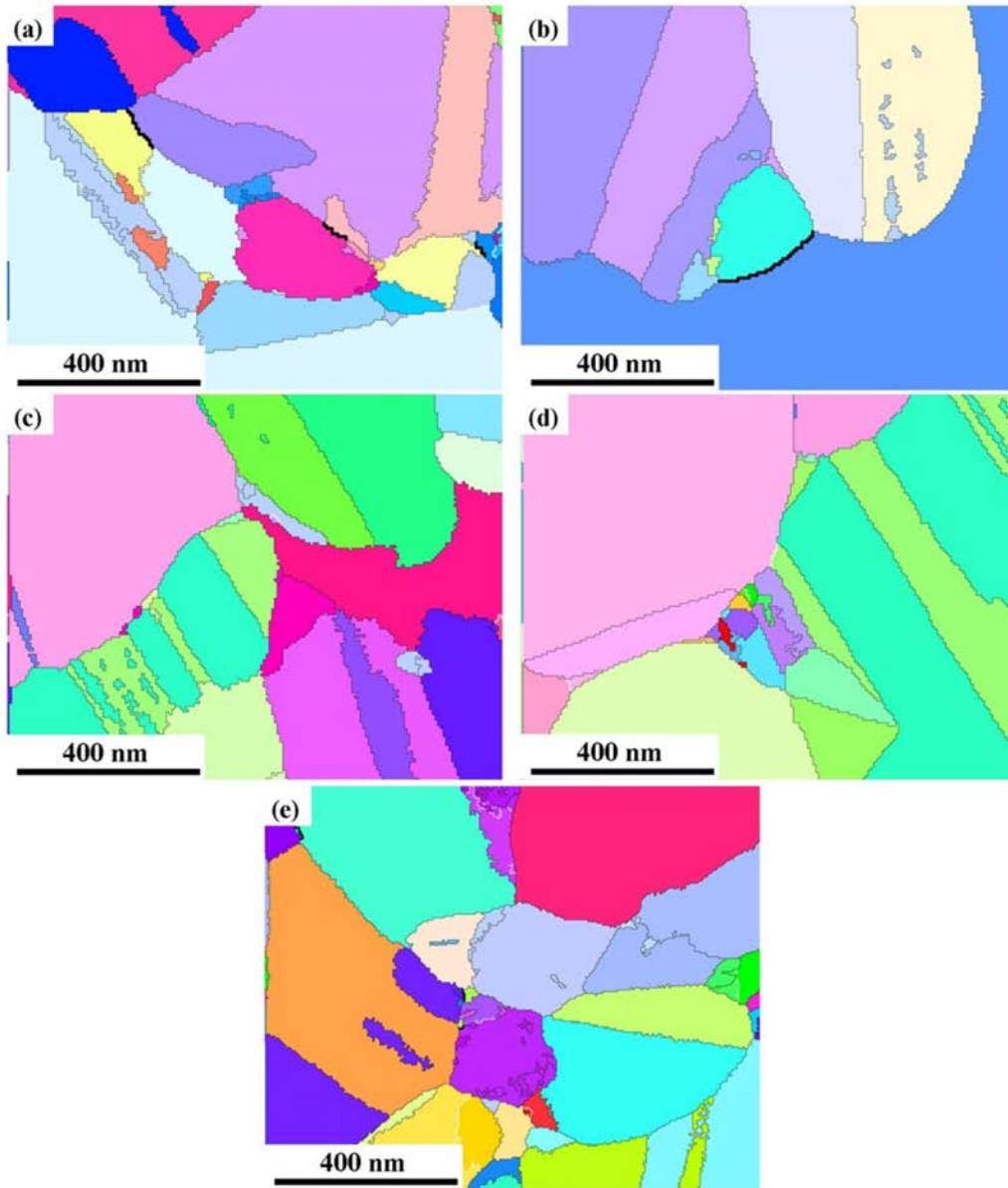


Figure 74. Orientation maps of (a) Area 1, (b) Area 2, (c) Area 3, (d) Area 4, and (e) Area 5 in Lamella 1 (from Figure 59[a]).

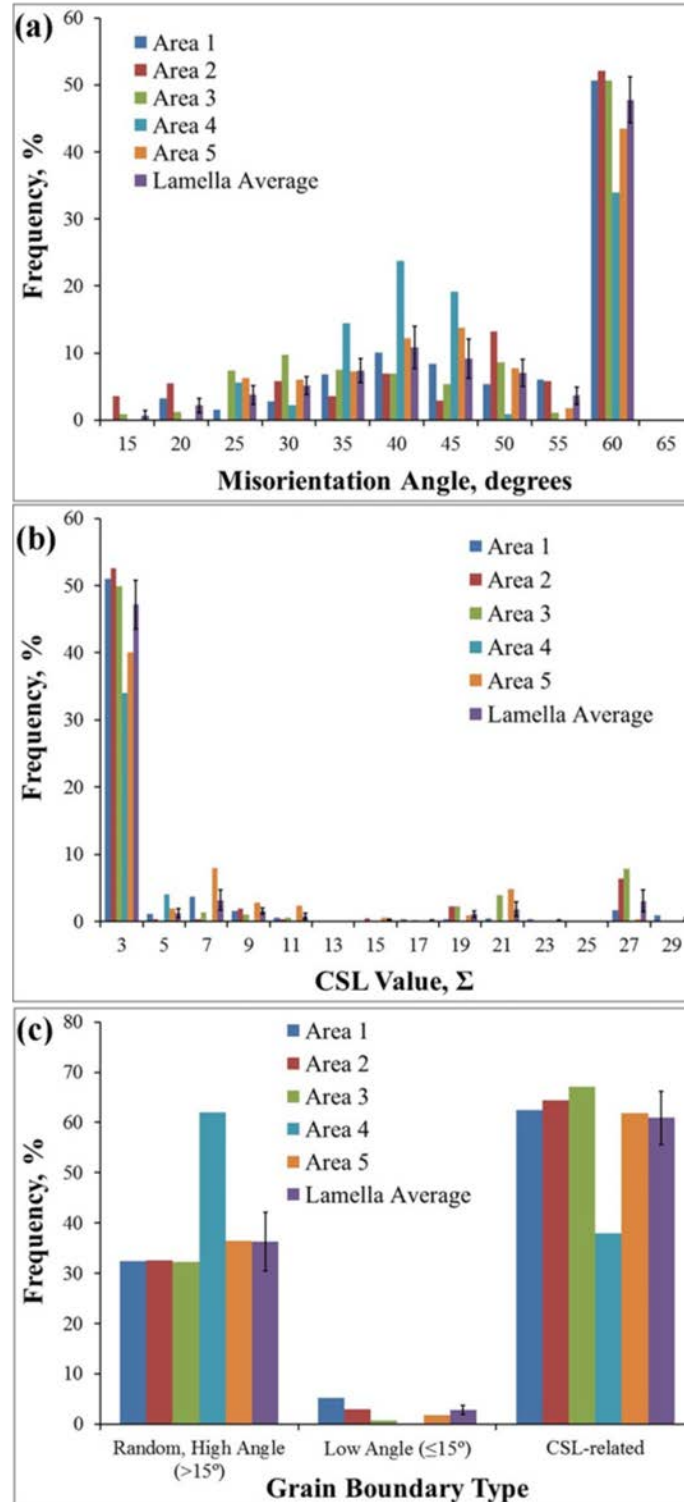


Figure 75. Distributions of (a) grain boundary misorientation angles, (b) value of CSL-related grain boundaries, and (c) grain boundary types in each area analyzed on the inner Lamella (Lamella 1, Figure 47[c] and Figure 59[a]), as well as the averaged distributions with the accompanying standard error bars.

**3.2.4.2 Misorientation Angle Distribution.** The plots in Figure 76(a) show that the SiC grain structure in the inner, center, and outer areas are dominated by the 60-degree misorientation, which coincides with the misorientation associated with twin grain boundaries. (The larger error bars on the outer sample at 60 degrees in Figure 76(a) are from the analysis of only two areas where the grain size was quite large. These error bars would likely be reduced and similar to those of the distributions for the inner and center samples had additional areas been analyzed with PED.) A second smaller peak in the misorientation angle distribution is found to occur around 40 degrees. Generally, the misorientation angle distributions are similar for the inner, center, and outer samples and most differences are not statistically significant.

**3.2.4.3 Distribution of Coincident Site Lattice-Related Grain Boundaries.** Figure 76(b) shows that the twin-related grain boundaries (CSL-designation,  $\Sigma 3$ ) dominate the distribution of grain boundaries that are CSL-related, as illustrated by the peak at 60 degrees in the misorientation angle distribution plot of Figure 76(a). There are very few CSL-related grain boundaries with CSL values other than  $\Sigma 3$ . The higher order twins (i.e.,  $\Sigma 9$  and  $\Sigma 27$ ) make up the majority of the remaining CSL-related grain boundaries, although significant numbers of  $\Sigma 5$ ,  $\Sigma 7$ , and  $\Sigma 21$  are also present.

The CSL distributions of the three samples can be averaged to yield fractions of CSL values for the entire SiC layer. For comparison purposes, only the fraction of twins, including higher order twins (i.e.,  $\Sigma 3$ ,  $\Sigma 9$ , and  $\Sigma 27$ ), have been included in Table 47. These values can then be compared directly to the work of Kirchhofer et al., (2013), who reported the grain boundary distributions in the SiC layer of unirradiated AGR-1 TRISO particles obtained from SEM-based EBSD measurements. The values they found for the SiC layer in a TRISO particle made using Variant 1 fabrication conditions are consistent with those reported in Table 47. They report fractions of 39% for  $\Sigma 3$ , 6% for  $\Sigma 9$ , and 1% for  $\Sigma 27$  twin boundaries. When the standard error given in Table 47 is also taken into account, the Kirchhofer values are very similar to those found here, although the  $\Sigma 9$  fraction in AGR1-531-038 may be statistically higher than that reported by Kirchhofer. Differences, if truly present, may be due to the use of SEM-based EBSD and analysis of a larger area compared to this work. Particle-to-particle variation may account for the observed differences between the two studies, but does not appear to be large. Furthermore, there appears to be no statistical difference between this particle and AGR1-531-031 that was reported in Table 30. Therefore, the variation between the SiC layers of these two Variant 1 TRISO particles appears to be small. Furthermore, comparison of the irradiated particles in this study with the results from the unirradiated particle of the Kirchhofer study seems to indicate that neutron irradiation does not have a large effect on the CSL grain boundary distribution in the SiC layer. However, the actual neutron fluence experienced by the two particles in this study needs to be determined before definitive conclusions can be made. Comparisons of these results with other particles from the different variant fuel types will be discussed in Section 4.4.

Table 47. Average fraction of twin-related grain boundaries in the SiC layer from Particle AGR1-531-038.

CSL value, $\Sigma$	Fraction, %	Std. Error
3	44.3	5.0
9	1.9	1.1
27	1.6	1.2

**3.2.4.4 Distribution by Grain Boundary Type.** The distribution by grain boundary type for AGR1-531-038 is shown in Figure 76(c). The fraction of low-angle grain boundaries (misorientation angle less than 15 degrees) is generally low (i.e., generally less than 10%, as shown in Figure 76(c)) with the exception of the outer sample where the low-angle grain boundary fraction was found to be around 25%. However, only two areas were analyzed in the outer region and the grain size is relatively large, which results in a reduced number of grain boundaries used in the calculation of the distribution for the

outer region and the relatively large error bars. CSL-related grain boundaries represent the largest fractions of grain boundaries in each of the samples, although the fractions of high-angle grain boundaries (misorientation angle greater than 15 degrees) are nearly as large (Figure 76[c]), except in the outer sample. The error bars indicate there is no significant difference in the distributions between the inner (AGR1-531-038-1) and center (AGR1-531-038-2) samples of Figure 76(c).

The average random, high-angle grain boundary fraction in the SiC layer in Table 48, at 32.2%, is significantly higher than that found for AGR1-531-031 (Figure 55[c] and Table 31), which was found to be on the order of 22.5%. Comparisons of the average values of grain boundary types in Table 48 can also be made to those reported for the SiC layer in an unirradiated, AGR-1 Variant 1, TRISO fuel particle (Kirchhofer et al., 2013) using SEM-based EBSD methods. Generally, the values found here for AGR1-531-038 are consistent with those of the study on the SiC layer in an unirradiated Variant 1, TRISO particle, which are reported to be 54% for CSL-related grain boundaries, 42% for high-angle grain boundaries, and 4% for low-angle grain boundaries. Comparison of the unirradiated grain boundary distribution of the Kirchhofer study and the irradiated AGR1-531-038 grain boundary distribution suggests the microstructure of the SiC layer does not change significantly due to the irradiation conditions of the AGR-1 experiment; however, additional particles should be analyzed and the actual neutron fluence experienced by each particle needs to be determined before this observation can be confirmed. Furthermore, the standard error values given in Table 48 are quite large and make comparisons somewhat tenuous. For instance, results from AGR1-531-031 show a considerable difference in the random, high-angle and low-angle grain boundary fractions compared to the Kirchhofer results. Large errors associated with the AGR1-531-038 data may be masking significant differences in the unirradiated and irradiated Variant 1 grain boundary distributions. Therefore, there may be subtle differences in the grain boundary distributions among different particles as well as irradiated and unirradiated particles of the same variant. Ultimately, these differences may be relevant to fission product release because AGR1-531-038 and AGR1-531-031 exhibited extremely different Ag release behavior. The implications of these differences are discussed in Section 3.2.5 of this report.

Table 48. Average fraction of grain boundary types in the SiC layer from Particle AGR1-531-038.

Grain Boundary Type	Fraction, %	Std. Error
Low angle, <15°	9.8	7.0
High angle, >15°	32.2	10.7
CSL-related	58.0	4.6

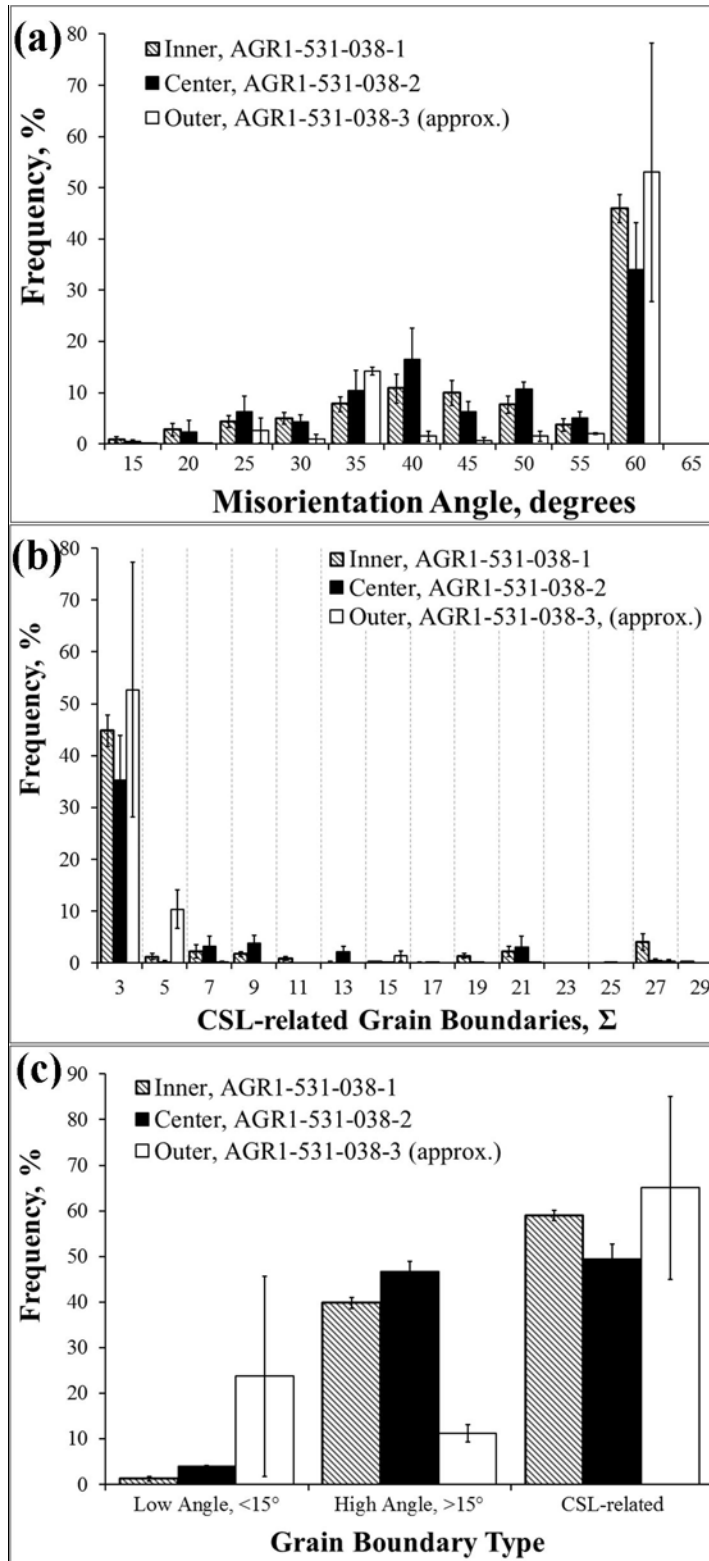


Figure 76. Distributions averaged over all areas analyzed for each sample: (a) misorientation angle, (b) CSL designation, and (c) grain boundary type for the SiC grain boundaries of samples taken from AGR1-531-038.

#### **3.2.4.5 Grain Boundary Data for Grain Boundaries Containing Fission Product**

**Precipitates.** The inner and center samples (AGR1-531-038-01 and AGR1-531-038-02, respectively) exhibited a number of grain boundary fission product precipitates. These precipitates were analyzed qualitatively for the presence of various fission product elements using EDS, and the associated grain boundary character was analyzed using the PED data. Unfortunately, it was difficult in some cases to match fission product precipitates found in the HAADF image to the same locations in the PED orientation maps. It is likely that overlapping SiC grains prevented easy identification of the desired boundaries in the PED orientation images. Only those areas and precipitates that could be confidently identified in the PED orientation images were analyzed for the grain boundary characteristics and reported here. Therefore, although a relatively large number of precipitates were found in HAADF images and analyzed with EDS, only about half could be correlated to the PED orientation data, resulting in the limited dataset (i.e., 21 precipitates for the inner sample and 26 precipitates for the center sample) presented in the following subsections. (Although the compositional information of fission product precipitates in the outer sample was determined, the PED information associated with these grain boundary precipitates was not obtained because this sample was lost prior to PED analysis.)

**3.2.4.5.1 Area Nearest Inner Pyrolytic Carbon Layer (Inner Sample, AGR1-531-038-01).** The areas analyzed on this sample (Lamella 1) are indicated in Figure 59(a). Area 1 was located very near the IPyC/SiC interface and the successive areas were located at increasing distances from this interface. The bright features in this HAADF image indicates precipitates of higher average atomic number than SiC, indicating the presence of fission product precipitates. Fission product precipitates in these areas were analyzed qualitatively for composition to determine whether a particular fission product element was present (i.e., 0.2 at.% was taken as the limits of detection for EDS data) and the grain boundary parameters on which they were located were determined using PED orientation data. The results of these analyses are summarized in Table 49. Pd was frequently present in the fission product precipitates, while a few precipitates exhibited significant amounts of U, which was always found in conjunction with Pd, and some exhibited the presence of Ag, which is typically, but not always, in conjunction with Pd. Only one precipitate was found to exhibit a significant amount of Ce, which was associated with both U and Pd. The majority of the fission product elements reside on high-angle grain boundaries; although a significant fraction is associated with CSL-related grain boundaries (about 33% considering CSL  $\Sigma$  values up to 29). Finally, Table 49 shows only one fission product precipitate (containing only Pd) was found on a low-angle grain boundary.

It must be kept in mind that the areas analyzed here represent only a small fraction of the total SiC layer. It is possible that additional fission products and fission product precipitate/grain boundary-type associations may be present elsewhere in this TRISO particle, but were not present within the final samples produced in this study. Indeed, in other micro-analysis characterization work on different TRISO particles, other fission product elements (e.g., Ce and Cd) were found in vicinities close to the IPyC/SiC interface. However, only Ag, U, and Pd-containing fission product precipitates were found at significant distances away from this interface. This would indicate that other, fission products (e.g., Ce and Cd) may diffuse relatively slowly along grain boundaries compared to Ag, U, and Pd. Also, it is likely that performance of the kernel, buffer layer, and IPyC also influence the fission products that ultimately make their way into the SiC layer and the location where they enter the SiC layer. This is why the samples studied here were taken from the area of the SiC layer that was in closest proximity to the cracked buffer layer and kernel protrusion (Figure 47). Distribution of fission product elements will likely be different at areas away from the buffer layer fractures. However, this work was mainly interested in transport of fission products and focused only on the damaged area.



**3.2.4.5.2 Results for the Center Sample (AGR1-531-038-02).** The areas analyzed on this sample that were taken from the center of the SiC layer, Lamella 2 in Figure 47(c), are shown in Figure 59(b). Again, the fission products in each of these areas were analyzed in a manner similar to that of the inner sample (AGR1-531-038-01) reported above. The results are summarized in Table 50. As with the inner sample (AGR1-531-038-01), Pd is the most prevalent fission product element in the precipitates. The fraction of precipitates exhibiting the presence of U is significantly lower, while only one precipitate exhibited significant amounts of Ag. Again, U-containing precipitates always contained significant amounts of Pd. The one Ag-containing precipitate also contained a significant amount of Pd. No fission products precipitates exhibiting Ce were found.

Again, most of the fission product precipitates were found on random, high-angle grain boundaries. Only a small fraction of precipitates were located on CSL-related grain boundaries (i.e., about 15% considering  $\Sigma$  values up to 29) and no precipitates were located on low-angle grain boundaries.

Table 49. Summary of fission product precipitate analysis for the inner sample (AGR1-531-038-01).

Fission Product Precipitate ID	Misorientation Angle (degree)	Misorientation Axis			CSL Designation		Fission Product Element or Transuranic Element			
		x	y	z	$\Sigma$	Deviation (degree)	U	Pd	Ag	Ce
Area 1	1	3.3	5	-19	11	—	—	•		
	2	41.3	-12	-17	-15	—	—	•		
	3	54	-18	-13	-18	—	—	•		
	4	33	-3	4	11	33b	2	•		
Area 2	1	44.5	0	-3	-1	37b	1.4	•		
	2	53.3	-17	-24	-8	—	—	•		
	3	51	1	7	-8	—	—	•		
	4	35.6	-1	-15	8	27b	2.2		•	
	5	59.1	1	-1	-1	3	1.2	•		
Area 3	1	52.1	7	6	-9	—	—	•	•	
	2	38.4	4	-22	13	—	—	•	•	
	3	32.3	-20	0	21	27a	1.1	•		
	4	37.2	-5	12	22	—	—	•		
Area 4	1	40.7	-1	-3	-28	5	5.7	•	•	
	2	28.4	3	-7	-8	—	—	•	•	•
Area 5	1	29.4	-5	12	15	—	—	•		
	2	39.1	-2	15	0	5	5.4	•		
	3	42.7	-21	-1	21	9	4	•		
	4	47.8	2	5	2	—	—	•	•	
	5	46.1	-1	26	-15	15	3.8	•	•	
	6	30.9	17	-23	-7	—	—	•		

**3.2.4.5.3 Comparison of Lamella 1 and Lamella 2.** The data for each sample in Table 49 and Table 50 are summarized and analyzed in Discussion **of Results for Particle AGR1-531-038**. Since the datasets for Lamellae 1 and 2 were relatively small, they were combined to yield distributions relevant to the entire SiC layer.

Pd-containing precipitates (i.e., Pd only, Pd with Ag, and Pd with U) were the most common throughout the SiC layer (**Error! Not a valid bookmark self-reference.** and Figure 78). Only one precipitate was found that exhibited only Ag and no other fission products above the detectable limit of 0.2 at.%. U, assumed to have originated in the UCO fuel kernel, was always found in conjunction with Pd but never by itself or associated with Ag.

**3.2.4.5.4 Table 51.** Also, the distribution of grain boundary types containing fission products in the inner and center sample can be compared in Figure 77. In general, the distribution of fission product precipitates in the inner and center lamellae exhibit similar trends that indicate precipitates are most prevalent on random, high angle grain boundaries with a significant number also found on CSL-related grain boundaries but very few on low angle grain boundaries. The dataset for each area is relatively small and the sample locations in the SiC layer significantly overlap each other (see Figure 47[c], Lamellae 1 and 2), making further comparisons between the two region relatively meaningless. Such comparisons would require considerably more data to make meaningful conclusions on the apparent differences in the two distributions.. However, it can be concluded that precipitates prefer to form on random, high-angle grain boundaries, but will also form on CSL-related grain boundaries to a lesser degree. Precipitates rarely form on low-angle grain boundaries and the only precipitates identified on low-angle boundaries contained only Pd in detectable quantities.

Table 50. Summary of fission product precipitate analysis for the center sample (AGR1-531-038-02).

Fission Product Precipitate ID	Misorientation Angle (degree)	Misorientation Axis			CSL Designation		Fission Product Element or Transuranic Element			
		x	y	z	$\Sigma$	Deviation (degree)	U	Pd	Ag	Ce
Area 2	1	41.4	-23	13	-7	—	—	•		
	2	50.8	-15	17	6	—	—	•		
	3	47	9	-1	22	—	—	•		
	4	54.5	-12	16	-21	—	—	•	•	
	5	54.4	-12	16	-21	—	—	•	•	
Area 3	1	36.6	21	12	8	—	—	•		
	2	45.5	12	-3	-11	—	—	•		
	3	45.5	12	-3	-11	—	—	•		
Area 4	1	41	-22	-13	-14	—	—	•		
	2	48.1	-11	11	15	—	—	•		
	3	15.8	-7	2	26	—	—	•		
	4	49.3	18	10	-15	—	—	•	•	
	5	56.7	19	-14	10	—	—	•		
Area 5	1	41.7	1	-13	14	9	3.7	•	•	
	2	46.9	-15	23	8	—	—	•		

Table 50. (continued).

Fission Product Precipitate ID	Misorientation Angle (degree)	Misorientation Axis			CSL Designation		Fission Product Element or Transuranic Element			
		x	y	z	$\Sigma$	Deviation (degree)	U	Pd	Ag	Ce
3	52	-20	-7	-13	39b	2.1	•	•		
4	44.6	-2	-23	19	—	—		•		
5	49	17	9	5	—	—		•		
6	40.1	-5	8	27	—	—		•		
7	34.3	-1	-11	-11	—	—		•		
Area 6	1	21	1	-21	9	0.7	•	•		
	2	1	6	13	—	—	•	•		
	3	-1	-21	17	—	—		•		
	4	4	4	-3	13b	3.7		•		
	5	-1	-1	1	3	0.7	•	•		
	6	-13	-16	1	—	—		•		

**3.2.4.5.1 Discussion of Results for Particle AGR1-531-038.** Since the datasets for Lamellae 1 and 2 were relatively small, they were combined to yield distributions relevant to the entire SiC layer.

Pd-containing precipitates (i.e., Pd only, Pd with Ag, and Pd with U) were the most common throughout the SiC layer (**Error! Not a valid bookmark self-reference.** and Figure 78). Only one precipitate was found that exhibited only Ag and no other fission products above the detectable limit of 0.2 at.%. U, assumed to have originated in the UCO fuel kernel, was always found in conjunction with Pd but never by itself or associated with Ag.

Table 51. Summary of the distribution of fission product elements.

	Pd Only	Ag only	U only	Pd & Ag	Pd & U	Ag & U
<b>Inner Sample</b>						
Number of grain boundaries	13	1	0	2	5	0
Percentage of all boundaries with fission products, %	61.9	4.8	0.0	9.5	23.8	0.0
Low angle, %	7.6	0.0	—	0	0.0	—
Random, high angle, %	46.2	0.0	—	100	60.0	—
CSL, %	46.2	100.0	—	0	40.0	—
<b>Center Sample</b>						
Number of grain boundaries	18	0	0	1	7	0
Percentage of all boundaries with fission products, %	69.2	0.0	0.0	3.8	26.9	0.0
Low angle, %	0.0	—	—	0.0	0.0	—
Random, high angle, %	94.4	—	—	0.0	57.1	—
CSL, %	5.6	—	—	100.0	42.9	—

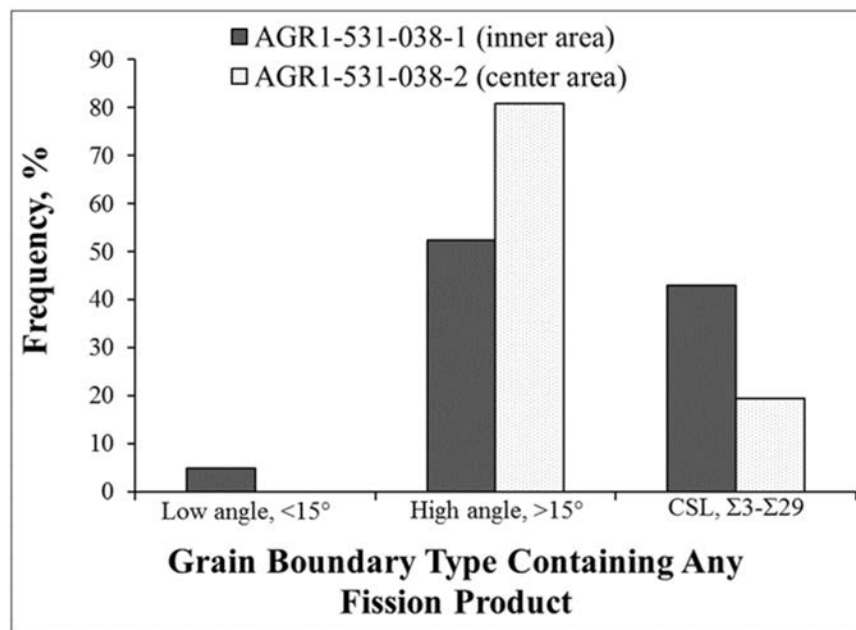


Figure 77. Comparison of the distribution of grain boundary types that contained any fission product precipitates.

Regardless of the fission product elements present, the precipitates showed a preference for random, high-angle grain boundaries (Figure 79), as found in a similar analysis on an irradiated, Baseline TRISO particle from Compact 6-3-2 (Figure 35; Lillo and van Rooyen 2016). Precipitates on CSL-related grain boundaries are much less prevalent and precipitates on low-angle grain boundaries are infrequently observed (Figure 79). Pd was found to precipitate on all grain boundary types, although only Pd-only precipitates occurred on low-angle grain boundaries (Figure 80). Ag or U, whether associated with Pd or not, were never observed on low-angle grain boundaries. The single Ag-only precipitate was found to reside on a CSL-related grain boundary, which was Σ27b. (Since only one Ag-only precipitate was found and analyzed, the Ag-only data in Figure 80 is somewhat misleading. The grain boundary parameters of more Ag-only precipitates need to be determined to represent the distribution accurately of Ag-only as a function of grain boundary type.)

In summary, Pd-containing precipitates are most prevalent and are found on low-angle, high-angle, and CSL-related grain boundaries, while Ag-containing precipitates are found on random, high-angle and CSL-related grain boundaries. Overall, precipitation is favored on random, high-angle grain boundaries. Precipitation on low-angle grain SiC grain boundaries is rare in this irradiated TRISO particle. The preference of fission product precipitates for specific grain boundary types can be explained based on grain boundary energy (Lillo and van Rooyen 2016). In general, low-angle and CSL-related grain boundaries have lower energy than random, high-angle grain boundaries, although the grain boundary habit plane has a strong influence on grain boundary energy. The addition of fission product elements and/or U to a grain boundary tends to raise the energy of the boundary, mainly due to the atomic size mismatch. However, random, high-angle grain boundaries typically have a greater amount of free volume, and incorporation of atoms with a different atomic radius in this type of grain boundary results in a smaller increase in energy as opposed to either low-angle or CSL-related grain boundaries that tend to have less free volume.

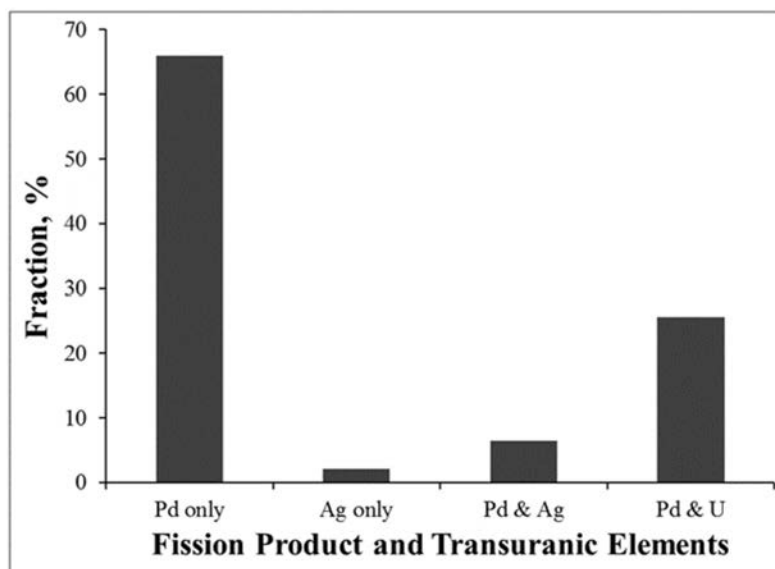


Figure 78. Composition distribution of the grain boundary precipitates.

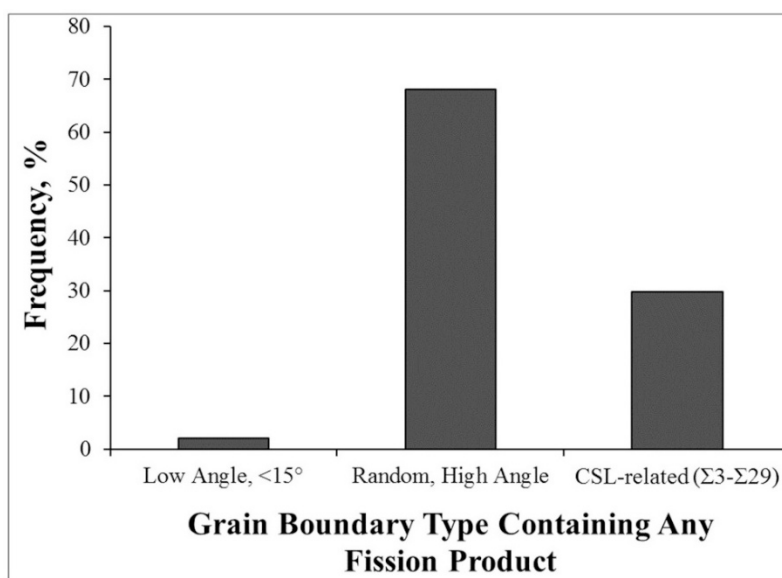


Figure 79. Distribution of fission product precipitates on various boundary types as a percentage.

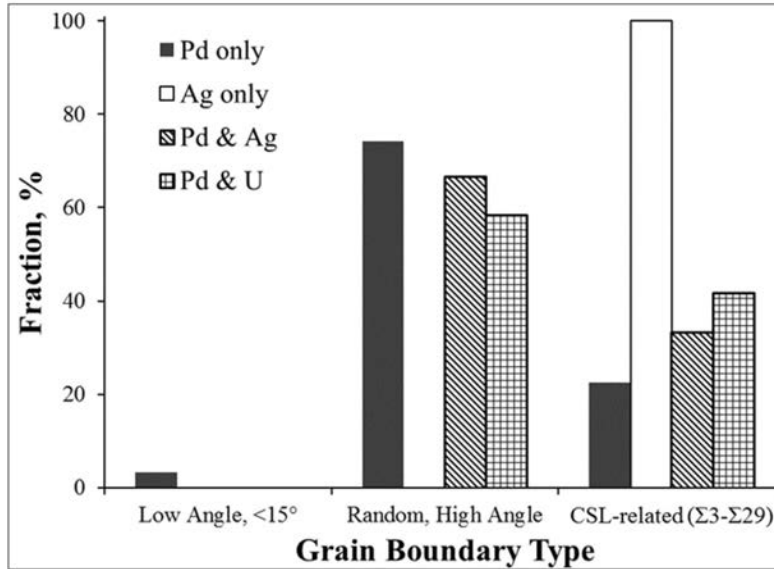


Figure 80. Distributions of fission product elements, as a percentage, by grain boundary type.

### 3.2.5 Crystallographic Characteristic Comparison and Main Findings on Compact 5-3-1 Particles

**3.2.5.1 Crystallographic Characteristic Comparison.** The two particles from Compact 5-3-1 exhibited radically different fission product release behavior even though they were in the same compact during the AGR-1 experiment. AGR1-531-038 showed a retention of Ag-110m of less than 19% compared to that predicted from physics calculations; however, AGR1-531-031 exhibited 105% retention compared to predicted, theoretical values (indicating complete retention). The reasons for the different behavior are either due to differences in the local experimental testing conditions or SiC microstructure. Experimentally, even though both particles were in the same compact in nominally the same position in the reactor during the irradiation experiment, the local conditions (primarily temperature, but also fluence, and burnup) may have been significantly different for each particle and significantly different from the values averaged over the compact. The irradiation temperature of a fuel particle will vary depending on the location of a given particle within the compact. This temperature variation may approach 300°C between the hottest part of compact and the coldest part of the same compact (Hawkes and Murray 2014). Alternatively, differences in microstructure, especially the grain boundary structure, could theoretically give rise to differences in fission product transport behavior.

**3.2.5.2 General Grain Boundary Distribution.** Comparisons of the misorientation angle distributions, CSL boundary distributions, and the grain boundary-type distributions between AGR1-531-038 and AGR1-531-031 are shown in Figure 81. Where the data for all the lamellae for a given particle has been averaged to yield values relevant to the SiC layer as a whole. A notable difference in the misorientation angle distribution of Figure 81(a) is the fraction of grain boundaries with a 60-degree misorientation, which is statistically lower in AGR1-531-038 compared to AGR1-531-031. Although this misorientation angle is associated with twin boundaries (equivalent to a CSL value of Σ3) in SiC, the Σ3 fractions in Figure 81b, though somewhat greater for AGR1-531-031, are not statistically different between the two particles, based on the standard error bars not being statistically different between the two particles. Thus, a significant number of grain boundaries are near the 60-degree twin orientation in AGR1-531-031 with a deviation that exceeds the Brandon criteria for Σ3 boundaries. (The Brandon criterion was used in this study to determine whether a given grain boundary misorientation is sufficiently close to that of a given Σ value to be considered as having the characteristic associated with

that  $\Sigma$  value and is given by  $\Delta\theta = 15^\circ \times \Sigma^{1/2}$ .) For  $\Sigma 3$  grain boundaries, the Brandon criterion indicates the deviation from exact coincidence,  $\Delta\theta$ , must be less than or equal to 8.7 degrees (Randle 1993).

Perhaps more interesting is the difference in the grain boundary-type distributions in Figure 81(c). In this figure, it is evident that the low-retention particle, AGR1-531-038, has a significantly higher fraction of random, high-angle grain boundaries than the high-retention Particle AGR1-531-031. This difference in the overall fraction of random, high-angle grain boundaries results mainly from contributions of the inner and center regions of AGR1-531-038. These regions have significantly higher fractions of random, high-angle grain boundaries than in the same regions of AGR1-531-031 when compared with the high-angle grain boundary fractions in the inner and center regions for Figure 76(c) and Figure 55(c) for AGR1-531-038 and AGR1-531-031, respectively. Random, high-angle grain boundaries generally exhibit higher grain boundary energies than CSL-related grain boundaries (although the boundary plane of CSL boundaries significantly affects grain boundary energy). Higher-energy grain boundaries generally exhibit higher diffusivities and are more amenable to precipitation. The low-Ag retention particle (AGR1-531-038) had a greater fraction of random, high-angle grain boundaries than the high-retention particle (AGR1-531-031). The high-Ag retention particle, AGR1-531-031, also exhibited a greater low-angle grain boundary fraction. These low-angle grain boundaries also exhibit a low diffusivity for impurity diffusion (essentially pipe diffusion). The differences in the observed grain boundary-type fractions may contribute to differences in observed fission product retention.

**3.2.5.3 Microstructural Comparison.** During characterization of the microstructure of AGR1-531-031, it was noted that the center and outer samples were not only essentially devoid of fission product precipitates, but pores in the SiC layer were noted, Figure 56. No pores were identified in the microstructure of AGR1-531-038, which exhibited fission product precipitates in the center and outer samples from its SiC layer.

No Pu was observed in the precipitates from Particle AGR1-531-031, with Pd, Ag, and U migration through the SiC layer identified up to 0.9, 1.7, and 8.7  $\mu\text{m}$ , respectively, away from the IPyC/SiC interface. This is significantly less than the movement of 34, 11, and 30  $\mu\text{m}$  into the SiC layer for Particle AGR1-531-038. Although, it should be considered that these lamellae were only prepared from a single location in the circumference of the SiC layer and there may be some bias in these values because there was a significant difference observed in the grain boundary characteristics of these two coated particles as demonstrated in Section 3.2.5.1.

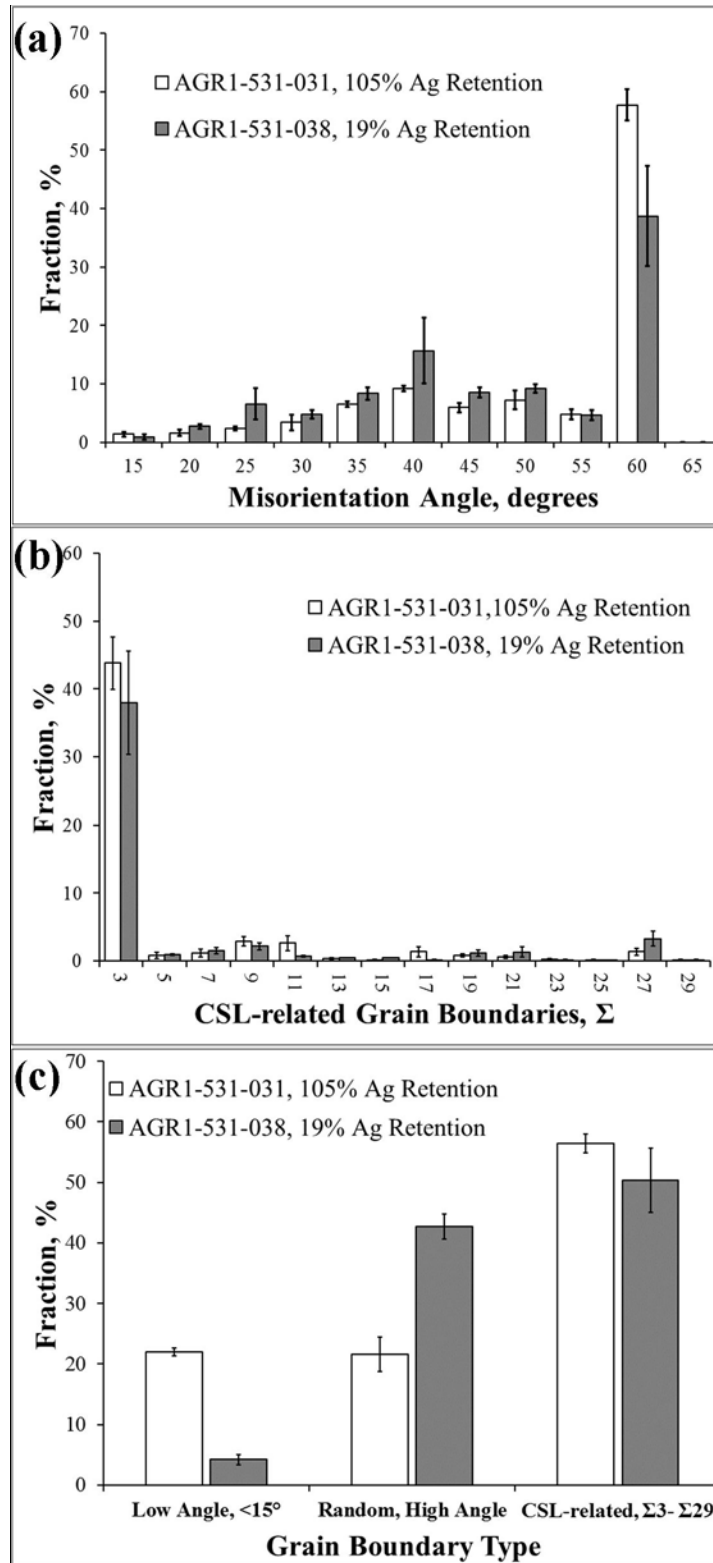


Figure 81. Comparison of the (a) misorientation angle distributions, (b) CSL boundary distributions, and (c) grain boundary-type distributions between AGR1-531-031 and AGR1-531-038.



### 3.3 Irradiated Variant 1 Fuel Examination: Compact 5-2-3

This section describes the advanced microscopy examination of a Variant 1 TRISO fuel particle (AGR1-523-SP01) with failed IPyC and SiC layers. Advanced microscopy methods were used to establish a potential difference in microstructure and fission product composition near the IPyC crack and in areas where the IPyC layer remained intact. Preliminary SEM analysis suggested the SiC degradation contained large C-rich features and notable build-up of Pd. The SEM analysis also indicated Pd-Si features located along the IPyC crack away from SiC layer degradation, suggesting the IPyC crack served as a pathway for Si transport away from the SiC layer and Pd transport toward the SiC layer (Hunn et al., 2014, Hunn et al., 2015). Given these initial observations, advanced microscopy was performed during this study to further understand SiC degradation and fission product transport in the SiC degradation region. Because this work is described in detail in journal publications, only a short summary of the results are provided. (Wen et al., 2015, Wen et al., 2016, and Wen and van Rooyen 2016). Crystallographic characteristic information and compositional trend graphics were not available at the time of this report. The reported fission product precipitate compositions (atomic %) are qualitative or semi-quantitative in nature (Section 2.1.2.3).

#### 3.3.1 Particle Selection and Lamellae

Compact 5-2-3, a Variant 1 fuel, was irradiated in the ATR to an average burnup of 17.42% FIMA, a time-averaged and volume-averaged temperature of 1059°C, and an average fast fluence of  $3.77 \times 10^{25} \text{ n/m}^2$  ( $E > 0.18 \text{ MeV}$ ) (Hunn et al., 2015).

During PIE of TRISO particles from Compact 5-2-3, gamma activity measurements determined that Cs had been released by two specific particles out of 4,088 particles deconsolidated from the compact and surveyed, whereas the other particles exhibited no measurable Cs release. The fractional Cs and Ag releases were determined, by comparing the measured inventory (from gamma counting) to the predicted inventory (from physics calculations) for Cs-134, Cs-137, and Ag-110m. For one of the two Cs-releasing particles (i.e., Particle AGR1-523-SP01), the fractional releases of Cs and Ag were about 30% and 85%, respectively. The particle had no detectable Ce or Eu release (i.e., measured activities were within normal distribution for measured isotopes). Non-destructive, 3D, x-ray tomography performed on this particle (Figure 82) revealed degradation of the SiC layer; this degradation was localized to one specific region that was connected to a crack in the IPyC layer that terminated at the IPyC-SiC interface. Buffer fractures and buffer/IPyC delamination are also evident in Figure 82.

**3.3.1.1 Lamellae Preparation.** Figure 83 shows the crack and area of examination with the locations where STEM lamellae were prepared using FIB. Ten TEM lamellae were cut from different locations of the TRISO particle cross section (shown in Figure 83[a] and [b]). The examination results obtained from Lamellae 1 through 4 will be used for comparative STEM studies from other compacts. Lamella 4 was perpendicular to the IPyC-SiC interface. Lamellae 5 through 10 are specifically prepared for obtaining information on the cracked region to supplement the SEM data already collected by ORNL. Lamella 7 was extracted from a location in the IPyC layer adjacent to the crack, Lamella 8 was right at the crack tip and approximately parallel to the IPyC-SiC interface and it contained mostly IPyC, and Lamella 10 was close to the crack tip and in the SiC layer. Lamellae 5, 6, and 9 were all approximately perpendicular to the IPyC-SiC interface and were in regions slightly away from the crack.

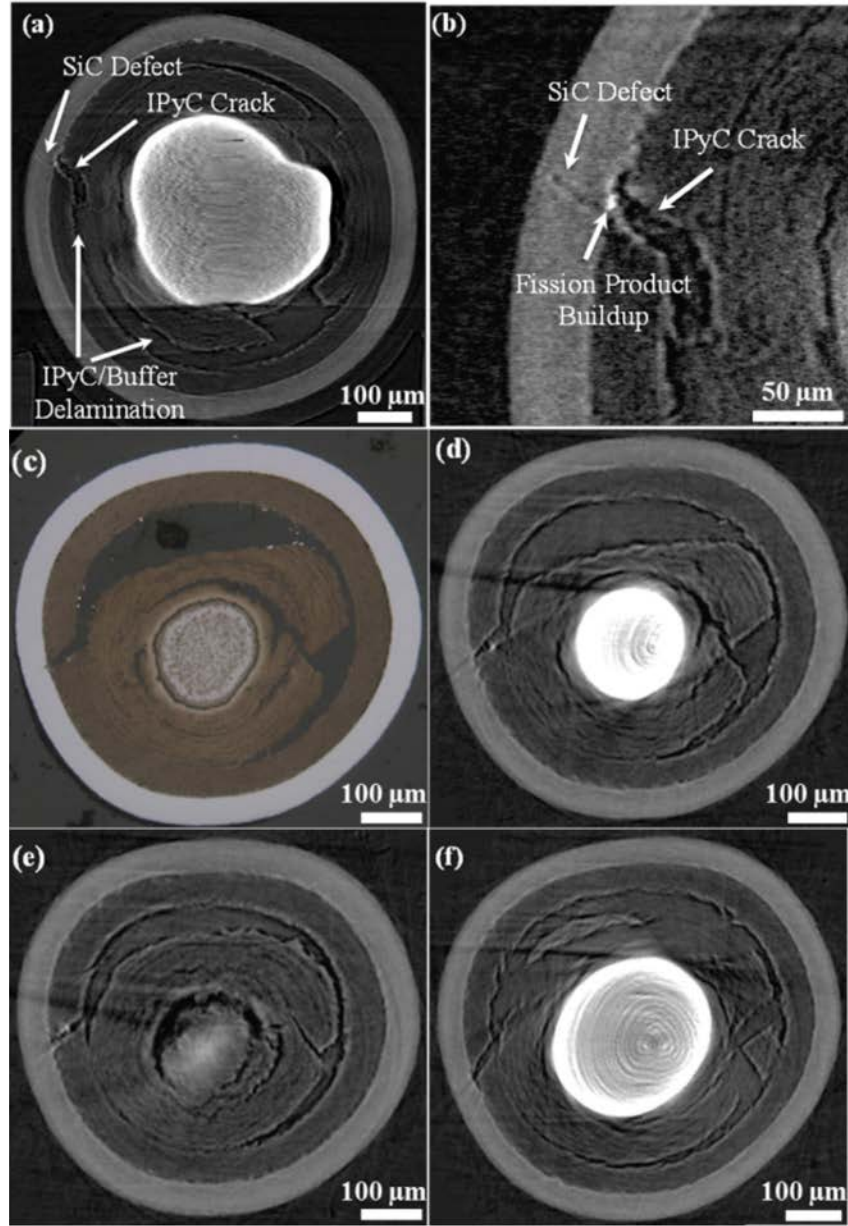


Figure 82. X-ray tomographs and a reference optical micrograph of TRISO Particle AGR1-523-SP01: (a) near-mid plane showing indication of a localized defect through SiC layer thickness; (b) close-up view of the SiC layer defect in (a), indicating that fission product build-up at the IPyC-SiC interface and that the SiC defect traverses the whole SiC layer; (c) optical micrograph of particle cross section produced by metallographic preparation of the particle from the plane orthogonal to that shown in (a); (d) matching tomographic slice to that shown in (c), showing correlation of layer construction with that of the analyzed particle cross-section; (e) plane approximately 25  $\mu\text{m}$  above (d) in the same orientation; and (f) plane approximately 25  $\mu\text{m}$  below (d) in the same orientation. The progression of images from (e) to (d) to (f) show the nature of crack termination at the IPyC-SiC interface and indicate that the SiC defect/degradation is localized to one location along the exposed SiC surface that is greater than 50  $\mu\text{m}$  (Wen et al., 2016).

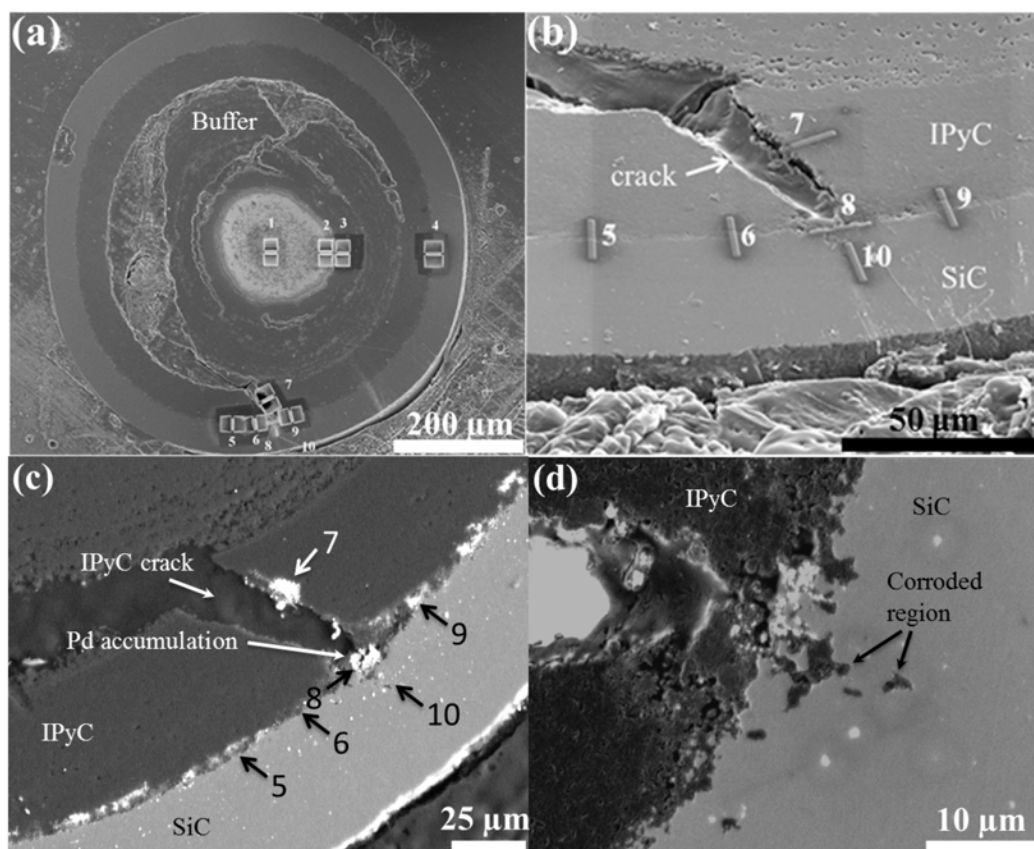


Figure 83. SEM images of the cross section of the studied AGR1-523-SP01 TRISO-coated particle. (a), (b) and (d) are secondary electron images and (c) is a back-scattered electron image. In (a), (b), and (c), the numbers indicate the locations where TEM lamellae were sectioned. The bright spots/areas in (c) are fission product precipitates.

### 3.3.2 Microstructural Examination

STEM and EDS were carried out to study the distribution and composition of fission product precipitates across the IPyC and SiC layers in different locations close to and away from the major crack. The general distribution of fission products in Lamellae 4, 5, and 6 (Figure 84[a], [b], and [c]) were similar because the number density of precipitates close to or at the IPyC-SiC interface was relatively low overall and the precipitate sizes were small. Note there were similarities among fission product distributions in Lamellae 4, 5, 6, and 9 (Figure 84[a], [b], [c], and [f]) that were away from the major IPyC crack.

Approximately 30% of the precipitates in the SiC layer adjacent to the crack contain Cs, with concentrations usually in the range of about 0.40 to 0.80 at.%, with the highest concentration being 2.20 at.%. No precipitates containing only Cs were observed. Ag and/or Cd-containing precipitates were also identified by EDS point scans at grain boundaries or triple junctions. The qualitative Ag concentration in these precipitates is 0.22 to 7.95 at.% and the Cd concentration is 0.20 to 1.31 at.%. Ag and/or Cd may exist by themselves or coexist with Pd. The number of Cs-containing precipitates is significantly higher than that of Ag or Cd-containing precipitates; however, the Cs concentration in the precipitates is usually significantly lower than the Ag or Cd concentration (see the Compact 1-3-1 and Compact 6-3-2 results). Analysis revealed the aligned nano-voids and Pd-rich precipitates in the SiC grains (Figure 85). Most of the nano precipitates are too small for the STEM-EDS detector.

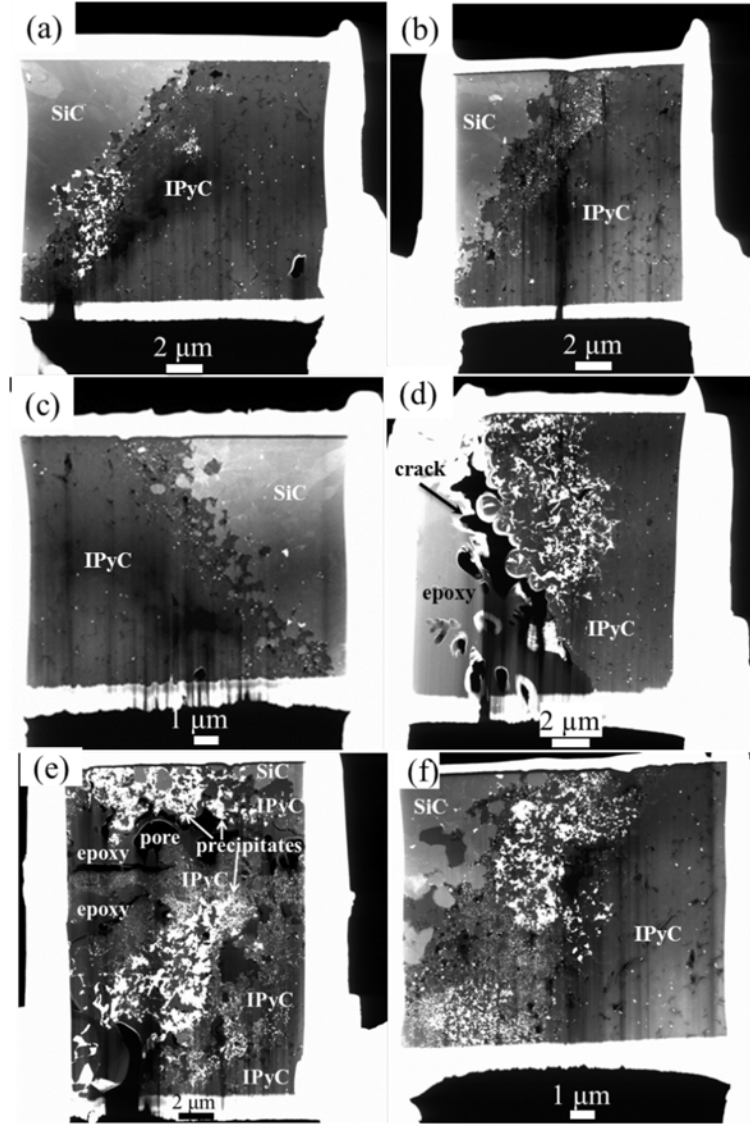


Figure 84. Low-magnification STEM images of TEM Lamellae 4 (a), 5 (b), 6 (c), 7 (d), 8 (e), and 9 (f), showing the general distribution of fission products.

Finding Ag inside a SiC grain is significant. An Ag-Pd-Cd precipitate was identified at a stacking fault inside a SiC grain in Particle AGR1-532-SP01 Lamella 10 (Figure 86). Previously, Ag was predominantly identified at grain boundaries and triple junctions, with evidence of Ag inside a SiC grain in a Lamella of Particle AGR1-632-035 (Leng et al., 2016). This study confirmed with STEM, TEM, STEM-EDS, and inverse fast Fourier transformation (IFFT) that the precipitate is indeed at a stacking fault and not at a grain boundary.

Figure 87 shows an example of a Pd-U-Ce and Pd-Si precipitates with corresponding diffraction patterns. From the diffraction patterns, the Pd-U-Ce precipitate in (b) is amorphous and the Pd-Si precipitate in (c) is semi-crystalline. For another Pd-U-Ce precipitate in (d), the lower-left part is amorphous, whereas the upper-right part is semi-crystalline. This further demonstrates the complex nature of precipitates that cannot be resolved at this resolution.

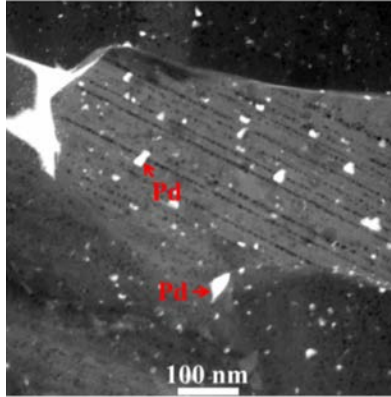


Figure 85. STEM image showing aligned nano voids (dark) and Pd nano precipitates (light features) in a SiC grain of Lamella 10.

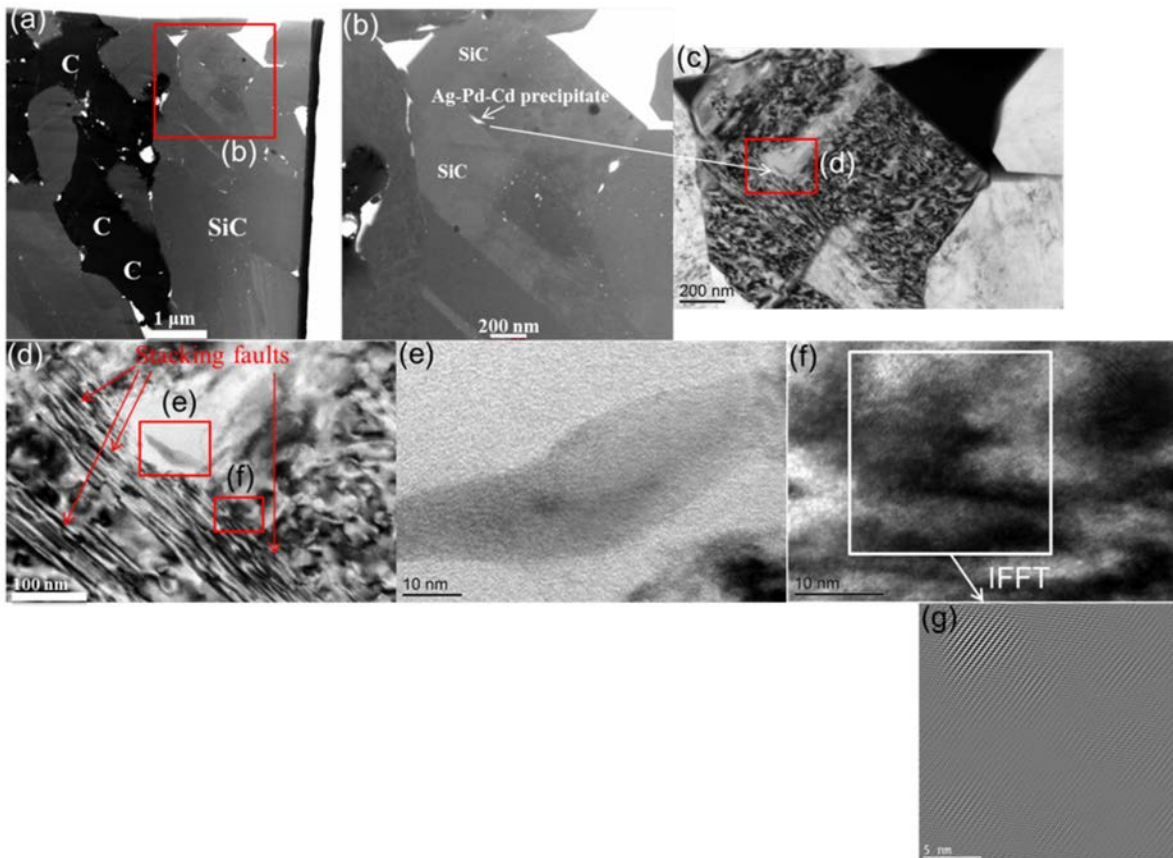


Figure 86. An Ag-Pd-Cd precipitate at stacking fault inside a SiC grain from Lamella 10. (a) and (b) STEM images show the location of the Ag-Pd-Cd precipitate, whose composition was determined by EDS; (c) TEM image corresponding to (b); (d) a magnification of the red rectangle in (c); (e) a magnification of the red rectangle in (d) where the Ag-Pd-Cd precipitate is located; (f) a magnification of the red rectangle in (d) where stacking faults are present; (g) inverse fast Fourier transform of the white square in (f), where the continuous lattice fringes indicate absence of grain boundary and confirm the presence of stacking faults.



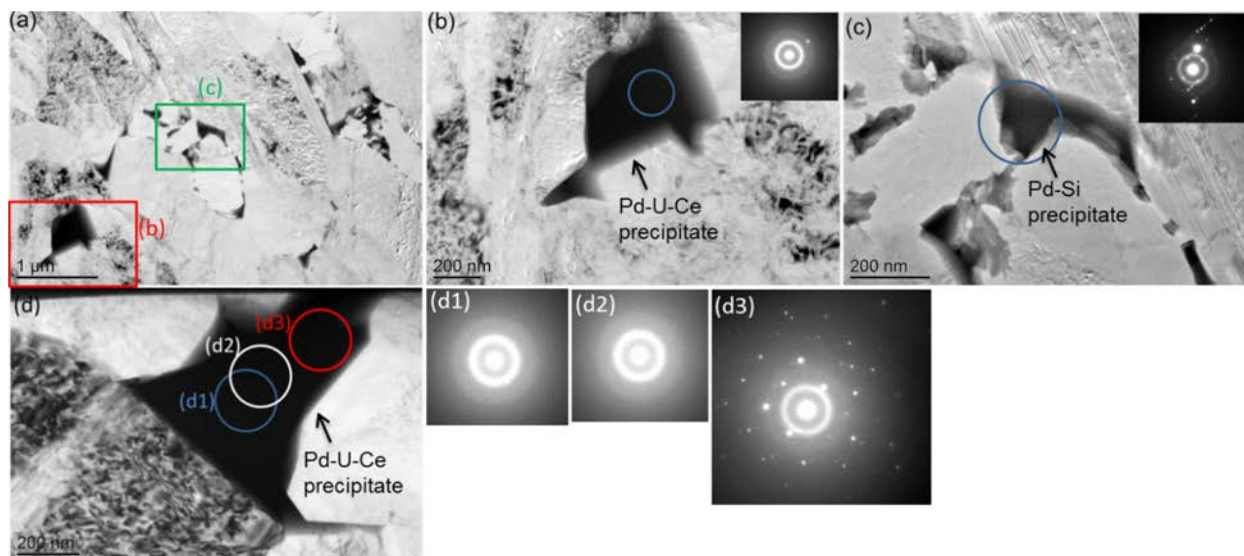


Figure 87. Selected area electron diffraction on precipitates from Lamella 10 from Particle AGR1-523-SP01. (a) A low-magnification TEM image; (b) a magnification of the red rectangle in (a), with diffraction performed on the blue circle and the corresponding diffraction pattern presented in the inset; (c) a magnification of the green rectangle in (a), with diffraction performed on the blue circle and the corresponding diffraction pattern presented in the inset; (d) TEM image of another precipitate, with diffraction performed on the blue, white, and red circles and the corresponding diffraction patterns presented in (d1), (d2), and (d3), respectively. Precipitate in (b) and (d) are Pd-U with small Ce concentrations and precipitate in (c) is Pd-Si, as determined by EDS in STEM. From the diffraction patterns, precipitate in (b) is amorphous, and precipitate in (c) is semi-crystalline; for the precipitate in (d), the lower-left part is amorphous, whereas the upper-right part is semi-crystalline.

### 3.3.2.1 Conclusions from Investigation of Corroded Area in Silicon Carbide Layer.

Summary and conclusions are based on work from Wen et al., (2015 and 2016) and Wen and Van Rooyen (2016).

- There were pure C areas in the SiC layer close to the crack, with Pd<sub>2</sub>Si or PdSi inside these areas, indicating corrosion of SiC by Pd. These corroded areas were not observed in locations in the SiC layer away from the crack.
- A locally elevated Pd concentration was among the necessary conditions for significant chemical reaction between Pd and SiC. In areas in the SiC layer close to the IPyC crack tip, local accumulation of Pd was present, which initiated the reaction between Pd and SiC. In addition, silicides formed by the reaction migrated away from the reaction site, leaving C areas behind, and silicides were observed in the IPyC layer. These high-C areas in the SiC layer allowed for easier transport of additional Pd and Pd silicides, which allowed the reaction to progress. Without these conditions and in the SiC layer away from the IPyC crack, Pd migrated in the SiC layer via diffusion without an observable chemical reaction with SiC; silicide formation was repressed.
- Ag and/or Cd were frequently identified in Pd silicides and Pd precipitates located in the high-C areas in the SiC layer, sometimes with very significant concentrations. This suggests that Ag/Cd partition to Pd silicides and Pd in the high-C areas and that Pd silicides and Pd may assist Ag/Cd transport through the high-C areas and across the SiC layer. Additionally, Ag and Pd migrate in the short range through nanocracks in the high-C areas (Pd and Ag were found in nanocracks).
- Xe was identified separately in nanocracks in the high-C areas in the SiC layer, indicating that nanocracks provide short-range pathways for Xe transport.

- The C areas in the SiC layer may have provided pathways (called carbon “channel”) for Cs transport. Nanocracks in the C areas would make rapid short-range pathways for Cs migration; however, no Cs was identified in the areas investigated.
- Some Pd silicides in the C areas contain small concentrations of Ce, suggesting that Pd silicides may assist Ce transport.
- Some Pd silicides in the pure C areas in the SiC layer also contain small concentrations of U; U and Ce usually coexist in Pd silicides and Ag/Cd usually do not coexist with U or Ce in Pd silicides.

### **3.3.2.2 Conclusions from Uncorroded SiC Investigation.**

- Ag and/or Cd-containing precipitates are present in the uncorroded SiC areas that are close to the corroded SiC areas. Ag/Cd also migrates through the uncorroded SiC areas. Ag/Cd may exist alone or coexist with Pd.
- Most of the Ag/Cd-containing precipitates contained Pd, meaning Ag/Cd usually co-exists with Pd and Pd may assist Ag/Cd transport.
- Most Ag/Cd-containing precipitates are located at SiC grain boundaries, indicating that Ag/Cd predominantly transports along grain boundaries.
- An Ag-Pd-Cd precipitate was identified at a stacking fault inside a SiC grain, indicating that intragranular transport of Ag/Cd is also a possible transport mechanism, although intragranular migration rarely occurs.
- Precipitates in the SiC layer are mostly Pd, Pd-Si, Pd-U, and Pd-Si-U. Pd precipitates are present at both SiC grain boundaries and inside SiC grain interiors, and Pd precipitates at SiC grain boundaries are usually significantly larger than those inside SiC grains. Pd-Si, Pd-U, and Pd-Si-U precipitates are all located at SiC grain boundaries. Pd-Si in the unreacted SiC areas are from the Pd-Si created in the carbon “channel” or at the IPyC-SiC interface.
- For a majority of the Pd-Si-U and Pd-U precipitates, the U concentrations are much lower than the Pd concentrations. Pd-Si-U precipitates in the uncorroded SiC areas are from Pd-Si-U created at the IPyC-SiC interface where Pd and U with locally elevated concentrations react with SiC to form Pd-Si-U. Unreacted U at the IPyC-SiC interface migrates into the SiC layer together with Pd, meaning Pd assists the transport of U. All Pd-Si-U and Pd-U precipitates in the SiC layer are observed at grain boundaries.
- Some of the Pd-rich precipitates (especially large ones) contain small concentrations of Ce. Ce frequently coexists with U in Pd-rich precipitates close to the corroded area. No precipitates containing only Ce were observed. Ce migrates in the unreacted SiC areas only with the assistance of Pd.
- Ag/Cd do not coexist with U or Ce.
- Fission product precipitates in the SiC layer can be crystalline, semi-crystalline, amorphous, or partly amorphous and partly semi-crystalline, owing to the non-equilibrium state and to the high density of defects generated during neutron irradiation.

### 3.3.3 Electron Probe Micro-Analysis

Particle AGR1-523-SP01, mounted by ORNL in a custom-designed metallography mount, was used for EPMA method development for the first EPMA measurements of irradiated TRISO particles at INL during FY 2014. This particle was analyzed to gather micrometer-scale quantitative chemical analyses of a number of features, including the compositional changes that occur across a radial traverse and the composition of precipitates formed between the SiC and IPyC layer. In addition, X-ray maps of those same features were collected. An image of the particle highlighting the path of the radial traverse chemical composition measurements is shown in Figure 88. Quantitative measurements were taken every 3  $\mu\text{m}$  along this radial line. Figure 89 through Figure 91 show the concentrations of different elements measured along the radial traverse. Error bars represent 99% confidence intervals. Where error bars are not apparent, the symbol exceeds the size of the error bars. The locations for the kernel, recoil zone (RZ) (Kleykamp 1975), buffer, IPyC, and SiC are approximate.

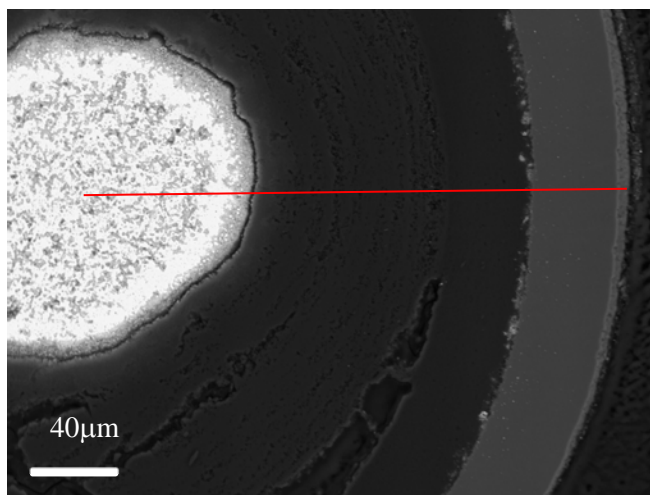


Figure 88. Backscattered electron image of the TRISO particle showing the path of the radial traverse measurement.

These plots show that rare earth elements (Ce, Eu, La, Nd, Pr, and Sm) remain largely in the kernel. Other elements (such as Xe, Cs, and I) appear to penetrate into the buffer. Still others (such as Pd, Cs, and Ba) not only penetrate the buffer, but accumulate between the SiC and IPyC layer. This is particularly evident in Figure 92 and Figure 93, which show via X-ray maps the spatial location of select fission products. Of note is Kleykamp's (1975) "recoil zone." The recoil zone refers to the approximately 15- $\mu\text{m}$  thick region between the kernel and the buffer. In this zone, the uranium concentration drops precipitously at the same time the carbon concentration rapidly increases (e.g., Figure 92 [b] and [f]). Concentrations of Ru, Mo, Zr, Cs, Ba, Xe, Sr, and Te are sufficiently elevated that the elevation is detectable via X-ray maps (Figure 92 and Figure 93).



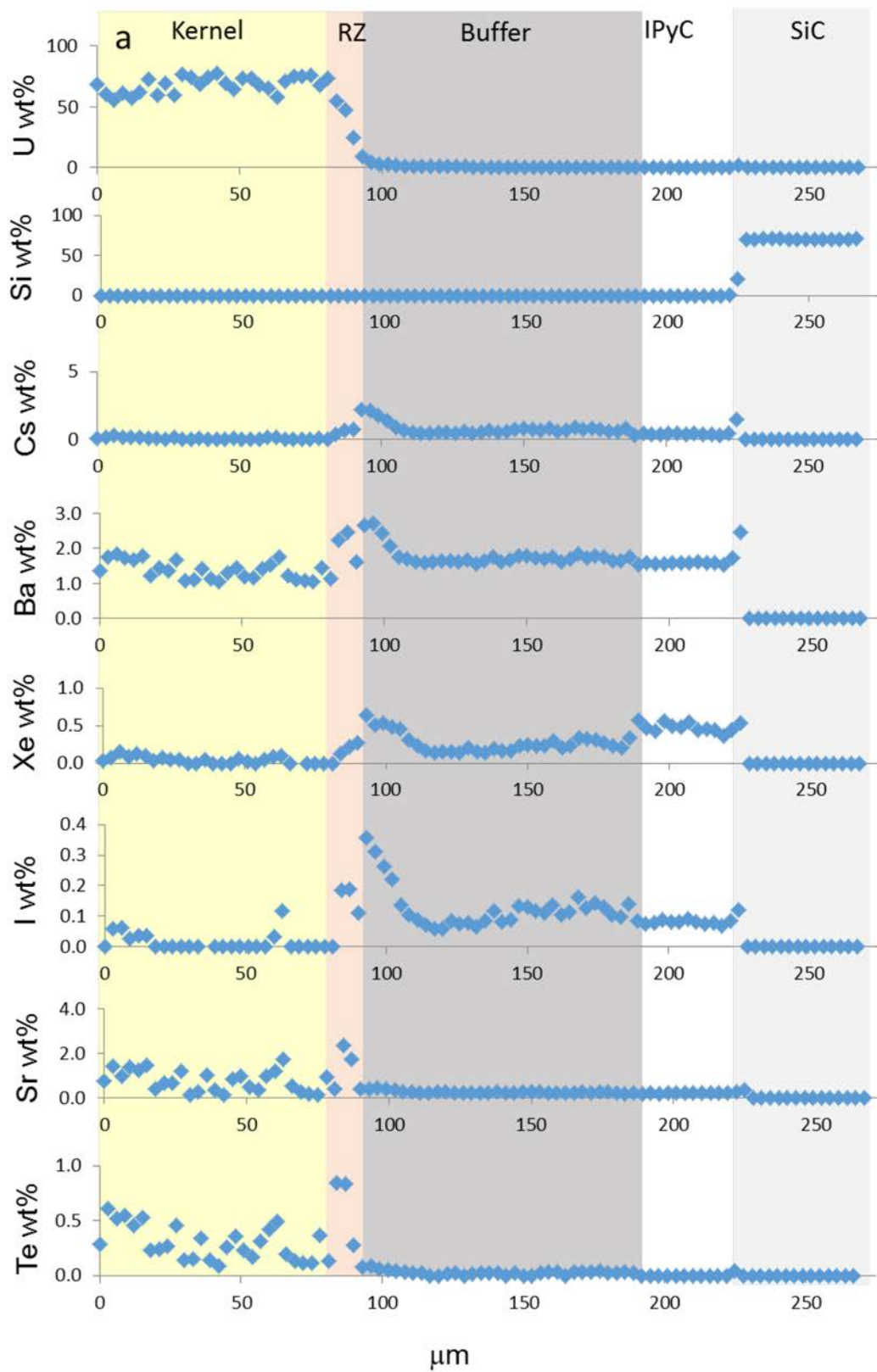


Figure 89. Elemental concentrations along the radial traverse for U, Si, Cs, Ba, Xe, I, Sr, and Te.

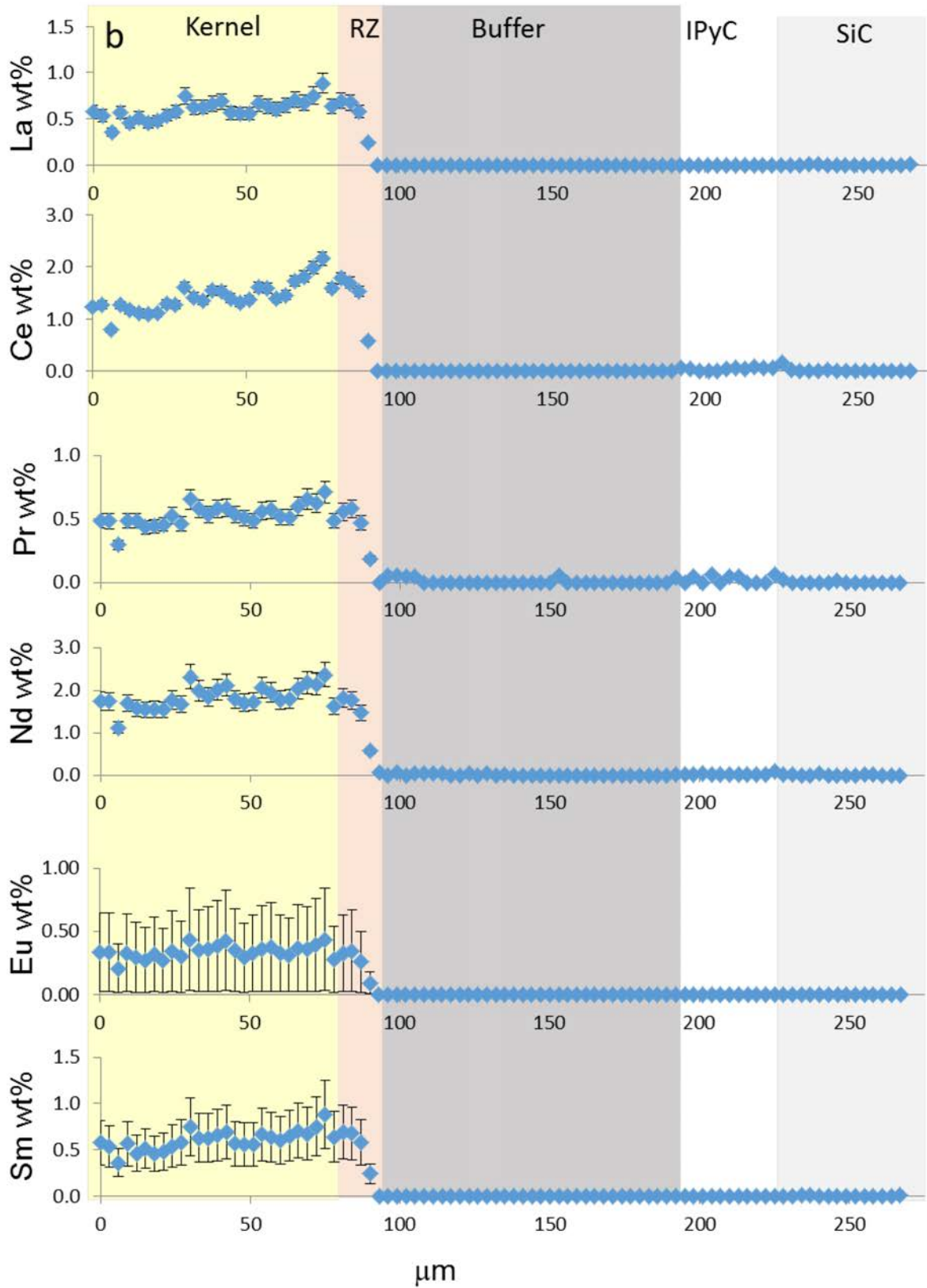


Figure 90. Elemental concentrations along the radial traverse for La, Ce, Pr, Nd, Eu, and Sm.

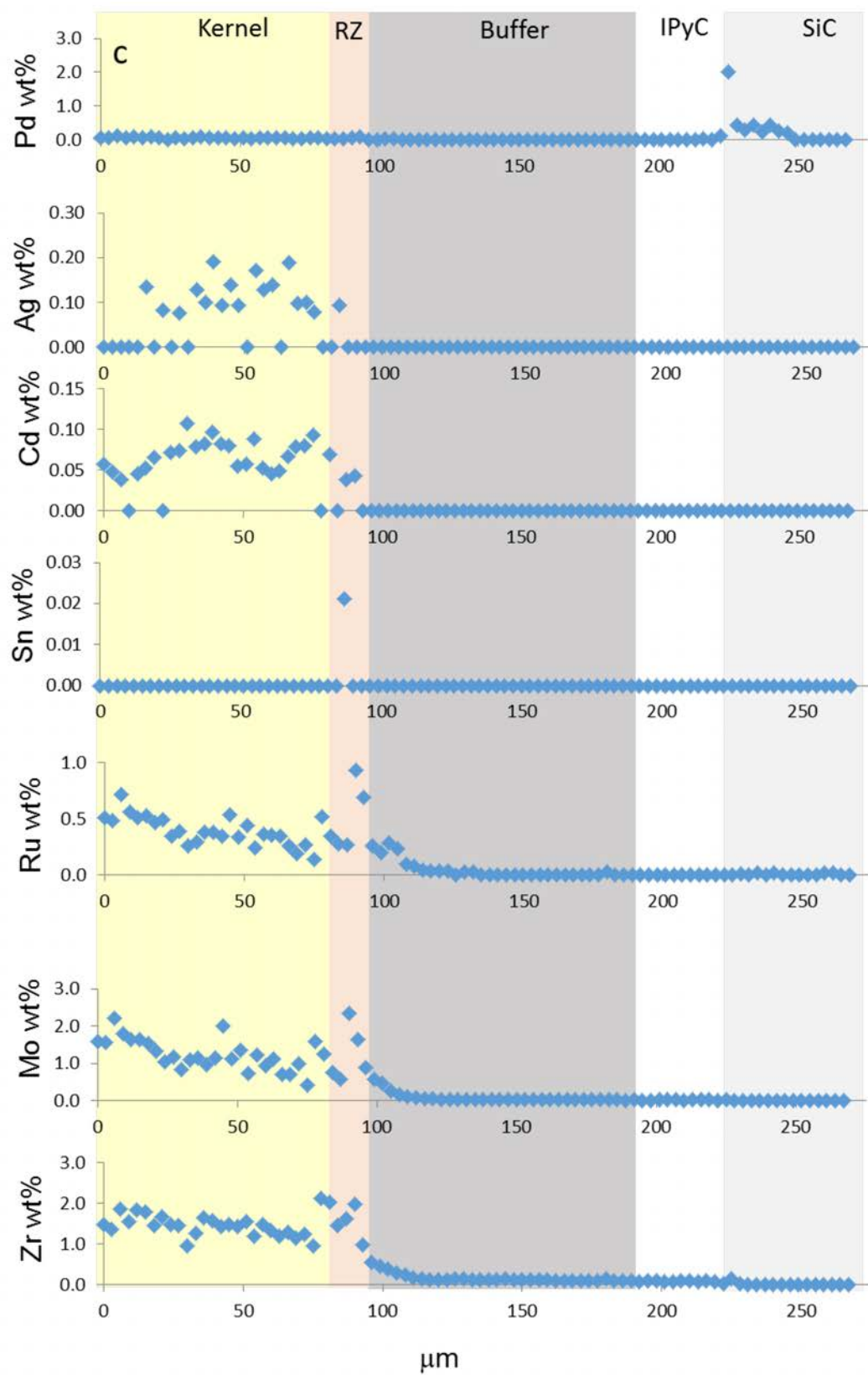


Figure 91. Elemental concentrations along the radial traverse for Pd, Ag, Cd, Sn, Ru, Mo, and Zr.

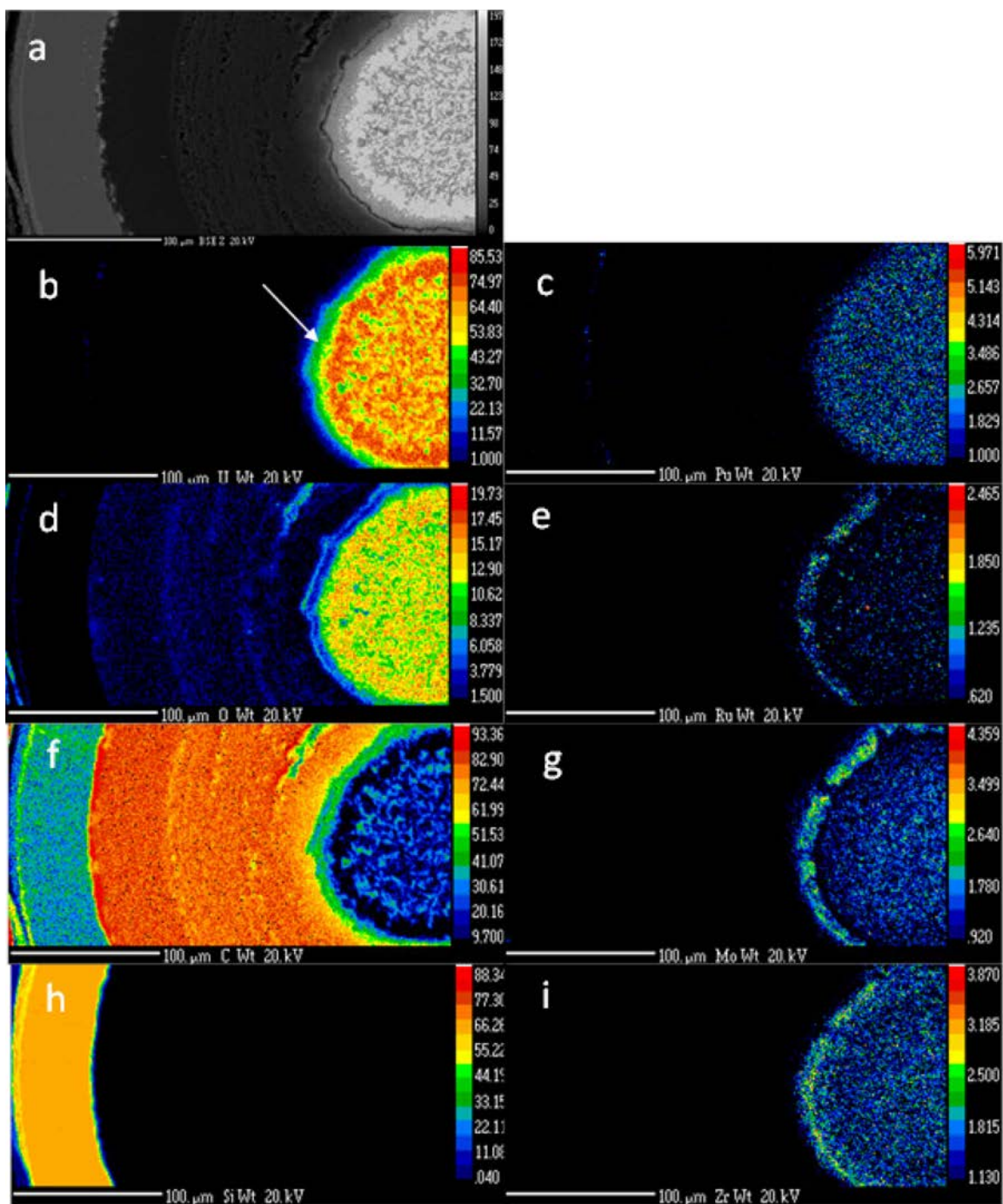


Figure 92. Backscattered electron image of irradiated TRISO particle (a) and quantitative X-ray maps of U, Pu, O, Ru, C, Mo, Si, and Zr (b–i). Recoil zone is shown with the white arrow in (b).



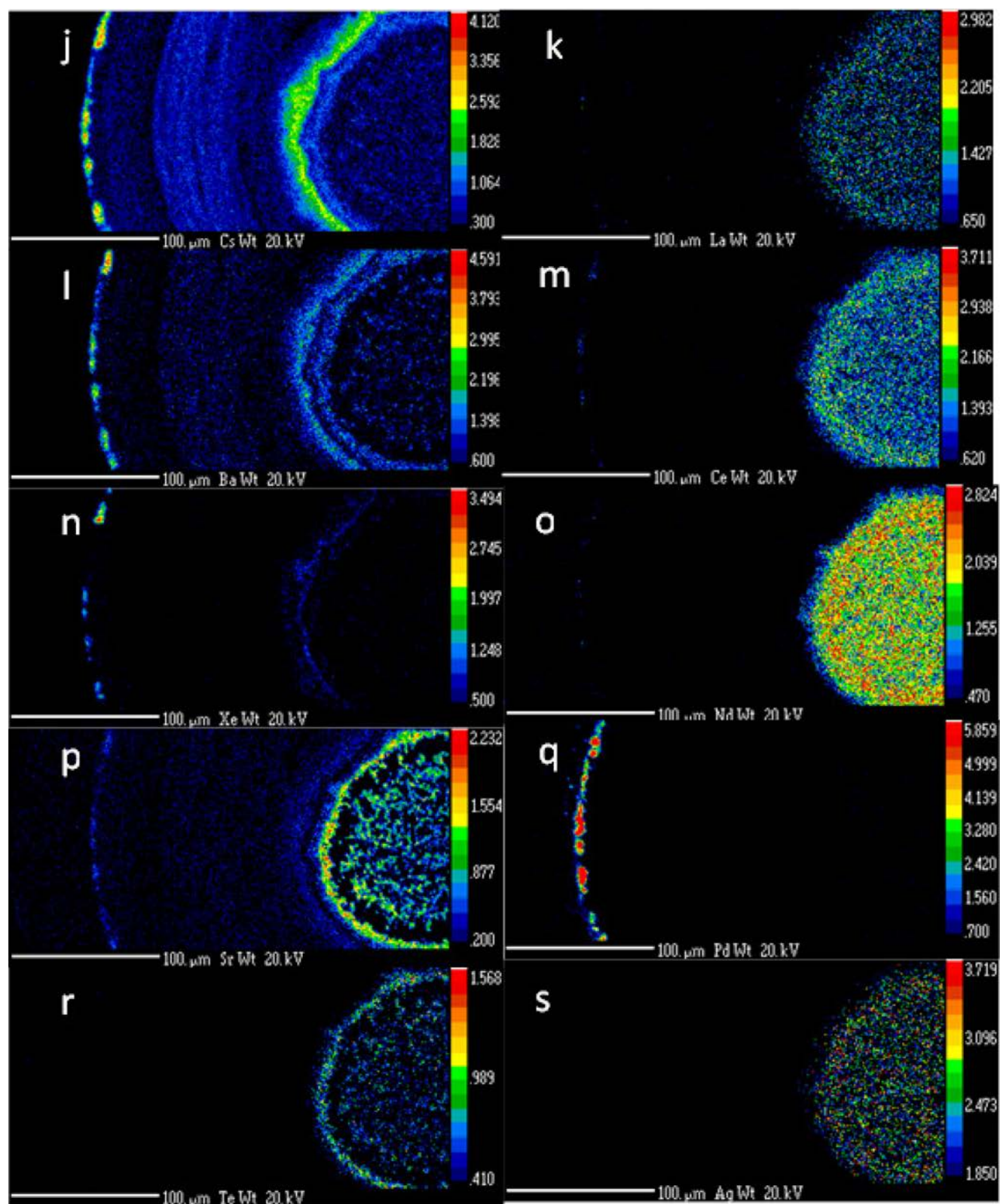


Figure 93. Quantitative X-ray maps of Cs, La, Ba, Ce, Xe, Nd, Sr, Pd, Te, and Ag (j-s).

**3.3.3.1 Kernel Analysis.** X-ray mapping analysis detected the fission products Sr, Ba, Te, La, Ce, Nd, Ru, Mo, and Zr in the kernel. Of particular interest are the elements Ru, Mo, and Zr (Figure 94).

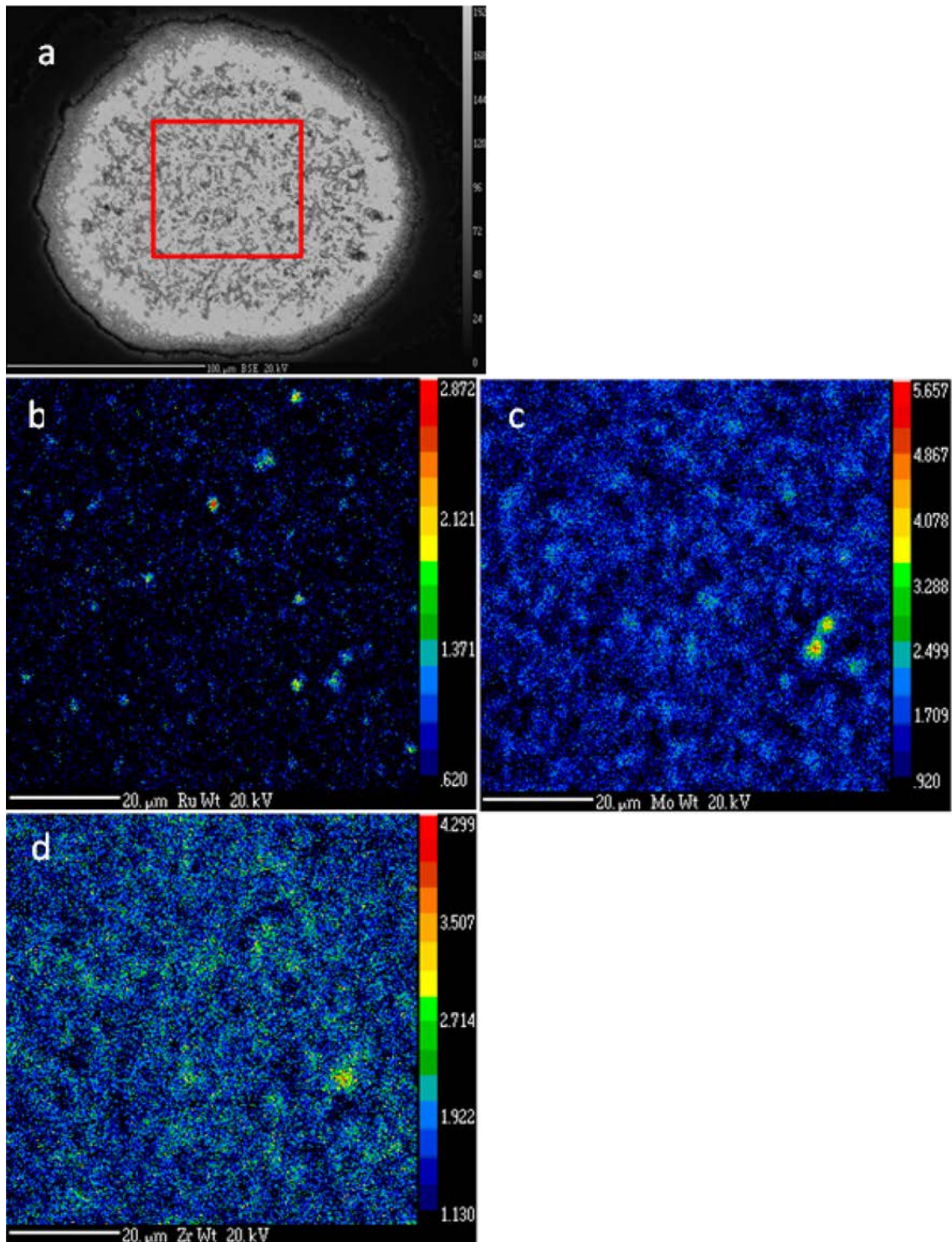


Figure 94. Shows a backscattered electron image of the kernel (a) and X-ray maps of Ru, Mo, and Zr (b-d) in the area outlined by the red square.



Previously, researchers (Minato et al., 1994, Barrachin et al., 2011) reported the presence of metal inclusions in the kernel. Minato et al., 1994 described several types of inclusions in the irradiated UO<sub>2</sub> kernel, including (1) Mo-Tc-Ru-Rh-Pd, (2) Pd-Te, (3) containing Sn, and (4) predominantly Mo. Barrachin et al., (2011) describe Ru-Mo inclusions with little Pd.

With respect to AGR1-523-SP01, kernel mapping shows small (i.e., less than 5  $\mu\text{m}$ ) Ru-rich precipitates, some of which appear to contain Mo and possibly Zr. More analyses using longer count times are necessary to clarify the nature of these inclusions in AGR-1 fuel. Understanding these inclusions is desirable because the stoichiometry of such inclusions can yield data concerning oxygen potential in the kernel and, thus, mobility of the fission products.

**3.3.3.2 Precipitate Analysis.** It is important when constructing X-ray maps that peak overlap correction is employed, just as it is for traditional point analysis. Figure 95 shows a backscattered electron image of precipitates in the crack of the IPyC layer and X-ray maps of fission products whose analytical measurement peaks overlap with one another. It can be seen, particularly with Pd, Cd and Ag, that the images are not identical, demonstrating that peak deconvolution is effective and precipitates are chemically heterogeneous.

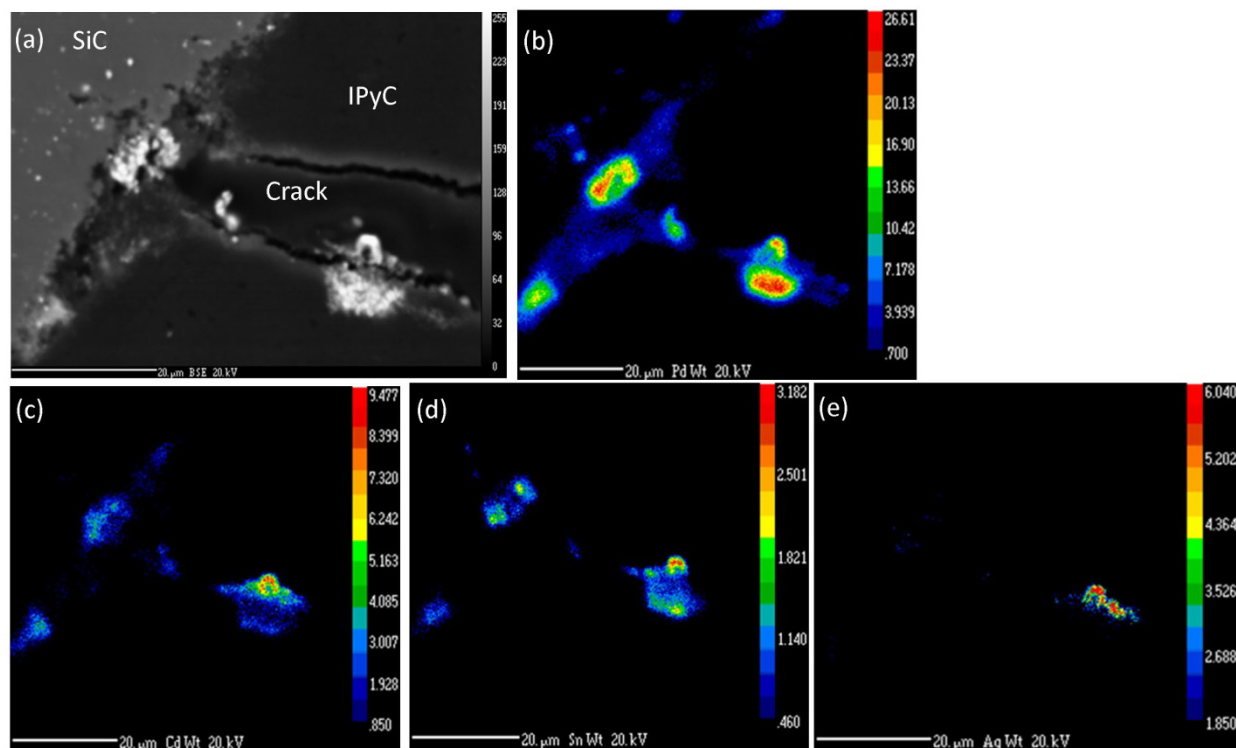


Figure 95. Backscattered electron image of precipitates in the IPyC crack (a) and X-ray maps of (b) Pd, (c) Cd, (d) Sn, and (e) Ag. X-ray maps were corrected for peak overlaps.

Locations for quantitative point analysis of precipitates are shown in Figure 96, with analyses shown in Table 52. Note the considerable discrepancies between the concentrations for analytes shown in Table 52, compared to the apparent concentration of the same feature as indicated by the X-ray map (Figure 95). In particular, the Ag X-ray map appears to show a maximum concentration of approximately 6 wt%, while the spot analysis shows 0.2 wt%. The source of this discrepancy is not clear, but may relate to the fact that the mapping program measures one background point and assumes the background intensity on either side of the peak is the same, whereas the spot analysis measures a background on each side of the peak and uses the average. If the intensity of the two background peaks is quite different (as can occur with complex, overlapping peaks), the net intensity of the peak can be incorrectly determined.

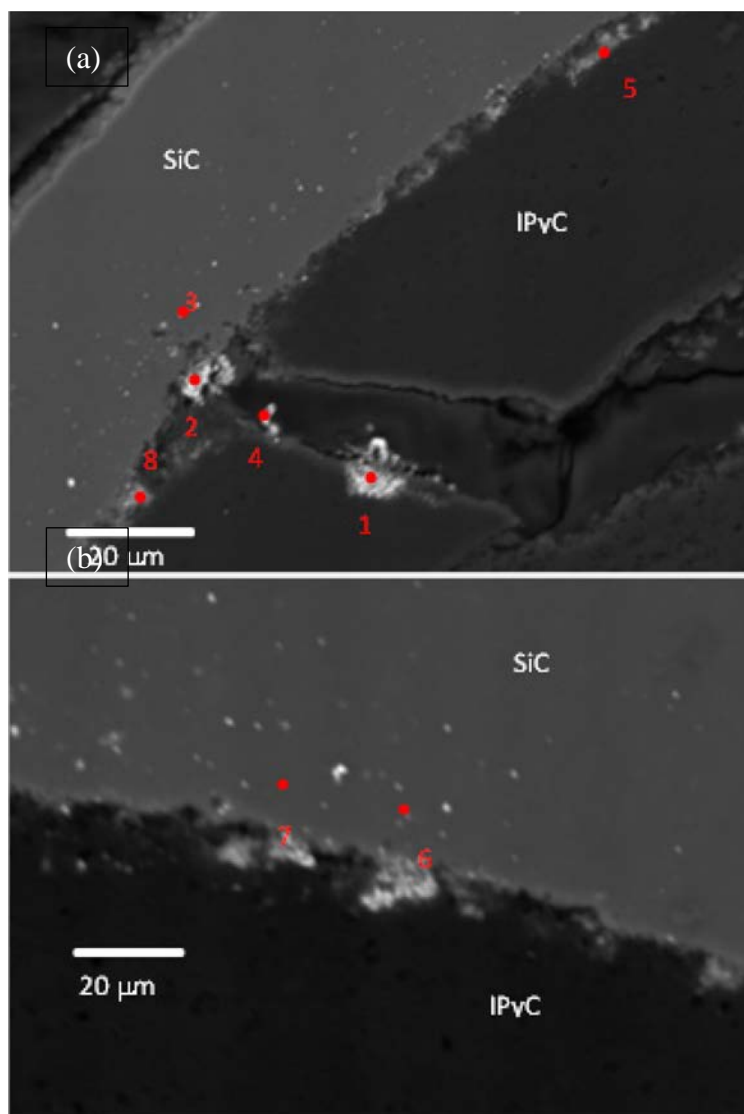


Figure 96. Locations of analyzed precipitates in the crack in the IPyC (a) and between the IPyC and SiC layer (b). Analyses are shown in Table 52.

Nonetheless, Figure 95, Figure 96, and Table 52 serve to illustrate the following features of these precipitates:

1. Precipitates are chemically heterogeneous, but are dominated by Pd, Si, and C. It is not clear whether these precipitates are silicides or whether the measured Si comes from the surrounding material.
2. Tin is present in several of the precipitates.
3. In these precipitates, Cd is either a minor element or is not detected.
4. The analytical totals for the point analyses (particularly analyses within the IPyC and SiC) are not as close to 100% as would be desirable for microprobe analysis. The reasons for this are not clear; however, porosity in the buffer layer and at layer interfaces will contribute to such issues. In addition, inadequate matrix matching between standards and unknowns, especially with light elements, can contribute to error.



Table 52. Analyses of spots (in weight percent) whose location is shown in Figure 96.

Element	Detection Limit (wt%)	Chemical Analysis (wt%) at each Spot No.							
		1	2	3	4	5	6	7	8
U	0.04	5.95	6.51	0.35	4.30	3.87	5.17	4.20	2.55
C	0.132	34.1	37.3	27.0	46.9	58.2	48.7	64.7	46.0
O	0.044	5.18	5.04	1.79	11.3	2.14	1.93	1.51	4.01
Si	0.004	5.27	11.1	51.4	1.57	4.52	5.46	19.1	3.25
Pu	0.054	3.89	4.59	0.30	1.26	0.83	2.19	1.22	1.43
Sr	0.012	0.25	0.35	0.02	0.07	0.48	0.35	0.25	0.37
Cs	0.025	0.69	0.38	<0.025	0.41	2.59	1.23	1.36	1.22
Xe	0.015	0.13	0.09	0.04	0.05	2.33	1.14	0.34	0.44
I	0.015	0.31	0.28	<0.015	0.08	0.28	0.16	0.11	0.32
Te	0.015	0.23	0.25	0.03	0.10	0.12	0.14	0.08	0.17
Ba	0.021	1.38	0.84	<0.021	0.38	3.43	2.49	1.62	2.12
Pd	0.024	26.1	29.2	4.47	11.1	6.6	12.9	8.5	18.2
Cd	0.025	1.57	3.68	<0.025	1.84	<0.025	<0.025	<0.025	4.59
Ag	0.051	0.20	0.26	<0.051	0.10	<0.051	0.06	<0.051	0.59
Sn	0.014	1.70	1.79	0.20	0.39	0.12	0.13	0.07	1.32
Ru	0.016	0.05	0.02	<0.016	<0.016	<0.016	<0.016	<0.016	<0.016
Mo	0.015	<0.015	<0.015	<0.015	<0.015	<0.015	0.02	0.02	0.04
Zr	0.017	0.11	0.14	0.04	0.03	0.11	0.27	0.14	0.67
La	0.031	0.62	0.80	0.07	0.19	0.12	0.37	0.19	0.29
Ce	0.031	2.13	2.91	0.19	0.80	0.56	1.50	0.94	0.90
Pr	0.027	0.40	0.63	0.03	0.15	0.24	0.37	0.20	0.20
Nd	0.025	1.08	1.47	0.12	0.47	0.25	0.74	0.45	0.45
Sm	0.024	0.19	0.26	0.03	0.09	0.08	0.14	0.11	0.07
Eu	0.034	0.08	0.04	<0.034	0.04	0.05	0.05	0.05	0.05
Total		91.7	107.9	86.2	81.5	87.0	85.5	105.1	89.3

### 3.3.3.3 Electron Probe Micro-Analysis Conclusions.

1. While the behavior of Ag transport out of the kernel has been difficult to explain, other fission products (such as Cs, Ba, Pu, I, Xe, and Pd) are also transported out of the kernel.
2. Ru forms precipitates within the kernel, the precise nature of which requires additional study.
3. The chemical compositions of precipitates along the SiC-IPyC interface and crack are chemically heterogeneous.
4. Cs, Ba, I, and Xe are spread throughout the buffer but appear to concentrate in and near the recoil zone. In addition, they appear to accumulate along the SiC-IPyC interface.

**3.3.3.4 Lessons Learned with the Irradiated Particle and Path Forward.** The main purpose for analyzing this irradiated particle was to determine the steps necessary to generate valid fuel morphological and fission product distribution analyses for an irradiated fuel particle.

Lessons learned include the following:

1. Sample handling techniques developed for irradiated samples appear to be effective in the absence of permanent shielding or remote handling equipment.
2. U-C and U-O analysis within the kernel remains problematic due to the lack of UC and UO<sub>2</sub> standards to use as check standards or to use as primary standards. Efforts should be made to acquire these standards.
3. Peak overlap correction is vital for accurate analysis of the overlapping peaks that occur in irradiated fuels. Though the peak overlaps are not as pronounced as they would be using an EDS, they still exist and must be corrected.
4. Because of the high density of U, 20 kV is the minimum usable accelerating voltage for kernel analysis. However, in the porous carbon matrices and the lower density SiC, it creates an overly large electron interaction volume that substantially reduces the spatial resolution of the analysis. Future analyses should take into account the very different densities of the matrices coupled with the required over-voltage of the analytes to determine an optimum accelerating voltage for each matrix. This will require instrument calibration at each desired accelerating voltage and increase the overall analysis time.
5. To minimize error from counting statistics, it would be beneficial to increase peak counting integrations so peak counts total at least 10,000 counts. For many trace elements, this will require a peak integration count time of about 600 seconds, with an equal amount for background counting. This could result in about 60 minutes to count one spot. In low-density or beam-sensitive materials, such as the buffer and IPyC, this lengthy count time will likely destroy the sample in proximity to the beam. Therefore, trace elements measurements in those matrices will be problematic.

### **3.3.4 Conclusions and Main Findings**

The main conclusions reached from these studies are as follows:

- An Ag-Pd-Cd precipitate was identified at a stacking fault inside a SiC grain, indicating that intragranular transport of Ag/Cd is also a possible transport mechanism, although intragranular migration rarely occurs.
- There were pure C areas in the SiC layer close to the crack, with Pd<sub>2</sub>Si or PdSi inside these areas, indicating corrosion of SiC by Pd. These corroded areas were not observed in locations in the SiC layer away from the crack.
- A locally elevated Pd concentration was among the necessary conditions for significant chemical reaction between Pd and SiC. In areas in the SiC layer close to the IPyC crack tip, local accumulation of Pd was present, which initiated the reaction between Pd and SiC. In addition, silicides formed by the reaction migrated away from the reaction site, leaving C areas behind; silicides were observed in the IPyC layer. These C areas allowed for easier transport of additional Pd and Pd silicides, which allowed the reaction to progress. Without these conditions, Pd migrated in the SiC layer via diffusion without observable chemical reaction with SiC and silicide formation was repressed.
- Significant concentrations of Ag and/or Cd were frequently identified in Pd silicides and Pd precipitates located in the high-C areas in the SiC layer near the crack. This suggests that Ag/Cd partition to Pd silicides and Pd in the high-C areas and that Pd silicides and Pd may assist Ag/Cd transport through the high-C areas and across the SiC layer. Additionally, Ag and Pd migrate in the short range through nanocracks in the high-C areas.

- U and Ce usually coexist in Pd silicides and Ag/Cd usually do not coexist with U or Ce in Pd silicides.
- Ag/Cd usually coexist with Pd and Pd assists Ag/Cd transport.
- Some Pd silicides in the pure C areas in the SiC layer also contain small concentrations of U. U and Ce usually coexist in Pd silicides and Ag/Cd usually do not coexist with U or Ce in Pd silicides.
- Fission product precipitates in the SiC layer can be crystalline, semi-crystalline, amorphous, or partly amorphous and partly semi-crystalline, owing to the non-equilibrium state and to the high density of defects generated during neutron irradiation.
- No precipitates containing Cs were detected in the areas examined with EDS. EPMA measurements showed that Cs was found throughout the buffer, but they appear to concentrate in and near the recoil zone. In addition, they appear to accumulate along the SiC-IPyC interface.
- Pd precipitates are present at both SiC grain boundaries and inside SiC grain interiors; Pd precipitates at SiC grain boundaries are usually significantly larger than those inside SiC grains.
- The EPMA method has been established for subsequent analysis on irradiated samples and lessons learned have been noted.

### **3.4 Irradiated Variant 3 Fuel Examination: Compact 1-3-1**

This section contains a large body of unpublished results from particles AGR1-131-066 and AGR1-131-099, which include the grain boundary characteristics of particles, fission product identification and distribution, and phase identification of micro-sized precipitates. This section also describes limited HRTEM results on phase identification of micron-sized precipitates and the first HRTEM images of the fuel kernel (kernel microscopy results are not fully discussed in this report). The reported fission product precipitate compositions (atomic %) are qualitative or semi-quantitative in nature (Section 2.1.2.3).

#### **3.4.1 Particle Selection and Analysis Performed**

Two TRISO-coated particles from Compact 1-3-1 of the AGR-1 experiment were selected based on the measured-to-predicted Ag-110m activity ratio (shown in Figure 97), to investigate microstructural characteristics related to Ag retention (Demkowicz et al., 2016b). From these distributions, particles were chosen to represent a low (Particle AGR1-131-099: <6%.) and relatively high (AGR1-131-066: 39%) Ag-110m measured-to-predicted ratio. A high measured-to-predicted ratio indicates a high degree of fission product retention in the particle. Conversely, a low measured-to-predicted ratio indicates a low degree of retention (a high degree of release). Figure 97 indicates that particles exhibit a maximum Ag retention of about 50% of the predicted inventory, so while the 39% retention value for AGR1-131-066 is considered low in absolute terms, it is near the high end of the distribution of particles analyzed from Compact 1-3-1. Examinations using STEM, PED, and HRTEM were completed on both particles, with additional EFTEM analyses performed on Particle AGR1-131-099 to target elemental quantification (Table 53).

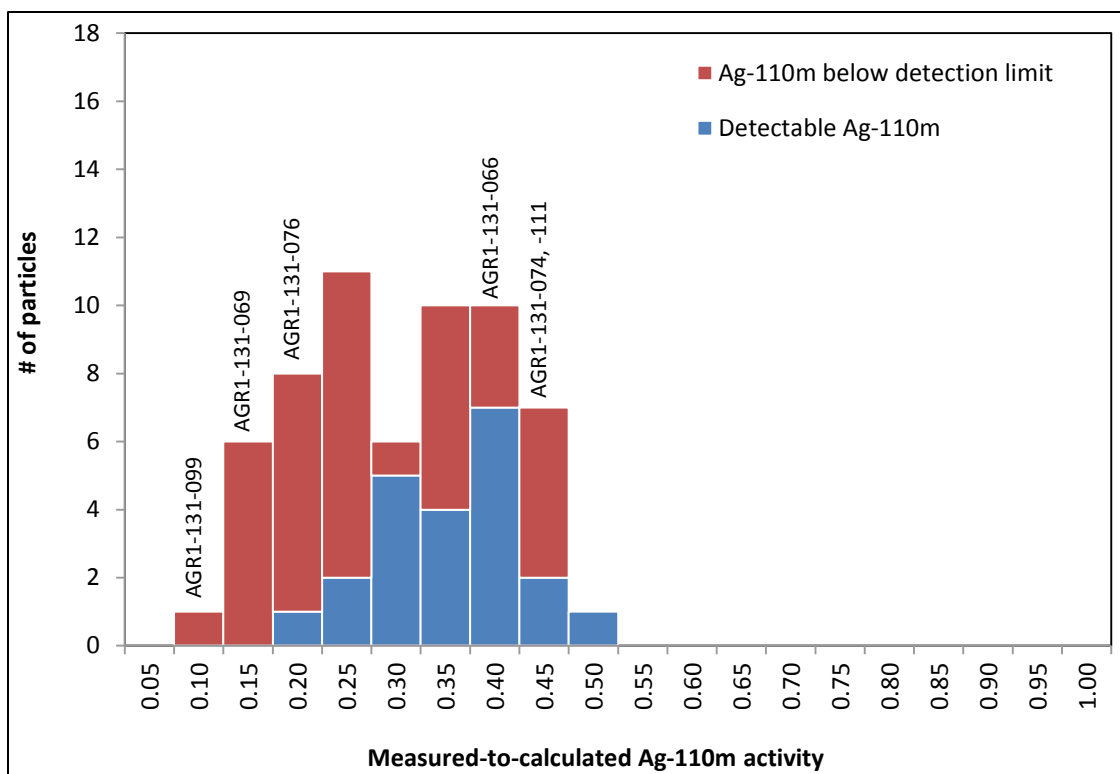


Figure 97. Distribution of the measured-to-calculated Ag-110m activity ratio for the irradiated Compact 1-3-1 particles (Demkowicz et al., 2016b).

Table 53. Advanced microscopy and micro-analysis examination performed on Compact 1-3-1 particles.

Technique	SEM <sup>a</sup> EDS/WDS	EELS/ EFTEM	STEM	EPMA	PED	APT	HRTEM
Compact 1-3-1 (Variant 3)							
AGR1-131-099 (Low (<6%) Ag retention)	X	X	X	—	X	—	X
AGR1-131-066 (High (39%) Ag retention)	X	—	X	—	X	—	X (kernel only)

<sup>a</sup>. Reported in separate report by van Rooyen et al., 2017.

**3.4.1.1 Lamella Locations for Particles AGR1-131-066 and AGR1-131-099.** Figure 98 and Figure 99 show low-magnification cross sections and the locations on the particles where TEM sample lamellae were prepared by standard FIB methods for particles AGR1-131-066 and AGR1-131-099, respectively. Lamellae 5, 6, and 7 on AGR1-131-066 (Figure 98[b]) correspond to inner, center, and outer regions of the SiC layer. Only Lamellae 2, 4, and 3 on Particle AGR1-131-099 correspond to the inner, center, and outer area of the SiC layer, respectively (Figure 99[b]).

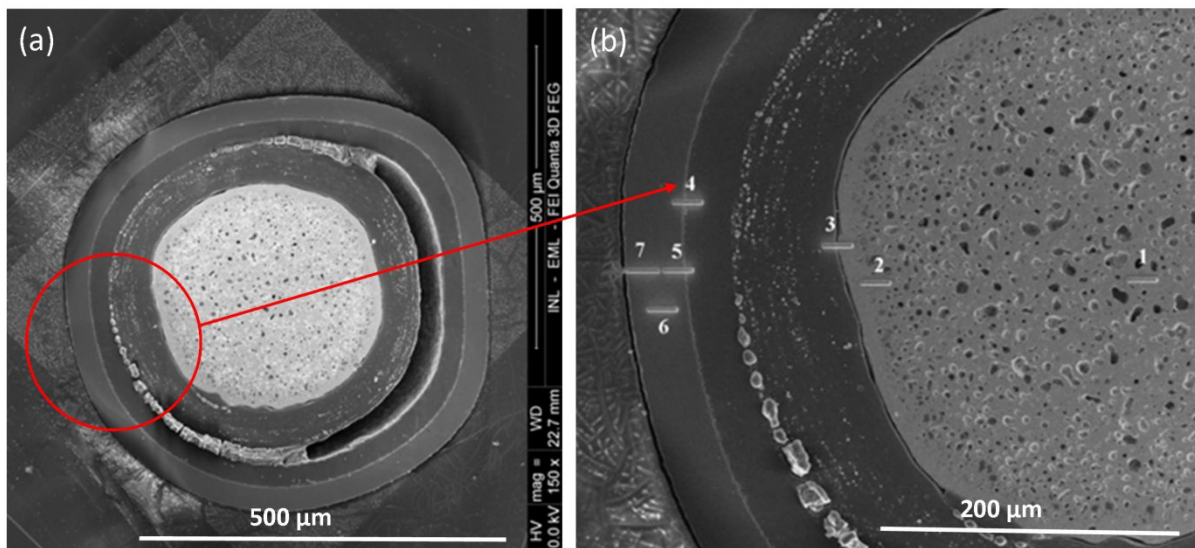


Figure 98. Figure showing (a) cross section from Particle AGR1-131-066 with (b) the corresponding SiC layer FIB lamellae (4 to 7) and fuel kernel FIB lamellae (1 to 3) for AGR1-131-066.

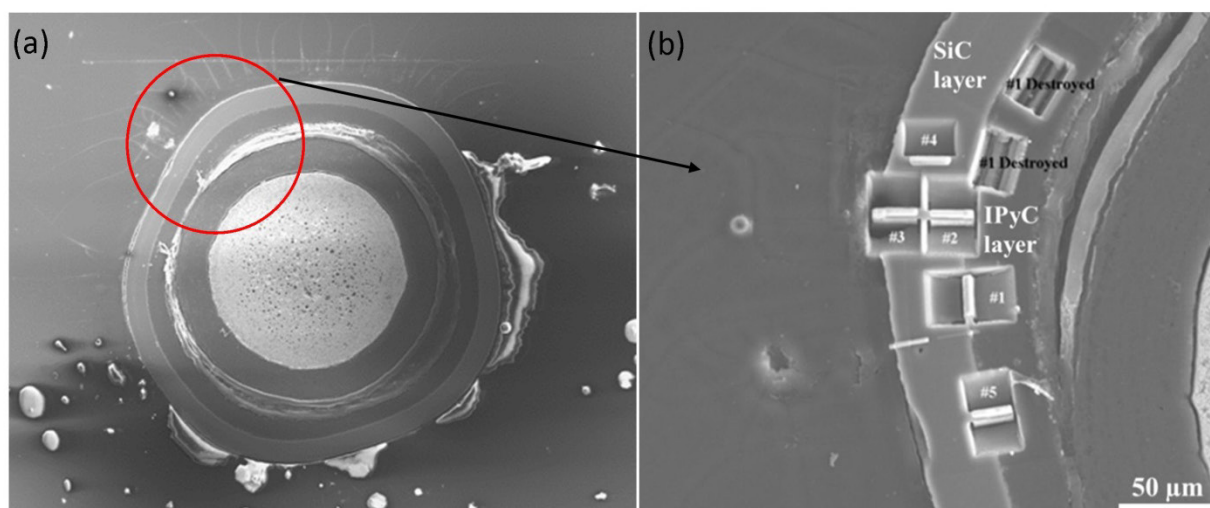


Figure 99. Figure showing (a) cross section from Particle AGR1-131-099 with (b) the corresponding SiC layer FIB- lamellae (1 to 5).

### 3.4.2 Chemical Composition and Distribution of Fission Products in Precipitates from Particle AGR1-131-066

This section reports the qualitative chemical composition of minor elements on Particle AGR1-131-066 to determine the type of fission products present, the location of these fission product precipitates in relation to the SiC layer thickness, and the fission product elemental composition. Areas where microstructural analyses were carried out on the SiC layer of AGR1-131-066 of lamellae 4 to 7 are shown in Figure 100.

For precipitates in the SiC layer, the exact Si concentrations in the precipitates cannot be determined because of the significant contribution of the SiC matrix to the measured EDS spectra of the precipitates. A rough estimate of the Si concentration in the precipitates in the SiC layer can be obtained by subtracting

the C concentration from the Si concentration in the EDS result, assuming that Si and C concentrations contributed by the SiC matrix to the EDS result are exactly identical. If the Si concentration is equal to or smaller than the C concentration in the EDS result, it is interpreted that no Si exists in the precipitate. However, all the compositions presented in this report are raw data from EDS results, without the subtraction described above. It is emphasized that this study is only intended to establish if Si is present in the precipitates, rather than determine the exact Si content in them. For precipitates in the IPyC layer or in the C areas of the SiC layer, Si concentrations from raw EDS results are considered to be accurate because there is no interference from SiC. Thus, when interpreting the results, there is no need to subtract the C concentration from the Si concentration; C concentrations can be simply ignored because they are from the C in the IPyC layer.

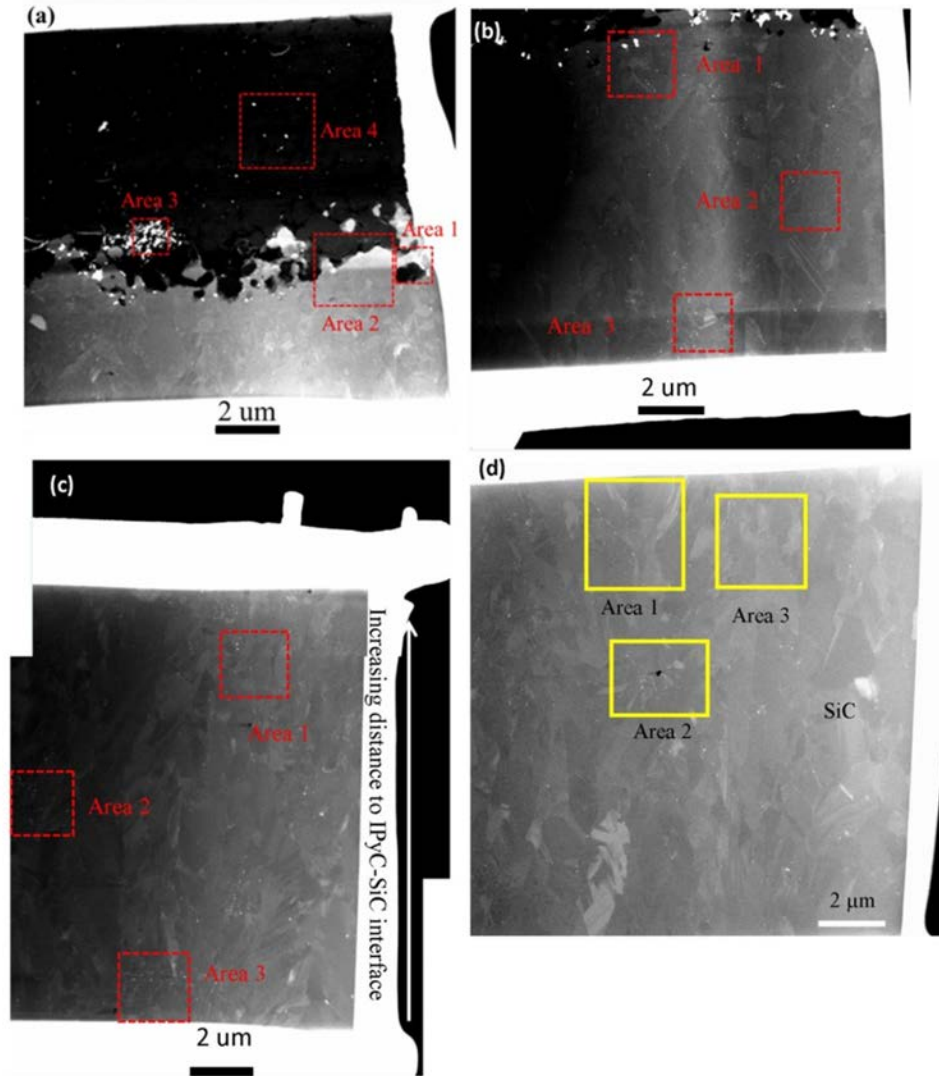


Figure 100. Images of (a) Lamella 4 (b) Lamella 5, (c) Lamella 6, and (d) Lamella 7, where microstructural analyses were carried out on the SiC layer of AGR1-131-066.

### 3.4.2.1 Chemical Composition in the Inner Area of the Silicon Carbide Layer (Lamellae 4 and 5).

**3.4.2.1.1 Lamella 4 Inner Region of the Silicon Carbide Layer.** Figure 101 shows the STEM and TEM images of Lamella 4 (Figure 98 and Figure 100), which was sectioned perpendicular to the IPyC-SiC interface. It is evident at the IPyC-SiC interface of only a relatively low number density of precipitates, and the precipitates are relatively small. This observation is in contrast with the phenomena observed in particles from other compacts where precipitates at the IPyC-SiC interface are typically large with a high number density (van Rooyen et al., 2014b, van Rooyen et al., 2014c). In addition, pores are present at the IPyC-SiC interface. The distribution of precipitates and the presence of pores at the IPyC-SiC interface are consistent with those in AGR1-131-099 (Wen et al., 2015a).

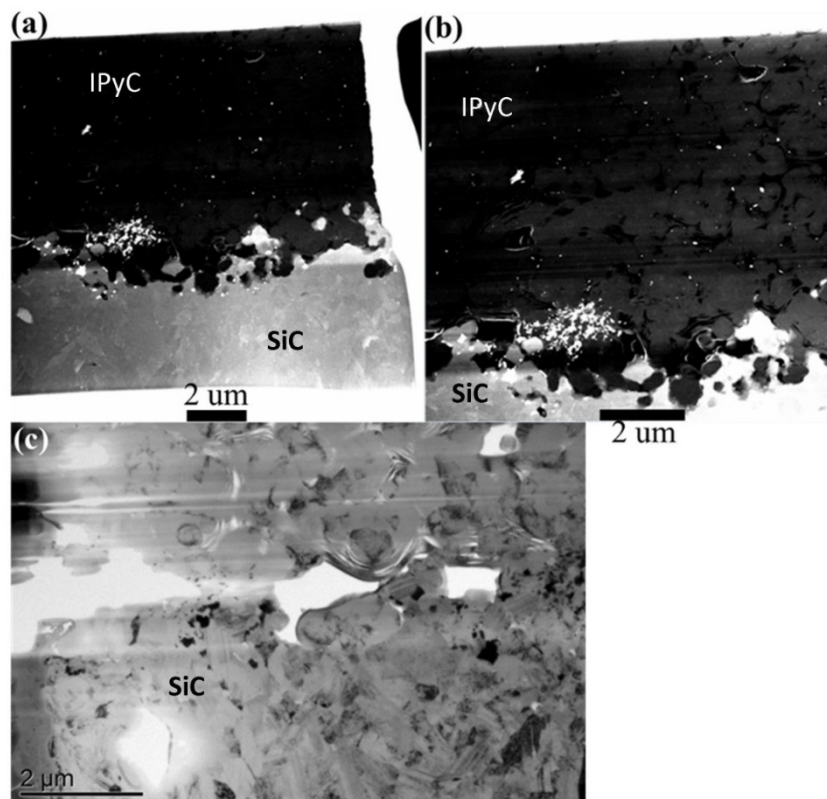


Figure 101. (a)(b) STEM images and (c) TEM image of TEM Lamella 4, showing a relatively low number density of precipitates at the IPyC-SiC interface. Precipitates are relatively small. Porosity is present at the IPyC-SiC interface.

Figure 102 shows STEM images of the areas close to the IPyC-SiC interface. In the figure, precipitates indicated by arrows or circles were subjected to EDS composition analyses; these precipitates are representative of precipitates in the SiC layer very close to the IPyC-SiC interface. The precipitate compositions from EDS are displayed in Table 54. It is evident that the majority of precipitates in the SiC layer very close to the IPyC-SiC interface are Pd-Si-U or Pd-U, with a small fraction of U-rich precipitates and Pd precipitates. Most precipitates contain U, but the U concentration is typically low. These results indicate that U from the fuel kernel has significantly migrated to the IPyC-SiC interface. This observation is different from that in particles from other compacts, where the fraction of precipitates containing U at the IPyC-SiC interface is not very high (van Rooyen et al., 2014c, Wen et al., 2015).



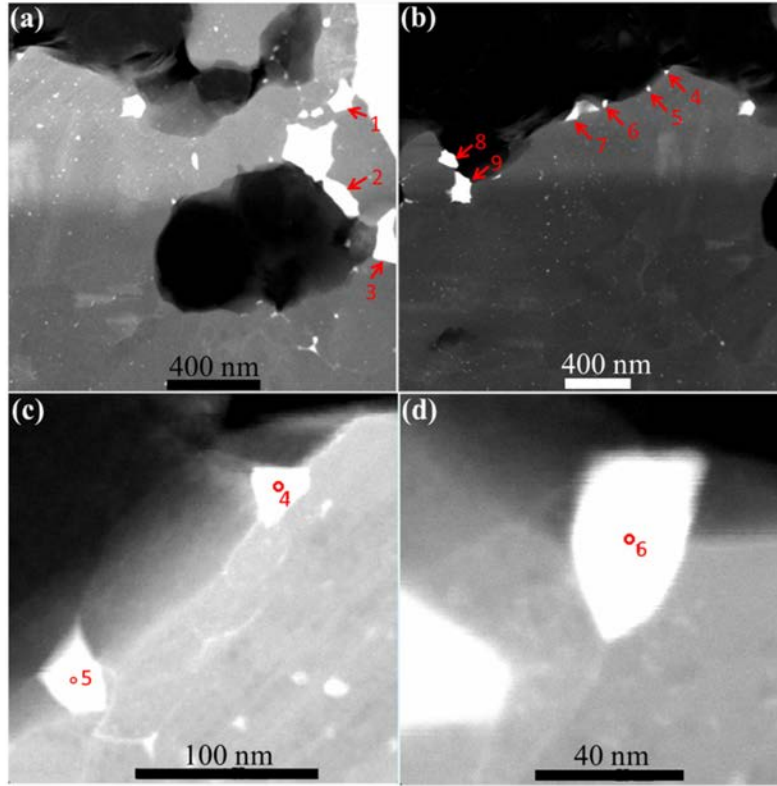


Figure 102. STEM images of precipitates in the SiC layer very close to the IPyC-SiC interface (Areas 1 and 2 on Lamella 4 [shown in Figure 98 and Figure 100]), where precipitates indicated by arrows or circles were subjected to EDS composition analyses. Chemical composition is reported in Table 54.

Table 54. EDS compositions correspond to precipitates indicated in Figure 102 from Areas 1 and 2 from Lamella 4. The majority of the precipitates are Pd-Si-U or Pd-U. Most precipitates contain U, but U concentration is typically low.

Precipitate Number	Concentration (at.%)												Precipitate Identification
	C	O	Si	U	Pd	Cs	Ce	Ag	Cd	I	Sr	Te	
Point Scan 1	43.65	0.03	52.17	0.95	3.07	0	0.10	0	0	0	0	0	Pd-Si-U
Point Scan 2	44.78	0.08	51.15	0.69	3.22	0	0	0	0	0	0.05	0	Pd-Si-U
Point Scan 3	39.51	0	44.19	1.43	14.38	0	0.14	0	0	0	0.33	0	Pd-Si-U-Sr
Point Scan 4	56.13	0.76	41.62	1.03	0.33	0.07	0	0	0	0	0.03	0	U-Pd
Point Scan 5	55.39	0	37.76	0	6.81	0.01	0	0	0	0	0	0	Pd
Point Scan 6	71.80	0	25.46	2.21	0.03	0.43	0	0	0	0	0.03	0	U-Cs
Point Scan 7	49.71	0	41.91	1.65	6.50	0	0.10	0	0	0	0.09	0	Pd-U
Point Scan 8	69.11	0.24	21.16	1.61	7.65	0	0.11	0	0	0	0.05	0.01	Pd-U
Point Scan 9	37.34	0.27	31.20	5.58	25.38	0	0.17	0	0	0	0	0.02	Pd-U



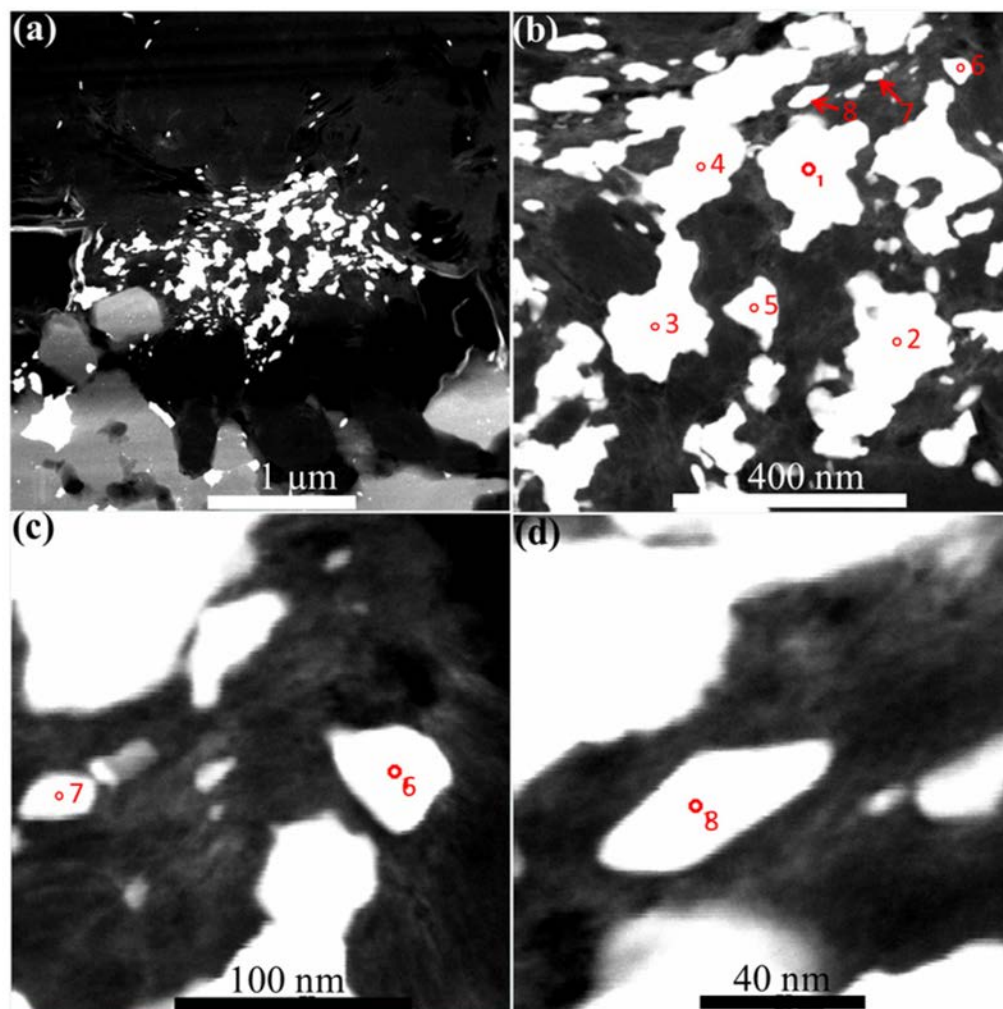


Figure 103. STEM images of (a) precipitates in the IPyC layer close to the IPyC-SiC interface (Area 3 on Lamella 4 [shown in Figure 98 and Figure 100]), (b) where precipitates indicated by arrows or circles, and (c–d) larger magnification images of precipitate numbers 6 through 8 were subjected to EDS composition analyses. Majority of precipitates are Pd-Si-U, with a small fraction of Pd-Si. Chemical composition is reported in Table 55.

Figure 103 shows STEM images of precipitates in the IPyC layer close to the IPyC-SiC interface (Area 3 on Lamella 4 as shown in Figure 98 and Figure 100), where precipitates indicated by arrows or circles were subjected to EDS composition analyses. These precipitates are representative of precipitates in the IPyC layer close to the IPyC-SiC interface. The precipitate compositions from EDS are displayed in Table 55. It is seen that majority of precipitates are Pd-Si-U, with a small fraction of Pd-Si. The Pd-Si-U and Pd-Si precipitates in the IPyC layer close to the IPyC-SiC interface are from Pd-Si-U and Pd-Si precipitates at the IPyC-SiC interface created by reaction between Pd or Pd-U and SiC. Note that the Si concentrations in the precipitates in the IPyC layer measured by EDS are accurate.

Figure 104 displays STEM images of precipitates in the IPyC layer away from the IPyC-SiC interface (Area 4 on Lamella 4 as shown in Figure 98 and Figure 100), where precipitates indicated by arrows or circles were subjected to EDS composition analyses. These precipitates are representative of precipitates in the IPyC layer away from the IPyC-SiC interface. The precipitate compositions from EDS are displayed in Table 56. It can be seen that precipitates are small (usually less than 30 nm in diameter) with a low number density. Most precipitates are U and U-Si. These U-rich precipitates are believed to be from

the fuel kernel where U migrates away from the fuel kernel and across the buffer layer and the IPyC layer. When U reaches the IPyC-SiC interface, its transport is slowed down and it accumulates at the interface. It is noted that Pd also accumulates at the IPyC-SiC interface. Pd and U at the interface (Pd has a higher concentration than U) react with SiC to form Pd-Si-U, which is rich in Pd and contains a small concentration of U. In addition, Pd at the IPyC-SiC interface also reacts with SiC to form Pd-Si. The Pd-Si-U and Pd-Si created at the IPyC-SiC interface migrate into the IPyC layer and the SiC layer.

Table 55. EDS compositions corresponding to the precipitates indicated in Figure 103. The majority of the precipitates are Pd-Si-U, with a small fraction of Pd-Si.

Precipitate Number	Concentration (at.%)												Precipitate Identification
	C	O	Si	U	Pd	Cs	Ce	Ag	Cd	I	Sr	Te	
Point Scan 1	73.89	1.17	9.09	1.06	14.57	0.09	0	0	0	0	0.09	0	Pd-Si-U
Point Scan 2	90.04	0.12	3.95	1.30	4.50	0	0.04	0	0	0	0.02	0	Pd-Si-U
Point Scan 3	62.05	0.13	14.80	3.05	19.68	0	0.10	0	0	0	0.15	0	Pd-Si-U
Point Scan 4	88.60	0.39	4.57	1.32	4.37	0.09	0.06	0	0.12	0.02	0.41	0	Pd-Si-U-Sr
Point Scan 5	92.15	0.01	3.16	0.86	3.76	0.02	0.01	0	0	0	0	0	Pd-Si-U
Point Scan 6	84.40	1.85	5.65	1.24	5.75	0.31	0.04	0.02	0	0	0.62	0.06	Pd-Si-U-Sr-Cs
Point Scan 7	97.14	0.06	1.32	0.09	1.15	0.14	0	0	0	0	0.07	0	Pd-Si
Point Scan 8	92.06	0.03	4.08	0.69	2.77	0.23	0	0	0	0	0.09	0	Pd-Si-U-Cs

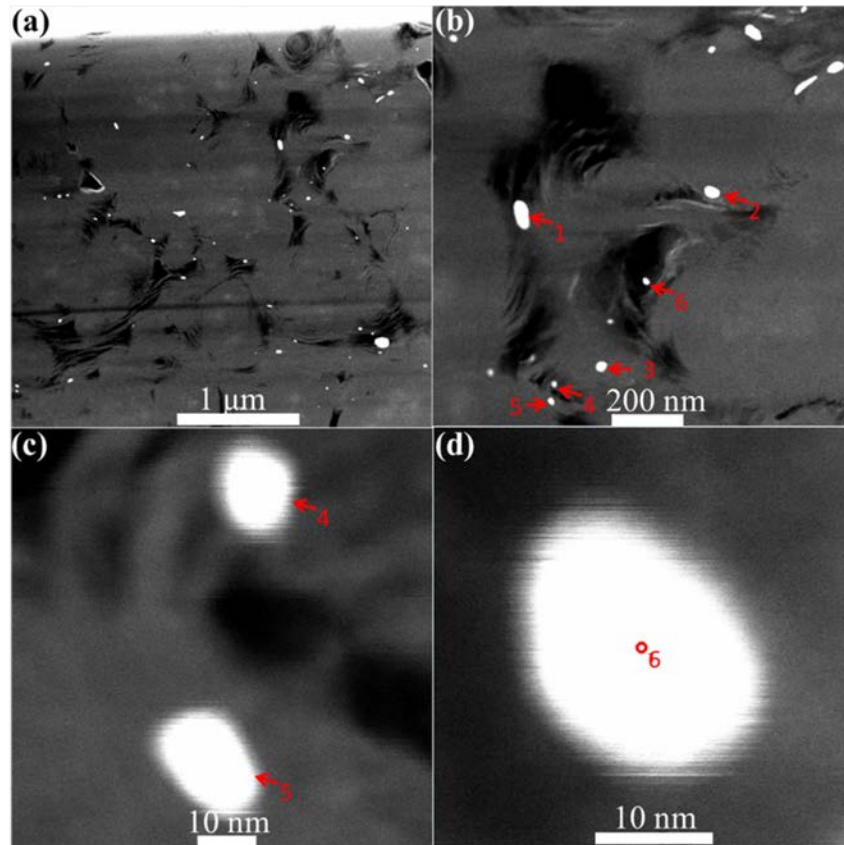


Figure 104. STEM images of precipitates in the IPyC layer away from the IPyC-SiC interface (a) (Area 4, Lamella 4), where precipitates indicated by arrows or circles were subjected to EDS composition analyses (b) with larger magnification images of precipitate Number 4 to 6 (c and d). Precipitates are small with a low number density. Chemical composition is reported in Table 56.

Table 56. EDS compositions correspond to precipitates indicated in Figure 104 from Area 4 on Lamella 4 from Particle AGR1-131-066. Most precipitates are U and U-Si.

Precipitate Number	Concentration (at.%)												Precipitate Identification
	C	O	Si	U	Pd	Cs	Ce	Ag	Cd	I	Sr	Te	
Point Scan 1	94.82	0.47	2.37	0.85	1.40	0	0.05	0	0	0	0	0.01	Pd-Si-U
Point Scan 2	96.03	0	2.92	0.96	0	0	0	0	0	0	0.06	0	U-Si
Point Scan 3	98.64	0.18	0.17	0.86	0.01	0.06	0.02	0	0	0	0	0.01	U
Point Scan 4	99.55	0	0.10	0.31	0	0.02	0	0	0	0	0.01	0	U
Point Scan 5	99.39	0	0.33	0.25	0	0.01	0	0	0	0	0	0	U-Si
Point Scan 6	99.23	0	0.23	0.43	0	0	0	0.01	0.02	0	0	0.03	U-Si

**3.4.2.1.2 Lamella 5 Inner Region of the Silicon Carbide Layer.** Lamella 5 was sectioned from the inner region of the SiC layer, and precipitates of three areas were analyzed. Figure 105 shows STEM images of precipitates in the SiC layer within about 2  $\mu\text{m}$  from the IPyC-SiC interface, where precipitates indicated by arrows or circles were subjected to EDS composition analyses. The precipitate compositions from EDS are displayed in Table 57. It can be seen that precipitates in this area are Pd, Pd-Si, Pd-U, and Pd-Si-U. Note that Precipitates 1 through 5 are within about 300 nm from the IPyC-SiC interface, and most of them (1, 2, 3, and 5) contain U. In contrast, Precipitates 6 through 14 are beyond about 300 nm from the IPyC-SiC interface and they are either Pd or Pd-Si. As discussed above, Pd-Si and Pd-Si-U in the SiC layer are from the Pd-Si and Pd-Si-U created at the IPyC-SiC interface by the reaction between Pd or Pd-U with SiC. Unreacted U at the IPyC-SiC interface migrates into the SiC layer along with Pd in the form of Pd-U. This means Pd assists the transport of U in the SiC layer. Pd readily migrates in the SiC layer because the diffusivity of Pd in SiC is high.

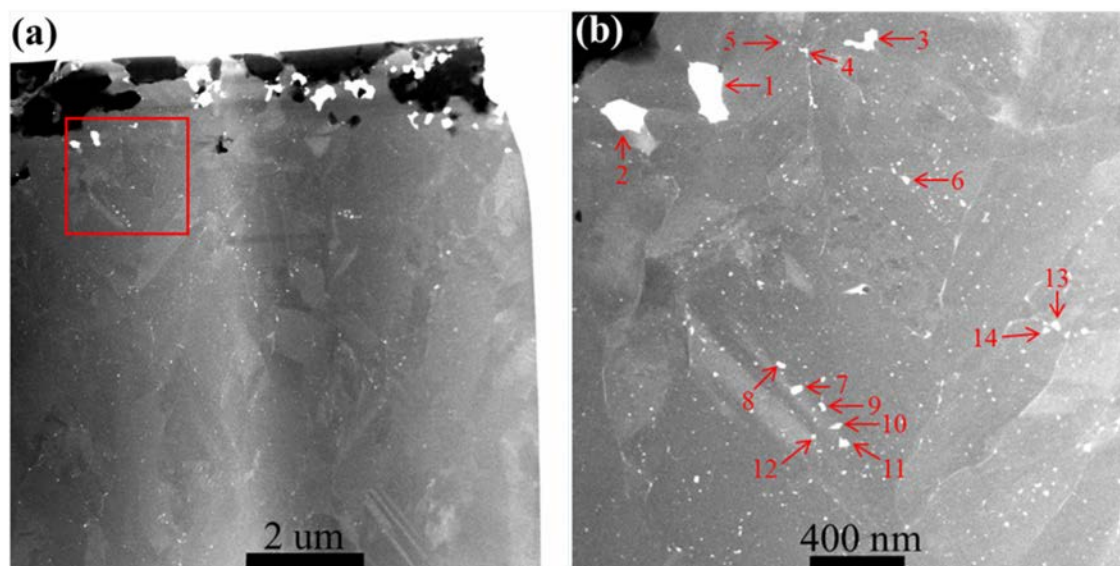


Figure 105. STEM images of precipitates in the SiC layer within about 2  $\mu\text{m}$  from the IPyC-SiC interface (Area 1, Lamella 5), where precipitates indicated by arrows or circles were subjected to EDS composition analyses. Chemical composition is reported in Table 57. Most precipitates within about 300 nm from the IPyC-SiC interface (Precipitates 1, 2, 3, and 5) contain U.

Table 57. EDS compositions correspond to precipitates indicated in Figure 105 from Area 1 on Lamella 5 from Particle AGR1-131-066. Precipitates are Pd, Pd-Si, Pd-U, and Pd-Si-U. Most precipitates within about 300 nm from the IPyC-SiC interface contain U.

Precipitate Number	Concentration (at.%)												Precipitate Identification
	C	O	Si	U	Pd	Cs	Ce	Ag	Cd	I	Sr	Te	
Point Scan 1	41.80	0	38.25	3.88	15.61	0	0.28	0	0	0	0.16	0	Pd-U-Ce
Point Scan 2	6.66	0.28	67.04	4.97	18.76	0	0.36	0	0	0	1.63	0.27	Pd-Si-U-Sr-Ce
Point Scan 3	48.71	0	41.68	2.08	7.39	0	0.06	0	0	0	0.05	0	Pd-U
Point Scan 4	49.56	0.07	46.29	0	4.07	0	0	0	0	0	0	0	Pd
Point Scan 5	53.72	0.07	43.34	0.24	2.58	0	0	0	0	0	0	0.02	Pd-U
Point Scan 6	45.12	0.10	48.29	0	6.47	0	0	0	0	0	0	0	Pd-Si
Point Scan 7	42.36	0	50.27	0	7.36	0	0	0	0	0	0	0	Pd-Si
Point Scan 8	43.88	0	44.40	0	11.69	0	0	0	0	0	0	0	Pd
Point Scan 9	48.79	0.20	45.76	0	5.22	0	0	0	0	0	0	0	Pd
Point Scan 10	45.24	0	50.80	0	3.95	0	0	0	0	0	0	0	Pd-Si
Point Scan 11	46.95	0.09	47.55	0	5.39	0	0	0	0	0	0	0	Pd
Point Scan 12	46.14	0.02	48.17	0	5.65	0	0	0	0	0	0	0	Pd
Point Scan 13	47.67	0.44	46.91	0	4.96	0	0	0	0	0	0	0	Pd
Point Scan 14	47.95	0.09	48.25	0	3.69	0	0	0	0	0	0	0	Pd

Figure 106 shows STEM images of precipitates in the SiC layer about 6 to 7  $\mu\text{m}$  from the IPyC-SiC interface, where precipitates indicated by arrows or circles were subjected to EDS composition analyses. The precipitate compositions from EDS are displayed in Table 58. Precipitates in this area are Pd, Pd-Si, and Pd-U. The majority of the precipitates are Pd, with a small fraction of Pd-Si and Pd-U. Note that the fraction of Pd-Si-U, Pd-U, and Pd-Si precipitates is significantly reduced compared to that in Figure 105.

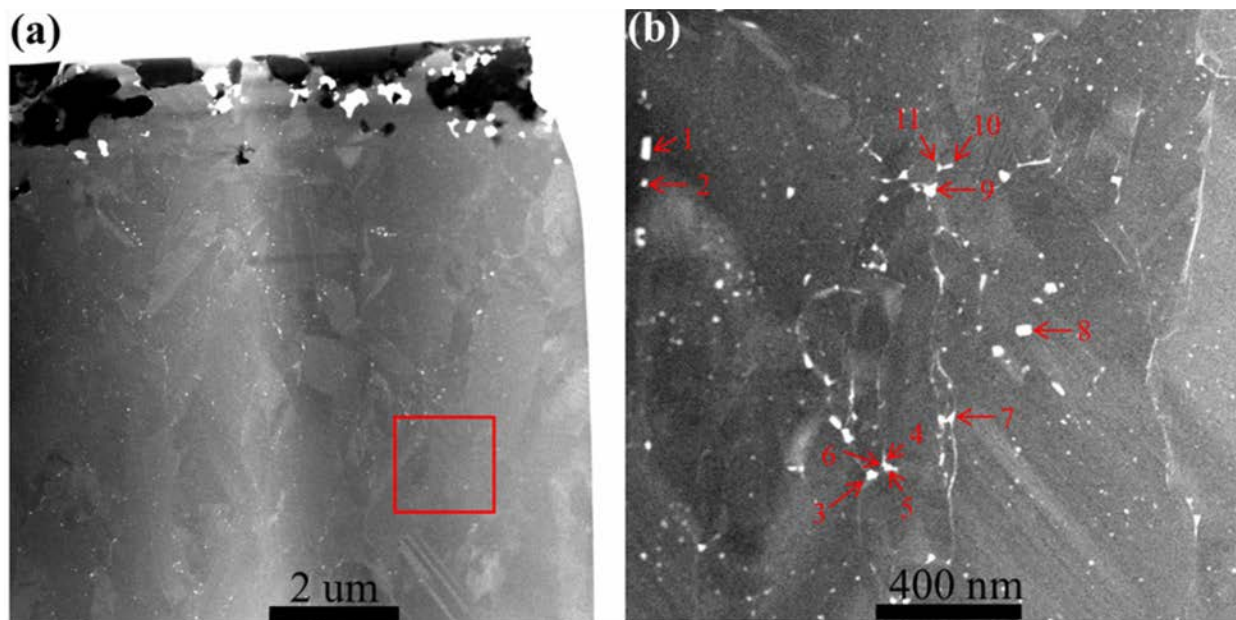


Figure 106. STEM images of precipitates in the SiC layer about 6 to 7  $\mu\text{m}$  from the IPyC-SiC interface (Area 2, Lamella 5), where precipitates indicated by arrows or circles were subjected to EDS composition analyses. Chemical composition of precipitates is reported in Table 58.

Table 58. Qualitative EDS compositions corresponding to precipitates indicated in Figure 106 from Area 2 on Lamella 5 from Particle AGR1-131-066. Majority of precipitates are Pd, with a small fraction of Pd-Si and Pd-U.

Precipitate Number	Concentration (at.%)												Precipitate Identification
	C	O	Si	U	Pd	Cs	Ce	Ag	Cd	I	Sr	Te	
Point Scan 1	50.20	0	45.31	0	4.29	0	0	0.17	0	0	0	0	Pd
Point Scan 2	50.27	0.06	46.31	0	3.23	0	0	0.04	0.05	0	0	0	Pd
Point Scan 3	46.22	0.10	40.98	0	12.66	0	0	0	0	0	0	0	Pd
Point Scan 4	48.52	0.11	46.18	0	5.17	0	0	0	0	0	0	0	Pd
Point Scan 5	47.57	0.31	45.75	0.32	6.02	0	0	0	0	0	0	0	Pd-U
Point Scan 6	49.62	0.19	46.01	0	4.16	0	0	0	0	0	0	0	Pd
Point Scan 7	52.10	0.01	45.36	0	2.42	0	0	0.05	0.04	0	0	0	Pd
Point Scan 8	45.67	0	49.00	0.02	5.28	0	0	0.01	0	0	0	0	Pd-Si
Point Scan 9	45.65	0.20	37.68	0	16.45	0	0	0	0	0	0	0	Pd
Point Scan 10	53.46	0.11	43.27	0	3.14	0	0	0	0	0	0	0	Pd
Point Scan 11	49.16	0.08	47.30	0	3.44	0	0	0.01	0	0	0	0	Pd

Figure 107 shows STEM images of precipitates in the SiC layer about 9 to 10  $\mu\text{m}$  from the IPyC-SiC interface, where precipitates indicated by arrows or circles were subjected to EDS composition analyses. The precipitate compositions from EDS are displayed in Table 59. Precipitates in this area are Pd-Si and Pd. No Pd-Si-U precipitates were observed. Here, no Pd-Si-U and no Pd-U precipitates were found in comparison to Figure 105 that had a number of these precipitates. The area in Figure 107 is close to that in Figure 106. Comparing the results in Figure 106 and Figure 107 with those in Figure 105, it is evident that the number density of Pd-Si-U and Pd-U precipitates in the SiC layer decreases with increasing distance from the IPyC-SiC interface, probably owing to the limited diffusivity of Pd-Si-U and Pd-U



precipitates in the SiC layer (Pd-Si-U and Pd-U precipitates diffuse from the IPyC-SiC interface into the SiC layer). This observation is consistent with that in AGR1-131-099 (Wen et al., 2015a).

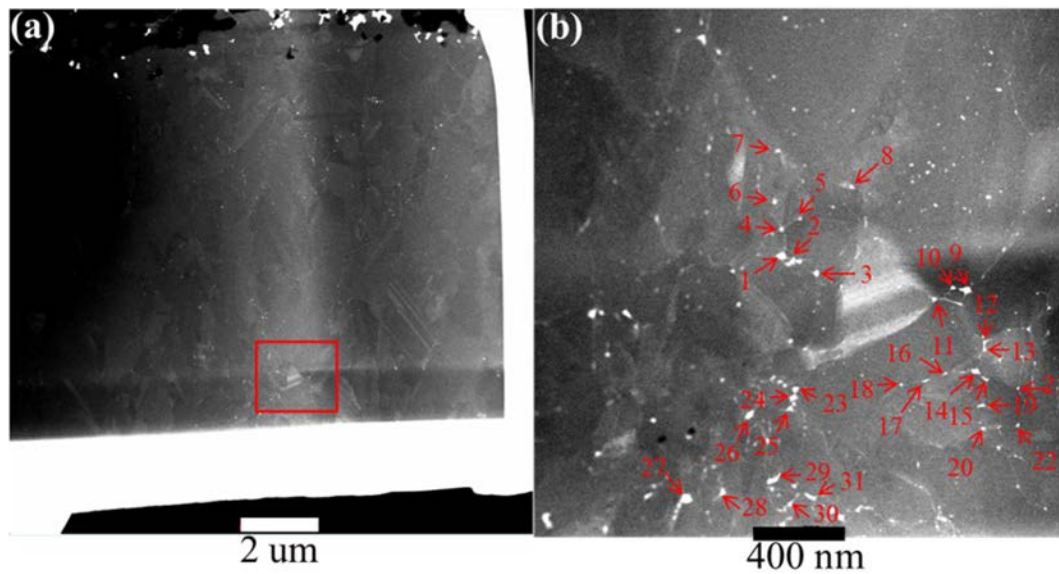


Figure 107. STEM images of precipitates in the SiC layer about 9 to 10  $\mu\text{m}$  from the IPyC-SiC interface (Area 3, Lamella 5), where precipitates indicated by arrows or circles were subjected to EDS composition analyses. Chemical composition is reported in Table 59.

Table 59. Qualitative EDS compositions correspond to precipitates indicated in Figure 107 from Area 3 on Lamella 5 from Particle AGR1-131-066. The majority of the precipitates are Pd and Pd-Si, with a small fraction of Pd-Si-U.

Precipitate Number	Concentration (at.%)												Precipitate Identification
	C	O	Si	U	Pd	Cs	Ce	Ag	Cd	I	Sr	Te	
Point Scan 1	39.89	0.06	52.12	0	7.91	0	0	0	0	0	0	0	Pd-Si
Point Scan 2	45.37	0.11	50.57	0	3.92	0	0	0	0	0	0	0	Pd-Si
Point Scan 3	41.14	0	54.60	0	4.24	0	0	0	0	0	0	0	Pd-Si
Point Scan 4	43.87	0.10	51.46	0	4.55	0	0	0	0	0	0	0	Pd-Si
Point Scan 5	46.43	0.11	49.56	0	3.88	0	0	0	0	0	0	0	Pd-Si
Point Scan 6	45.48	0.30	49.58	0	4.60	0	0	0	0	0	0.01	0	Pd-Si
Point Scan 7	45.86	0.55	47.39	0	6.17	0	0	0	0	0	0	0	Pd
Point Scan 8	46.20	0.02	49.55	0	4.22	0	0	0	0	0	0	0	Pd-Si
Point Scan 9	46.43	0.29	44.39	0	8.85	0	0	0	0	0	0	0	Pd
Point Scan 10	47.67	0.04	48.71	0	3.56	0	0	0	0	0	0	0	Pd
Point Scan 11	48.16	0	47.95	0	3.88	0	0	0	0	0	0	0	Pd
Point Scan 12	48.51	0.34	47.82	0	3.31	0	0	0	0	0	0	0	Pd
Point Scan 13	46.84	0	48.74	0	4.41	0	0	0	0	0	0	0	Pd-Si
Point Scan 14	46.84	0.17	49.29	0	3.68	0	0	0	0	0	0	0	Pd-Si
Point Scan 15	49.52	0	47.99	0	2.48	0	0	0	0	0	0	0	Pd
Point Scan 16	45.72	0	50.79	0	3.47	0	0	0	0	0	0	0	Pd-Si
Point Scan 17	47.02	0.27	50.49	0.48	1.70	0	0	0	0	0	0.02	0	Pd-Si-U
Point Scan 18	46.86	0.05	49.73	0	3.24	0	0	0.03	0.05	0	0	0	Pd-Si
Point Scan 19	46.97	0	49.06	0	3.96	0	0	0	0	0	0	0	Pd-Si
Point Scan 20	42.21	0.15	48.69	0	8.90	0	0	0.01	0	0	0	0.01	Pd-Si
Point Scan 21	42.98	0.20	52.18	0	4.59	0	0.01	0	0.02	0	0	0	Pd-Si
Point Scan 22	45.50	0	52.84	0.36	1.27	0	0.01	0	0	0	0	0	Pd-Si-U
Point Scan 23	42.22	0.08	50.11	0	7.57	0	0	0	0	0	0	0	Pd-Si
Point Scan 24	45.02	0.34	46.96	0.02	7.64	0	0	0	0	0	0	0	Pd-Si
Point Scan 25	44.15	0	52.21	0	3.62	0	0	0	0	0	0	0	Pd-Si
Point Scan 26	36.26	0.28	53.48	0	9.81	0.04	0.01	0	0.05	0	0	0.03	Pd-Si
Point Scan 27	39.03	0.58	46.95	0	13.38	0	0	0	0	0	0.03	0	Pd-Si
Point Scan 28	43.69	0	48.06	0.01	8.23	0	0	0	0	0	0	0	Pd-Si
Point Scan 29	42.20	0.05	51.00	0	6.72	0	0	0	0	0	0	0	Pd-Si
Point Scan 30	40.80	0.36	54.07	0	4.74	0	0	0	0	0	0	0	Pd-Si
Point Scan 31	42.03	0.39	50.66	0.03	6.77	0	0	0.04	0.03	0	0.01	0	Pd-Si

### 3.4.2.2 Chemical Composition in the Center Area of the Silicon Carbide Layer

**(Lamella 6).** AGR1-131-066 Lamella 6 was sectioned from the middle region in the SiC layer. Three areas in this Lamella were investigated by STEM-EDS, as shown in Figure 100(c). Note that among the three areas, Area 3 is closest to the IPyC-SiC interface, and Area 1 is closest to the OPyC layer (OPyC layer is removed after deconsolidation leach-burn-leach; there is no longer an OPyC layer).

Figure 108 shows STEM images of precipitates in Area 1 of AGR1-131-066 Lamella 6, where precipitates indicated by arrows were subjected to EDS composition analyses. The precipitate compositions from EDS are displayed in Table 60. It is seen that most of the precipitates examined in this area are Pd, with a small fraction of Pd-Si precipitates.

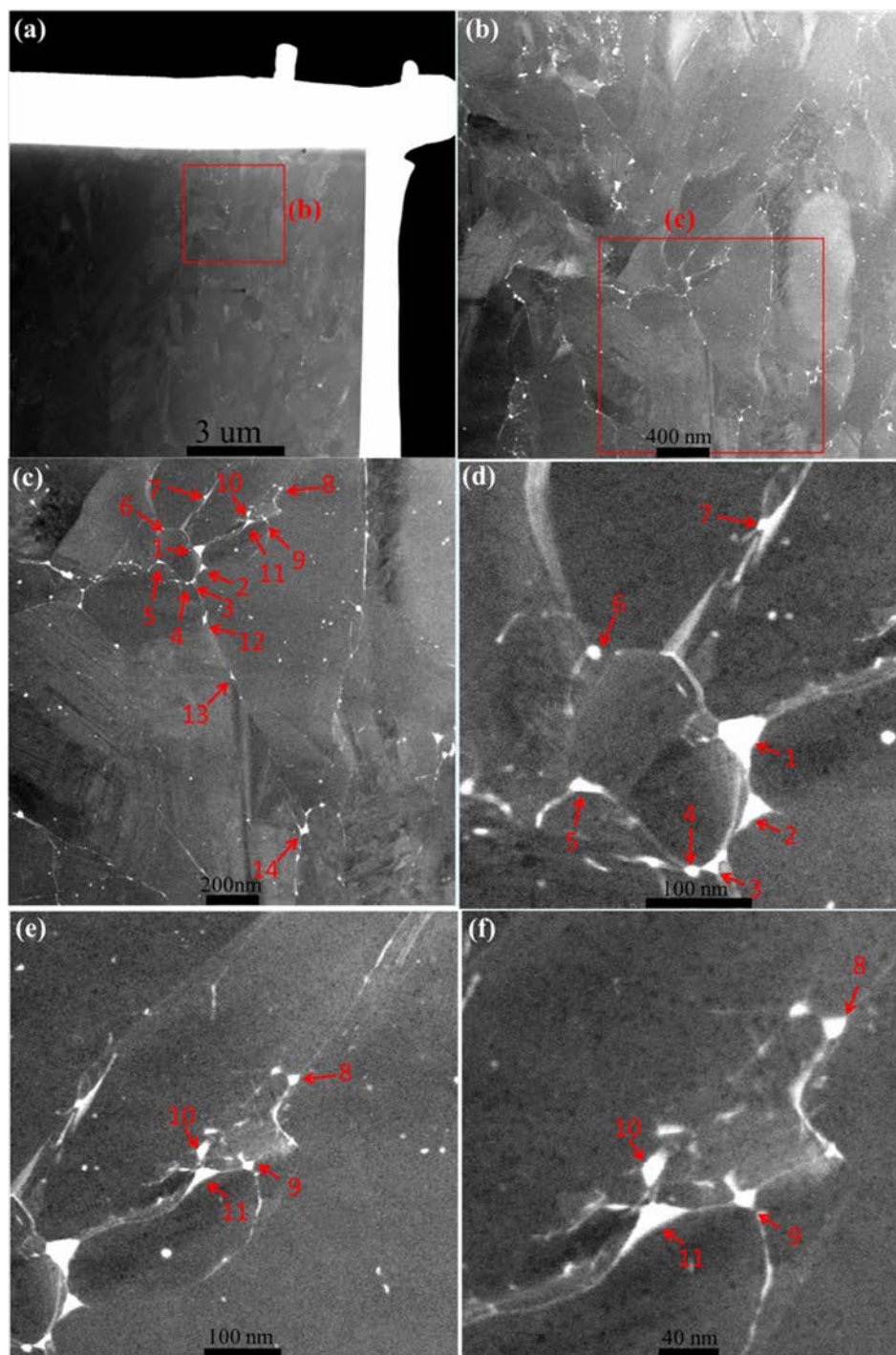


Figure 108. STEM images of (a) Area 1 of AGR1-131-066 Lamella 6 (Figure 100), where precipitates indicated by arrows (b through f) were subjected to EDS composition analyses. Qualitative chemical composition is reported in Table 60.



Table 60. Qualitative EDS compositions correspond to precipitates (indicated in Figure 108) of Area 1 of AGR1-131-066 Lamella 6. Most precipitates are Pd, with a small fraction of Pd-Si precipitates.

ICP-MS 650 Laundia 6 lowest precipitates are Pd, with a small fraction of Pd-Si precipitates.														
Precipitate Number	Concentration (at.%)												Precipitate Identification	
	C	O	Si	U	Pd	Cs	Ce	Ag	Cd	I	Sr	Te		
Point Scan 1	41.58	0.06	42.26	0	16.06	0	0	0	0	0	0	0	Pd	
Point Scan 2	47.38	0	47.95	0	4.65	0	0	0	0	0	0	0	Pd	
Point Scan 3	47.94	0	46.58	0.01	5.45	0	0	0	0	0	0	0	Pd	
Point Scan 4	52.66	0	45.50	0	1.82	0	0	0	0	0	0	0	Pd	
Point Scan 5	48.61	0	48.52	0	2.86	0	0	0	0	0	0	0	Pd	
Point Scan 6	49.80	0.28	47.62	0	2.27	0	0	0	0	0	0	0	Pd	
Point Scan 7	48.54	0.14	47.85	0	3.44	0	0	0	0	0	0.01	0	Pd	
Point Scan 8	54.55	0.76	42.51	0	2.15	0	0	0	0	0	0	0	Pd	
Point Scan 9	49.36	0.12	47.66	0	2.84	0	0	0	0	0	0	0	Pd	
Point Scan 10	50.97	0	46.34	0	2.68	0	0	0	0	0	0	0	Pd	
Point Scan 11	49.89	0.44	45.52	0	4.12	0	0	0	0	0	0	0	Pd	
Point Scan 12	47.90	0.08	47.53	0	4.46	0	0	0	0	0	0	0	Pd	
Point Scan 13	47.34	0.68	48.12	0.01	3.83	0	0	0	0	0	0	0	Pd	
Point Scan 14	45.62	0.03	49.67	0	4.66	0	0	0	0	0	0	0	Pd-Si	

Figure 109 shows STEM images of Area 2 of AGR1-131-066 Lamella 6, where precipitates indicated by arrows were subjected to EDS composition analyses. The precipitate compositions from EDS are displayed in Table 61. Based on these EDS results, precipitates in Area 2 are Pd, Pd-Si, and Pd-Si-U. The majority of the precipitates are Pd, with a small fraction of Pd-Si and Pd-U.

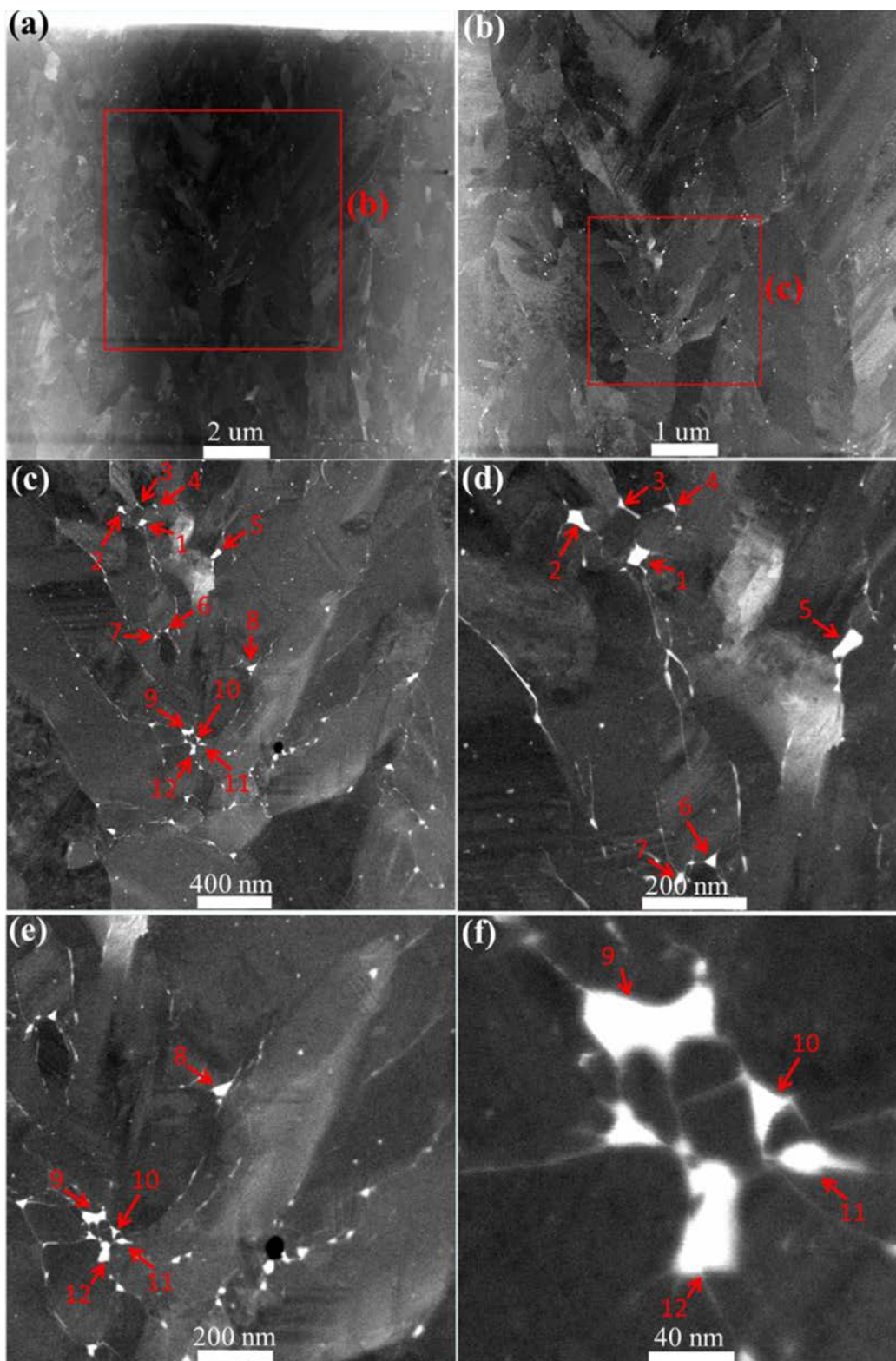


Figure 109. STEM images of Area 2 of AGR1-131-066 Lamella 6 (Figure 100), where precipitates indicated by arrows were subjected to EDS. Composition analyses are reported in Table 61.

Table 61. Qualitative EDS compositions correspond to precipitates indicated in Figure 109. The majority of the precipitates are Pd, with a small fraction of Pd-Si and Pd-U precipitates.

Precipitate Number	Concentration (at.%)												Precipitate Identification
	C	O	Si	U	Pd	Cs	Ce	Ag	Cd	I	Sr	Te	
Point Scan 1	48.99	0.14	45.35	0	5.50	0	0	0	0	0	0	0	Pd
Point Scan 2	47.38	0.49	42.86	0	9.05	0	0	0.12	0.05	0	0.01	0	Pd
Point Scan 3	4.83	0	91.93	0	3.21	0	0	0	0	0.01	0	0	Pd-Si
Point Scan 4	48.56	0.24	47.24	0.73	3.20	0	0	0	0	0	0	0	Pd-U
Point Scan 5	43.46	0	44.71	0	11.81	0	0	0	0	0	0	0	Pd
Point Scan 6	47.81	0	44.60	0	7.57	0	0	0	0	0	0	0	Pd
Point Scan 7	52.09	0.08	43.72	0.66	3.39	0	0.01	0	0	0	0	0.02	Pd-U
Point Scan 8	50.34	0.47	42.68	0	6.49	0	0	0	0	0	0	0	Pd
Point Scan 9	47.03	0.12	43.59	0	9.21	0	0	0	0	0	0	0.02	Pd
Point Scan 10	51.89	0.25	41.72	0	6.11	0	0	0	0	0	0	0	Pd
Point Scan 11	54.97	0.05	38.11	0.02	6.82	0	0	0	0	0	0	0	Pd
Point Scan 12	54.70	0.16	39.82	0	5.30	0	0	0	0	0	0	0	Pd

STEM images of Area 3 of AGR1-131-066 Lamella 6 are displayed in Figure 110. Figure 110(a) is a low-magnification STEM image; the red rectangle in (a) is magnified in (b). Precipitates indicated by arrows in the STEM images ([c] through [f]) were subjected to qualitative EDS composition analyses, and the precipitate compositions from EDS are displayed in Table 62. The majority of precipitates are Pd, with a noticeable fraction of Pd-Si precipitates and a small fraction of Pd-Si-U precipitates.

Comparing the results in Figure 108 to Figure 110, it is observed that for Areas 3–1, with increasing distance from the IPyC-SiC interface, the number density decreases of Pd-Si-U, Pd-U, and Pd-Si precipitates in the SiC layer. Comparing the results on Lamella 6 with those on Lamella 5, it is evident that the total number density of precipitates is reduced compared to that in Lamella 5, which was sectioned from the inner region in the SiC layer. Also, the number density of Pd-Si-U, Pd-U, and Pd-Si precipitates in the SiC layer decreases with increased distance from the IPyC-SiC interface. These observations are consistent with those in AGR1-131-099.

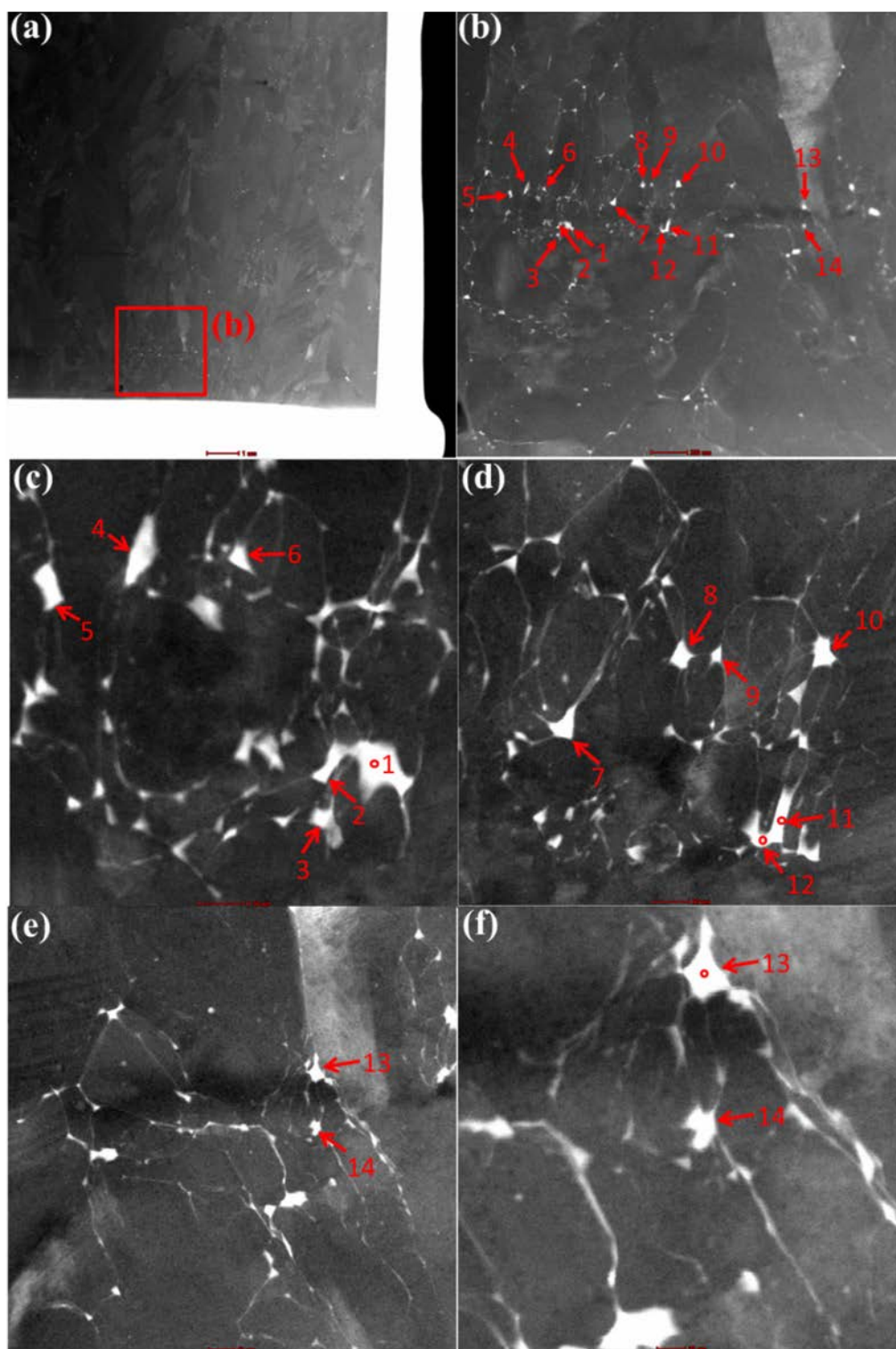


Figure 110. STEM images of Area 3 of AGR1-131-066 Lamella 6 (Figure 100), where precipitates are indicated by arrows, were subjected to EDS composition analyses. Chemical composition of precipitates is reported in Table 62.

Table 62. Qualitative EDS compositions correspond to precipitates indicated in Figure 110 from Area 3 of AGR1-131-066 Lamella 6. The majority of the precipitates are Pd, with a noticeable fraction of Pd-Si precipitates and a small fraction of Pd-Si-U precipitates.

Precipitate Number	Concentration (at.%)											Precipitate Identification	
	C	O	Si	U	Pd	Cs	Ce	Ag	Cd	I	Sr		Te
Point Scan 1	44.33	0.07	48.50	0	7.04	0	0	0	0	0.01	0	0.01	Pd-Si
Point Scan 2	51.23	0.38	43.69	0	4.66	0	0	0	0	0	0	0	Pd
Point Scan 3	47.59	0.35	48.12	0	3.91	0	0	0	0	0	0	0	Pd
Point Scan 4	54.21	0.20	42.56	0	3.02	0	0	0	0	0	0	0	Pd
Point Scan 5	49.68	0	45.31	0	5.00	0	0	0	0	0	0	0	Pd
Point Scan 6	44.87	0.18	48.30	0	6.63	0	0	0	0	0	0	0	Pd-Si
Point Scan 7	40.74	1.27	39.91	0	18.05	0	0	0	0	0	0	0	Pd
Point Scan 8	47.54	0	47.62	0	4.82	0	0	0	0	0	0	0	Pd
Point Scan 9	50.03	0.98	43.38	0	5.59	0	0	0	0	0	0	0	Pd
Point Scan 10	45.38	0.57	45.84	0	8.18	0	0.01	0	0	0	0	0	Pd
Point Scan 11	22.09	0	67.90	0.02	9.80	0.04	0.02	0.09	0	0	0	0	Pd-Si
Point Scan 12	44.42	0.21	46.40	0	8.94	0	0	0	0	0	0	0	Pd-Si
Point Scan 13	46.68	0.31	46.20	0	6.78	0	0	0	0	0	0	0	Pd
Point Scan 14	41.79	0.17	49.83	0.25	7.93	0	0	0	0	0	0	0	Pd-Si-U

### 3.4.2.3 Chemical Composition in the Outer Area of the Silicon Carbide Layer

**(Lamella 7).** STEM-based dark field imaging coupled with point-resolved EDS was performed to track individual fission product precipitates within Particle AGR1-113-066. In the outer area of the SiC layer close to the OPyC layer, shown in Figure 100(d), three individual areas were tracked that contained nanometer-scale fission product precipitates. Contained within Area 1 (shown in Figure 111[a]) are five subtended areas and within each area there are precipitates on grain boundaries and triple point junctions. Over the areas, labeled 1a through 1e (Figure 111[b] through [f]), precipitates indicated by circles were subjected to EDS composition analyses. All precipitates analyzed contain Pd, with no traces of Ag reported in Table 63. In Area 1a (Figure 111[b]), there are traces of Ce and U present in the precipitates analyzed.

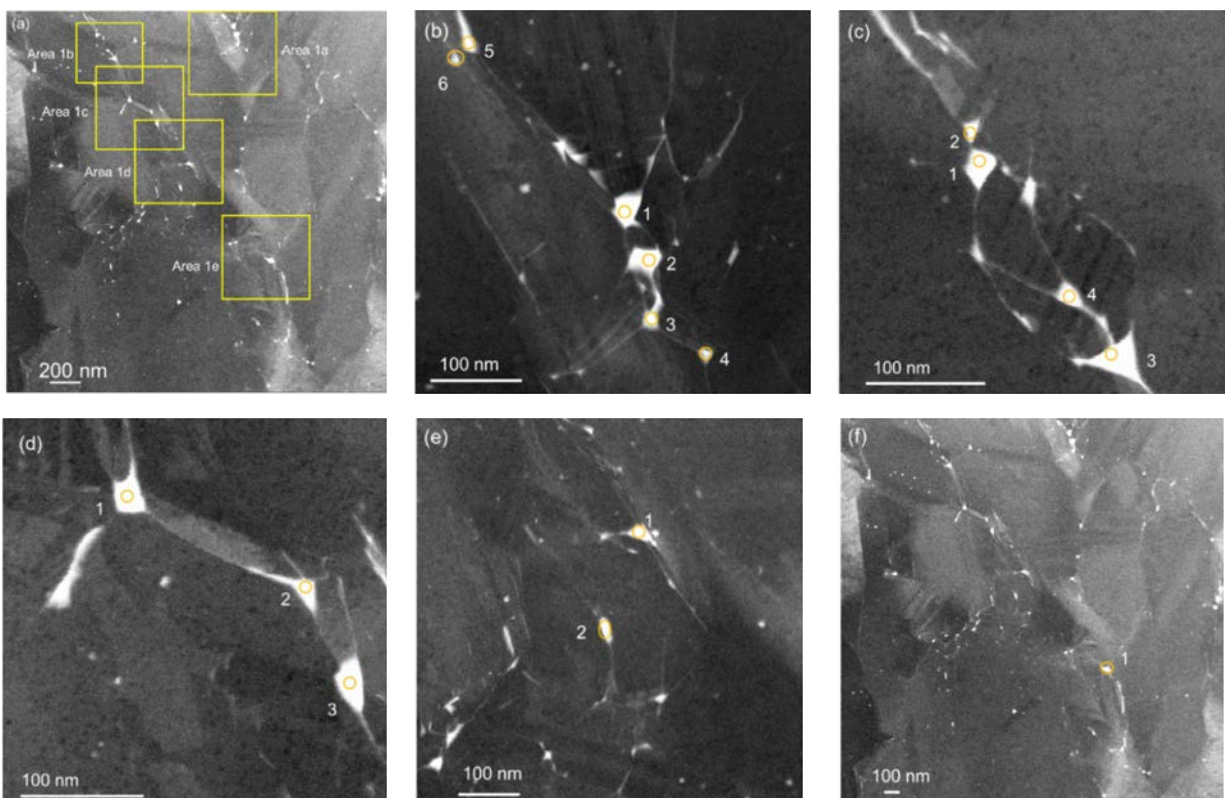


Figure 111. (a) STEM HAADF image combined with EDS labeling to track the chemical composition of fission product precipitates from the outer area (Lamella 7, Area 1 shown previously in Figure 100) of TRISO Particle AGR1-131-066. Within Area 1, five subtended areas (b) 1a, (c) 1b, (d) 1c, (e) 1d, and (f) 1e were studied with point-resolved EDS. Note the reported chemical compositions are in Table 63.



Table 63. Reported qualitative EDS compositions from the outer area (Lamella 7) of TRISO Particle AGR1-131-066, taken from subtended Areas 1a, 1b, 1c, 1d, and 1e from Figure 111.

Precipitate Number	Concentration (at.%)									Precipitate Identification
	C	Si	Pd	Ag	Cs	Ce	Eu	U	Pu	
Area 1a										
1	37.53	50.35	11.21	0.04	0.06	0.00	0.00	0.00	0.12	Pd
2	45.54	47.99	4.96	0.00	0.00	0.00	0.00	0.00	0.00	Pd
3	41.46	50.04	5.40	0.00	0.00	1.43	0.00	0.00	0.00	Pd-Ce
4	42.12	55.19	2.01	0.00	0.00	0.00	0.00	0.65	0.00	Pd-U
5	31.50	59.89	6.11	0.00	0.00	2.13	0.00	0.22	0.11	Pd-Ce-U
6	41.56	53.35	4.99	0.06	0.00	0.00	0.00	0.00	0.00	Pd
Area 1b										
1	51.71	43.02	5.08	0.01	0.00	0.00	0.00	0.00	0.00	Pd
2	49.23	46.17	2.25	0.00	0.00	0.13	0.00	0.93	0.00	Pd-U
3	50.47	40.16	8.87	0.00	0.00	0.00	0.00	0.00	0.00	Pd
4	49.69	45.17	3.36	0.00	0.00	0.23	0.00	0.00	0.00	Pd-Ce
Area 1c										
1	39.53	50.08	10.03	0.09	0.00	0.00	0.00	0.00	0.00	Pd
2	53.48	42.21	4.19	0.00	0.00	0.00	0.00	0.00	0.00	Pd
3	54.30	38.36	6.85	0.00	0.00	0.00	0.00	0.00	0.00	Pd
Area 1d										
1	51.06	41.85	6.69	0.00	0.00	0.00	0.00	0.00	0.00	Pd
2	48.58	46.81	4.12	0.00	0.00	0.00	0.00	0.00	0.00	Pd
Area 1e										
1	46.44	44.06	9.19	0.01	0.00	0.00	0.00	0.00	0.00	Pd

Similarly, in Sub-area 2 (highlighted in Figure 100), two individual areas were tracked containing nano-scale fission product precipitates. Contained within Area 2 (shown in Figure 112[a]) are two areas that contain precipitates circled at grain boundaries and triple point junctions. From the low-magnification STEM image in Figure 112(a), the number density of precipitates is compared to the composition of Area 1. Over the two areas within Area 2, labeled 2a (Figure 112[b]) and 2b (Figure 112[c]), all areas only contain the Pd precipitates reported in Table 64. Similarly, over Area 3 (highlighted in Figure 100), point analyses were performed over the points highlighted in Figure 113; Pd and Pd-Ce precipitates are reported in Table 65.

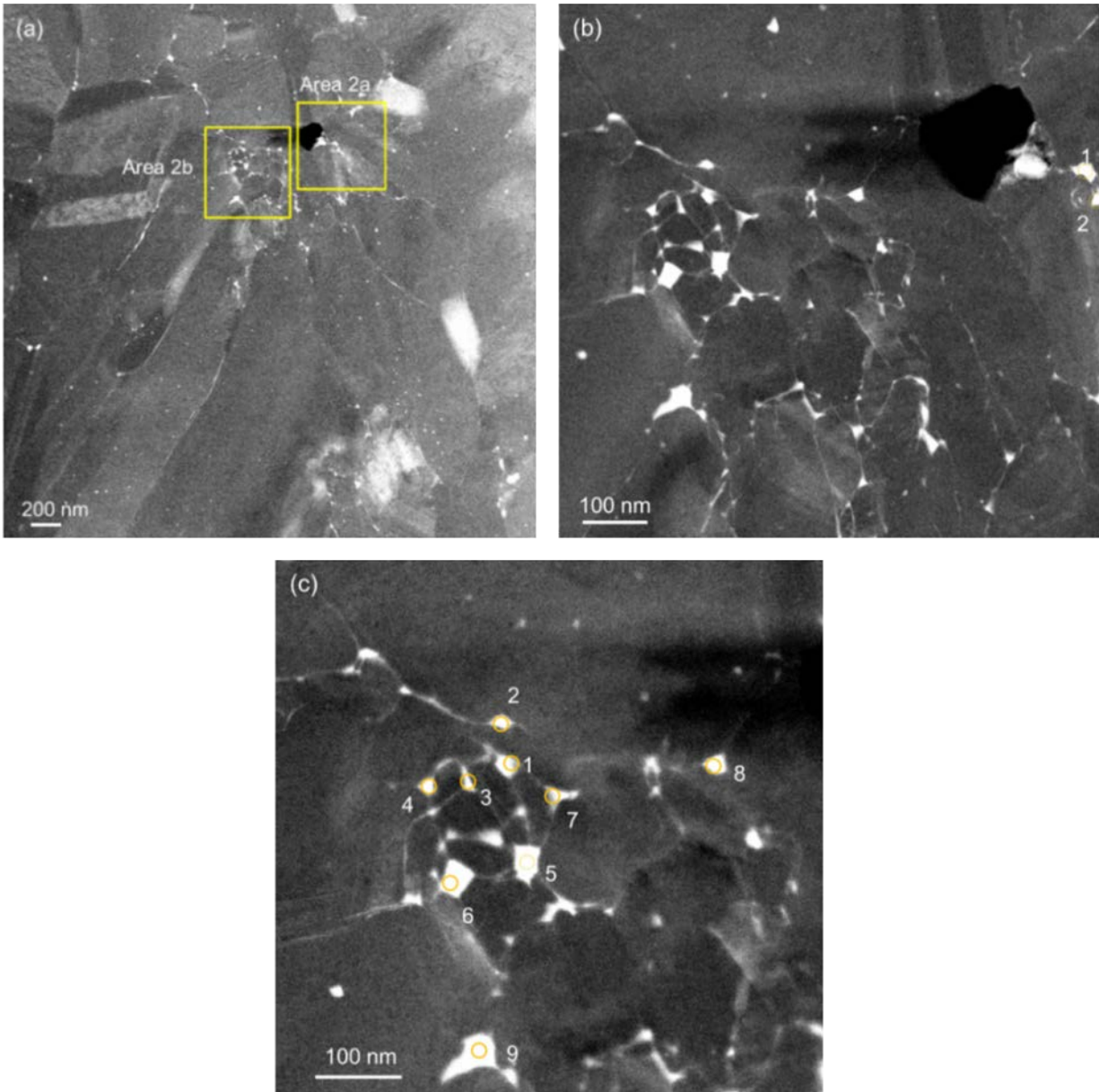


Figure 112. (a) STEM HAADF image combined with EDS labeling to track the chemical composition of fission product precipitates from the outer area (Lamella 7) of TRISO Particle AGR1-131-066 within subtended Area 2 (see Figure 100). Within Area 2, two subtended Areas (b) 2a and (c) 2c were studied with point-resolved EDS. Note the reported chemical compositions are in Table 64.



Table 64. Reported qualitative EDS compositions from the precipitates (Figure 112) from the outer area (Lamella 7) of TRISO Particle AGR1-131-066 (Figure 100), taken from subtended Areas 2a and 2b.

Precipitate Number	Concentration (at.%)									Precipitate Identification
	C	Si	Pd	Ag	Cs	Ce	Eu	U	Pu	Fission Product
<b>Area 2a</b>										
1	58.98	36.05	4.74	0.08	0.01	0.00	0.00	0.04	0.00	Pd
2	64.49	32.02	3.13	0.00	0.00	0.00	0.00	0.02	0.00	Pd
3	66.25	31.37	2.22	0.03	0.00	0.00	0.00	0.05	0.00	Pd
<b>Area 2b</b>										
1	71.16	27.50	0.66	0.00	0.00	0.00	0.00	0.39	0.02	Pd-U
2	69.59	26.76	3.44	0.00	0.00	0.00	0.00	0.00	0.00	Pd
3	73.79	24.19	1.96	0.01	0.00	0.00	0.00	0.01	0.05	Pd
4	71.71	25.54	2.66	0.00	0.00	0.00	0.00	0.00	0.00	Pd
5	67.48	26.73	5.71	0.00	0.00	0.00	0.00	0.00	0.00	Pd
6	69.49	27.10	3.24	0.06	0.00	0.00	0.00	0.00	0.00	Pd
7	72.86	24.79	2.14	0.02	0.00	0.00	0.00	0.00	0.00	Pd
8	70.62	25.59	3.57	0.00	0.00	0.00	0.00	0.00	0.00	Pd
9	45.02	49.81	5.15	0.00	0.00	0.00	0.00	0.00	0.00	Pd

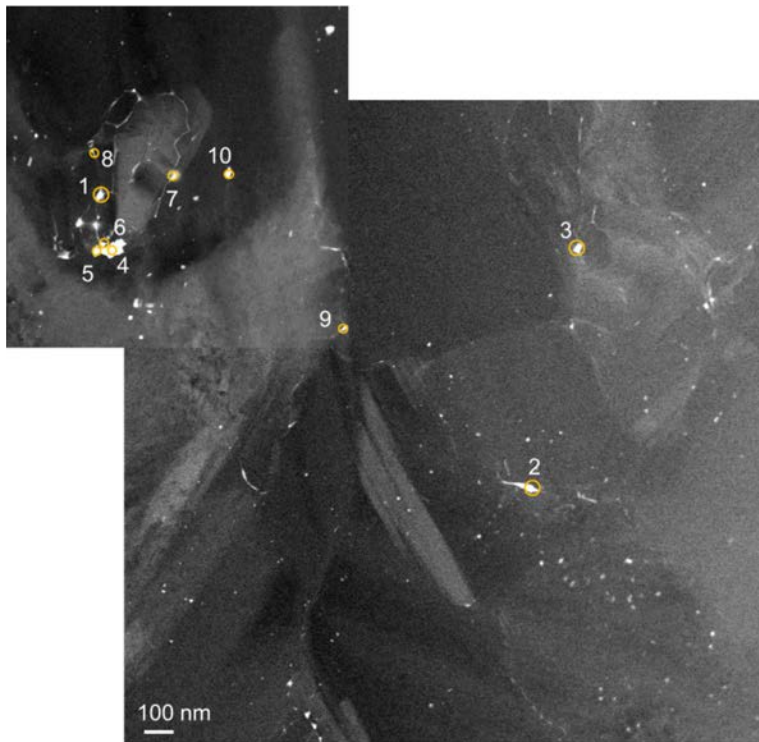


Figure 113. STEM HAADF image combined with EDS labeling to track the chemical composition of fission product precipitates from the outer area (Lamella 7) of TRISO Particle AGR1-131-066 within subtended Area 3 (see Figure 100). Note the reported chemical compositions are in Table 65.

Table 65. Reported qualitative EDS compositions from the precipitates (Figure 113) from the outer area (Lamella 7) of TRISO Particle AGR1-131-066 (Figure 100), taken from Area 3.

Precipitate Number	Concentration (at.%)									Precipitate Identification
	C	Si	Pd	Ag	Cs	Ce	Eu	U	Pu	
1	63.95	29.30	5.17	0.04	0.00	0.94	0.00	0.00	0.00	Pd-Ce
2	69.66	26.57	3.38	0.00	0.00	3.38	0.00	0.00	0.00	Pd-Ce
3	58.89	27.76	4.90	0.00	0.00	0.89	0.00	0.00	0.00	Pd-Ce
4	26.90	52.46	19.82	0.00	0.00	0.80	0.00	0.00	0.00	Pd-Ce
5	51.69	41.26	5.30	0.00	0.00	0.67	0.00	0.00	0.00	Pd-Ce
6	48.95	45.69	4.32	0.00	0.00	0.00	0.00	0.00	0.00	Pd
7	68.75	27.80	3.39	0.03	0.00	0.00	0.00	0.00	0.00	Pd
8	74.22	23.86	1.43	0.00	0.00	0.00	0.00	0.00	0.00	Pd
9	73.61	24.32	2.00	0.00	0.00	0.00	0.00	0.00	0.05	Pd
10	54.53	39.21	6.17	0.00	0.00	0.00	0.00	0.04	0.02	Pd

Based on EDS results reported from each of these three areas, the majority of precipitates are Pd, with a very small fraction of Pd-Ce and Pd-U. It appears that AGR1-131-066 is less permeable to Ag and U and/or its irradiation temperature was on the lower end of the temperature variations within the compact, resulting in reduced temperature-dependent diffusion. This reduced Ag and U permeability or diffusion may manifest as a higher degree of Ag retention (AGR1-131-066 Ag retention was 39% compared to less than 6% for AGR1-131-099). The different behavior in fission product and transport may be due to differences in neutron irradiation temperature and/or in microstructural characteristics for example grain boundary characteristics, phase and chemical composition.

**3.4.2.4 Crystallographic Information Obtained on Particle AGR1-131-066.** Figure 100 shows the areas on Lamellae 5, 6, and 7 (Figure 100[b], [c], and [d], respectively) subjected to advanced microstructural characterization, including qualitative compositional analysis of fission product precipitates using EDS and SiC grain orientation mapping using PED.

**3.4.2.4.1 General Grain Boundary Distributions across the Silicon Carbide Layer.** The PED-derived grain orientation maps of the areas analyzed on the inner sample (Lamella 5, Figure 100[b]) are shown in Figure 114. The orientation maps and other grain information on this Lamella and the other lamellae can be found in Lillo et al., (2017). Grain orientation data were used to calculate grain boundary distributions such as those shown in Figure 115, which show the distributions for the areas in Lamella 5. Because the areas are relatively small compared to the grain size, data for the three areas were also combined to yield average distributions representative of the inner region of the SiC layer with error bars showing the standard error. Similar averaged distributions were also calculated for Lamellae 6 and 7. These averaged distributions for the different regions, inner (Lamella 5), center (Lamella 6), and outer (Lamella 7) are compared in Figure 116.

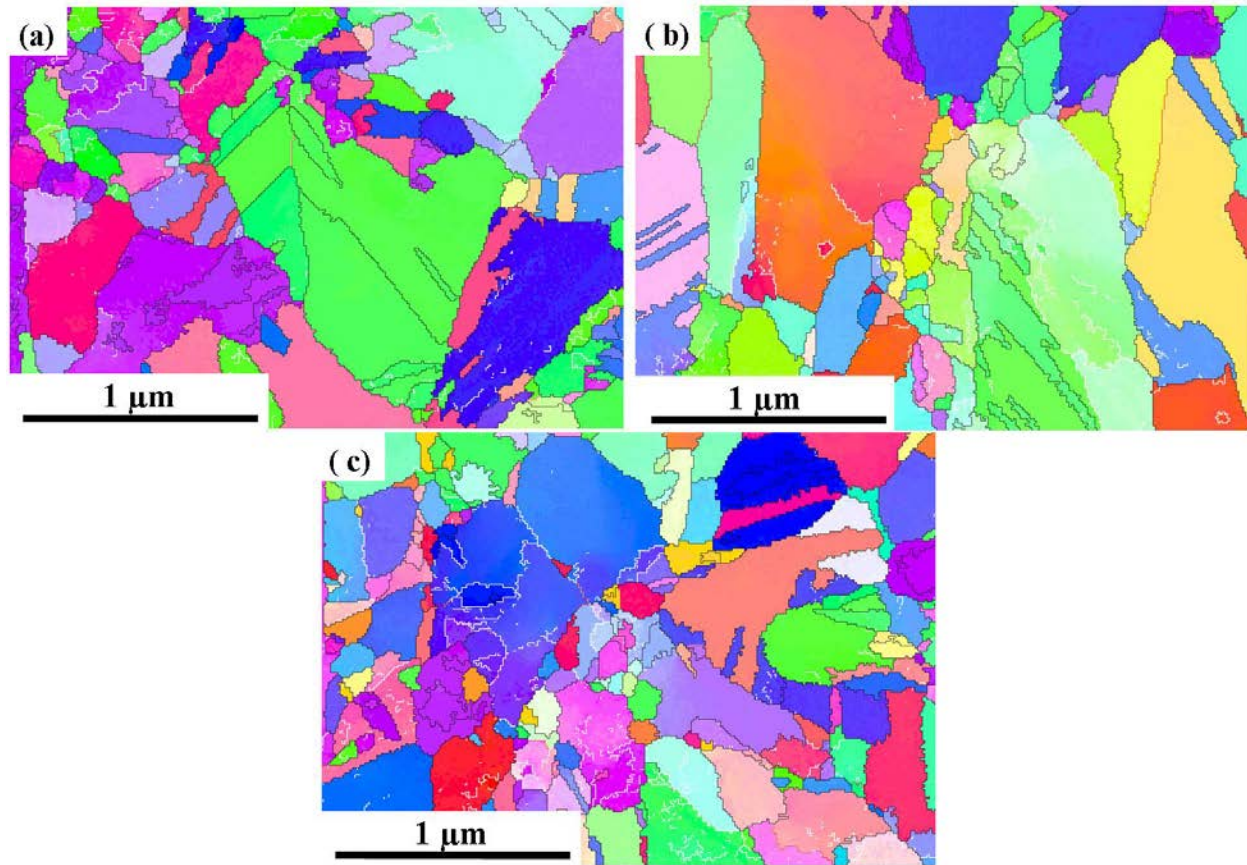


Figure 114. SiC grain orientation maps from the areas analyzed in Figure 100[b]: (a) Area 1, (b) Area 2, and (c) Area 3.

**3.4.2.4.1 Misorientation Angle Distribution.** The averaged distributions of the grain boundary misorientation angle for the inner, center, and outer sample are shown in Figure 116(a). The misorientation associated with twin boundaries ( $\theta = 60$  degrees) dominates the distribution of all the areas, while a secondary peak in the distribution occurs around 40 degrees. Generally, the distributions in the three regions are similar and no statistically significant differences are observed.

**3.4.2.4.2 Distribution of Coincident Site Lattice-Related Grain Boundaries.** Figure 116(b) shows the distribution of grain boundaries that exhibit a CSL relationship. Twin boundaries, with CSL value of  $\Sigma 3$ , represent the major fraction of CSL-related grain boundaries. Higher order twin boundaries, especially  $\Sigma 9$  boundaries, make up the majority of the remaining grain boundaries. CSL boundaries with other values make up a relatively insignificant fraction of the CSL-related grain boundaries in the SiC layer.

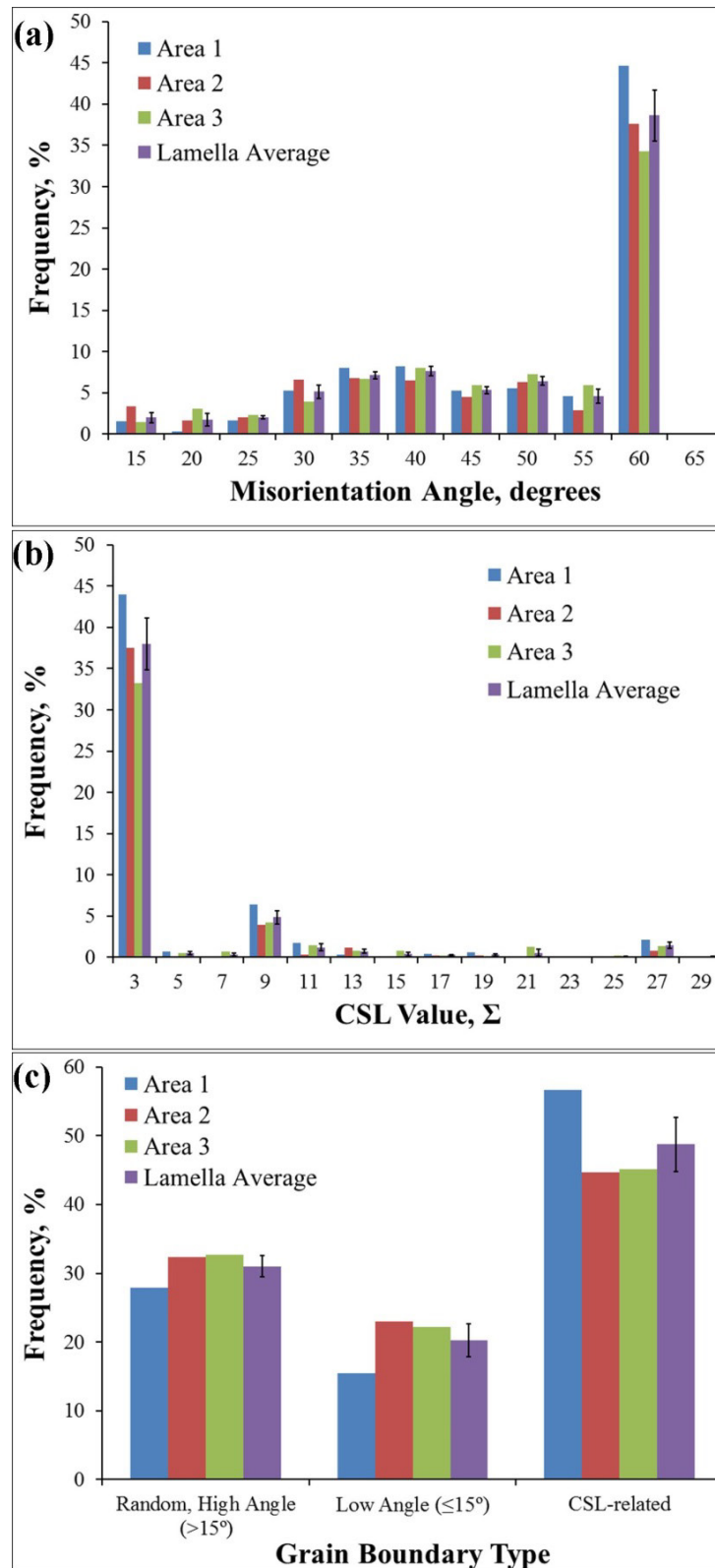


Figure 115. Distributions of the (a) grain boundary misorientation angle, (b) CSL distribution, and (c) grain boundary type for the areas in Lamella 5. The average distribution for Lamella 5 is included and consists of all data from the three areas.

Data for the three samples can be combined to yield a CSL value distribution representative of the entire SiC layer, especially because no significant statistical differences are noted among the different samples taken from the SiC layer. The twin (i.e.,  $\Sigma 3$ ) fractions, including the higher order twins of  $\Sigma 9$  and  $\Sigma 27$ , may be compared to those reported in literature for the SiC layer of unirradiated AGR-1 Variant 3 TRISO fuel particles (Kirchhofer et al., 2013) that were determined using SEM-based EBSD methods. For unirradiated TRISO particles, the values of  $\Sigma 3$ ,  $\Sigma 9$ , and  $\Sigma 27$  CSL boundaries are reported as 27%, 5%, and 1%, respectively. These values are generally close to those reported in Table 66 (no indication of the error associated with the study of Kirchhofer et al., 2013 is given, but due to the relatively large area analyzed in that study, the statistical variation in that study is expected to be no greater and probably less than that found in this study). Also, there is no indication that the high-temperature, neutron irradiation experienced by AGR1-131-066 had a large effect on the distribution of the CSL boundary values, provided the CSL distribution in the unirradiated TRISO particle in the Kirchhofer study accurately represented the pre-irradiated distribution in AGR1-131-066.

Table 66. Average fraction of twin-related grain boundaries in the SiC layer from Particle AGR1-131-066.

CSL value, $\Sigma$	Fraction, %	Std. Error
3	33.1	2.8
9	3.6	0.7
27	0.9	0.3

**3.4.2.4.3 Distribution by Grain Boundary Type.** The averaged distributions by grain boundary types for the inner, center, and outer samples of AGR1-131-066 are shown in Figure 116(c). CSL-related grain boundaries occur most frequently and random, high-angle grain boundaries are only slightly less common. The fraction of low-angle grain boundaries is nearly the same as that of the random, high-angle grain boundary fraction. Again, there appears to be little statistical variation between the inner, center, and outer samples.

The fraction of grain boundary types, averaged over all lamellae (Table 67) in this irradiated particle may be compared to the unirradiated values reported in Kirchhofer et al., (2013). That study reported values of 21%, 39%, and 40% for the low-angle, high-angle, and CSL-related grain boundary fractions, respectively. The value for the random high-angle grain boundaries in Table 67 appears to be significantly different between the two studies, while the values of the other types of grain boundaries generally agree within statistical error. The reason for the difference in the high-angle grain boundary fraction is not known, but it might be attributed to either particle-to-particle variations, differences in the techniques used to collect the orientation information (Kirchhofer et al., 2013 used SEM-based EBSD, while TEM-based PED was used in this study), or possibly temperature and neutron irradiation effects.

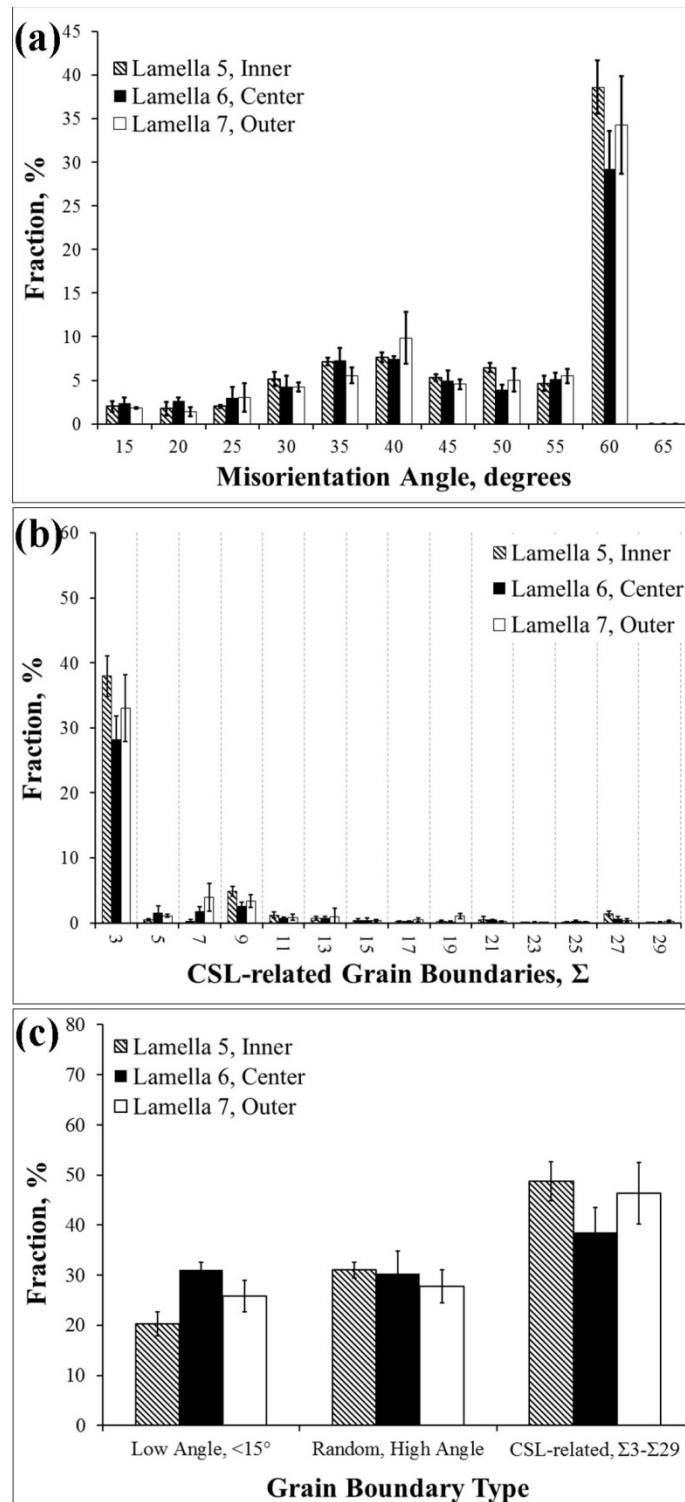


Figure 116. Distributions averaged over all areas analyzed for each sample, (a) misorientation angle, (b) CSL designation, and (c) grain boundary type for the SiC grain boundaries for samples taken from AGR1-131-066.

Table 67. Average fraction of grain boundary types in the SiC layer from Particle AGR1-131-066.

Grain Boundary Type	Fraction, %	Std. Error
Low angle, <15 degrees	25.7	3.1
High angle, >15 degrees	29.8	1.0
CSL-related	44.5	3.1

### 3.4.2.5 Grain Boundary Data for Grain Boundaries Containing Fission Product

**Precipitates.** The presence of various fission product and transuranic elements in the grain boundary fission product precipitates, determined using EDS, was correlated with information about the grain boundary on which the precipitate was found. The data are visualized in Figure 117 and summarized in Table 68. Generally, fission product precipitates are found most frequently on random, high-angle grain boundaries. Fission product precipitates are not as prevalent on CSL-related grain boundaries and are rarely associated with low-angle grain boundaries. Also, the fission product precipitates consisted of either Pd only or Pd with some U (Table 68). No other fission product elements above the limits of detection were found in any of the samples. As mentioned, the retention of Ag-110m, at about 39%, was fairly low (even though it was higher than that for AGR1-131-099 at less than 6%) and may be the reason why it was not found in the fission product precipitates of this particle.

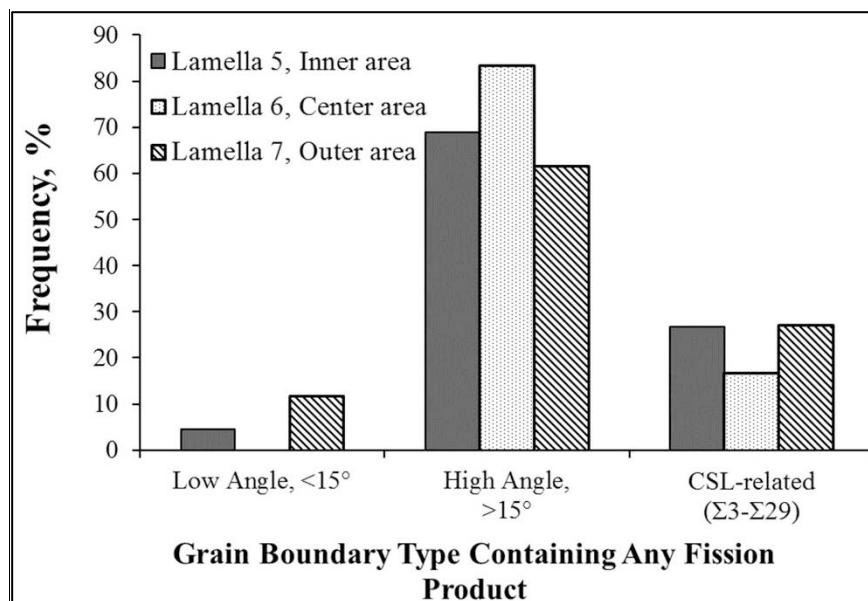


Figure 117. Comparison of the distribution of grain boundary types that contained any fission product precipitates.

As mentioned, precipitates occasionally appeared that were associated with CSL-related grain boundaries, but with much less frequency than random, high-angle grain boundaries. Pd-only precipitates occurred on  $\Sigma 3$  (10 times),  $\Sigma 9$  (one time),  $\Sigma 11$  (one time),  $\Sigma 13$  (one time),  $\Sigma 15$  (one time),  $\Sigma 17$  (one time), and  $\Sigma 21$  (one time). Precipitates containing Pd with U occurred on one  $\Sigma 9$  boundary and one  $\Sigma 15$  boundary. These results indicate that CSL-related grain boundaries are more easily occupied by Pd-only precipitates compared to when U is present with Pd. This is likely due to the relatively large atomic size differential between U and Pd. The larger atomic radius of U likely results in greater strains within a grain boundary compared to Pd. Thus, U tends to occupy grain boundaries with greater excess free volume and higher energy.

Table 68. Summary of the distribution of fission product elements.

	Pd Only	Ag only	U only	Pd and Ag	Pd and U	Pd+Pu	Pd+U+Pu	Pd+Ag+U
<b>Lamella 5, Inner Sample</b>								
Number of grain boundaries	38	0	0	0	7	0	0	0
Fraction of all boundaries with fission products, %	84.4	0.0	0.0	0.0	15.6	0.0	0.0	0.0
Low angle, %	5.3	—	—	—	0.0	—	—	—
Random, high angle, %	65.8	—	—	—	85.7	—	—	—
CSL, %	28.9	—	—	—	14.3	—	—	—
<b>Lamella 6, Center Sample</b>								
Number of grain boundaries	12	0	0	0	0	0	0	0
Fraction of all boundaries with fission products, %	100.0	0.0	0.0	0.0	0.0	0.0	0.0	0.0
Low angle, %	0.0	—	—	—	—	—	—	—
Random, high angle, %	83.3	—	—	—	—	—	—	—
CSL, %	16.7	—	—	—	—	—	—	—
<b>Lamella 7, Outer Sample</b>								
Number of grain boundaries	22	0	0	0	4	0	0	0
Fraction of all boundaries with fission products, %	84.6	0.0	0.0	0.0	15.4	0.0	0.0	0.0
Low angle, %	13.6	—	—	—	0.0	—	—	—
Random, high angle, %	63.6	—	—	—	50.0	—	—	—
CSL, %	22.7	—	—	—	50.0	—	—	—

**3.4.2.6 Discussions of Results for AGR1-131-066.** The total number of fission product precipitates for the three samples summarized in Table 68 is relatively small (i.e., only 83 precipitates). Therefore, precipitate data for the three regions was combined to yield a more statistically relevant data set that represents the entire SiC layer. As expected, the trend seen for the individual regions is further reinforced in the combined distributions:

- The precipitates are mainly of the Pd-only type; although a small fraction also contain U (Figure 118).
- Fission products prefer random, high-angle grain boundaries (Figure 119); although some CSL-related grain boundaries contain fission product precipitates while relatively few low-angle grain boundaries contain precipitates.
- Pd-only fission product precipitates occur on low-angle, high-angle, and CSL-related grain boundaries while Pd and U precipitates occur only on random, high-angle and some CSL-related grain boundaries (Figure 120). Precipitates containing Pd and U were not found on low-angle grain boundaries.



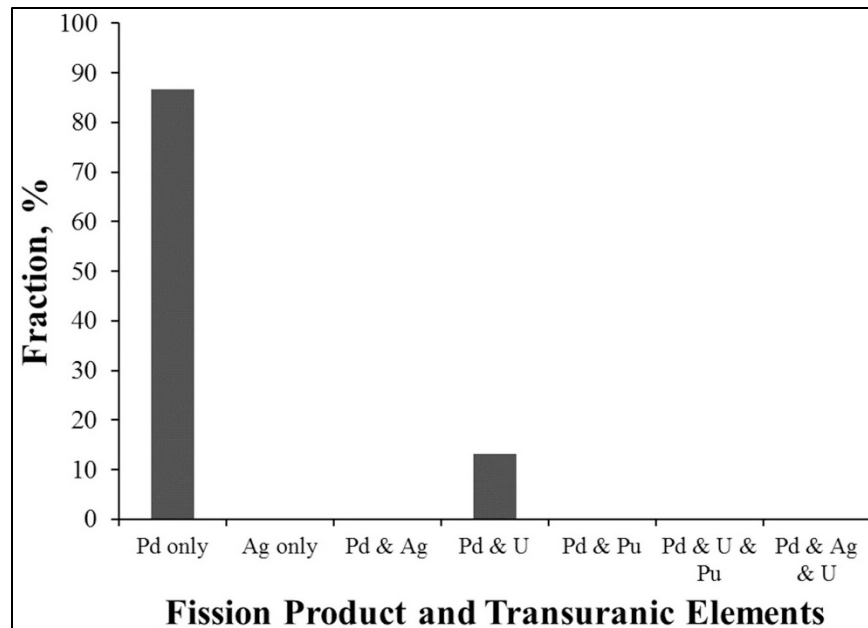


Figure 118. Composition distribution of the grain boundary precipitates in Particle AGR1-131-066.

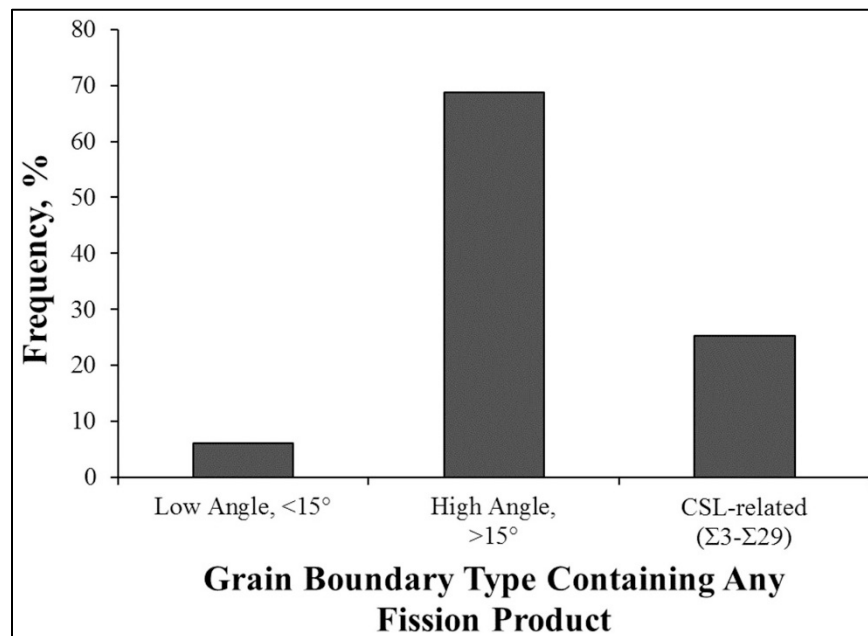


Figure 119. Distribution of fission product precipitates on the various grain boundary types in Particle AGR1-131-066.

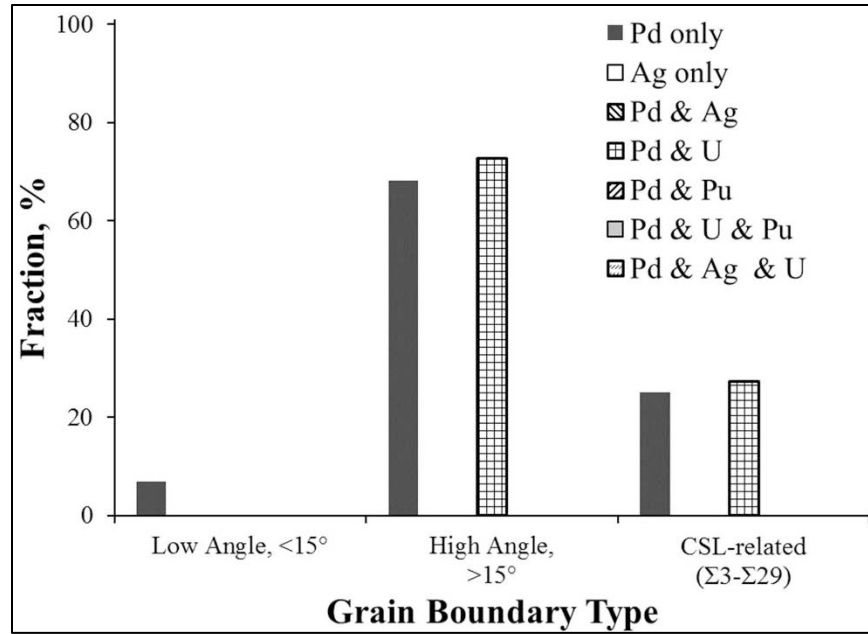


Figure 120. Distributions of fission product elements by grain boundary type for Particle AGR1-131-066.

**3.4.2.7 Kernel Microstructural Examination.** Results reported in this section are some of the first HRTEM results reported on UCO fuel kernels; this work was initiated in December 2015. It should be noted that these are only preliminary data and are not fully analyzed. (These results on kernel examination will be reported in a separate report at a later stage.) The initial phase of this electron microscopy examination focused on the identification survey of phases and structures present in and near the fuel kernel of a neutron-irradiated TRISO particle. Spectral imaging and point EDS analyses were carried out to identify the salient features and compositions. Overall, the specimens were suitable for survey work. However, additional localized thinning and polishing of areas of interest are necessary to obtain good diffraction data (selected area and convergent beam diffraction patterns), high-resolution images, and compositional data. Because it appears that the precipitates in graphitic areas originate from a specific phase in the uranium-containing fuel material, it is important to identify these phases in the kernel areas first. This will facilitate identification of particles in the graphitic area.

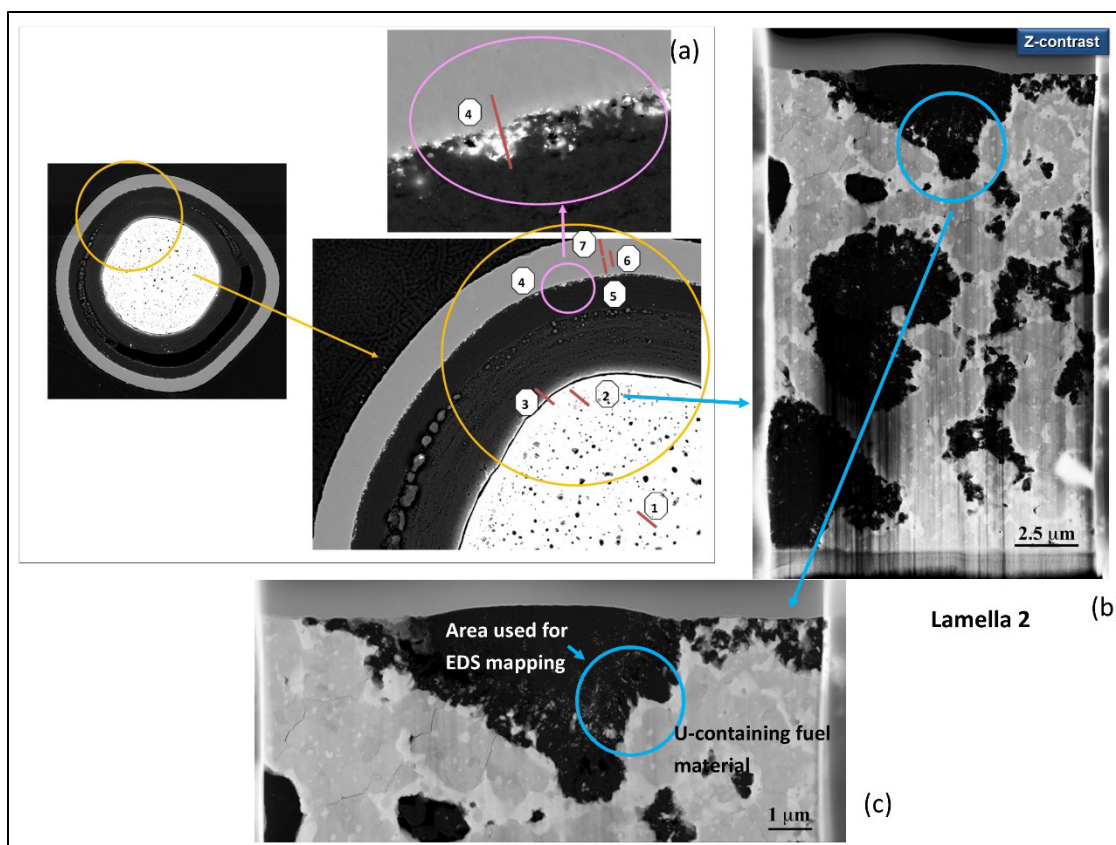


Figure 121. Images showing (a) the location of Lamella 2 of Particle AGR1-131-066 (Figure 98) examined in this study; with higher magnification and STEM Z-contrast images (b) and (c) showing where further STEM examination of the irradiation effects and EDS chemical composition were obtained.

Initial scoping results are provided for Particle AGR1-131-066 Lamella 2 (the location of Lamella 2 is shown in Figure 98). Figure 122 shows a STEM Z contrast image of the fuel kernel from Particle AGR1-131-066, which shows the overall structure after neutron irradiation. Two phases are identified in the uranium-containing material in a core shell-type arrangement. The outer or shell material is uranium-rich; it contains some Zr, Mo, and Ru, and is nearly metallic in nature. The core material is a U-(O,C) of approximate composition 1:2. The STEM BF image and EDS spectral images in Figure 123 showed that nearly all nanoparticles in the graphite are U-based, containing Zr, Mo, and Ru. They are similar in composition to the shell material of the composite fuel particles. The notable exception is that these small particles contain much more oxygen. A small amount of Cs could be detected within the graphite. No Pd or Ag was found in detectable quantities in these areas. The indicated spectral imaging compositional ranges are the maximum and minimum extents of each element in the maps. As indicated, Zr, Mo, and Ru do comprise a considerable fraction of the nanoparticles. HRTEM images (Figure 124) were obtained of some U (Zr, Mo, Ru)(C, O) nanoparticles found within the map region described in Figure 123. Selected area diffraction patterns could not be fully obtained due to the thickness of the lamellae. This will be further explored in future work.

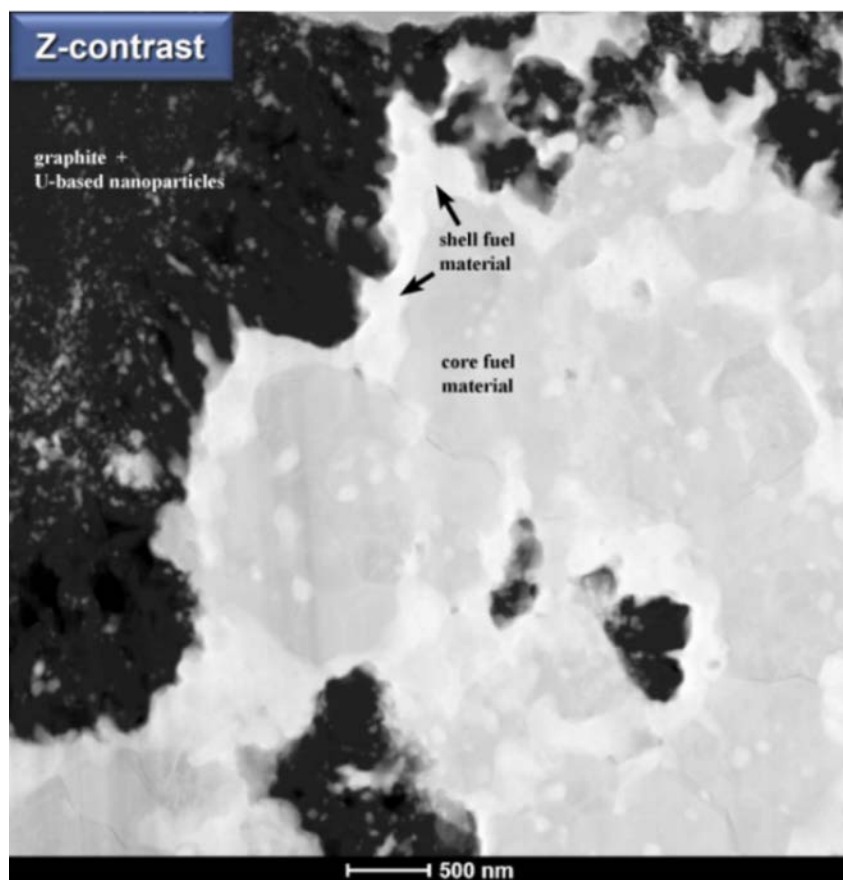


Figure 122. STEM Z contrast image of the fuel kernel from Particle AGR1-131-066 Lamella 2, showing the overall structure after neutron irradiation. Two phases are identified in the uranium-containing material in a core shell type of arrangement. The outer or shell material is U-rich, contains some Zr, Mo, and Ru, and is nearly metallic in nature. The core material is a U-(O,C) of approximate composition of 1:2.

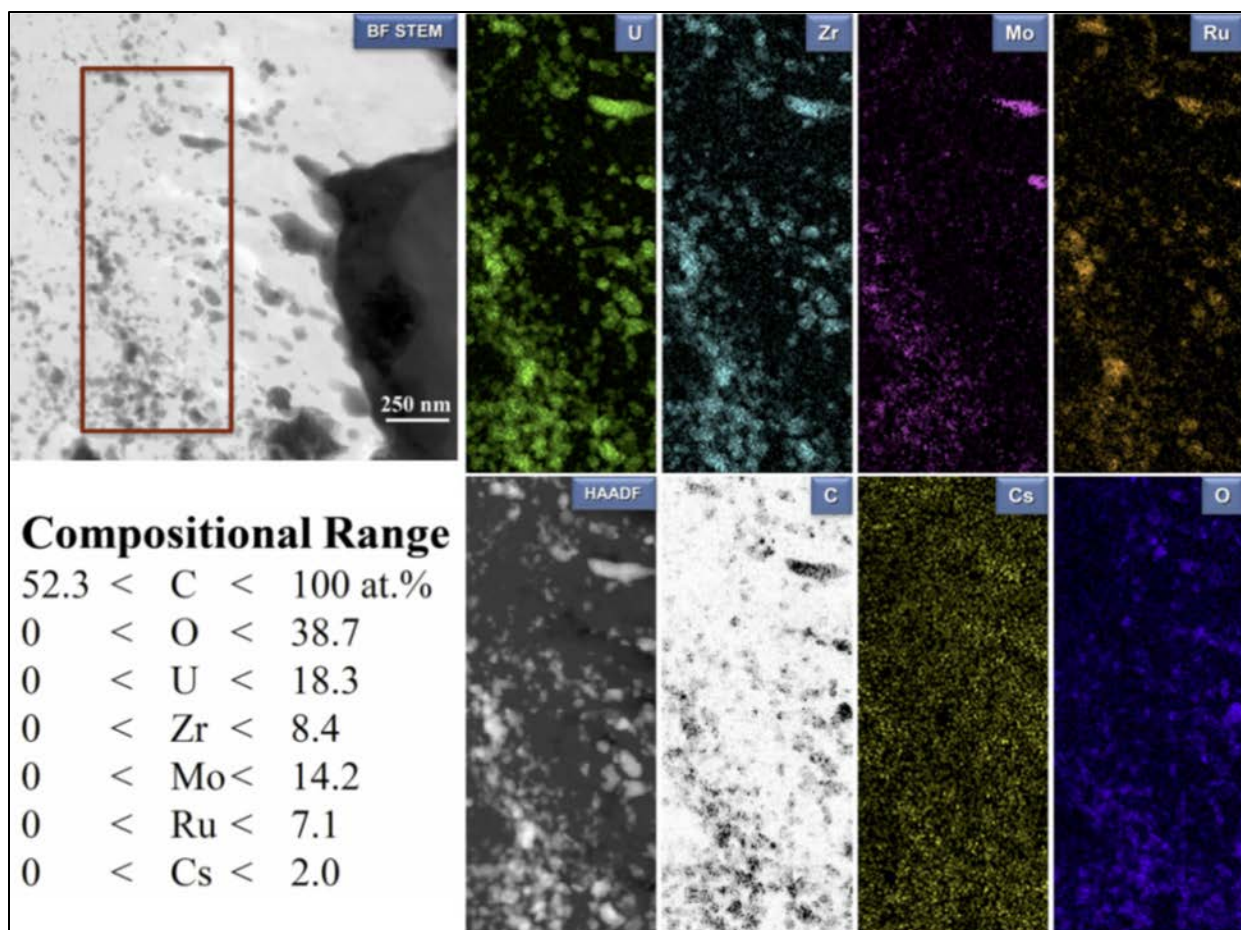


Figure 123. STEM BF image and EDS spectral images from the indicated region (Figure 121[c]) of the fuel kernel from Particle AGR1-131-066 Lamella 2.

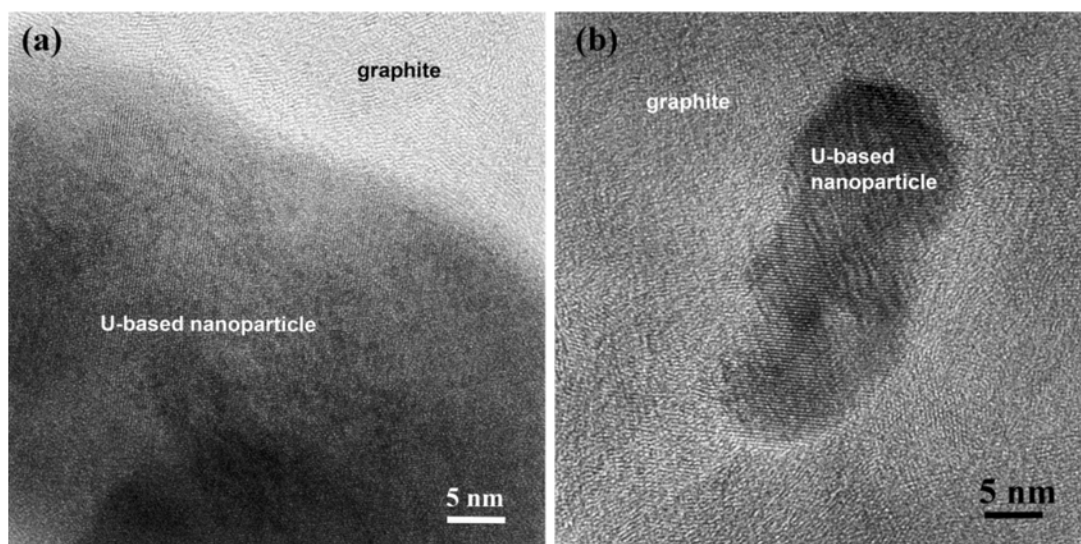


Figure 124. HRTEM images of some U (Zr, Mo, Ru)(C, O) nanoparticles found within the map region of the fuel kernel from Particle AGR1-131-066 Lamella 2 described above in Figure 123.



### 3.4.3 Chemical Composition and Distribution of Fission Products in Precipitates from Particle AGR1-131-099

This section reports the qualitative chemical composition of minor elements on Particle AGR1-131-099 to determine the type of fission products present, the location of these fission products in relation to the SiC layer thickness, and the fission product elemental composition. The reported fission product precipitate compositions (atomic %) are qualitative or semi-quantitative in nature (Section 2.1.2.3). Images of the TEM Lamella from Lamellae 1 through 5 with the indicated areas of microstructural analysis are shown in Figure 125.

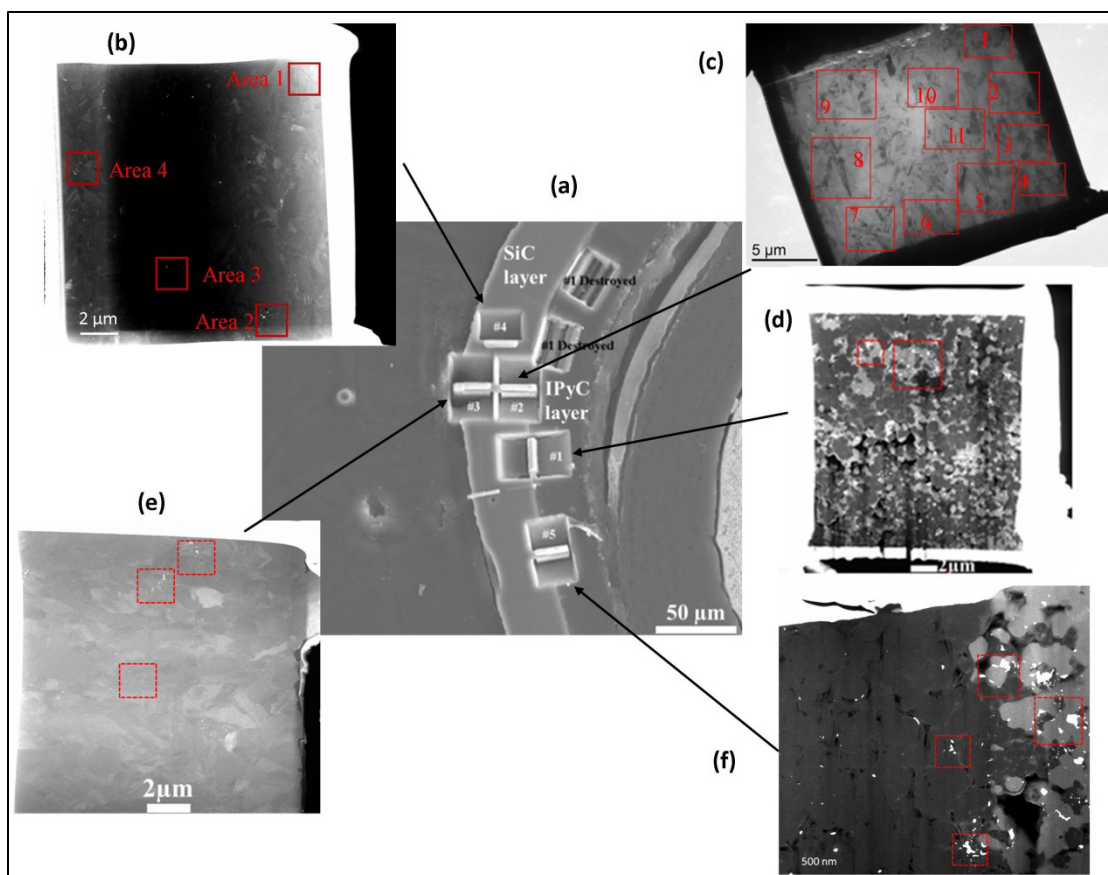


Figure 125. Images of the TEM Lamella from Particle AGR1-131-099 showing (a) SEM image showing the Lamella locations in the SiC layer (b) Lamella 4 with PED areas marked (EDS analysis completed on precipitates located in Area 2), (c) Lamella 2 with PED areas marked (EDS locations indicated in Section 3.4.3.1.3), (d) Lamella 1 with EDS precipitate analysis areas marked, (e) Lamella 3 with EDS precipitate analysis areas marked, and (f) Lamella 5 with EDS precipitate analysis areas marked.

#### 3.4.3.1 Chemical Composition in the Inner Area of the SiC Layer (Lamellae 1, 2, and 5).

**3.4.3.1.1 Lamella 1.** AGR1-131-099 Lamella 1 was sectioned from the IPyC-SiC interface. The length of this Lamella is parallel to the interface and the Lamella was taken exactly at the IPyC-SiC interface. Figure 126 shows STEM and TEM images of this lamella. Note the IPyC-SiC interface is not “sharp.” Therefore, there is a “mixture” of IPyC and SiC in the lamella, which is evident in the STEM images (Figure 126). There is a relatively low number density of precipitates at the IPyC-SiC interface and precipitates are not large. This is different from particles from other compacts, where there is typically a high number density of large precipitates at the IPyC-SiC interface. From the STEM images, pores are present at the IPyC-SiC interface, which are also evident in the TEM image.

Figure 127 shows STEM images of precipitates at the IPyC-SiC interface, where precipitates indicated by arrows were subjected to qualitative EDS composition analyses. In the STEM images, Precipitates 3 and 4 are in the IPyC, and others are in the SiC. Precipitates in SiC are larger than those in the IPyC. This is different from the phenomenon observed in TRISO particles from other compacts, where precipitates in the IPyC layer close to the IPyC-SiC interface are larger than precipitates in the SiC layer. The precipitate compositions from EDS are displayed in Table 69. These compositions are representative of the precipitate compositions in Lamella 1. From the EDS results, precipitates at the IPyC-SiC interface are Pd-Si-U, Pd-U, U, and U-Si. The majority of the precipitates are Pd-U or Pd-Si-U, with a small fraction of U and U-Si. Almost all precipitates at the IPyC-SiC interface contain U, which is different from the observation in the TRISO particles from other compacts where the fraction of U-containing precipitates at the IPyC-SiC interface is not high. Cs and Ce are also present in some of the precipitates.

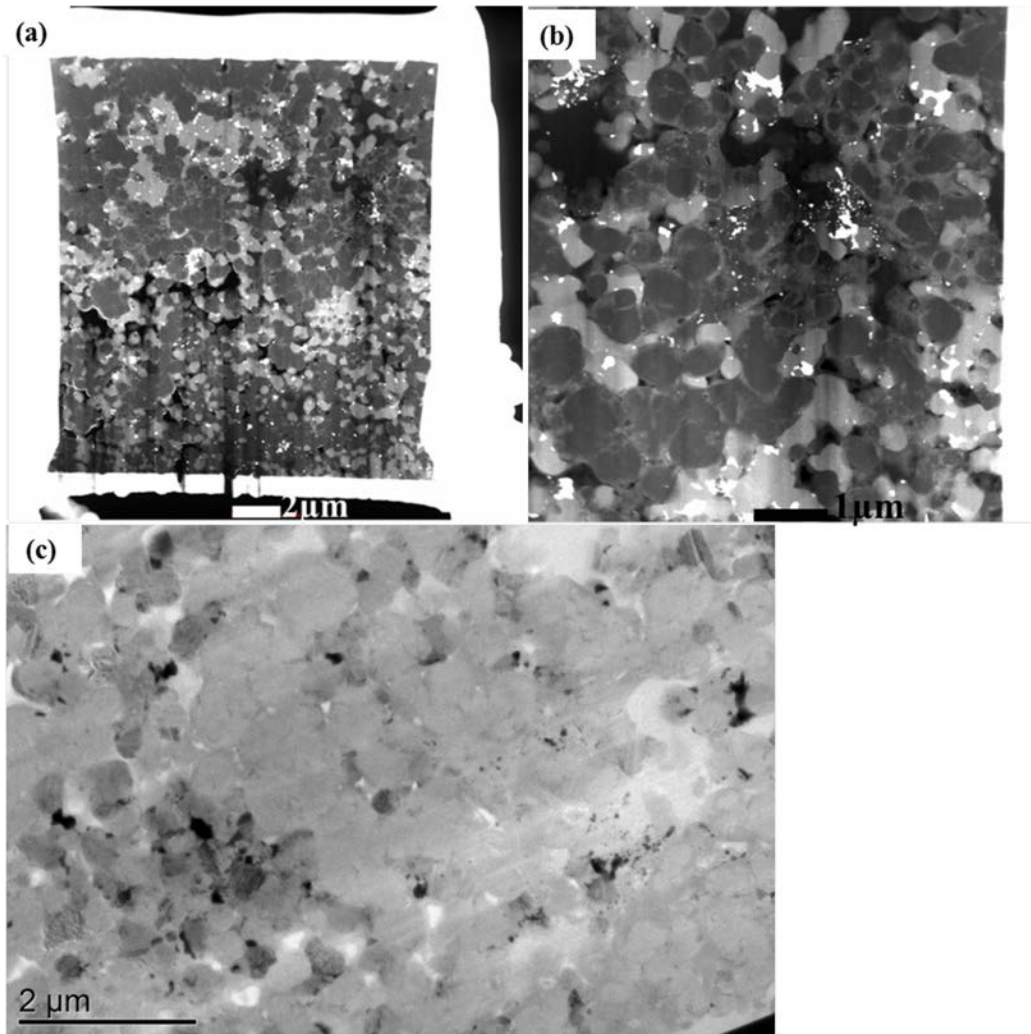


Figure 126. (a) (b) STEM images and (c) TEM image of AGR1-131-099 Lamella 1 that was sectioned from the IPyC-SiC interface (Lamella is parallel to the interface).

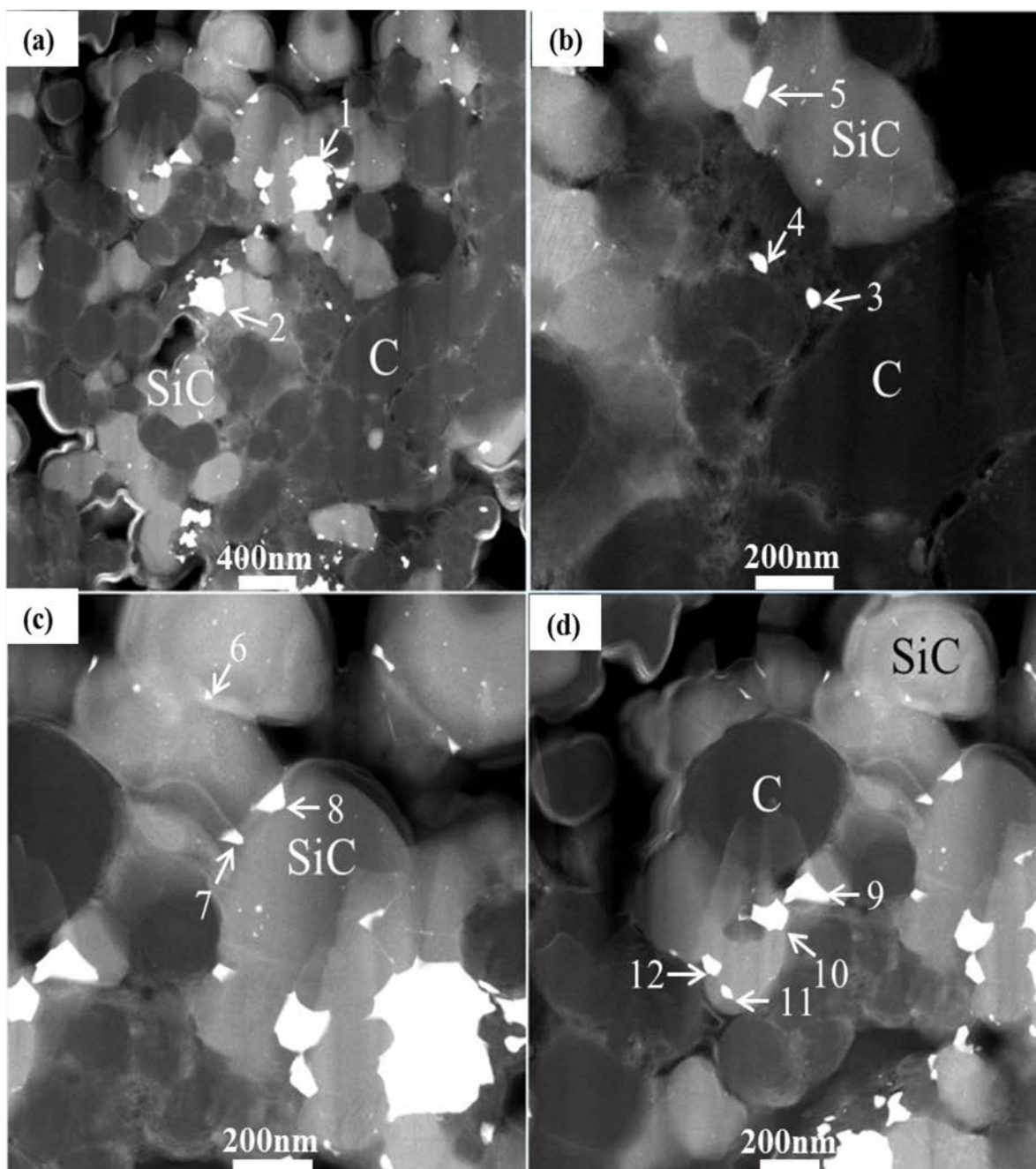


Figure 127. STEM images of precipitates in Lamella 1 (at the IPyC-SiC interface), where precipitates indicated by arrows were subjected to EDS point scan. The qualitative compositions corresponding to the EDS point scans are displayed in Table 69. The majority of the precipitates are Pd-U or Pd-Si-U, with a small fraction of U and U-Si. All precipitates contain U.



Table 69. Representative composition of precipitates in TEM Lamella 1 (at the IPyC-SiC interface). These compositions correspond to precipitates indicated in Figure 127. 0.2 at.% is taken as the detection limit for Pd, Ag, Cs and Ce, and 0.1 at.% for U. Any element with concentration below the detection limit is considered not to be present.

Precipitate Number	Concentration (at.%)												Precipitate Identification
	C	O	Si	U	Pd	Cd	Ag	Cs	Ce	Sr	I	Te	
Point Scan 1	79.5	0.2	8.4	2.1	8.1	0.1	0	0.5	0.2	0.6	0.1	0.3	Pd-U-Cs-Ce-Sr-Te
Point Scan 2	35.5	0.4	47.7	2.6	13.5	0	0	0	0.2	0.1	0	0	Pd-U-Ce
Point Scan 3	88.9	0.5	5.7	0.6	4.1	0	0	0.3	0	0.1	0	0	Pd-Si-U-Cs
Point Scan 4	89.0	0.1	6.0	1.3	3.5	0	0	0	0	0.1	0	0	Pd-Si-U
Point Scan 5	41.1	0	52.4	0.8	5.5	0	0	0	0.1	0.1	0	0	Pd-U
Point Scan 6	61.9	1.9	35.3	0.6	0.3	0	0	0	0	0	0	0	U
Point Scan 7	75.0	0.7	20.8	0.6	2.8	0.1	0.1	0	0	0	0	0	Pd-U
Point Scan 8	59.8	3.0	26.5	1.4	7.8	0	0	0.5	0.3	0.7	0	0.01	Pd-U-Cs-Ce-Sr
Point Scan 9	45.2	0	45.2	1.6	7.8	0	0	0	0.1	0.1	0	0	Pd-U
Point Scan 10	56.2	0	37.0	0.9	5.7	0	0	0	0.1	0.2	0	0	Pd-U-Sr
Point Scan 11	47.3	0.1	48.6	3.9	0.1	0	0	0	0	0	0	0	U
Point Scan 12	8.6	0.6	79.8	8.6	0.8	0	0	0.7	0.1	0	0.2	0.6	U-Cs-Pd-I-Te

**3.4.3.1.2 Lamella 5.** Multiple pores were observed in the microstructure of the SiC of this Lamella (shown in Figure 128), which is in contrast with most other particles from other compacts examined. Distribution of precipitates in the IPyC layer is demonstrated in Figure 128(b), which shows qualitatively to be smaller than the precipitates found in the SiC layer. This corresponds with the general trend observed in examining precipitates from other particles and compacts. Compositions of the precipitates shown in Figure 129 are indicated in Table 70. Note that Precipitates 1 through 6 are in the SiC layer and close to the IPyC-SiC interface, and that Precipitates 7 through 12 are in the IPyC layer and are also close to the IPyC-SiC interface. It can be seen that precipitates in the SiC layer have the following types of compositions: Pd-Si-U, Pd-Si, Pd-U, Pd, and U. The EDS results show that large precipitates (about 0.1 to 0.3  $\mu\text{m}$ ) at the IPyC-SiC interface are typically Pd-Si-U. However, there are some exceptions.

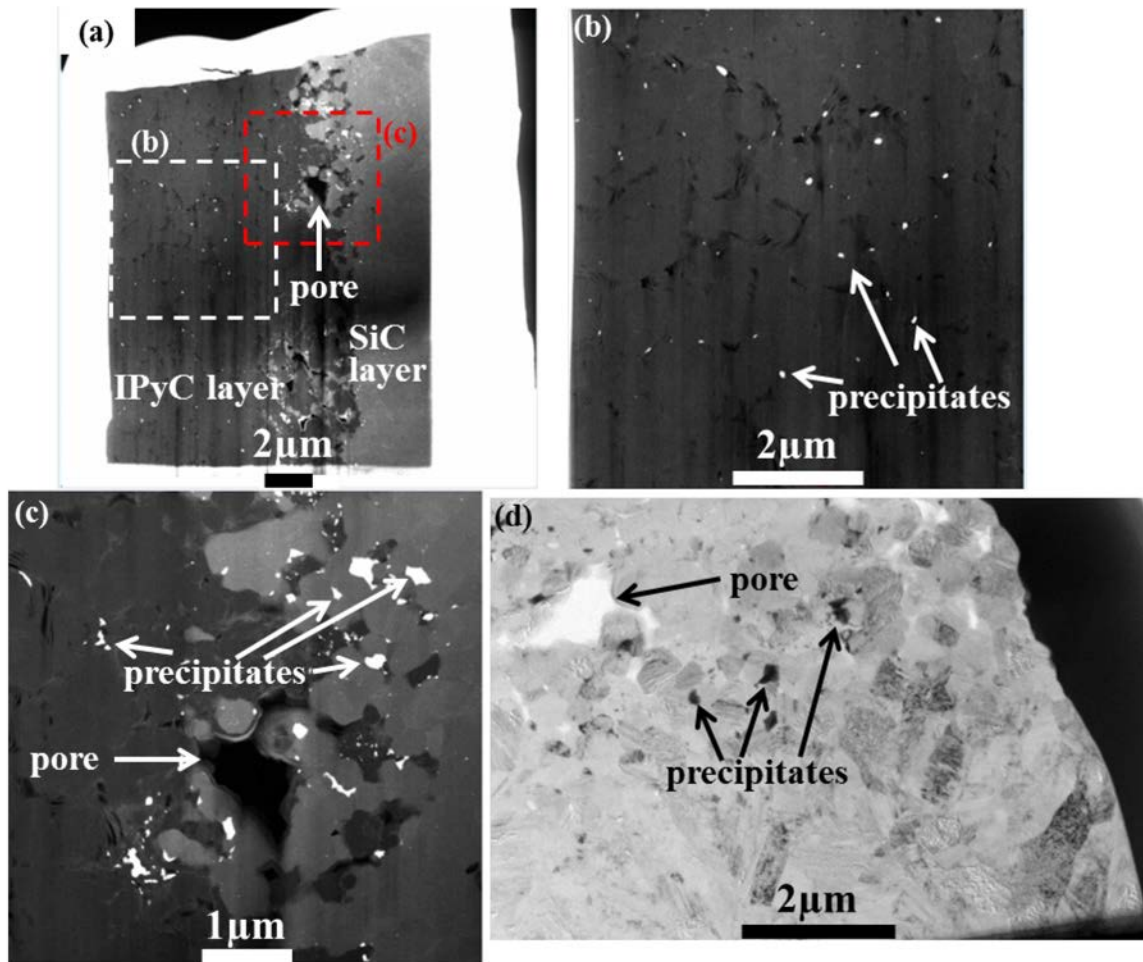


Figure 128. (a) (b) (c) STEM images of TEM Lamella 5 (across the IPyC-SiC interface), showing the whole sample (a), the IPyC layer (b), and the IPyC-SiC interface (c), and (d) TEM image of an area close to the IPyC-SiC interface.

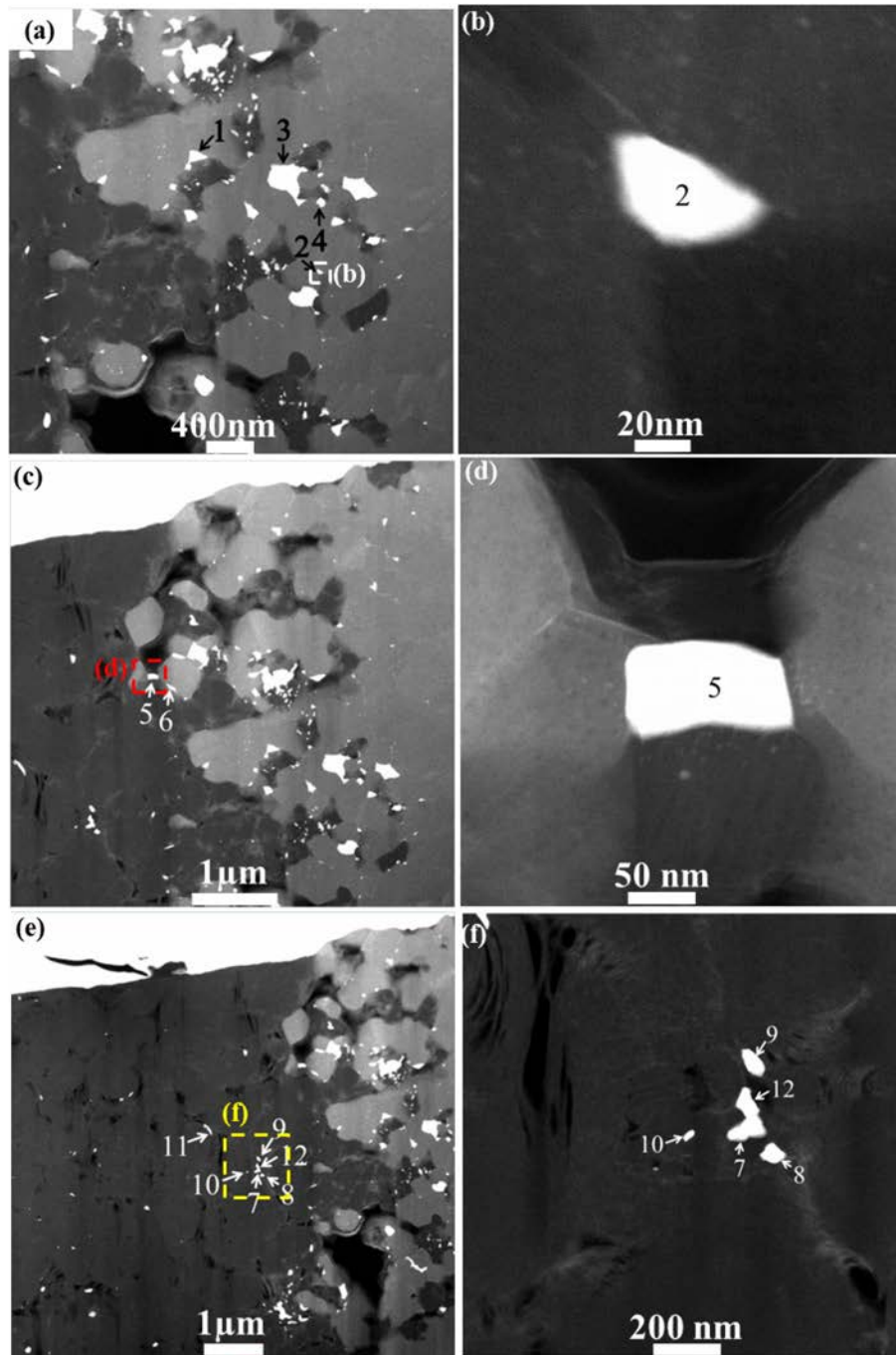


Figure 129. Images (a) through (f) are STEM images of precipitates in TEM Lamella 5 (across the IPyC-SiC interface), where precipitates indicated by arrows and numbers were subjected to an EDS point scan. The qualitative compositions corresponding to the EDS point scans are displayed in Table 70. Images (a), (c), and (e) are of low-magnification and show the locations of the investigated precipitates relative to the IPyC-SiC interface, and (b), (d), and (f) are higher magnification images showing the exact precipitates on which EDS point scans were performed. Precipitates 1 through 6 are in the SiC layer and Precipitates 7 through 12 are in the IPyC layer. The majority of the precipitates in the SiC layer are Pd-Si-U, Pd-U, or U, with a small fraction of Pd-Si and Pd (not shown in the figure). Precipitates in the IPyC layer are Pd-Si-U, Pd-Si, U-Si, or U.

Table 70. Representative composition of precipitates in TEM Lamella 5 (across the IPyC-SiC interface). These compositions correspond to precipitates indicated in Figure 129. The 0.2 at.% is taken as the detection limit for Pd, Ag, Cs, and Ce and 0.1 at.% for U. Any element with a concentration below the detection limit is considered to not be present.

Precipitate Number	Concentration (at.%)												Precipitate Identification
	C	O	Si	U	Pd	Cd	Ag	Cs	Ce	Sr	I	Te	
Point Scan 1	39.4	0.4	48.7	1.5	9.8	0	0.1	0	0	0.1	0	0	Pd-Si-U
Point Scan 2	60.5	0	33.8	5.0	0.6	0	0	0	0	0.1	0	0	U-Pd
Point Scan 3	28.2	0	28.9	0.6	42.3	0	0	0	0	0	0	0	Pd-U
Point Scan 4	78.3	0.1	18.0	3.6	0	0	0	0	0	0	0	0	U
Point Scan 5	79.2	0	9.3	1.5	8.9	0.1	0	0.1	0.3	0.6	0	0	Pd-U-Ce-Sr
Point Scan 6	8.3	1.2	79.3	8.6	0.9	0	0	0.1	0	0.7	0	0.8	U-Si-Pd-Sr-Te
Point Scan 7	88.2	1.0	4.0	0	6.7	0	0	0.1	0	0	0	0	Pd
Point Scan 8	96.5	0.3	1.3	1.6	0	0.1	0	0	0	0.2	0	0	U
Point Scan 9	80.9	0.2	7.7	1.8	7.3	0.1	0	0	0.2	1.2	0.2	0.2	Pd-U-Ce-Sr-I-Te
Point Scan 10	96.4	0.4	0.6	2.2	0.1	0.1	0.1	0	0	0	0	0	U
Point Scan 11	83.9	1.7	6.0	0.6	7.5	0	0.1	0	0	0	0	0	Pd-U
Point Scan 12	83.0	0.2	8.0	1.2	7.4	0	0	0	0	0.3	0	0	Pd-U-Sr

**3.4.3.1.3 Lamella 2.** Chemical composition and precipitate distribution are discussed in detail by Wen et al., (2015a). EDS point scans were conducted on numerous precipitates in the SiC layer in TEM Lamella 2. Figure 130 shows lower magnification images of Lamella 2, where bright specs in Figure 130(b) represent precipitates. Figure 131 shows precipitates with representative compositions, and Table 71 indicates the compositions of the precipitates labeled in Figure 131 on which EDS point scans were performed. From STEM images in Figure 131(b), Figure 131(d), and Figure 131(f), it is evident that an extensive network of small precipitates is present in the SiC layer, both at the grain boundaries and inside grain interiors. Precipitates at the grain boundaries are generally larger than those inside the grain interiors. Note that Precipitates 1 through 5 are almost right at the IPyC-SiC interface, Precipitates 6 and 7 are about 500 nm away from the IPyC-SiC interface, Precipitates 8 and 9 are about 2.5  $\mu\text{m}$  from the interface, and Precipitates 10 and 11 are about 9  $\mu\text{m}$  from the interface. From the EDS results, precipitates in the SiC layer have the following types of compositions: Pd-Si-U, Pd-Si, Pd, Pd-U, U, and U-Si. It should be noted that only a few precipitates inside grain interiors were analyzed by EDS and these precipitates contain only Pd.

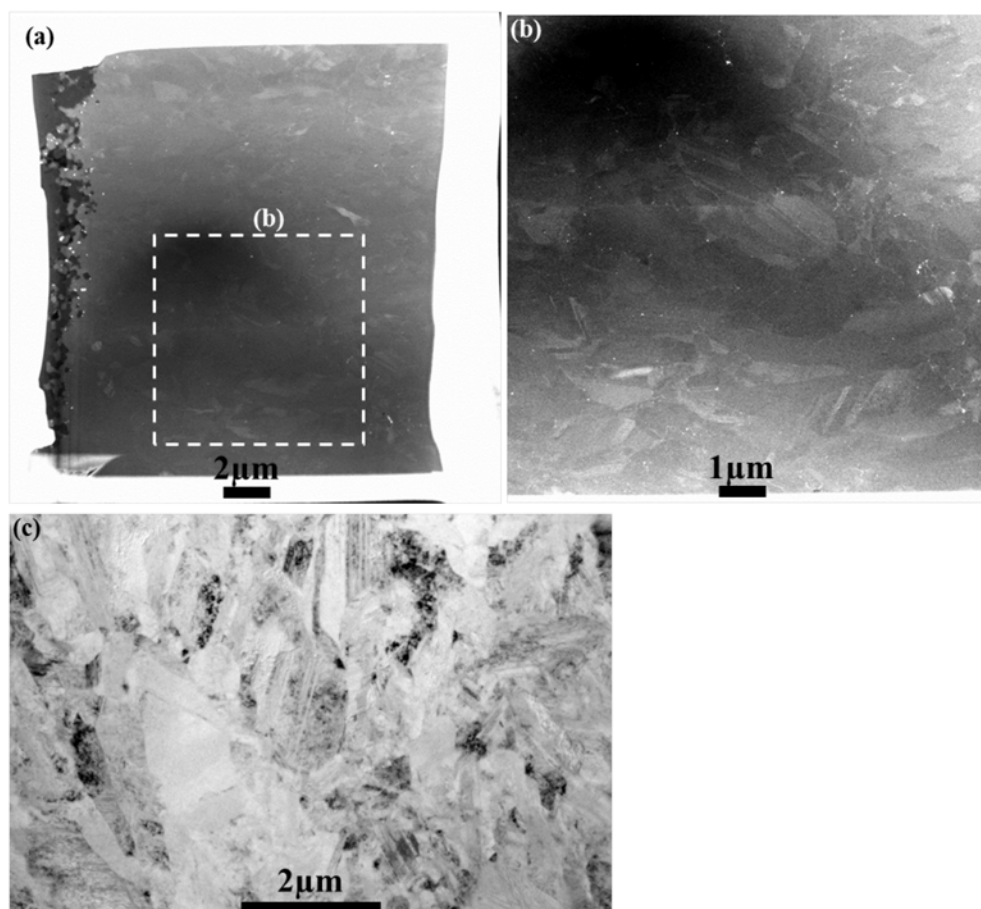


Figure 130. (a) and (b) STEM images of TEM Lamella 2 (from the inner region of the SiC layer), with different magnifications, showing the whole sample (a) and part of the sample (b). (c) TEM image of a selected area.

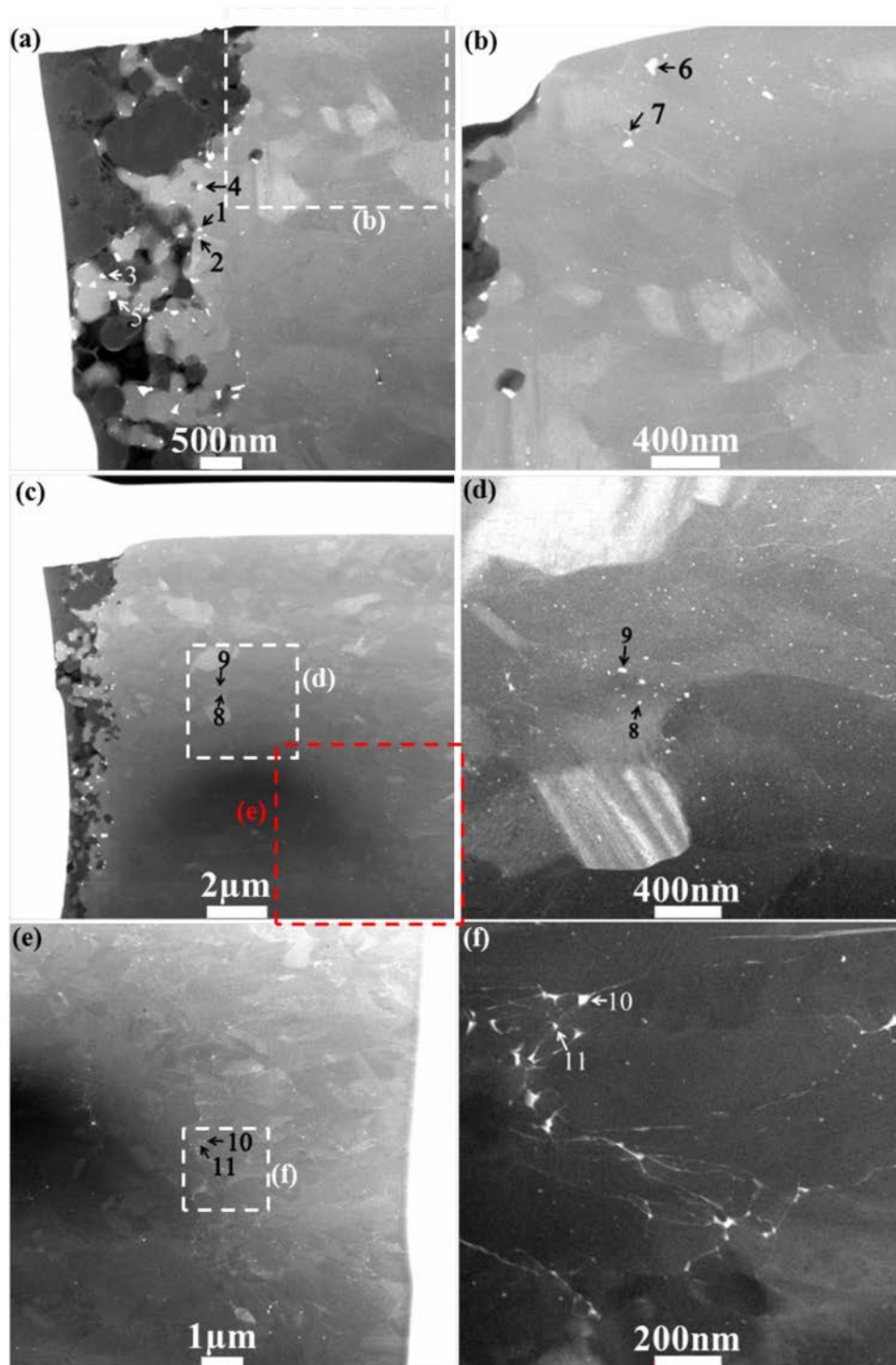


Figure 131. STEM images of precipitates in TEM Lamella 2 (from the inner region of the SiC layer), where precipitates indicated by arrows and numbers were subjected to EDS point scan. The quantified compositions corresponding to the EDS point scans are displayed in Table 71. Precipitates are Pd-Si-U, Pd-Si, Pd-U, Pd, U, or U-Si.

Table 71. Representative compositions of precipitates in TEM Lamella 2 (from the inner region of the SiC layer). These compositions correspond to precipitates indicated in Figure 131. A 0.2 at.% is taken as the detection limit for Pd, Ag, Cs, and Ce and 0.1 at.% for U. Any element with a concentration below the detection limit is considered to not be present.

Precipitate Number	Concentration (at.%)												Precipitate Identification
	C	O	Si	U	Pd	Cd	Ag	Cs	Ce	Sr	I	Te	
Point Scan 1	34.6	0.1	58.1	1.2	5.6	0.1	0.1	0	0.1	0	0	0	Pd-Si-U
Point Scan 2	46.6	0.4	52.0	1.0	0	0	0	0	0	0	0	0	U-Si
Point Scan 3	90.2	0.3	8.0	1.5	0	0	0	0	0	0	0	0	U
Point Scan 4	42.6	0.1	50.5	1.2	5.5	0	0	0	0	0.1	0	0	Pd-Si-U
Point Scan 5	57.6	0.3	34.3	1.1	6.5	0	0	0	0.1	0.2	0	0	Pd-U-Sr
Point Scan 6	31.8	1.0	56.5	0.3	10.4	0	0.1	0	0	0	0	0	Pd-Si-U
Point Scan 7	41.1	0	54.7	0	4.2	0	0	0	0	0	0	0	Pd-Si
Point Scan 8	37.8	0	54.0	0	8.0	0.1	0.1	0	0	0	0	0	Pd-Si
Point Scan 9	20.9	0.9	68.2	0	9.6	0.1	0	0	0	0	0.1	0.2	Pd-Si-Te
Point Scan 10	53.4	0.1	37.3	0	9.1	0	0	0	0	0	0	0	Pd
Point Scan 11	60.2	0.2	36.2	0.2	3.2	0	0	0	0	0	0	0	Pd-U

### 3.4.3.2 Chemical Composition in the Center Area of the Silicon Carbide Layer (Lamella 4).

**3.4.3.2.1 Lamella 4.** AGR1-131-099 Lamella 4 was sectioned from the middle region of the SiC layer. Figure 132 shows STEM and TEM images of this lamella. From STEM images, only a moderate number density of precipitates is evident in this lamella. From TEM images, SiC grain diameters are on the order of 1  $\mu\text{m}$ , which are larger than the SiC grain sizes close to the IPyC-SiC interface.



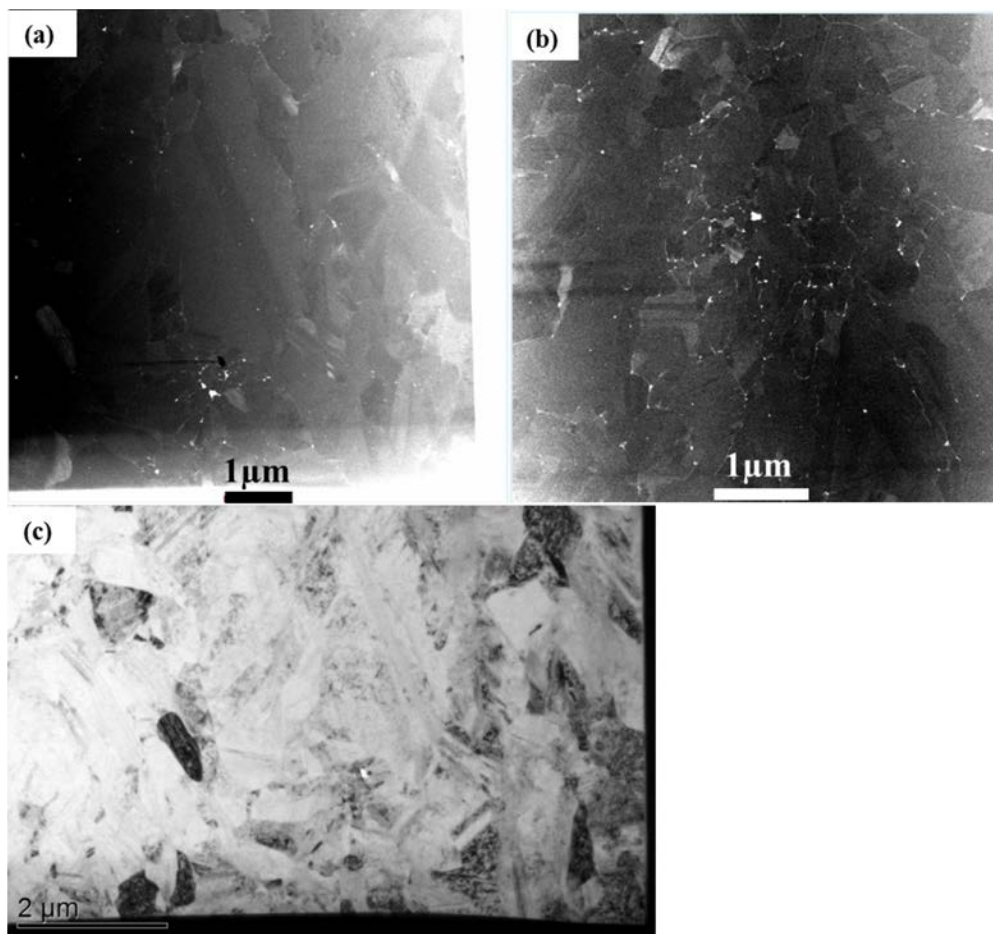


Figure 132. (a) (b) STEM images and (c) TEM image of AGR1-131-099 Lamella 4 that was sectioned from the middle region of the SiC layer.

Figure 133 shows STEM images of precipitates in the middle region of the SiC layer, where precipitates indicated by arrows or circles were subjected to EDS composition analyses. Figure 133(a) is a low magnification STEM image, (b) is a magnification of the red rectangle in (a), and (c) is a magnification of the blue rectangle in (a). Figure 133(b) and (c) are two areas in the Lamella where larger precipitates and a higher number density of precipitates are found. With increased distance from the IPyC-SiC interface, a network of precipitates become less evident, more precipitates are located at grain boundaries, few precipitates are located inside grain interiors, and precipitates become smaller. The precipitate compositions from EDS are displayed in Table 72. From EDS results, precipitates are Pd and Pd-U and the fraction of Pd is higher than that of Pd-U. It is evident that with increased distance from the IPyC-SiC interface, the number density of U-containing precipitates in the SiC layer decreases.



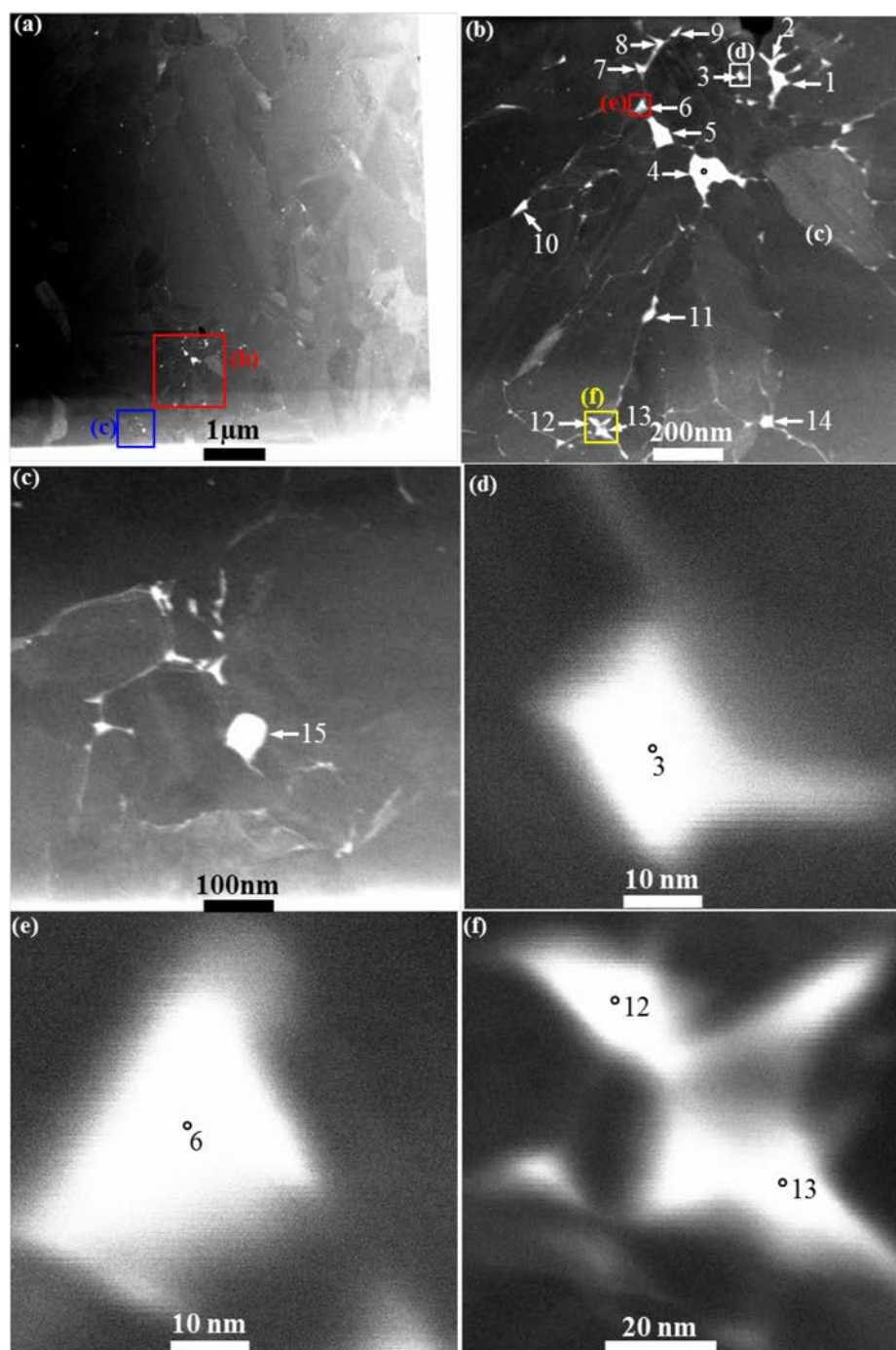


Figure 133. STEM images of precipitates in TEM Lamella 4 (in the middle region of the SiC layer), where precipitates indicated by arrows were subjected to EDS composition analyses. The quantified compositions correspond to the EDS point scans are displayed in Table 72. Precipitates are Pd or Pd-U. A small fraction of Pd-Si-U precipitates is also present in the TEM lamella, but is not shown in this figure.

Table 72. Representative qualitative compositions of precipitates in TEM Lamella 4 (from the middle region of the SiC layer). These compositions correspond to precipitates indicated in Figure 133. A 0.2 at.% is taken as the detection limit for Pd, Ag, Cs, and Ce and 0.1 at.% for U. Any element with a concentration below the detection limit is considered to not be present.

Precipitate Number	Concentration (at.%)											Precipitate Identification	
	C	O	Si	U	Pd	Cd	Ag	Cs	Ce	Sr	I		Te
Point scan 1	49.27	0	40.88	1.58	8.04	0.11	0	0	0	0.08	0	0	Pd-U
Point scan 2	52.13	0	43.78	0.86	3.12	0	0	0	0	0.01	0	0.07	Pd-U
Point scan 3	67.97	0	31.03	0.61	0.24	0.01	0	0.02	0	0	0	0.07	Pd-U
Point scan 4	37.72	0	21.29	0	40.98	0	0	0	0	0	0	0	Pd
Point scan 5	43.93	0.46	24.57	0	31.03	0	0	0	0	0	0	0	Pd
Point scan 6	65.01	0.32	30.42	0.02	4.19	0	0.02	0	0	0	0	0	Pd
Point scan 7	61.41	0	34.17	0.72	3.52	0	0.1	0	0	0.03	0	0	Pd-U
Point scan 8	56.6	0.36	32.29	0	10.7	0	0	0	0	0.02	0	0	Pd
Point scan 9	58.39	0	33.48	0	8.05	0	0.06	0	0	0	0	0	Pd
Point scan 10	50.32	2.03	33.82	0	13.8	0	0	0	0	0	0	0	Pd
Point scan 11	56.25	0.28	36.42	0	6.91	0.02	0.09	0	0	0	0	0	Pd
Point scan 12	55.09	0	37.08	0	7.79	0	0.02	0	0	0	0	0	Pd
Point scan 13	57.19	0.43	35.98	0	6.32	0	0.05	0	0	0	0	0	Pd
Point scan 14	48.66	0.13	38.37	0	12.71	0	0.1	0	0	0	0	0	Pd
Point scan 15	51.21	0	43.21	1.56	3.99	0	0	0	0	0	0	0	Pd-U

### 3.4.3.3 Chemical Composition in the Outer Area of the Silicon Carbide Layer

(**Lamella 3**). STEM and TEM images of Lamella 3 which was sectioned from the outer region of the SiC layer are displayed in Figure 134. Only a low-number density of precipitates is evident from the low-magnification STEM image. From the TEM image, the grain diameters in the SiC layer are on the order of 2  $\mu\text{m}$ , which is larger than the grain diameters (1  $\mu\text{m}$ ) observed in the middle of the SiC layer and larger than the grain diameters (0.2 to 0.3  $\mu\text{m}$ ) observed at the IPyC-SiC interface. Numerous precipitates in the SiC layer in TEM Lamella 3 were also analyzed using EDS point scans. Figure 135 displays precipitates with representative compositions and Table 73 indicates the compositions of the precipitates labeled in Figure 135 on which EDS point scans were performed. Note that in Figure 135(a) and Figure 135(f), from left to right, the distance from the IPyC-SiC interface is increased. Therefore, in Figure 135, Precipitates 14 and 15 are closest to the IPyC-SiC interface.

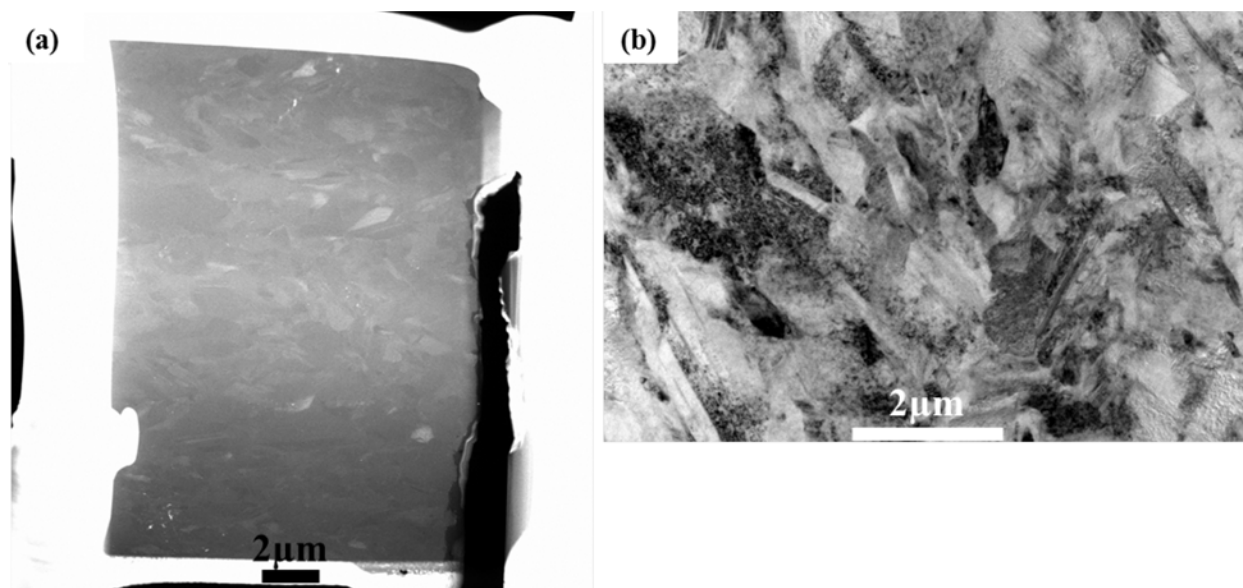


Figure 134. (a) STEM image of TEM Lamella 3 (from the outer region of the SiC layer) and showing the whole sample; (b) TEM image of a selected area.

Table 73. Representative compositions of precipitates in TEM Lamella 3 (from the outer region of the SiC layer). These compositions correspond to precipitates indicated in Figure 135. A 0.2 at.% is taken as the detection limit for Pd, Ag, Cs, and Ce and 0.1 at.% for U. Any element with a concentration below the detection limit is considered to not be present.

Precipitate Number	Concentration (at.%)												Precipitate Identification
	C	O	Si	U	Pd	Cd	Ag	Cs	Ce	Sr	I	Te	
Point Scan 1	27.7	0	59.5	4.3	8.2	0	0	0	0	0.3	0	0	Pd-Si-U-Sr
Point Scan 2	30.8	0.1	59.9	2.9	6.3	0	0	0	0	0	0	0	Pd-Si-U
Point Scan 3	29.3	0	63.4	0	7.2	0	0	0	0	0	0	0	Pd-Si
Point Scan 4	29.7	0.2	59.1	0	11.1	0	0	0	0	0	0	0	Pd-Si
Point Scan 5	6.5	0.3	73.6	6.2	12.8	0	0.1	0.1	0	0.2	0	0.3	Pd-Si-U-Sr-Te
Point Scan 6	31.8	0	64.9	0.6	2.6	0.1	0	0	0	0	0	0	Pd-Si-U
Point Scan 7	26.6	0.3	61.1	2.4	9.5	0	0	0	0.1	0	0	0	Pd-Si-U
Point Scan 8	19.9	0	69.3	0	10.8	0	0	0	0	0	0	0	Pd-Si
Point Scan 9	20.8	0	64.0	0	15.2	0	0	0	0	0	0	0	Pd-Si
Point Scan 10	34.1	0.5	61.8	0	3.5	0	0	0	0	0	0	0	Pd-Si
Point Scan 11	24.1	0	67.0	0	8.8	0	0.1	0	0	0	0	0	Pd-Si
Point Scan 12	22.9	0.2	72.4	0	4.5	0	0	0	0	0	0	0	Pd-Si
Point Scan 13	21.7	0	73.2	1.1	4.0	0	0	0	0	0	0	0	Pd-Si-U
Point Scan 14	35.7	0.4	55.4	2.3	6.2	0	0	0	0	0.1	0	0	Pd-Si-U
Point Scan 15	32.1	1.1	49.4	0	17.3	0	0	0	0	0	0	0	Pd-Si

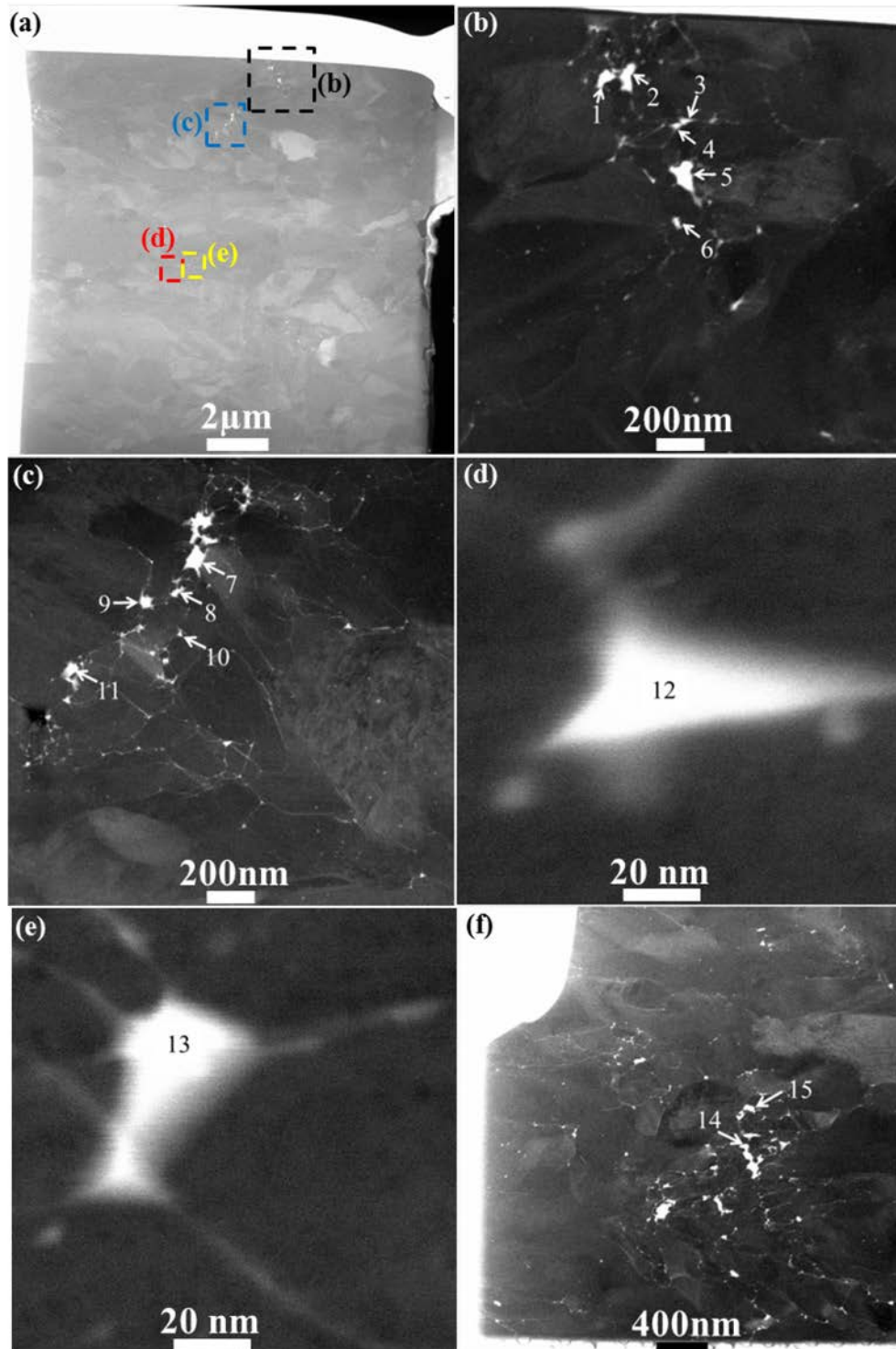


Figure 135. STEM images of precipitates in TEM Lamella 3 (from the outer region of the SiC layer), where precipitates indicated by arrows and numbers were subjected to EDS point scan. The quantified compositions corresponding to the EDS point scans are displayed in Table 73. Precipitates are Pd-Si-U or Pd-Si. A small fraction of Pd precipitates is also present in the TEM lamella, but is not shown in this figure.

### 3.4.4 Crystallographic Information Obtained on Particle AGR1-131-099

Figure 125 shows the TEM Lamella with the areas analyzed marked with red boxes for Lamella 2, inner and Lamella 4, center, respectively, from Particle AGR1-131-099. For Lamella 2, only SiC orientation data were collected; no compositional data on any precipitates were collected. However, both SiC orientation information and compositional data of the grain boundary precipitates were collected for Lamella 4.

**3.4.4.1 General Grain Boundary Distributions for the Inner (Lamella 2) and Center (Lamella 4) Regions.** The PED-derived grain orientation maps of the areas analyzed on the center sample (Lamella 4) Figure 125(b), are shown in Figure 136. The other grain orientation maps for Lamella 2 can be found in Lillo et al., (2017). The grain boundary distributions derived from the SiC grain orientation data are shown in Figure 137 for the four areas analyzed in Lamella 4, Figure 125(b). In addition to the individual distributions for each area that was analyzed, there is also an averaged distribution consisting of all data from all four areas. The averaged distributions also contain standard error bars based on the statistical variation between the four areas. A similar analysis was performed on data from the areas in Lamella 2 and the averaged distributions for Lamellae 2 and 4 are compared.

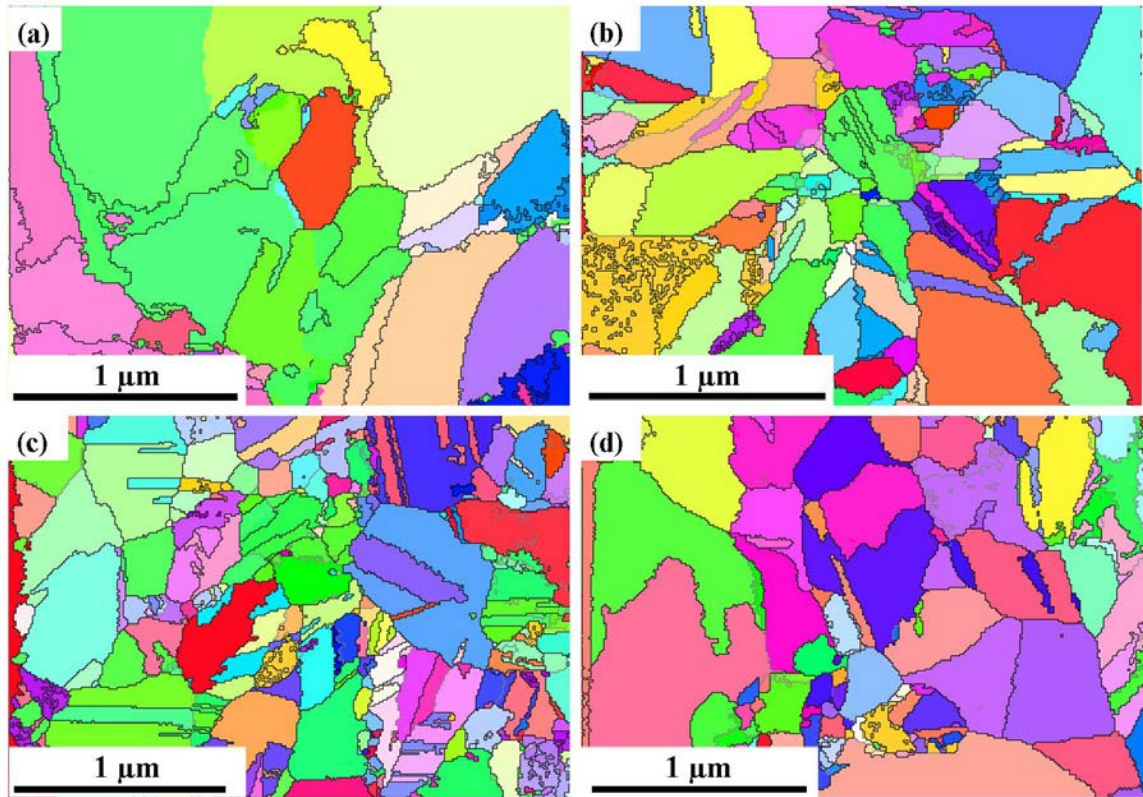


Figure 136. SiC grain orientation maps for (a) Area 1, (b) Area 2, (c) Area 3, and (d) Area 4 from Lamella 4 (center), Figure 125(b), of AGR1-131-099.



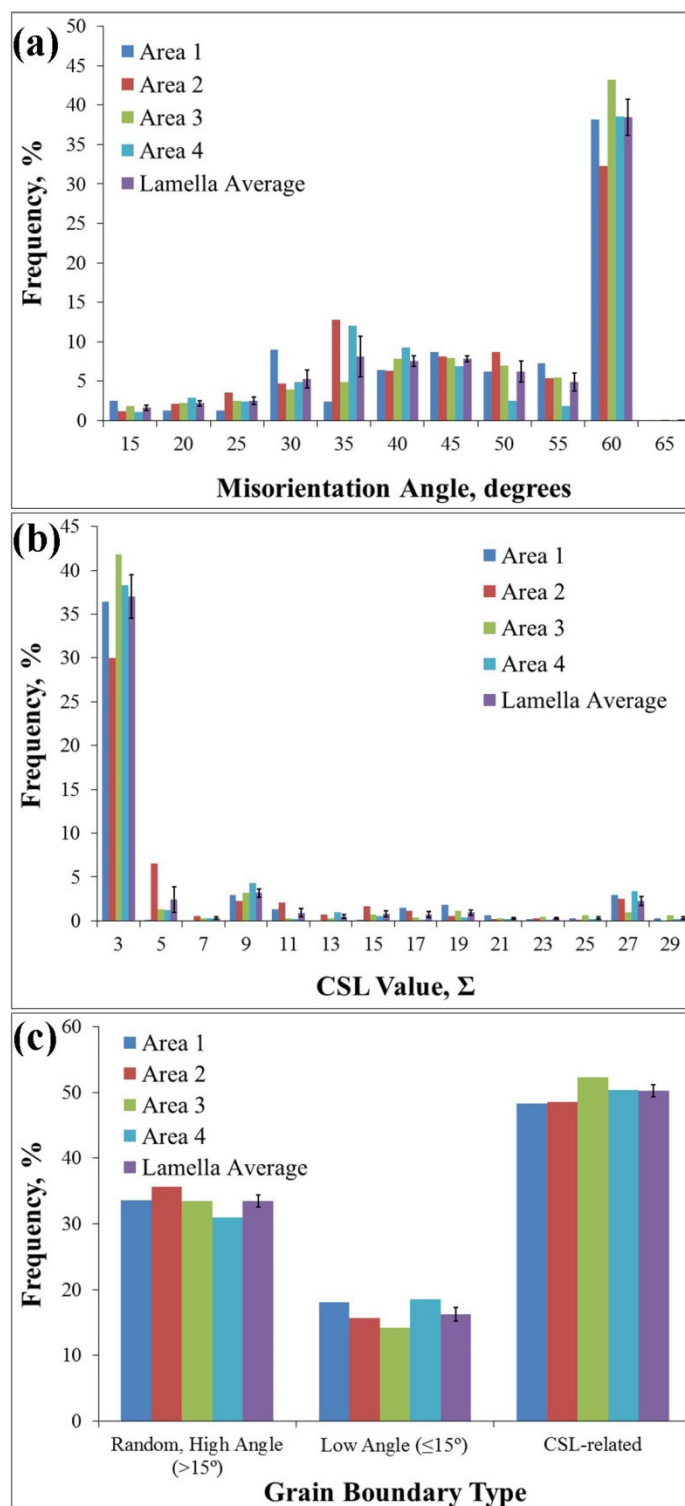


Figure 137. Distributions of the (a) grain boundary misorientation angle, (b) CSL distribution, and (c) grain boundary type for the areas in Lamella 4. The averaged distributions for Lamella 4 are included and are a combination of all data from all four areas.

**3.4.4.2 Misorientation Angle Distribution.** The distributions for the inner and center samples are shown in Figure 138(a). Both distributions are quite similar and exhibit a high fraction of twin grain boundaries ( $\theta = 60$  degrees) with a secondary peak in the distributions around 40 degrees. Statistically, the two distributions are identical.

**3.4.4.3 Distributions of Coincident Site Lattice-Related Grain Boundaries.** Figure 138(b) shows the distributions of grain boundaries that exhibit a CSL relationship. Again, twin boundaries, identified by a CSL value of  $\Sigma 3$ , represent the major fraction of CSL-related grain boundaries. Higher order twins (i.e.,  $\Sigma 9$  and  $\Sigma 27$ ) comprise the majority of the remaining CSL-related grain boundaries. Again, the distributions for Sites 2 and 4 are virtually identical. If the two data sets are combined, the resulting fractions of the twins and higher order twins are shown in Table 74. Values of 27%, 5%, and 1% for  $\Sigma 3$ ,  $\Sigma 9$ , and  $\Sigma 27$ , respectively, are reported in the literature (Kirchhofer et al., 2013) for the SiC layer from an unirradiated AGR-1 TRISO particle made with Variant 3 parameters. This irradiated particle exhibits a significantly higher  $\Sigma 3$  twin boundary fraction, although no statistical error is reported for the Kirchhofer data. It is not known at this time whether irradiation effects, data acquisition methods (SEM-based versus TEM-based), or simply particle-to-particle variations are responsible for this difference. Analysis of additional irradiated and unirradiated particles will be necessary to determine the specific cause of the observed differences.

Table 74. Average fraction of twin-related grain boundaries in the SiC layer of Particle AGR1-131-099.

CSL value, $\Sigma$	Fraction, %	Std. Error
3	40.3	1.9
9	3.5	0.2
27	1.9	0.2

**3.4.4.4 Distribution by Grain Boundary Type.** Figure 138(c) compares the types of grain boundaries present in both lamellae. CSL-related grain boundaries represent the major fraction of grain boundaries while random, high-angle grain boundaries are also present in significant numbers. Generally, low-angle grain boundaries represent about 18% of all grain boundaries in these areas. Again, there appears to be little difference in the two distributions.

The values in Table 75 show the grain boundary fractions after combining data from Lamellae 2 and 4. Values reported by Kirchhofer et al., 2013 for low-angle, random, high-angle, and CSL-related grain boundary fractions for the SiC layer in an unirradiated, Variant 3 TRISO particle are 21%, 39%, and 40%, respectively, which is significantly different than found in this study. Again, reasons for these differences are not clear at this time and can only be resolved by analysis of additional irradiated and unirradiated particles.

Table 75. Average fraction of grain boundary types in the SiC layer of Particle AGR1-131-099.

Grain Boundary Type	Fraction, %	Std. Error
Low angle, <15 degrees	17.8	0.9
High angle, >15 degrees	29.1	2.5
CSL-related	53.1	1.6

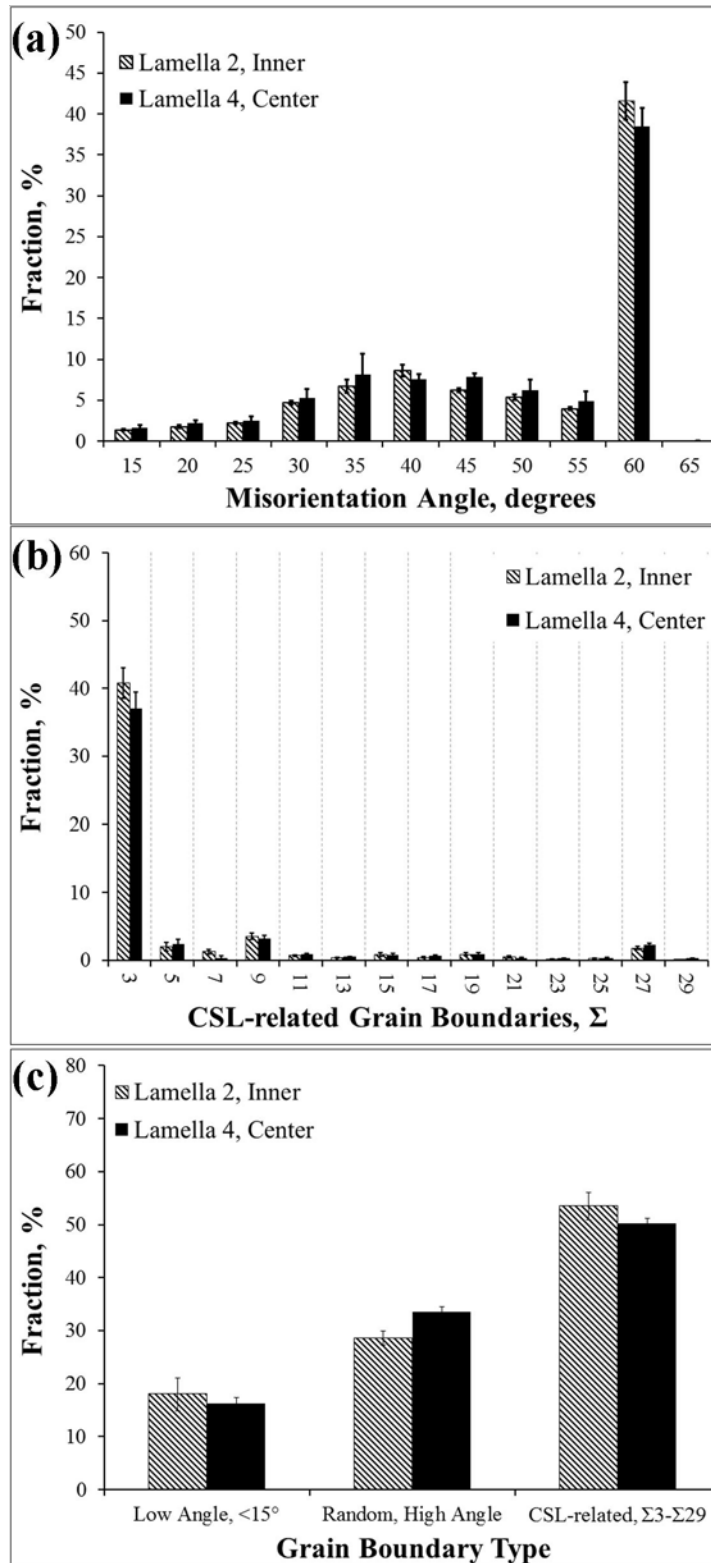


Figure 138. Distributions averaged over all areas analyzed for each sample: (a) misorientation angle, (b) CSL designation, and (c) grain boundary type for the SiC grain boundaries for samples taken from AGR1-131-099.



### 3.4.4.5 Grain Boundary Data for Grain Boundaries Containing Fission Product

**Precipitates.** The qualitative composition of fission product precipitates obtained using EDS was correlated with information about the grain boundaries on which they resided. This correlation was performed on fission product precipitates only in Lamella 4 (center area) Figure 125(b). The correlation data are summarized in Table 76. Generally, fission product precipitates are found most often on random, high-angle grain boundaries (Figure 139) and contain only Pd or Pd with U (Figure 140). However, fission product precipitates do occur on CSL-related grain boundaries, but rarely on low-angle grain boundaries (Figure 139 and Table 76).

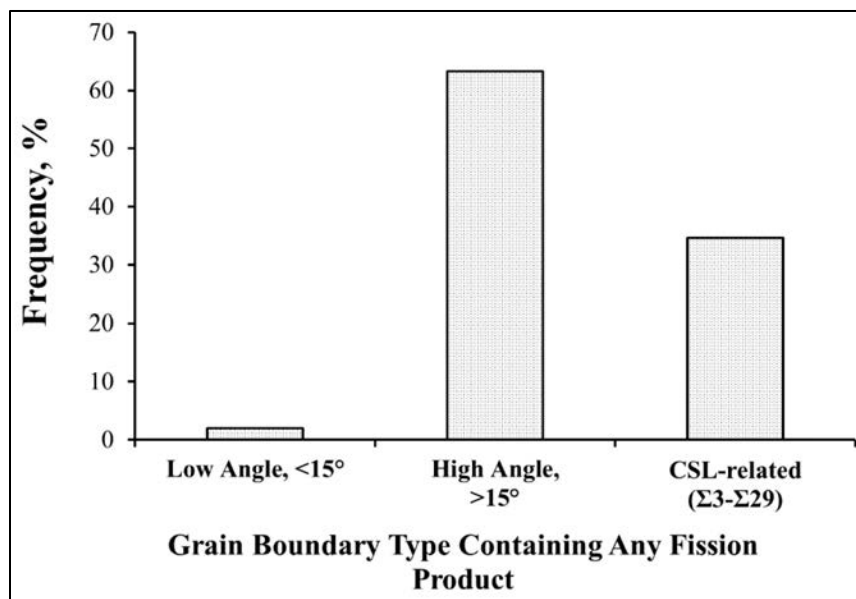


Figure 139. Distribution of grain boundary types that contained any fission product precipitate for Lamella 4 (center) AGR1-131-099, Figure 125(b).

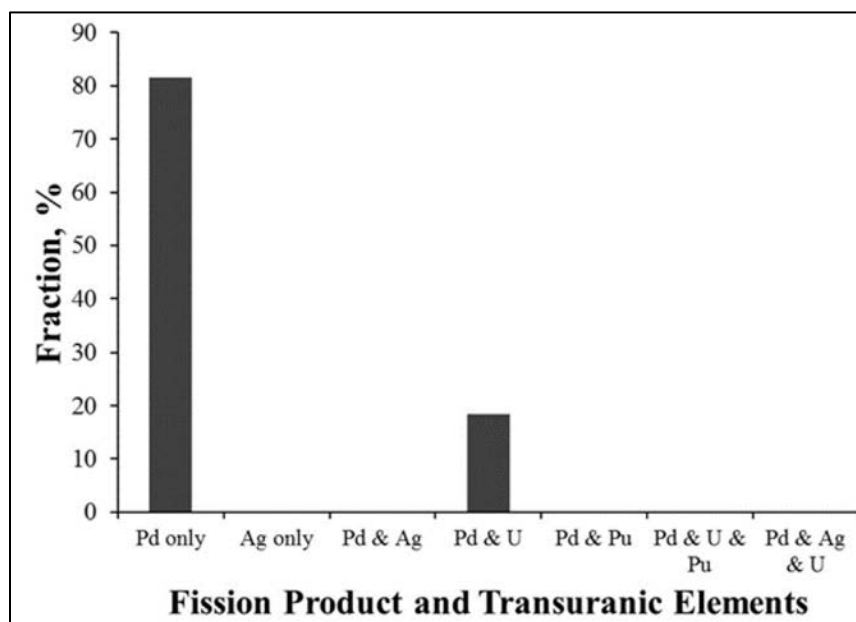


Figure 140. Composition distribution of the grain boundary precipitates for Lamella 4 (center) AGR1-131-099, Figure 125(b).

Table 76. Summary of the distribution of fission product elements.

	Pd Only	Ag only	U only	Pd and Ag	Pd and U	Pd+Pu	Pd+U+Pu	Pd+Ag+U
<b>Lamella 4, Center Sample</b>								
Number of grain boundaries	40	0	0	0	9	0	0	0
Fraction of all boundaries with fission products, %	81.6	0.0	0.0	0.0	18.4	0.0	0.0	0.0
Low angle, %	2.5	—	—	—	0.0	—	—	—
Random, high angle, %	62.5	—	—	—	66.7	—	—	—
CSL, %	35.0	—	—	—	33.3	—	—	—

**3.4.4.6 Discussion of Results for Particle AGR1-131-099.** The database on the correlation between fission product precipitates and grain boundary parameter contains only four areas within the center region and resulted in only 49 precipitates that were correlated with grain boundary information. However, the trends are similar to those for the other particles analyzed in this work and reported in other sections. Specifically, it appears that:

- About 82% of the precipitates contain only Pd; sometimes U is also present with Pd while ~18% of the precipitates contain U as well as Pd, as shown in Table 76.
- Fission product precipitates prefer random, high-angle grain boundaries although they can occur on CSL-related boundaries and, to a much lesser extent, low-angle grain boundaries.
- Pd-only fission product precipitates occur on low-angle, random high-angle, and CSL-related grain boundaries, while Pd and U precipitates occur only on random, high-angle and some CSL-related grain boundaries (Figure 141). Pd and U precipitates were not found on low-angle grain boundaries.
- Ag, Pu, or any other fission product elements were not found in any of the precipitates that could be correlated with grain boundary parameters (Figure 141).

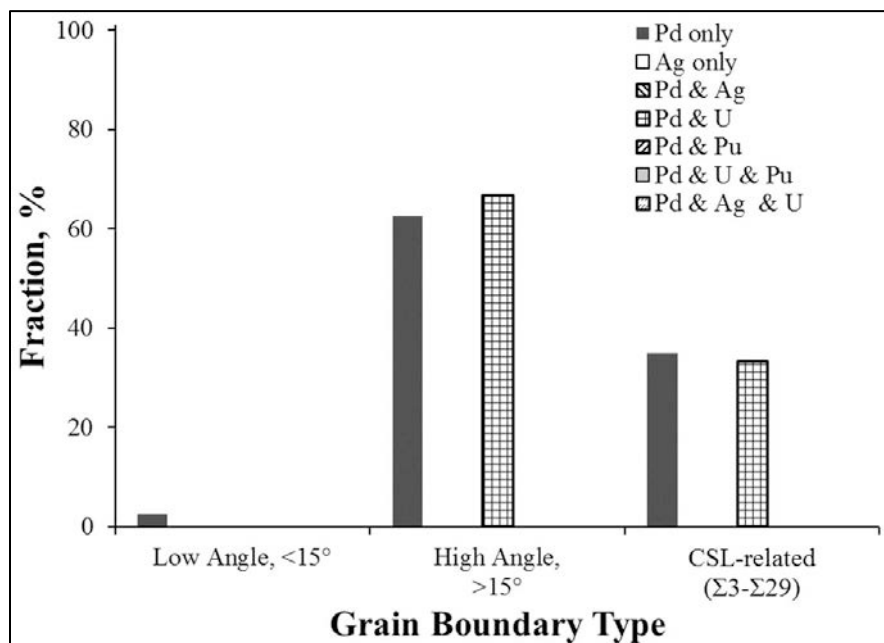


Figure 141. Distribution of fission product elements, as a percentage, by grain boundary type AGR1-131-099.

### 3.4.5 Precipitate Phase and Structure Evaluation (High-Resolution Transmission Electron Microscopy Performed at Los Alamos National Laboratory)

Preliminary HRSTEM of Particle AGR1-131-099, Lamella 1, was performed on May 21, 2015, at LANL, using an FEI Titan 80-300TM with 0.07 nm and 0.20 nm TEM and STEM resolution, respectively. This initial work was performed to establish a U.S.-based facility in lieu of the successful research conducted in 2013 at the Nelson Mandela Metropolitan University (NMMU) electron microscopy facility, in South Africa. The preliminary electron microscopy performed at LANL showed promise although the resolution is not as high as that from the NMMU JEOL ARM 200F TEM, which is equipped with two CEOS spherical aberration correctors.

Figure 142 to Figure 144 are examples of the microscopy performed at LANL that demonstrate the additional information obtained from this work. A SiC grain and precipitate interface was investigated with the goal of obtaining more knowledge on the phase and structure of the precipitate. Although analysis and interpretation are still in progress, a preliminary conclusion can be reached that the precipitate consists of one phase, as the fast Fourier transformation (FFT) of Areas 1, 2, 3, and 4 in Figure 144 shows that the crystal structure is identical with only slight misorientation differences. The small misorientation may be due to a difference in dislocation density between the top and bottom parts of the precipitate. This work will need to be continued in the future on a larger number of precipitates to establish a statistical base.

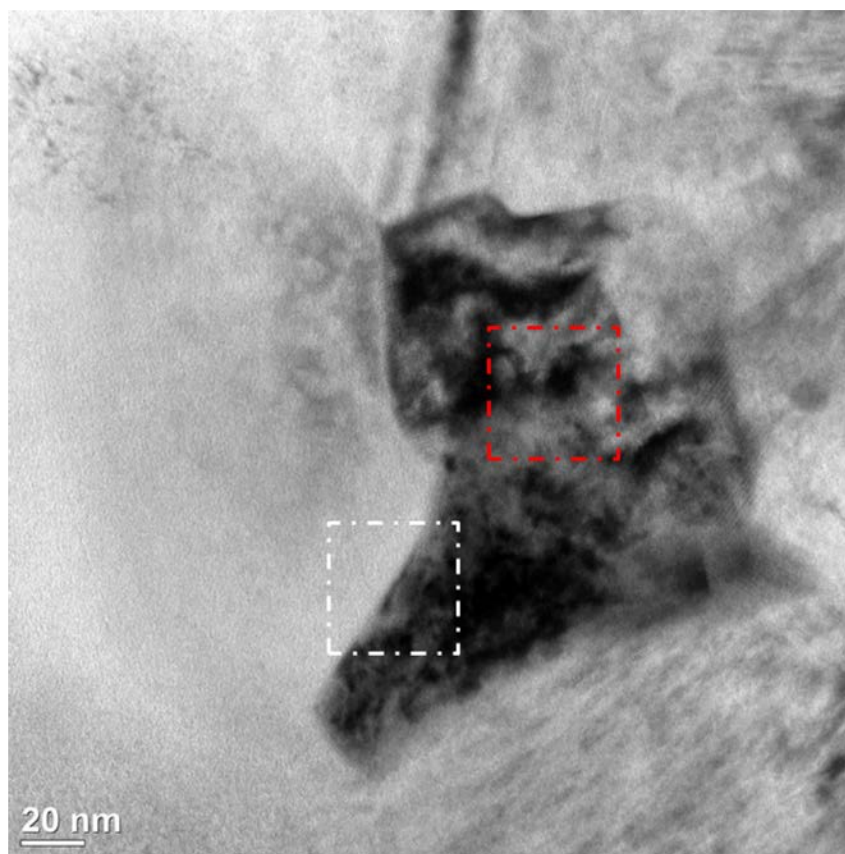


Figure 142. A precipitate at the SiC grain boundary.

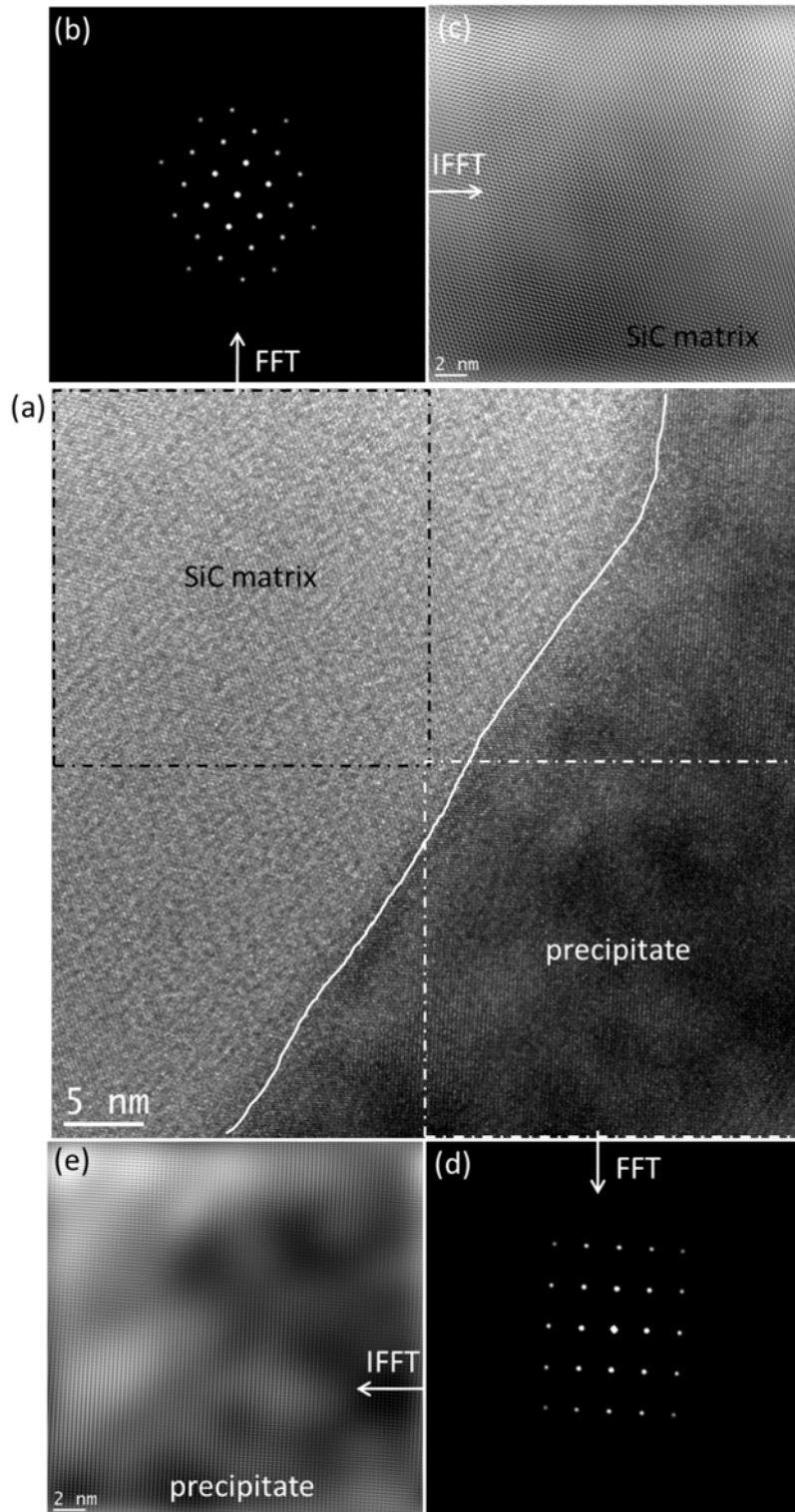


Figure 143. Interface between the precipitate in Figure 142 and the SiC matrix. (a) HRTEM showing the interface between the precipitate and the SiC matrix (a magnification of the white square in Figure 142); (b) FFT of the black square area in (a); (c) inverse FFT of (b); (d) FFT of the white square area in (a); and (e) inverse FFT of (d).

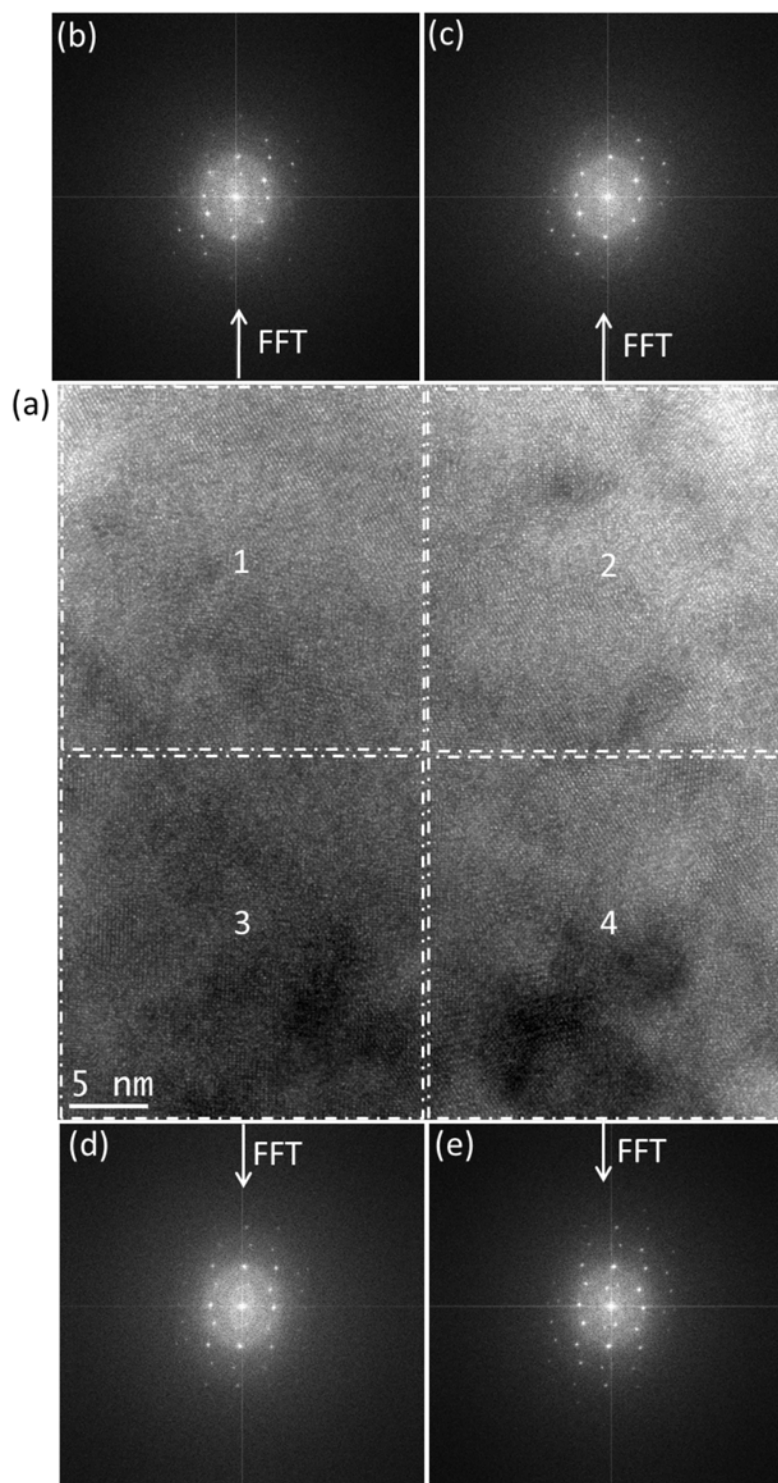


Figure 144. (a) HRTEM image of the precipitate in Figure 142 (a magnification of the red square in Figure 142); (b)(c)(d)(e) FFT of the areas 1, 2, 3, and 4 in (a), respectively. From (b) through (d), the top part of the precipitate has a slight misorientation (within a few degrees) with the bottom part of the precipitate; however, the crystal structure is identical. The small misorientation may be due to a difference in dislocation density between the top and bottom parts of the precipitate.

Subsequent HRSTEM examinations focused on chemical composition (including EDS point, line, and mapping analysis) of precipitates in Particle AGR1-131-099. Figure 145 shows a HRSTEM image and EDS elemental mapping of a small area containing precipitates in the IPyC layer close to the IPyC-SiC interface. From these maps, the large precipitate in the red rectangle area consists of multiple phases. The small part at the upper-left corner is U-Zr, whereas the other parts of the precipitate are Pd-Si with small concentrations of U and Pu. It should be noted that Pu L edges overlap with Sr K edges; however, other edges of Pu that do not overlap with Sr or other elements are also present. Therefore, it appears that Pu is present in the precipitate. This will be confirmed by a more detailed analysis. In addition, it is noted that significant Cs concentrations appear to be present in the IPyC area, with lower concentrations in the precipitate; this observation also needs to be confirmed with a more detailed analysis. Note that during EDS mapping, the dwell time for each point was only 4 seconds; therefore, it is considered as qualitative only.

Figure 146 shows an HRSTEM image and EDS elemental mapping of another small area containing precipitates in the IPyC layer close to the IPyC-SiC interface. From the maps, the two small precipitates (highlighted with red arrows) at the upper-left and lower-left corners are single-phase U-Zr. In contrast, the large precipitate at the upper-right corner has multiple phases. The top part of this precipitate is Pd-Si with concentrations of U, Pu, and Zr, whereas the bottom part is Pd-Si with a Zr concentration. Figure 147 shows an HRSTEM image and EDS mapping of an area containing precipitates in the SiC layer close to the IPyC-SiC interface. Precipitates 1 and 2 are single-phase precipitates and both of them are Pd-U-Pu. Precipitate 3 appears to be a multi-phase precipitate. The lower-left part of this precipitate is Pd with a small concentration of Zr, whereas the upper-right part is U-Pu. Note that multi-phase precipitates have also been found in other compacts. In STEM, fission product precipitates all appear bright; a precipitate that appears to have one single-phase may actually have multiple phases (the multiple phases all appear bright and cannot be distinguished in STEM). In EDS mapping or point analyses, the multiple phases in a precipitate can be distinguished if they have different compositions.

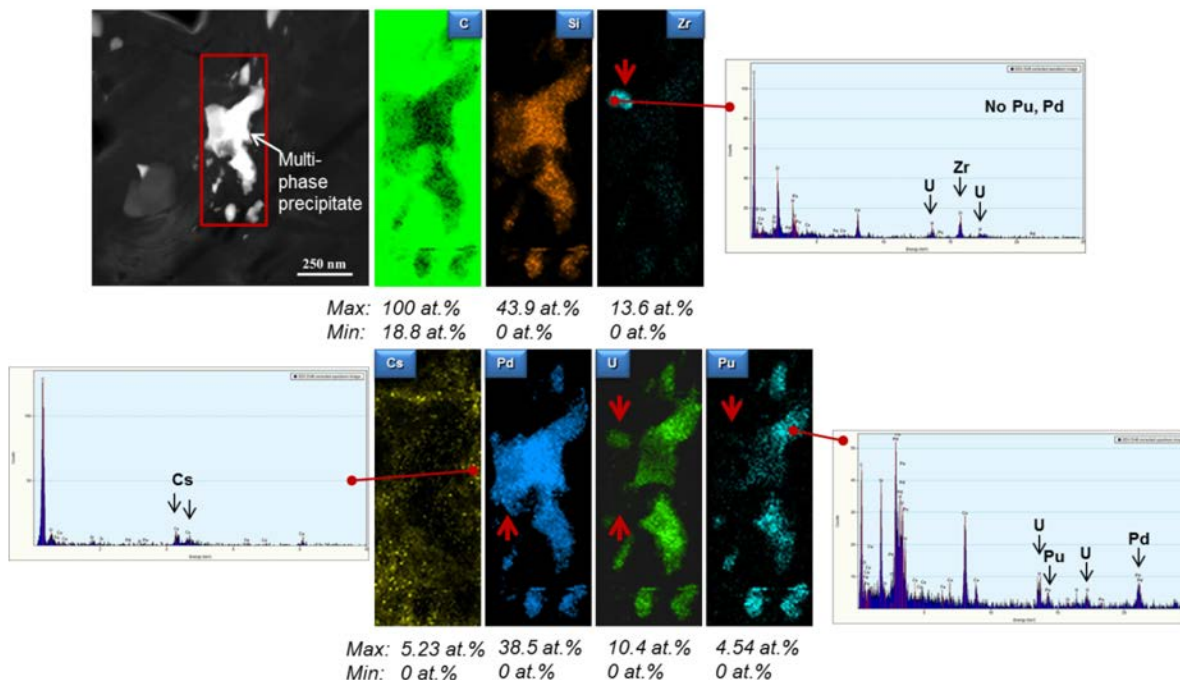


Figure 145. HRSTEM image and EDS mapping of a small area containing precipitates in the IPyC layer of Particle AGR1-131-099 close to the IPyC-SiC interface. Maximum and minimum concentration values for the elements with the maps are listed. The EDS spectra are extracted from the spectral maps.



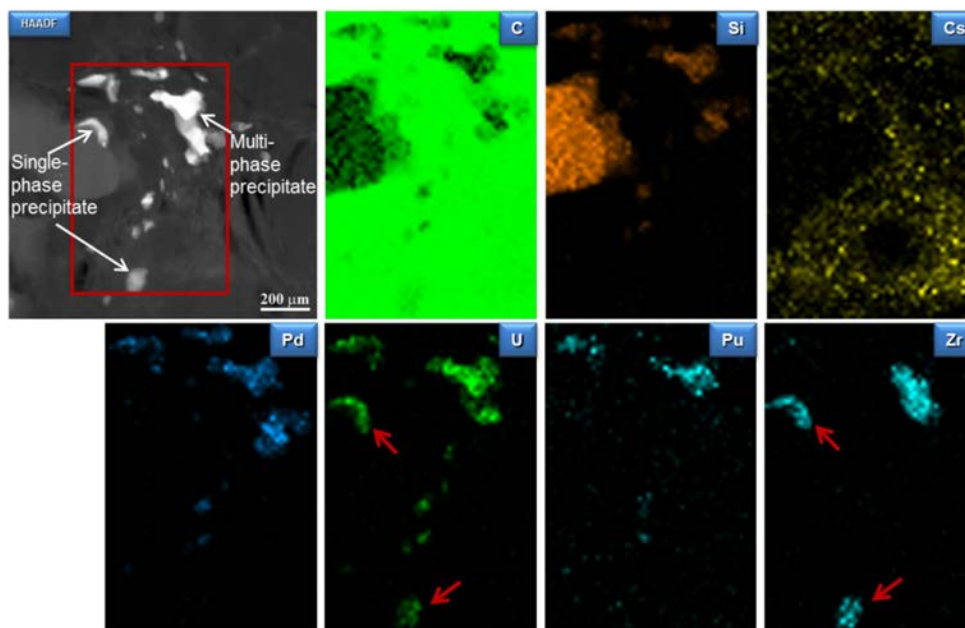


Figure 146. HRSTEM image and EDS mapping of a small area containing precipitates in the IPyC layer of Particle AGR1-131-099) close to the IPyC-SiC interface.

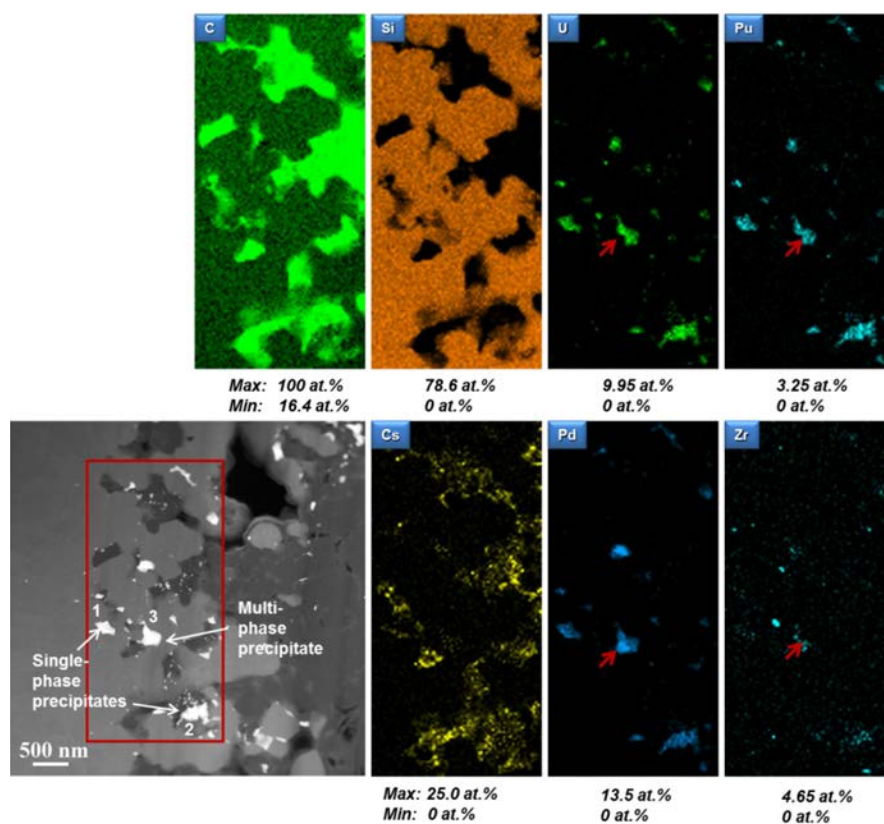


Figure 147. HRSTEM image and EDS mapping of an area containing precipitates in the SiC layer of Particle AGR1-131-099 close to the IPyC-SiC interface.



The interface between SiC and the fission product precipitate is well defined and free of porosity (Figure 148). From the change in the tilt of the atomic layers across this interface, it appears that the secondary phase is not aligned to the SiC in any well-defined manner.

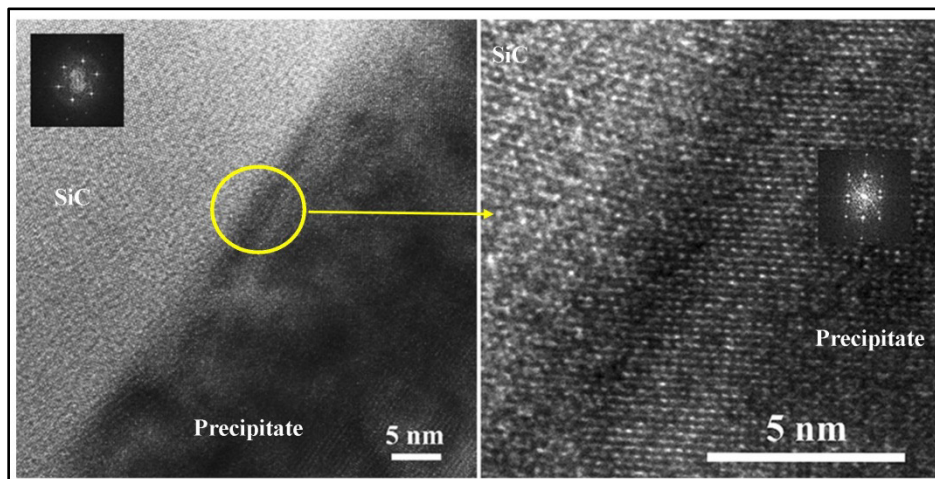


Figure 148. HRTEM images of the interface between a particle and the SiC matrix of Particle AGR1-131-099 Lamella 1.

High-resolution imaging of random grain boundary phases and precipitates is shown in Figure 149 and Figure 150, respectively. FFT of the indicated area in Figure 149 revealed lattice parameters consistent with  $\text{Pd}_2\text{Si}$ . The grain boundary precipitate shown in Figure 150 has some structure as suggested by the bands (i.e., arrows) rising from mass contrast in the image. (Chemical analysis of the structure was not obtained during this run of experiments.)

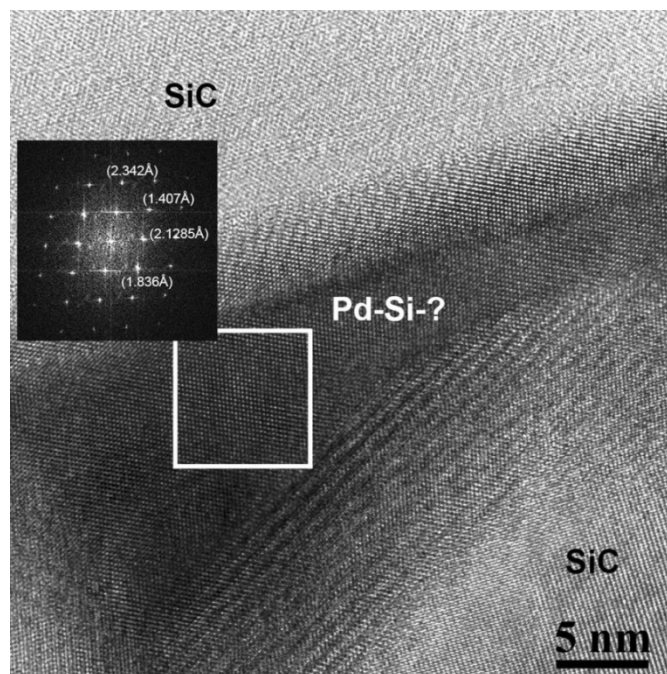


Figure 149. HRTEM image of a grain boundary phase in the SiC layer. The inset is a FFT of the area outlined by the box. Indicated lattice spacings are also shown and are consistent with  $\text{Pd}_2\text{Si}$ , although it is not confirmed by chemical analysis.

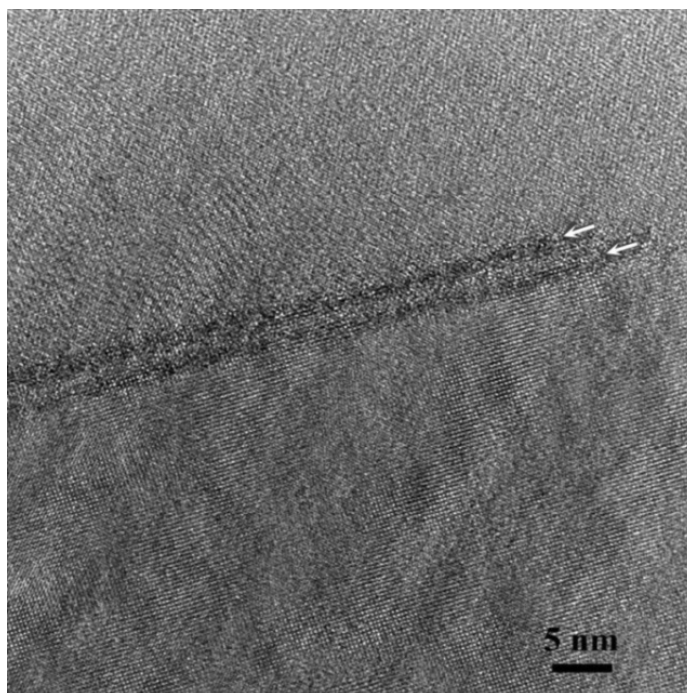


Figure 150. HRTEM image of a precipitate along the grain boundary between SiC grains. The bands rising from the mass contrast suggest a more complex structure to this precipitate.

### 3.4.6 Precipitate Chemical Composition Quantification Using Energy-Filtered Transmission Electron Microscopy Performed at Los Alamos National Laboratory

Very limited EFTEM was performed on a precipitate of Particle AGR1-131-099 to quantify the Ag, U, and Pd concentrations of the precipitate. Earlier EDS analysis showed the presence of these three elements.

Shown in Figure 151 are images taken at zero-loss and 71-eV loss (window size for imaging was 2 eV with the use of a 10-micron objective aperture). The 71-eV loss image was chosen to avoid imaging with low-loss signals around near the Pd and Ag lines around 50 eV and Si and U edges around 90 eV, yet maintain a good intensity in the acquired image. The primary reason to use these image-filtered images is to reduce the amount of scattering that can blur the images due to the relative thick nature of the FIB specimen and to highlight some aspects of the particles themselves. As such, a layered morphology of the particle can clearly be seen in the zero-loss images, suggesting that the particle is lying between SiC grains. The gray arrows in this image indicate layer edges of the particle. Further corroborating this observation is the low-loss image taken at 71 eV that clearly shows several different sets of Moire fringes. Furthermore, these fringes are everywhere in the particle showing that any through-thickness volume through the particle is a composite of SiC and the Pd particle. Hence, no probe technique would be able to get a completely accurate composition from this particle. Note that it was one of the larger particles found in the SiC area of this FIB lamella.

Despite the fact that the particle is partially obscured by SiC, one can use EFTEM to evaluate the relative distributions of the elements in the particle. Shown in Figure 152 is a set of EFTEM maps and image of the large particle taken after all the maps were acquired. The images shown in Figure 151 were taken before the spectral images were acquired. These maps were derived from the jump ratio method, which divides the signal isolated in a window above the edge of interest from that of the background just before the edge. The Pd image shows a very high contrast between the particle and surrounding matrix in

agreement with the EDS results, which show a Pd-rich particle. Conversely, the U and Ag maps do show some contrast between the particle and surrounding SiC suggesting that these elements are present in the particle, albeit at very low concentrations. These elements were not detected by the EDS spectral scans for this particle.

Figure 153 contains an atomic resolution image of the particle and a corresponding FFT of the image to extract a diffractogram. Similar imaging around the particle and the corresponding extraction of the diffractograms via FFT all show the same general structure indicating a single overall orientation for the particle. Note that the diffraction pattern obtained in this manner is somewhat smeared because of the overlap with the SiC matrix. Accurate phase identification from this one diffraction pattern is difficult, given the uncertainty in the overall composition. The pattern could be indexed to a cubic structure with  $a = 3.495$  Angstrom. For reference, the crystal structure of pure Pd is  $a = 3.8907$  Angstrom (cubic close pack structure). Alloying with any of the other elements present such as Si, C, U, or Ag (small amounts) and/or strain effects from the surrounding SiC matrix may explain the differences.

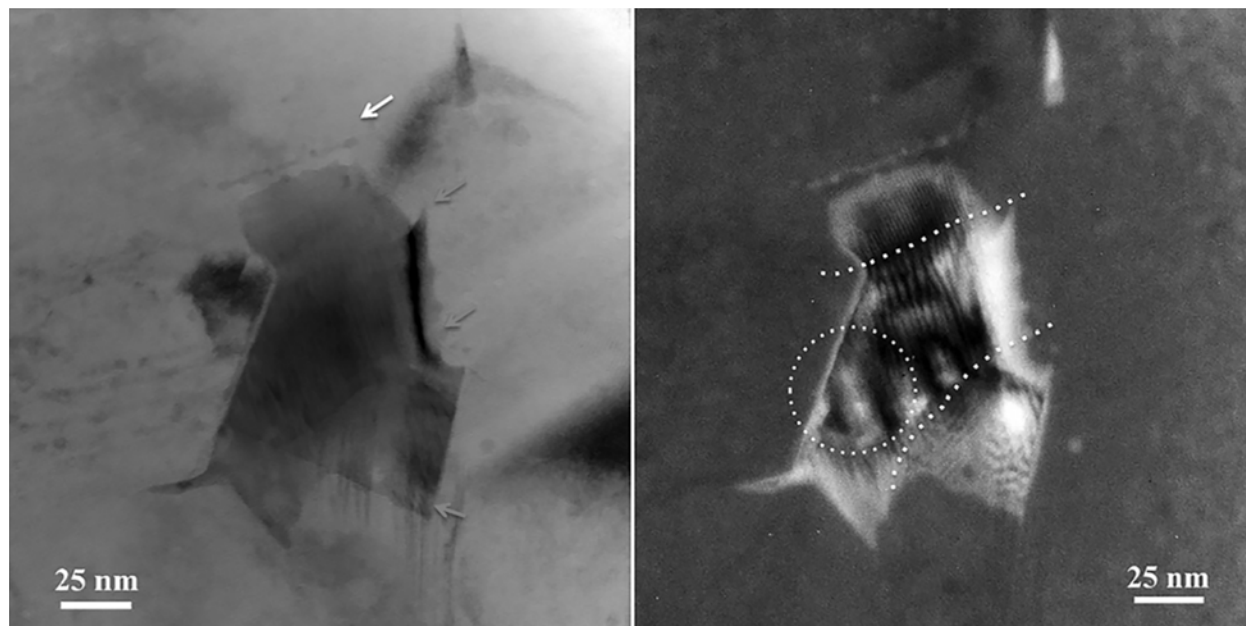


Figure 151. EFTEM images take at (left) zero loss and at an energy loss of 71 eV (right). A layered structure nestled between SiC grains is suggested by the zero-loss image and the different sets of Moiré fringes shown in the 71-eV loss image.

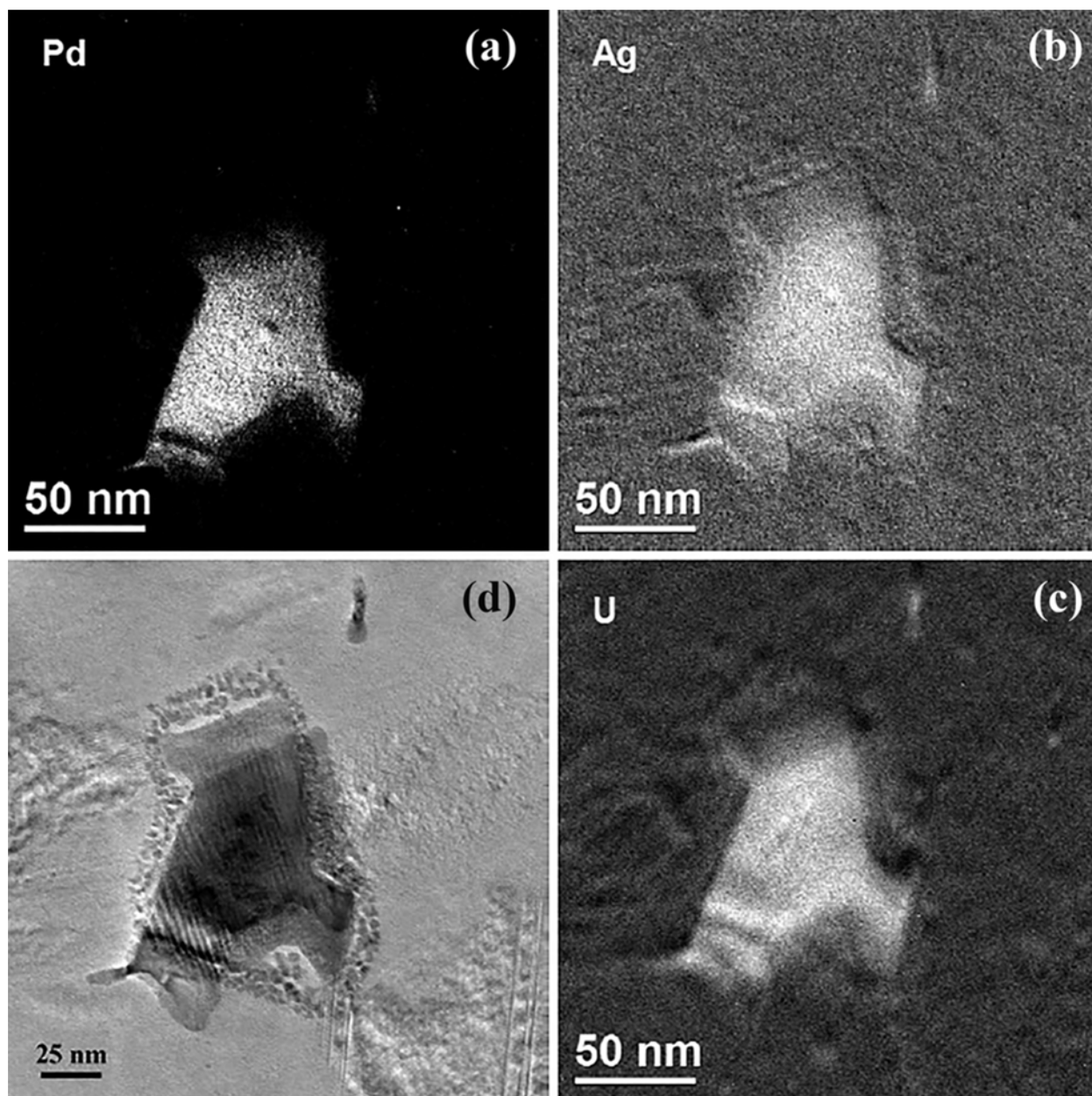


Figure 152. EFTEM maps derived from the jump ratio method to show the relative distributions of (a) Pd, (b) Ag, and (c) U in the particle. The EFTEM image in (d) shows some of the damage to the area from the imaging process, which is primarily occurring in the nearby SiC matrix.

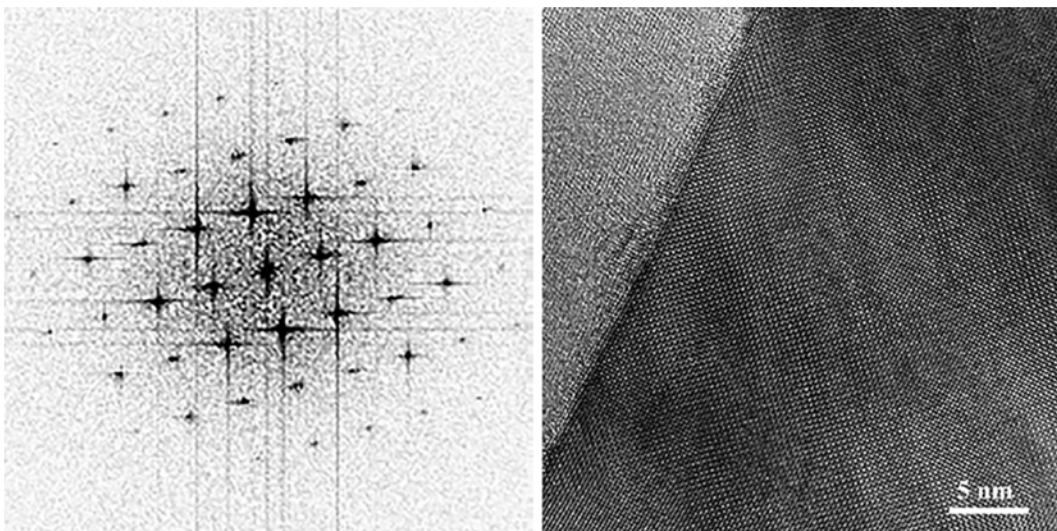


Figure 153. Atomic resolution image of the edge of the precipitate (right) and a corresponding diffractogram (left) from a precipitate in Particle AGR1-131-099.

### 3.4.7 Summary and Main Findings on Coated Particles from Compact 1-3-1

Both particles from this compact that were analyzed using advanced microscopy techniques exhibited relatively low retention of Ag-110m. Even so, the particles exhibited significant differences in release behavior with AGR1-131-066 exhibiting an Ag-110m retention of about 39% while AGR1-131-099 exhibited virtually no retention of Ag-110m (i.e., complete release). The following comparison is provided to provide possible insight about whether (and what) microstructural factors may be responsible for the difference in the observed release behavior.

**3.4.7.1 General Grain Boundary Distributions.** Figure 154 shows the comparison between the two particles for distributions of the misorientation angle (Figure 154[a]), CSL grain boundary distribution (Figure 154[b]), and grain boundary type (Figure 154[c]). From these plots, it appears there are slight, but statistically significant, differences in the twin boundary/CSL boundary fractions and the low-angle grain boundary fractions. AGR1-131-066 has a lower fraction of  $\Sigma 3$  and total CSL-related grain boundary fractions, but a higher low-angle grain boundary fraction than AGR1-131-099. Generally, twin boundaries exhibit a lower diffusivity for impurity atoms and would tend to promote fission product retention (Peterson 1983, Priester 1989). Diffusion of fission product elements in low-angle grain boundaries is also limited because one or more arrays of discrete dislocations and impurity transport are accomplished by dislocation pipe diffusion. Therefore, one would expect the major microstructural parameter affecting the migration of fission products through the SiC to be the fraction of random, high-angle grain boundaries. However, Figure 154(c) shows the random, high-angle grain boundary fraction for both particles to be virtually identical. Additionally, the fractions of the random, high-angle grain boundaries in the inner regions of both particles, where fission product elements would enter the SiC layer, are statistically identical when comparing the random, high-angle grain boundary fractions in Figure 116(c) and Figure 138(c), Lamellae 5 and 2, respectively. Therefore, no obvious differences are apparent in the grain boundary distributions of Figure 116, Figure 138, and Figure 154 that might explain the difference in Ag-110m release behavior between these two particles. However, it should be mentioned that grain boundary diffusivity of CSL-related grain boundaries is strongly related to grain boundary plane, and just being a CSL-related grain boundary does not necessarily equate to a low diffusivity for impurity atoms (Priester 1989). A remote possibility exists that the low Ag-110m retention particle might have a larger fraction of CSL boundaries that are associated with high diffusivity grain boundary planes than the high Ag-110m particle. Thus, differences in the fractions of low diffusivity and high-diffusivity CSL-related grain boundaries may be responsible for the differences in Ag-110m retention between these



two particles. Unfortunately, currently no method exists for quickly determining the grain boundary habit plane; furthermore, the grain boundary habit plane is rarely straight, but rather it is typically curved and the habit plane is continually changing along the grain boundary, resulting in continually changing grain boundary energy.

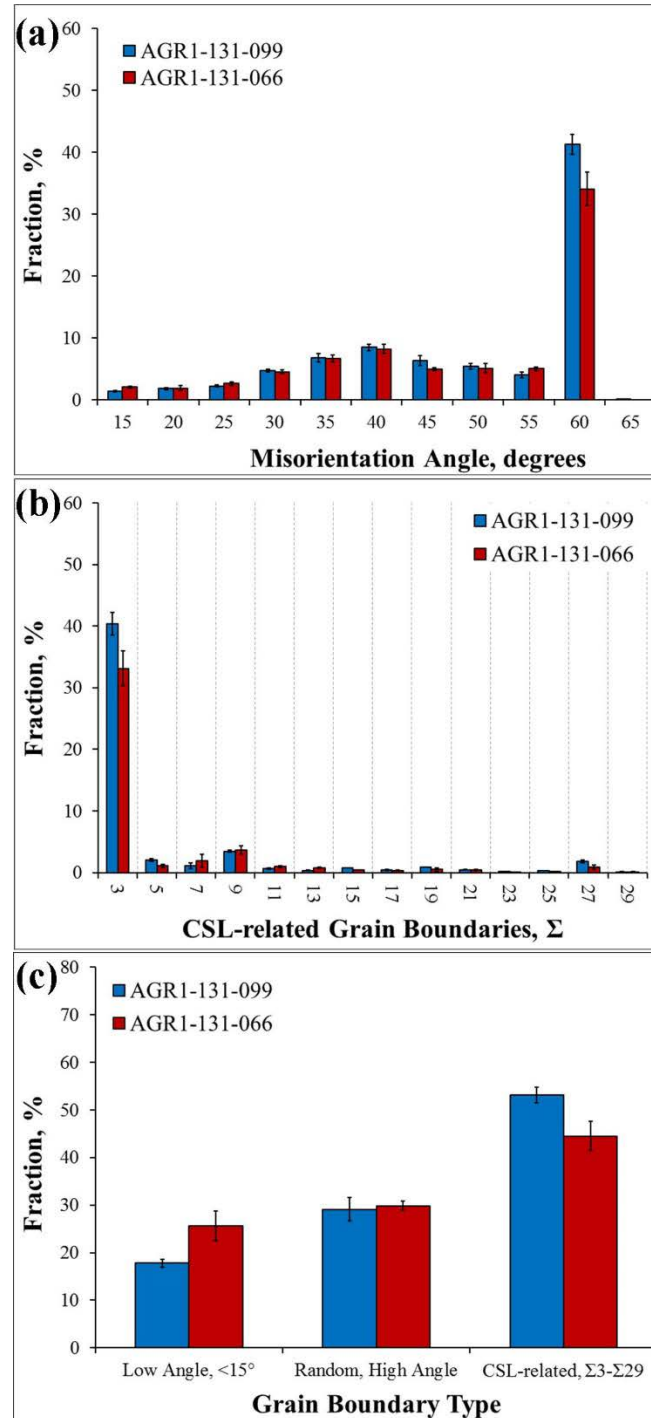


Figure 154. Comparison of the (a) misorientation angle distributions; (b) CSL boundary distributions, and (c) grain boundary-type distributions between AGR1-131-066 and AGR1-131-099.

### 3.4.7.2 Fission Product Precipitate Elements and Associated Grain Boundary Type.

Figure 155(a) compares the distribution of fission product elements for precipitates in the SiC layer of the two particles. Both exhibit precipitates that are composed of only Pd or Pd with U and these two precipitate types occur in roughly the same fractions in both particles. The notable feature in this plot is the lack of other fission products (such as Ag and transuranic elements, including Pu), which have been found in the analyses of other TRISO particles from the AGR-1 experiment. However, the Ag-retention characteristics of those other TRISO particles are generally better than those observed for both particles and Ag concentrations at the grain boundaries in these particles may have been too low to form Ag-containing precipitates. Furthermore, the concentration of Pu may have been too low to form Pu-containing precipitates.

Figure 155(b) shows the distribution of fission product precipitates as a function of grain boundary type for the two particles. Both indicate a precipitate preference for random, high-angle grain boundaries and a lack of precipitates on low-angle grain boundaries. Precipitation occurs on CSL-related grain boundaries but at a lower fraction than that of random, high-angle grain boundaries. Again, the grain boundary habit plane of CSL-related grain boundaries likely plays a significant role in whether a precipitate will form on these types of grain boundaries. Otherwise, there is no significant difference in the distributions in Figure 155(b) for the two particles.

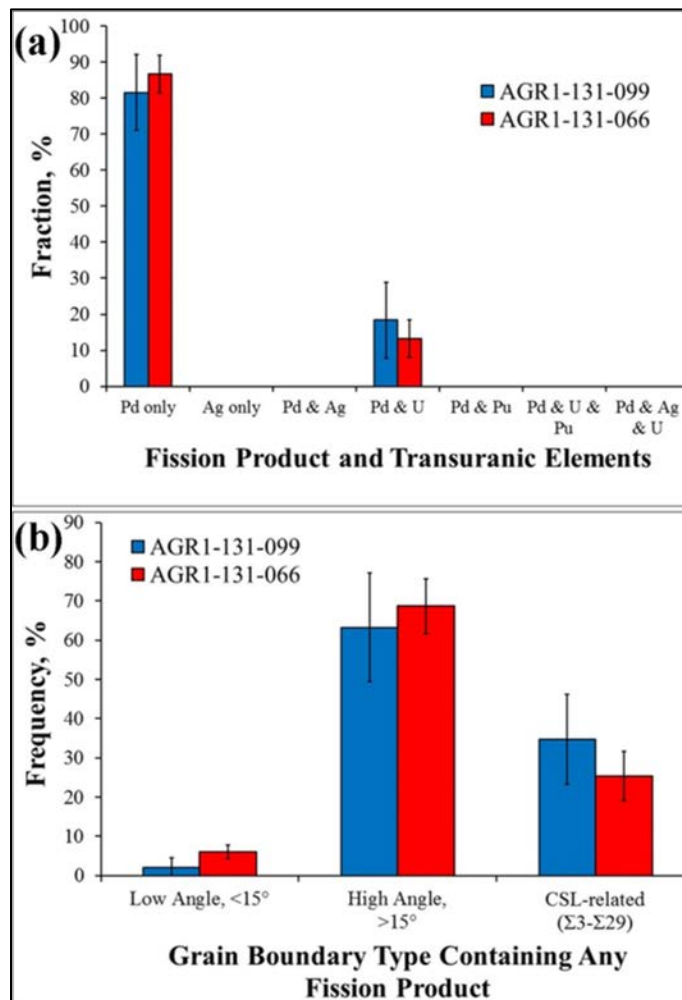


Figure 155. Comparison of (a) the fission product element distribution and (b) the distribution of fission product precipitates as a function of grain boundary type for AGR1-131-066 and AGR1-131-099.



**3.4.7.3 Precipitate Identification (Energy Dispersive X-ray Spectroscopy and Energy-Filtered Transmission Electron microscopy).** Figure 156 shows a schematic presentation summary of the main elements present in the precipitates in Particle AGR1-131-099.

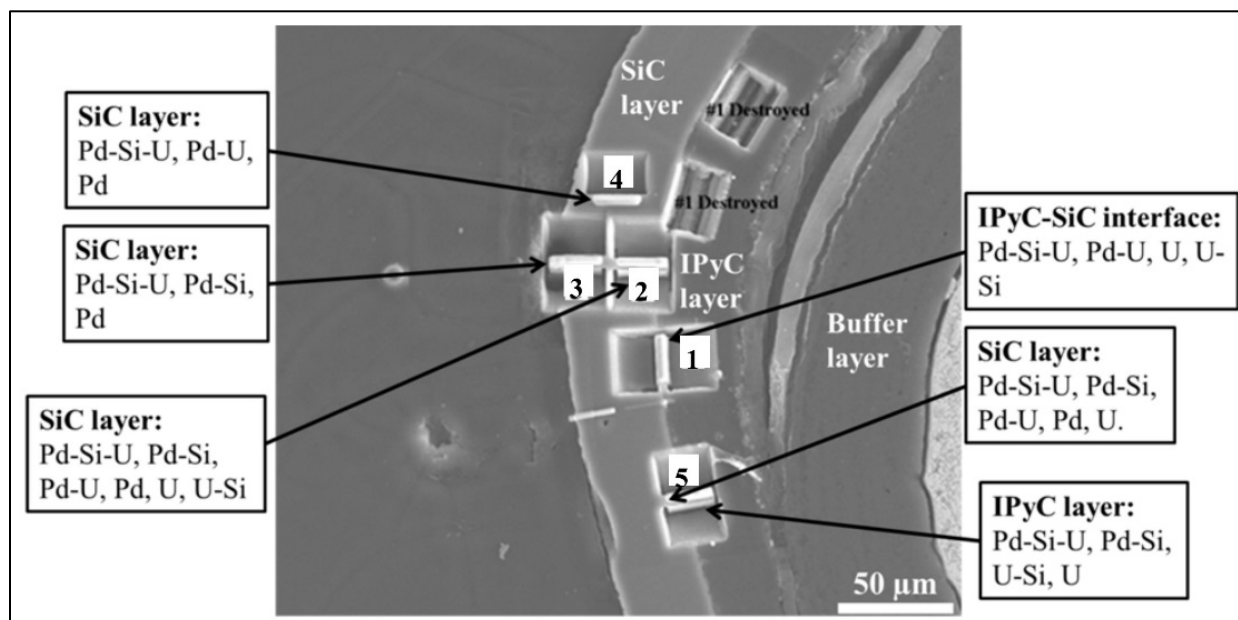


Figure 156. Summary of precipitate compositions in different TEM lamellae from AGR1-131-099.

**3.4.7.4 Phase and Structural Examination (High-Resolution Transmission Electron Microscopy).**

- Multi- and single-phased precipitates were identified in both the IPyC layer and the SiC layer. These results emphasize the complex nature of the precipitates; no definite trend is yet determined because only very few precipitates were examined using HRTEM.
- The interface between SiC and the fission product precipitate examined is well defined and free of porosity. From the change in the tilt of the atomic layers across this interface, it appears the precipitate is not aligned to the SiC in any well-defined manner.
- FFT of a random triple-point precipitate revealed lattice parameters consistent with  $\text{Pd}_2\text{Si}$ .
- Bands arising from mass contrast were identified for a precipitate along the grain boundary between SiC grains and suggest a more complex structure to this precipitate. (It was too small to determine chemical composition.)

## 3.5 Irradiated Variant 3 Fuel Examination: Compact 4-1-1

### 3.5.1 Particle Selection and Analysis Performed

The Ag retention of Compact 4-1-1 was relatively high and the Ag-110m measured-to-calculated ratio for 58 gamma ray-counted particles from Compact 4-1-1 ranged from 0.75 to 1.45. Coated Particle AGR1-411-030 was selected because it exhibited an average level of retained Ag-110m with a measured-to-calculated Ag-110m ratio of 0.90 (Figure 157). Deconsolidation leach-burn-leach data from Demkowicz et al., (2016c) indicate that 3% of the Compact 4-1-1 Ag-110m inventory was retained in the graphitic matrix. It has been concluded that, on average, there was a relatively low release of Ag from the particles in this compact. The decay-corrected activity for Ag-110m measured by gamma ray counting of the AGR1-411-030 particle is  $6.45 \times 10^4$  Bq (1.74  $\mu\text{Ci}$ ) (Demkowicz et al., 2016c).

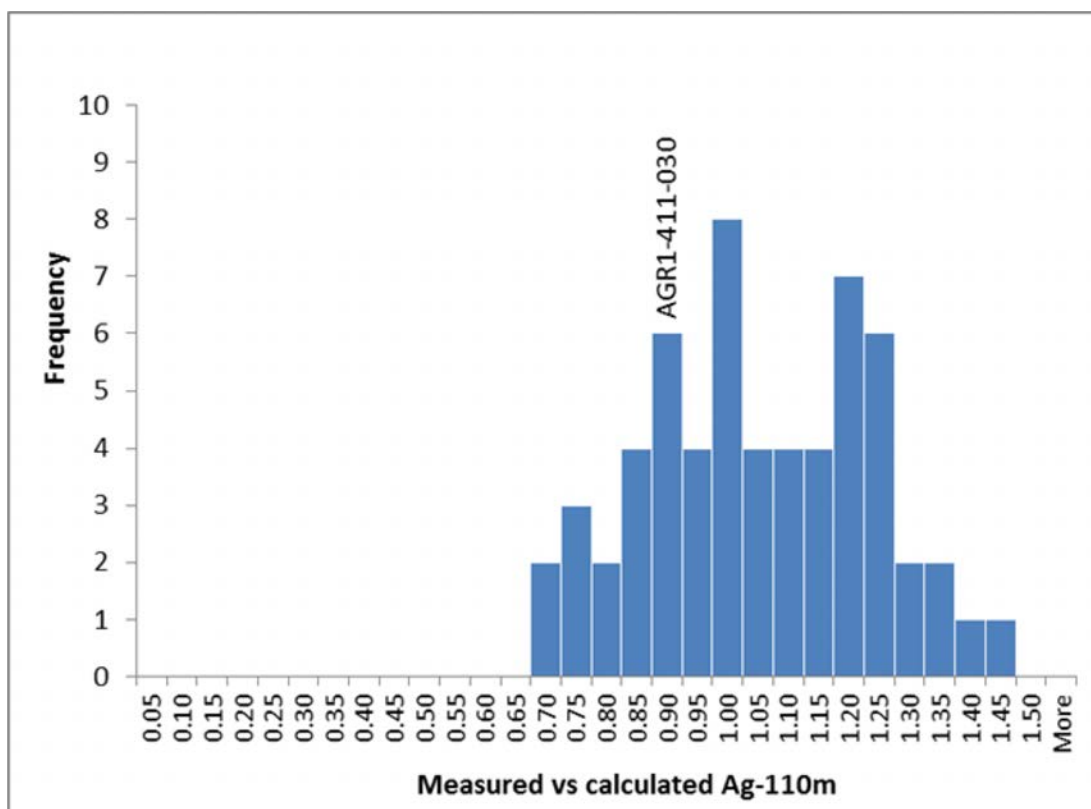


Figure 157. Distribution of measured-to-calculated Ag-110m activity ratios, normalized by the Cs-137 activity to account for variations in fissile content and burnup (Demkowicz et al 2016c).

Because this particle was chosen for the first exploratory HRTEM examination at NMMU and the crystallographic characteristic method development was not yet established, no crystallographic measurements were performed on these particles prior to shipment to NMMU. Only limited SEM and TEM examinations were performed (see Table 77).

Table 77. Advanced microscopy and micro-analysis examination performed on Compact 4-1-1 particles.

Technique	SEM <sup>a</sup> EDS/WDS	EELS/ EFTEM	STEM	EPMA	PED	APT	HRTEM
<b>Compact 4-1-1 (Variant 3)</b>							
AGR-411-030 (Average (90 %) Ag retention)	X	—	—	—	—	—	X

a. Reported in a separate report by van Rooyen et al., 2017.

**3.5.1.1 Lamellae Locations.** Although two coated particles from Compact 4-1-1 (i.e., AGR1-411-021 and AGR1-411-030) were examined as part of the basic SEM examination, the original number of samples (positions) to be examined at the TEM was decreased due to equipment availability and budget constraints. This resulted in no TEM examinations for AGR1-411-021. FIB lamellae at Position 1b, 1c, and 2 were extracted from locations perpendicular to the SiC-IPyC interface in Particle AGR1-411-030 (see Figure 158). Lamellae 1b and 2 contain parts of both the IPyC and SiC layers, while FIB Lamella 1c is from the outer interface between the SiC and OPyC layer, which is the furthest away from the IPyC-SiC interface. FIB Lamella 1a contained only a small area of the SiC layer close to the IPyC-SiC interface and was cut parallel to the IPyC-SiC interface. Because Lamella 1a contained only small areas of the SiC layer at the IPyC-SiC interface, it was not examined for this report.

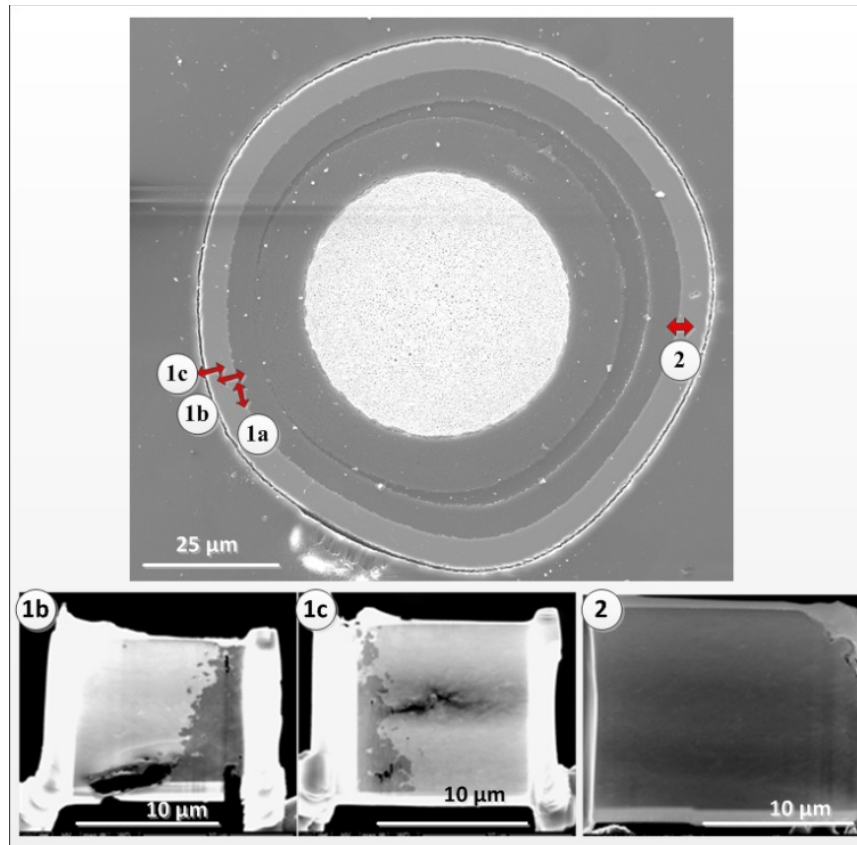


Figure 158. SEM image showing the AGR1-411-030 FIB SEM lamellae sectioned at Positions 1b, 1c, and 2 as indicated on the cross section of the coated particle.

### 3.5.2 Microstructural Examination

TEM examination was performed in January and February 2013 and provided a good basic overview on the properties of the SiC layer, including the following:

- The TEM-EDS analysis on the micron-sized precipitates showed Pd-rich precipitates with no U and Ag detected. This is in contrast with the EDS analysis previously performed on Compact 6-3-2's micron-sized precipitates where U was identified.
- Selected Area Diffraction (SAD) measurements showed no correspondence to those of  $\text{UPd}_2\text{Si}_2$  previously found in the Compact 6-3-2 specimens that were investigated. From both the qualitative EDS and the SAD patterns, the precipitates are different between the two compacts.
- Slight indications of debonding at localized areas of the IPyC-SiC interface are noted. No indications of macro-scale debonding were observed for the Compact 4-1-1 specimens (Figure 159).
- Cs precipitates were found in a porous region of the buffer area in specimen AGR1-411-030 (Figure 160).

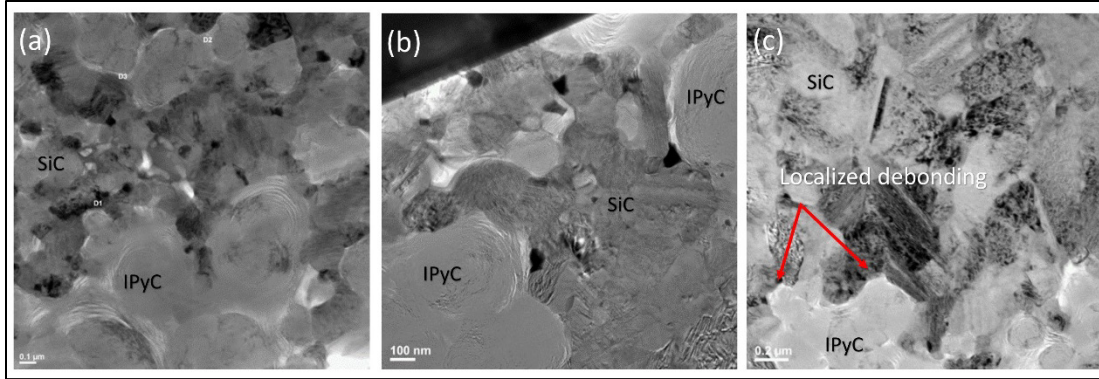


Figure 159. Localized areas at the IPyC-SiC interface showing intact interfaces at (a) Lamella 1a; (b) Lamella 1b; and (c) slight localized indications of debonding observed at the IPyC-SiC interface at Lamella 2 as shown by the red arrows. Indications of debonding were not observed previously on specimens from Compact 6-3-2.

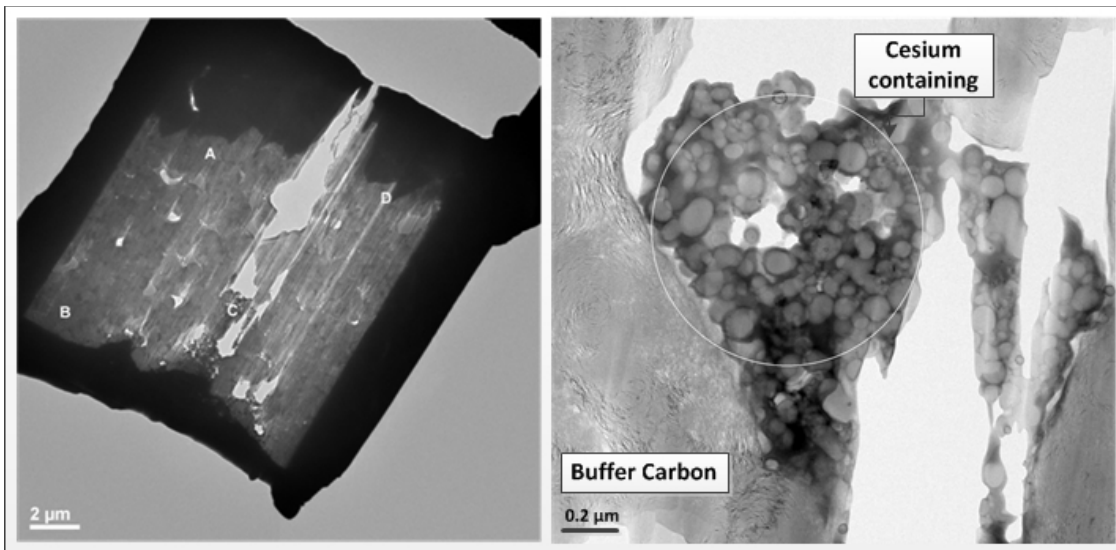


Figure 160. Image showing the presence and morphology of Cs in the buffer layer of the AGR1-411-030 particle (FIB Position 3 in Figure 159).

**3.5.2.1 High-Resolution Transmission Electron Microscopy.** An HRTEM examination was performed at NMMU on AGR1-411-030 Lamellae 1b and 2 that were prepared via FIB (Figure 159). The main objective of this examination was to obtain very high-resolution images at an atomic level of the fission products. Following is a brief summary of the main findings of the first analytical HRSTEM performed on TRISO-coated particles as reported by van Rooyen et al., (2014a).

With STEM imaging, Pd accumulation at the IPyC-SiC interface (Figure 161) was observed, which is an indication that Pd diffuses rapidly through the PyC layers until it reaches the SiC where transport is much slower. This confirms the effectiveness of the SiC layer and the morphology of the IPyC/SiC interlayer as the main fission product barrier. Additionally, no significant Pd corrosion of SiC was observed, which confirmed earlier SEM observations and indicated that Pd can penetrate the SiC without significantly corroding the surface.

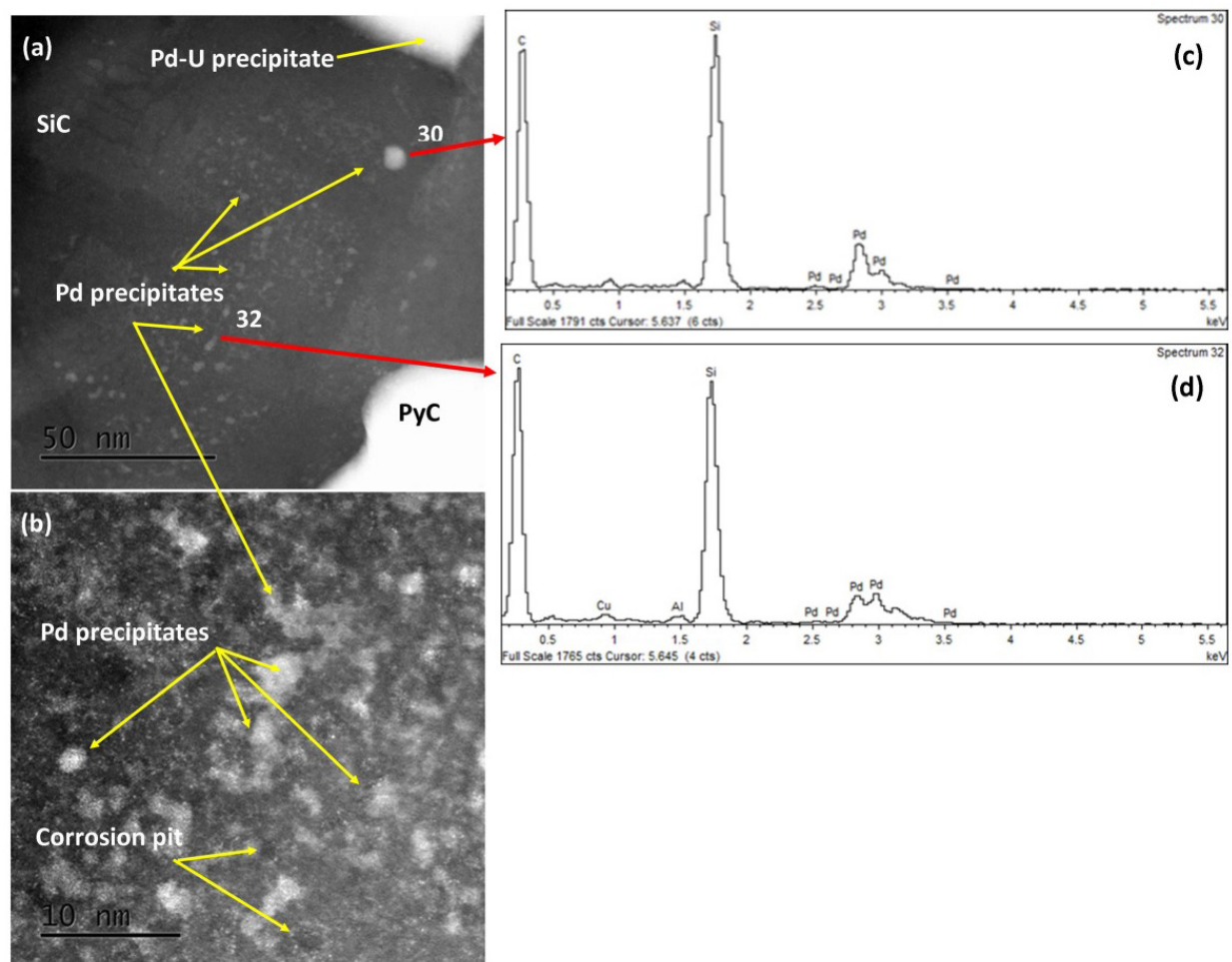


Figure 161. HAADF STEM images showing (a) accumulation of Pd at the IPyC-SiC interface, (b) no significant corrosion except for a few approximate 1-nm diameter corrosion pits only visible at this magnification, and (c) and (d) the presence of Pd in two spectra of associated areas in (a).

Atomic resolution images were obtained showing Pd and Ag atoms co-existing on the same location of the SiC grain boundaries (Figure 162 to Figure 165). In contrast with the STEM results obtained from Particle AGR1-632-035 to date, it was found that Ag and Pd always co-exist in the same triple point. At some locations, EDS analyses only indicated the presence of Pd. However, the possible presence of Ag or Cd at these locations in concentrations below the EDS detection limit cannot be ruled out. Ag decay is most likely the primary source of the Cd observed in the fission product nodules. Therefore, Cd is expected to be present in close proximity to Ag at the end of irradiations. If Cd accumulations were observed without any Ag, it could indicate that a source of Cd was fission in the kernel.



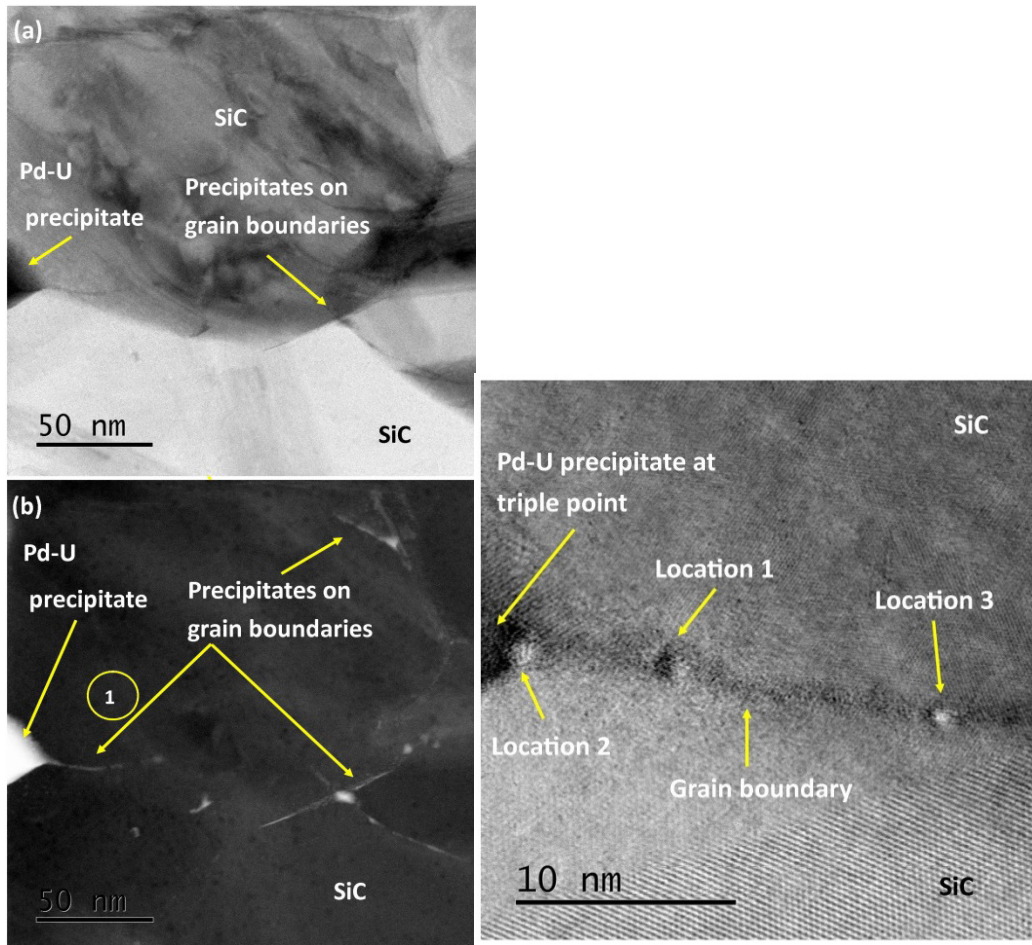


Figure 162. BF (a) and dark field (b) STEM images of fission product networks at grain boundaries and triple points of specimen AGR-411-030 Position 1b. (c) High-resolution BF STEM image Pd-Ag-Cd accumulations co-existing at Location 1 at a SiC grain boundary of specimen AGR1-411-030 Position 1b. Only Pd was found at Locations 2 and 3. (Adapted from van Rooyen et al., 2014a).

Pd was also observed inside SiC grains in proximity to planar defects such as stacking faults or nano twins. This is an interesting observation because the majority of Pd precipitates are usually found along SiC grain boundaries. Previous STEM work by Van Rooyen et al., (2014b) also showed the presence of spherical nano Pd precipitates inside grains on particles from Compact 6-3-2. It was not possible to provide more positional information on these Pd precipitates inside the SiC grains, although evidence of fission products was found when comparing HAADF with corresponding BF images (it was not possible to obtain compositional quantification and identification of these precipitates due to low concentration). This HRTEM study provides this new information. It is proposed that the same mechanism that governs movement of Pd along SiC grain boundaries is responsible for migration of Pd along planar defects in SiC. Grain boundaries contain high concentrations of dislocations due to relative misorientation between adjacent grains; therefore, they have a comparatively open structure. This results in diffusivities for grain boundary transport that are much larger than analogous values for lattice diffusion. Enhanced diffusion along dislocation cores will also occur. SiC grains containing high concentrations of stacking faults (or nano-twins) bounded by partial dislocations will also have a high concentration of easy diffusion paths created by the stacking faults and partial dislocation cores.

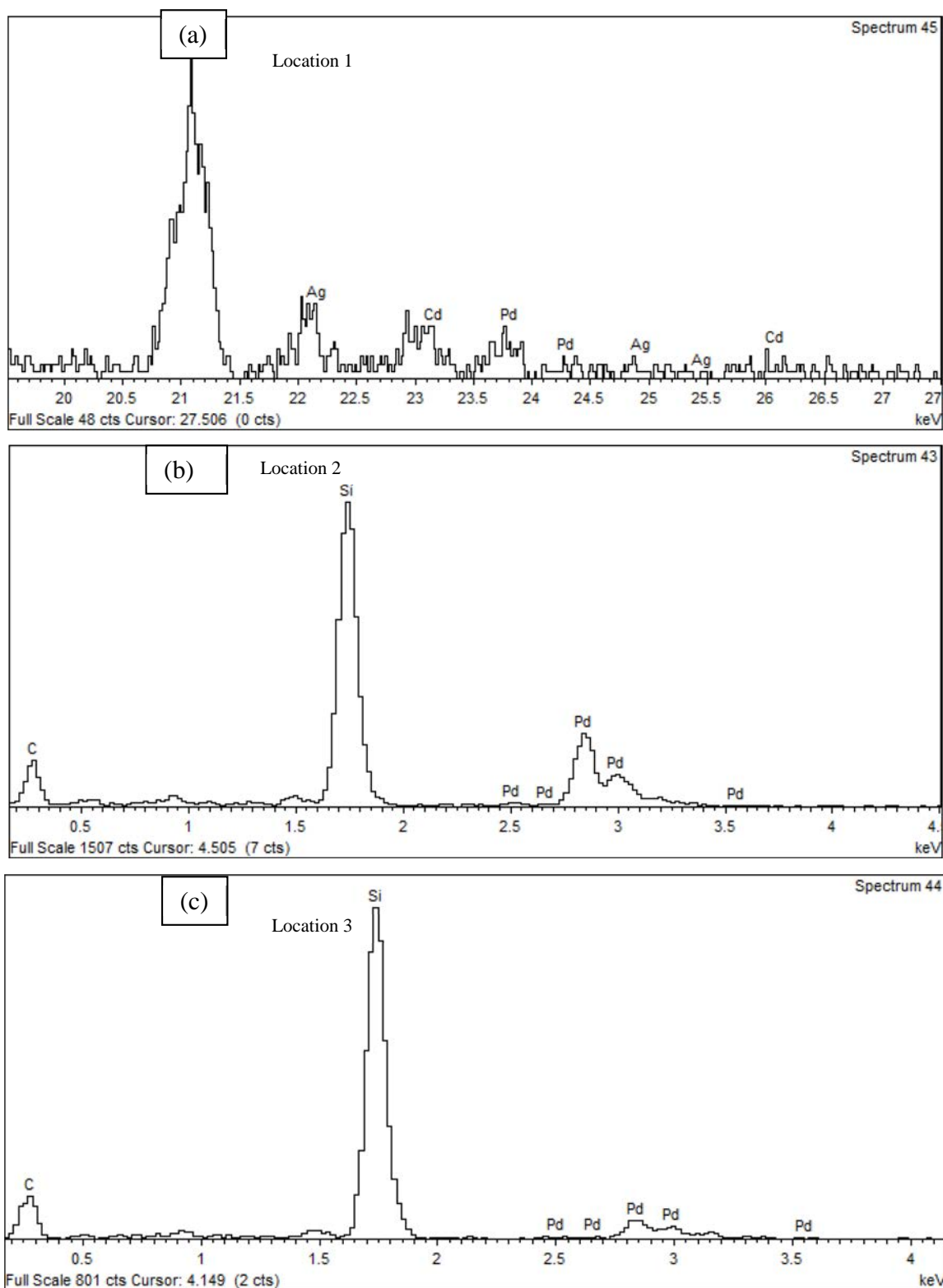


Figure 163. EDS spectra showing (a) co-existence of Pd, Ag, and Cd at Location 1 of specimen AGR1-411-030 Position 1b. The peaks for Ag and Cd passed the 2-sigma test as determined by the Oxford software. Therefore, the peaks are deemed to be statistically relevant and show that only Pd was found at Locations 2 and 3 (shown in [b] and [c]).



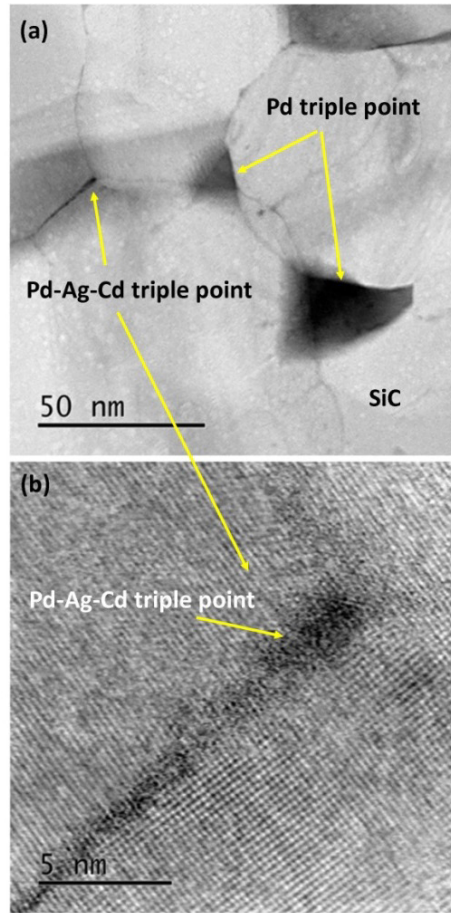


Figure 164. BF STEM image (a) of a Pd-Ag-Cd containing triple point with the corresponding high-resolution BF STEM image (b).

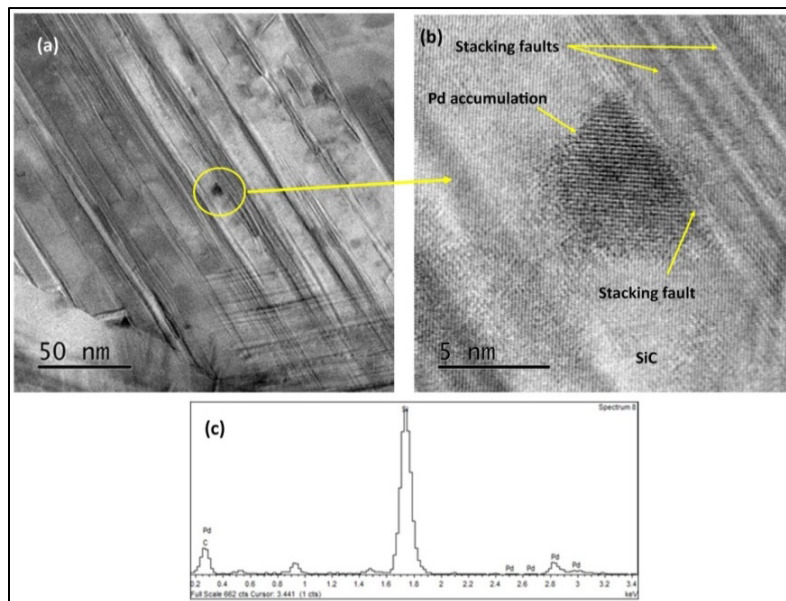


Figure 165. BF STEM image in (a) showing the position of the Pd accumulation at a stacking fault in a SiC grain with a high-resolution BF STEM image in (b) with the corresponding EDS spectrum in (c).

The first finding of phosphorus (P) in the SiC layer of neutron-irradiated, TRISO-coated particles is reported in this work. P is usually produced by neutron transmutation of Si. No direct link between the presence of P and Ag transport could be made from this study. P was detected in association with Pd and Ag at the SiC grain boundary at Point 1, while, in contrast, no P was detected in the SiC grain at Positions 5 and 6 (see Figure 166 for analysis positions with Figure 167 and Figure 168 for the EDS spectra)). Further analysis of grain boundaries at an additional site also revealed P on grain boundaries (shown in Figure 168), specifically at Points 1 and 2. This suggests segregation of P at the boundaries and triple points. The software identifies and quantifies it to be within a 3-sigma level. This is the first finding of P in the SiC layer grain boundaries of neutron-irradiated, TRISO-coated particles.

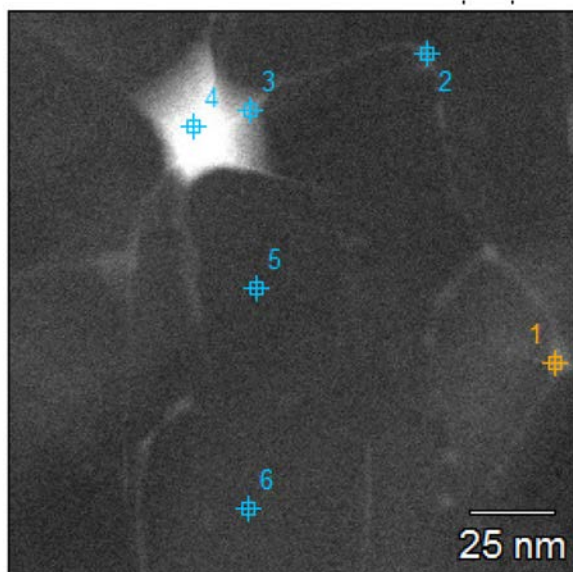


Figure 166. Selected HRSTEM image showing the six locations where EDS analysis was completed using the new higher-resolution EDS detector.

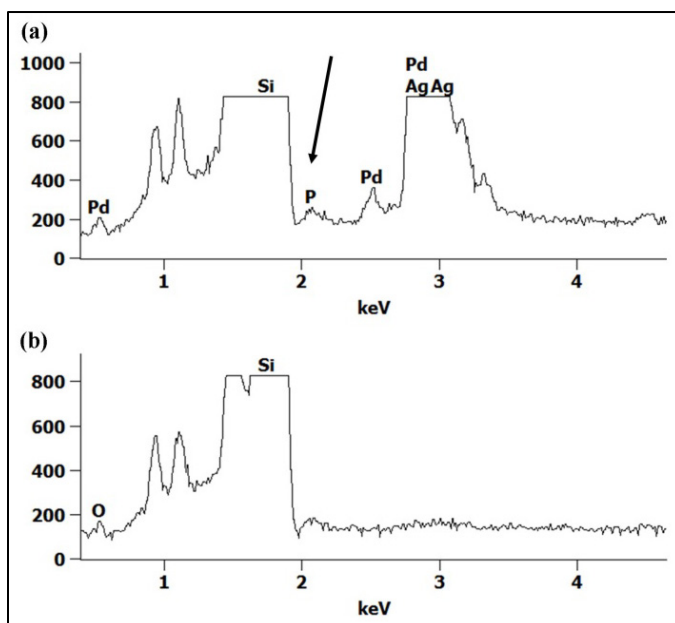


Figure 167. HRSTEM-EDS spectra at points 1(a) and 5(b) showing the presence of P (as indicated by the arrow) at the grain boundary but not in the SiC grain, respectively.

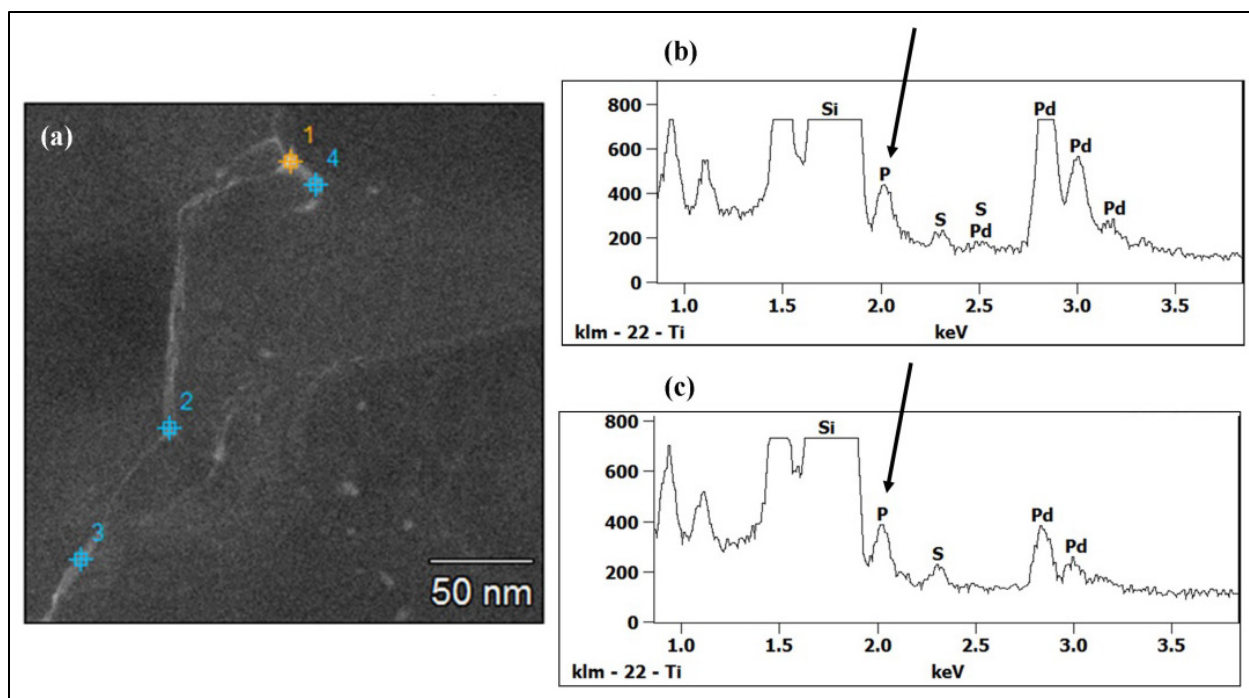


Figure 168. Selected HRSTEM image (a) showing the four locations where EDS analysis was completed using the new higher-resolution EDS detector. HRSTEM-EDS spectra at Points 1(b) and 2(c) showing the presence of P (as indicated by the arrow) at the grain boundary triple points.

### 3.5.3 Summary and Main Findings on Compact 4-1-1 Particles

Main findings from the TEM and HRTEM examinations on Particle AGR1-411-030 were as follows:

- The TEM-EDS analysis on the micron-sized precipitates showed Pd-rich precipitates with no U or Ag detected. This is in contrast with the EDS analysis previously performed on Compact 6-3-2, which identified micron-sized precipitates containing U. However, U was identified in the HRTEM examination in triple points and grain boundaries in Particle AGR1-411-030.
- SAD measurements on micro-sized precipitates showed no correspondence to those of  $\text{UPd}_2\text{Si}_2$  previously found in the investigated Compact 6-3-2 specimens. From both the qualitative EDS and SAD patterns, the precipitates are different between these two compacts. No explanation for this difference can be provided at this point.
- Except for slight indications of debonding at localized areas at the IPyC-SiC interface are noted, no significant debonding were observed. No indications of debonding were observed for the Compact 6-3-2 specimens.
- Cs precipitates were found in a porous region of the buffer area in specimen AGR1-411-030; no Cs was found in the SiC layer in the areas examined.
- Pd was observed inside SiC grains in proximity to planar defects (e.g., stacking faults).
- Ag co-existing with Pd and Cd may suggest a Pd-assisted transport mechanism.
- First finding of P produced by Si neutron transmutation in the SiC layer of neutron-irradiated, TRISO-coated particles. No direct link to Ag transport was found.
- No significant Pd corrosion of SiC observed, even in high-resolution images.

### 3.6 Irradiated and Safety-Tested Variant 3 Fuel Examination: Compact 4-3-3

This section contains a large body of unpublished results for particles AGR1-433-001, AGR1-433-003, AGR1-433-004, and AGR1-433-007, which includes, grain boundary characteristics of particles, and fission product identification and distribution (STEM and EPMA). Focused structural and phase evaluations were performed on all areas where the grain boundary character and qualitative chemical composition were determined. This extensive battery of tests demonstrates the cohesive focused examinations strategy formed from all the lessons learned from the AGR-1 advanced microscopy campaign.

#### 3.6.1 Particle Selection and Lamellae Locations

Two TRISO-coated particles from AGR-1 Compact 4-3-3, safety-tested to a temperature of 1600°C, were selected based on the measured Ag-110m activity and the predicted activity ratio, as shown in Figure 169, to investigate microstructural characteristics related to Ag retention (Demkowicz et al., 2016d). From these distributions, particles were chosen to represent particles having a low (Particle AGR1-433-001: 66%) and high (AGR1-433-004: 98%) Ag-110m measured-to-calculated ratio. Figure 169 indicates that particles exhibit a range of Ag retention from about 25 to 105% of the predicted inventory. Examination using STEM, PED, and HRTEM were completed for both particles (see Table 78 for the examination matrix).

Particles AGR1-433-003 and AGR1-433-007, with measured-to-calculated Ag-110m inventories of less than 22% and 100%, respectively, were chosen to further explore EPMA as a tool for obtaining more information on the quantification and distribution of fission products on larger areas and, therefore, become a more effective analytical tool for providing distribution patterns. These two particles were further selected for comparative electron microprobe analysis to determine whether the distribution or abundance of fission products differed proximally and distally from the deformed kernel in AGR1-433-003 and how this compared to fission product distribution in AGR1-433-007 (see Figure 170).

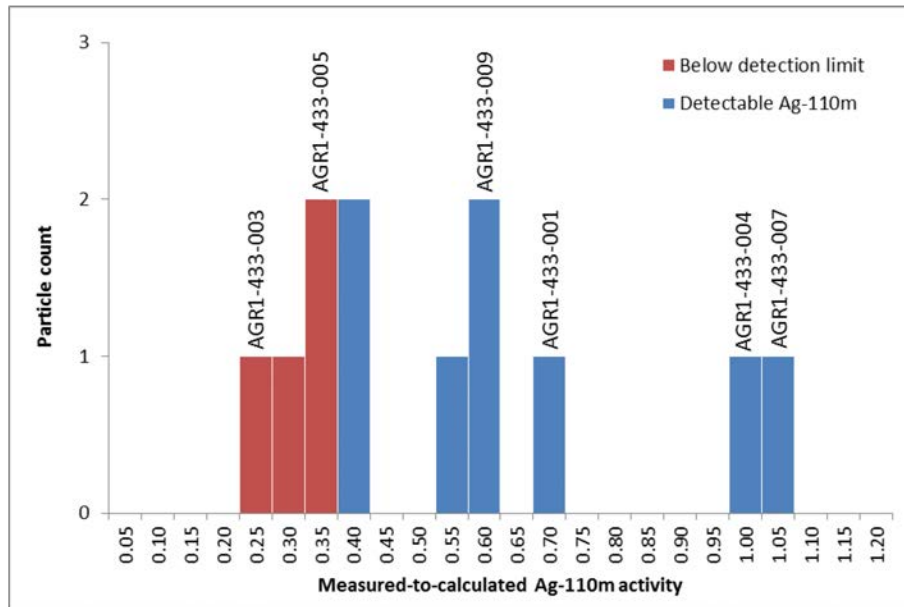


Figure 169. Distribution of the measured-to-calculated Ag-110m activity ratio for the irradiated Compact 4-3-3 particles (Demkowicz et al., 2016d).



Table 78. Advanced microscopy and micro-analysis examination performed on Compact 4-3-3 particles.

Technique	SEM <sup>a</sup> EDS/WDS	EELS/ EFTEM	STEM	EPMA	PED	APT	HRTEM
Compact 4-3-3 (Variant 3; 1600°C safety tested)							
AGR1-433-003 (Low (< 22%) Ag retention)	—	—	—	X	—	—	—
AGR1-433-007 (High (100%) Ag retention)	—	—	—	X	—	—	—
AGR1-433-001 (Low (66%) g retention)	X	—	X	—	X	—	X
AGR1-433-004 (High (98%) Ag retention)	X	—	X	—	X	—	X

a. Reported in separate report by van Rooyen et al., 2017.

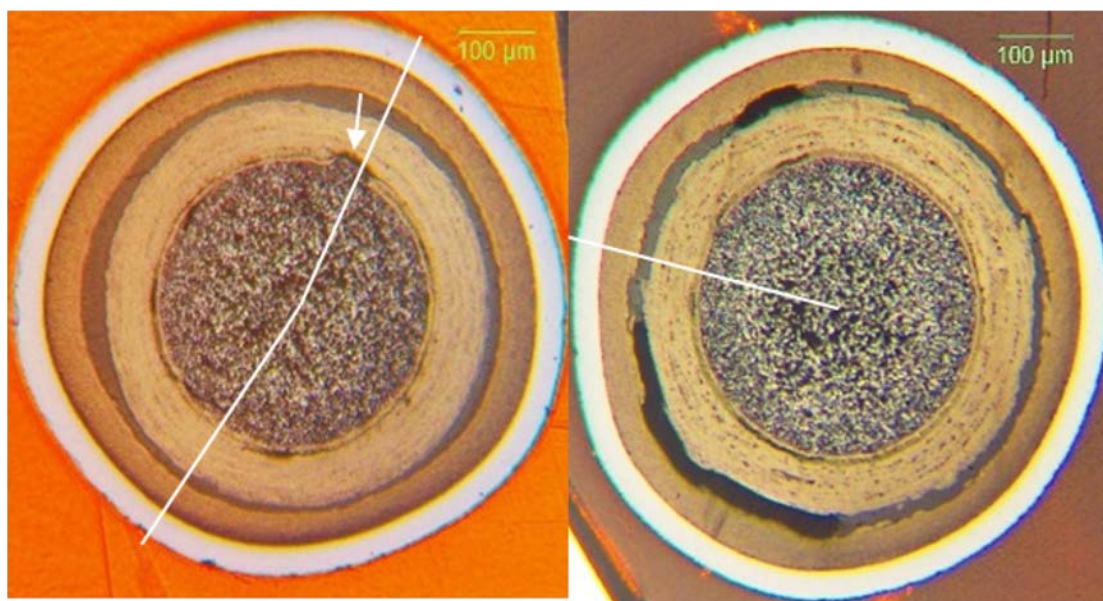


Figure 170. Optical microscope image of AGR1-433-003 (left) and AGR1-433-007 (right). Paths of radial traverses EPMA elemental composition measurements are shown with white lines. The arrow in the left image highlights kernel extrusion (deformation) into a fractured region of the buffer layer.

**3.6.1.1 Lamella Locations of Particles AGR1-433-001 and AGR1-433-004.** The rationale for choosing Lamella locations was driven by a previous study on a corroded sample from Compact 5-2-3 with a cracked buffer and IPyC layer. In the case of Particle AGR1-433-001, in addition to its relatively low Ag retention in comparison with that of Particle AGR1-433-004, the optical ceramography examination revealed multiple cracks in the buffer layer. Therefore, as seen in Figure 171, multiple lamellae were identified in these areas. Lamellae 5 through 7 were chosen again to provide a through thickness evaluation of the SiC, while Lamella 10 was chosen away from the breached buffer to provide comparative results with Lamellae 4 and 5. For Particle AGR1-433-004, Lamellae 5 through 7 represent the through thickness Lamella and Lamellae 4 and 5 were chosen in areas of fission product clusters (Figure 172).

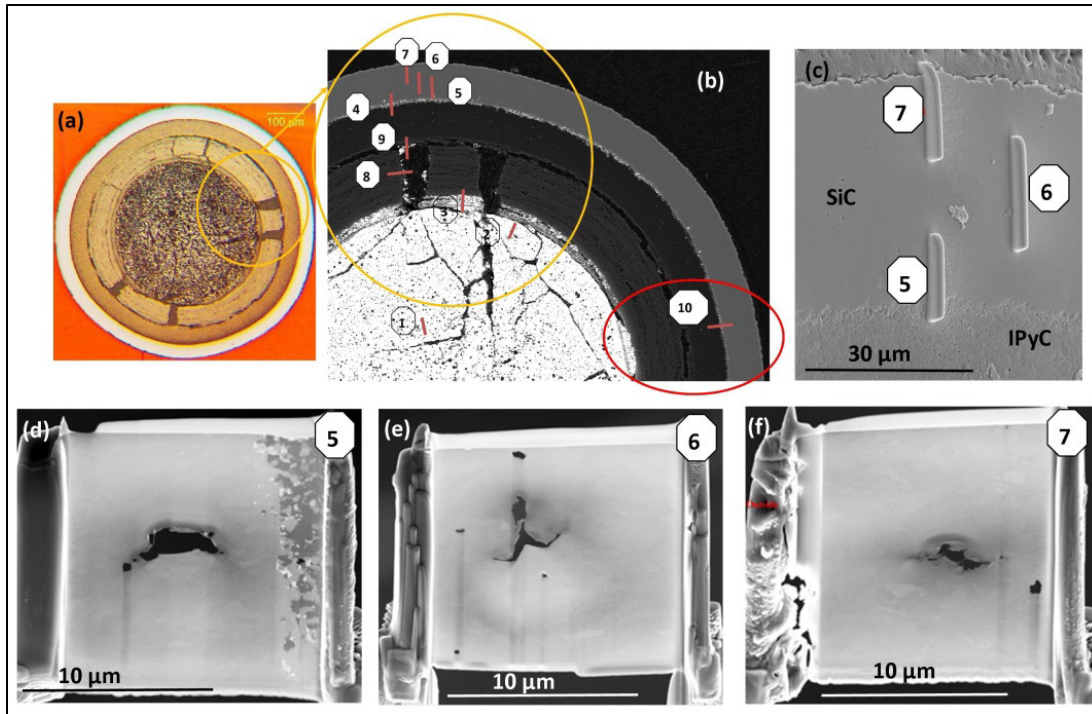


Figure 171. Images from Particle AGR1-433-001 showing the (a) cross section of the particle, (b) all FIB preparation locations labeled 1 through 10, (c) actual locations marked on the SiC layer ready for FIB lamellae preparation on the areas used for HRTEM, and (d) through (f) actual Lamellae 5 to 7, respectively, used for HRTEM examination.

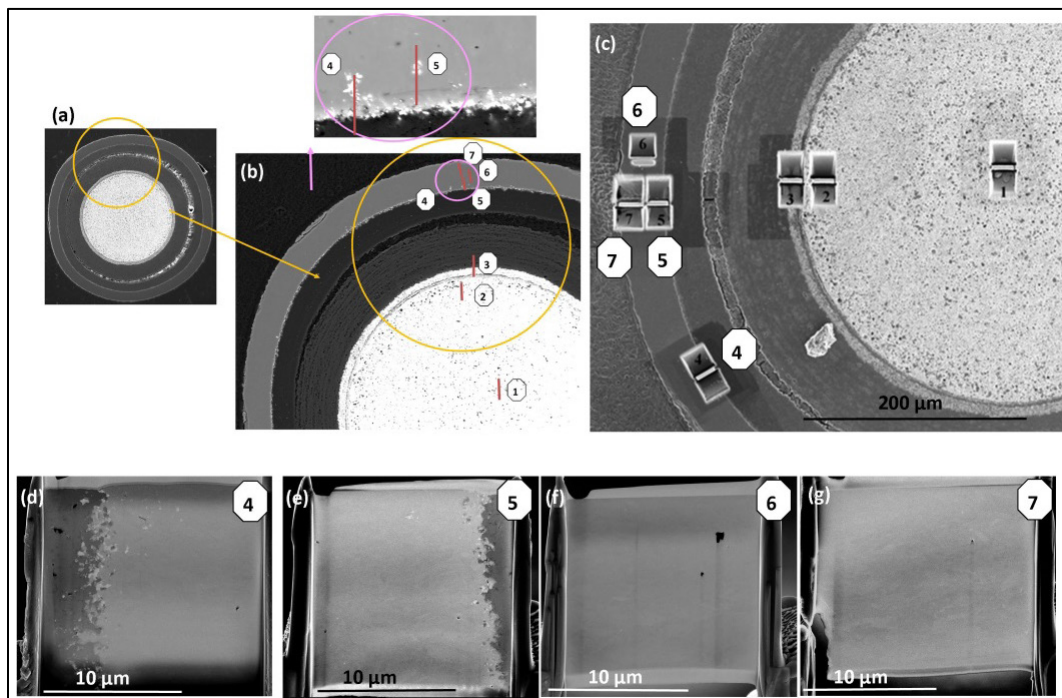


Figure 172. Images from Particle AGR1-433-004 showing (a) the cross section of the particle, (b) all FIB preparation locations labeled 1 through 7, (c) actual FIB locations ready for lift-out of the lamellae, and (d) through (f) actual Lamellae 4 to 7, respectively, used for HRTEM examination.

### 3.6.2 Coated Particle AGR1-433-001 (Low [66%] Ag Retention)

Results from qualitative chemical composition, fission product identification, crystallographic characteristics, and HRTEM examination will be provided for Particle AGR1-433-001.

Table 79. Identification of minor elements present in fission product precipitates in the SiC layer of Particle AGR1-433-001.

Lamella	Area	Elements Present									Precipitate Summary
		C	Si	Pd	Ag	Cs	Ce	Eu	U	Pu	
Inner, Lamella 4	Area 1	X	X	X	X		X		X	X	Pd, Pd-Ag, Pd-Pu, Pd-Ag-Ce, Pd-Ce-U-Pu
	Area 1B	X	X	X	X		X		X		Pd-Ag, Pd-Ag-U, Pd-U, Pd-Ce-U
	Area 2	X	X	X			X		X		Pd, Pd-Ce-U, Ce-U
	Area 3	X	X	X	X		X		X	X	Pd, Pd-Ce-U, Pd-U, Pd-Ag, Pd-U-Pu, Pd-Ce
Inner, Lamella 5	Area 1	X	X	X	X	X	X	X	X	X	Pd-Eu-U-Pu, Pd-Ce-Pu, Ag, Ag-Cs, Pd-Ce-Eu-U, Pd-Ag, Pd
	Area 2	X	X	X					X		Pd-U, Pd
	Area 3	X	X	X							Pd
Inner, Lamella 10	Area 1	X	X	X	X		X		X	X	Pd, Ag, Pd-Ag, Pd-U-Pu, Pd-Ce-U-Pu
	Area 2	X	X	X					X	X	Pd, Pd-U-Pu, Pd-Pu-U
	Area 3	X	X	X	X		X		X	X	Pd-U-Pu, U, Pd-Ag-Ce-U-Pu, Pd-U-Pu-Ce, Pd-U
	Area 4	X	X	X					X	X	Pd, Pd-U-Pu
Inner Summary		X	X	X	X	X	X	X	X	X	
Center, Lamella 6	Area 1	X	X	X					X		Pd, Pd-U
	Area 1B	X	X	X			X				Pd
	Area 2	X	X	X	X	X	X	X	X	X	Pd-Ag-Cs-Eu-U, Pd-Ag-Ce-Eu-U-Pu, Pd-Ce-Eu-Pu, Pd-Cs-Pu, Pd-Ce-Eu, Pd-Ag-Ce-Eu
Center Summary		X	X	X	X	X	X	X	X	X	
Outer, Lamella 7	Area 1	X	X	X							Pd
	Area 2	X	X	X	X	X		X	X		Pd-Ag, Pd-Eu, Pd-Eu-U, Pd-Ag-Cs-Eu-U, Pd-Ag, Pd
	Area 3	X	X	X	X		X	X			Pd, Pd-Ce, Pd-Ag
Outer Summary		X	X	X	X	X	X	X	X		
Final Summary		X	X	X	X	X	X	X	X	X	

**3.6.2.1 Chemical Composition of Minor Elements of Particle AGR1-433-001.** This section reports the qualitative chemical composition of minor elements on Particle AGR1-433-001 to determine the type of fission products present, the location of these fission product precipitates in relation to the SiC layer thickness, and the fission product elemental composition. The reported fission product precipitate compositions (atomic %) are qualitative or semi-quantitative in nature (Section 2.1.2.3). A summary of the minor elements present in these three lamellae are shown in Table 79, with Sections 3.6.2.2 to 3.6.2.4 describing the precipitates found in the inner, center, and outer areas. From these qualitative analyses, it was determined that precipitates containing Pd, Ag, Ce, Eu, Cs, U, and Pu were found in all the areas of the SiC



layer, with the exclusion of Pu, which is not present in the outer region of the SiC layer (Table 79 and Figure 171).

Figure 173 shows a qualitative trend analysis of precipitate composition (Pd, Ag, and U only) as a function of the approximate distance from the SiC-IPyC interface of Particle AGR1-433-001. This schematic presentation shows the movement of Pd, Ag, and U to an approximate depth of 38.5, 35.5, and 35.5  $\mu\text{m}$ , respectively. The slight trend observed for the U distribution (shown in Figure 174) is similar to those for Particle AGR1-531-031. However, more work is necessary to use these trend analyses in a mathematical model for prediction and quantification. The trend analysis of Pd/U and Pd/Ag ratios in relation to distance also show no observable correlation.

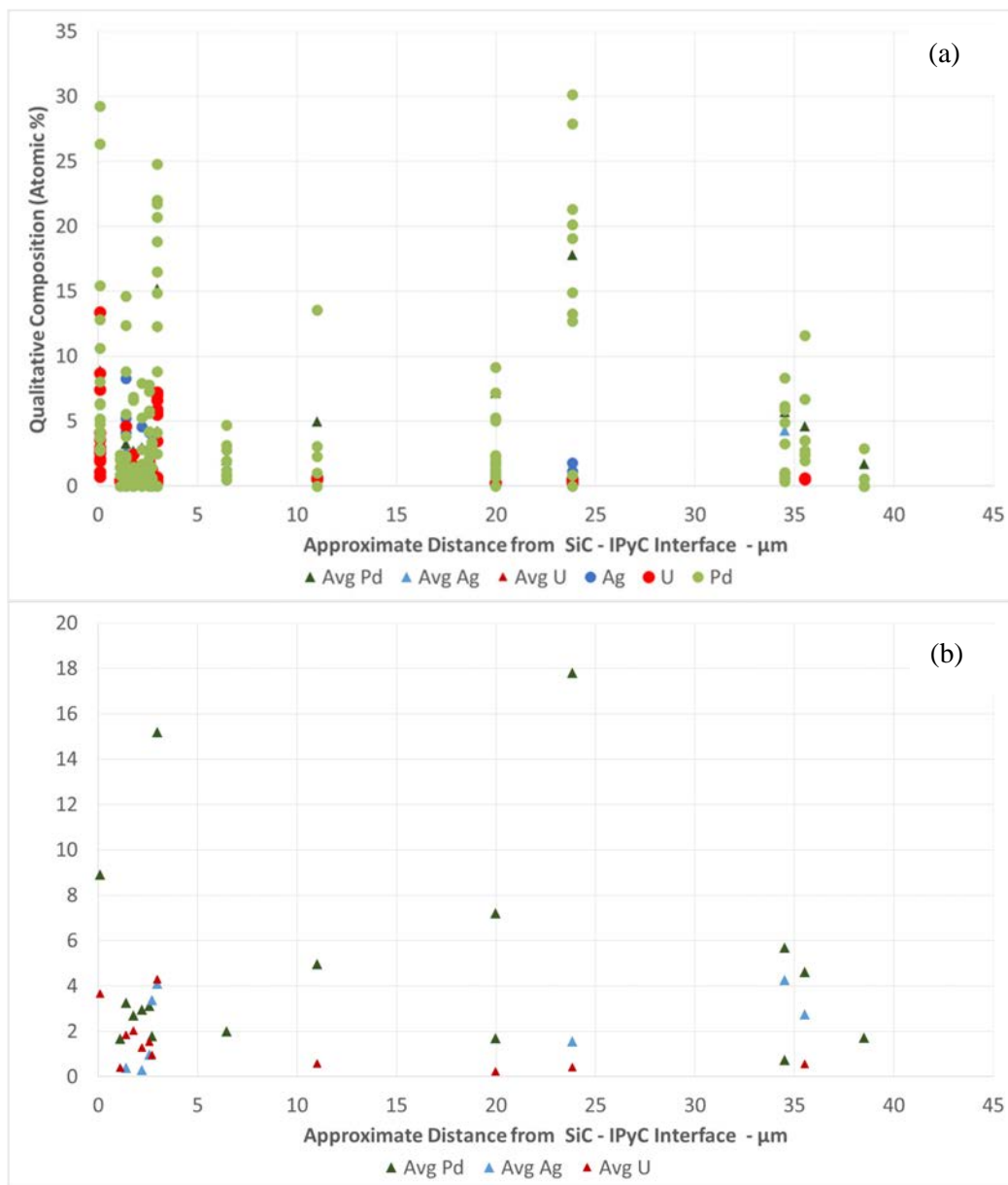


Figure 173. Qualitative trend analysis of precipitate composition (Pd, Ag, and U only) as a function of the approximate distance from the SiC-IPyC interface of Particle AGR1-433-001 with (a) a plot of the individual concentrations and averages, and (b) only the average concentration trend analysis for better clarity.

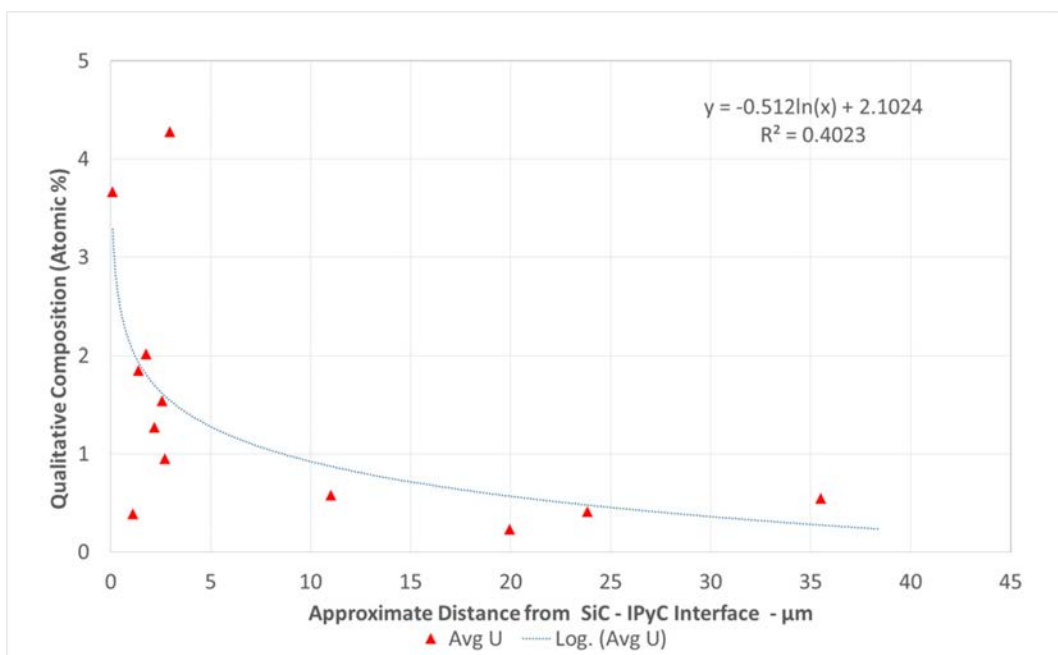


Figure 174. Qualitative trend analysis of precipitate composition for U as a function of the approximate distance from the SiC-IPyC interface of Particle AGR1-433-001.

**3.6.2.2 Inner Silicon Carbide Region (Lamellae 4, 5, 10, and 6).** Precipitates in four lamellae will provide information on the qualitative chemical composition and the presence of minor elements.

**3.6.2.2.1 Lamella 4.** Three subareas in Lamella 4 were randomly chosen (shown in Figure 175). Seven precipitates contained Ce and the majority of these contained co-existing U (six out of seven). In the single instance where U did not coexist with Ce, Ag is present in a Pd-Ag-Ce grain boundary precipitate. U was found to co-exist with Ag and Pd in one instance at a grain boundary precipitate. Only one Pd-U-Pu grain boundary precipitate is identified. No Cs was found in this Lamella of the SiC layer.

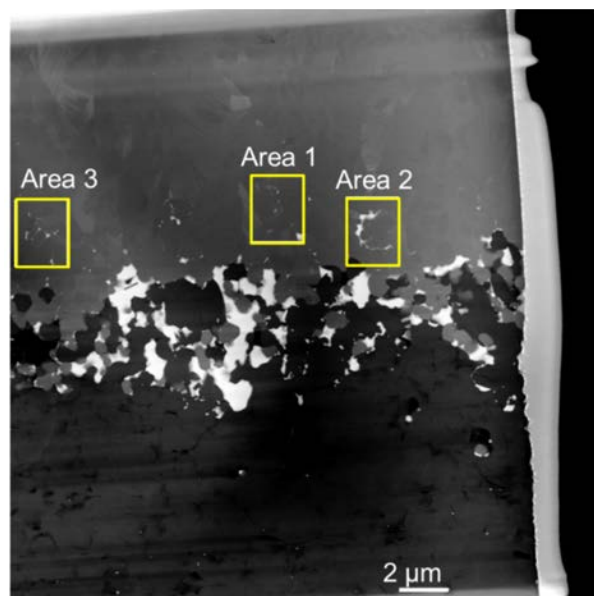


Figure 175. Large field of view STEM dark field image taken from the inner area (Lamella 4, Figure 171[b]) of TRISO Particle AGR1-433-001 at the IPyC/SiC interface showing three analysis areas (labeled 1 to 3) in the SiC layer.

Table 80. Reported qualitative EDS compositions (at.%) from the outer area (Lamella 4) of TRISO Particle AGR1-433-001, taken from subtended Areas 1a and 1b that are shown in Figure 176.

Precipitate Number	Concentration (at.%)									Precipitate Identification
	C	Si	Pd	Ag	Cs	Ce	Eu	U	Pu	
Area 1a										
1	52.45	43.35	0.55	0.00	0.00	0.09	0.00	0.03	0.04	Pd
2	48.43	35.78	0.84	8.28	0.00	0.00	0.00	0.00	0.00	Pd-Ag
3	45.53	39.55	5.26	0.00	0.00	0.15	0.00	0.12	0.38	Pd-Pu
4	43.88	43.93	0.22	0.27	0.00	3.12	0.00	0.06	0.00	Pd-Ag-Ce
5	51.82	31.60	7.93	0.07	0.00	0.67	0.00	1.27	1.10	Pd-Ce-U-Pu
Area 1b										
1	42.39	50.89	1.56	4.56	0.00	0.00	0.00	0.00	0.00	Pd-Ag
2	40.59	51.70	2.80	0.00	0.00	0.00	0.00	0.00	0.14	Pd
3	40.99	48.47	1.72	0.32	0.00	0.00	0.00	0.20	0.01	Pd-Ag-U
4	45.20	40.29	0.13	0.00	0.00	0.00	0.00	0.99	0.01	Pd-U
5	47.30	47.14	1.09	0.00	0.00	0.45	0.00	0.18	0.03	Pd-Ce-U

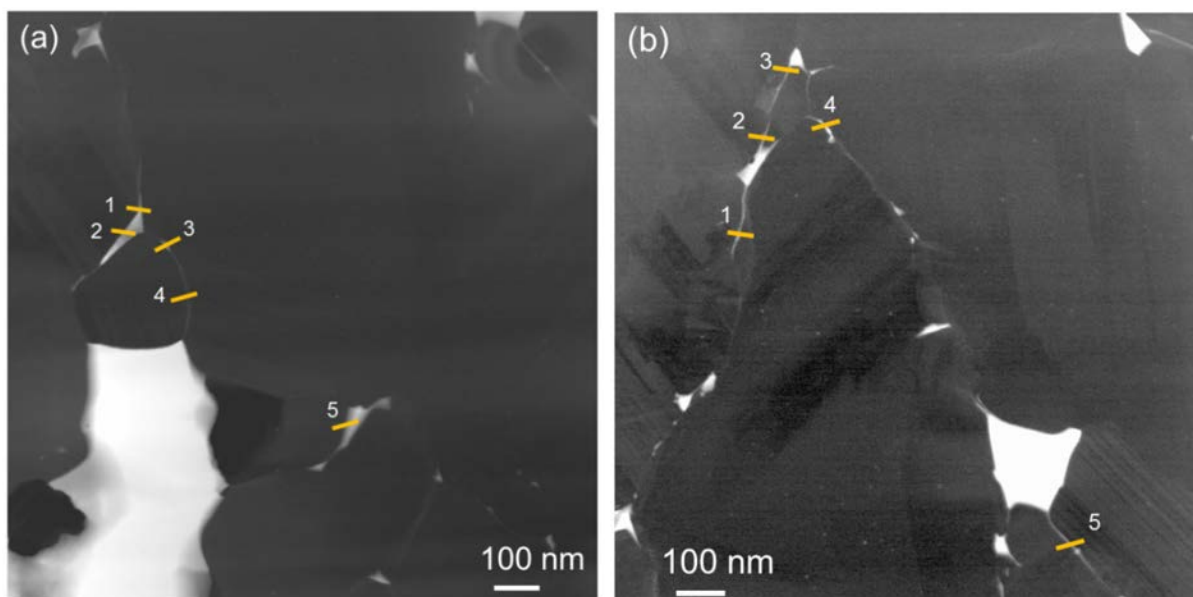


Figure 176. STEM HAADF image combined with EDS labeling to track the chemical composition of fission product precipitates from the inner area (Lamella 4) of TRISO Particle AGR1-433-001 within the subtended Area 1, which was subdivided into two Areas (a) 1a and (b) 1b. Note the reported chemical compositions are in Table 80.

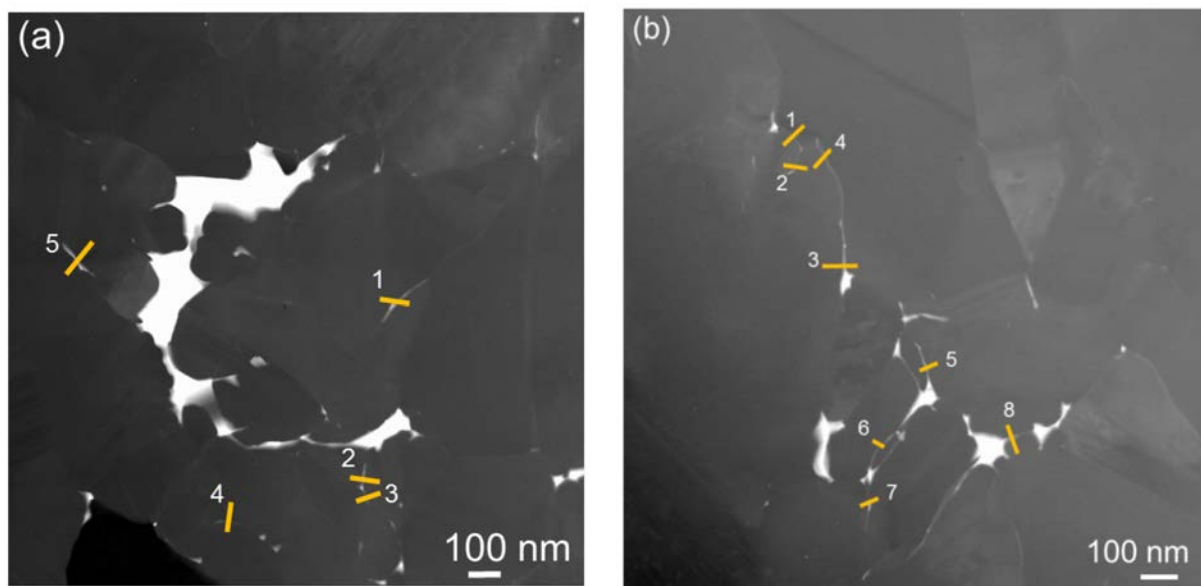


Figure 177. STEM HAADF image combined with EDS labeling to track the chemical composition of fission product precipitates from the inner area (Lamella 4) of TRISO Particle AGR1-433-001 within the subtended Areas (a) 2 and (b) 3. Note the reported chemical compositions are in Table 81.

Table 81. Reported qualitative EDS compositions (at.%) from precipitates (Figure 177) from the outer area (Lamella 4) of TRISO Particle AGR1-433-001, taken from subtended Areas 2 and 3 (Figure 175).

Precipitate Number	Concentration (at.%)									Precipitate Identification
	C	Si	Pd	Ag	Cs	Ce	Eu	U	Pu	
Area 2										
1	40.97	54.05	2.39	0.00	0.00	1.47	0.00	0.12	0.19	Pd-Ce
2	45.32	50.35	2.03	0.01	0.00	0.13	0.00	0.44	0.07	Pd-U
3	49.96	47.60	0.05	0.00	0.00	0.46	0.00	0.35	0.00	Ce-U
4	48.71	48.89	0.86	0.00	0.00	0.00	0.00	0.00	0.05	Pd
5	49.97	46.02	1.47	0.00	0.00	0.00	0.00	0.13	0.03	Pd
Area 3										
1	43.41	53.68	0.66	0.00	0.00	0.38	0.00	0.00	0.06	Pd-Ce
2	47.12	51.02	0.02	0.02	0.00	0.00	0.00	0.01	0.04	
3	49.20	43.73	3.16	0.00	0.00	1.42	0.00	0.00	0.00	Pd-Ce
4	47.09	49.38	0.41	0.00	0.00	0.00	0.00	0.62	0.07	Pd-U
5	45.53	46.54	0.52	4.11	0.00	0.00	0.00	0.02	0.04	Pd-Ag
6	49.90	46.74	1.47	0.00	0.00	0.00	0.00	0.00	0.02	Pd
7	40.80	53.19	3.40	0.04	0.00	0.00	0.00	1.29	0.67	Pd-U-Pu
8	37.78	58.67	2.94	0.00	0.00	0.43	0.00	0.07	0.08	Pd-Ce

**3.6.2.2.2 Lamella 5.** Three subareas containing precipitates in Lamella 5 (shown in Figure 171[d]) were chosen and shown in Figure 178. One of each of the following precipitates was found in this lamella: Pd-Eu-U-Pu, Pd-Ce-Pu, Pd-Ce-Eu-U, and Ag-Cs. However, the majority of the precipitates were either Ag or Pd alone or Pd-Ag and Pd-U. Precipitate details are provided in Figure 179, Figure 180, Table 82, and Table 83.

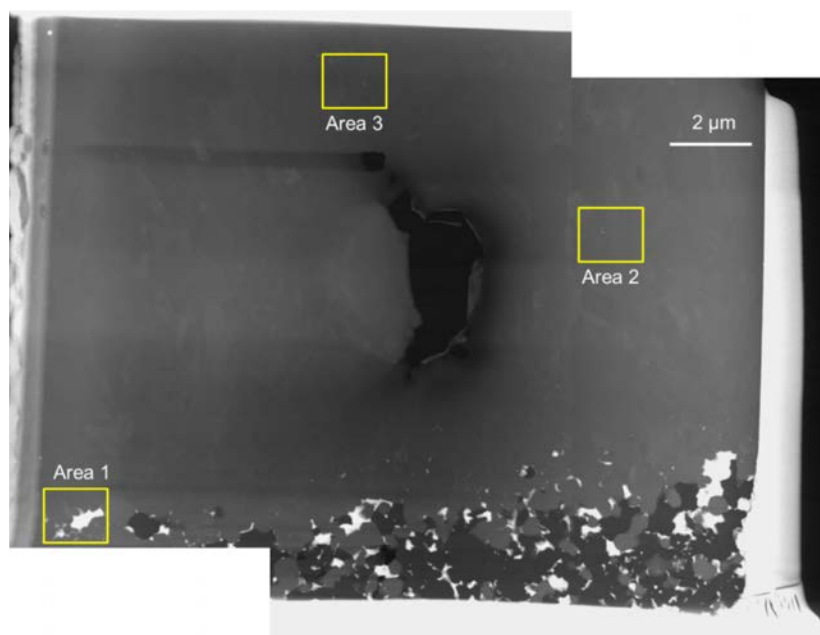


Figure 178. Large field of view STEM dark field image taken from the inner area of TRISO Particle AGR1-433-001 (Lamella 5) showing three areas (labeled 1 to 3) in the SiC layer.

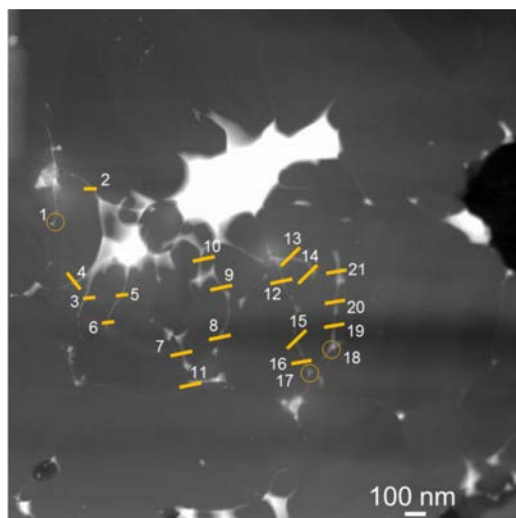


Figure 179. STEM HAADF image combined with EDS labeling to track the chemical composition of fission product precipitates from the inner area (Lamella 5 in Figure 178) of TRISO Particle AGR1-433-001 within subtended area 1. Note the reported chemical compositions are in Table 82.

Table 82. Reported qualitative EDS compositions (at.%) from precipitates (Figure 179) from the inner area (Lamella 5) of TRISO Particle AGR1-433-001, taken from subtended Area 1 (Figure 178).

Precipitate Number	Concentration (at.%)									Precipitate Identification
	C	Si	Pd	Ag	Cs	Ce	Eu	U	Pu	
1	58.68	19.57	14.61	0.00	0.00	0.18	0.74	4.61	1.61	Pd-Eu-U-Pu
2	30.98	55.52	12.38	0.07	0.00	0.42	0.24 <sup>a</sup>	0.00	0.39	Pd-Ce-Pu
3	41.03	54.83	0.00	4.10	0.00	0.02	0.02	0.00	0.00	Ag
4	42.77	50.93	0.40	4.56	0.56	0.47	0.26 <sup>a</sup>	0.00	0.05	Ag-Cs-Pd-Ce
5	33.29	61.30	3.83	0.00	0.13	0.21	0.34	0.74	0.17	Pd-Ce-Eu-U
6	38.58	51.83	0.25	1.40	0.00	0.00	0.00	0.05	0.00	Pd-Ag
7	21.53	62.96	8.82	0.29	0.00	0.00	0.00	0.08	0.82	Pd-Ag-Pu
8	34.34	55.55	0.69	1.99	0.00	0.00	0.00	0.00	0.00	Pd-Ag
9	30.65	59.20	1.44	0.00	0.00	0.00	0.00	0.03	0.04	Pd
10	35.88	53.65	2.32	0.00	0.00	0.00	0.00	0.00	0.00	Pd
11	35.98	54.23	5.55	0.12	0.00	0.00	0.00	0.21	0.00	Pd-U
12	41.41	47.93	0.23	1.73	0.00	0.00	0.00	0.00	0.00	Pd-Ag
13	39.62	48.43	0.82	0.07	0.00	0.00	0.00	0.00	0.02	Pd
14	35.54	50.82	0.34	5.21	0.00	0.00	0.00	0.00	0.00	Pd-Ag
15	39.41	50.83	0.54	1.44	0.00	0.00	0.00	0.00	0.02	Pd-Ag
16	43.67	48.36	0.11	0.00	0.00	0.00	0.00	0.00	0.00	
17	35.53	54.22	0.02	2.46	0.00	0.00	0.00	0.00	0.00	Ag
18	39.57	45.01	0.15	4.71	0.00	0.00	0.00	0.00	0.00	Ag
19	41.75	44.27	0.29	2.29	0.00	0.00	0.00	0.06	0.02	Ag-Pd
20	38.28	51.28	1.04	0.00	0.00	0.00	0.00	0.00	0.00	Pd
21	43.03	45.82	2.11	0.00	0.00	0.00	0.00	0.00	0.00	Pd

a. Cannot differentiate between Eu and Fe.

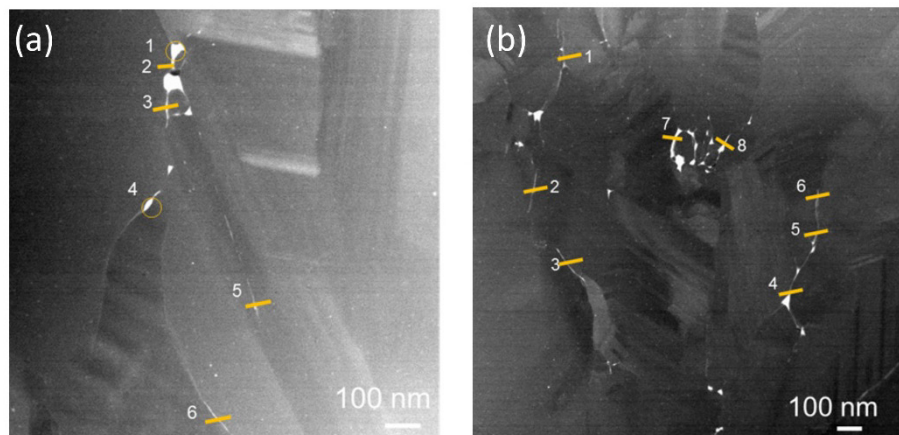


Figure 180. (a) STEM HAADF image combined with EDS labeling to track the chemical composition of fission product precipitates from the inner area (Lamella 5) of TRISO Particle AGR1-433-001 within subtended Area 2. Note the reported chemical compositions are in Table 82. (b) STEM HAADF image combined with EDS labeling to track the chemical composition of fission product precipitates from the inner area (Lamella 5) of TRISO Particle AGR1-433-001 within subtended Area 3. Note the reported chemical compositions are in Table 83.

Table 83. Reported qualitative EDS compositions (at.%) from the inner area (Lamella 5) of TRISO Particle AGR1-433-001, taken from subtended Areas 2 and 3 (Figure 178).

Precipitate Number	Concentration (at.%)									Precipitate Identification
	C	Si	Pd	Ag	Cs	Ce	Eu	U	Pu	
Area 2										
1	37.72	48.65	13.54	0.03	0.00	0.02	0.05	0.00	0.00	Pd
2	41.87	55.57	2.27	0.00	0.00	0.09	0.05	0.07	0.08	Pd
3	50.31	49.59	0.07	0.00	0.00	0.00	0.01	0.00	0.02	
4	41.85	54.37	3.06	0.00	0.00	0.00	0.01	0.63	0.08	Pd-U
5	41.31	57.11	1.01	0.00	0.00	0.00	0.03	0.53	0.00	Pd-U
6	50.75	49.11	0.11	0.00	0.00	0.00	0.03	0.00	0.00	
Area 3										
1	65.44	33.88	0.50	0.00	0.05	0.03	0.11	0.00	0.00	Pd
2	64.53	32.66	2.79	0.00	0.00	0.01	0.01	0.00	0.00	Pd
3	60.93	38.22	0.83	0.00	0.00	0.00	0.02	0.00	0.00	Pd
4	57.21	40.82	1.97	0.00	0.00	0.00	0.01	0.00	0.00	Pd
5	61.54	37.20	1.23	0.00	0.00	0.00	0.03	0.00	0.00	Pd
6	62.21	36.93	0.85	0.00	0.00	0.00	0.00	0.00	0.00	Pd
7	52.28	42.99	4.71	0.00	0.00	0.00	0.02	0.00	0.00	Pd
8	45.61	51.04	3.14	0.00	0.00	0.00	0.00	0.00	0.20	Pd-Pu

**3.6.2.2.3 Lamella Position 10.** Four subareas in Lamella 10 were chosen at the SiC-IPyC interface (shown in Figure 181). Only one of each of the following precipitates is present in this lamella, which is on the opposite side of the breached buffer layer: Pd-Ce-U-Pu, Pd-Ag-Ce-U-Pu, Ag, and U, with the majority of the precipitates being either Pd or Ag alone or Pd-U-Pu.



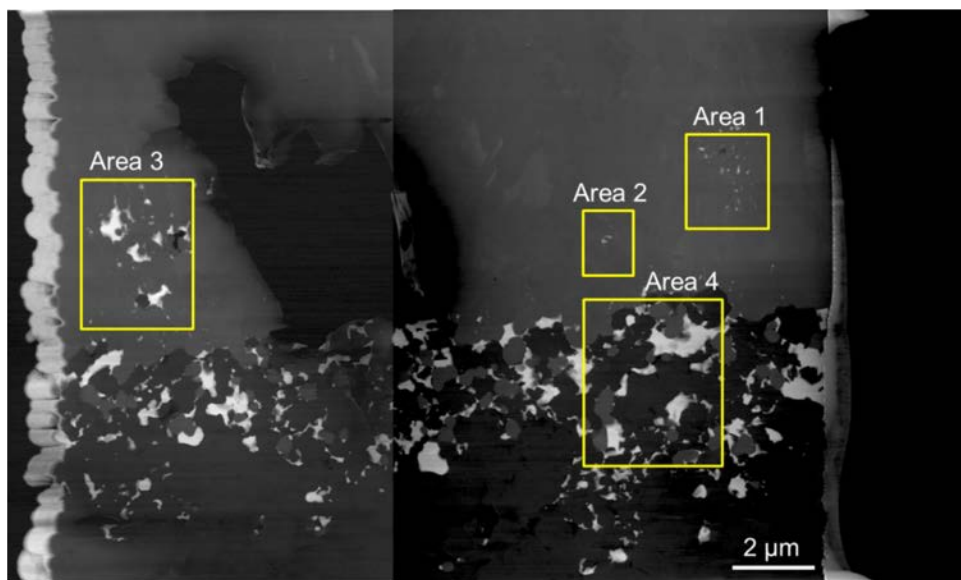


Figure 181. Large field of view STEM dark field image taken from the inner area (Lamella 10) of TRISO Particle AGR1-433-001 at the IPyC/SiC interface showing three areas of analysis in the SiC layer (Areas 1-3) and one (Area 4) in the IPyC/SiC interface.

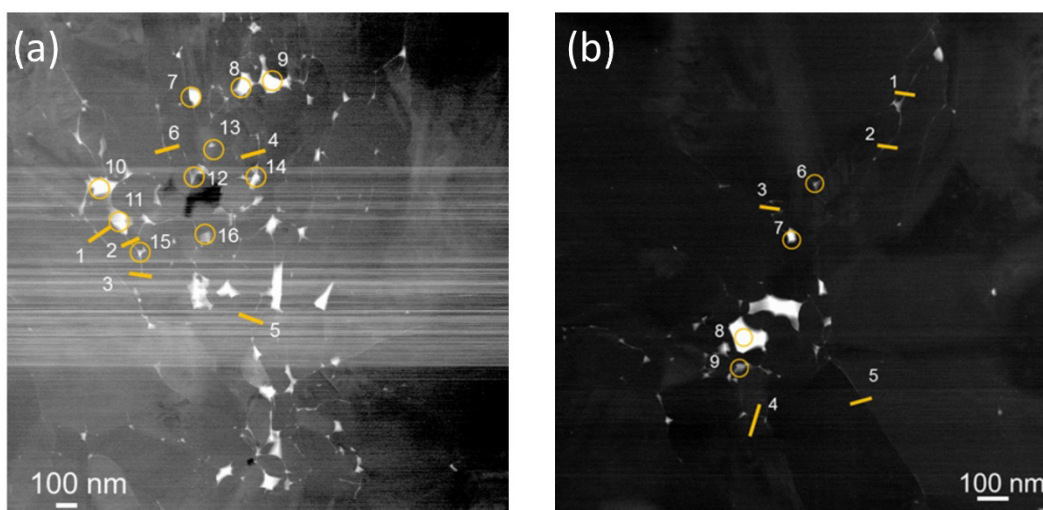


Figure 182. (a) STEM HAADF image combined with EDS labeling to track the chemical composition of fission product precipitates from the inner area at the IPyC-SiC interface (Lamella 10) of TRISO Particle AGR1-433-001 within subtended Area 1. Note the reported chemical compositions are in Table 84. (b) STEM HAADF image combined with EDS labeling to track the chemical composition of fission product precipitates from the inner area (Lamella 10) of TRISO Particle AGR1-433-001 within subtended Area 2. Note the reported chemical compositions are in Table 84.

Table 84. Reported qualitative EDS compositions (at.%) from precipitates (Figure 182) from the inner area (Lamella 10) of TRISO Particle AGR1-433-001, taken from subtended Areas 1 and 2 (Figure 181).

Precipitate Number	Concentration (at.%)									Precipitate Identification
	C	Si	Pd	Ag	Cs	Ce	Eu	U	Pu	
Area 1										
1	54.35	44.58	0.28	0.07	0.00	0.00	0.00	0.00	0.00	Pd
2	45.61	53.75	0.21	0.00	0.00	0.00	0.00	0.00	0.00	Pd
3	57.33	40.40	0.23	0.35	0.00	0.00	0.00	0.00	0.00	Pd-Ag
4	52.31	45.21	1.07	0.00	0.00	0.00	0.00	0.00	0.00	Pd
5	55.30	43.41	0.00	0.00	0.00	0.00	0.00	0.00	0.00	
6	70.24	29.40	0.29	0.0	0.00	0.00	0.00	0.00	0.00	Pd
7	35.58	56.82	5.66	0.00	0.00	0.00	0.00	1.67	0.25	Pd-U-Pu
8	49.11	36.54	7.29	0.03	0.00	0.51	0.00	1.80	0.76	Pd-Ce-U-Pu
9	43.87	48.15	5.79	0.00	0.00	0.00	0.00	1.67	0.49	Pd-U-Pu
10	44.58	41.82	7.78	0.00	0.00	0.00	0.00	1.92	0.81	Pd-U-Pu
11	47.17	45.99	5.59	0.00	0.00	0.00	0.00	0.00	0.00	Pd
12	47.43	49.23	2.20	0.00	0.00	0.00	0.00	0.00	0.00	Pd
13	48.49	47.07	2.66	0.00	0.00	0.00	0.00	0.19	0.05	Pd
14	43.18	51.49	4.21	0.00	0.00	0.00	0.00	0.64	0.43	Pd-U-Pu
15	46.52	48.30	0.12	2.78	0.00	0.00	0.00	0.00	0.00	Ag
16	49.13	48.92	0.65	0.0	0.00	0.0	0.00	0.09	0.03	Pd
Area 2										
1	55.08	43.92	0.20	0.09	0.00	0.00	0.00	0.00	0.00	Pd
2	58.52	39.63	0.74	0.00	0.00	0.00	0.00	0.00	0.00	Pd
3	52.87	47.12	0.00	0.00	0.00	0.00	0.00	0.00	0.00	
4	59.85	39.65	0.00	0.00	0.00	0.00	0.00	0.00	0.00	
5	60.65	38.19	0.00	0.00	0.00	0.00	0.00	0.00	0.00	
6	48.56	50.80	0.44	0.00	0.00	0.00	0.00	0.00	0.04	Pd
7	42.93	47.61	6.61	0.00	0.00	0.00	0.00	1.60	0.46	Pd-U-Pu
8	43.76	45.90	6.84	0.00	0.00	0.00	0.00	2.45	0.50	Pd-Pu-U
9	55.84	42.68	1.46	0.00	0.00	0.00	0.00	0.00	0.00	Pd

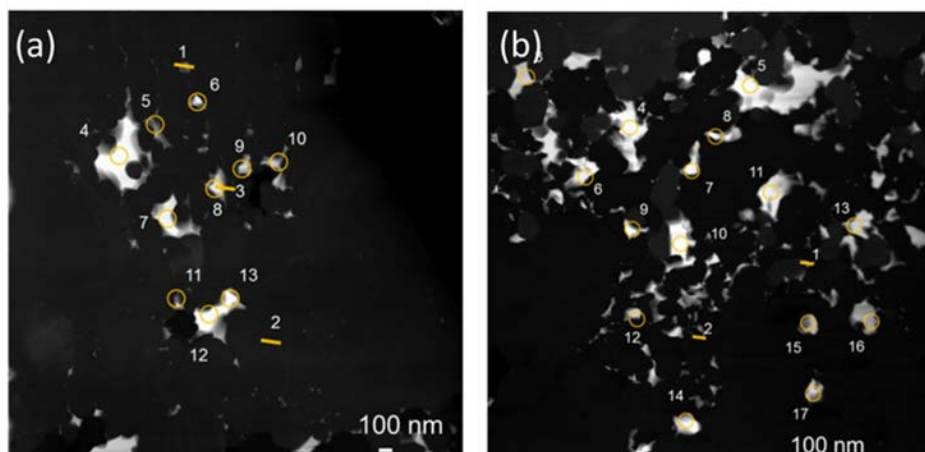


Figure 183. (a) STEM HAADF image combined with EDS labeling to track the chemical composition of fission product precipitates from the IPyC-SiC interface (Lamella 10) of TRISO Particle AGR1-433-001 within subtended Area 3 (from the inner area of the SiC layer). Note the reported chemical compositions are in Table 85. (b) STEM HAADF image combined with EDS labeling to track the chemical composition of fission product precipitates from the IPyC-SiC interface (Lamella 10) of TRISO Particle AGR1-433-001 within the subtended Area 4 that is within the IPyC layer. Note the reported chemical compositions are in Table 85.

Table 85. Reported qualitative EDS compositions (at.%) from precipitates (Figure 183) from the inner area (Lamella 10) of the SiC layer of TRISO Particle AGR1-433-001, taken from subtended Areas 3 and 4 (Figure 181).

Precipitate Number	Concentration (at.%)									Precipitate Identification
	C	Si	Pd	Ag	Cs	Ce	Eu	U	Pu	
Area 3										
1	50.57	45.68	2.50	0.00	0.00	0.00	0.00	0.68	0.38	Pd-U-Pu
2	62.64	36.07	0.16	0.00	0.00	0.00	0.00	0.42	0.00	U
3	47.99	46.22	4.13	0.00	0.00	0.00	0.00	0.27	0.60	Pd-U-Pu
4	49.73	23.09	18.82	0.00	0.00	0.00	0.00	5.93	2.41	Pd-U-Pu
5	48.26	36.51	14.85	0.00	0.00	0.00	0.00	0.00	0.00	Pd
6	35.99	31.66	20.70	3.39	0.00	2.35	0.00	3.47	0.90	Pd-Ag-Ce-U-Pu
7	52.52	21.77	16.51	0.00	0.00	0.00	0.00	5.69	1.48	Pd-U-Pu
8	29.01	29.74	21.73	0.00	0.00	8.39	0.00	6.63	4.43	Pd-U-Pu-Ce
9	52.59	24.88	22.00	0.00	0.00	0.00	0.00	0.00	0.00	Pd
10	45.09	29.55	24.78	0.00	0.00	0.00	0.00	0.00	0.00	Pd
11	45.71	35.89	12.29	0.00	0.00	0.00	0.00	5.49	0.59	Pd-U-Pu
12	67.50	11.56	8.81	0.00	0.00	0.00	0.00	7.23	0.42	Pd-U-Pu
13	75.47	13.58	0.19	0.00	0.00	0.00	0.00	6.99	0.00	Pd-U
Area 4										
1	91.30	3.85	3.72	0.00	0.00	0.00	0.00	0.07	0.12	Pd-U-Pu
2	94.84	2.12	2.91	0.00	0.00	0.00	0.00	0.00	0.12	Pd-Pu
3	32.37	31.56	26.34	0.00	0.00	0.00	0.00	7.41	2.18	Pd-U-Pu

Table 85. (continued).

Precipitate Number	Concentration (at.%)									Precipitate Identification
	C	Si	Pd	Ag	Cs	Ce	Eu	U	Pu	
4	72.40	7.80	5.17	0.00	0.00	0.05	0.00	8.68	0.42	Pd-U-Pu
5	54.21	20.76	15.44	0.00	0.00	0.00	0.00	4.13	1.44	Pd-U-Pu
6	86.40	5.24	4.15	0.00	0.00	0.00	0.00	2.57	0.33	Pd-U-Pu
7	83.21	7.82	6.29	0.00	0.00	0.00	0.00	1.98	0.67	Pd-U-Pu
8	90.25	4.10	4.11	0.00	0.00	0.00	0.00	1.11	0.39	Pd-U-Pu
9	60.54	27.93	8.06	0.00	0.00	0.00	0.00	2.77	0.68	Pd-U-Pu
10	67.66	13.45	12.80	0.00	0.00	0.00	0.00	3.57	1.39	Pd-U-Pu
11	23.13	29.00	29.26	0.00	0.00	0.00	0.00	13.39	5.19	Pd-U-Pu
12	90.09	4.79	3.69	0.00	0.00	0.00	0.00	0.71	0.27	Pd-U-Pu
13	70.42	12.27	10.62	0.00	0.00	0.00	0.00	2.98	1.06	Pd-U-Pu
14	86.13	6.24	4.78	0.11	0.00	0.00	0.00	2.13	0.59	Pd-U-Pu
15	94.11	2.20	2.74	0.00	0.00	0.00	0.00	0.74	0.07	Pd-U-Pu
16	83.53	7.47	6.38	0.00	0.00	0.00	0.00	1.93	0.59	Pd-U-Pu
17	88.80	4.26	5.13	0.00	0.00	0.00	0.00	1.09	0.23	Pd-U-Pu

### 3.6.2.3 Chemical Composition in the Center Area of the Silicon Carbide Layer

**(Lamella 6).** Two random areas in Lamella 6 were chosen for analysis (shown in Figure 184). Area 1 is further subdivided into two areas (1a and 1b) (shown in Figure 185). The precipitates in Area 1 consists only of Pd alone or in two instances Pd-U, while the precipitates in Subarea 2 differ significantly with more multi-elemental precipitates containing three or more elements from Eu, Ag, Pd, Pu, Ce, and Cs. No explanation for this behavior is currently obvious.

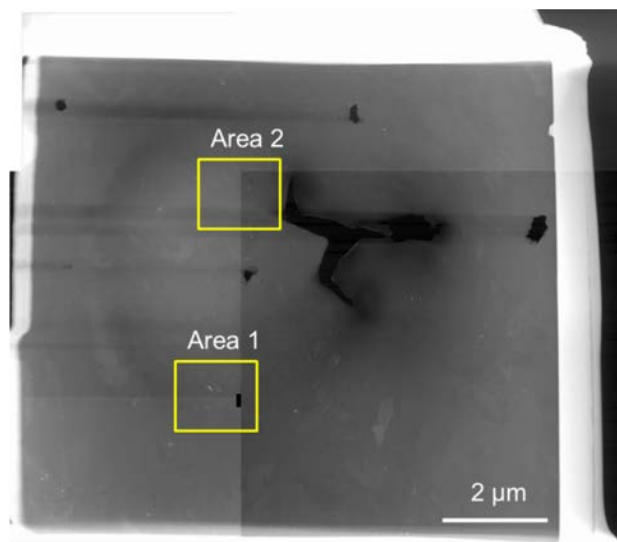


Figure 184. Large field of view STEM dark field image taken from the center area (Lamella 6) of TRISO Particle AGR1-433-001.

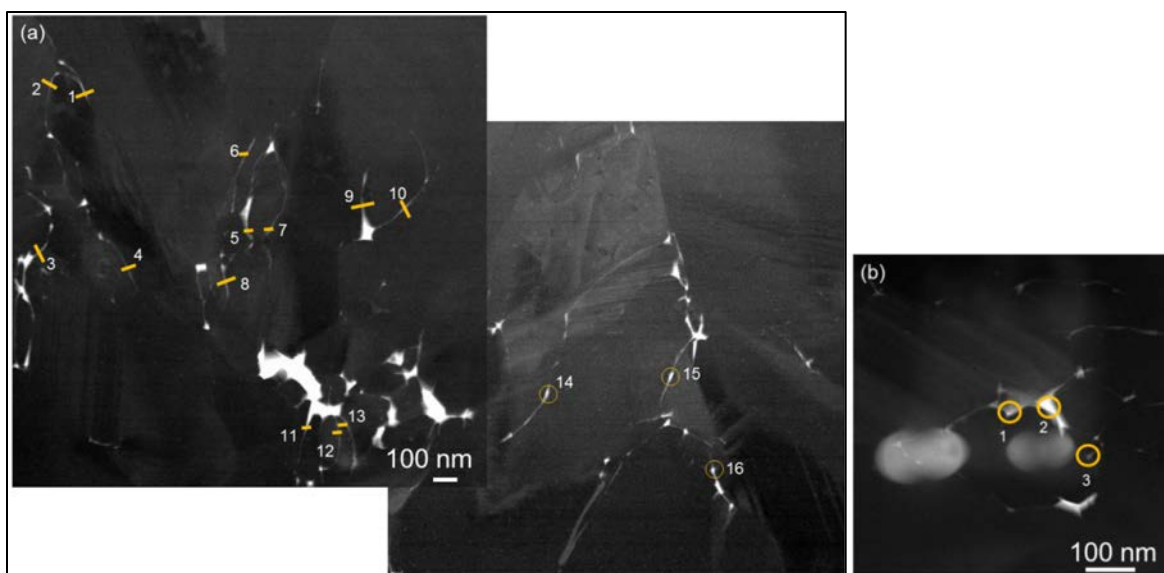


Figure 185. STEM HAADF image combined with EDS labeling to track the chemical composition of fission product precipitates from the center area (Lamella 6) of TRISO Particle AGR1-433-001 within subtended Areas (a) 1a and (b) 1b. Note the reported chemical compositions are in Table 86 (note that Figure 185(a) consists of a combination of 2 images that overlap).

Table 86. Reported qualitative EDS compositions (at.%) from the precipitates (Figure 185) from the center area (Lamella 6) of TRISO Particle AGR1-433-001, taken from subtended Areas 1a and 1b (Figure 184).

Precipitate Number	Concentration (at.%)									Precipitate Identification
	C	Si	Pd	Ag	Cs	Ce	Eu	U	Pu	
Area 1a										
1	51.55	45.73	2.36	0.00	0.00	0.14	0.18	0.04	0.00	Pd
2	53.99	44.88	0.88	0.00	0.00	0.06	0.18	0.00	0.00	Pd
3	59.57	38.82	1.59	0.00	0.00	0.00	0.02	0.00	0.00	Pd
4	60.38	38.65	0.78	0.00	0.00	0.02	0.18	0.00	0.00	Pd
5	58.91	39.05	1.97	0.00	0.00	0.00	0.07	0.00	0.00	Pd
6	53.70	45.40	0.69	0.00	0.00	0.07	0.14	0.00	0.00	Pd
7	52.34	46.29	1.18	0.19	0.00	0.00	0.00	0.00	0.00	Pd
8	58.15	41.11	0.73	0.00	0.00	0.00	0.00	0.00	0.00	Pd
9	57.38	40.86	1.75	0.00	0.00	0.00	0.02	0.00	0.00	Pd
10	57.36	42.44	0.14	0.00	0.00	0.01	0.05	0.01	0.00	
11	54.47	40.47	5.01	0.00	0.00	0.00	0.00	0.00	0.00	Pd
12	55.02	42.94	1.04	0.11	0.00	0.00	0.00	0.00	0.00	Pd
13	54.51	42.46	1.15	0.00	0.00	0.00	0.00	0.03	0.00	Pd
14	56.35	41.31	2.32	0.00	0.00	0.00	0.00	0.00	0.00	Pd
15	51.53	46.13	1.84	0.00	0.00	0.00	0.00	0.26	0.00	Pd-U
16	48.57	48.41	2.22	0.00	0.00	0.00	0.00	0.21	0.00	Pd-U

Table 86. (continued).

Precipitate Number	Concentration (at.%)									Precipitate Identification
	C	Si	Pd	Ag	Cs	Ce	Eu	U	Pu	
Area 1b										
1	39.78	44.12	5.26	0.00	0.00	0.00	0.00	0.00	0.06	Pd
2	36.59	44.75	7.19	0.00	0.00	0.69	0.00	0.00	0.14	Pd-Ce
3	37.86	46.68	9.16	0.09	0.00	0.00	0.00	0.00	0.03	Pd

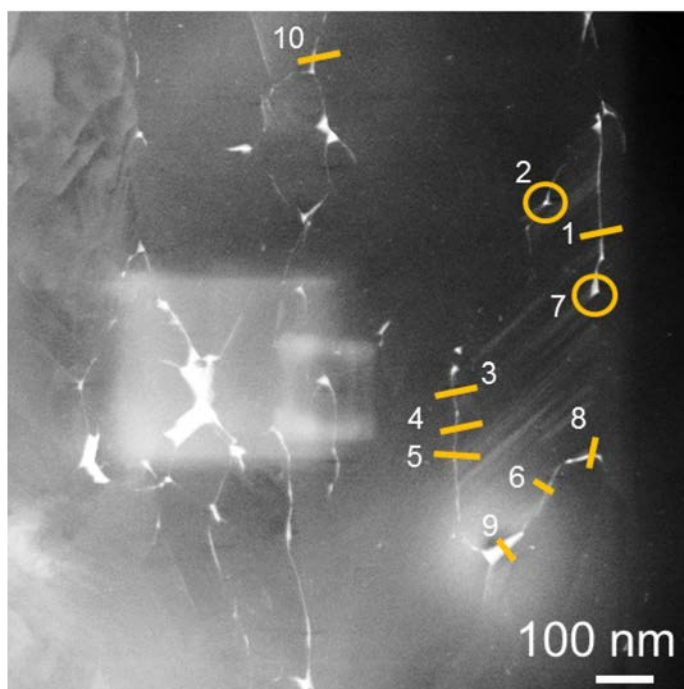


Figure 186. STEM HAADF image combined with EDS labeling to track the chemical composition of fission product precipitates from the center area (Lamella 6) of TRISO Particle AGR1-433-001 within subtended area 2. Note the reported chemical compositions are in Table 87.

Table 87. Reported qualitative EDS compositions (at.%) from precipitates (Figure 186) from the center area (Lamella 6) of TRISO Particle AGR1-433-001, taken from subtended Area 2 (Figure 184).

Precipitate Number	Concentration (at.%)									Precipitate Identification
	C	Si	Pd	Ag	Cs	Ce	Eu	U	Pu	
1	29.54	55.58	13.28	0.10	0.00	0.61	0.87	0.00	0.00	Pd-Ce-Eu
2	20.79	55.73	21.30	0.30	0.45	0.00	0.88	0.51	0.00	Pd-Ag-Cs-Eu-U
3	21.83	61.47	12.71	0.73	0.00	1.16	0.87	0.49	0.70	Pd-Ag-Ce-Eu-U-Pu
4	22.20	58.60	14.92	1.78	0.00	0.54	1.01	0.25	0.65	Pd-Ag-Ce-Eu-U-Pu
5	24.09	54.10	20.12	0.00	0.00	0.49	0.90	0.00	0.26	Pd-Ce-Eu-Pu
6	21.55	56.34	18.55	0.00	0.00	0.44	0.70	0.00	0.24	Pd-Ce-Eu-Pu
7	17.34	49.85	30.13	0.00	0.76	0.00	0.07	0.00	1.82	Pd-Cs-Pu

Table 87. (continued).

Precipitate Number	Concentration (at.%)									Precipitate Identification
	C	Si	Pd	Ag	Cs	Ce	Eu	U	Pu	
8	22.66	47.62	27.89	0.06	0.00	0.56	1.18	0.00	0.00	Pd-Ce-Eu
9	21.55	56.34	19.08	1.12	0.00	0.80	1.09	0.00	0.00	Pd-Ag-Ce-Eu
10	49.44	48.06	0.85	0.00	0.00	0.00	0.00	0.15	0.00	Pd-Eu

**3.6.2.4 Chemical Composition in the Outer Area of the Silicon Carbide Layer (Lamella 7).** Three selected subareas were examined as shown in Figure 187. The bulk of the precipitates contain only Pd with one of each of the following precipitates: Pd-Ag-Cs-Eu-U, Pd-Eu-U, Pd-Eu, and Pd-Ce with four Pd Ag precipitates.

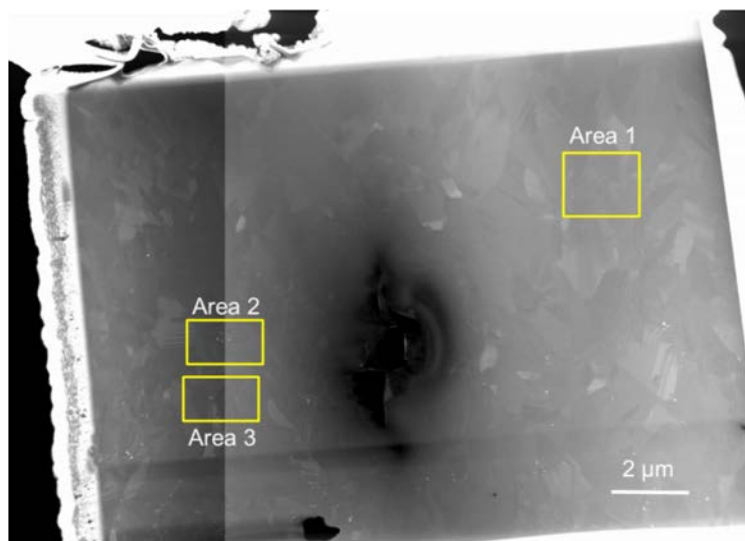


Figure 187. Large field of view STEM dark field image taken from the outer area (Lamella 7) of TRISO Particle AGR1-433-001.



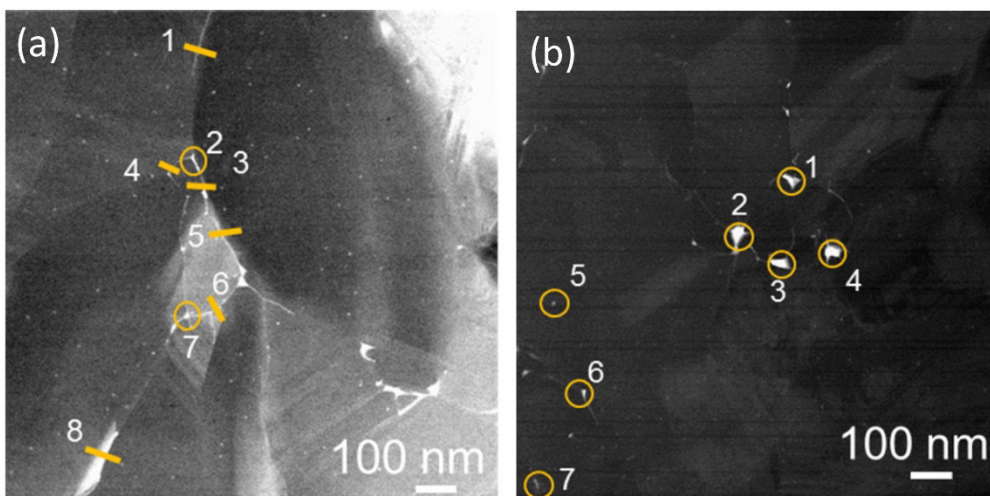


Figure 188. STEM HAADF image combined with EDS labeling to track the chemical composition of fission product precipitates from, (a) the outer area (Lamella 7) of TRISO Particle AGR1-433-001, within subtended area 1. Note the reported chemical compositions are in Table 88; (b) STEM HAADF image combined with EDS labeling to track the chemical composition of fission product precipitates from the outer area (Lamella 7) of TRISO Particle AGR1-433-001 within subtended Area 2. Note the reported chemical compositions are in Table 88.

Table 88. Reported qualitative EDS compositions (at.%) from precipitates (showing in Figure 188) from the outer area (Lamella 7) of TRISO Particle AGR1-433-001, taken from subtended Area 1 and 2 (Figure 187).

Precipitate Number	Concentration (at.%)									Precipitate Identification
	C	Si	Pd	Ag	Cs	Ce	Eu	U	Pu	
Area 1										
1	50.43	49.06	0.19	0.00	0.00	0.16	0.17	0.00	0.00	
2	55.87	43.55	0.56	0.00	0.00	0.00	0.00	0.03	0.00	Pd
3	39.06	60.85	0.07	0.00	0.00	0.01	0.00	0.00	0.00	
4	50.41	49.22	0.00	0.09	0.07	0.07	0.14	0.00	0.00	
5	53.78	46.00	0.06	0.00	0.00	0.09	0.06	0.00	0.00	
6	51.31	48.35	0.11	0.00	0.00	0.07	0.14	0.00	0.01	
7	49.43	50.20	0.19	0.00	0.00	0.06	0.10	0.02	0.00	
8	48.18	48.58	2.88	0.10	0.00	0.05	0.19	0.00	0.03	Pd
Area 2										
1	55.21	40.99	3.50	0.10	0.00	0.08	0.10	0.00	0.02	Pd-Ag
2	53.95	38.84	6.68	0.00	0.00	0.14	0.39	0.00	0.00	Pd-Eu
3	56.69	40.43	1.94	0.01	0.00	0.13	0.29	0.51	0.00	Pd-Eu-U
4	47.14	39.50	11.61	0.20	0.39	0.15	0.41	0.60	0.00	Pd-Ag-Cs-Eu-U
5	49.20	47.54	2.40	0.61	0.00	0.00	0.17	0.00	0.08	Pd-Ag
6	55.34	41.86	2.71	0.03	0.00	0.00	0.06	0.00	0.00	Pd
7	49.05	47.02	3.51	0.00	0.00	0.18	0.24	0.00	0.00	Pd-Eu

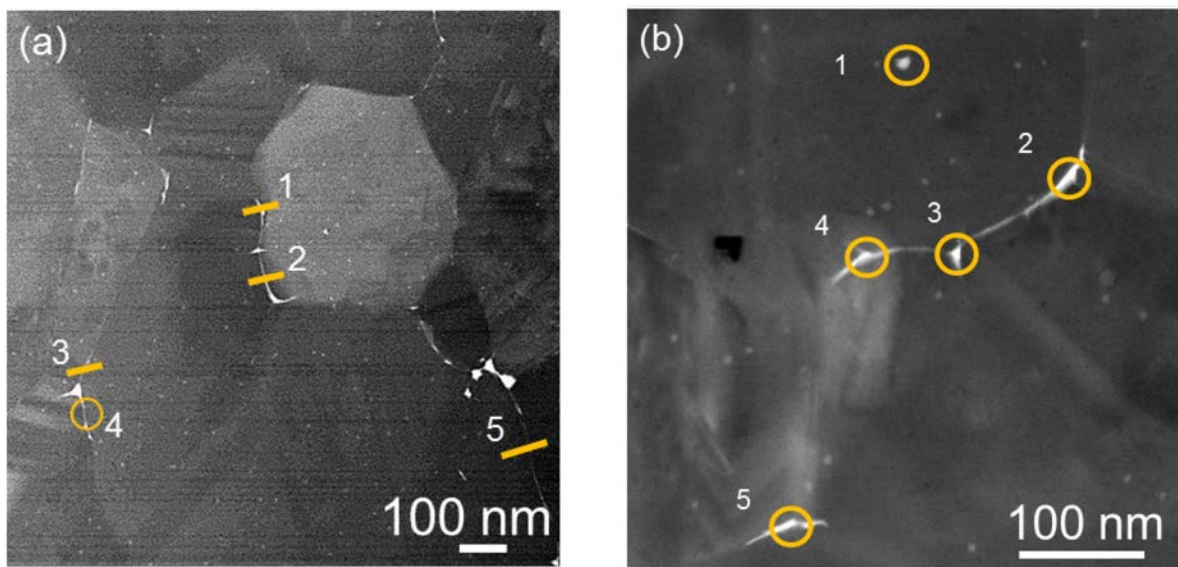


Figure 189. STEM HAADF image combined with EDS labeling to track the chemical composition of fission product precipitates from the outer area (Lamella 7) of TRISO Particle AGR1-433-001, within subtended Areas (a) 3a and (b) 3b. Note the reported chemical compositions are in Table 89.

Table 89. Reported qualitative EDS compositions (at.%) from precipitates (Figure 189) from the outer area (Lamella 7) of TRISO Particle AGR1-433-001, taken from subtended Areas 3a and 3b (Figure 187).

Precipitate Number	Concentration (at.%)									Precipitate Identification
	C	Si	Pd	Ag	Cs	Ce	Eu	U	Pu	
Area 3a										
1	44.84	48.82	6.16	0.10	0.00	0.08	0.00	0.00	0.00	Pd
2	51.75	42.36	5.89	0.00	0.00	0.00	0.00	0.00	0.00	Pd
3	58.34	37.85	3.26	0.00	0.00	0.29	0.26 <sup>a</sup>	0.00	0.00	Pd-Ce
4	49.07	42.22	8.31	0.39	0.00	0.00	0.00	0.00	0.00	Pd-Ag
5	57.94	36.77	4.91	0.20	0.00	0.05	0.13	0.00	0.00	Pd-Ag
Area 3b										
1	51.19	44.42	0.35	0.00	0.00	0.00	0.00	0.00	0.00	Pd
2	42.49	49.57	0.87	0.00	0.00	0.00	0.00	0.00	0.00	Pd
3	53.40	41.07	1.04	0.00	0.00	0.00	0.00	0.00	0.00	Pd
4	50.09	42.87	0.60	0.00	0.00	0.00	0.00	0.00	0.00	Pd
5	54.65	40.17	0.87	0.00	0.00	0.00	0.00	0.00	0.00	Pd

a. Cannot differentiate between Eu and Fe

a. Cannot differentiate between Eu and Fe

**3.6.2.5 Crystallographic Information Obtained on Particle AGR1-433-001.** The TEM lamellae from this particle consisted of three inner samples: Lamella 4 (near a buffer crack), Lamella 5 (near a buffer crack), Lamella 10 (far away from any buffer cracks), and one center sample (Lamella 6) and one outer sample (Lamella 7) that is closest to the OPyC/SiC interface. Grain boundary fission product precipitates were analyzed for composition and grain boundary parameters using EDS and PED, respectively, in the TEM.

**3.6.2.5.1 General Grain Boundary Distributions across the Silicon Carbide Layer.**

The grain orientation maps of the areas analyzed on the inner sample (Lamella 5) are shown in Figure 190. (Grain orientation maps of the other areas analyzed on the other TEM Lamella from AGR1-433-001 can be found in Lillo et al., [2017].) The grain orientations were used to determine the grain boundary distributions in each area. The distributions of grain boundary misorientation angles, CSL values, and grain boundary types for each area analyzed on the inner sample (Lamella 5) are shown in Figure 191(a), (b), and (c), respectively. The areas were relatively small compared to the SiC grain size, and significant variability is observed in the distributions from each area. Therefore, the standard error in the averaged distributions was calculated by dividing the standard deviation for each value and dividing by the square root of the number of areas analyzed. These averaged distributions are used in comparisons among the various lamellae.

**Misorientation Angle Distribution:** The average distributions of the grain boundary misorientation angle for the inner, center, and outer samples are shown in Figure 192(a). The twin boundary fraction, indicated by a 60-degree misorientation, dominates the misorientation angle distribution. A secondary peak in the distribution occurs around a misorientation angle of 40 degrees. The error bars indicate there are virtually no statistically significant differences between the distributions of the inner, center, and outer samples in the SiC layer of this TRISO particle made with Variant 3 fabrication conditions. The distributions for the three inner samples (i.e., Lamellae 4, 10, and 5) do not show variations exceeding the standard error associated with the measurement. Therefore, it appears there are no significant variations in the misorientation angle distribution at three different inner locations around this SiC layer; the location-to-location variation in the distribution of misorientation angles at inner regions of the SiC layer appears small.

**Distribution of CSL-Related Grain Boundaries:** Figure 192(b) shows the distribution of grain boundaries that exhibit a CSL relationship. Again, twin boundaries (i.e.,  $\Sigma 3$ ) are the major CSL-related grain boundary type in all regions of the SiC layer. The higher order twins (i.e.,  $\Sigma 9$  and  $\Sigma 27$ ) make up a majority of the remaining CSL-related grain boundaries; however, small but significant fractions of  $\Sigma 5$  and  $\Sigma 7$  CSL grain boundaries exist in the inner, center, and outer regions analyzed.

The fraction of each CSL value in the CSL distributions for the five samples can be mathematically averaged to give an average CSL distribution for the entire SiC layer because no statistical differences are observed in the individual distributions of the inner, center, and outer regions. The twin fraction, including the higher order twin fractions, shown in Table 90 can be compared to literature values reported by Kirchhofer et al., (2013) from an SEM-based EBSD study. For the SiC layer of an unirradiated Variant 3 TRISO particle Kirchhofer et al., (2013) reports values of 27%, 5%, and 1% for  $\Sigma 3$ ,  $\Sigma 9$ , and  $\Sigma 27$  CSL-related grain boundaries, respectively. The fraction of  $\Sigma 3$  grain boundaries in the Kirchhofer et al., (2013) study is significantly lower than that found in this work. However, the statistical error in the CSL fractions is not given in the Kirchhofer study. It is expected to be similar to, and most likely less than, the error reported in this study because the total area analyzed here was not as large as that in Kirchhofer et al., (2013) study. However, it remains to be seen whether the difference in the  $\Sigma 3$  fraction reported here is due to a statistical variation, systematic differences in the method used to obtain CSL data, or irradiation and temperature effects. The fractions of the higher order twins are generally in agreement with that reported in the Kirchhofer study.

Table 90. Average fraction of twin-related grain boundaries in the SiC layer from Particle AGR1-433-001.

CSL value, $\Sigma$	Fraction, %	Std. Error
3	42.4	3.8
9	4.1	0.7
27	2.1	0.3

**Distribution by Grain Boundary Type:** The averaged distributions by grain boundary types for the inner, center, and outer samples are shown in Figure 192c. As expected, the CSL-related grain boundaries make up the majority of the grain boundaries at approximately 62% (see Table 91), while the random, high-angle grain boundary fraction appears to be virtually constant at approximately 26% across the entire SiC layer (Figure 192[c]). There appears to be considerable variation in the low-angle fractions of grain boundaries and, to a lesser extent, the CSL-related grain boundary fractions between the inner, center, and outer regions of the SiC layer. The fraction of random, high-angle grain boundaries is quite consistent among the five lamellae.

The values in Table 91, derived by averaging the results from the inner, center and outer lamellae, may be compared to the values reported by Kirchhofer for the entire SiC layer of an unirradiated, Variant 3 TRISO particle. The values reported by Kirchhofer et al., are 21%, 39%, and 40% for low-angle, high-angle, and CSL-related grain boundaries, respectively. These values are considerably different than those reported in Table 91. At this time, the reason for these differences is not known, although the possible reasons for them are the same as those stated for the differences found in the CSL distributions (i.e., statistical variations among particles, different data collection methods, and possibly irradiation and temperature effects).

Table 91. Average fraction of grain boundary types in the SiC layer from Particle AGR1-433-001.

Grain Boundary Type	Fraction, %	Std. Error
Low angle, $<15^\circ$	12.1	2.5
High angle, $>15^\circ$	26.4	0.9
CSL-related	61.5	3.1

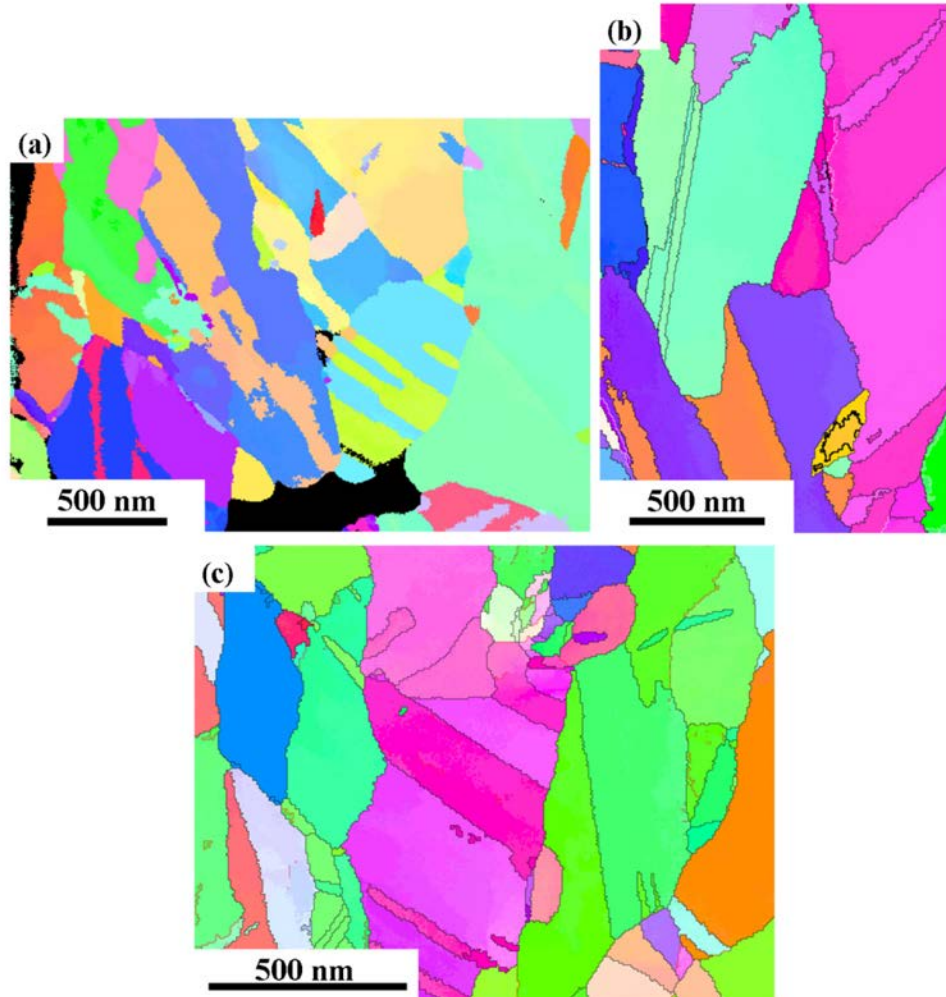


Figure 190. SiC grain orientation maps of the areas analyzed in Lamella 5 (Figure 171[c], Figure 178): (a) Area 1, (b) Area 2, and (c) Area 3. The black areas in (a) represent large fission product precipitates.

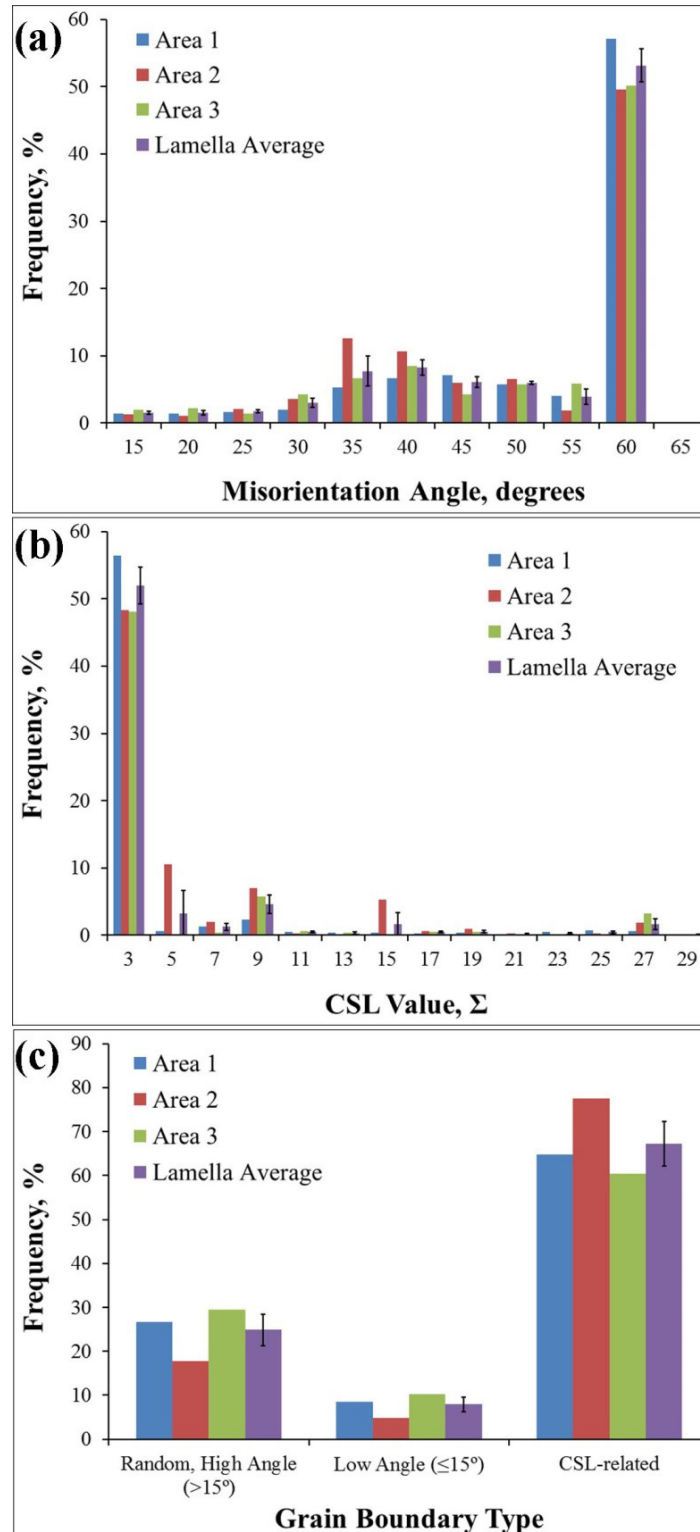


Figure 191. Distributions of (a) grain boundary misorientation angle, (b) value of CSL-related grain boundaries, and (c) grain boundary types in each area analyzed on the inner Lamella (Lamella 5, Figure 171[c]) and the averaged distribution with error bars calculated from the standard error.

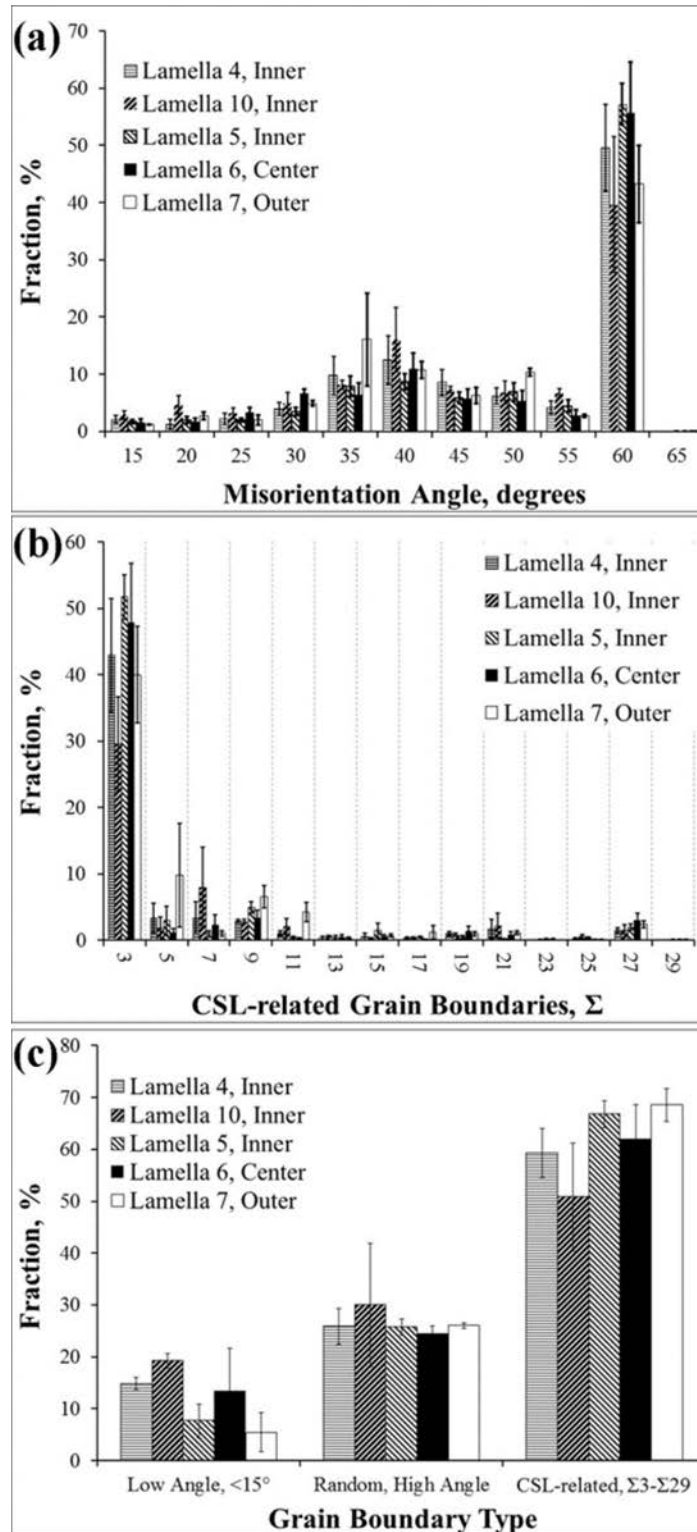


Figure 192. Distributions averaged over all areas analyzed for each lamella: (a) misorientation angle, (b) CSL designation, and (c) grain boundary type for the SiC grain boundaries in samples taken from AGR1-433-001.



**3.6.2.5.2 Grain Boundary Data for Grain Boundaries Containing Fission Product Precipitate.** Grain boundary fission product precipitates found in the STEM HAADF images were analyzed for the presence of various fission product elements using EDS and then correlated with the grain boundary misorientation data obtained with PED. The EDS data correlated with the PED data are summarized in Table 92 and Figure 193. The results are discussed in the following subsection. In this particle, there were also indications that other fission product and transuranic elements (e.g., Pu, Eu, Cs, and Ce) might be present in extremely low concentrations. However, the short x-ray data acquisition time prevented these elements from being definitively identified in the samples. Therefore, these elements were not included in the correlation of fission products with the grain boundary type that follows.

**Inner Samples (Lamellae 4, 10, and 5):** Pd-containing precipitates were most prevalent in all the inner lamellae (Table 92). A considerable number of Ag-containing precipitates (either Ag only or Ag+Pd) were also found, as were Pd+U precipitates. U was never found alone or in conjunction with Ag. Figure 193 shows that fission product precipitates in the inner regions of the SiC layer were found on random, high-angle grain boundaries, CSL-related boundaries and, to a lesser extent, low-angle grain boundaries; however, they are most prevalent on random, high-angle grain boundaries and least prevalent on low-angle grain boundaries. When broken down by fission product element, it is evident from Table 92 that most of the precipitates are Pd-containing. Precipitates that contain only Ag were found almost exclusively on random, high-angle grain boundaries, with one exception (Table 92, Lamella 5), which was found on a  $\Sigma 15$  CSL-related grain boundary.

**Center Sample (Lamella 6):** In this region further from the IPyC-SiC interface and the UCO fuel kernel, the grain boundary precipitates are still found on all types of grain boundaries (Figure 193). Pd-only precipitates were found on all grain boundary types, while Pd+U precipitates were found mainly on random, high-angle grain boundaries. However, one Pd+U precipitate was found on a CSL-related grain boundary (Table 92, Lamella 6), which was determined to be a  $\Sigma 9$  grain boundary. Ag-only and Pd+Ag type precipitates were not found in this center sample. These types of Ag-containing precipitates may be in other areas of the center region because only two areas were sampled on this lamella.

**Outer Sample (Lamella 7):** In the outer regions, the precipitates were found on either random, high-angle grain boundaries or CSL-related grain boundaries (Figure 193). No precipitates were found on low-angle grain boundaries (Figure 193). Furthermore, the precipitates are almost exclusively of the Pd-only variety (Table 92), except for one that was found to be of the type Pd+Ag on a CSL-related grain boundary determined to be on a  $\Sigma 25b$  grain boundary. Four Pd-only precipitates were found on CSL-related grain boundaries (i.e., a  $\Sigma 5$ ,  $\Sigma 19a$ ,  $\Sigma 21b$ , and a  $\Sigma 27a$ ).

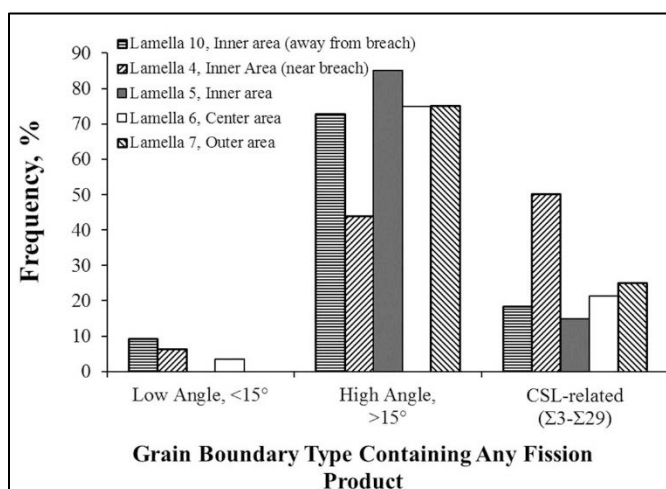


Figure 193. Comparison of the distribution of grain boundary precipitates on the various grain boundary types in various regions of the SiC layer of AGR1-433-001.

Table 92 Summary of the distribution of fission product elements.

	<b>Pd Only</b>	<b>Ag only</b>	<b>U only</b>	<b>Pd and Ag</b>	<b>Pd and U</b>	<b>Pd+Pu</b>	<b>Pd+U+Pu</b>	<b>Pd+Ag+U</b>
<b>Lamella 4, Inner Sample</b>								
Number of grain boundaries	7	0	1	3	1	1	2	1
Fraction of all boundaries with fission products, %	43.8	0.0	6.3	18.8	6.3	6.3	12.5	6.3
Low angle, %	0.0	—	0.0	0.0	0.0	100.0	0.0	0.0
Random, high angle, %	28.6	—	0.0	66.7	100.0	0.0	100.0	0.0
CSL, %	71.4	—	100.0	33.3	0.0	0.0	0.0	100.0
<b>Lamella 10, Inner sample</b>								
Number of grain boundaries	6	0	0	1	0	0	4	0
Fraction of all boundaries with fission products, %	54.5	0.0	0.0	9.1	0.0	0.0	36.4	0.0
Low angle, %	16.7	—	—	0	—	—	0.0	—
Random, high angle, %	83.3	—	—	100	—	—	50.0	—
CSL, %	0	—	—	0	—	—	50.0	—
<b>Lamella 5, Inner Sample</b>								
Number of grain boundaries	14	4	0	8	1	0	0	0
Fraction of all boundaries with fission products, %	51.9	14.8	0.0	29.6	3.7	0.0	0.0	0.0
Low angle, %	0.0	0.0	—	0.0	0.0	—	—	—
Random, high angle, %	85.7	75.0	—	87.5	100.0	—	—	—
CSL, %	14.3	25.0	—	12.5	0.0	—	—	—
<b>Lamella 6, Center Sample</b>								
Number of grain boundaries	24	0	0	0	4	0	0	0
Fraction of all boundaries with fission products, %	85.7	0.0	0.0	0.0	14.3	0.0	0.0	0.0
Low angle, %	4.2	—	—	—	0.0	—	—	—
Random, high angle, %	75.0	—	—	—	75.0	—	—	—
CSL, %	20.8	—	—	—	25.0	—	—	—
<b>Lamella 7, Outer Sample</b>								
Number of grain boundaries	19	0	0	1	0	0	0	0
Fraction of all boundaries with fission products, %	95.0	0.0	0.0	5.0	0.0	0.0	0.0	0.0
Low angle, %	0.0	—	—	0.0	—	—	—	—
Random, high angle, %	78.9	—	—	0.0	—	—	—	—
CSL, %	21.1	—	—	100.0	—	—	—	—

**3.6.2.5.3 Discussion of Results for Particle AGR1-433-001.** The correlations of fission products with grain boundary parameters for the various areas analyzed on each sample that are summarized in Table 92 were combined to yield distributions representative of the entire SiC layer that are discussed in the following subsections.

**Fission Product and Transuranic Element Distribution:** Figure 194 indicates that most grain boundary precipitates in the SiC layer contain Pd, either alone or in conjunction with other elements such as Ag or U. Ag-only precipitates are not prevalent, but do occur in significant numbers in one Lamella from the inner region of the SiC layer, Lamella 5, Table 92. Pu is present in conjunction with Pd or Pd and U. (Pu was not found in the other AGR-1 TRISO that had *not* been safety tested.).

**Associations of Fission Products with Grain Boundary Types – Low-Angle, High-Angle, and  $\Sigma$ :** Fission product precipitates show a preference for random, high-angle grain boundaries, regardless of the elements present in the precipitate (Figure 195). Precipitation on low-angle grain boundaries is infrequent and is limited to precipitates containing only Pd, or Pd and Pu (only one precipitate of each kind was found on low-angle grain boundaries, Table 92, Lamellae 10 and 4, respectively) (Figure 196). Precipitation on CSL-related grain boundaries occurs and is more common, at about 25% of all precipitates, than precipitation on low-angle grain boundaries at about 3% of the precipitates, Figure 195. Of the four Ag-only precipitates analyzed, three were found on random, high-angle grain boundaries and one was found on a CSL-related grain boundary, which was determined to be a  $\Sigma 15$  CSL boundary. The Pd-containing precipitates on CSL-related grain boundaries in Figure 196 occurred on a variety of CSL values between  $\Sigma 3$  and  $\Sigma 29$ , including on twin ( $\Sigma 3$ ) boundaries.

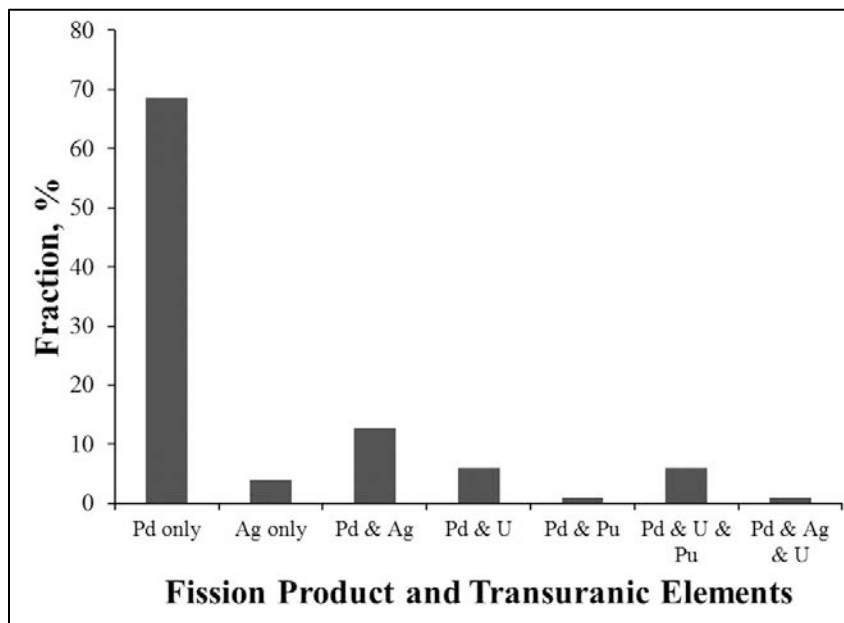


Figure 194. Composition distribution of the grain boundary precipitates AGR1-433-001.

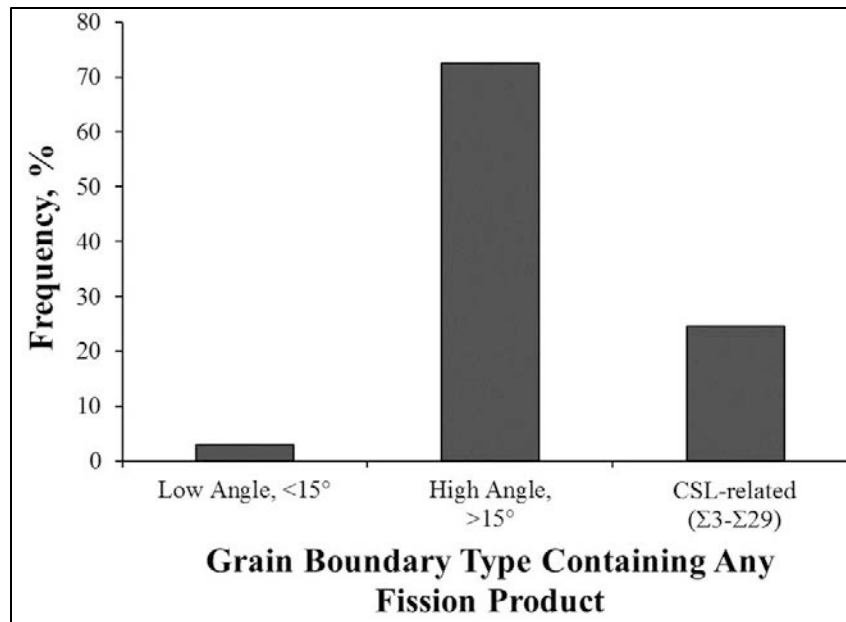


Figure 195. Distribution of fission product precipitates on the various boundary types as a percentage AGR1-433-001.

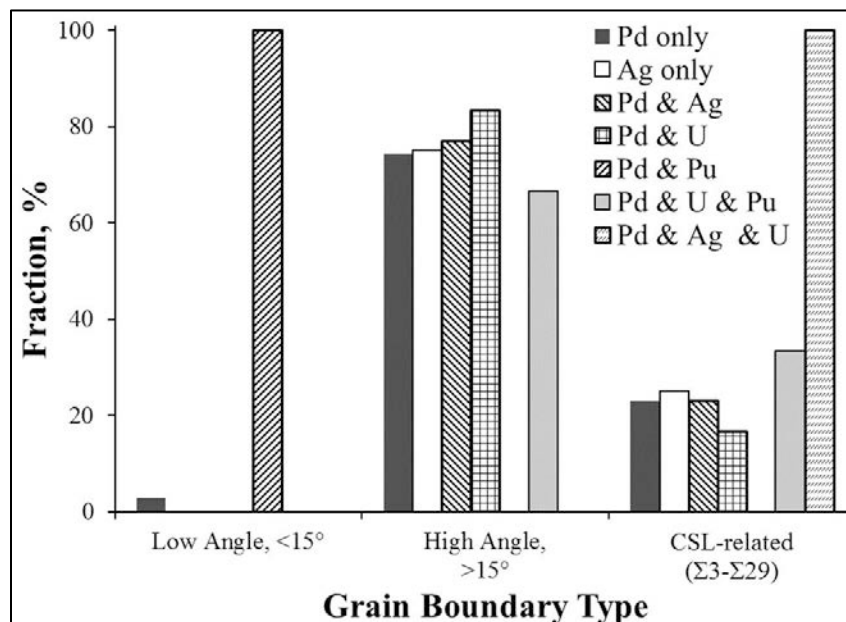


Figure 196. Distributions of fission product elements, as a percentage, by grain boundary type AGR1-433-001.

**3.6.2.6 Fission Product Precipitate Structure and Phase Identification of Particle AGR1-433-001 (High-Resolution Transmission Electron Microscopy).** The information from this advanced microscopy study is presented in the following sections for different layers of the sample. For the microstructure determination, a variety of techniques inside the TEM were used, including HAADF STEM, HRTEM, and EDS. The material composition of the samples was determined and profiled using STEM EDS linescans, individual points, and composite two-dimensional spectral images.

### 3.6.2.6.1 Inner Area of the Silicon Carbide Layer: Lamella AGR1-433-001-05.

Figure 197(a) is a large-scale field of view of AGR1-433-001-05, including two areas containing precipitates. Within each of these areas, the precipitates were analyzed using HRTEM. Using atomic contrast, HAADF STEM imaging (Figure 197(b)) is a magnified field of view containing the identified areas where fission product precipitates neighbor on intact SiC grains, including low- and high-angle grain boundaries. Area 1 contains Pd-Ag fission product precipitates that form at triple point junctions in the SiC. Simultaneous HAADF and low-angle annular BF STEM images in Figure 197(c) and Figure 197(d), respectively, reveal the size and atomic contrast differences associated with these precipitates. Similarly, over the second area of interest, STEM HAADF and annular BF reveal in Figure 197(e) and Figure 197(f), respectively, similarly sized fission product precipitates decorating triple point junctions. For each of these areas, detailed chemical and structural analysis was then performed using HRTEM as described in the following paragraphs.

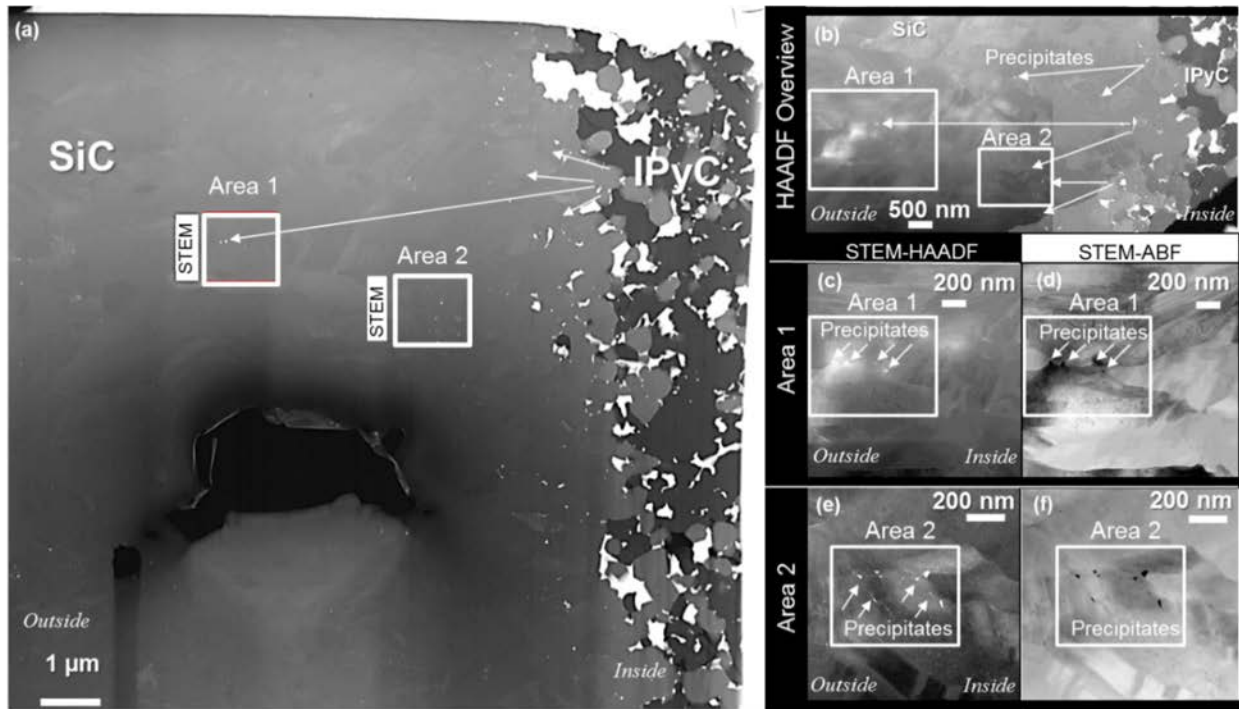


Figure 197. (a) Large field of view atomic contrast HAADF image from the inner area of TRISO Particle AGR1-433-001, where Areas 1 and 2 containing precipitates were analyzed using STEM and HRTEM imaging away from the SiC-IPyC interface contained within Lamella 5. (b) Atomic contrast dark field imaging centered over each of the two areas reveals a network of fission product precipitates, which migrate under neutron irradiation along SiC grain boundary interiors and nucleate in large concentrations at triple point junctions. (c) STEM HAADF, and (d) low-angle annular BF centered over the first area reveal Pd-Ag fission product precipitates concentrated at triple point junctions reported in Table 93. Similarly, centered over the second area (e) STEM-HAADF and (f) annular BF reveal similarly sized fission product precipitates, with a large concentration located at triple-point junctions. Note the composition of precipitates contained in each of these areas is reported in Table 93.

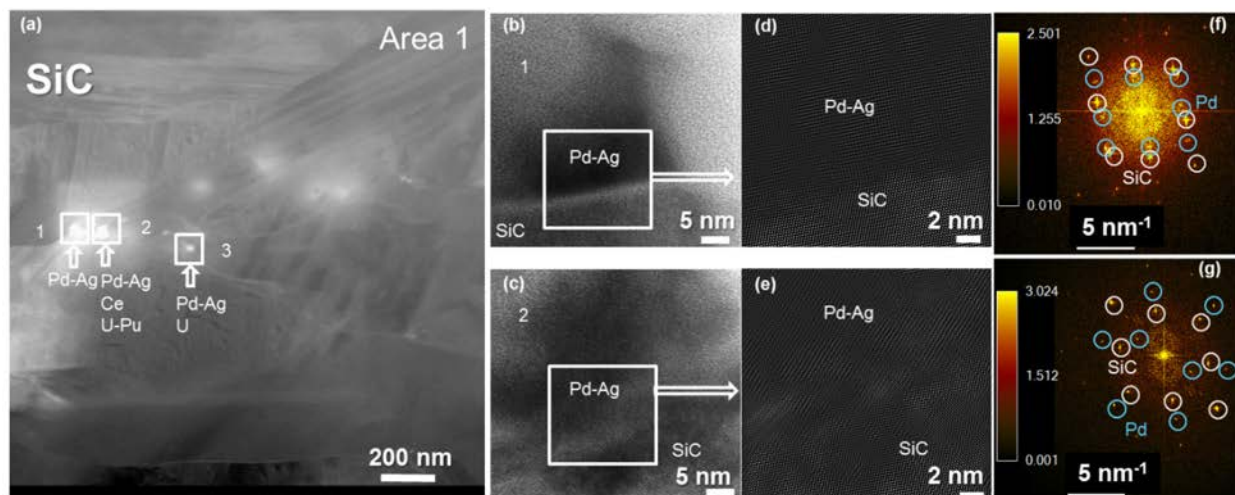


Figure 198. (a) Large field of view centered covered the subtended Area 1, from the inner area of TRISO Particle AGR1-433-001. Three individual fission product precipitates are located and labeled, and two precipitates (1, 2) were subsequently imaged with HRTEM from Lamella 5. The third precipitate could not be resolved with HRTEM lattice imaging due to significant SiC grain overlap. For fission product Precipitate (b) 1 and (c) 2, both contain Pd and Ag and are located at triple point junctions within the SiC lattice. To address overlapping SiC grains and raw image signal to noise, a filtered inverse FFT was also performed for each of these areas, including Precipitate (d) 1 and (e) 2. To identify the structural and crystallographic details, FFTs were calculated for Precipitate (f) 1 and (g) 2. Each of the respective FFTs reveal the cubic SiC and Pd-Ag lattice points labeled by white and blue circles, respectively. Note the composition of precipitates contained in this area is reported in Table 93.

Over Area 1, the fission product precipitates imaged with dark field STEM were studied with HRTEM. Figure 198(a) is a large field of view of the inner area from TRISO Particle AGR1-433-001 (Lamella 5), Area 1, containing three individual fission product precipitates. Two of the three fission product precipitates could be imaged with HRTEM due to significant SiC overlap and lack of material contained within the third fission product precipitate. Over the remaining two fission product precipitates, 1 (Figure 198[b]) and 2 (Figure 198[c]), STEM EDS point scans determined their individual chemical composition and are reported in Table 96. Both precipitates, located triple point junctions within the intact SiC lattice and have significant overlap with neighboring SiC grains. To address the overlap, select points in the FFT were used to calculate inverse fast-Fourier image over each of these images. A closer look at Figure 198(d) and Figure 198(e) reveal both areas containing SiC and Pd-Ag are arranged in cubic arrangement. This was further verified and checked by indexing the FFT for each Precipitate 1 (Figure 198[f]) and 2 (Figure 198[g]). The cubic SiC and Pd-Ag diffraction lattice spots for each crystal type were confirmed.

Within the second area, fission product precipitates were imaged with both dark field STEM and HRTEM. Figure 199(a) is enlarged field of view where both STEM and HRTEM were used to image six individual fission product precipitates contained within Lamella AGR1-433-001-05, Area 2. Figure 199(b) is the same area imaged using BF TEM, and each of the corresponding fission product precipitates imaged using STEM are labeled in Figure 199(a). Note the lack of contrast in TEM, owing to the lack of phase contrast differences between the precipitates and surrounding SiC, hence the importance of atomic contrast STEM imaging for locating precipitates. For the six labeled fission product precipitates, Figure 200 and Figure 201 provide a series of HRTEM and FFTs for each. For fission product Precipitate 1, Figure 200(a) shows overlapping lattice fringes corresponding to the precipitate, and the surrounding SiC lattice. This is verified in Figure 200(b) where the cubic SiC lattice points can be indexed. Figure 200(c) shows fission product Precipitate 2, where a distinct Pd-Ag lattice is resolved. The

FFT corresponding to Precipitate 2 (Figure 200[d]) shows only the Pd-Ag lattice points. Comparing Precipitates 1 and 2, it is apparent that a significant difference in the placement of the fission product precipitate is key to atomic scale imaging, where precipitate location along a triple point with no grain overlap is ideal compared to the less-desirable location on top of the SiC grains. Similar, to fission product Precipitates 1 and 2, Figure 200(e) shows overlapping lattice fringes and the lack of fission product material does not offer enough phase contrast for fission product Precipitate 3. Subsequently in Figure 200(f) only the SiC lattice can be resolved in atomic detail. HRTEM imaging of fission product Precipitate 4, Figure 201(a) shows both Pd-Ag and SiC lattice with minimal overlap. Subsequently in Figure 201(b) both the Pd-Ag and SiC lattice points are resolved. Similar to fission product Precipitates 5 and 6, Figure 201(c) shows only SiC lattice structure. This is again confirmed in the accompanying FFT Figure 201(d), where only the corresponding spots indicating cubic SiC are observed. For fission product Precipitate 6, Figure 201(e) reveals strong overlapping lattice fringes between Pd-Ag and SiC. All SiC lattice spots are found in Figure 201(f), but only one family of lattice planes can be indexed to cubic Pd-Ag.

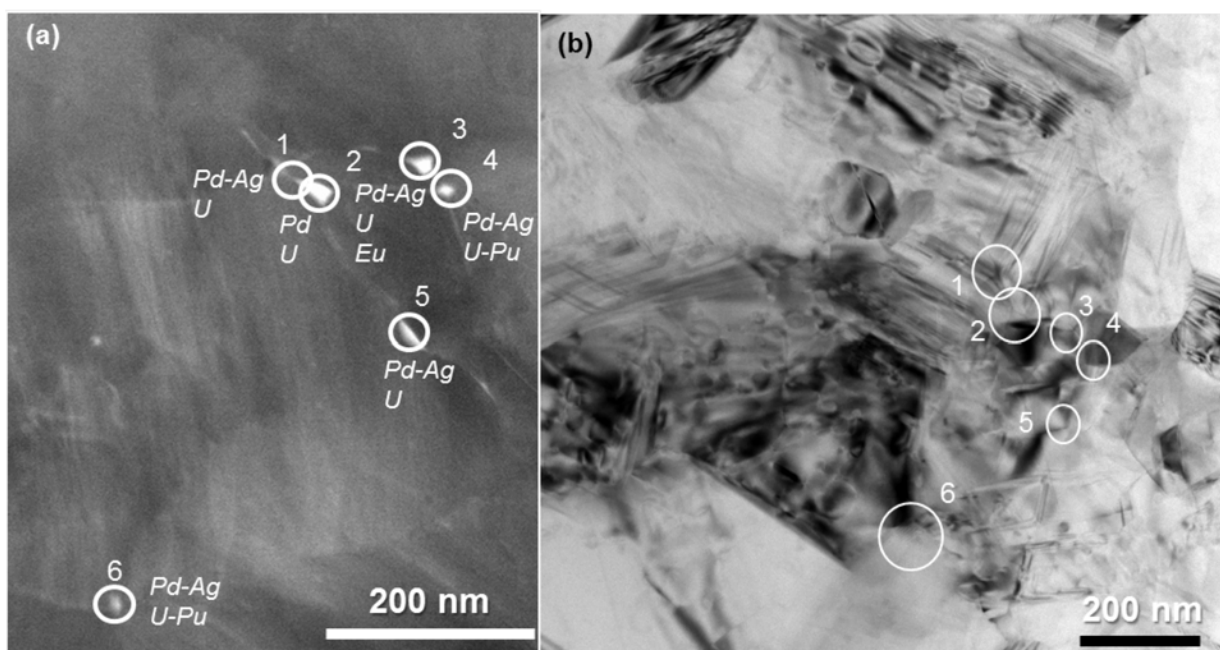


Figure 199. (a) STEM dark field imaging centered over area 2 from the inner area of TRISO Particle AGR1-433-001 exposes individual fission product precipitates that have been later identified and analyzed using both STEM and HRTEM from Lamella 5. (b) Over the same area, TEM was performed and each area containing a precipitate is labeled. For each of these precipitates, HRTEM and EDS was utilized to image and determine intact fission product precipitate structure and chemistry. Note the chemical compositions of the fission product precipitates contained within Area 2 are reported in Table 93.



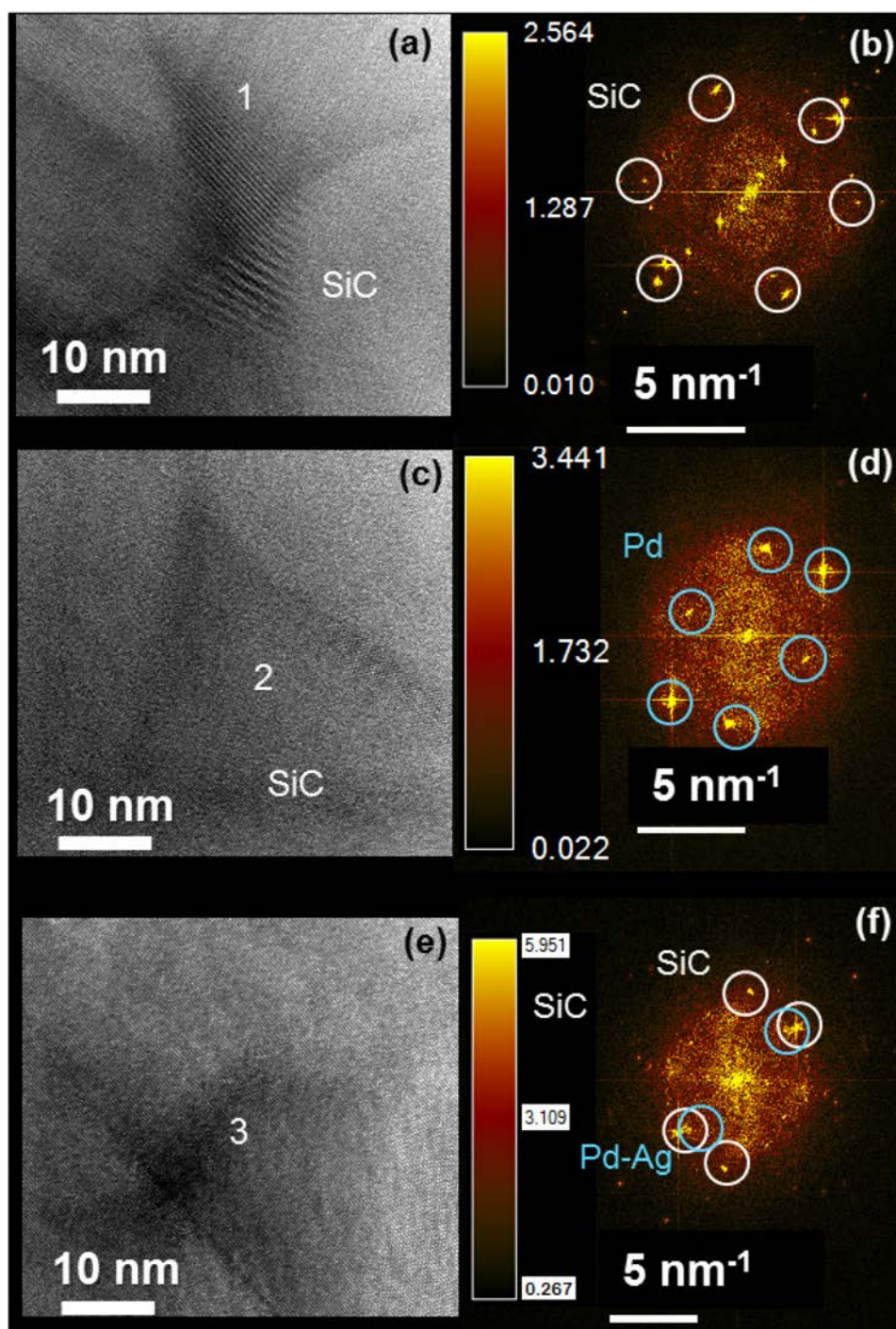


Figure 200. Atomic scale HRTEM imaging and FFTs of individual fission product precipitates contained within the subtended area 2 from the inner area of TRISO Particle AGR1-433-001, including (a–b) 1, (c–d) 2, and (e–f) 3 from Lamella 5. For each of the respective FFTs, white circles label the cubic SiC and blue circles highlight the Pd and Pd-Ag lattice points.

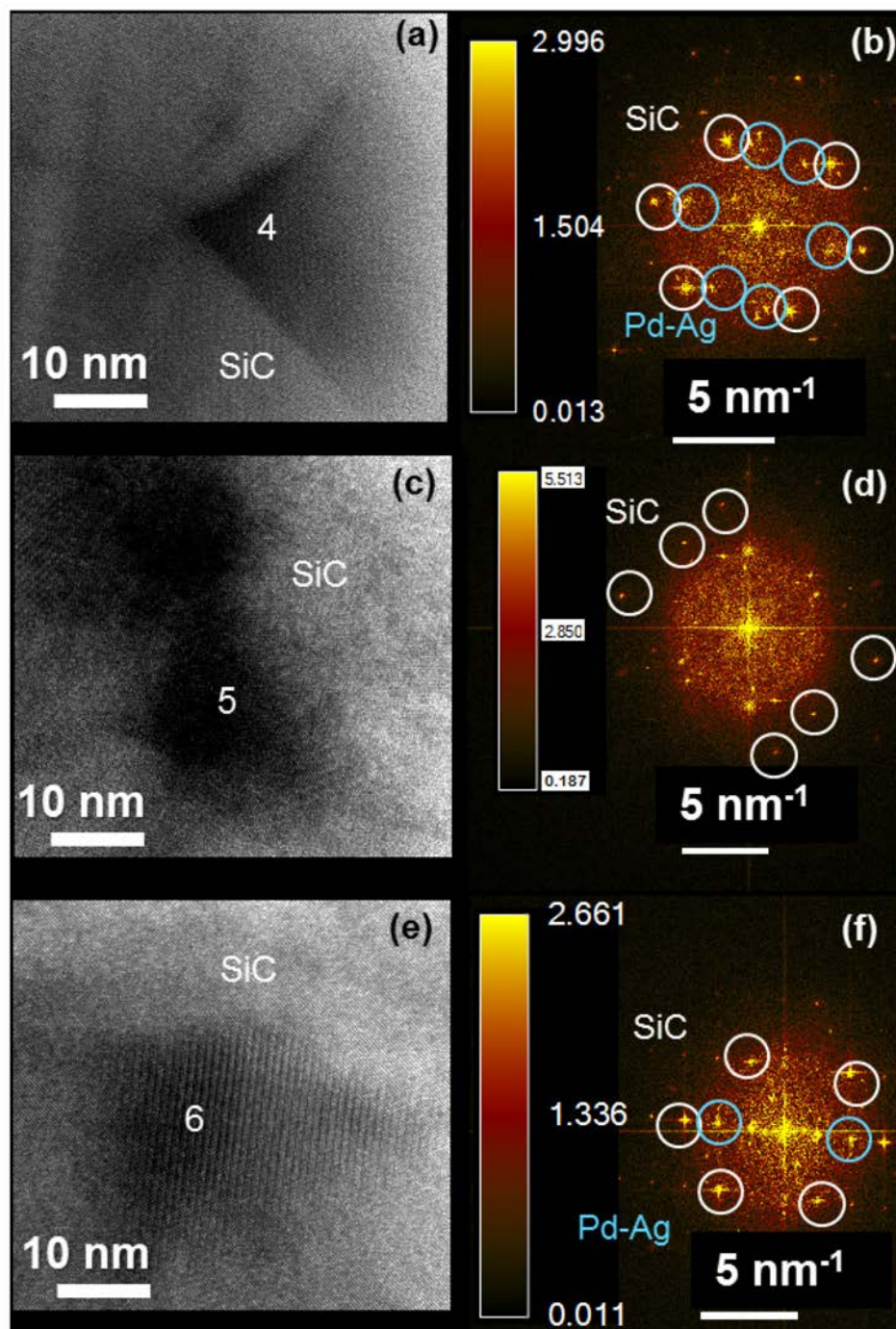


Figure 201. Atomic scale HRTEM imaging and FFTs of individual fission product precipitates contained within the subtended area 2 from the inner silicon carbide area of TRISO Particle AGR1-433-001, including (a–b) 4, (c–d) 5, and (e–f) 6 from Lamella 5. For each of the respective FFTs, white circles label the cubic SiC and blue circles highlight the Pd and Pd-Ag lattice points. For a closer examination of the fission product precipitation chemistry along each of the specific grain boundaries, point-resolved STEM EDS chemical profiling was used to identify elements, contained within each fission product precipitate. Table 93 reports the most and least abundant fission product elements, measuring less than 1 at.% for some.

Table 93. Qualitative fission product precipitate chemistry reported in atomic % from the inner area of the silicon carbide layer of TRISO Particle AGR1-433-001 taken from subtended Area 1 and 2 of Lamella 5 as highlighted in Figure 197 and labeled in Figure 198 and Figure 199.

Precipitate Number	Concentration (at.%)									Precipitate Identification
	C	Si	Pd	Ag	Cs	Ce	Eu	U	Pu	
Area 1										
1	34.21	44.99	3.53	1.54	0.00	0.00	0.00	0.00	0.00	Pd-Ag
2	38.24	40.28	2.52	0.78	0.00	0.08	0.00	0.56	0.12	Pd-Ag-U
3	39.33	41.25	2.83	1.33	0.00	0.00	0.00	0.51	0.00	Pd-Ag-U
Area 2										
1	39.15	60.53	1.53	0.31	0.00	0.00	0.00	2.27	0.00	Pd-Ag-U
2	39.15	60.53	0.09	0.00	0.00	0.00	0.00	2.27	0.00	U
3	43.61	54.18	0.49	0.42	0.00	0.00	0.02	0.17	0.00	Pd-Ag
4	42.84	55.63	0.32	0.23	0.00	0.00	0.00	0.17	0.44	Pd-Ag-Pu
5	39.25	54.65	1.51	0.33	0.00	0.00	0.00	2.24	0.00	Pd-Ag-U
6	41.67	54.38	1.33	0.12	0.00	0.00	0.00	0.17	0.19	Pd-U-Pu

**3.6.2.6.2 Concluding Remarks AGR1-433-001-05.** The following concluding remarks are made concerning the structure and chemistry of AGR1-433-001-05 based on HRTEM results:

- Pd-Ag and Pd precipitates constitute the areas sampled, as reported earlier by Lillo and van Rooyen (2016)

Differences between Pd-Ag and Pd precipitates based on FFT analysis cannot be resolved given the close proximity to neighboring lattice spots ( $\pm 0.08 \text{ \AA}$ ). Similar limitations exist for differentiating Pd-U, Pd-Pu, and Pd-U-Si precipitates (see Appendix C).

- Based on the detailed microscopy in these areas, the structure and lattice of Pd-Ag and Pd precipitates are cubic in nature
- The lack of a pattern in fission product orientation raises a question as to whether the incorporation of fission product precipitates into the SiC lattice does not follow conventional nucleation and kinetics of a secondary phase.

**3.6.2.6.3 Center Area of the SiC Layer: Lamella AGR1-433-001-06.** Figure 202(a) shows a large-scale field of view of the center of TRISO Particle AGR1-433-001, Lamella 6 including two areas containing fission product precipitates. Using atomic contrast and dark field STEM imaging, Figure 202(b) is a magnified field of view containing the identified areas. Similarly, Figure 202(c) is the simultaneous STEM BF image that reveals significant grain texturing over this same area. A closer examination with STEM dark (Figure 202[d]) and BF (Figure 202[e]) reveal the size and location of precipitates contained within each of these areas. Subsequently, each of these fission product precipitates were studied with HRTEM. These precipitates will be discussed in detail in the following paragraphs.

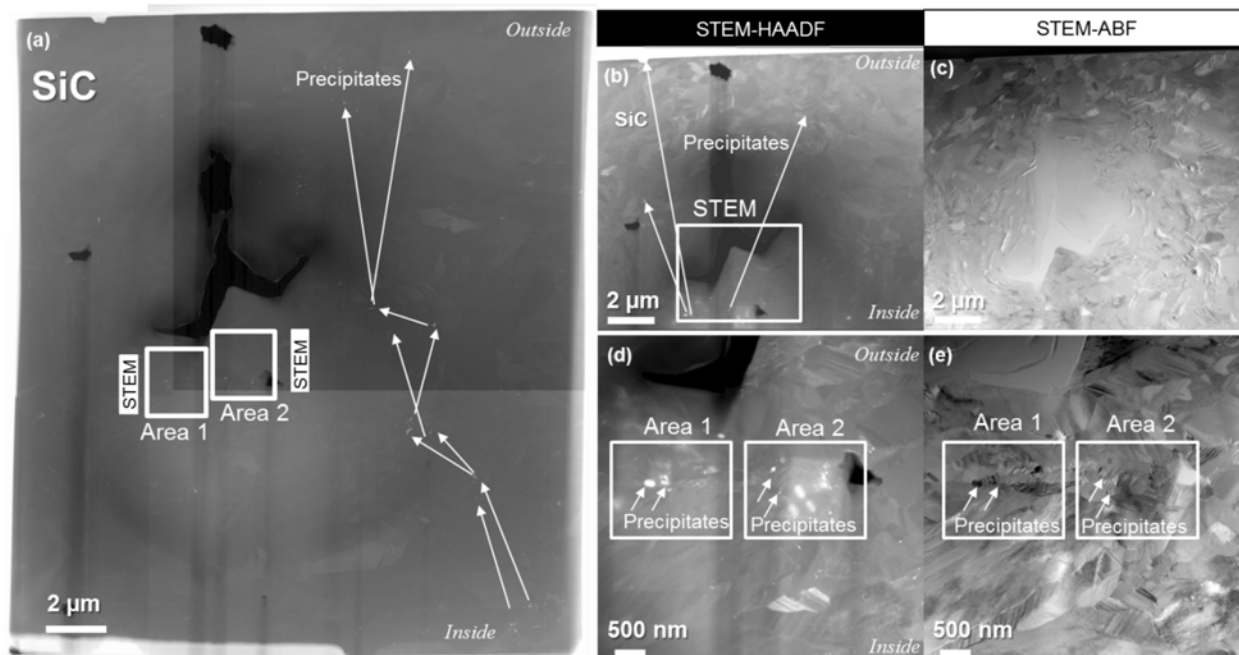


Figure 202. (a) STEM HAADF large field of view image taken over the center of the SiC layer of the TRISO coated Particle AGR1-433-001, where two areas containing precipitates were analyzed using STEM imaging within the SiC layer contained within Lamella 6 (the arrows indicating the presence of other precipitates although not measured in this study). Atomic contrast (b) dark field and (c) BF imaging centered over each of these two areas, reveals a network of fission product precipitates that migrate under neutron irradiation and are found in this middle cross section of the SiC layer. A closer examination of the area containing these two areas, (d) STEM dark and (e) BF, reveal Pd-Ag fission product precipitates concentrated within these two areas. Subsequently, over these two areas STEM, EDS, and HRTEM was performed. Note the chemical composition of fission product precipitates contained in these areas is reported in Table 94.

Over Area 1, the individual fission product precipitates were imaged with dark field STEM and HRTEM. Figure 203(a) is a dark field STEM image of the Lamella AGR1-433-001-06, Area 1, containing three individual fission product precipitates. Figure 203(b) is the accompanying simultaneous, STEM BF image that reveals grain texture and clearly shows fission product precipitates are centered at triple point junctions. Each of these fission product precipitates were imaged with HRTEM. For each of the fission product precipitates labeled 1 (Figure 204[a] and [b]), 2 (Figure 204[c] and [d]), and 3 (Figure 204[e] and [f]), point resolved EDS was used to determine their individual chemical composition and was reported in Table 94. Located primarily at triple point junctions within the SiC lattice, fission product precipitates in some cases having significant grain overlap. For fission product Precipitate 1, Figure 204(a) shows overlapping lattice fringes corresponding to the precipitate and the SiC lattice. Subsequently, in Figure 204(b) both the SiC and Pd-Ag lattice are resolved. Fission product Precipitate 2 (Figure 204[c]) shows a Pd-Ag fission product on top of the SiC lattice. Only the SiC lattice points are resolved in Figure 204(d). Fission product Precipitate 3 (Figure 204[e]) shows both the Pd-Ag and SiC lattice. Each of the crystals is resolved in Figure 204(f).



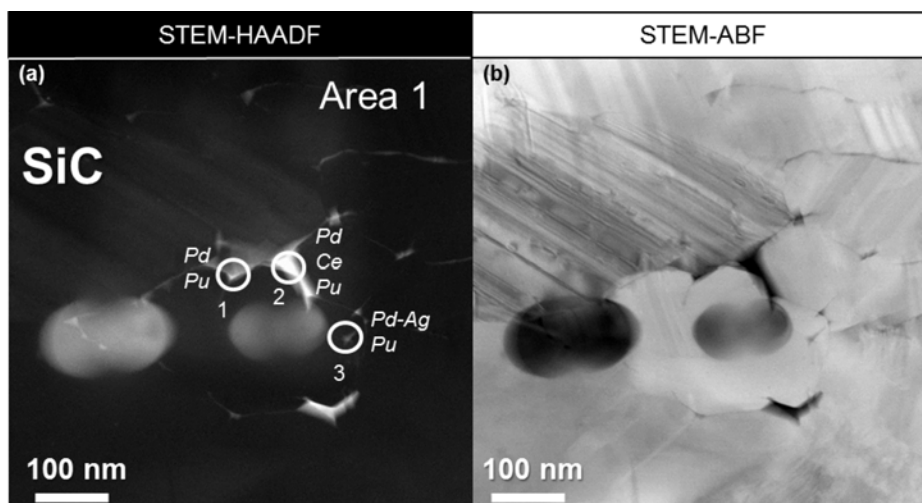


Figure 203. (a) STEM dark and (b) BF imaging centered over subtended Area 1 from the center area of TRISO Particle AGR1-433-001, reveals each of individual fission product precipitates within Lamella 6 that have been later identified and analyzed using HRTEM and EDS. Note the report chemical compositions for each of these fission product precipitates are reported in Table 94.

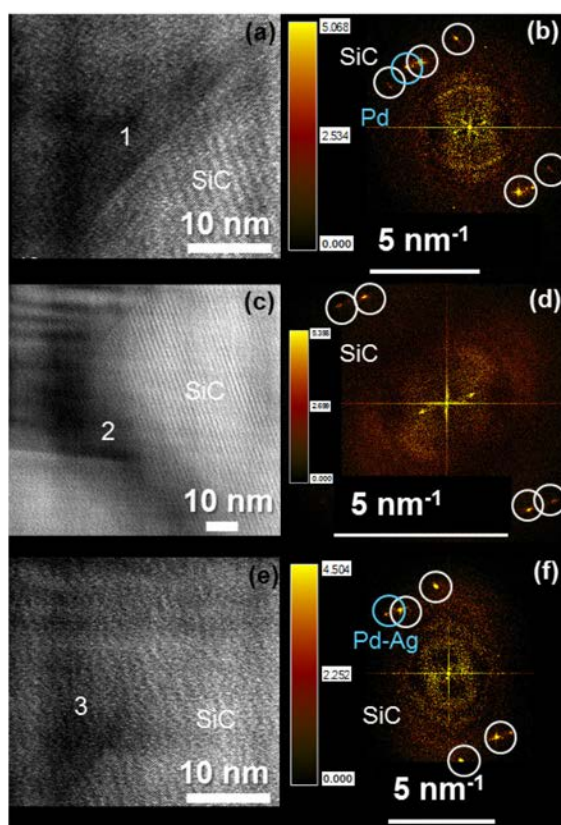


Figure 204. Atomic-scale, high-resolution TEM imaging and FFTs of individual fission product precipitates contained within Area 1 from the center of the silicon carbide layer of TRISO Particle AGR1-433-001, including (a–b) 1, (c–d) 2, and (e–f) 3 from Lamella 6. For each of the respective FFTs, white circles label the cubic SiC and blue circles highlight the Pd and Pd-Ag lattice points. Over Area 2, fission product precipitates were imaged with dark field STEM and HRTEM to reveal both their structural and chemical details.

Figure 205(a) is a STEM dark field of view of Lamella AGR1-433-001-06, Area 2, containing three fission product precipitates. From over the same area, Figure 205(b) is the STEM BF image that reveals the surrounding SiC grain texture and location of each fission product precipitate. For the three fission product precipitates, Figure 206 provides a series of HRTEM and FFTs for each. For fission product Precipitate 1, Figure 206(a) shows lattice fringes corresponding to both SiC and Pd-Ag. The accompanying FFT in Figure 206(b) confirms these lattice structures. Similarly, for fission product Precipitate 2, Figure 206(c) shows both the Pd-Ag and SiC lattice are resolved with no overlap. Subsequently, these are each confirmed in Figure 206(d), the accompanying FFT. Similarly, fission product Precipitate 3 (shown in Figure 206[e]) reveals no overlapping lattice fringes, where both the SiC and Pd-Ag atomic configurations are found. This is verified in Figure 206(f), where both lattices extending up to third interatomic planar distances are observed.

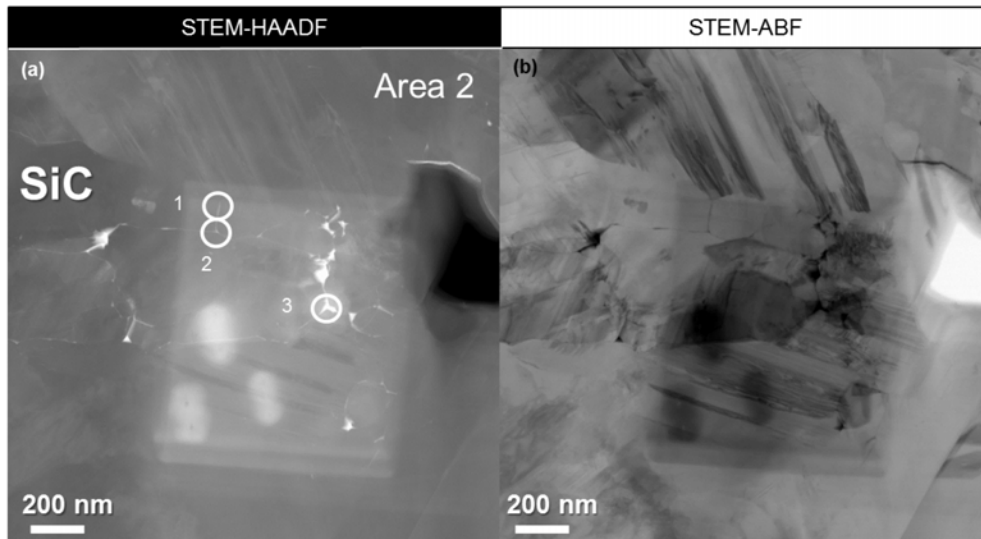


Figure 205. (a) STEM dark and (b) BF imaging centered over Area 2 from the center of the silicon carbide layer of TRISO Particle AGR1-433-001, reveals the individual fission product precipitates that have been later identified and analyzed using both STEM and HRTEM contained within Lamella 6. Over the same Area 2, HRTEM was performed for each of these three fission product precipitates labeled. Note the report chemical compositions are reported in Table 94.

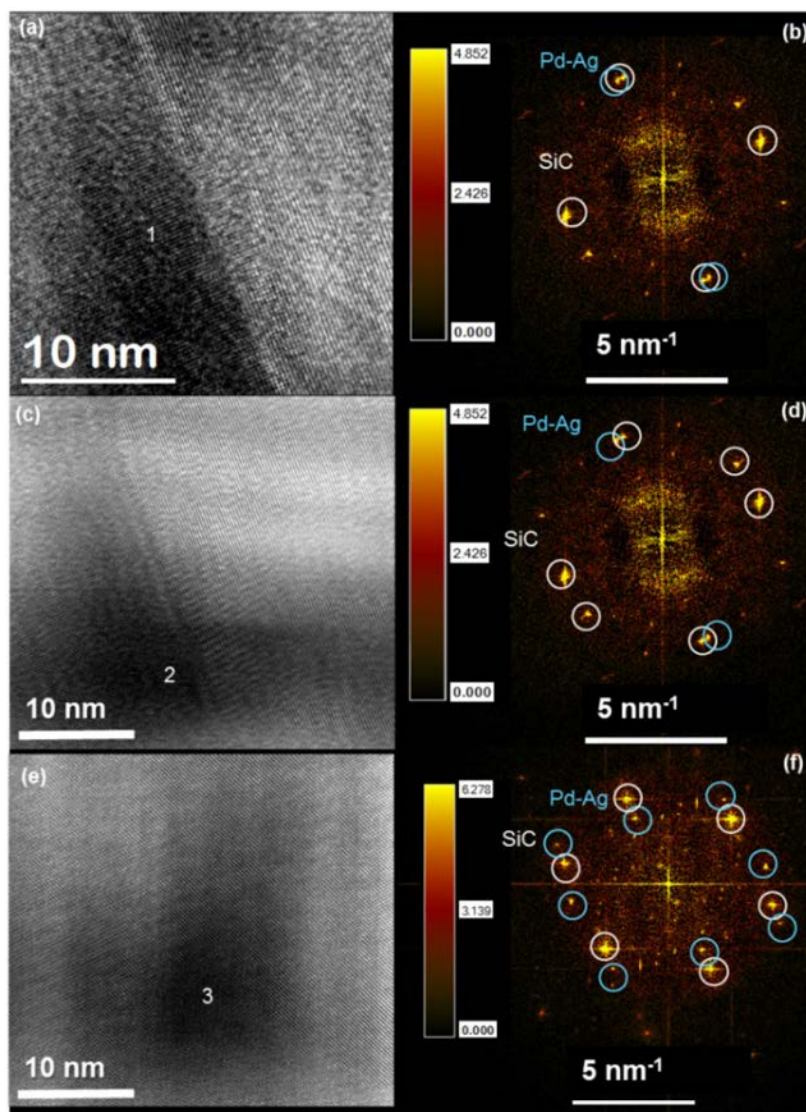


Figure 206. Atomic-scale, high-resolution TEM imaging and FFTs of individual fission product precipitates, including (a–b) 1, (c–d) 2, and (e–f) 3 with from area 2 of the center of the silicon carbide layer of TRISO Particle AGR1-433-001 contained within Lamella 6. For each of the respective FFTs, white circles label the cubic SiC and blue circles Pd-Ag lattice points.

Chemistry for each of the fission product precipitates contained in Areas 1 and 2 were resolved with EDS chemical profiling. Table 94 reports the most and least abundant fission product elements, measuring less than 1 at.%, for each of the identified fission product precipitates within Areas 1 and 2.



Table 94. Qualitative fission product precipitate chemistry reported in atomic % from the center area of the silicon carbide layer of TRISO Particle AGR1-433-001 taken from subtended Areas 1 and 2 of Lamella 6 as highlighted in Figure 202 and labeled in Figure 203 and Figure 205.

Precipitate Number	Concentration (at.%)									Precipitate Identification
	C	Si	Pd	Ag	Cs	Ce	Eu	U	Pu	
Area 1										
1	39.78	44.12	5.26	0.00	0.00	0.00	0.00	0.00	0.06	Pd
2	36.59	44.75	7.19	0.00	0.00	0.69	0.00	0.00	0.14	Pd-Ce
3	37.86	46.68	9.16	0.09	0.00	0.00	0.00	0.00	0.03	Pd
Area 2										
1	46.18	44.83	6.78	0.00	0.00	0.00	0.00	0.00	0.00	Pd
2	48.8	42.43	7.3	0.00	0.00	0.00	0.00	0.00	0.00	Pd
3	44.16	38.2	14.09	0.03	0.00	0.00	0.00	0.00	0.00	Pd

**3.6.2.6.4 Concluding Remarks AGR1-433-001-06.** The following concluding remarks are made concerning the structure and chemistry of AGR1-433-001-06 based on the HRTEM results:

- In the precipitates sampled, Pd is the most abundant and a minor trace of Ce was found.
- Similar to AGR1-433-001-05, the structure and lattice of Pd-Ag and Pd precipitates are cubic
- Precipitates sampled do not contain U.

**3.6.2.6.5 Outer Area of the Silicon Carbide Layer: Lamella AGR1-433-001-07.**

Figure 207(a) is large-scale field of view of the outer area of TRISO Particle AGR1-433-001, Lamella 7, including one area of interest containing precipitates, where HRTEM was used to image each precipitate. Figure 207 (b) is a magnified STEM dark field view containing the identified area for AGR1-433-001-07. The area contains Pd fission product precipitates, where simultaneous STEM dark and BF imaging in Figure 207(c) and Figure 207(d), respectively, reveal these precipitates and the surrounding intact SiC layer. Detailed chemical and structural analyses were performed.

Over the single area, Figure 208(a) is a dark field STEM image of the AGR1-433-001-07 lamella, containing five individual fission product precipitates. Figure 208(b) is the simultaneous, STEM BF image that reveals grain texture and clearly shows the fission product precipitates are centered at triple point junctions. Fission product precipitates within Sub-area 1 (highlighted in Figure 207[d]) were then imaged with HRTEM. Fission product precipitates labeled 3 (Figure 209[a] through [c]) and 4 (Figure 209[d] through [f]) were the only nano-precipitates adequate for HRTEM imaging. For fission product Precipitate 3, Figure 209(a) shows overlapping Si-C lattice fringes, it was suspected the Pd precipitate is buried within the surrounding lattice. Only over some partial area is another lattice direction and spacing consistent with a Pd precipitate observable. At higher magnification, Figure 209(b) shows those same overlapping lattice areas more clearly, where Figure 209(c) shows both the SiC and Pd-Ag lattice are clearly resolved. For fission product Precipitate 4, Figure 216(c) shows a Pd-Ag fission product precipitate lattice, where at higher magnification in Figure 209(d), a lattice other than SiC is observed. This was then subsequently verified using an FFT centered over the precipitate shown in Figure 209(e).

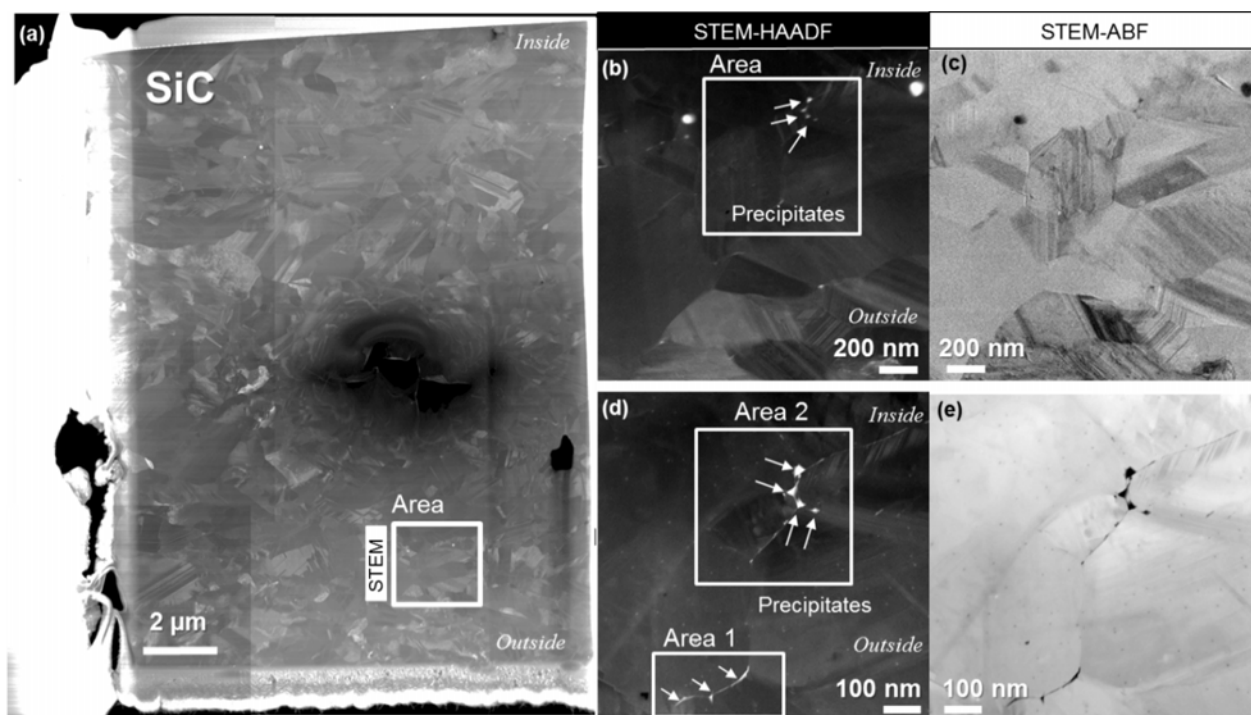


Figure 207. (a) Large field of view from the outer area of TRISO Particle AGR1-433-001, where one area containing precipitates was analyzed using STEM imaging within the SiC layer contained within Lamella 7. Atomic contrast (b) dark field and (c) BF imaging centered over the area, reveals a network of fission product precipitates within the SiC layer that migrate under neutron irradiation. A closer examination of the area, (d) STEM dark and (e) BF reveal Pd-Ag fission product precipitates concentrated within the area of interest. Note the chemical composition of the fission product precipitates contained within this one area is provided in Table 95.

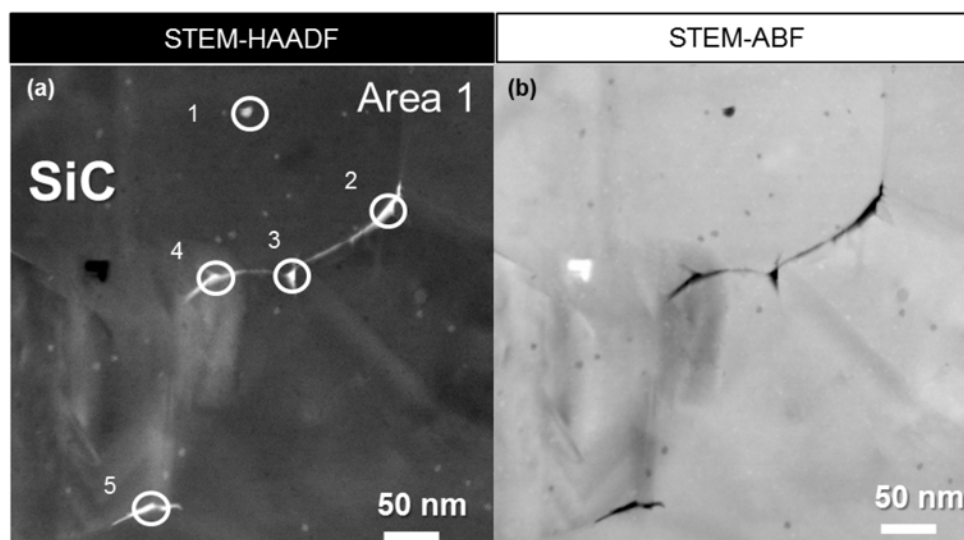


Figure 208. (a) STEM dark and (b) BF imaging centered over area 1 reveals the individual fission product precipitates contained with Area 1 from the outer area of TRISO Particle AGR1-433-001 of Lamella 7 that have been later identified and analyzed using both STEM and HRTEM. Over the same Area 1, HRTEM was performed for fission product Precipitates 3 and 4. Note the report chemical compositions for each of these labeled fission product precipitates are reported in Table 95.

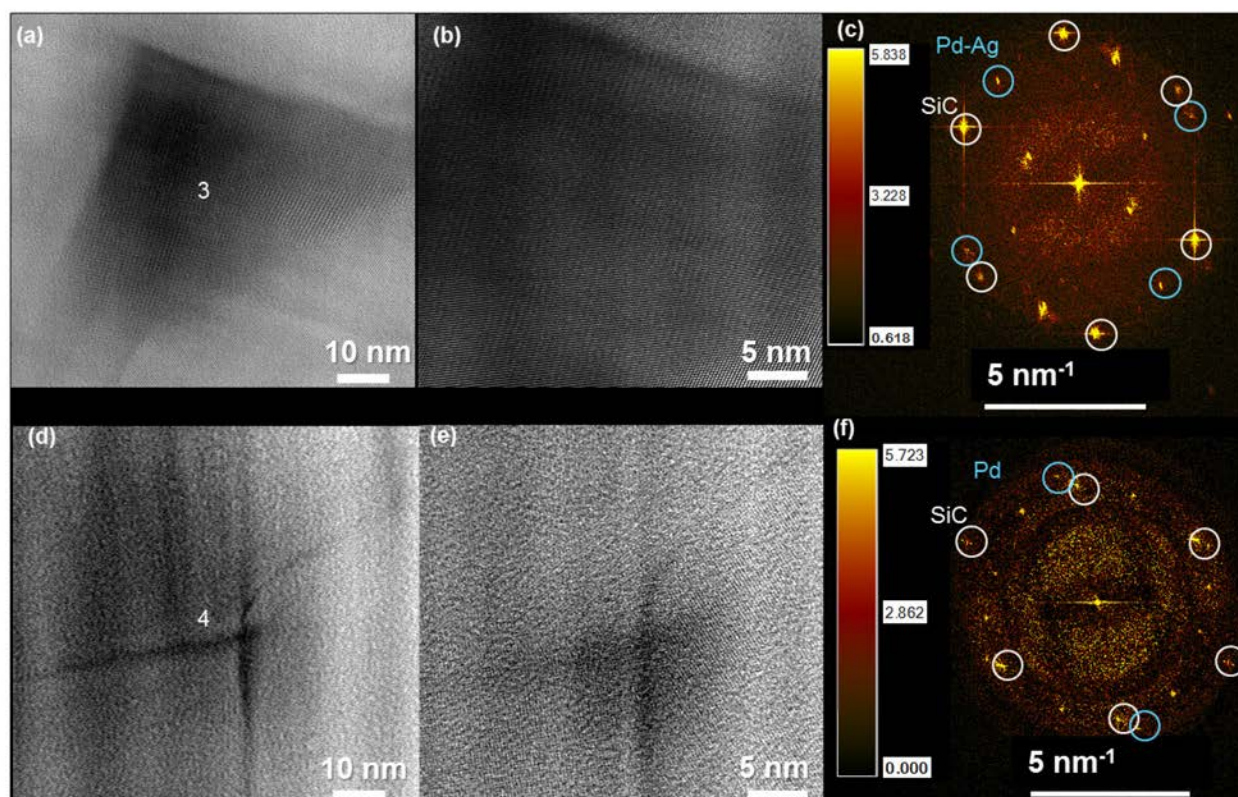


Figure 209. Atomic-scale HRTEM imaging and FFTs of individual fission product precipitates, including (a and b) 3 and (d through f) 4, taken from Area 1 within the outer area of TRISO Particle AGR1-433-001 contained within Lamella 7. From (a) low to (b) higher magnification, fission product Precipitate 3 is resolved with HRTEM. (c) The accompanying FFT reveals both the Pd-Ag and SiC lattice spots for fission product Precipitate 3. Similarly, for fission product Precipitate 4, (d) low to (e) higher magnification HRTEM was used to image the atomic structure of the precipitate and accompanying FFT pattern. For each of the respective FFTs, white and blue circles label the cubic SiC and blue circles label the Pd and Pd-Ag lattice points.

Fission product precipitates contained within the area were also imaged with dark field (Figure 210[a]) and BF (Figure 210[b]) STEM. Because of the significant grain overlap, these fission product precipitates were not imaged with HRTEM, but were analyzed with STEM EDS and their individual chemistry is reported in Table 95.

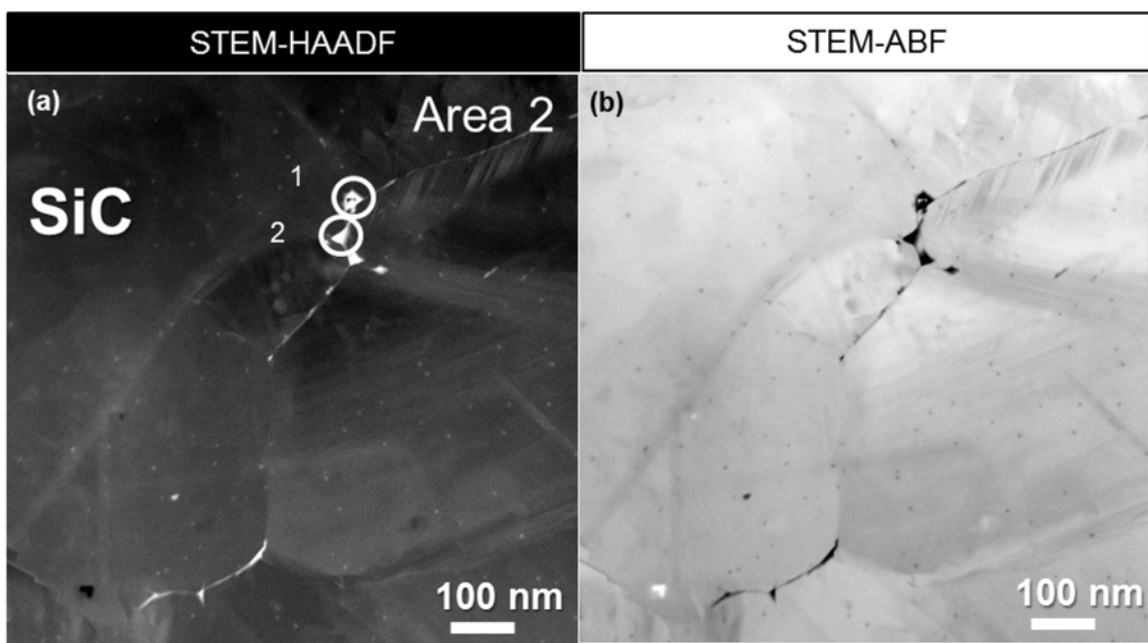


Figure 210. (a) STEM dark and (b) BF imaging centered over Area 2 from the outer area of TRISO Particle AGR1-433-001, reveals the individual fission product precipitates that have been later identified and analyzed using both STEM and EDS contained within Lamella 7. Note the report chemical compositions are reported in Table 95.

Chemistry for each of the fission product precipitates contained in Areas 1 and 2 was resolved with EDS chemical profiling. Table 95 reports the most- and least-abundant fission product elements for Areas 1 and 2 in Lamella AGR1-433-001-07.

Table 95. Qualitative fission product precipitate chemistry reported in atomic % from the outer area of the silicon carbide layer of TRISO Particle AGR1-433-001 taken from subtended Areas 1 and 2 of Lamella 7 as highlighted in Figure 207 and labeled in Figure 208 and Figure 210.

Precipitate Number	Concentration (at.%)									Precipitate Identification
	C	Si	Pd	Ag	Cs	Ce	Eu	U	Pu	
Area 1										
1	51.19	44.42	0.35	0.00	0.00	0.00	0.00	0.00	0.00	Pd
2	42.49	49.57	0.87	0.00	0.00	0.00	0.00	0.00	0.00	Pd
3	53.4	41.07	1.04	0.00	0.00	0.00	0.00	0.00	0.00	Pd
4	50.09	42.87	0.60	0.00	0.00	0.00	0.00	0.00	0.00	Pd
5	54.65	40.17	0.87	0.00	0.00	0.00	0.00	0.00	0.00	Pd
Area 2										
1	55.62	37.04	3.47	0.00	0.00	0.00	0.00	0.00	0.00	Pd
2	44.36	50.05	1.59	0.00	0.00	0.00	0.00	0.00	0.00	Pd

**3.6.2.6.6 Concluding Remarks AGR1-433-001-07.** Based on the leading observations, the following concluding remarks are made concerning the structure and chemistry of precipitates from Lamella AGR1-433-001-07, based on HRTEM results:

- In the precipitates sampled, Pd is the only element found.
- Precipitates are networked along grain boundaries concentrated at triple points. It is suspected that the migration of fission product precipitates occurs along grain boundaries and triple points throughout the TRISO-coated particle.
- Similar to precipitates from lamellae AGR1-433-001-05/06, the structure and lattice of Pd/Ag and Pd precipitates is observed to be cubic in nature
- Precipitates sampled in this area do not contain U or Pu.
- The majority of precipitates are concentrated at triple-point junctions, where these areas offer enough material continuity to image using HRTEM. These are areas where they are not overlapped with surrounding intact SiC grains

### 3.6.3 Coated Particle AGR1-433-004 (High [98%] Ag Retention)

Results from qualitative chemical composition measurement, fission product identification, crystallographic characteristics, and HRTEM examination will be provided for Particle AGR1-433-004 on precipitates from two areas each from four lamellae (see Figure 211 for Lamellae 4 to 7). The areas chosen on Lamella 4 are closer to the SiC-IPyC interface than those of Lamella 5.

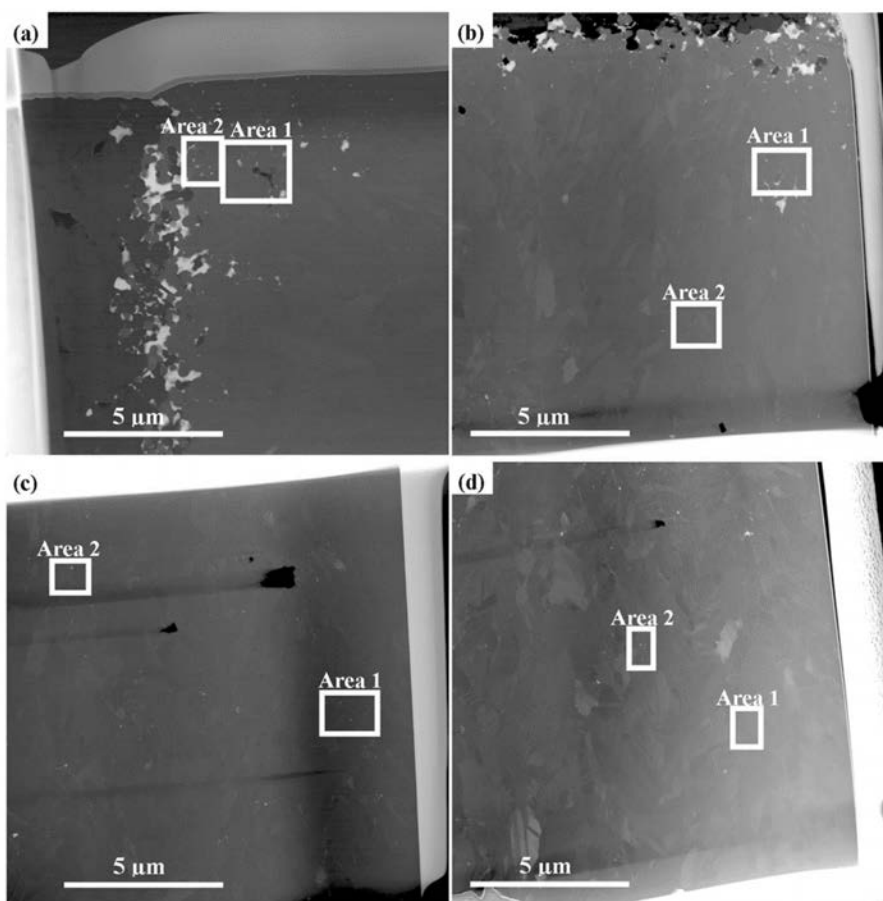


Figure 211. Overview of the TEM Lamella from AGR1-433-004 showing the analysis areas for (a) inner, Lamella 4, (b) inner, Lamella 5, (c) center, Lamella 6, and (d) outer, Lamella 7.

**3.6.3.1 Chemical Composition of Minor Elements of Particle AGR1-433-004.** This section reports the qualitative chemical composition of elements on Particle AGR1-433-004 to determine the type of fission products present, the location of these particles in relation to the SiC layer thickness, and the fission product elemental composition. The reported fission product precipitate compositions (atomic %) are qualitative or semi-quantitative in nature (Section 2.1.2.3). A summary of the minor elements present in these four lamellae are shown in Table 96, with Sections 3.6.3.2 to 3.6.3.3 describing the precipitates found in the inner, center, and outer areas. A significant number of precipitates and features identified within AGR1-433-004, Sites 4, 5, 6, and 7 contain sites where the chemistry of the feature cannot be reported due to reported low counts over background for elements identified in the tables. Despite a STEM EDS scan or point over the feature identified (a precipitate, grain boundary, or triple-point junction), the quantified and reported composition for these features is not above the 0.2 at.% uncertainty limit to be considered significant. Over these featured areas, many of the precipitates and features are smaller than the foil thickness where the majority of electron beam passes through the entire thickness of the lamellae, not generating a large X-ray emission field compared to the surrounding SiC. Because of these limitations of studying nanometer-sized features with STEM EDS, these studies are only intended to establish if the elements are present in the fission product precipitates, but to do so, they need to be measured above 0.2 at. % for the microscope configuration used in this study.

The qualitative trend analysis of precipitate composition (Pd, Ag, and U only) as a function of the approximate distance from the SiC-IPyC interface of Particle AGR1-433-004 is shown in Figure 212. No significant trends are identified; however, Ag is identified approximately through the full SiC layer thickness. Cs was found only in the outer region of the SiC layer with U and Pu only in the inner region, with Eu and Ag identified in the inner and outer regions. Ce was not found in the outer region.

Table 96. Identification of minor elements present in fission product precipitates in the SiC layer of Particle AGR1-433-004.

Lamellae	Area	Elements Present									Precipitate Identification
		C	Si	Pd	Ag	Cs	Ce	Eu	U	Pu	
Inner, Lamella 4	Area 1	X	X	X			X	X	X		Pd, Pd-Eu, Pd-Ce, Pd-U
	Area 2	X	X	X	X		X				Pd, Pd-Ag, Pd-Ce
Inner, Lamella 5	Area 1	X	X	X	X		X		X	X	Pd, Ag, Pd-U, Pd-Ag, Pd-U-Pu, Pd-Ce-Pu
	Area 2	X	X	X	X		X			X	Pd, Pd-Ag, Pd-Ag-Ce
Inner Summary		X	X	X	X		X	X	X	X	
Center, Lamella 6	Area 1	X	X	X							Pd
	Area 2	X	X	X			X				Pd, Pd-Ce
Center Summary		X	X	X			X				
Outer, Lamella 7	Area 1	X	X	X							Pd
	Area 2	X	X	X	X	X		X			Pd, Pd-Ag, Pd-Cs-Eu
Outer Summary		X	X	X	X	X		X			
Final Summary		X	X	X	X	X	X	X	X	X	

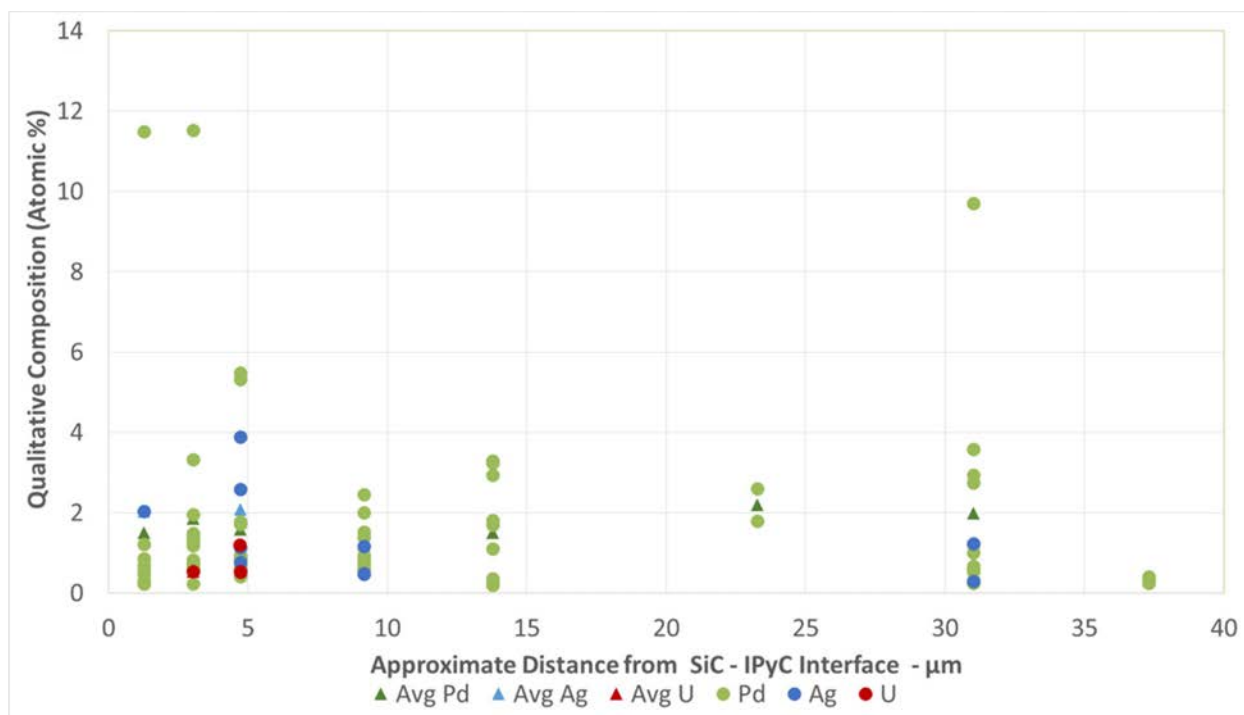


Figure 212. Qualitative trend analysis of precipitate composition (Pd, Ag, and U only) as a function of the approximate distance from the SiC-IPyC interface of Particle AGR1-433-004.

**3.6.3.2 Inner Area of the Silicon Carbide Layer (Lamellae 4 and 5).** As indicated in Figure 211, two lamellae (Lamellae 4 and 5) represent the inner area of the SiC layer.

**3.6.3.2.1 Lamella 4.** Figure 213 shows a higher magnification view of the two chosen areas in Lamella 4 marked in yellow and labeled Areas 1 and 2, respectively. Precipitates in these areas were examined and the composition determined by qualitative EDS analysis (presented in Table 97, Table 98, Figure 214, and Figure 215). One Pd-Ag and Pd Ce and three Pd-U precipitates are found in this inner area Lamella with the majority containing only Pd. The single Pd-Ag precipitate is found in Area 2, which is closest to the SiC-IPyC interface.



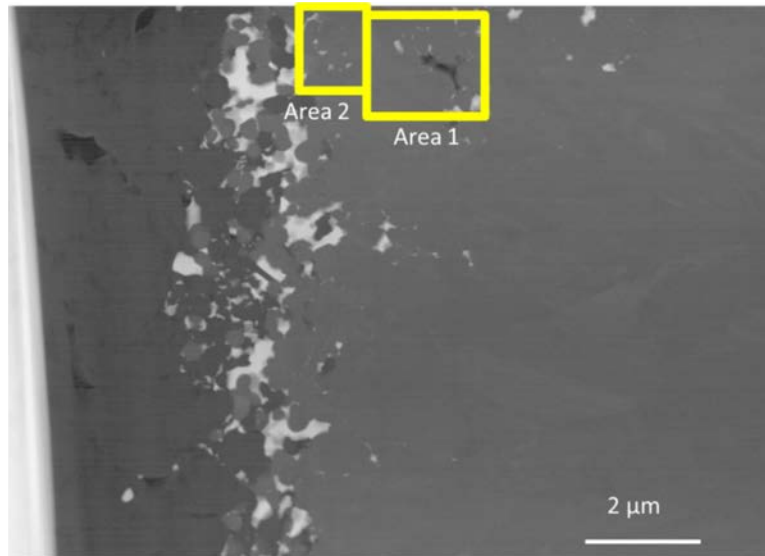


Figure 213. Large field of view STEM dark field image taken from the inner area (Lamella 4) of TRISO Particle AGR1-433-004.

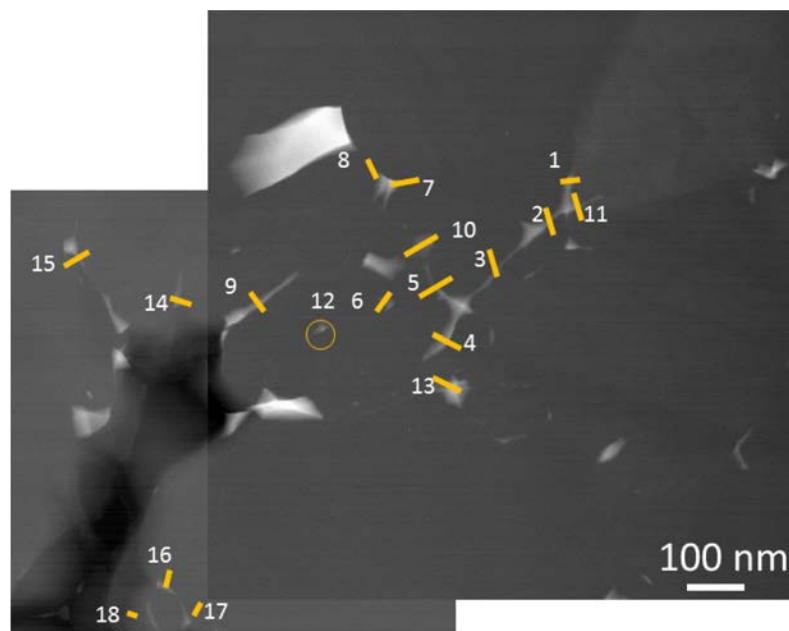


Figure 214. STEM HAADF image combined with EDS labeling to track the chemical composition of fission product precipitates from the inner area (Lamella 4) of TRISO Particle AGR1-433-04 within subtended Area 1. Note the reported chemical compositions are in Table 97.

Table 97. Reported qualitative EDS compositions from precipitates (Figure 214) from the inner area of TRISO Particle AGR1-433-004, measured in subtended Area 1 (Figure 213).

Precipitate Number	Concentration (at.%)									Precipitate Identification
	C	Si	Pd	Ag	Cs	Ce	Eu	U	Pu	
1	51.45	46.73	1.22	0.00	0.00	0.13	0.29	0.02	0.16	Pd-Eu
2	41.26	57.36	1.28	0.00	0.00	0.00	0.00	0.00	0.10	Pd
3	51.97	47.88	0.15	0.00	0.00	0.00	0.00	0.00	0.00	
4	48.76	49.56	1.35	0.03	0.00	0.00	0.00	0.14	0.16	Pd
5	62.10	37.19	0.70	0.00	0.00	0.00	0.00	0.00	0.00	Pd
6	56.11	42.67	1.22	0.00	0.00	0.00	0.00	0.00	0.00	Pd
7	56.69	42.13	1.18	0.00	0.00	0.00	0.00	0.00	0.00	Pd
8	46.23	42.09	11.53	0.00	0.00	0.00	0.00	0.00	0.15	Pd
9	53.40	43.27	3.33	0.00	0.00	0.00	0.00	0.00	0.00	Pd
10	58.81	40.15	0.57	0.00	0.00	0.46	0.00	0.00	0.00	Pd-Ce
11	62.87	36.97	0.13	0.00	0.00	0.00	0.00	0.00	0.04	
12	45.23	52.16	1.96	0.00	0.00	0.00	0.00	0.54	0.10	Pd-U
13	53.72	44.78	1.49	0.00	0.00	0.00	0.00	0.00	0.00	Pd
14	51.09	48.67	0.24	0.00	0.00	0.00	0.00	0.00	0.00	Pd
15	48.02	51.09	0.83	0.00	0.00	0.00	0.00	0.00	0.06	Pd
16	51.30	47.94	0.76	0.00	0.00	0.00	0.00	0.00	0.00	Pd
17	51.99	46.80	0.63	0.00	0.00	0.59	0.00	0.00	0.00	Pd-Ce
18	48.67	49.92	1.42	0.00	0.00	0.00	0.00	0.00	0.00	Pd

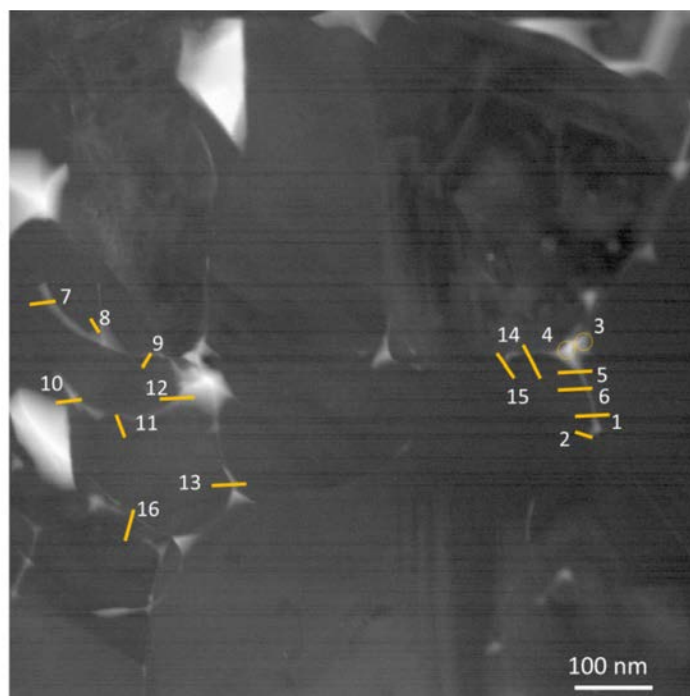


Figure 215. STEM HAADF image combined with EDS labeling to track the chemical composition of fission product precipitates from the inner area (Lamella 4) of TRISO Particle AGR1-433-004, within subtended Area 2. Note the reported chemical compositions are in Table 98.

Table 98. Reported qualitative EDS compositions from precipitates (Figure 215) from the inner area of TRISO Particle AGR1-433-004, taken from subtended Area 2 (Figure 213).

Precipitate Number	Concentration (at.%)									Precipitate Identification
	C	Si	Pd	Ag	Cs	Ce	Eu	U	Pu	
1	56.34	43.55	0.09	0.00	0.00	0.00	0.00	0.02	0.00	
2	46.71	50.93	0.32	2.04	0.00	0.00	0.00	0.00	0.00	Pd-Ag
3	44.82	43.51	11.50	0.13	0.00	0.00	0.00	0.00	0.04	Pd
4	57.64	42.09	0.27	0.00	0.00	0.00	0.00	0.00	0.00	Pd
5	59.46	40.43	0.11	0.00	0.00	0.00	0.00	0.00	0.00	
6	57.67	42.23	0.10	0.00	0.00	0.00	0.00	0.00	0.00	
7	48.61	50.65	0.48	0.00	0.00	0.25	0.00	0.00	0.00	Pd-Ce
8	53.36	46.55	0.08	0.00	0.00	0.00	0.00	0.00	0.01	
9	53.81	45.96	0.23	0.00	0.00	0.00	0.00	0.00	0.00	Pd
10	55.52	44.26	0.23	0.00	0.00	0.00	0.00	0.00	0.00	Pd
11	52.55	46.74	0.71	0.00	0.00	0.00	0.00	0.00	0.00	Pd
12	51.05	47.66	1.22	0.00	0.00	0.00	0.00	0.07	0.00	Pd
13	55.11	44.30	0.58	0.00	0.00	0.00	0.00	0.00	0.00	Pd
14	54.70	45.10	0.13	0.00	0.00	0.00	0.00	0.08	0.00	
15	53.47	46.11	0.26	0.00	0.00	0.16	0.00	0.00	0.00	Pd
16	52.19	46.95	0.86	0.00	0.00	0.00	0.00	0.00	0.00	Pd

**3.6.3.2.2 Lamella 5.** Two random areas are selected for chemical analysis and are shown in Figure 216 and are marked in yellow and labeled Areas 1 and 2, respectively. Precipitates in these areas were examined and the composition determined by qualitative EDS analysis (presented in Table 99 and Figure 217).

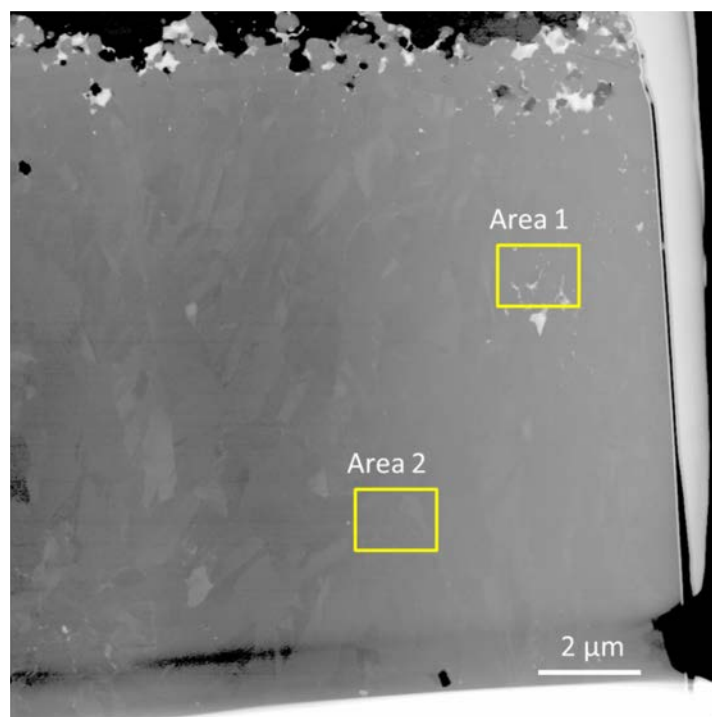


Figure 216. Large field of view STEM dark field image taken from the inner area (Lamella 5) of TRISO Particle AGR1-433-004.

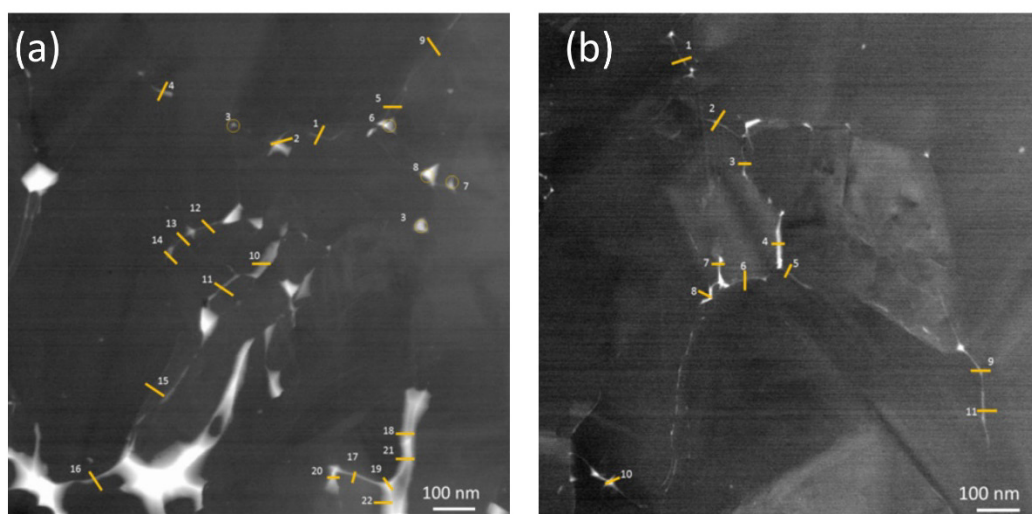


Figure 217. (a) STEM HAADF image combined with EDS labeling to track the chemical composition of fission product precipitates from the center area (Lamella 5) of TRISO Particle AGR1-433-004 within subtended Area 1. Note the reported chemical compositions are in Table 99(b), The STEM HAADF image combined with EDS labeling to track the chemical composition of fission product precipitates from the center area (Lamella 5) of TRISO Particle AGR1-433-004 within subtended Area 2. Note the reported chemical compositions are in Table 99.

Table 99. Reported qualitative EDS compositions from precipitates (Figure 217) from the center area (Lamella 5) of TRISO Particle AGR1-433-004, taken from subtended Areas 1 and 2 (Figure 216).

Precipitate Number	Concentration (at.%)									Precipitate Identification
	C	Si	Pd	Ag	Cs	Ce	Eu	U	Pu	
Area 1										
1	44.00	55.92	0.07	0.00	0.00	0.00	0.00	0.00	0.00	
2	36.94	60.29	0.19	2.59	0.00	0.00	0.00	0.00	0.00	Ag
3	51.32	48.68	0.00	0.00	0.00	0.00	0.00	0.00	0.00	
4	38.50	59.83	0.94	0.15	0.00	0.00	0.00	0.53	0.06	Pd-U
5	38.71	61.23	0.00	0.00	0.00	0.00	0.00	0.06	0.00	
6	44.81	53.09	0.89	0.00	0.00	0.00	0.00	1.20	0.01	Pd-U
7	44.36	55.61	0.02	0.00	0.00	0.00	0.00	0.01	0.00	
8	34.54	62.89	1.78	0.02	0.00	0.00	0.00	0.55	0.21	Pd-U-Pu
9	45.61	54.34	0.03	0.00	0.00	0.02	0.00	0.00	0.00	
10	52.68	46.41	0.89	0.00	0.00	0.00	0.00	0.01	0.01	Pd
11	47.67	51.48	0.85	0.00	0.00	0.00	0.00	0.00	0.00	Pd
12	40.61	56.99	0.42	0.00	0.00	1.66	0.00	0.07	0.26	Pd-Ce-Pu
13	43.87	55.39	0.45	0.00	0.00	0.00	0.00	0.13	0.15	Pd-U
14	48.20	51.26	0.54	0.00	0.00	0.00	0.00	0.00	0.00	Pd
15	44.45	54.92	0.63	0.00	0.00	0.00	0.00	0.00	0.00	Pd
16	38.53	61.43	0.04	0.00	0.00	0.00	0.00	0.00	0.00	
17	37.07	62.01	0.16	0.76	0.00	0.00	0.00	0.00	0.00	Ag
18	35.32	59.23	5.33	0.00	0.00	0.00	0.00	0.00	0.11	Pd
19	39.20	59.52	0.15	1.14	0.00	0.00	0.00	0.00	0.00	Ag
20	40.29	55.13	0.65	3.89	0.01	0.00	0.00	0.00	0.03	Pd-Ag
21	41.31	56.98	1.71	0.00	0.00	0.00	0.00	0.00	0.00	Pd
22	36.36	58.02	5.48	0.00	0.00	0.00	0.00	0.00	0.14	Pd
Area 2										
1	53.37	45.94	0.69	0.00	0.00	0.00	0.00	0.00	0.00	Pd
2	39.79	58.90	0.95	0.00	0.00	0.00	0.00	0.00	0.36	Pd-Pu
3	47.73	51.04	0.62	0.47	0.00	0.00	0.00	0.14	0.00	Pd-Ag
4	52.42	45.58	2.00	0.00	0.00	0.00	0.00	0.00	0.00	Pd
5	39.90	58.69	0.90	0.50	0.00	0.00	0.00	0.00	0.00	Pd-Ag
6	53.93	45.93	0.15	0.00	0.00	0.00	0.00	0.00	0.00	
7	39.59	53.29	1.40	1.17	0.00	4.54	0.00	0.00	0.00	Pd-Ag-Ce
8	53.44	44.10	2.46	0.00	0.00	0.00	0.00	0.00	0.00	Pd
9	49.99	48.99	0.91	0.11	0.00	0.00	0.00	0.00	0.00	Pd
10	41.92	57.30	0.78	0.00	0.00	0.00	0.00	0.00	0.00	Pd
11	51.92	46.55	1.53	0.00	0.00	0.00	0.00	0.00	0.00	Pd

**3.6.3.2.3 Lamella 6.** As indicated in Figure 218, two random areas were identified for chemical analysis in the center area of the SiC layer. Pd is identified as the main fission product with only one Pd-Ce precipitate identified. Precipitate details are provided in Figure 219, Figure 220, Table 100, Table 82 and Table 101.

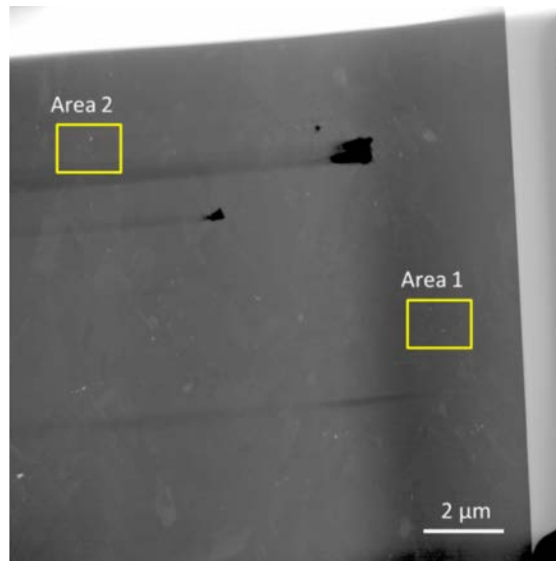


Figure 218. Large field of view STEM dark field image taken from the center area (Lamella 6) of TRISO Particle AGR1-433-004.

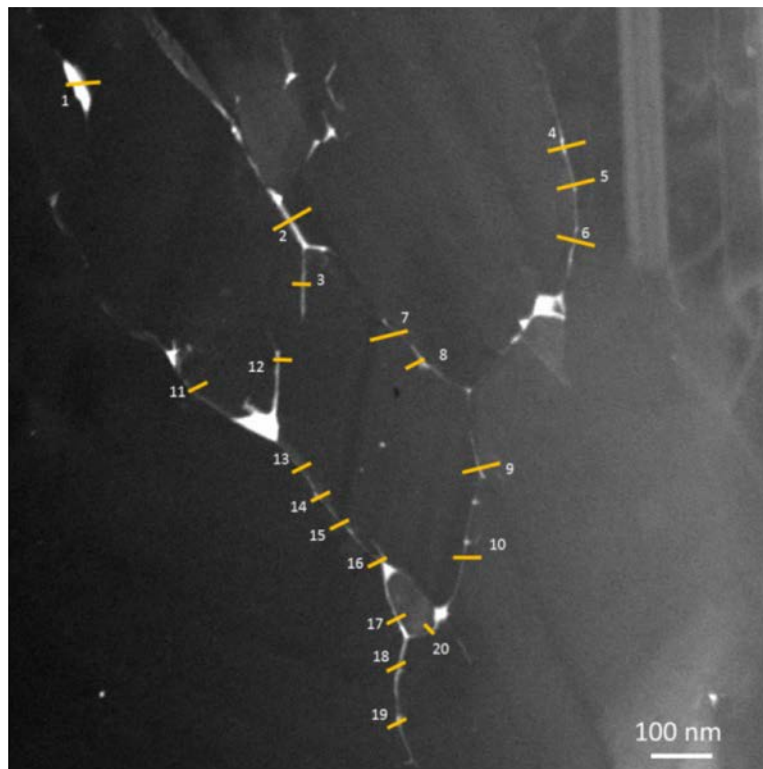


Figure 219. STEM HAADF image combined with EDS labeling to track the chemical composition of fission product precipitates from the center area (Lamella 6) of TRISO Particle AGR1-433-004, within subtended Area 1. Note the reported chemical compositions are in Table 100.

Table 100. Reported qualitative EDS compositions from precipitates (Figure 219) from the center area (Lamella 6) of TRISO Particle AGR1-433-004, taken from subtended Area 1 (Figure 218).

Precipitate Number	Concentration (at.%)									Precipitate Identification
	C	Si	Pd	Ag	Cs	Ce	Eu	U	Pu	
1	61.09	36.31	2.60	0.00	0.00	0.00	0.00	0.00	0.00	Pd
2	61.13	38.80	0.07	0.00	0.00	0.00	0.00	0.00	0.00	
3	53.11	46.86	0.00	0.00	0.00	0.00	0.00	0.00	0.03	
4	55.20	44.76	0.04	0.00	0.00	0.00	0.00	0.00	0.00	
5	57.70	42.25	0.00	0.00	0.00	0.00	0.00	0.00	0.04	
6	44.19	54.02	1.80	0.00	0.00	0.00	0.00	0.00	0.00	Pd
7	61.40	38.54	0.07	0.00	0.00	0.00	0.00	0.00	0.00	
8	62.16	37.71	0.13	0.00	0.00	0.00	0.00	0.00	0.00	
9	61.38	38.62	0.00	0.00	0.00	0.00	0.00	0.00	0.00	
10	58.44	41.48	0.08	0.00	0.00	0.00	0.00	0.00	0.00	
11	63.12	36.87	0.00	0.00	0.00	0.00	0.00	0.00	0.00	
12	60.26	39.74	0.00	0.00	0.00	0.00	0.00	0.00	0.00	
13	59.75	40.11	0.14	0.00	0.00	0.00	0.00	0.00	0.00	
14	62.96	36.97	0.07	0.00	0.00	0.00	0.00	0.00	0.00	
15	60.48	39.34	0.17	0.00	0.00	0.00	0.00	0.00	0.00	
16	61.45	38.44	0.12	0.00	0.00	0.00	0.00	0.00	0.00	
17	59.02	40.94	0.04	0.00	0.00	0.00	0.00	0.00	0.00	
18	61.37	38.55	0.04	0.00	0.00	0.00	0.00	0.04	0.00	
19	60.68	39.30	0.02	0.00	0.00	0.00	0.00	0.00	0.00	
20	58.11	41.87	0.03	0.00	0.00	0.00	0.00	0.00	0.00	

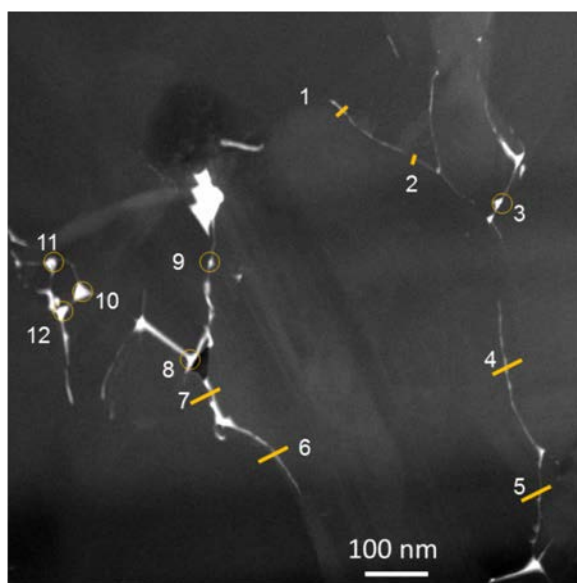


Figure 220. STEM HAADF image combined with EDS labeling to track the chemical composition of fission product precipitates from the center area (Lamella 6) of TRISO Particle AGR1-433-004 within subtended Area 2. Note the reported chemical compositions are in Table 101.



Table 101. Reported qualitative EDS compositions from the center area (Lamella 6) of TRISO Particle AGR1-433-004, taken from subtended Area 2.

Precipitate Number	Concentration (at.%)									Precipitate Identification
	C	Si	Pd	Ag	Cs	Ce	Eu	U	Pu	
1	46.96	51.22	1.81	0.00	0.00	0.00	0.00	0.00	0.00	Pd
2	54.64	43.65	1.70	0.00	0.00	0.00	0.00	0.00	0.00	Pd
3	56.00	43.78	0.22	0.00	0.00	0.00	0.00	0.00	0.00	Pd
4	47.61	51.80	0.36	0.00	0.00	0.23	0.00	0.00	0.00	Pd-Ce
5	54.73	45.09	0.19	0.00	0.00	0.00	0.00	0.00	0.00	
6	55.75	43.15	1.10	0.00	0.00	0.00	0.00	0.00	0.00	Pd
7	52.70	47.09	0.21	0.00	0.00	0.00	0.00	0.00	0.00	Pd
8	56.39	43.40	0.21	0.00	0.00	0.00	0.00	0.00	0.00	Pd
9	56.17	40.53	3.30	0.00	0.00	0.00	0.00	0.00	0.00	Pd
10	52.65	44.10	3.25	0.00	0.00	0.00	0.00	0.00	0.00	Pd
11	52.71	44.28	2.94	0.08	0.00	0.00	0.00	0.00	0.00	Pd
12	57.08	42.76	0.12	0.05	0.00	0.00	0.00	0.00	0.00	

**3.6.3.3 Outer Area of the Silicon Carbide Layer Lamella 7.** Two areas were randomly selected as shown in Figure 221 and the qualitative chemical analysis from precipitates shown are reported in Table 102 and Table 103. Only one Pd-Cs-Eu and Pd Ag precipitate and predominant Pd-containing precipitates are visible in this outer area of the SiC layer.

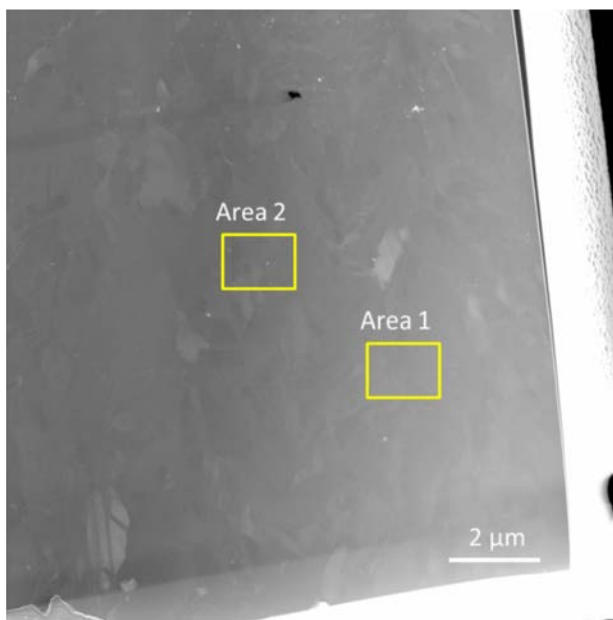


Figure 221. Large field of view STEM dark field image taken from the outer area (Lamella 7) of TRISO Particle AGR1-433-004.

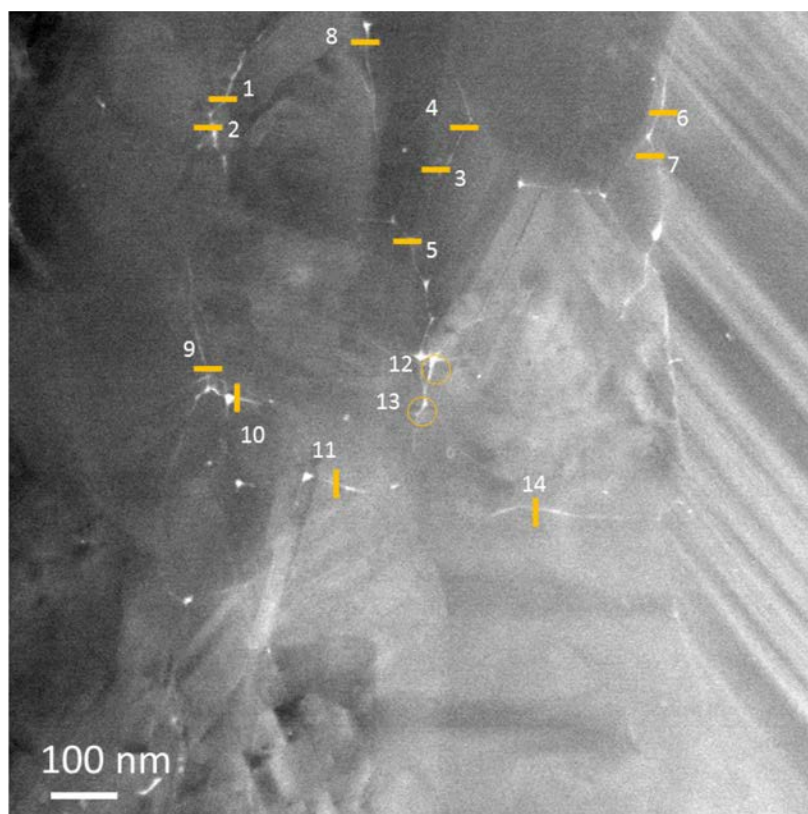


Figure 222. STEM HAADF image combined with EDS labeling to track the chemical composition of fission product precipitates from the outer area (Lamella 7) of TRISO Particle AGR1-433-004 within subtended Area 1. Note the reported chemical compositions are in Table 102.

Table 102. Reported qualitative EDS compositions from precipitates (Figure 222) from the outer area (Lamella 7) of TRISO Particle AGR1-433-004, measured in subtended Area 1 (Figure 221).

Precipitate Number	Concentration (at.%)									Precipitate Identification
	C	Si	Pd	Ag	Cs	Ce	Eu	U	Pu	
1	51.28	48.31	0.41	0.00	0.00	0.00	0.00	0.00	0.00	Pd
2	45.25	54.49	0.26	0.00	0.00	0.00	0.00	0.00	0.00	Pd
3	38.75	61.05	0.02	0.00	0.00	0.00	0.00	0.18	0.00	U
4	47.42	52.56	0.02	0.00	0.00	0.00	0.00	0.00	0.00	
5	51.91	48.06	0.03	0.00	0.00	0.00	0.00	0.00	0.00	
6	51.35	48.53	0.12	0.00	0.00	0.00	0.00	0.00	0.00	
7	47.15	52.56	0.28	0.00	0.00	0.00	0.00	0.00	0.00	Pd
8	52.26	47.56	0.17	0.00	0.00	0.00	0.00	0.00	0.00	
9	52.89	46.76	0.33	0.00	0.02	0.00	0.00	0.00	0.00	Pd
10	50.82	49.10	0.09	0.00	0.00	0.00	0.00	0.00	0.00	
11	51.91	48.06	0.03	0.00	0.00	0.00	0.00	0.00	0.00	
12	49.76	50.16	0.02	0.00	0.06	0.00	0.00	0.00	0.00	
13	47.95	51.69	0.36	0.00	0.00	0.00	0.00	0.00	0.00	Pd

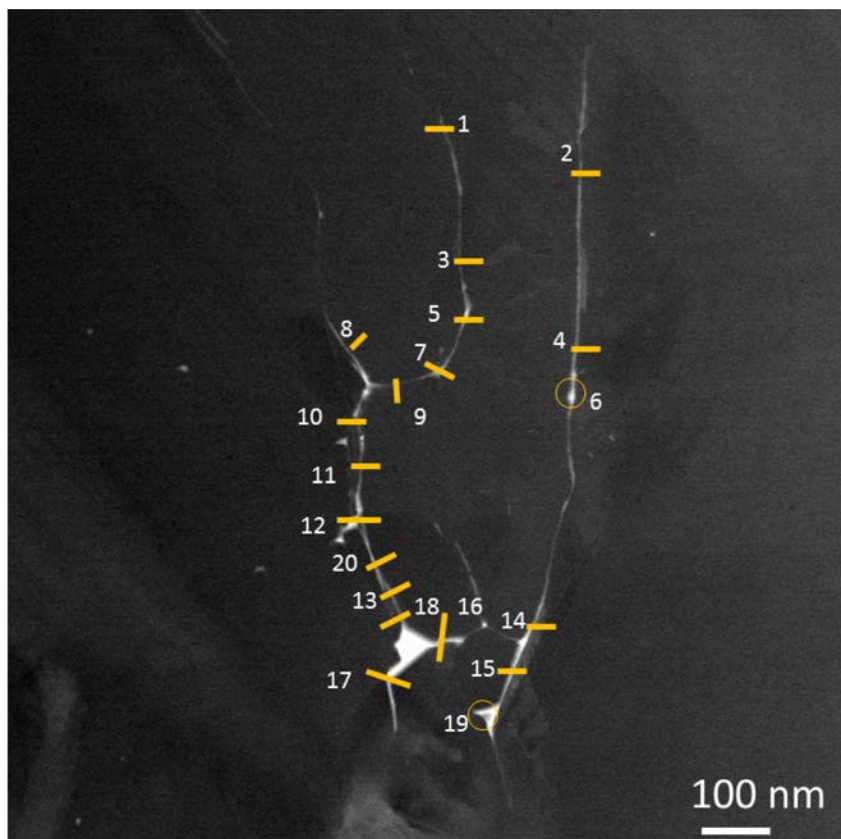


Figure 223. STEM HAADF image combined with EDS labeling to track the chemical composition of fission product precipitates from the outer area (Lamella 7) of TRISO Particle AGR1-433-004 within subtended Area 2. Note the reported chemical compositions are in Table 103.

Table 103. Reported qualitative EDS compositions from precipitates (Figure 223) from the outer area (Lamella 7) of TRISO Particle AGR1-433-004, taken from subtended Area 2 (Figure 221).

Precipitate Number	Concentration (at.%)									Precipitate Identification
	C	Si	Pd	Ag	Cs	Ce	Eu	U	Pu	
1	55.70	43.98	0.32	0.00	0.00	0.00	0.00	0.00	0.00	Pd
2	56.69	42.26	1.01	0.04	0.00	0.00	0.00	0.00	0.00	Pd
3	57.33	42.39	0.28	0.00	0.00	0.00	0.00	0.00	0.00	Pd
4	55.66	43.67	0.67	0.00	0.00	0.00	0.00	0.00	0.00	Pd
5	58.59	40.19	1.22	0.00	0.00	0.00	0.00	0.00	0.00	Pd
6	39.45	56.36	2.95	1.24	0.00	0.00	0.00	0.00	0.00	Pd-Ag
7	59.22	40.64	0.14	0.00	0.00	0.00	0.00	0.00	0.00	
8	62.92	36.49	0.60	0.00	0.00	0.00	0.00	0.00	0.00	Pd
9	59.26	40.19	0.55	0.00	0.00	0.00	0.00	0.00	0.00	Pd
10	62.14	37.79	0.07	0.00	0.00	0.00	0.00	0.00	0.00	
11	62.48	37.44	0.02	0.00	0.05	0.00	0.00	0.00	0.00	
12	59.88	39.98	0.14	0.00	0.00	0.00	0.00	0.00	0.00	Pd
13	62.37	37.55	0.08	0.00	0.00	0.00	0.00	0.00	0.00	
14	59.58	40.17	0.25	0.00	0.00	0.00	0.00	0.00	0.00	Pd
15	61.35	38.51	0.14	0.00	0.00	0.00	0.00	0.00	0.00	Pd
16	41.42	58.39	0.00	0.00	0.00	0.00	0.00	0.09	0.10	
17	61.96	37.99	0.05	0.00	0.00	0.00	0.00	0.00	0.00	
18	46.22	42.92	9.71	0.11	0.55	0.13	0.29	0.06	0.00	Pd-Cs-Eu
19	48.17	47.80	3.59	0.30	0.00	0.00	0.12	0.00	0.02	Pd-Ag
20	58.47	38.74	2.75	0.01	0.00	0.00	0.02	0.00	0.00	Pd

**3.6.3.4 Crystallographic Characteristic of Particle AGR1-433-004.** The TEM Lamella from this particle consisted of two inner samples (Lamellae 4 and 5), one center sample (Lamella 6), and one outer sample (Lamella 7). The areas analyzed on these samples are shown in Figure 211. Two areas were analyzed on each sample. Both fission product precipitate composition and grain boundary parameters from PED analysis were determined to correlate fission product precipitate composition with grain boundary types.

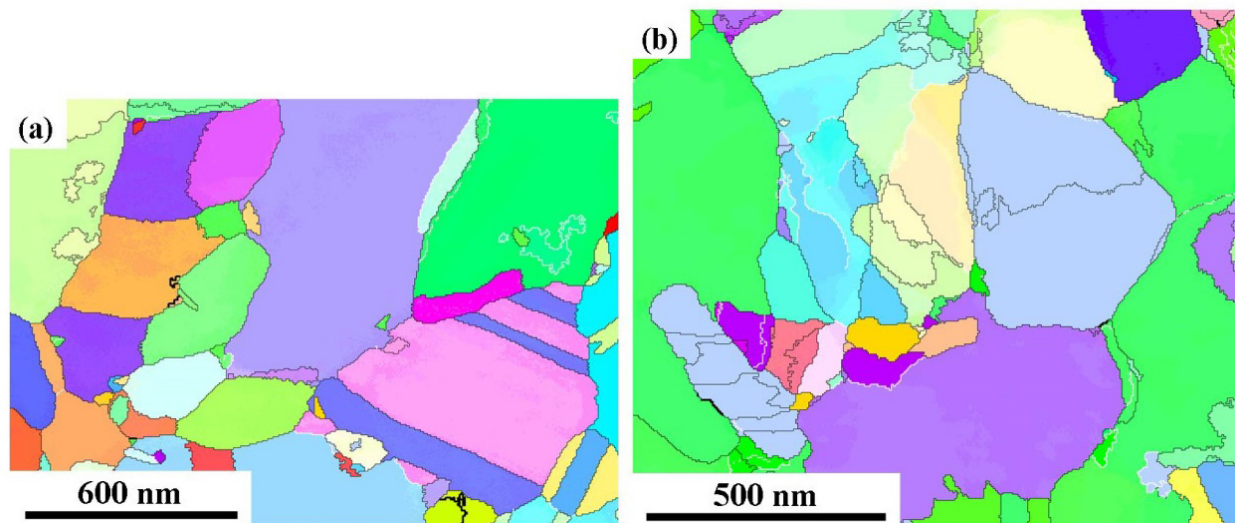


Figure 224. Orientation maps of (a) Area 1 and (b) Area 2 on the inner sample, Lamella 4, AGR1-433-004.

#### **3.6.3.4.1 General Grain Boundary Distributions across the Silicon Carbide Layer.**

Examples of the orientation maps from the areas analyzed on the inner sample (Lamella 4) are shown in Figure 224. The grain orientations were used to determine the grain boundary distributions in each area, which included misorientation angle distribution, CSL-value distribution, and grain boundary type distribution. Examples of these distributions for the inner (Lamella 4) are shown in Figure 225. Observations on the individual areas of a sample were combined and the standard error in the distributions were calculated (standard error = standard deviation/ $\sqrt{\text{number of areas analyzed}}$ ). The averaged distributions were used to compare the SiC microstructure in the inner, center, and outer regions of the SiC layer.

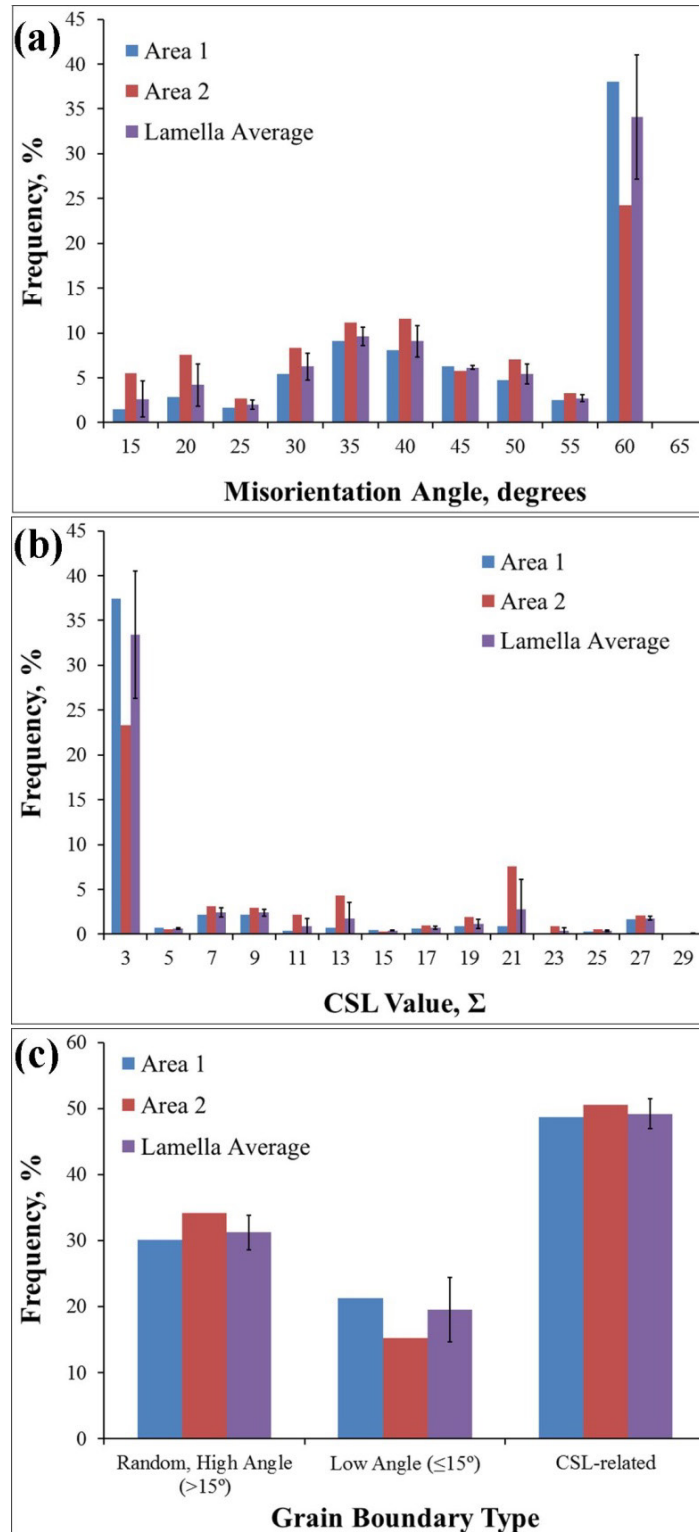


Figure 225. Distributions of (a) grain boundary misorientation angles, (b) value of CSL-related grain boundaries, and (c) grain boundary types in each area analyzed on the inner sample (Lamella 4, Figure 211[a]) AGR1-433-004. Averaged distributions are included.

**Misorientation Angle Distribution:** The averaged distributions of the grain boundary misorientation angle for the inner, center, and outer samples are shown in Figure 226(a). The twin boundary fraction ( $\theta = 60$  degrees), at a fraction around 50% dominates the distributions on the different lamellae from the SiC layer. A secondary peak is observed around  $\theta = 40$  degrees. Statistically, there are not significant differences in the distributions as a function of location in the SiC layer. Also, the two inner areas, Lamellae 4 and 5, closely resemble each other; therefore, it would appear that variations in the misorientation angle distribution at different inner locations are relatively small.

**Distribution of CSL-Related Grain Boundaries:** Figure 226(b) shows the distribution of grain boundaries that exhibit a CSL relationship. The twin boundaries,  $\Sigma 3$ , again dominate the distribution in all lamellae and, therefore, all areas in the SiC layer. Higher order twins (i.e.,  $\Sigma 9$  and  $\Sigma 27$ ) make up a majority of the remaining CSL-related grain boundaries. CSL boundaries  $\Sigma 7$  and  $\Sigma 21$  also make significant contributions to the CSL grain boundary distributions. Based on the standard error in the distribution, it appears that there are statistically fewer  $\Sigma 3$  (twin) grain boundaries in the inner regions of the SiC layer compared to the center and outer regions.

The distributions can be averaged to give a CSL distribution representative of the entire SiC layer. This allows the CSL distribution to be compared to that reported in literature for the SiC layer of an unirradiated TRISO particle (Kirchhofer et al., 2013). Table 104 reports the fractions of twin boundaries calculated from the data in this study. Kirchhofer et al., (2013) reports values of 27%, 5%, and 1% for  $\Sigma 3$ ,  $\Sigma 9$ , and  $\Sigma 27$  boundaries, respectively, for an unirradiated TRISO particle fabricated with Variant 3 parameters. The value for the  $\Sigma 3$  boundaries in this study is considerably higher, while the higher order twin fractions are similar in both studies. The reason behind the difference in the  $\Sigma 3$  fractions is not known at this time but may be due to particle-to-particle variations, irradiation and temperature effects, or differences in the methods used to collect the grain orientation data.

Table 104. Average fraction of twin-related grain boundaries in the SiC layer from Particle AGR1-433-004.

CSL value, $\Sigma$	Fraction, %	Std. Error
3	43.6	6.7
9	3.4	0.5
27	1.9	0.4

**Distributions by Grain Boundary Type:** The averaged distributions by grain boundary type for the inner, center, and outer samples are shown in Figure 226(c). Again, the distributions of the two inner samples (Lamellae 4 and 5) are quite similar and statistically identical. The center and outer samples appear to have higher fractions of CSL-related grain boundaries and lower fractions of low-angle grain boundaries than the inner samples.

The results from the four lamellae in this study have been averaged to yield values representative of the entire SiC layer and they have been tabulated in Table 105. These values, when compared to the values given by Kirchhofer for an unirradiated particle, low-angle = 21%, high-angle = 39%, and CSL-related = 40%, are significantly different. Again, this could be indicative of irradiation and temperature effects, particle-to-particle variation, and/or data collection methods.



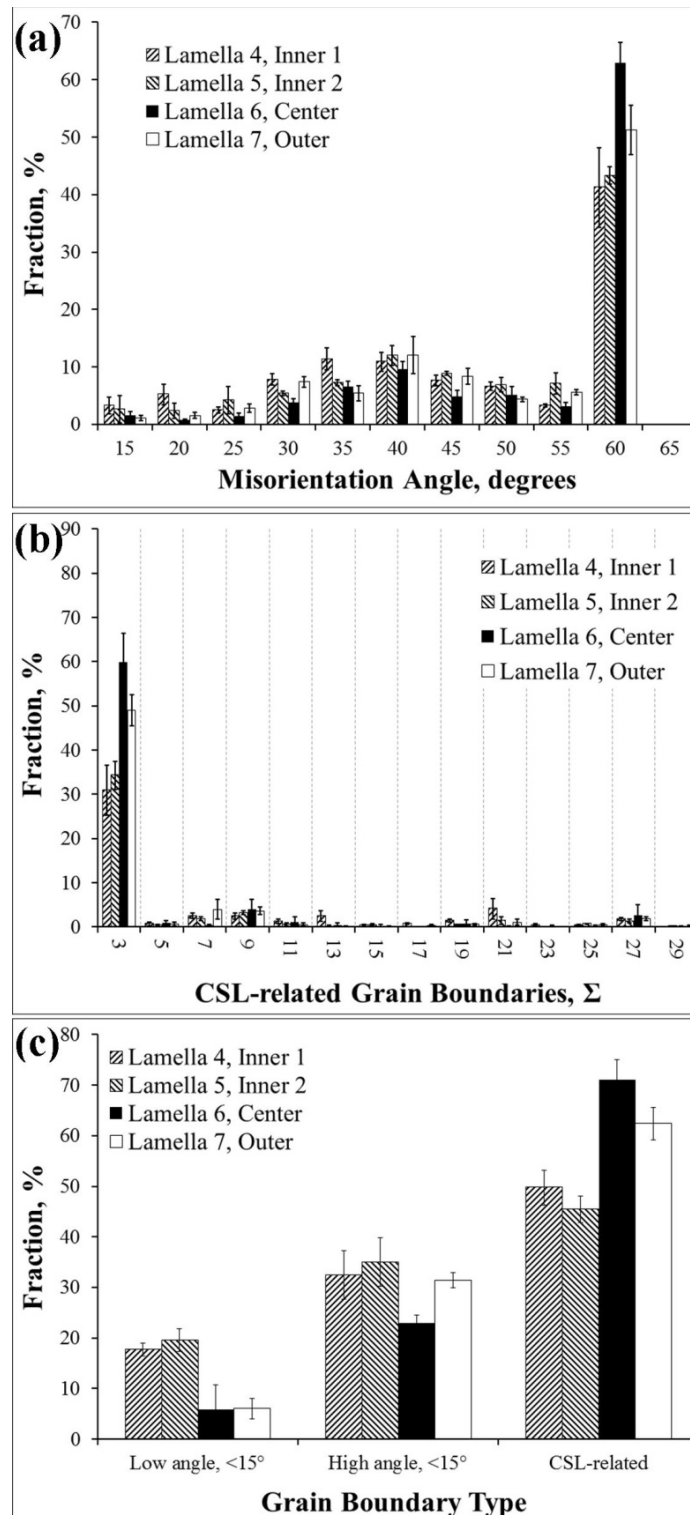


Figure 226. Grain boundary distributions averaged over all areas analyzed on each sample, (a) misorientation angle, (b) CSL value, and (c) grain boundary type for the SiC samples taken from AGR1-433-004.

Table 105. Average fraction of grain boundary types in the SiC layer from Particle AGR1-433-004.

Grain Boundary Type	Fraction, %	Std. Error
Low angle, <15°	12.3	3.7
High angle, >15°	30.5	2.6
CSL-related	57.2	5.9

**3.6.3.4.2 Grain Boundary Data for Grain Boundaries Containing Fission Product Precipitates.** Analysis of the grain boundary fission product precipitates in the SiC layer of this particle definitively indicated the presence of Pd, Ag, U, and Pu. Additional analyses described elsewhere in this report indicated that other fission product elements (e.g., Eu, Cs, and Ce) may also be present in low concentrations in these precipitates. However, the short x-ray data acquisition time prevented these elements from being definitively identified as being present. Therefore, these other elements were not included in the correlation of fission products with grain boundary type that follows.

**Inner Samples (Lamellae 4 and 5):** Pd-containing precipitates were the most prevalent near the IPyC-SiC interface. These precipitates also frequently contained either Ag, U, Pu, or U with Pu (Table 106). Additionally, some precipitates were found to contain only Ag. The transuranic elements (U and Pu) were never found by themselves in grain boundary precipitates, but always in conjunction with Pd. Figure 227 shows that fission product precipitates were found on high-angle and CSL-related grain boundaries with a preference for random, high-angle grain boundaries. In Table 106, only one Pd and Ag precipitate was found on a CSL-related grain boundary (Table 106, Lamella 4), determined to be a  $\Sigma 15$  CSL boundary and only one Ag-only precipitate was found on a CSL-related grain boundary (Table 106, Lamella 5), determined to be a  $\Sigma 7$  CSL boundary. Also, one Pd and Pu precipitate was found on a CSL-related grain boundary (Table 106, Lamella 4) determined to be a  $\Sigma 29b$  CSL boundary. No precipitates were found on low-angle grain boundaries. Clearly, the fission product precipitates preferred random, high-angle grain boundaries.

**Center Sample (Lamella 6):** This sample was farther from the source of fission product and transuranic elements, and all precipitates contained only Pd; no precipitates with other elements or combination of elements were found. Grain boundary precipitation on random, high-angle grain boundaries was still most prevalent but precipitation was also found to a much lesser extent, on CSL-related grain boundaries and, to an even lesser extent, on low-angle grain boundaries (Figure 227). Pd-only precipitates were found on all types of grain boundaries, but were most prevalent on random, high-angle grain boundaries (Table 106). Two precipitates were found on CSL-related grain boundaries that were determined to be a  $\Sigma 5$  and a  $\Sigma 27a$  CSL boundary.

**Outer Sample (Lamella 7):** This sample, near the OPyC/SiC interface, was farthest from the source of fission product and transuranic elements. Only two of the precipitates contained Pd with Ag, while all others only contained Pd (Table 106). Precipitates were most prevalent on random, high-angle grain boundaries, but also were found on CSL-related grain boundaries (a  $\Sigma 3$  and a  $\Sigma 9$  boundary) (Figure 227). The precipitates on the CSL-related grain boundaries contained only Pd (Table 106).

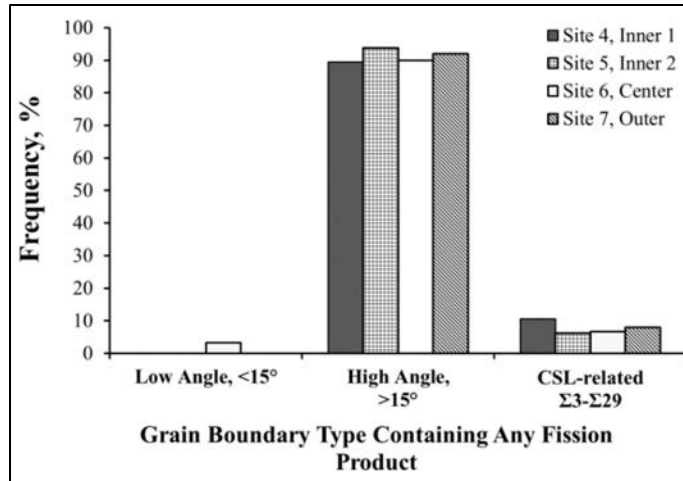


Figure 227. Comparison of the distribution of grain boundary types that contain any fission product precipitates in different regions of the SiC layer in TRISO particle, AGR1-433-004.

Table 106. Summary of the distribution of fission product elements in the SiC layer of AGR1-433-004.

	Pd Only	Ag Only	U Only	Pd and Ag	Pd and U	Ag and U	Pd and Pu	Pd, U, and Pu
<b>Lamella 4, Inner Sample</b>								
Number of grain boundaries	4	3	0	7	1	0	1	3
Fraction of all boundaries with fission products, %	21.1	15.8	0.0	36.8	5.3	0.0	5.3	15.8
Low angle, %	0.0	0.0	—	0.0	0.0	—	0.0	0.0
Random, high angle, %	100.0	100.0	—	85.7	100.0	—	0.0	100.0
CSL, %	0.0	0.0	—	14.3	0.0	—	100.0	0.0
<b>Lamella 5, Inner Sample</b>								
Number of grain boundaries	13	2	0	0	0	0	0	1
Fraction of all boundaries with fission products, %	81.3	12.5	0.0	0.0	0.0	0.0	0.0	6.3
Low angle, %	0.0	0.0	—	—	—	—	—	0.0
Random, high angle, %	100.0	50.0	—	—	—	—	—	100.0
CSL, %	0.0	50.0	—	—	—	—	—	0.0
<b>Lamella 6, Center Sample</b>								
Number of grain boundaries	30	0	0	0	0	0	0	0
Fraction of all boundaries with fission products, %	100.0	0.0	0.0	0.0	0.0	0.0	0.0	0.0
Low angle, %	3.3	—	—	—	—	—	—	—
Random, high angle, %	90.0	—	—	—	—	—	—	—
CSL, %	6.7	—	—	—	—	—	—	—
<b>Lamella 7, Outer Sample</b>								
Number of grain boundaries	23	0	0	2	0	0	0	0
Fraction of all boundaries with fission products, %	92.0	0.0	0.0	8.0	0.0	0.0	0.0	0.0
Low angle, %	0.0	—	—	0.0	—	—	—	—
Random, high angle, %	91.3	—	—	100.0	—	—	—	—
CSL, %	8.7	—	—	0.0	—	—	—	—

**3.6.3.4.3 Discussion of Results for Compact 4-3-3, Particle 4 (AGR1-433-004).** The individual correlation results summarized in Table 106 were combined to yield distributions representative of the entire SiC layer. The relationships between fission products and grain boundary parameters across the SiC layer are discussed in the following subsections.

**Fission Product and Transuranic Element Distribution:** Figure 228 shows that most grain boundary precipitates in the SiC layer contain Pd. These precipitates are mainly of the Pd-only variety with a small fraction of Pd combined with Ag, U, or Pu. Ag-only precipitates are fairly uncommon, but occur in significant numbers. Also, it should be noted that in this particle, significant quantities of Pu were found. This appears to be unique to this particle and not reported for the other particles from this compact (AGR1-433-001) (Section 3.6.2.5).

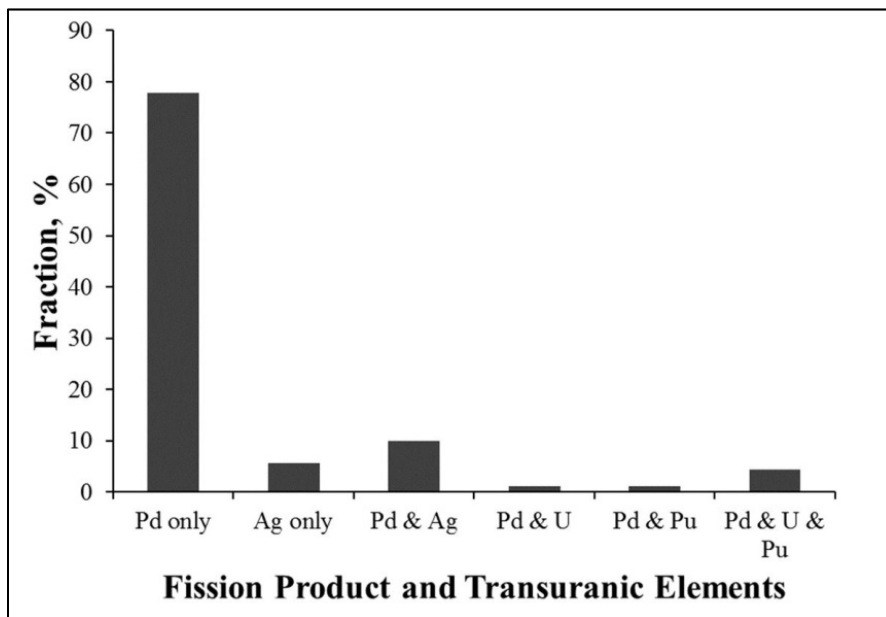


Figure 228. Composition distribution of the various fission product-containing grain boundary precipitates in the SiC layer of AGR1-433-004.

**Associations of Fission Products with Grain Boundary Types – Low-Angle, High-Angle, and  $\Sigma$ :** Regardless of the fission product elements present, the precipitates showed a preference for random, high-angle grain boundaries (Figure 229), as found in a similar analysis on an irradiated Baseline TRISO particle from Compact 6-3-2 (Lillo and van Rooyen 2016). Precipitation on low-angle grain boundaries was infrequent and limited to Pd-only precipitate types (Figure 229 and Figure 230). Precipitation on CSL-related boundaries is also infrequent, but more prevalent than precipitation on low-angle grain boundaries (Figure 229). However, precipitation on CSL-related grain boundaries is not limited to Pd-only type precipitates as it is with low-angle grain boundaries. One Ag-only precipitate was found on a CSL-related grain boundary (a  $\Sigma 7$  boundary), while Pd-containing precipitates were found on a variety of CSL-related boundaries that ranged from low to relatively high  $\Sigma$  values (e.g.,  $\Sigma 3$  to  $\Sigma 29$ ).

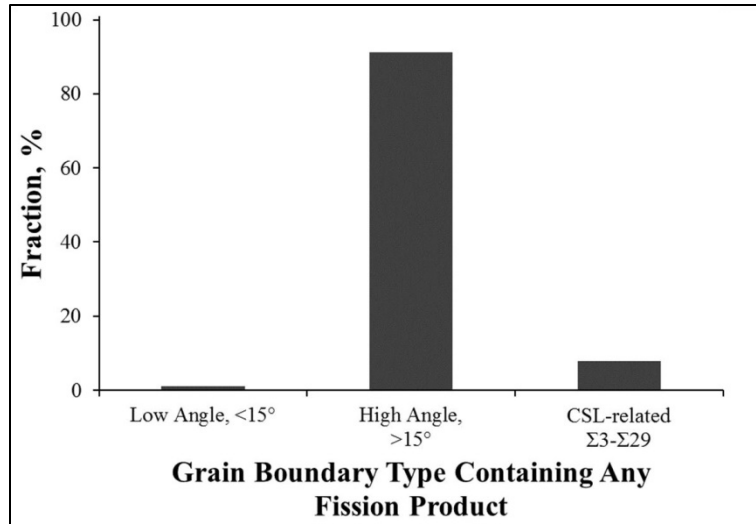


Figure 229. Distribution of the fission product-containing precipitates on the various boundary types, as a percentage, in the SiC layer of AGR1-433-004.

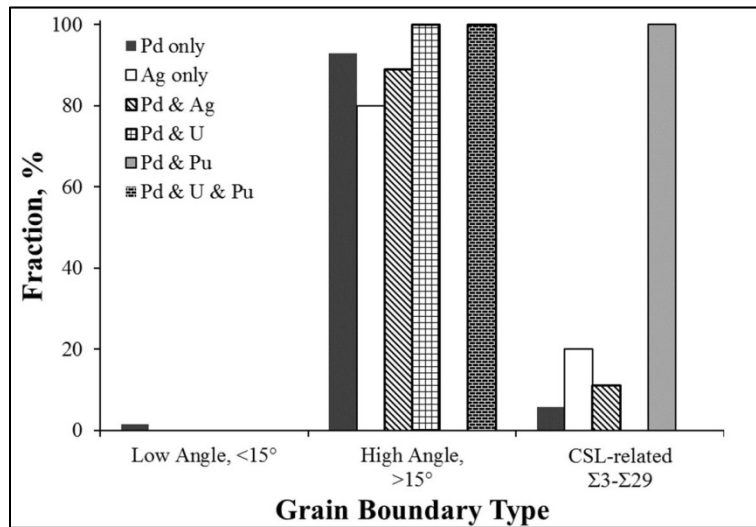


Figure 230. Distributions of precipitates containing specific fission product elements or their combination, as a percentage, by grain boundary type in the SiC layer of AGR1-433-004.

**Effects of Grain Boundary Energy:** As mentioned previously, the precipitation behavior is likely governed by grain boundary energy considerations. Low-angle grain boundaries and CSL-related grain boundaries tend to be of lower energy than random, high-angle grain boundaries. (Grain boundary habit plane plays a significant role in determining the grain boundary energy; therefore, some CSL-related grain boundaries may not be of particularly low energy; therefore, they are susceptible to precipitation of fission product elements. See Lillo and van Rooyen (2016) for a discussion of the role of grain boundary habit plane on grain boundary energy. Low-energy grain boundaries exhibit relatively good atomic matching across the grain boundary plane. Precipitation and even transporting atoms with a differing atomic radius than the matrix atoms can result in localized strains in the grain boundary, which tend to increase the system energy. Therefore, low-energy grain boundaries are not conducive to transporting impurity atoms or precipitation of second phases. Typically, high-energy grain boundaries do not have good atomic matching across the grain boundary plane and have excess free volume associated with the grain boundary (Wolf 1989, Wolf 1990) that can accommodate impurity atoms of different atomic radii

and precipitation of second phases. To correlate grain boundary energy with the observed precipitation behavior, it is necessary to know the grain boundary habit plane. Modeling can then provide an estimate of grain boundary energy. However, as mentioned previously, currently no method exists for quickly determining the grain boundary habit plane; furthermore, the grain boundary habit plane is rarely straight, but rather it is typically curved and the habit plane is continually changing along the grain boundary, resulting in continually changing grain boundary energy.

It should also be kept in mind that this particle was safety tested at higher temperatures than those used in fabrication, as well as those in the AGR-1 experiment. The rather lengthy time (~300 hours) at the safety testing temperature of 1600°C, could have enabled significant microstructural changes, including significant changes to the atomic structure of grain boundaries, and impurity diffusion. These microstructural changes and additional impurity diffusion may be responsible for the presence of Pu in the SiC layer of this particle, which was not seen in the other AGR-1 TRISO particles in this report that were not safety tested, especially since Pu was also found in the other safety tested particle, AGR1-433-001 (Table 92).

**3.6.3.4.4 Comparison of AGR1-433-001 and AGR1-433-004.** The two particles from Compact 4-3-3 exhibited significantly different fission product release behavior even though they were in the same compact during the AGR-1 experiment. AGR1-433-001 showed a retention of Ag-110m of 66% compared to that calculated on a theoretical basis, while AGR1-433-004 exhibited 98% retention compared to theoretical values. The reasons for the different behavior are either experiment-based or microstructure-based. Experimentally, even though both particles were in the same compact in nominally the same position in the reactor during the experiment, the local conditions (i.e., temperature, fluence, and burnup), may have been significantly different for each particle and different from the values averaged over the compact. The microstructure-based reasons postulate that differences in microstructure and especially the grain boundary structure give rise to differences in fission product transport behavior.

The advanced microstructural analysis task, the results of which are reported here, was designed to explore the viability of differences in microstructure as the reason for the difference in fission product release behavior. Identification of microstructural causes for differences in release behavior would then permit intelligent modification of the TRISO fabrication process to minimize microstructural differences and mitigate the potential for significant release of fission products. Therefore, the following compares the grain boundary distributions in an effort to reveal microstructural differences that may be related to fission product release behavior.

**General Grain Boundary Distributions:** Comparisons of the misorientation angle distributions, CSL boundary distributions and the grain boundary-type distributions between AGR1-433-001 and AGR1-433-004, are shown in Figure 231(a–c), respectively and is, representative of the entire SiC layer. Although slight differences are observed between the different distributions, no differences are statistically significant, except the fraction of  $\Sigma 5$  boundaries in Figure 231(b) and perhaps a slightly greater fraction of random, high-angle grain boundaries in Figure 231(c). As such, there does not appear to be anything in the grain boundary distributions of the entire SiC layer that would suggest a reason for the observed difference in release behavior. Additional measurements would be required to reduce the error bars and potentially reveal minor differences in one or more of the distributions.

However, it should be pointed out that there may be significant differences in the distributions for the two particles in the inner region. Comparison of Figure 192 and Figure 226 shows significant differences between the inner regions of the two particles. AGR1-433-001 exhibits a higher fraction of  $\Sigma 3$  grain boundaries and a lower fraction of random, high-angle grain boundaries in the inner region (Lamellae 4, 5, and 10 [Figure 192]) compared to AGR1-433-004 (Lamellae 4 and 5 [Figure 226]). However, this is not intuitively expected since AGR1-433-004 has a higher Ag-110m retention. A higher random, high-angle grain boundary would be expected to promote Ag release rather than tend to minimize it. Also, the difference in the random, high-angle grain boundary fraction between the two particles is not great, ~27%

for AGR1-433-001 versus ~33% for AGR1-433-004, and it is questionable whether this difference could result in such a large difference in Ag-110m retention behavior (66% versus 98%). Also, the random, high-angle grain boundary fraction may have altered significantly during the high temperature and long duration of the safety test. Release may have been occurred early during the safety test, while modification of the grain boundary distribution may not have occurred until later in the safety test; therefore, no correlation between the grain boundary distribution and the Ag-110m release can be (or should be) made.

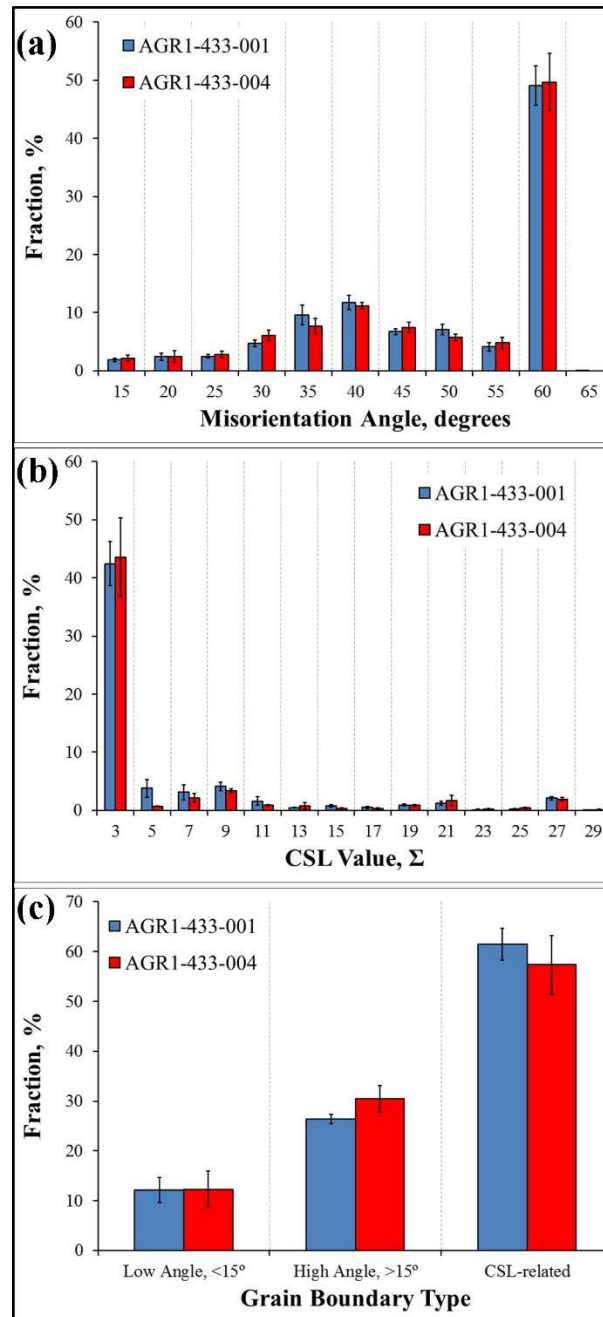


Figure 231. Comparison of the (a) misorientation angle, (b) CSL-related, and (c) grain boundary-type distributions in the SiC layers of AGR1-433-001 and AGR1-433-004.



**Fission Product Precipitate Type:** Figure 232(a) shows the distribution of precipitates containing various fission product elements for particles AGR1-433-001 and AGR1-433-004. The distributions for the two particles are very similar, and no statistically significant differences can be found. However, analyses of additional particles may reduce the size of the error bars and reveal significant differences.

Figure 232(b) shows the fission product precipitate distributions of the two particles as a function of grain boundary type. It would appear that the high-retention particle (AGR1-433-004) has a higher fraction of fission product precipitates associated with high-angle grain boundaries and fewer associated with CSL-related grain boundaries than the low-retention particle. The significance of this difference is unclear at this time.

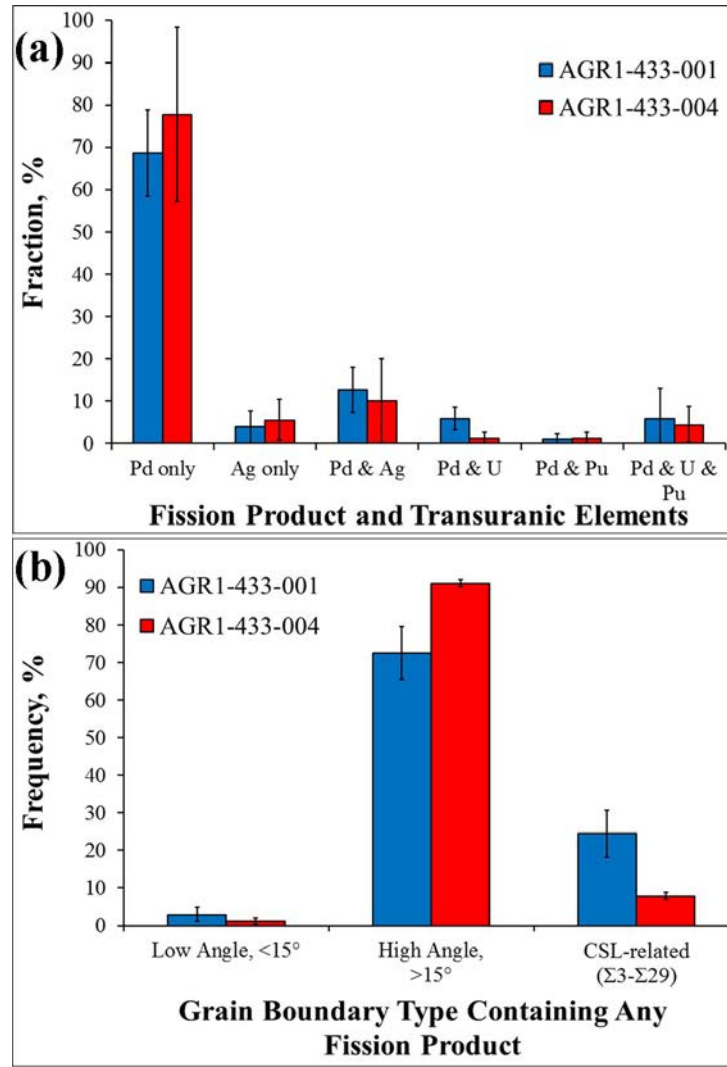


Figure 232. Comparison of (a) the precipitate distribution for grain boundary precipitates containing various fission product elements, and (b) the distribution of fission product precipitates as a function of grain boundary type for the safety-tested TRISO particles (AGR1-433-001 and AGR1-433-004).

**3.6.3.5 Fission Product Precipitate Structure and Phase Identification of Particle AGR1-433-004 (High-Resolution Transmission Electron Microscopy).** For the microstructure determination, a variety of techniques were used inside the TEM, including HAADF STEM, HRTEM, and EDS. The material composition of the samples was determined and profiled using STEM EDS linescans, individual points, and composite two-dimensional spectral images.

#### **3.6.3.5.1 Inner Area of the Silicon Carbide Layer.**

**AGR1-433-004-04:** A closer look at Lamella 4, Figure 233(a) is enlarged field of view from the inner area of TRISO Particle AGR1-433-004, including two areas containing precipitates, where each area was analyzed using HRTEM. Using atomic contrast, STEM dark field imaging, Figure 233(b) is a magnified field view containing the identified areas where nanoscale fission product precipitates, neighbor on intact SiC grain boundaries and triple point junctions. Area 1 contains Pd-Ag fission product precipitates formed mostly at triple point junctions within SiC.

Simultaneous BF imaging in Figure 233(c) clearly reveals the grains structure over this same area. Similarly, over the second area of interest, Area 1b STEM dark field and BF images (Figure 233[d] and Figure 233[e]) reveal similarly sized fission product precipitates near the SiC/IPyC interface. For each of these areas that contain fission product precipitates, detailed chemical and structural analysis was performed (discussed below in detail).

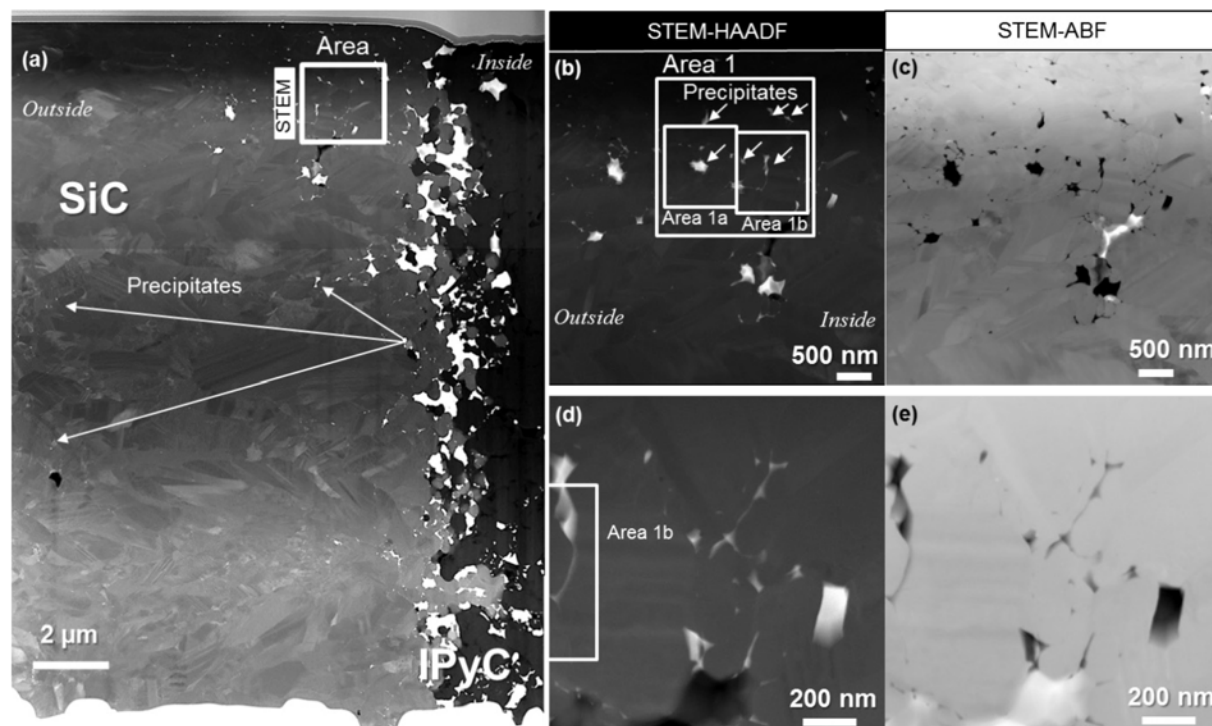


Figure 233. (a) STEM dark field large field of view taken over the inner area from TRISO Particle AGR1-433-004, where two areas containing fission product precipitates were analyzed using STEM imaging near the SiC/IPyC interface contained within Lamella 4. Atomic contrast (b) dark field and (c) BF imaging centered over the area found within the SiC layer, near the SiC/IPyC interface. A closer examination of the area, (d) STEM dark and (e) BF reveal Pd-Ag fission product precipitates concentrated within the area of interest. Note the chemical composition for the fission product precipitates contained within Area 1 is reported in Table 107.

Over the area identified in Figure 233, there are several individual fission product precipitates. These two subtended areas were imaged with both dark and BFSTEM imaging. Figure 234(a) is a dark field STEM image of the Lamella AGR1-433-004-04, Area 1a, containing two individual fission product precipitates. Figure 234(b) is the accompanying simultaneous, STEM BF image that shows significant grain overlap accompanying the locations where fission product precipitates are collocated. Similarly, over the second area, Area 1b Figure 234(c) is a dark field STEM image of the AGR1-433-004-04 Area 1b, which contains two individual fission product precipitates. Figure 234(d) is the accompanying simultaneous STEM BF image for Area 1b. HRTEM was performed to determine the atomic lattice arrangement of each precipitate in each of these areas. For each of the labeled fission product precipitates, point-resolved EDS was used to determine their individual chemical compositions reported in Table 107.

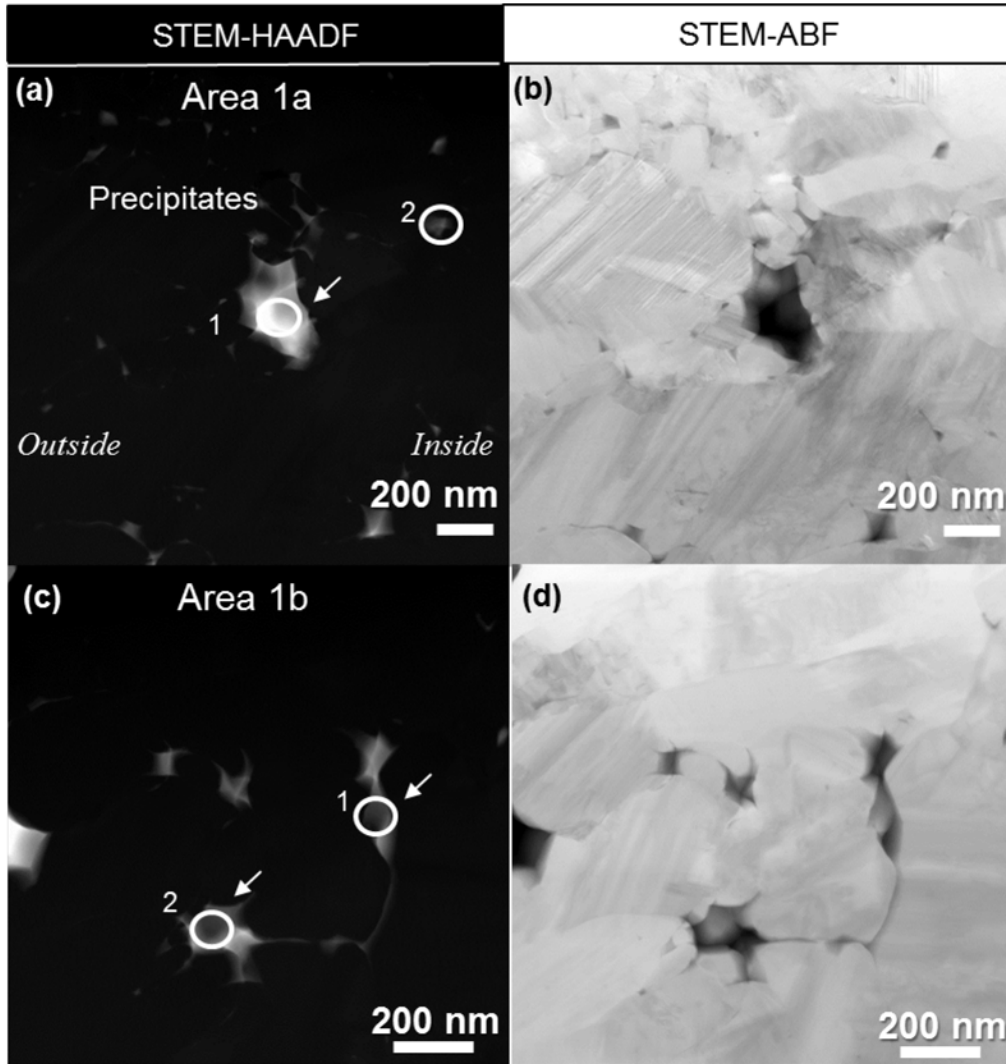


Figure 234. (a) STEM dark field (from Figure 233[b]) and (b) BF centered over the first subtended Area 1a (from Figure 233c) reveal Pd-Ag fission product precipitates concentrated along grain boundaries and triple point junctions from the inner area of TRISO Particle AGR1-433-004 contained within Lamellae 4. Similarly, centered over the second subtended Area 1b STEM (c) dark (from Figure 233[d]) and (d) BF (from Figure 233[e]) from the inner area of TRISO Particle AGR1-433-004 with subtended Area 1b reveals similarly sized fission product precipitates, with a large concentration of precipitates nucleated at triple-point junctions.

**Revealing Precipitate Chemistry in AGR1-433-004-04:** Figure 235 is a series of conventional BF and dark field TEM images showing that the lack of elemental uniformity within each of the fission product precipitates. Selected area electron diffraction (SAED) was used to image and index the crystallography associated with SiC and the accompanying precipitates. Based on the SAED pattern, dark field imaging was taken with the {022} fundamental reflection spot for the cubic structure shared by Pd, Pd-Ag, Pd-U, and Pd-Pu (i.e., circled in a white outline), using a 10  $\mu\text{m}$ -objective aperture for simultaneous dynamic BF and dark field TEM imaging. From subtended Area 1a, conventional BF (Figure 235[b]) and dark (Figure 235[c]) field images show the distribution of Pd. Over the area, there are scattered white spots that are a direct measurement of differences in scattering intensity and structural variation within the precipitate. Similarly, for the second subtended Area 1b, Figure 235(d) is a BF TEM image, where Figure 235(e) is the accompanying dark field TEM image that reveals similarly sized spots contained within the fission product precipitates. Accompanying the TEM analysis, the chemical composition based on point-resolved STEM EDS is reported in Table 107.

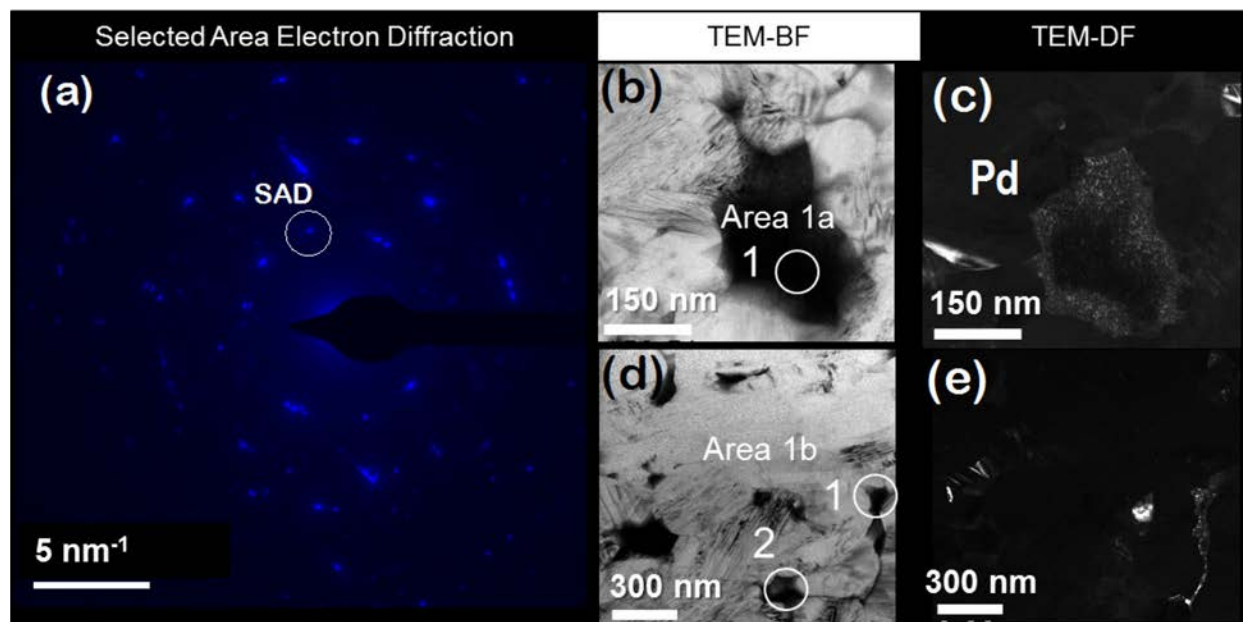


Figure 235. (a) SAED was collected from a larger field of view containing Areas 1a and 1b within the inner area of TRISO Particle AGR1-433-004, Lamella 4. Based on the SAED pattern, the {022} fundamental reflection spot for the cubic face center cubic (FCC) structure corresponding to Pd, Pd-Ag, Pd-U, and Pd-Pu was selected (i.e., circled in a white outline) for dynamic dark field TEM imaging. (b) From subtended Area 1a, Precipitate 1, a BF and (c) dark field image centered over a large precipitate reveals scattered intensities, consistent with a spatially varying distribution contained within the fission product precipitate. Similarly, for Area 1b, (d) BF and (e) dark field TEM reveal similarly sized points within the fission product precipitate. Note Areas 1a and 1b were highlighted in Figure 234.

Table 107. Qualitative fission product precipitate chemistry reported in at. % from the inner area of TRISO Particle AGR1-433-004 taken from subtended Areas 1a and 1b of Lamellae 4 as highlighted in and labeled in Figure 235.

Precipitate Number	Concentration (at.%)									Precipitate Identification
	C	Si	Pd	Ag	Cs	Ce	Eu	U	Pu	
<b>Area 1a</b>										
1	33.17	36.62	19.64	0.00	0.00	0.00	0.00	6.76	1.82	Pd-U-Pu
2	35.34	46.9	16.26	0.04	0.00	0.00	0.00	0.00	0.23	Pd-Pu
<b>Area 1b</b>										
1	36.35	47.3	17.34	0.19	0.00	0.00	0.00	0.00	0.00	Pd
2	44.36	50.05	1.59	0.00	0.00	0.00	0.00	0.00	0.00	Pd

Revealing spatially varying chemistry differences between and within fission product precipitates, STEM-based EDS point scans over a larger number of fission product precipitates were used to tabulate the individual chemistries with statistical significance, included in Area 1b of Lamella AGR1-433-004-04. Figure 236 is a STEM dark field image, containing a series of fission product precipitates, numbered from 1 to 24, which were individually analyzed for elemental composition using point-resolved STEM EDS scans. The compositions are reported in atomic % in Table 108. Over single precipitates, a series of points span two separate fission product precipitates. Points 8 through 12 span one precipitate and points 16 through 19 extend over a second precipitate. Each of these precipitates is highlighted in the series of points in Table 107. The overall chemistry between each of these precipitates varies, as well as their individual subtended point resolved chemistries. The fission product (labeled by points 8 through 12) shows a near constant Pd, U, and Pu content all within 1 at.%, whereas for the second precipitate (labeled by points 16 through 19), the Pd content varies by over 10 at.%, the U content varies by more than 1.5 at.%, and similarly Pu content varies by 1 atomic %. Each of these precipitates are similarly sized and furthermore are within about 600 nms of the other. Based on these results, it is suspected that several different types of fission product precipitates are attainable. Among precipitates and within a single precipitate there is a wide degree of chemical segregation pertaining to the elements of Pd, Ag, U, and Pu. This suggests the effective temperature-dependent atomic diffusivity for each of these elements is different within the SiC layer under irradiation. Determining whether the distribution of elements is primarily due to temperature or neutron damage or combination of both cannot be determined at this time.

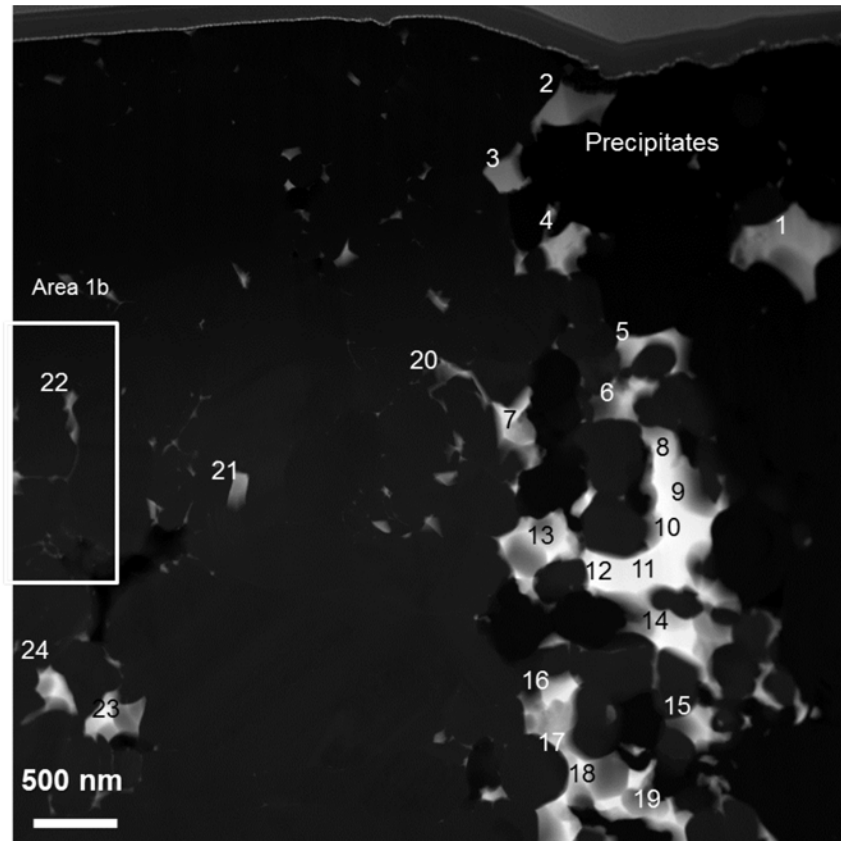


Figure 236. STEM dark field image taken over the larger field of view containing subtended Area 1b from the inner area of TRISO Particle AGR1-433-004, where a series of point-resolved EDS scans were acquired over fission product precipitates and their respective chemical composition is tabulated and reported in Table 108 contained within Lamella 4.

Table 108. Qualitative fission product precipitate chemistry, reported in atomic %, for precipitates from the subtended inner Area 1b of TRISO Particle AGR1-433-004, Lamella 4 taken as highlighted and labeled in Figure 236. Shading indicates overlapping points considered to be contained within the same fission product precipitate.

Precipitate Number	Concentration (at.%)									Precipitate Identification
	C	Si	Pd	Ag	Cs	Ce	Eu	U	Pu	
1	43.46	24.57	24.63	0.00	0.00	0.00	0.00	4.35	1.34	Pd-U-Pu
2	48.91	20.44	23.66	0.00	0.00	0.00	0.00	3.48	0.64	Pd-U-Pu
3	43.26	24.07	25.38	0.00	0.00	0.00	0.00	4.24	0.66	Pd-U-Pu
4	41.93	25.49	24.79	0.01	0.00	1.21	0.00	3.83	0.95	Pd-Ce-U-Pu
5	39.61	30.39	23.63	0.00	0.00	1.19	0.00	3.92	1.25	Pd-Ce-U-Pu
6	48.01	27.14	19.70	0.01	0.00	0.00	0.00	3.51	1.15	Pd-U-Pu
7	38.06	30.37	25.12	0.00	0.00	0.00	0.00	3.98	1.14	Pd-U-Pu
8	31.98	30.22	29.27	0.00	0.00	1.54	0.00	4.81	1.53	Pd-Ce-U-Pu
9	31.67	31.17	28.29	0.00	0.00	1.63	0.00	4.40	1.49	Pd-Ce-U-Pu
10	31.20	31.23	29.81	0.00	0.00	0.00	0.00	5.00	1.95	Pd-U-Pu
11	31.51	31.39	29.69	0.00	0.00	0.00	0.00	5.10	1.31	Pd-U-Pu
12	30.83	29.94	29.92	0.00	0.00	1.63	0.00	4.61	1.54	Pd-Ce-U-Pu
13	33.88	44.18	17.64	0.00	0.00	0.00	0.00	2.78	1.01	Pd-U-Pu
14	30.87	37.36	23.78	0.00	0.00	1.29	0.00	4.25	1.55	Pd-Ce-U-Pu
15	45.70	32.13	16.64	0.00	0.00	1.10	0.00	2.37	1.11	Pd-Ce-U-Pu
16	29.81	37.85	25.26	0.00	0.00	0.00	0.00	4.32	1.35	Pd-U-Pu
17	30.98	32.37	29.26	0.00	0.00	0.00	0.00	4.59	1.55	Pd-U-Pu
18	40.71	43.37	12.52	0.00	0.00	0.00	0.00	2.25	0.54	Pd-U-Pu
19	55.06	21.08	18.26	0.00	0.00	0.00	0.00	2.68	0.88	Pd-U-Pu
20	37.32	48.75	12.50	0.00	0.00	0.36	0.00	0.00	0.14	Pd-Ce
21	32.36	52.20	11.13	0.00	0.00	0.76	0.00	1.95	0.57	Pd-Ce-U-Pu
22	35.34	46.90	16.26	0.04	0.00	0.00	0.00	0.00	0.23	Pd-Pu
23	34.93	53.32	8.00	0.00	0.00	0.43	0.00	1.30	0.28	Pd-Ce-U-Pu
24	23.93	39.22	27.82	0.00	0.00	1.55	0.00	3.90	1.72	Pd-Ce-U-Pu

#### Concluding Remarks for AGR1-433-004-04.

- Similar to AGR1-433-001, the structure and lattice of Pd, Pd-Ce, and actinide containing Pd fission product precipitates (U, Pu) are observed and cubic in nature within the inner silicon carbide of AGR1-433-004-4
- Precipitates are inhomogeneous, with a distribution of elements scattered throughout; this is observed in STEM EDS point scan work in Table 108.



Neutron irradiation and the effect of different temperature gradients in materials are well-known to affect materials, especially polycrystalline materials containing a multitude of different grain boundary types. Neutron irradiation induced segregation and intermixing of elements has been previously reported in the literature, by Aguiar et al., (2015) on model thin films using proton irradiation and previously by Bruemmer et al., (1999) and was for materials exposed to reactor type environments. Although differences in fission product precipitate chemistry are found in this study; comparing model crystal structures for Pd, Pd-Ag, and Pd-U/Pu, the terminating atomic structure and lattice parameter can not fully be resolved as differences in crystal structure are not resolvable based on HRTEM (see Appendix C), where distinguishing differences in atomic structure are within the 0.7 Å point-point resolution of the aberration-corrected HRTEM. The differences in fission product precipitate chemistry can, at this point in our studies, only reveal themselves based on collected STEM EDS data.

**AGR1-433-004-05:** Figure 237(a) is large-scale field of view of Lamella AGR1-433-004-05, including one area containing precipitates near the IPyC/SiC interfaces, where within these areas, HRTEM was used to identify the atomic structure of fission product precipitates. Using atomic contrast, STEM dark field imaging, Figure 237(b) is a magnified field view containing the identified areas, where fission product precipitates neighbor on intact SiC grains. The complementary STEM BF image is provided in Figure 237(c). Higher magnification images from STEM dark (Figure 237[d]) and BF (Figure 237[e]) imaging are also included. These images reveal that the same precipitates are heavily concentrated at triple points within the SiC layer, whereas for the smaller precipitates, there is significant SiC grain overlap. For this area within AGR1-433-004-05, detailed chemical and structural analysis was performed.

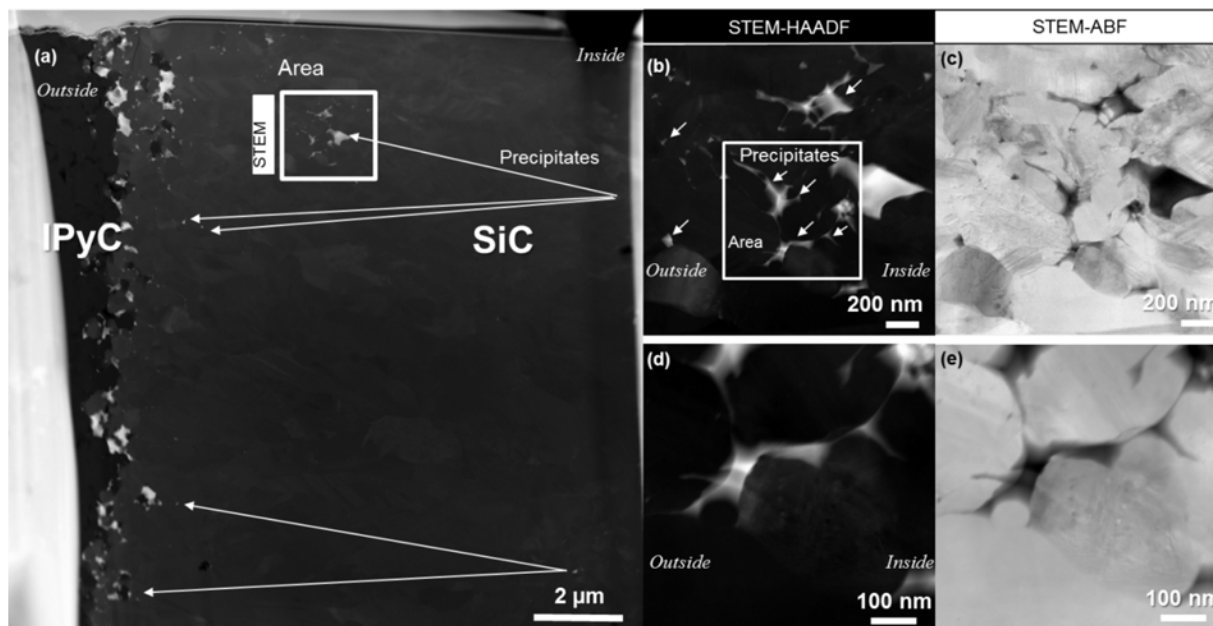


Figure 237. (a) Large field of view taken from the outer area of TRISO Particle AGR1-433-004, where a single area containing precipitates was analyzed using STEM and HRTEM imaging near the outer SiC/OPyC interface contained in Lamella 5. Atomic contrast (b) dark field and (c) BF imaging centered over the area, reveals a network of fission product precipitates that migrate under neutron irradiation and are found within the SiC layer. A closer examination of the area, STEM (d) dark and (e) BF reveal Pd-Ag fission product precipitates concentrated within the area of interest.

Figure 238(a) is a dark field STEM image of Lamella AGR1-433-004-05, taken over the outer area of the silicon carbide layer, which indicates fission product precipitates that were imaged with HRTEM. Figure 238(b) is the complementary STEM BF image that clearly shows that fission product precipitates

are centered at triple point junctions within the SiC and, for specific areas, are overlapped within the surrounding SiC lattice. Each of the four fission product precipitates were labeled and; chemically profiled with EDS, and their chemistries are reported in Table 109. From the four fission product precipitates two were suitable to be studied with HRTEM to where there are partial areas not containing overlapping SiC grains. For fission product Precipitate 2, low (Figure 239[a]) and higher (Figure 239[b]) magnification HRTEM imaging shows only the Pd lattice near the triple point junction. The accompanying FFT (see Figure 239[c]) validates this point.

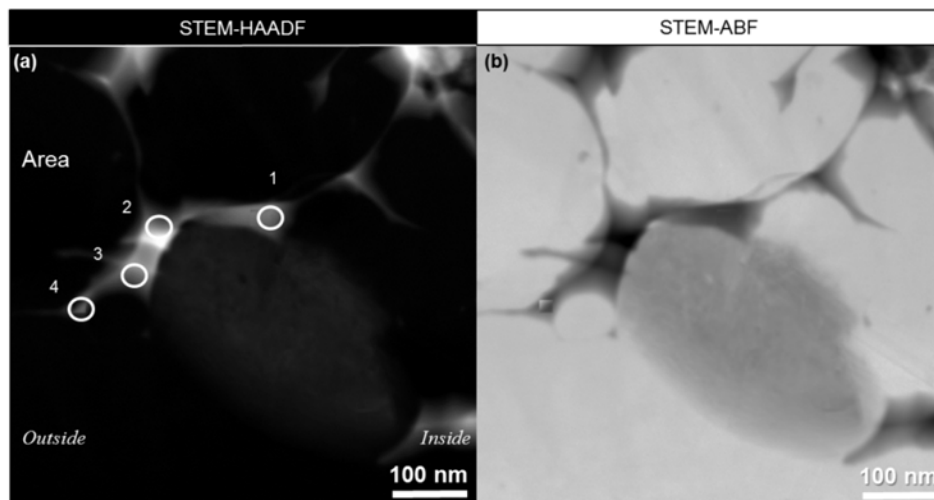


Figure 238. From the outer silicon carbide layer of TRISO Particle AGR1-433-004 (a) STEM dark field and (b) BF imaging centered over the area of interest, revealing a Pd fission product precipitate contained within Lamella 5. Note the chemistry at each of these points along a single fission product precipitate circled in white is reported in Table 109.

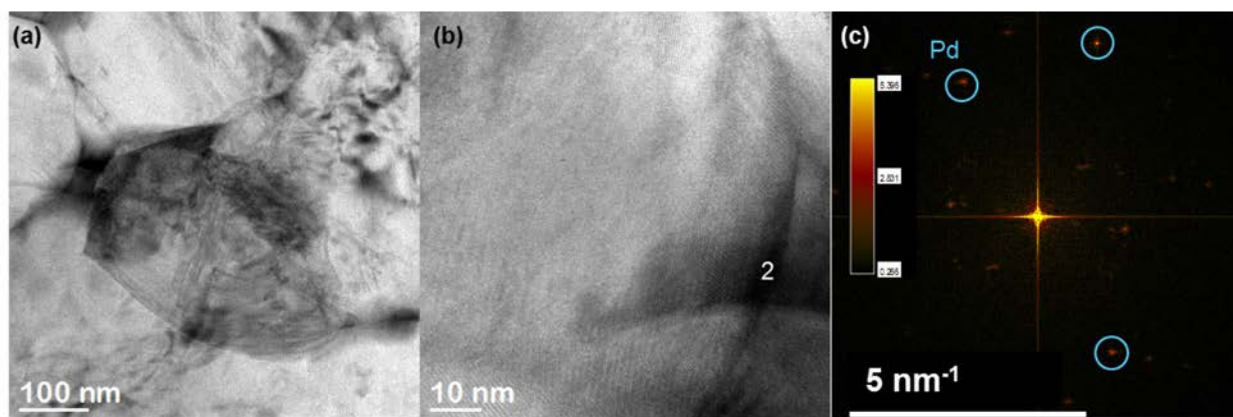


Figure 239. (a) TEM and (b) high-resolution imaging centered over fission product Precipitate 2 from the outer silicon carbide layer of TRISO Particle AGR1-433-004 reveals lattice fringes pertaining to the Pd precipitate contained within Lamella 5. (c) The observed lattice was confirmed with FFT analyses centered over the precipitate showing cubic Pd lattice spots.

Table 109. Qualitative fission product precipitate chemistry, reported in atomic % from outer silicon carbide layer of TRISO Particle AGR1-433-004 taken from subtended Area 1 of Lamella 5 as highlighted in Figure 237 and labeled in Figure 238.

Precipitate Number	Concentration (at.%)									Precipitate Identification
	C	Si	Pd	Ag	Cs	Ce	Eu	U	Pu	
Area 1										
1	33.5	55.39	9.57	0.00	0.00	0.00	0.00	0.00	0.00	Pd
2	32.67	46.49	20.74	0.00	0.00	0.08	0.00	0.00	0.00	Pd
3	31.71	51.27	16.73	0.00	0.00	0.00	0.07	0.00	0.00	Pd
4	33.08	59.59	6.9	0.03	0.00	0.00	0.00	0.04	0.02	Pd

**Concluding Remarks for AGR1-433-004-05.** Based on the leading observations, the following concluding remarks are made concerning the structure and chemistry of AGR1-433-004-05 from HRTEM results:

- Pd precipitates are found
- Precipitates imaged are networked at triple-point junctions
- Similar to AGR1-433-001, the structure and lattice of Pd precipitates are cubic in nature.

#### 3.6.3.5.2 Outer Area of the Silicon Carbide Layer Lamella AGR1-433-004-06.

Figure 240(a) is a large-scale field of view taken over the outer silicon carbide layer from Lamella AGR1-433-004-06, including a single area containing fission product precipitates. Using atomic contrast, dark field STEM imaging, Figure 240(b) is a magnified field view containing the identified area. Similarly, Figure 240(c) is the complementary STEM BF image. At even higher magnification, STEM dark field (Figure 240[d]) and BF (Figure 240[e]) images, reveal these precipitates are heavily networked in the sample. Detailed chemical and structural analyses were performed to identify the atomic structure of these precipitates.

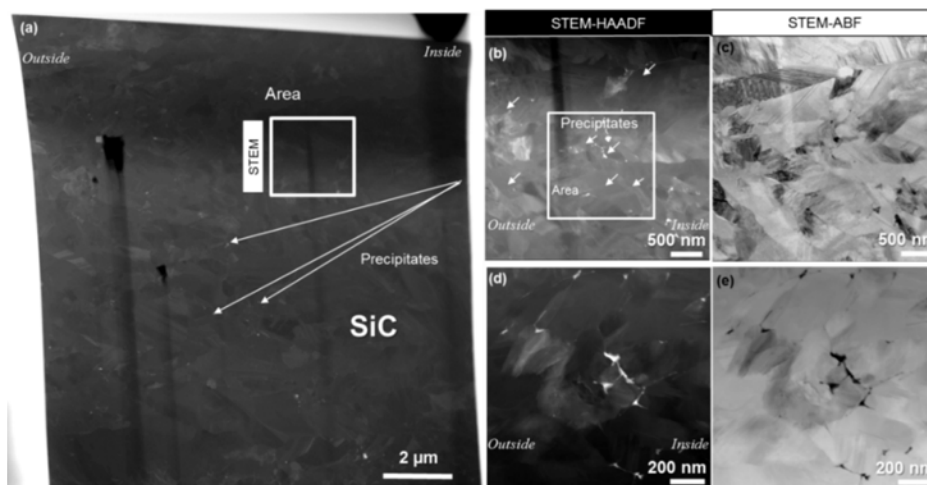


Figure 240. (a) Large field of view taken over the outer silicon carbide layer from TRISO particle of Lamella AGR1-433-004-06, where a single area was analyzed using STEM and HRTEM imaging within the outer SiC layer. Atomic contrast (b) dark field and (c) BF imaging centered over the area reveals the vicinity of precipitates from one another. At higher magnification, STEM (d) dark and (e) BF imaging reveals the individual fission product precipitates concentrated within the area of interest that were analyzed with HRTEM.

Over the single area, Figure 241(a) is a dark field STEM image of the Lamella AGR1-433-004-06, containing five individual fission product precipitates. Figure 241(b) is the complementary, STEM BF image centered over the same area revealing the detailed network of fission product precipitates. Again, fission product precipitates are nucleated at triple point junctions, where the larger and non-overlapping fission product Precipitates 1, 2, and 3 were subsequently imaged with HRTEM. For each of these fission product precipitates labeled 1 (Figure 242[a] and [b]), 2 (Figure 242[c] and [d]), and 3 (Figure 242[e] and [f]), these precipitates were the only precipitates suitable for HRTEM imaging. For fission product Precipitate 1, Figure 242(a) shows overlapping Pd and Si-C lattice fringes, where we suspect the Pd precipitate is significantly overlapped in part by the surrounding SiC lattice. Only in some partial areas is another lattice direction and spacing observed. At this higher magnification, the complementary FFT in Figure 242(b) shows both the SiC and Pd-Ag lattice are actually resolved in the image, extending the results. For fission product Precipitate 2, Figure 242(c) again shows both the Pd fission product precipitate and SiC lattice, where at atomic resolution Figure 242(d) shows both the Pd and SiC cubic lattice are observed in the image. This image and accompanying FFT clearly shows the precipitate lattice, where in most cases the fission product precipitate is off-tilt from the surrounding SiC lattice. Similarly, near perpendicular to the triple point and the TEM beam direction, fission product Precipitate 3 in Figure 242(e) shows both the Pd and surrounding SiC lattice structures. Consequently, this is verified using an FFT centered over the same precipitate in Figure 242(f) where both lattice points for each material are observed.

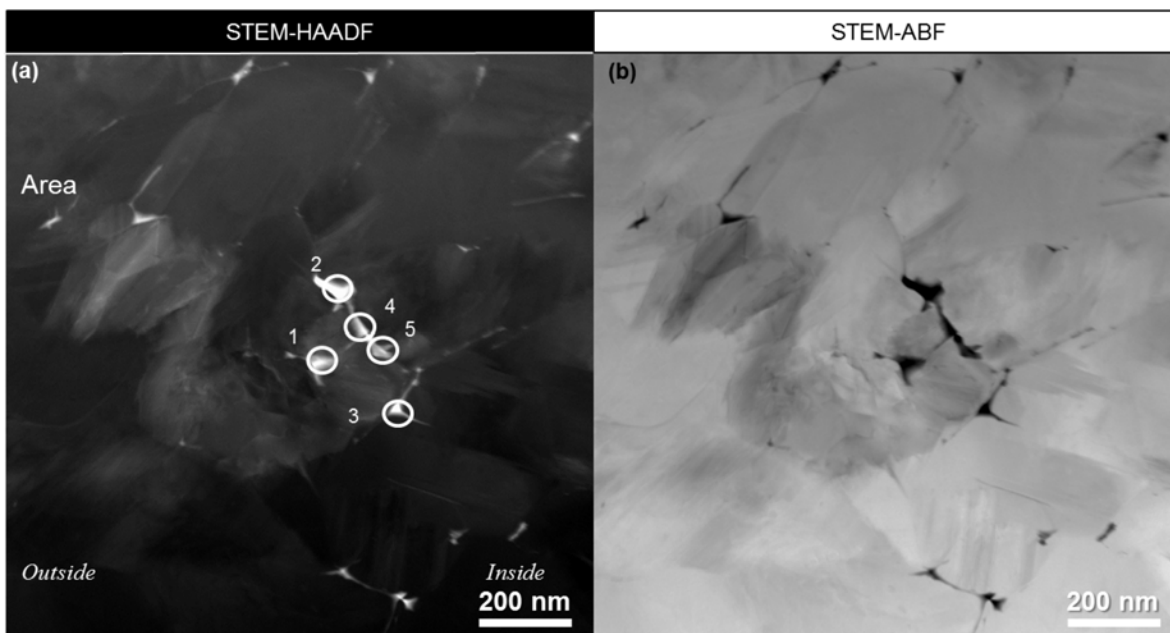


Figure 241. Over the outer silicon carbide layer from TRISO Particle AGR1-433-004, Lamella 6, (a) STEM dark field and (b) BF imaging, reveal fission product precipitates that were analyzed in detail with both HRTEM and point-resolved EDS. STEM EDS was collected from five fission product precipitates and three of which were adequate for HRTEM. Note the reported chemical composition for each of these fission product precipitates is provided in Table 110.

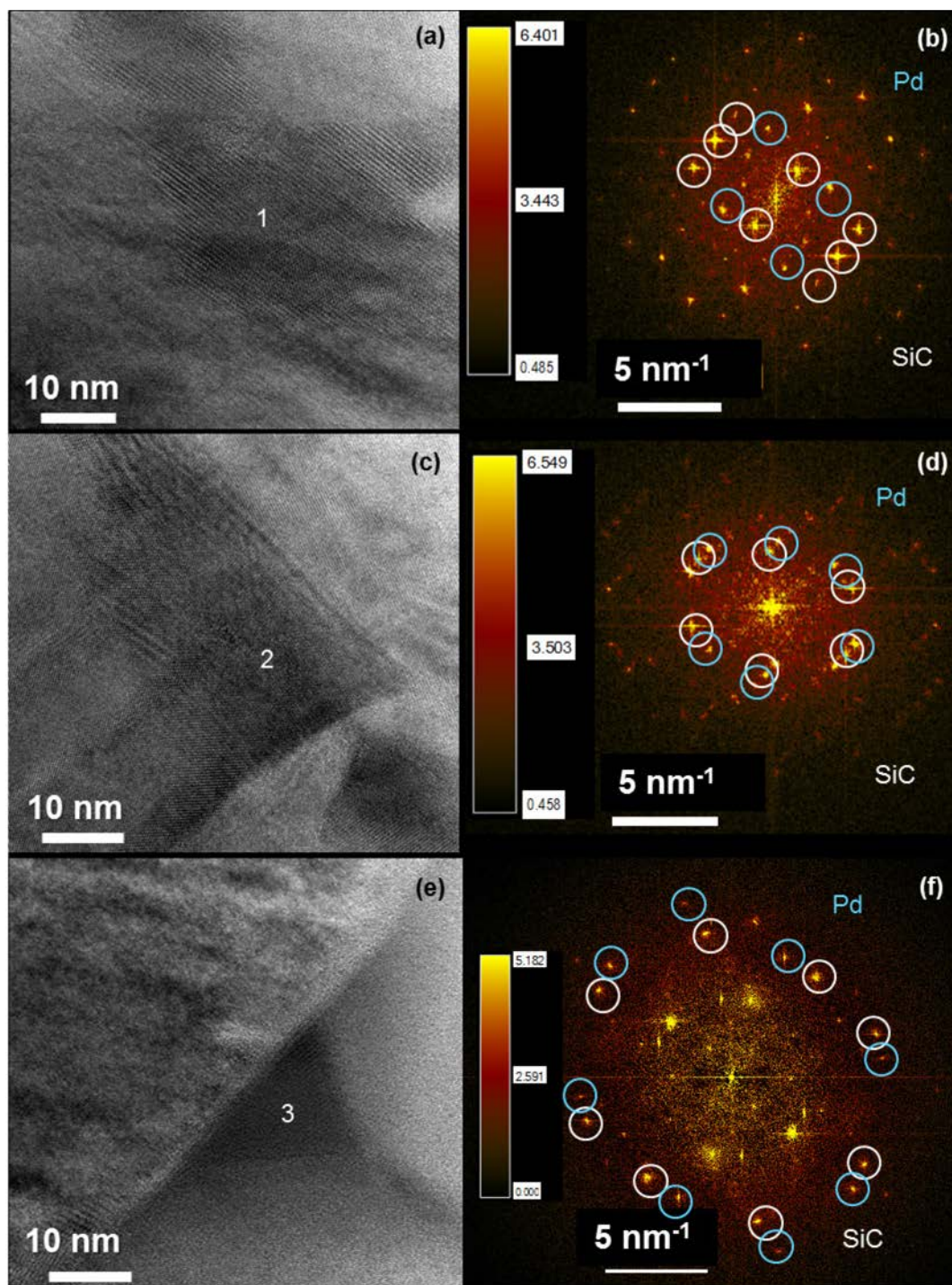


Figure 242. Atomic-scale, high-resolution TEM imaging and FFTs of individual fission product precipitates, including (a–b) 1, (c–d) 2, and (e–f) 3 within the outer silicon carbide layer identified for Particle AGR1-433-004 contained within Lamella 6.

Point-resolved STEM EDS chemical profiling was used to identify the most and least abundant elements, including Pd and Ag, within each of the fission products precipitates reported in Lamella 6 from Particle AGR1-433-004. Table 110 reports the most and least abundant fission product elements.



Table 110. Qualitative fission product precipitate chemistry reported in atomic % from outer silicon carbide layer of TRISO Particle AGR1-433-004 taken from subtended Area 1 of Lamella 6 as highlighted in Figure 240 and labeled in Figure 241.

Precipitate Number	Concentration (at.%)									Precipitate Identification
	C	Si	Pd	Ag	Cs	Ce	Eu	U	Pu	
Area 1										
1	39.74	42.23	10.87	0.00	0.00	4.7	0.03	0.00	0.09	Pd-Ce
2	51.33	39.94	8.28	0.00	0.00	0.00	0.02	0.00	0.00	Pd
3	47.2	40.16	10.3	0.00	0.00	0.00	0.2	0.00	0.78	Pd-Eu-Pu
4	44.69	38.76	9.99	0.00	0.00	4.33	0.02	0.00	0.08	Pd-Ce
5	44.69	38.76	9.99	0.00	0.00	4.33	0.02	0.00	0.08	Pd-Ce

**Concluding Remarks for Lamella AGR1-433-004-06.** The following concluding remarks are made concerning the structure and chemistry of AGR1-433-004-06 from the HRTEM results:

- Pd precipitates are found
- Similar to AGR1-433-001, the structure and lattice of Pd-only precipitates are observed and cubic in nature
- Lamella contains a higher percentage of minor trace elements, including Eu and Ce, and other elements are not sufficiently above background to make an identification.

### 3.6.3.5.3 Outer Area of the Silicon Carbide Layer Lamella AGR1-433-004-07.

Figure 243(a) is a large-scale field of view taken over the outer area of the silicon carbide layer from TRISO Lamella AGR1-433-004-07, including one area containing precipitates within the SiC, where HRTEM was used to identify the atomic structure of fission product precipitates. Using atomic contrast, STEM dark field imaging, Figure 243(b) is a magnified field view containing the identified areas where nanoscale fission product precipitates, neighbor intact SiC grain boundaries. The complementary STEM BF is provided in Figure 243(c). Higher magnification images from STEM dark field (Figure 243[d]) and BF (Figure 243[e]) reveal these same fission product precipitates. The same images also show a heavy fission product precipitate concentration segregated to triple points within the SiC layer. For this area within AGR1-433-004-07, detailed chemical and structural analysis was then performed combining HRTEM, STEM, and EDS.

Over the single area, Figure 244(a) is a dark field STEM image of precipitates contained with Lamella AGR1-433-004-07, including three individual fission product precipitates that were analyzed with EDS. Their chemistries are reported in Table 111. Figure 244(b) is the complementary, STEM BF image centered over the same area, revealing the same distribution of fission products decorating 1  $\mu\text{m}$  to sub-100 nm SiC grains. Fission product precipitates are nucleated at triple point junctions, where the larger and non-overlapping fission product Precipitates 1 and 3 were subsequently imaged with HRTEM. HRTEM imaging and accompanying FFTs analysis was performed for each of these fission product precipitates labeled 1 (Figure 245[a] and [b]) and 3 (Figure 245[c] and [d]). For fission product Precipitate 1, Figure 245(a) shows overlapping Pd and Si-C lattice fringes, where we suspect the Pd precipitate is overlapped in part by the surrounding SiC lattice. Because of these physical limitations, another lattice direction and spacing is only over partial areas of the precipitate observed to be consistent with the presence of a Pd-Ag alloy. Similarly, in Figure 245(b), the FFT shows both the SiC and Pd-Ag lattice are resolved. For fission product Precipitate 3, Figure 245(c) shows both the Pd-rich precipitate and SiC lattice are strongly overlapping, resulting in Moire fringes. For a part of the Pd (rich) precipitate, a lattice consistent with cubic symmetry is observed. This image and accompanying FFT shown in Figure 245(d), both lattices are resolved; however, due to orientation and position of the precipitate, a clear HRTEM image is difficult.

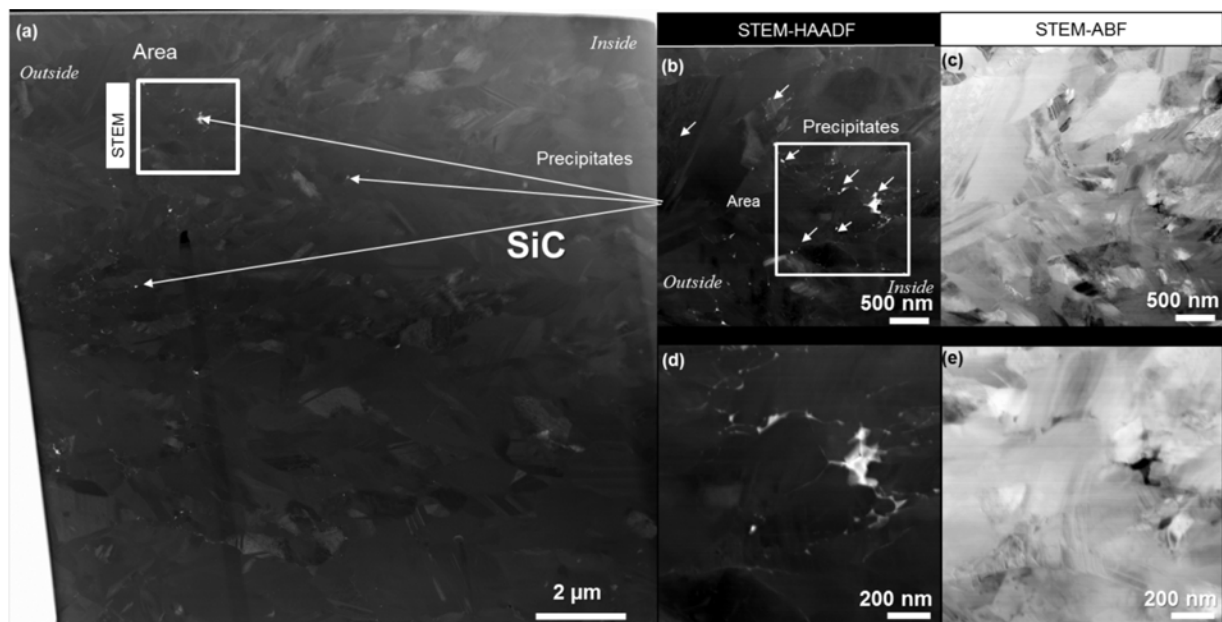


Figure 243. (a) Large field of view taken over the outer area of the silicon carbide layer from TRISO Particle AGR1-433-004, Lamella 7, where a single area was analyzed using STEM and HRTEM imaging within the SiC layer. Atomic contrast (b) dark field and (c) BF imaging centered over the area reveals the vicinity of precipitates from one another. At higher magnification, STEM (d) dark and (e) BF imaging reveals the individual fission product precipitates concentrated within the area of interest that were analyzed with HRTEM.

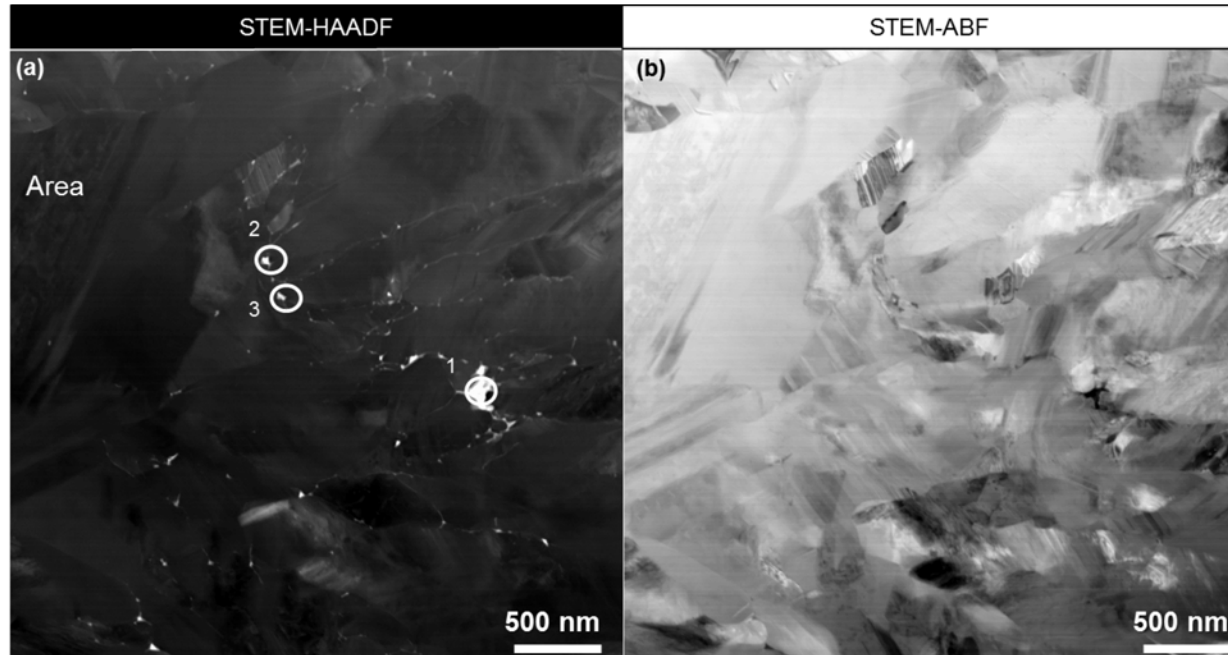


Figure 244. (a) STEM dark field and (b) BF imaging centered over Area 1 from TRISO Particle AGR1-433-004, revealing three fission product precipitates contained within Lamella 7 lifted out from outer silicon carbide layer that were analyzed in detail with point-resolved STEM EDS and two of which were adequate for HRTEM. Note the report chemical compositions are reported in Table 111.



For each of the three fission product precipitates, STEM EDS chemical profiling was used to identify the most- and least-abundant elements, including Pd and Ag. Table 111 reports the chemical composition for each of these precipitates, where the most- and least-abundant fission product elements are reported in atomic percentages.

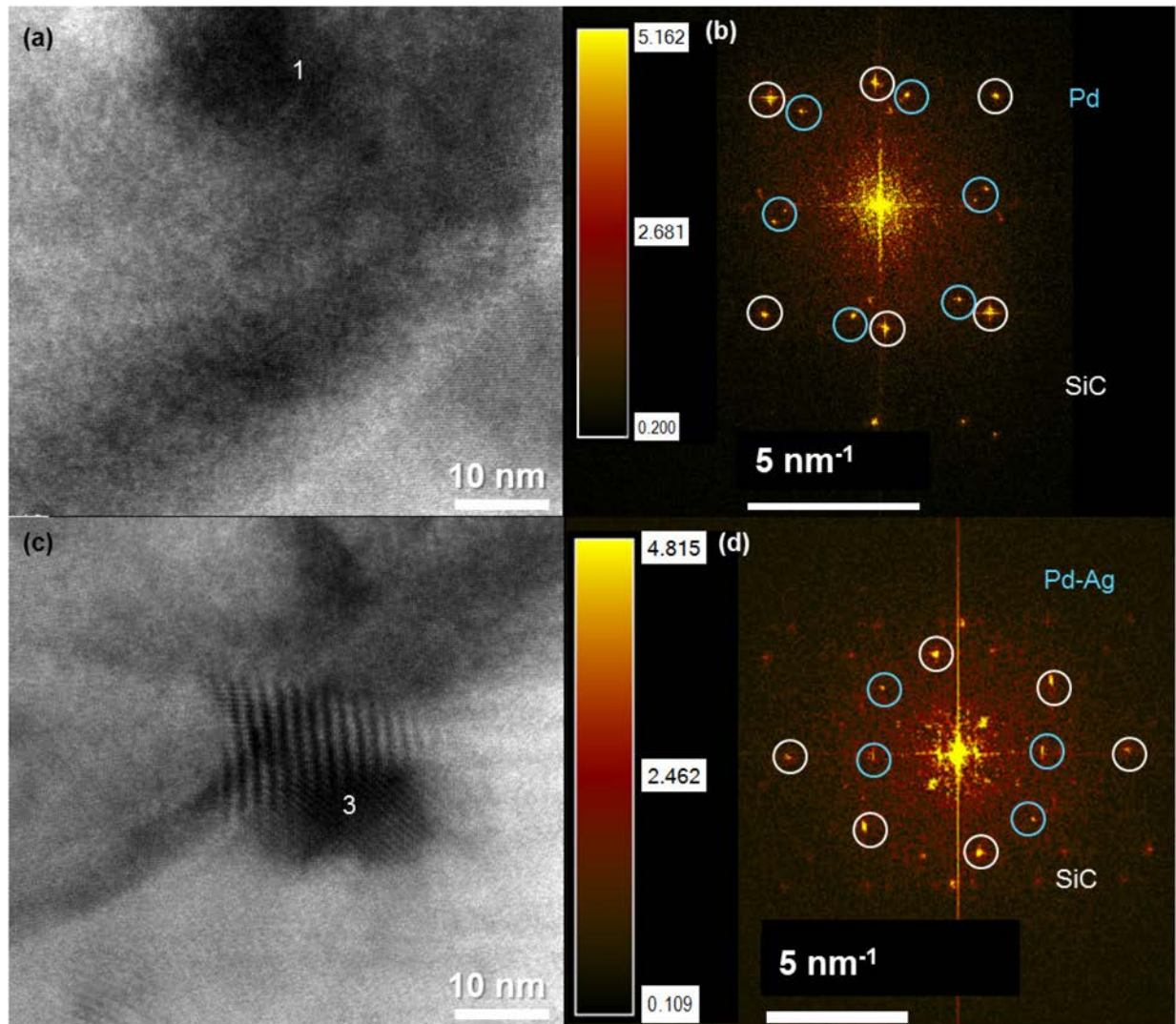


Figure 245. Atomic-scale HRTEM imaging and FFTs of individual fission product precipitates, including (a, b) 1 and (c, d) 3 within the outer silicon carbide layer identified for TRISO Particle AGR1-433-004, contained within Lamella 7. The precipitate labeled shown in (c) is overlapped with the surrounding SiC lattice, where Moiré fringes are resolved.

Table 111. Qualitative fission product precipitate chemistry, reported in atomic % from outer silicon carbide layer of TRISO Particle AGR1-433-004 taken from subtended Area 1 of Lamella 7 as highlighted in Figure 243 and labeled in Figure 244.

Precipitate Number	Concentration (at.%)									Precipitate Identification
	C	Si	Pd	Ag	Cs	Ce	Eu	U	Pu	
Area 1										
1	25.56	73.53	0.89	0.00	0.00	0.00	0.00	0.00	0.00	Pd
2	30.71	66.42	1.87	0.00	0.00	0.00	0.00	0.00	0.00	Pd
3	26.57	72.57	0.06	0.04	0.00	0.00	0.00	0.00	0.00	

**Concluding Remarks for Lamella AGR1-433-004-07.** The following concluding remarks are made concerning the structure and chemistry of AGR1-433-004-07, based on HRTEM results:

- Pd only precipitates are found (trace of Ag is negligible)
- Similar to AGR1-433-001, the structure and lattice of Pd-only precipitates are observed and cubic in nature.

U and Pu were not detected in the precipitates analyzed. The Pd fission products migrate to near microstructural surfaces, including triple-point junctions. Second, the effect of grain orientation and overlap can lead to issues where the atomic structure of a fission product precipitate cannot be clearly resolved due to competing lattice overlap. However, based on the measured HRTEM and subsequent FFT analysis, we determined the precipitates are cubic, similar to the other collected datasets. These analyses are based on analyzing the individual peaks and performing peak matching with known crystallographic orientations for cubic Pd.

### 3.6.3.6 Conclusions on the Fission Product Precipitates for Particle AGR1-433-004.

**3.6.3.6.1 Fission Product Precipitate Structure and Chemistry.** A systematic experimental investigation of the structure of fission product precipitates in TRISO-coated particles was reported. The goal was to understand and report on the atomic structure of fission products within the polycrystalline SiC layer for particles AGR1-433-001 and AGR1-433-004. Results demonstrate that despite chemistry differences, precipitates of Pd and Pd-Ag are cubic. The study concludes that the cubic fission products are found in abundance, especially at triple-point junctions, because they seem to migrate to areas of enough volume to nucleate.

**Chemistry of Pd and Ag:** Evidence of Pd and Pd-Ag co-existence was found with variability. Furthermore, multiple chemistries can exist within single-fission product precipitates, including a gradient in composition. Structurally, however, the fission product retains cubic symmetry. This dictates that the multiple chemistries resolved are the product of substitutional cation exchange between Pd and Ag. Cation substitution may also include Si, U, and Pu cations. Pd-U-Si alloys have been reported extensively in the literature, for a narrow range of U composition (less than 2 at.%), where the phase diagram noting the stable compounds and their formation energies are shown in Figure 246 (Shen et al., 1986). Poon et al., and references therein, reported the electron diffraction patterns for Pd-U-Si alloys are consistent with the current work. Only the presence of Pd within Pd-Si precipitates are reported in this examination because of our limited detection capabilities for Si with EDS. (Poon et al., 1985, Kofalt et al., 1987, Bretscher et al., 1987, Lugg et al., 2015). Differentiating Pd and Ag in these patterns is not resolvable given our uncertainty of measuring patterns within close proximity to neighboring lattice spots ( $\pm 0.08 \text{ \AA}$ ). For these more complicated compounds ( $\text{Pd}_2\text{Si}_2\text{U}$ ), we have not yet definitively resolved their presence in grainboundaries by our AGR TRISO HRTEM work using diffraction patterns in association with chemical composition. In previous work by Leng et al., (2016) and by van Rooyen et al., (2012), tetragonal  $\text{Pd}_2\text{Si}_2\text{U}$  precipitates were reported for AGR-1 samples.

Comparing similar datasets reported here with the previous work by Leng et al., (2016) and van Rooyen et al., (2012) there is a suggestion of  $\text{Pd}_2\text{Si}_2\text{U}$  in the nano-sized precipitates as well. Continued study is needed to confirm the presence of  $\text{Pd}_2\text{Si}_2\text{U}$  in nano-sized precipitates. Ongoing research attempts to combine HRTEM, EDS, and EELS for use on TRISO fuel particles, similar in nature to the X-ray absorption spectroscopy studies performed by Coulthard et al., (1996) for Pd-Ag alloys.

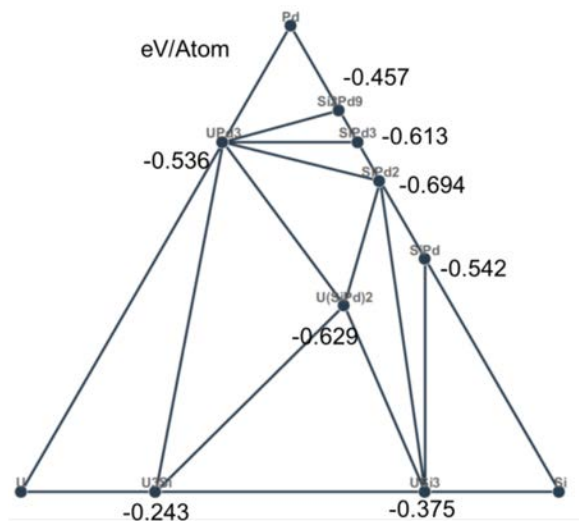


Figure 246. Predicted quaternary phase diagram for U-Si-Pd, based on ab-initio first principles-based calculations using materials project (Jain et al., 2011, 2013). The stable compounds and formation energies (eV/atom) are shown for U-Si-Pd stable containing compounds.

In the Pd-Ag alloy system there is complete miscibility within the FCC structure and very negligible cation volume effects. Furthermore, in the study reported by Kim et al., 2009, regardless of the composition and size of Pd-Ag bimetallic alloy clusters, the melting temperature is lower than found for the bulk, defined as macro-sized alloy rather than a nanometer cluster of atoms, and rises with cluster size expansion and Pd composition. Kim et al., (2009) reports the melting temperature is further lowered at grain boundaries and interfaces, forming a five-fold icosahedron structure. Cation exchange is predicted and favored for the Pd-Ag FCC metals and alloys, especially given the smaller nanoscale sizes of fission products. Using the embedded-atom method, Foiles et al., and references therein, report the alloy heats of formation in the bulk for single substitutional impurities between Pd for Ag is -0.36 eV and Ag for Pd is -0.24 eV (Coulthard and Sham 1996, Foiles et al., 1986, Foiles et al., 1988, Lu et al., 1991, Li et al., 2014). Experimentally, the value for incorporating Pd into an Ag FCC host is -0.11 eV and, similarly, Ag into a Pd host is -0.29 eV. There is a reported discrepancy between experiment and theory for these two elements in this study, where the trend for Pd and Ag is swapped. Other experimental studies have found both Pd (rich)-Ag and Ag (rich)-Pd alloys, including tetragonal  $\text{Ag}_3\text{Pd}$  (Coulthard and Sham 1996, Coles 1956, and Schwartz 1978). Comparing each of these predicted and experimental energies for incorporating one element into another FCC host based on the work by Folles et al., there is a preference for intermixing of both Pd and Ag regardless of the host species. As for the preference for one composition over another, in the later literature by Schwartz, the depletion of Ag can be qualitatively understood using a ternary solution model, where the details are discussed at length by Schwartz (1978). The bulk of the AGR-1 advanced microscopy work has found qualitatively that Pd composition is greater than Ag. The experimental results on resolving the chemistry of fission products are in agreement largely with these previous experimental results. This study's experimental data seems to suggest that neutron irradiation effects on precipitate formation still follow conventional equilibrium solute kinetics. It is however important to note that many of the precipitates contain other elements as well, and therefore should be considered during future work.

### 3.6.4 Coated Particles AGR1-433-003 and AGR1-433-007

Particles AGR1-433-003 and AGR1-433-007, with measured-to-calculated Ag-110m inventories of less than 22% and 100%, respectively, were chosen to further explore EPMA as a tool for determining and obtaining more information on the quantification and distribution of fission products on larger areas. These two particles were selected for comparative electron microprobe analysis to determine whether the distribution or abundance of fission products differed proximally and distally from the deformed kernel in AGR1-433-003 and how this compared to fission product distribution in AGR1-433-007 (Figure 247).

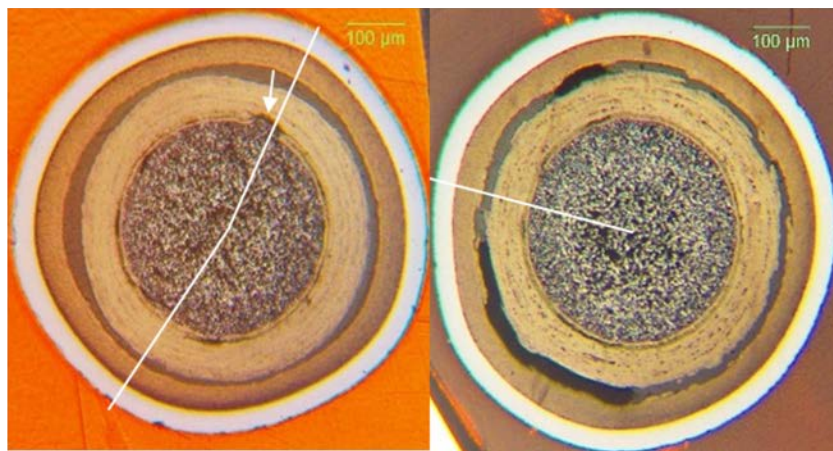


Figure 247. Optical microscope image of AGR1-433-003 (left) and AGR1-433-007 (right). Paths of measured radial traverses are shown with white lines. The arrow in the left image highlights kernel extrusion (deformation) into a fractured region of the buffer layer.

#### 3.6.4.1 Distribution of Fission Products Using Electron Probe Micro-Analyzer. A

Cameca SX100R electron microprobe was used to measure the chemical composition across two contrasting regions of irradiated Particle AGR1-433-003 and one region from Particle AGR1 433 007 (Figure 247). Twenty-four chemical elements were analyzed at each of the 85 points measured in each region. The analyzed regions were highlighted in Figure 247. Figure 248 shows the Eu, Sr, and Te concentrations, while Figure 249 shows the I, Xe, and Cs concentrations. Detailed results of this work are reported by Wright and van Rooyen 2016 and only selected conclusions are reported in this section.

Eu, Te, and Sr fission product concentrations are up to six times higher in the recoil zone (a 15- $\mu\text{m}$ -thick region immediately outside of the kernel) of the deformed side of the AGR1-433-003 kernel than on the non-deformed side of the kernel (Figure 248). They also exceed those in AGR1-433-007, but by a much smaller margin. Unlike other fission products, significant elevations of Eu, Te, and Sr are limited to the recoil zone.

Concentrations of I, Cs, and Xe in the recoil zone on the deformed side of AGR1-433-003 were up to two times higher than in the recoil zone on the non-deformed side of the kernel. Concentrations of I, Cs, and Xe in the recoil zone of AGR1-433-007 were up to 10% higher than those in the recoil zone of the deformed side of AGR1-433-003 (Figure 249).

Gases and fission products that are subject to recoil accumulate in higher concentrations in the recoil zone on the deformed side of AGR1-433-003 than on the intact side of that particle, or in the recoil zone of AGR1-433-007. However, the concentration of these elements in the buffer and IPyC of the three examined areas is quite similar. Concentrations of most fission products along the SiC-IPyC interface tend to be greater in Particle AGR1-433-007 compared to either measured interface in AGR1-433-003, suggesting that a deformed kernel does not necessarily increase fission product accumulation along that interface.



The particle that retained all its predicted inventory of silver (AGR1-433-007) had extensive Pd Ag deposits along a 110-degree arc within the SiC IPyC interface (Figure 250), while the particle that had <22% of its predicted Ag-110m inventory (AGR1-433-003) had a paucity of such deposits. Asymmetry of Pd Ag deposits could be the consequence of a lateral temperature gradient within Particle AGR1-433-007, wherein the precipitates are more common on the cold side of the particle. Montage analyses of two other coated particles of Compact 4-3-3 (Particles AGR1-433-001 and AGR1-433-004), however, showed a random distribution of fission product accumulation around the circumference (montages are presented in van Rooyen et al., 2016b). A random distribution of precipitates might suggest that these other two particles had a relatively uniform temperature distribution compared to AGR1-433-007.

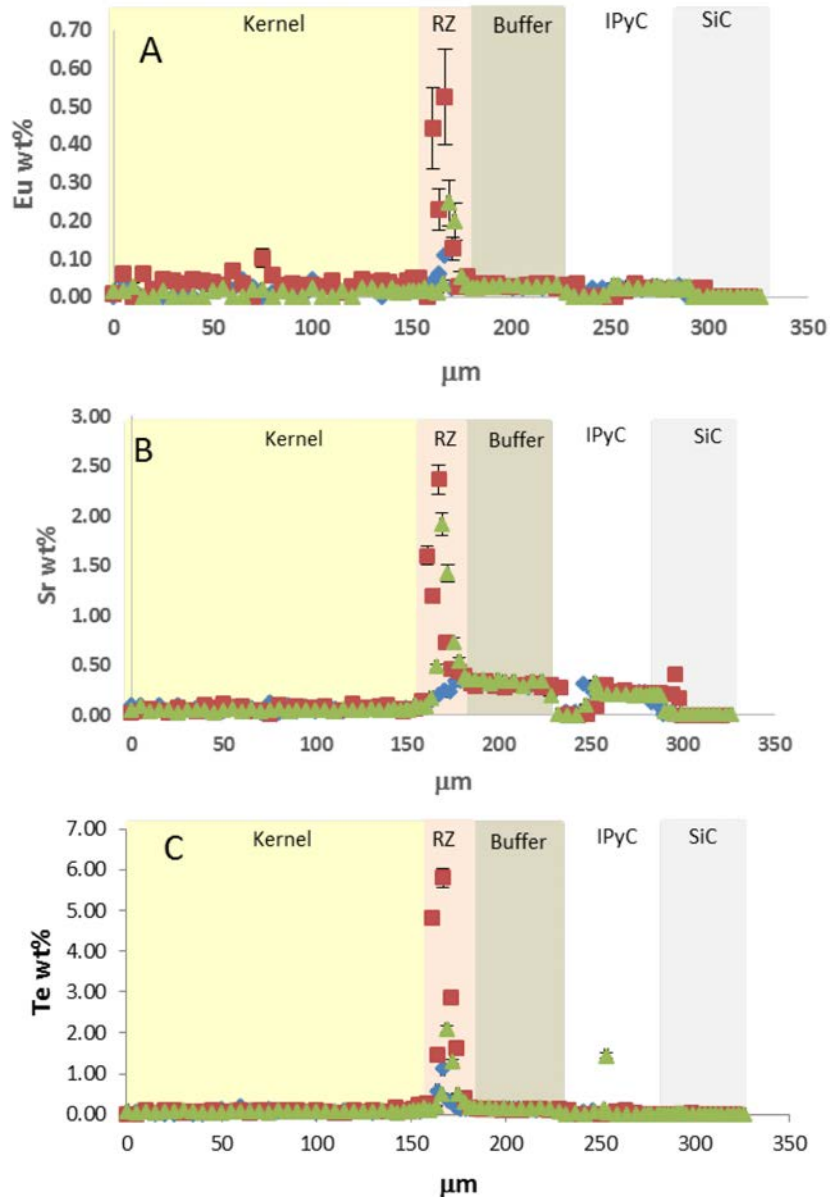


Figure 248. Eu concentration (A), Sr concentration (B), and Te concentration (C) in AGR1-433-003 and AGR1-433-007. Squares represent the radial traverse on the side with the deformed kernel of AGR1-433-003 and diamonds represent the radial traverse on the intact side. Triangles represent AGR1-433-007. If no error bars are visible, the error is smaller than the symbol.

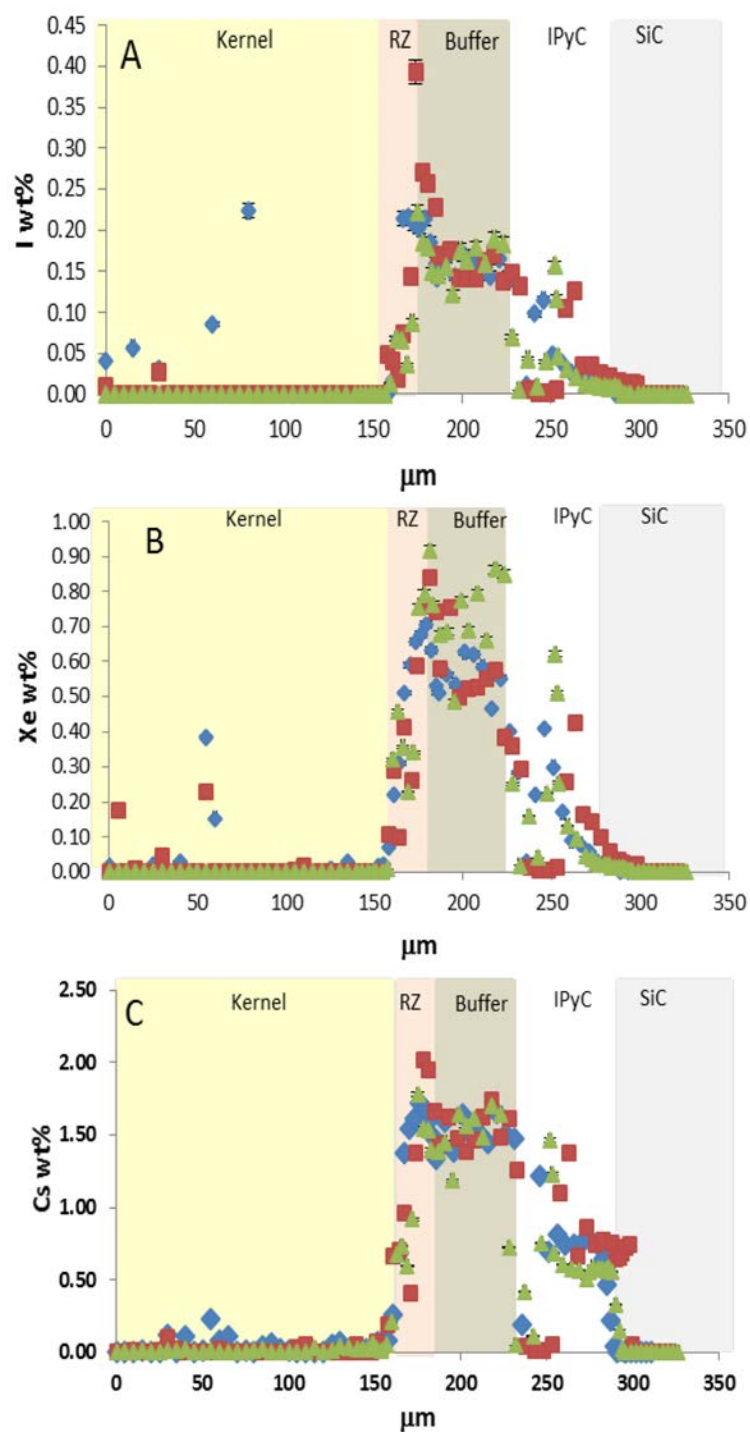


Figure 249. Concentration (A), Xe concentration (B), and Cs concentration (C) in AGR1-433-003 and AGR1 433-007. Squares represent the radial traverse on the side with the deformed kernel of AGR1-433-003 and diamonds represent the radial traverse on the intact side. Triangles represent AGR1-433-007. If no error bars are visible, the error is smaller than the symbol.

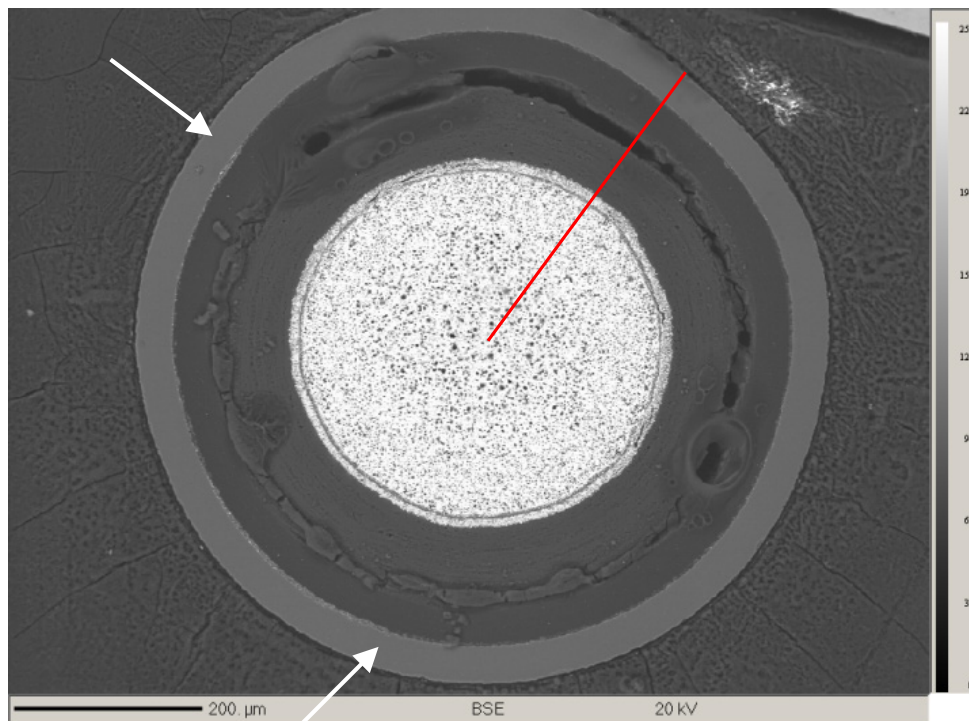


Figure 250. Backscattered electron images of AGR1-433-007 showing the 110-degree arc of precipitates (between the arrows) along the SiC-IPyC interface. The line indicates the path of the measured analytical traverse.

**3.6.4.2 Effect of Kernel Protrusion on Fission Product Distribution and Concentration from Particle AGR1-433-003 (Deformed Side versus Non-Deformed Side).** Table 112 shows the depth of fission product penetration into the SiC layer for both radial traverses of AGR1-433-003 and one radial traverse of AGR1-433-007. All measured elements, except Ag, Pr, and Te penetrate deeper into the SiC layer of the non-deformed side of AGR1-433-003 compared to the deformed side, while I and Tc become undetectable at the SiC-IPyC boundary of both the deformed and non-deformed side. While penetration depth for most fission products in AGR1-433-007 is similar to the non-deformed side of AGR1-433-003, for the elements La, Ce, Nd, Pr, Sm, Mo, U, and Pd, the highest concentration observed at the SiC-IPyC interface is at least double in AGR1-433-007 compared to either side the same interface of AGR1-433-003 (Figure 251, Table 112).



Table 112. Penetration of analyzed elements into the SiC layer.

Element	AGR1-433-003 Deformed Side SiC Penetration (μm)	Highest Concentration in Interface (wt.%)	AGR1-433-003 Non-deformed Side SiC Penetration (μm)	Highest Concentration in Interface (wt.%)	AGR1-433-007 SiC Penetration (μm)	Highest Concentration in Interface (wt.%)
I	Interface	<b>0.013</b>	Interface	0.011	Interface	0.007
Xe	Interface	<b>0.020</b>	6	0.013	6	0.014
Cs	6	<b>0.74</b>	20	0.64	20	0.56
Ba	2	<b>0.61</b>	18	0.58	6	0.63
Sr	Interface	<b>0.41</b>	10	0.20	Throughout	0.20
Eu	Interface	0.024	14	<b>0.032</b>	Interface	0.028
La	2	0.037	4	0.033	4	<b>0.067</b>
Ce	2	0.049	Throughout	0.050	4	<b>0.125</b>
Nd	2	0.064	4	0.051	4	<b>0.15</b>
Pr	6	0.015	4	0.019	4	<b>0.051</b>
Sm	2	0.016	4	0.011	4	<b>0.065</b>
Ru	Interface	<b>0.042</b>	4	0.016	4	0.034
Mo	Interface	0.005	6	0.005	4	<b>0.056</b>
Zr	Interface	0.022	6	<b>0.023</b>	4	0.013
Tc	Interface	0.008	Interface	0.004	4	0.008
U	2	1.14	Throughout	0.51	4	<b>1.98</b>
Pd	6	1.21	Throughout	0.42	Throughout	<b>2.05</b>
Cd	ND		ND		ND	
Ag	2	0.037	Interface	0.016	2	<b>0.052</b>
Sn	Interface	0.028	4	0.020	4	<b>0.040</b>
Te	Interface	0.030	ND		4	<b>0.032</b>

“Interface” indicates the element was found at the IPyC-SiC boundary.

“ND” indicates the element was not detected.

“Throughout” indicates the element was found intermittently or continuously throughout the SiC layer.

The concentration value indicates the highest concentration found in the SiC-IPyC interfacial region.

Concentration values in bold are the highest noted for the three interfacial regions measured.

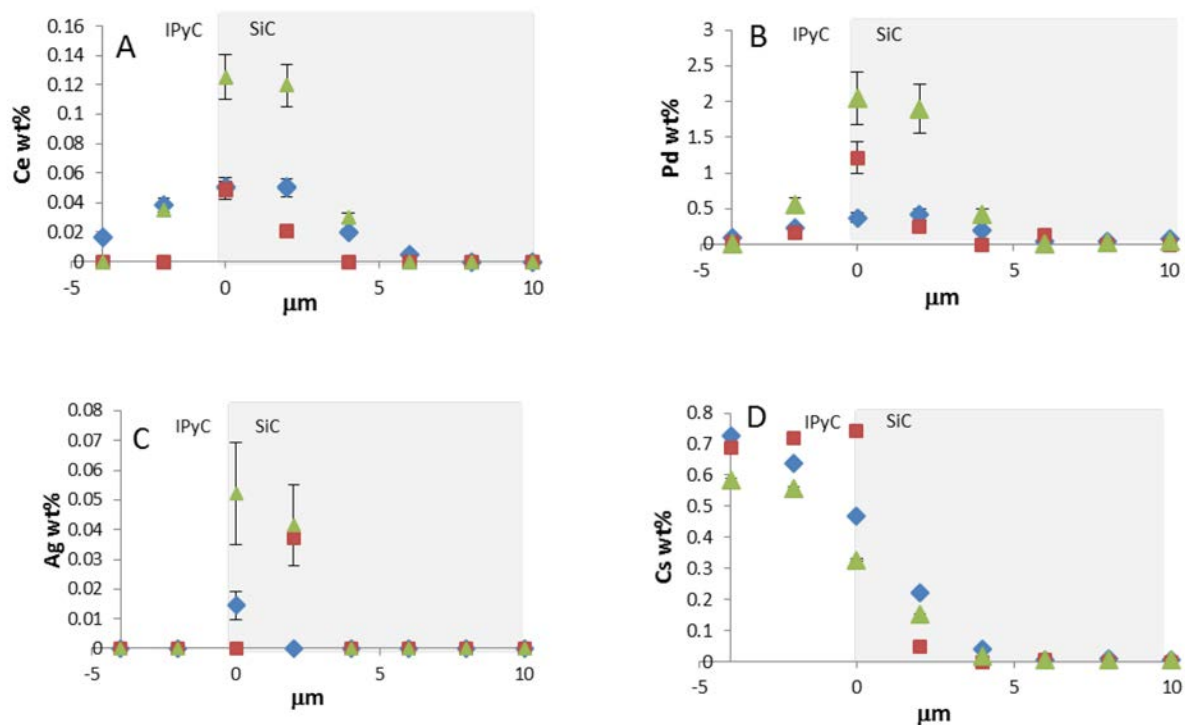


Figure 251. (A through D): Ce, Pd, Ag, and Cs wt%, respectively, across the IPyC-SiC interface. Squares represent the radial traverse on the side with the deformed kernel of AGR1-433-003; diamonds represent the radial traverse on the intact side. Triangles represent AGR1-433-007. Where no error bars are visible, the error is smaller than the symbol.

**3.6.4.3 Location of Palladium, Silver, Cadmium, and Tin.** With regard to Pd and Cd, there is very little difference in the observed accumulations of these elements in any of the examined kernel locations. While Cd is not detected beyond the buffer zone, Pd accumulates at the SiC-IPyC interface as small precipitates (Figure 252[a] and [b]). Tin is present in small amounts (<0.05 wt.%) for most examined kernel areas, with only two points exceeding that amount. Sn also accumulates along the SiC-IPyC interface (Figure 252[c]) in both AGR1-433-003 and AGR1-433-007 and is marginally greater in concentration in AGR1-433-007. Tin is also elevated at the kernel-recoil zone interface. With regard to Ag, AGR1-433-003 shows elevated concentrations (up to about 1 wt. %) on both measured sides of the AGR1-433-003 kernel, while Ag was not detected in the AGR1-433-007 kernel (Figure 252[d]). In addition, in the recoil zone on the deformed side of AGR1-433-003, Ag was elevated as high as 0.45 wt%, but was measured at 0.045 wt% on the non-deformed side of AGR1-433-003 and not detected in AGR1-433-007.

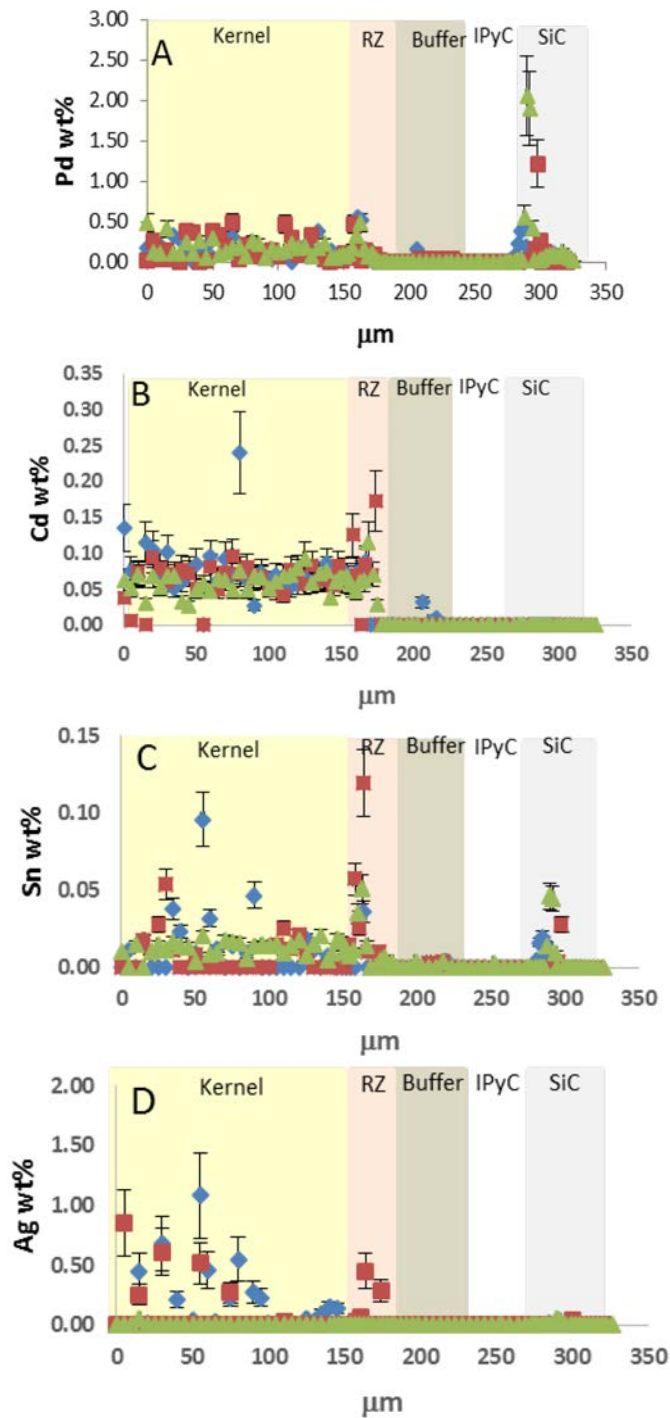


Figure 252. Pd concentration (A), Cd concentration (B), Sn concentration (C), and Ag concentration (D) in AGR1-433-003 and AGR1-433-007. Squares represent the radial traverse on the side with the deformed kernel of AGR1-433-003; diamonds represent the radial traverse on the intact side. Triangles represent AGR1-433-007. Where no error bars are visible, the error is smaller than the symbol.

Figure 252(d) shows small, sporadic concentrations of Ag in AGR1-433-003 are present in the kernel of both radial traverses; yet in AGR1-433-007, no Ag was detected along the measured traverse, except at the IPyC-interface. However, inspection of the IPyC-SiC interface in AGR1-433-007 shows an arc of approximately 110 degrees, which contains abundant Ag-Pd-U precipitates (Figure 250), many of which penetrate the SiC layer. The analogous interface in AGR1-433-003 contains very few precipitates and the precipitates that are present are much smaller ( $<1\ \mu\text{m}$ ), compared to those seen in AGR1-433-007.

This observation contrasts with SEM analysis of particles AGR1-433-001 and AGR1-433-004. Precipitate clusters in these particles were reported to occur in great abundance along the entire circumference of the SiC-IPyC interface. It is not possible to get a very accurate analysis of the precipitates. They are typically smaller than the electron beam interaction volume, which means that the beam may measure more than one particle or will include a large amount of matrix (e.g., C or SiC) in the analysis. However, it is possible to make some general comparisons between particles. Firstly, along the 110-degree precipitate-rich arc along the SiC-IPyC interface in AGR1-433-007, a total of 42 precipitates were identified and analyzed. The average Pd, Ag, and U concentrations were 3.1, 0.14, and 3.1 wt%, respectively. The highest concentration of these elements measured at the SiC-IPyC interface on the other side of AGR1-433-007 was 0.4, 0.014, and 0.5 wt%, respectively. This means that the precipitates on the precipitate-rich side were larger, had a greater concentration of those elements, or both, compared to the other side.

This suggests the presence of a lateral temperature gradient across the particle (Pd precipitates on the cold side of the particle). While the mechanism for Pd-Ag-U precipitation on the cold side of the particle is unclear, both Tiegs (1982) and Minato et al., (1994) describe this effect. Tiegs specifically describes the transport of Pd and rare earth elements down the temperature gradient. More investigation is required to clarify this phenomenon.

#### **3.6.4.4 Conclusions.**

- Concentrations of I, Cs, and Xe in the recoil zone on the deformed side of AGR1-433-003 are up to two times higher than in the recoil zone on the non-deformed side of the kernel.
- Eu, Sr, and Te concentrations in the recoil zone are up to six times higher on the deformed side of AGR1-433-003 compared to the non-deformed side. For the recoil zone of AGR1-433-007, these elements are up to four times higher than those in the recoil zone of the non-deformed side of AGR1-433-003.
- At the SiC-IPyC interface of AGR1-433-007, rare earth elements, U, and Pd concentrations are up to two times higher than at either interface side of AGR1-433-003; Mo is ten times higher. At the SiC-IPyC interface of AGR1-433-003, Sr and Ru concentrations are approximately two times higher on the deformed side than on the non-deformed side. I, Xe, Cs, and Ba are up to 50% higher at the SiC-IPyC interface on the deformed side compared to the non-deformed side or the SiC-IPyC interface of AGR1-433-007.
- Volatile fission products such as Ba, Cs, I, and Xe are not retained in the kernel, but rather they accumulate significantly in the buffer.

- Fission product accumulation in the recoil zone outside the deformed region of the kernel is greater than in the recoil zone outside the non-deformed region of the same kernel; however, a kernel showing no similar aberrations shows a larger accumulation of fission products along the SiC-IPyC interface, suggesting that fission product migration and precipitation may be more strongly influenced by factors other than kernel integrity. Fission product accumulation in the recoil zone does not necessarily result in a higher concentration of fission products in the buffer layer.
- The particle that retained all its predicted Ag-110m inventory had extensive Pd-Ag deposits along a 110-degree arc within the SiC-IPyC interface, while the particle that had less than 22% of its predicted 110m Ag inventory had a paucity of such deposits. Asymmetry of Pd-Ag deposits is suggestive of a lateral temperature gradient within Particle AGR1-433-007, wherein the precipitates are more common on the cold side of the particle.

## **4. DISCUSSION AND CONCLUSIONS OF ADVANCED MICROSCOPY AND MICRO-ANALYTIC EXAMINATION OF AGR-1 COMPACTS**

Identifying fission product distribution patterns was a main focus for the AGR-1 advanced microscopy and micro-analytical examination. The low levels of certain fission products (e.g., Ag, Eu, and Pu), varying size (i.e., several micron to 1 nm), unknown phase and structure of fission product precipitates, unknown transport mechanisms of various elements, and distribution of these elements in the SiC layers (and other TRISO layers) lead to exploration of various advanced techniques. Significant scientific success was achieved during the development phase of AGR PIE and the following sections highlight these advances. Lessons learned will be applied to develop the approach and battery of advanced characterization for the AGR-2 experiment and other subsequent AGR experiments.

### **4.1 Fission Product Identification and Distribution**

Because SiC is the main fission product barrier, and recent AGR1-PIE results showed the release of various metallic fission products (primarily Ag and Eu) through intact SiC layers, the focus of the chemical composition and fission product identification was mainly on SiC layers. However, limited work was performed on other layers, namely IPyC and buffer layers using STEM, HRTEM, and EPMA.

#### **4.1.1 Silver Found at Inter- and Intragranular Locations**

One of the first breakthroughs from advanced microscopy and micro-analysis was the identification of nano-sized Ag at grain boundaries and triple points in Particle AGR1-632-035 in the SiC layer at the SiC-IPyC interface using STEM and EDS. This finding was expanded by finding similar nano-Ag precipitates at grain boundaries and triple points in most of the other particles studied from other compacts and fabricated from the three fuel types examined.

Ag was found inside a SiC grain on two particles (AGR1-523-SP01 and AGR1-632-035); this is in contrast with the predominant finding of Ag at SiC grain boundaries and triple points of AGR-1 coated particles. Earlier out-of-pile research work and simulation studies revealed that bulk diffusion of Ag in SiC is rare and not favored (Xiao et al., 2012) At this point, it is not clear what would be the cause of the intragranular movement of Ag in these two specific cases because no obvious relation to fuel type (identified in Baseline and Variant 1 fuel types) and irradiation level (11.4 and 17.4% FIMA) could be made.

#### 4.1.2 Palladium Found at Inter- and Intragranular Locations

Spherical and rod-like Pd-rich precipitates were found intragranularly in the SiC layer of most particles examined. The intragranular Pd-rich precipitates were generally nano-sized and nodular and could also contain small concentrations of Cd and U. These nodules were sometimes observed within the vicinity of planar defects, such as stacking faults or nano twins (Van Rooyen et al., 2016a).

Additionally, Pd was found in most of the grain boundaries and triple points of the precipitates examined in all particles. Pd could be found alone or in a combination with other elements (see Section 3). Pd was found in variable-sized precipitates ranging from several microns to nanoscale precipitates. Pd was present in most of the precipitates examined.

#### 4.1.3 Fission Product Precipitate Composition

Qualitative chemical compositions were measured using EDS on various precipitates, and areas of each particle from the different compacts were examined. Generally, classification of areas and corresponding precipitates were made in three regions of the SiC layer called inner, center, and outer areas, respectively, with the inner area closest to the SiC-IPyC interlayer and the outer area the farthest from the SiC-IPyC interlayer. This identifies potential changes in chemical element distribution and the combinations of elements from the inside SiC edge to the outer edge.

Fission product precipitates were often found as a combination of elements (Table 113). Table 113 presents a summary of all element combinations found in the three SiC regions of the particles examined (detailed qualitative chemical compositions and element combinations for each precipitate are reported in Section 3). The combination of elements reported in Table 113 does not provide information on the effect of precipitate size and location (e.g., grain boundary or triple point, inter or intragranular precipitate) on the combination of elements. However, observations were made that provide information on potential relationships with fuel types and the distributions of fission products in the SiC layer based on results from the precipitates examined. However, full understanding of these relationships has not been established and will be further developed in the future. The observations from precipitates in the SiC layer are as follows:

- It was found that the combinations of elements in precipitates are complex and varying in nature; often, other elements (e.g., Eu, Ce, Pu, and Cs) can be present in precipitates that contain predominantly Pd, Si, Ag, and U, which complicates interpretation for determining possible trends with fuel type, Ag retention, and as SiC layer location.
- Generally, more element and element combinations exist for precipitates from low Ag retention particles compared to the high-retention particles regardless of fuel type.
- Qualitatively, the Pd composition is generally greater than the Ag, although no specific trend with regards to distribution in the SiC layer could be determined. In addition, it was found that the Pd-to-Ag ratios are not constant and no specific trend in this ratio could be observed for the different SiC areas.
- Pd dominated most of the examined fission products precipitates and was often found separately and throughout the SiC layer.
- U and Ag were only found as a combination in the low Ag retention safety-tested (1600°C) Particle AGR1-433-001.
- More combinations of elements are identified for the safety-tested particles from Compact 4-3-3 compared to the particles only exposed to irradiation. Additionally, it is observed that the low Ag retention particle (AGR1-433-001) exhibits the most element combinations and contains up to six different elements in a single precipitate.

- Ce was found in all particles examined; however, it was seldom found separately and mostly in combination with Pd.
- Cs was identified in all particles examined. Cs is mostly identified in the inner areas of the SiC layer and only found in the center and outer areas of the low-Ag-retention safety-tested particle (AGR1-433-001).
- Eu is not found in the PyC or SiC layers of high-Ag-retention Particle AGR1-531-031 (Variant 1 fuel) nor in both particles from Compact 1-3-1 (Variant 3).
- Pu was not found in precipitates from the high-Ag-retention AGR1-131-066 particle.
- U was only found by itself in precipitates from Compact 1-3-1 (a Variant 3 fuel compact).
- The elemental combinations of the precipitates from the Compact 5-3-1 particles in the outer layers of both particles are similar, with the only difference noted being that Cs and Ce exist only for Particle AGR1-531-031.
- Comparing the precipitate elemental combinations of the three fuel variants, no significant conclusions could be reached other than that the Variant 3 particles from Compact 1-3-1 contain no Eu in the SiC layer. Eu also was not observed in the high Ag-retention (Variant 1) Compact 5-3-1 particle.
- Specific observations made on precipitate composition from the safety-tested Variant 3 Compact 4-3-3 particles:
  - The Ce content found in the high-Ag-retention particle was significantly higher when compared with the lower retention particle.
  - Eu was found only in the higher Ag retention particle in the center lamella.
  - No Ag and U were found in the center and outer areas of the SiC from both particles.
  - Pu was found only in the inner and center areas of the SiC layer of AGR1-433-001 (low Ag retention) and only in the inner area of the high-Ag-retention particle (AGR1-433-004).
  - U was only found in the inner area of the high-Ag-retention particle (AGR1-433-004) in contrast with the low-Ag-retention particle (AGR1 433 001) where U was found in each area. Cs was only found in the outer area of the SiC layer for the high-retention particle while being present in all the areas of the low-Ag-retention particle.
  - Ag was found in all the areas for the lower Ag retention particle (AGR1-433-001) and in the inner and outer area of the high retention particle (AGR1-433-004).
  - Pd was present for both particles on all areas of the SiC layer.
  - More combinations of elements are identified for the lower retention particle (AGR1-433-001) compared to the high-retention particle (AGR1-433-004).



Table 113. Precipitate element combination summary (a detection limit of 0.2 at.% was used to determine if an element is present, as measured by STEM EDS analysis). For each particle, results are grouped by the specific area of the SiC layer (inner, center, or outer layer) and by the number of elements observed in the precipitates (one element, two elements, and three or more elements).

Particle	Precipitate Element Combinations in the SiC Layer <sup>b</sup>		
	Inner Area	Center Area	Outer Area
AGR1-632-035 (High [79%] Ag retention)	Pd, Ag	Pd, Ag, Ce	Pd
	Pd-Ag, Pd-Pu, Pd-U, Pd-Ce	Pd-Ag, Pd-U, Pd-Ce	Pd-Ag, Pd-Eu, Pd-Ce
	Pd-U-Pu, Pd-Ag-Cs-U, <sup>a</sup>		
	Pd-Ag-Cd <sup>a</sup>		Pd-Ag-Ce, Pd-Ce-Eu
AGR1-531- 038 (Low [<19%] Ag retention )	Pd	Pd, Ag	Pd
	Pd-U, Pd-Pu, Pd-Ag	Pd-Ag, Pd-Pu, Pd-U, Pd-Ce	
	Pd-Cs-Eu, Pd-Ce-Eu, Pd-Cs-Ag, Pd-U-Pu, Pd-Ag-Eu	Pd-Ag-U, Pd-U-Pu, Pd-Ag-Pu	Pd-U-Pu
AGR1-531-031 (High [105%] Ag retention)	Pd, Cs, Pu, U,		
	Ag-U, Cs-U, Ce-U, U-Pu		
AGR1-131-066 (High [39%] Ag retention)	Pd, U	Pd	Pd
	Pd-Si, U-Si, Pd-U, Cs-U	Pd-Si, Pd-U	Pd-U, Pd-Ce
	Pd-Si-U	Pd-Si-U	Pd-Ce-U
AGR1-131-099 (Low [<6%] Ag retention)	Pd, U	Pd	Pd
	Pd-U, U-Cs, Pd-U	Pd-U	Pd-U
	Pd-U-Ce, Pd-U-Cs, Pd-Si-U		
	Pd-U-Cs-Ce, Pd-U-Si-Cs		
AGR1-433-001 (Low [66%] Ag retention)	Ag, Pd	Pd	Pd
	Ag-Cs, Pd-Ce, Pd-Ag, Pd-U, Ce-U, Pd-Pu	Pd-U,	Pd-Ag, Pd-Eu, Pd-Ce
	Pd-Ag-Ce, Pd-Ce-U, Pd-Ce-Pu, Pd-U-Pu, Pd-Ag-U	Pd-Ce-Eu, Pd-Cs-Pu, Pd-Ce-U	Pd-Eu-U
	Pd-Ce-U-Pu, Pd-Eu-U-Pu, Pd-Ce-Eu-U, Pd-U-Pu-Ce	Pd-Ce-Eu-Pu, Pd-Ag-Ce-Eu	Pd-Ag-Cs-Eu-U
		Pd-Ag-Cs-Eu-U	
		Pd-Ag-Ce-Eu-U-Pu	
AGR1-433-004 (High (98%) Ag retention)	Pd, Ag	Pd	Pd
	Pd-U, Pd-Ce, Pd-Ag, Pd-Eu	Pd-Ce	Pd-Ag
	Pd-Ce-Pu, Pd-U-Pu, Pd-Ag-Ce		Pd-Cs-Eu
<p>a. Chemical analysis from TEM evaluation on various other areas (as example in lamellae shown in Figure 6) and not only in the lamellae specifically fabricated from the inner, center and outer regions as shown in Figure 6(c) (van Rooyen et al., 2012, 2012b, 2014, 2016 and Leng et al., 2016).</p> <p>b. The reported qualitative chemical composition for the particles examined focused for this study mainly on Pd, Ag, Cs, Ce, Eu, U, and Pu although other elements were also present and will be considered in future studies.</p>			

## 4.2 Fission Product Precipitate Phase and Structure

Characterization of the phase and crystal structure of fission product precipitates did not yield a conclusive result with regard to fission product behavior, partially because it is complicated by the size distribution of the precipitates, specifically the nano-sized precipitates located at grain boundaries, triple points, and in the SiC grains. The dataset was too small to determine any significant differences based on phase and precipitate structure to differentiate between the high- and low-Ag-retention particles.

SAD with associated qualitative chemical compositions using EDS was partially successful in identifying  $\text{UPd}_2\text{Si}_2$  precipitates in particles AGR1-632-034 and AGR1-632-035. SAD patterns were collected from numerous micron-sized precipitates from particles AGR1-632-034 and AGR1-632-035. All diffraction patterns could be indexed as  $\text{UPd}_2\text{Si}_2$  (tetragonal, space group  $I4/mmm$ ) and represented eight distinct zone axes. Some of the patterns had extra reflections that may either be from adjacent crystals or double diffraction involving both a precipitate and the adjacent matrix. Proportions of the U and Pd compositions from EDS data are not consistent with  $\text{UPd}_2\text{Si}_2$ . Thus, it seems likely that the precipitates all represent a single phase, which is similar to  $\text{UPd}_2\text{Si}_2$ , but does not have the stoichiometric composition.

To obtain additional clarification on the structure of the precipitates and phases present, especially on the smaller and nano-sized precipitates, HRTEM examination was performed on specific lamellae. The techniques are described under Section 2.1.2.4. HRSTEM examination of particles from Compacts 1-3-1 and 4-3-3 showed the complex nature of precipitate structure, with both single-phased and multi-phased precipitates being identified:

### Particle AGR1-131-099:

- For the IPyC layer both a single-phase (based on uniform elemental composition) U-Zr precipitate and a multiple phase precipitate (based on non-uniform elemental composition) were found. The top part of this multiple phase precipitate was identified as Pd-Si, with concentrations of U, Pu, and Zr, whereas the bottom part is Pd-Si with a Zr concentration.
- For the SiC layer, the Pd-U-Pu single-phase precipitates were identified, as well as a multi-phase precipitate with a part consisting of Pd with a small concentration of Zr, whereas the other part consists of U-Pu.
- The interface between SiC and a grain boundary fission product precipitate was found to be well defined and free of porosity. From the change in the tilt of the atomic layers across this interface, it appears that the precipitate was not aligned to the SiC in any well-defined manner. However, it should be taken into account that only a very small sample set was studied in this manner and no general trend could be made.
- FFT of a random triple-point precipitate revealed lattice parameters consistent with  $\text{Pd}_2\text{Si}$ . Bands arising from mass contrast were identified of a precipitate along the grain boundary between SiC grains and they suggest a more complex structure to this precipitate. (It was too small to determine chemical composition.)

### Particles AGR1-433-001 and AGR1-433-004:

- All nano precipitates examined in these particles are of a cubic nature. Because the lattice structures for Pd, Pd-Ag, Pd-U, and Pd-Pu share the same cubic structure and are within  $\pm 0.08 \text{ \AA}$  lattice spacing, it was not possible to differentiate between these different types of precipitates based on lattice spacing alone. Additionally, chemical composition measurements using EDS are only qualitative and will not be able to accurately determine the combination and ratio of precipitate elements. However, obtaining higher resolution images for more accurate FFT diagrams is recommended for potentially more accurate lattice space measurements. Evidence of Pd and Pd-Ag co-existence was found with variability among different precipitates of different compacts. Furthermore, within single fission

product precipitates, there can exist multiple chemistries, including a gradient in composition. However, structurally, the fission product retains cubic symmetry. This dictates that multiple resolved chemistries (i.e., combinations of elements) are the product of substitutional cation swapping of Pd and Ag, where they also may possibly include Si, U, and Pu cations.

### **4.3 Quantification and Distribution of Fission Products Using Electron Probe Micro-analysis and Atom Probe Tomography**

EPMA was performed on three irradiated particles (AGR1-523-SP01, AGR1-433-003, and AGR1-433-007) to establish the work method and perform comparative studies for determining the effect of kernel protrusion on fission product distribution and concentration. This work produced the following main findings:

- Compact 5-2-3 (AGR1-523-SP01)
  - While Ag transport out of the kernel has been a concern, other fission products (e.g., Cs, Ba, Pu, I, Xe, and Pd) are also transported out of the kernel.
  - Ru forms precipitates within the kernel, the precise nature of which requires additional study
  - The chemical composition of the precipitates along the SiC-IPyC interface and IPyC crack is chemically heterogeneous.
  - Cs, Ba, I, and Xe are spread throughout the buffer, but appear to concentrate in and near the recoil zone. In addition, they appear to accumulate along the SiC-IPyC interface.
  - Cd was rarely found in the analyzed precipitates.
  - The EPMA method has been established for subsequent quantification of fission product precipitates and analysis on irradiated samples with lessons learned noted.
- Compact 4-3-3 (AGR1-433-003 and AGR1-433-007)
  - Concentrations of I, Cs, and Xe in the recoil zone on the deformed side of AGR1-433-003 were up to two times higher than in the recoil zone on the non-deformed side of the kernel. Concentrations of I, Cs, and Xe in the recoil zone of AGR1-433-007 were up to 10% higher than those in the recoil zone of the deformed side of AGR1-433-003.
  - Eu, Sr, and Te concentrations in the recoil zone are up to six times higher on the deformed side of AGR1-433-003 compared to the non-deformed side. For the recoil zone of AGR1-433-007, these elements are up to four times higher than those in the recoil zone of the non-deformed side of AGR1-433-003.
  - At the SiC-IPyC interface of AGR1-433-007, rare earth element, U, and Pd concentrations are up to two times higher than at either the deformed or non-deformed interface side of AGR1-433-003; Mo is ten times higher. At the SiC-IPyC interface of AGR1-433-003, Sr and Ru concentrations are approximately two times higher on the deformed side than on the non-deformed side. I, Xe, Cs, and Ba are up to 50% higher at the SiC-IPyC interface on the deformed side compared to the non-deformed side or the SiC-IPyC interface of AGR1-433-007.
  - Volatile fission products (e.g., Ba, Cs, I, and Xe) are not retained in the kernel, but rather they accumulate significantly in the buffer.

- Fission product accumulation outside the deformed region of the kernel is greater than outside the non-deformed region of the same kernel; however, a kernel showing no similar aberrations shows larger accumulation of fission products along the SiC-IPyC interface. This suggests that fission product migration and precipitation may be more strongly influenced by factors other than kernel integrity.
- The particle (AGR1-433-007) that retained all its predicted Ag-110m inventory had extensive Pd-Ag deposits along a 110-degree arc within the SiC-IPyC interface, while the particle that had less than 22% of its predicted Ag-110m inventory had a paucity of such deposits (AGR1-433-003). Asymmetry of Pd-Ag deposits is suggestive of a lateral temperature gradient within Particle AGR1-433-007, wherein the precipitates are more common on the cold side of the particle (Tiegs 1982 and Minato et al., 1994).
- Success was recently achieved using APT on Particle AGR1-632-035, where a multi-phased Ag-Pd-U precipitate was quantified on a grain boundary. The 3D re-construction of this precipitate showed that elements are localized and not evenly distributed, which is significant for our understanding of transport mechanisms. Quantitative analysis within the Pd-Ag-U-rich phase shows the normalized concentrations of Pd, Ag, and U are 12.1 at.% (error 0.3 at.%), 3.5 at.% (error 0.2 at.%), and 3.3 at.% (error 0.1 at.%), respectively. The Si and C concentrations in the Pd-Ag-U-rich phase are 60.0 at.% (error 0.3 at.%) and 21.2 at.% (error 0.2 at.%), respectively.

## 4.4 Crystallographic Characteristic Discussion

In this study, particles were selected from compacts containing TRISO particles fabricated using different coating deposition parameters. The variants of TRISO particles studied included Baseline particles (Compact 6-3-2), Variant 1 particles (Compact 5-3-1), and Variant 3 particles (Compacts 4-3-3 and 1-3-1). The coating parameters for the SiC layer of the Baseline and Variant 1 particles were nominally the same, while the SiC layer in Variant 3 TRISO particles was deposited at a lower temperature (1425°C versus 1500°C for the Baseline and Variant 1 TRISO particles) (Hunn and Lowden 2006a, b, c). This lower deposition temperature resulted in a significantly smaller grain size (Kirchhofer et al., 2013). (The grain size was not determined in this study because the length scale of the analyses in this work was too small to accurately determine grain size in the SiC layer [Lillo, van Rooyen, and Wu, et al., 2016].) The differences in coating parameters—whether intentional, as in the case of Variant 3, or unintentional, such as those due to batch-to-batch and particle-to-particle variations—could potentially affect the microstructure in the SiC layer and, ultimately, Ag-110m retention behavior. Therefore, the discussion in the following subsections compares the microstructures found for the various particles analyzed and highlights potential differences that may affect Ag-110m retention behavior.

### 4.4.1 General Grain Boundary Distributions

A considerable amount of work has concluded that Ag transport through bulk SiC is negligible at temperatures on the order of that used in the AGR-1 experiment (Schrader et al., 2011, Khalil et al., 2011, Friedland et al., 2009, Xiao et al., 2012, Gerczak et al., 2015, Malherbe 2013) and grain boundary diffusion plays a major role in the release of Ag through the SiC layer (Malherbe 2013, O’Connell and Neethling 2004, Lopez-Honorato et al., 2010, Rabone and Lopez-Honorato 2015, Deng et al., 2015). If transport by grain boundaries is the dominant mechanism for fission product movement through the SiC layer, it follows that grain boundaries and individual grain boundary characteristics (Khalil et al., 2011, Szlufarska et al., 2010) play an important role in release of fission products in TRISO fuel. Therefore, high- and low-Ag-110m-retention TRISO particles would be expected to exhibit differences in the grain boundary distributions of their SiC layer (provided the particles compared experienced a similar irradiation temperature and neutron fluence, both of which can vary considerably with particle location within the compact [Hawkes and Murray 2014]), which is the main barrier to fission product migration out of the TRISO particle.

Figure 253 shows a comparison of the distributions of grain boundary types for the different particles of this work. The different variants are shown in different colors (i.e., Baseline is black, Variant 1 is red, and Variant 3 is green), while low- and high-Ag-110m-retention particles from the same compact are shown adjacent to one another. Additionally, distributions of grain boundary types in the SiC layer of unirradiated TRISO particle variants are also included from Kirchhofer et al., (2013). Figure 253 shows the distribution of grain boundary types for (a) inner regions, (b) center regions, (c) outer regions, and (d) all regions combined. However, it should be kept in mind that the irradiation parameters (i.e., time-averaged, volume-averaged temperature and neutron fluence) varied considerably from compact to compact and even from particle to particle due to location within the compact, as well as the local particle arrangement (Hawkes and Murray 2014). Furthermore, AGR1-433-001 and AGR1-433-004 were subjected to an additional safety testing at 1600°C for 300 hours after irradiation, which could have significantly altered the retained Ag-110m content and the grain boundary distribution as the safety test temperature was above both the AGR-1 test temperature and the SiC layer fabrication temperature.

#### 4.4.2 Inner Areas

The grain boundary distributions associated with the inner area of the SiC layer of all particles are compared in Figure 253(a). The distributions of grain boundary types from particle-to-particle show significant differences. In general, all particles exhibit grain boundary distributions where the CSL-related grain boundary fraction is most prominent followed by slightly lower fractions of random, high-angle grain boundaries and, finally, low-angle grain boundaries make up the smallest fraction of the distributions. The fractions of low-angle grain boundaries associated with unirradiated particles of the Kirchhofer et al., (2013) study are generally slightly higher than those of the irradiated particles for the same variant while the fractions of CSL-related grain boundaries in the Kirchhofer et al., (2013) study are generally lower than those in the irradiated particles.

No large and/or consistent differences between compacts are evident. Comparison of the high- and low-Ag-110m-retention particle pairs in Figure 253(a) shows that for Compact 5-3-1 the low-retention particle (AGR1-531-038) exhibits a smaller low-angle grain boundary fraction and a greater random, high-angle grain boundary fraction than the high-retention particle (AGR1-531-031) while the CSL-related grain boundary fractions are the same within the standard error of the measurements. However, for Compact 4-3-3, the only statistically significant differences are a greater CSL-related, grain boundary fraction and a slightly lower random, high-angle grain boundary fraction for the lower retention particle (AGR1-433-001). The high- and low-retention particles of Compact 1-3-1 show no statistically significant differences in their grain boundary type distributions; however, the high and low retention particle pairs from the different compacts show different relative retention characteristics (e.g., for Compact 4-3-3, “high” Ag-110m retention is considered to be 98% and “low” Ag-110m retention is considered to be 66%, while for Compact 1-3-1, “high” retention is considered to be 39% and “low” Ag-110m retention is considered to be 6%). Therefore, the high-Ag-110m-retention particle of Compact 1-3-1 has lower retention than the low-Ag-110m-retention particle from Compact 4-3-3.

Consequently, direct comparisons of grain boundary types in Figure 253 may not be the best approach. Therefore, the Ag-110m retention data were plotted as a function of random, high-angle grain boundary fractions, CSL grain boundary fractions, twin boundary fraction ( $\Sigma 3$ ), and low-angle grain boundary fraction for the inner regions of the SiC layer (Figure 254). Ag-110m retention plotted against random, high-angle grain boundary, CSL-related grain boundary, twin boundary ( $\Sigma 3$ , only), and low-angle grain boundary fractions are shown in Figure 254(a), (b), (c), and (d), respectively.

As mentioned above, the experimental and fabrication parameters vary among the particles studied. Therefore, comparisons should be made only for particles with the same fabrication conditions and irradiation parameters. Baseline and Variant 1 SiC fabrication conditions are the same and can be compared cautiously since the irradiation conditions for TRISO particles in this sample set will likely not be identical. (It is assumed here that the irradiation conditions of the individual particles were close enough among the

particles of the Baseline and Variant 1 sample set so that trends can be identified.) Variant 3 particles from Compacts 1-3-1 and 4-3-3 have a much smaller SiC grain size than the Baseline and Variant 1 particles and, thus, irradiated Variant 3 TRISO particles should not be compared directly with either Baseline or Variant 1 TRISO particles. Also, Compact 4-3-3 was safety tested at temperatures much higher than the SiC layer fabrication and irradiation temperatures, while Compact 1-3-1 was not; therefore, particles from these two Variant 3 compacts may exhibit release behavior for which their grain boundary distributions are not responsible for and should not be compared.

Only data from the Variant 1 and Baseline particles have been combined and fitted with a linear trend line in the plots of Figure 254 to explore possible correlations between the grain boundary types and Ag-110m retention. The linear fit to the data, defined by the  $R^2$  value (where  $R^2 = 1$  is perfect fit and an indication of high correlation), is quite poor in all plots except for Figure 254(d), where Ag-110m retention is plotted against the low-angle grain boundary fraction. A strong, positive correlation between the low-angle grain boundary fractions and Ag-110m retention for Baseline and Variant TRISO particles is indicated in this plot. Low-angle grain boundaries are low-diffusivity paths and an increasing fraction of low-angle grain boundaries results in a reduced fraction of higher diffusivity grain boundaries, leading to higher retention values.

#### 4.4.3 Center Areas

Figure 253(b) shows the grain boundary-type distributions in the central regions of the SiC layer. The high/low retention pair for Compact 5-3-1 exhibits significant differences in the low-angle and random, high-angle grain boundary fractions, with the low-retention particle (AGR1-531-038) having a smaller low-angle grain boundary fraction and a greater random, high-angle grain boundary fraction than the high-retention particle (AGR1-531-031). Compact 4-3-3 shows statistically significant differences only in the low-angle grain boundary fraction, with the lower retention particle (AGR1-433-001) having a greater low-angle grain boundary fraction than the higher retention particle (AGR1-433-004). No statistically significant difference is observed in the random, high-angle and CSL-related grain boundary fractions of the particles from Compact 4-3-3. The particles from Compact 1-3-1 show differences in the low-angle grain boundary fraction and the CSL-related grain boundary fraction, with the lower retention particle exhibiting a smaller low-angle grain boundary fraction and a greater CSL-related grain boundary fraction than the higher retention particle (AGR1-131-066), but no statistical difference in the random, high-angle grain boundary fractions.

From the differing behavior in the grain boundary distributions of the low- and high-Ag-retention particles for the different compacts, it is difficult to determine the correlation between the various grain boundary distribution parameters and Ag-110m retention. So, again, correlations are more easily seen when the Ag-110m retention is plotted as a function of grain boundary type (Figure 255). This figure shows there is a strong, negative correlation between the Ag-110m retention behavior and the random, high-angle grain boundary fraction (Figure 255[a]), as well as strong, positive correlations between Ag-110m retention and the CSL-related boundary fraction (Figure 255[b]), and the twin boundary fraction (Figure 255[c]). The correlations, as indicated by the  $R^2$  values, are very high ( $R^2 \approx 1$ ), although the fitted trend line consists of only three data points.

However, these correlations are those expected intuitively if SiC grain boundary structure is the dominant factor influencing Ag-110m retention. Random, high-angle grain boundaries are high-diffusivity paths for impurities, and an increasing random, high-angle grain boundary fraction would be expected to result in less Ag-110m retention (greater release), negative correlation between Ag-110m retention and random, and high-angle grain boundary fraction. Furthermore,  $\Sigma 3$  grain boundaries have relatively low values for grain boundary diffusivity, and an increasing fraction of  $\Sigma 3$  grain boundaries would be expected to prevent the release of Ag-110m and result in higher values of Ag-110m retention, resulting in a positive correlation between Ag-110m retention and twin boundary fraction, as observed in Figure 255(c). (Since twin boundary fraction [i.e.,  $\Sigma 3$  boundaries] dominate

the CSL-related grain boundary distributions of all the particles [e.g., Figure 31(b), Figure 55(b), Figure 76(b), Figure 116(b), Figure 138(b), Figure 192(b) and Figure 226(b)], a positive correlation between Ag-110m retention and the CSL-related grain boundary fraction, as observed in Figure 255[b], is also expected.) Finally, a positive correlation between Ag-110m and the low-angle grain boundary fraction is observed in Figure 255(d), although the correlation is not as strong as with the other grain boundary types.

Data from the Variant 3 particles do not always exhibit correlation relationships consistent with those of the Baseline and Variant 1 particles in this study. In some cases, data for the particles that were not safety tested (i.e., AGR1-131-066 and AGR1-131-099) follow the same correlation behavior as the Variant 1 and Baseline particles (i.e., the negative correlation for the random high-angle grain boundary fraction and the positive correlation with the low-angle grain boundary fraction, Figure 255[a] and [d]), but suggest opposite correlations compared to the Variant 1 and Baseline data for CSL-related and twin boundary fractions, Figure 255(b) and (c). However, since the standard error bars on the AGR1-131-066 and AGR1-131-099 data for the random, high angle, grain boundary fraction overlap, and nearly so for the  $\Sigma 3$  grain boundary fractions, the correlations of these quantities with Ag-110m retention, whether positive or negative, cannot be determined any certainty. Analyses of additional irradiated Variant 3 particles will be required to establish the true correlation between the fractions of random, high angle and  $\Sigma 3$  grain boundaries with Ag-110m retention, which can then be compared to the correlations exhibited by the Baseline and Variant 1 data.

Data from the safety-tested particles, AGR1-433-001 and AGR1-433-004, would appear to follow the same correlations found for the Variant 1 and Baseline particles, except for the low-angle grain boundary fraction (Figure 255[d]), where a negative correlation is observed and which is also opposite to the Compact 1-3-1 data for the low-angle grain boundary fraction. However, as mentioned, differences in the correlation behavior between fractions of various grain boundary parameters and Ag-110m retention may arise not be the same as that found for the Baseline and Variant 1 particles due to the smaller grain size and/or the safety testing of the Variant 3 TRISO particles studied here. Furthermore, this study has produced only two data points for the various grain boundary fractions of safety tested, Variant 3 particles and a third data point from the analysis of an additional particle is needed to establish the true correlation between the various grain boundary fractions and Ag-110m retention in safety tested particles. Only then can valid comparisons of the grain boundary correlations with Ag-110m retention found in safety tested, Variant 3 particles be made with Baseline, Variant 1 and non-safety tested Variant 3 particles.

Clearly the results for the center areas are interesting and tend to support a microstructure-based explanation for Ag-110m retention behavior. However, analysis of additional particles, exhibiting different Ag-110m retention characteristics under similar experimental test conditions, is required to verify the correlations presented here.

#### 4.4.4 Outer Areas

Figure 253(c) shows there are some small, statistically significant differences in the grain boundary distributions in the outer regions of the SiC layers of the Variant 1 and Baseline particles. However, the grain size tends to be larger in these outer regions (Kirchhofer et al., 2013), especially for Variant 1 (Compact 5-3-1). Therefore, fewer grain boundaries were analyzed, which resulted in greater statistical error. The increased statistical error may mask trends in these regions. The outer region of AGR1-131-099 was not analyzed and no comparison of the high- and low-retention particles could be made for this area.

When the Ag-110m retention for the Variant 1 and Baseline particle data are plotted against the fractions of the various grain boundary parameters of the outer regions of the SiC layer, a strong correlation with the random, high-angle grain boundary fraction is found (Figure 256[a]); however, it is a positive correlation, while a strong negative correlation existed in the center region of the SiC layer (Figure 255[a]). Because of the typically higher impurity diffusivities of random, high-angle grain boundaries, a negative correlation with Ag-110m retention is expected. The reason for the difference in correlation behavior in the outer region compared to the center regions of the SiC layer is not clear at this time, but one possible



explanation is that the microstructure in the outer region may have little effect on the overall retention behavior of the TRISO particle (at least for the particles in this study) if the microstructure in the center regions is dominating retention behavior; Ag-110m encounters the center microstructure first on its way to the outer region and its eventual release from the particle. Therefore, migration through the center region may be the controlling step in Ag-110m release.

Weak negative, correlations between the Ag-110m retention, the CSL-related grain boundary fraction, and the twin-related grain boundary fraction are found in the outer regions of the SiC layer, Figure 256(b) and (c), and are also opposite to the strong, positive correlations found in the central region of the SiC layer (Figure 255[b] and [c]). The negative correlation between Ag-110m retention and the twin/CSL-related boundary fraction in the outer regions of the SiC layer are opposite to intuition—twins ( $\Sigma 3$  grain boundaries) are low-diffusivity pathways for impurity atoms and a positive correlation is expected. Again, the relatively large standard error bars associated with the data in the outer region of the SiC layer may be preventing the true correlation behavior between grain boundary fractions and Ag-110m retention from being identified. Again, additional TRISO-coated particles with the same fabrication conditions for the SiC layer and similar irradiation histories need to be analyzed to verify the correlations found for the outer regions of the SiC layer. Not only would more particles be helpful to verify correlations, but so would multiple Lamella from the same particle (to confirm whether the grain boundary character distribution observed in inner, center, and outer areas is consistent from location to location).

#### 4.4.5 Combined Regions

Figure 253(d) shows the grain-boundary type distributions when all data from each particle are combined to provide a representative distribution for the entire SiC layer of each particle. Differences are even less pronounced than those in the plots for the individual regions (Figure 253[a] through [c]). Significant differences are seen in the low-angle grain boundary fractions for the Variant 1 and Baseline particles (AGR1-531-038, AGR1-531-031 and AGR1-632-035), respectively. Small, but significant, differences are also observed in the random, high-angle grain boundary fractions of the Variant 1 and Baseline particles. The high and low Ag-110m retention Variant 3 particles, AGR1-131-066 and AGR1-131-099, respectively, also show statistically significant differences in their low-angle and CSL-related grain boundary fractions while exhibiting nearly identical random, high-angle grain boundary fractions. The safety tested Variant 3 TRISO particles, AGR1-433-001 and AGR1-433-004, do not show any statistically significant differences in the fractions of the various grain boundary types.

Correlations for Variant 1 and Baseline fuel data between Ag-110m retention and the various grain boundary parameters are shown in Figure 257. A negative correlation between Ag-110m retention and the random, high-angle grain boundary fraction is still observed in this combined dataset; however, the  $R^2$  is reduced compared to that found in the center region of the SiC layer (Figure 255[a]). No correlation between Ag-110m retention and the CSL grain boundary fraction is observed in Figure 257(b) since there is no statistical difference in the CSL values. Positive correlations between Ag-110m retention and the twin boundary ( $\Sigma 3$ ) fraction and low-angle grain boundary fraction are also found in Figure 257(c) and (d), respectively. However, the  $R^2$  values for the best linear fit to the data are, again, lower than those found in the center region of the SiC layer (Figure 255[c] and [d]). Furthermore, the relatively large standard error bars on the data allow for actual correlations that could be positive or negative. If the grain boundary distribution found in the center of the SiC is truly controlling the Ag-110m retention then correlations exhibited in these combined regions may not be relevant.

#### 4.4.6 Conclusions

Strong correlations were found to exist in the center regions of the SiC layer for Variant 1 and Baseline particles (i.e., the center regions exhibited excellent correlations between Ag-110m retention and random, high-angle grain boundary fraction [negative correlation], CSL-related grain boundary fraction [positive correlation], twin boundary fraction [positive correlation], and the low-angle grain boundary fraction [positive correlation]). A good correlation also was found in the inner region between Ag-110m retention and the low-angle grain boundary fraction. A strong positive correlation was also found in the outer region between Ag-110m retention and the random, high-angle grain boundary fraction. Combining the datasets from the inner, center, and outer regions tended to weaken the correlations between Ag-110m and the various grain boundary parameters. The changing grain boundary distribution from the inner to outer regions for the Variant 1 and Baseline particles (AGR1-531-038, AGR1-531-031, and AGR1-632-035 in Figure 253[a] through [c]) appears to have created a region that controls the retention of Ag-110m; however, the correlations are based on data from only three particles.

The Variant 3 particles (AGR1-131-066, AGR1-131-099, AGR1-433-001, and AGR1-433-004) do not seem to exhibit a consistent change in the various grain boundary fractions from the inner to outer regions (Figure 253[a] through [c]); however, analysis of additional particles will be required to determine whether a similar controlling region and/or grain boundary distribution can be identified in Variant 3 particles. Additional analyses of irradiated Variant 1 and Baseline particles with similar irradiation histories also are needed to verify the trends and correlations found in this work. Not only would more particles be helpful to verify correlations, but so would multiple lamellae from the same particle (to confirm whether or not the grain boundary character distribution observed in the inner, center, and outer areas is consistent from location to location). Alternatively, collection of additional data could be performed with SEM-based EBSD on inner, center, and outer regions of the SiC layer at various locations on polished cross sections of irradiated TRISO particles to improve the statistics of the correlations between Ag-110m retention and grain boundary type as well as evaluate the location-to-location variation of the grain boundary character distribution in the SiC layer.

Correlations in the central region are reasonably explained. Here, it was found that increasing fractions of random, high-angle grain boundaries are associated with decreasing Ag-110m retention (negative correlation). Random, high-angle grain boundaries typically exhibit greater diffusivities for impurity atoms and a higher fraction of random, high-angle grain boundaries would be expected to transport more of the fission product elements across the SiC layer, resulting in a lower final retention. Also, the positive correlation between increasing twin boundary fraction,  $\Sigma 3$  fraction, and increasing Ag-110m retention (Figure 255[c]) is explainable using a similar argument, except that twin boundaries are generally poor paths for impurity diffusion; therefore, with more twin boundaries present, fewer high diffusivity paths for fission product transport exist, resulting in greater final Ag-110m retention.

The positive correlation between Ag-110m retention and the low-angle grain boundary fraction is also expected. Low-angle grain boundaries are composed of discrete sets of lattice dislocations. Diffusion along low-angle grain boundaries is generally by dislocation pipe diffusion, where the core of the dislocation is the conduit by which the impurity atom diffuses. The diffusivity of such boundaries is relatively low and an increasing fraction of low-angle boundaries would be expected to aid in Ag-110m retention. This positive correlation between Ag-110m retention and the low-angle grain boundary fraction was found in the center region of the SiC layer.

Data from Compact 4-3-3 was not included in the correlation analysis nor compared in depth to the other Variant 3 data from TRISO particles, AGR1-131-099 and AGR1-131-066. This compact was safety tested at 1600°C, while the other particles in this study were not. The safety test temperature represents greater than 0.6 melting point for SiC; generally, microstructural changes are considered possible at such temperatures. These particles also contained neutron damage prior to safety testing, which would also enhance grain boundary diffusion and might aid in microstructural changes. The largest effect would be expected on the fraction of low-angle grain boundaries. The elevated temperature would be expected to allow the reaction of the low-angle grain boundaries with other low-angle grain boundaries or high-angle grain boundaries to produce a single grain boundary of lower total energy. Comparison of the low-angle grain boundary fraction between the particles of Compact 4-3-3 and Compact 1-3-1 in Figure 253(d) may show a slight, possibly significant difference, with the safety tested particles (Compact 4-3-3) exhibiting a slightly smaller low-angle grain boundary fraction. Also, inclusion of Baseline and Variant 1 particles with Variant 3 particles in the analysis may obscure possible correlations between grain boundary parameters and Ag-110m retention. The smaller grain size in Variant 3 particles will translate into a higher number density of boundary types compared to Baseline and Variant 1 particles and different Ag-110m retention might be expected. Additionally, the time-averaged, volume-averaged irradiation temperature for the Variant 3 compacts was significantly higher than either the Variant 1 or Baseline particles, although the TAVA irradiation temperature of the compact may have little bearing on the actual irradiation temperature of the individual particles.

#### **4.4.7 Grain Boundary/Fission Product Precipitate Correlations**

Whether or not a precipitate will be found on a given boundary will depend mainly on the energy of the grain boundary and whether the solubility of the fission product in the grain boundary is exceeded. Generally, precipitation is easier on higher energy grain boundaries. Random, high-angle grain boundaries typically have the highest grain boundary energies, followed by CSL-related grain boundaries (although the grain boundary habit plane significantly affects the grain boundary energy) and then low-angle grain boundaries tend to have the lowest grain boundary energy. Thus, one would expect to find most of the precipitates on random, high-angle grain boundaries, some on CSL-related grain boundaries, and very few on low-angle grain boundaries. This is indeed the case in Figure 258(a), where the fraction of precipitates is plotted as a function of grain boundary type. The trend in relative grain boundary energy is followed by all particles analyzed, regardless of variant type. The other determining factor for grain boundary precipitation is whether the concentration level within a given grain boundary reaches a critical level that exceeds the solubility of the fission product in the grain boundary. If the supply of fission products is limited and/or the fission product diffusivity in the grain boundary is sufficient to prevent the impurity concentration from reaching a critical level, then no grain boundary precipitation will occur. The variation in the fraction of precipitates on high-angle grain and CSL-related grain boundaries in Figure 258 is possibly due to the local variation in fission product supply from particle to particle. For instance, AGR1-531-038 exhibited a failed buffer layer and a UCO fuel kernel protrusion toward the IPyC (Figure 47), and would be expected to provide a more ready supply of fission products due to the closer proximity of the UCO kernel to the SiC layer. Higher concentrations of the fission product elements at the IPyC/SiC interface give rise to higher concentration gradients and; higher chemical potential gradients, thus, a higher driving force for impurity atoms to enter SiC grain boundaries, and diffuse through the SiC layer. The higher driving force enables impurity atoms to enter lower energy grain boundaries (such as CSL-related grain boundaries and even  $\Sigma 3$  and low-angle grain boundaries if the driving force is high enough) as long as the energy of the system is reduced. The variant type is expected to have little influence on the fraction of precipitates residing on the various grain boundary type since grain boundary energy is only a function of grain boundary misorientation and grain boundary habit plane and not a function of the SiC layer fabrication conditions. However, grain size and the distribution of grain boundary types may affect the supply of fission product elements, which could affect precipitation (whether or not the critical concentration for a precipitate to form is attained) on grain boundaries of differing energy.

The distribution of fission product and transuranic elements in the precipitates analyzed is shown in Figure 258(b). Precipitates containing only Pd are most prevalent among all particles analyzed. One of the major differences is that Ag-containing precipitates were not found in the SiC layer of the particles of Compact 1-3-1 (Variant 3). However, gamma spectroscopy indicates a very low level of Ag-110m retention for these two particles so Ag-110m did transport through the SiC layer. Therefore, it is possible that the grain distributions in these two particles actually resulted in enhanced Ag-110m transport to the point the concentration of Ag never attained a critical value for the formation of Ag-containing precipitates. However, Ag and Pu were found in the safety-tested particles from Compact 4-3-3 (Variant 3). It is possible that the elevated temperature in the safety test enabled an enhanced Ag release from the UCO kernel and its subsequent migration to and into the SiC layer.

The other noticeable difference in the distribution of fission product and transuranic elements in the plot of Figure 258(b) is the presence of Pu in only the safety tested particles, AGR1-433-001 and AGR1-433-004. TRISO particles that were not subjected to safety testing did not exhibit the presence of Pu in precipitates in their SiC layer. Therefore, the temperature of the safety test was sufficient to allow the release of Pu from the UCO kernel and transport into the SiC layer.

#### **4.4.8 Recommendations**

Although enough data were collected in many cases to yield statistically relevant results, keep in mind that only a very small fraction of the SiC layer in any of the particles was analyzed. The extent of the location-to-location variation in the microstructure in the SiC layer is still not known and the areas analyzed may not have been those most important to Ag-110m transport. However, the areas analyzed do not show large variations in grain boundary distributions that might explain the large variation in Ag-110m retention, suggesting that the local temperature and neutron fluence may be the dominating factor in Ag-110m retention. The study did reveal some correlations (such as the decreasing Ag-110m retention with increasing random, high-angle grain boundary fraction in the center of the SiC layer that warrant further investigation.

To properly address the mechanism of fission product transport, especially Ag-110m, through the SiC layer, the following must be addressed:

- Analyze the SiC layer of additional particles with the same fabrication and irradiation parameters, but differing Ag-110m retention characteristics, to verify the Ag-110m retention/grain boundary type correlations found in the center region of the SiC layer in Variant 1 and Baseline particles (Figure 255). SEM-based EBSD can be used to gather the grain boundary character distributions on polished cross sections of the TRISO particles in this study. The SEM-based EBSD study should collect grain boundary character distributions for inner, center, and outer regions at various locations in the SiC layer. Additional data needs to be collected from AGR1-632-035, AGR1-531-031, AGR1-531-038, AGR1-131-066, and AGR1-131-099.
- Develop a method to accurately determine the irradiation conditions experienced by each particle that is analyzed (i.e., the actual particle temperature and neutron fluence). This will ensure the proper particles are included in correlation analyses and will help determine the influence of irradiation parameters on Ag-110m retention.
- Provide theoretical calculations of the amount of Ag-110m generated in each particle due the particle irradiation conditions (a record of which is contained in the irradiation defects in the SiC layer) to accurately determine the relative retention of Ag-110m in each particle analyzed and accurately determine the correlations between Ag-110m and grain boundary types.

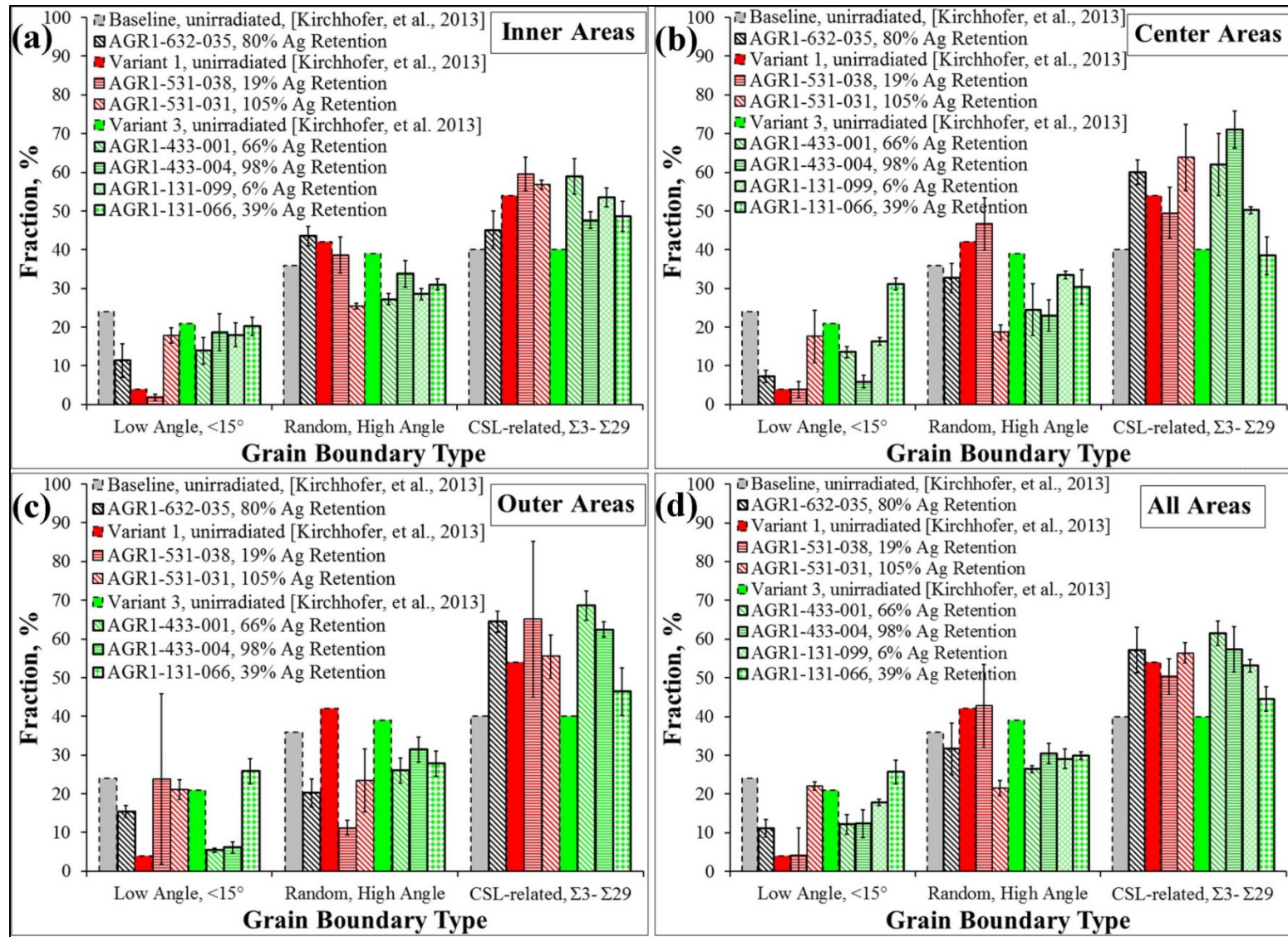


Figure 253. Comparison of the distributions of grain boundary types: (a) inner regions, (b) center regions, (c) outer regions, and (d) the combined regions are compared. Baseline in black, Variant 1 in red, and Variant 3 in green.

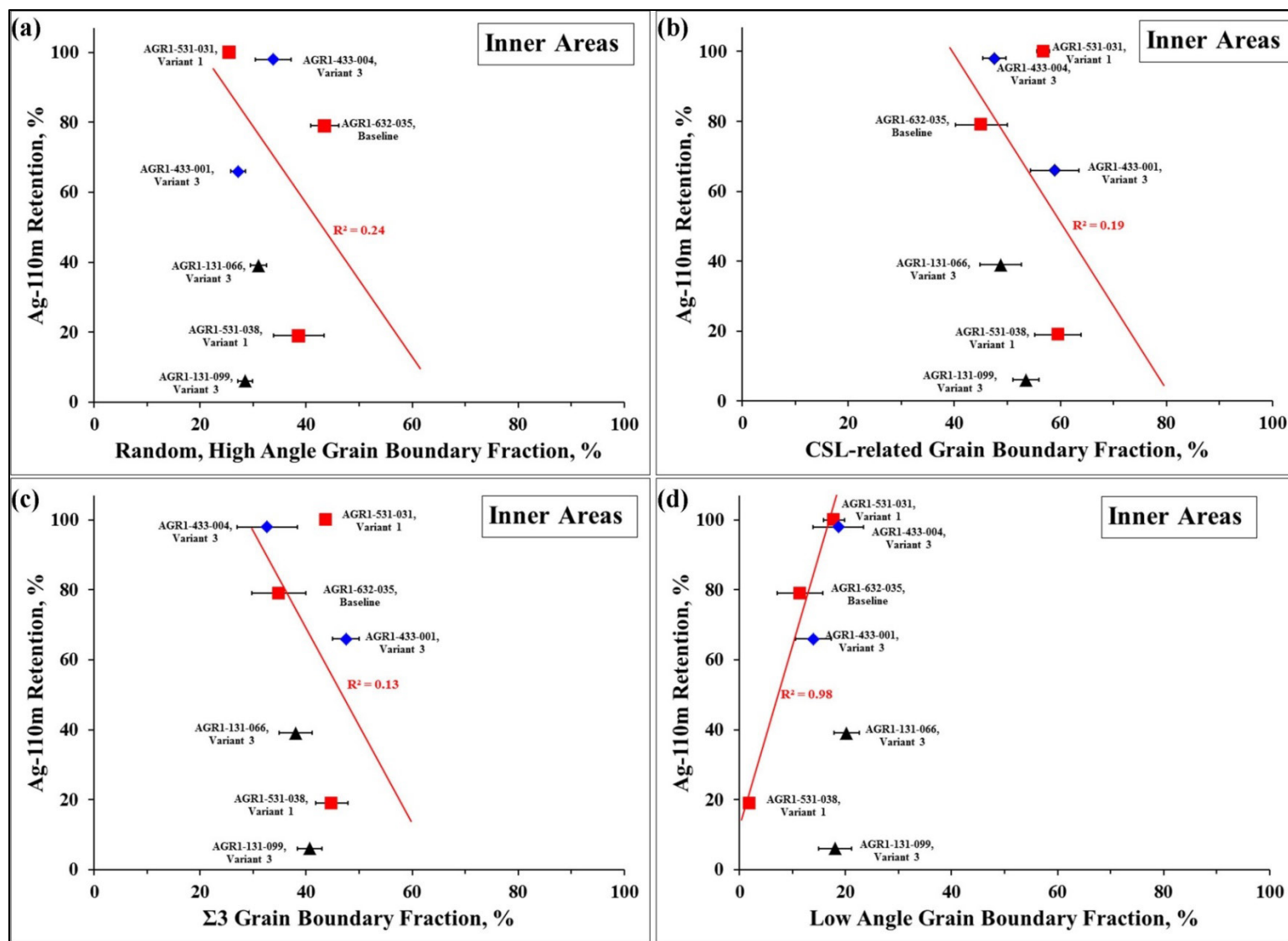


Figure 254. Correlations between the Ag-110m retention and (a) random, high-angle grain boundary fraction, (b) CSL-related grain boundary fraction, (c) twin boundary fraction, and (d) low-angle grain boundary fraction for inner regions of the SiC layer.



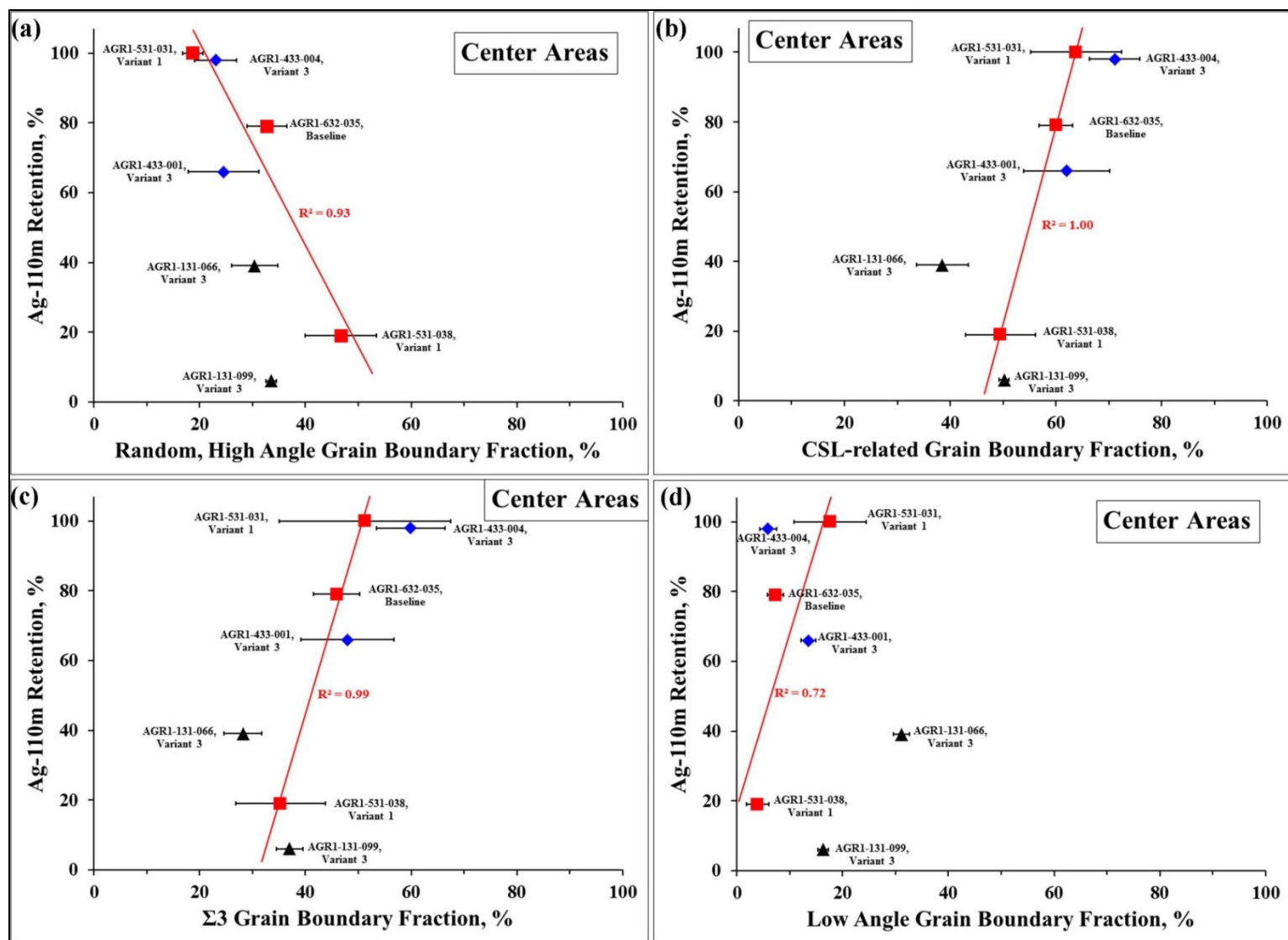


Figure 255. Correlations between the Ag-110m retention and (a) random, high-angle grain boundary fraction, (b) CSL-related grain boundary fraction, (c) twin boundary fraction, and (d) low-angle grain boundary fraction for central regions of the SiC layer.



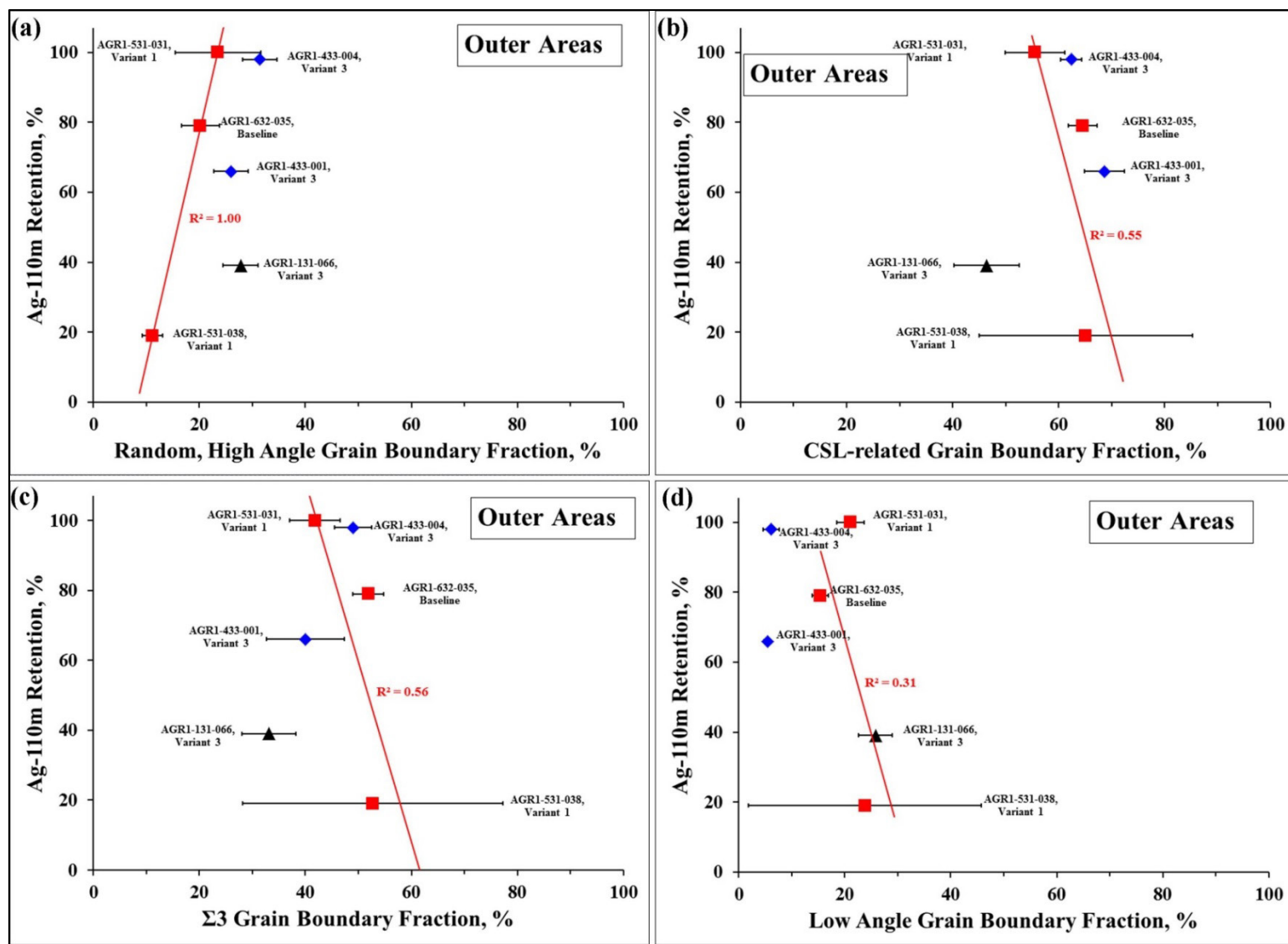


Figure 256. Correlations between the Ag-110m retention and (a) random, high-angle grain boundary fraction, (b) CSL-related grain boundary fraction, (c) twin boundary fraction, and (d) low-angle grain boundary fraction for outer regions of the SiC layer.

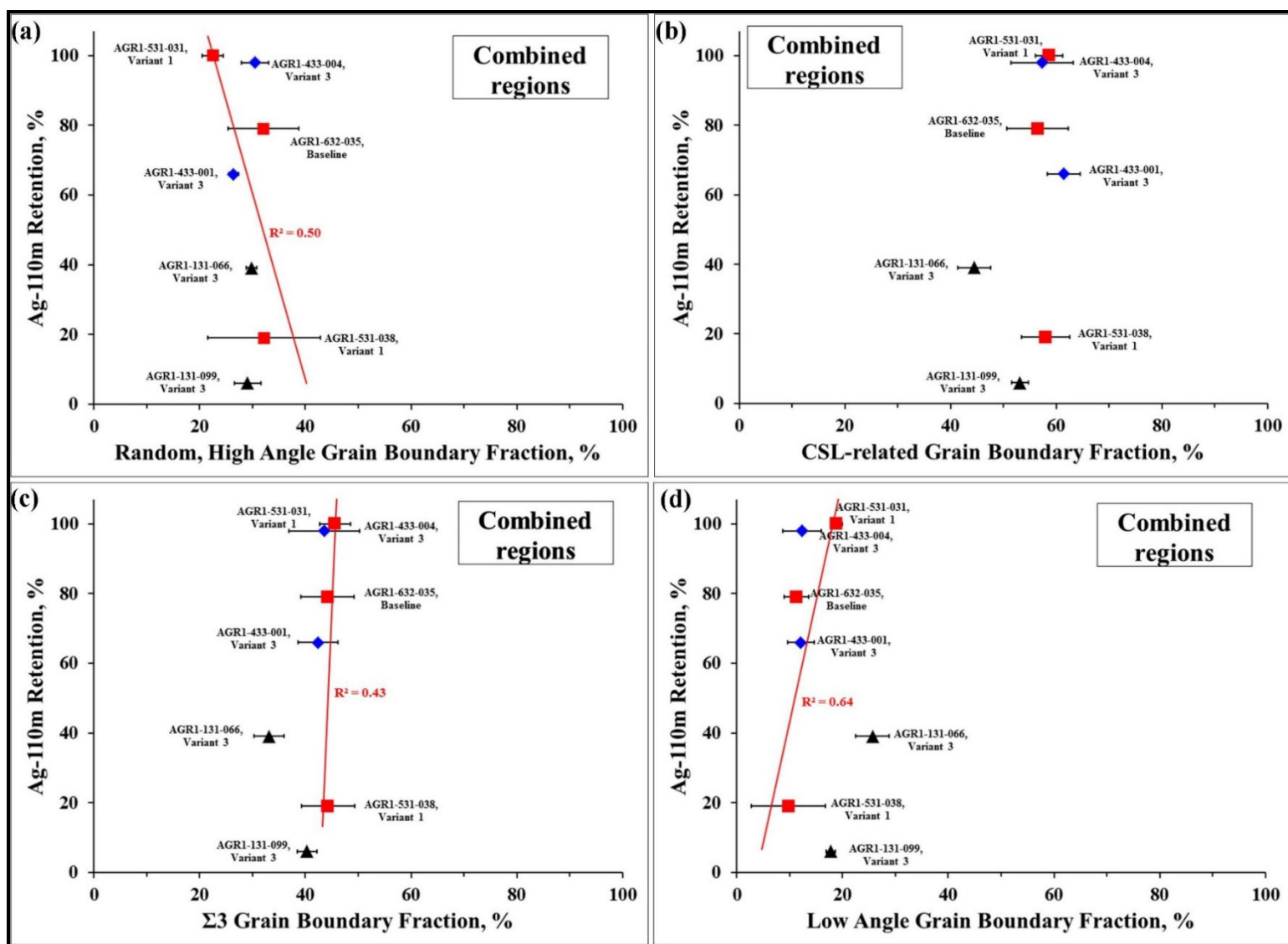


Figure 257. Correlations between the Ag-110m retention and (a) random, high-angle grain boundary fraction, (b) CSL-related grain boundary fraction, (c) twin boundary fraction, and (d) low-angle grain boundary fraction for all regions of the SiC layer combined to yield correlations representative of the entire SiC layer.

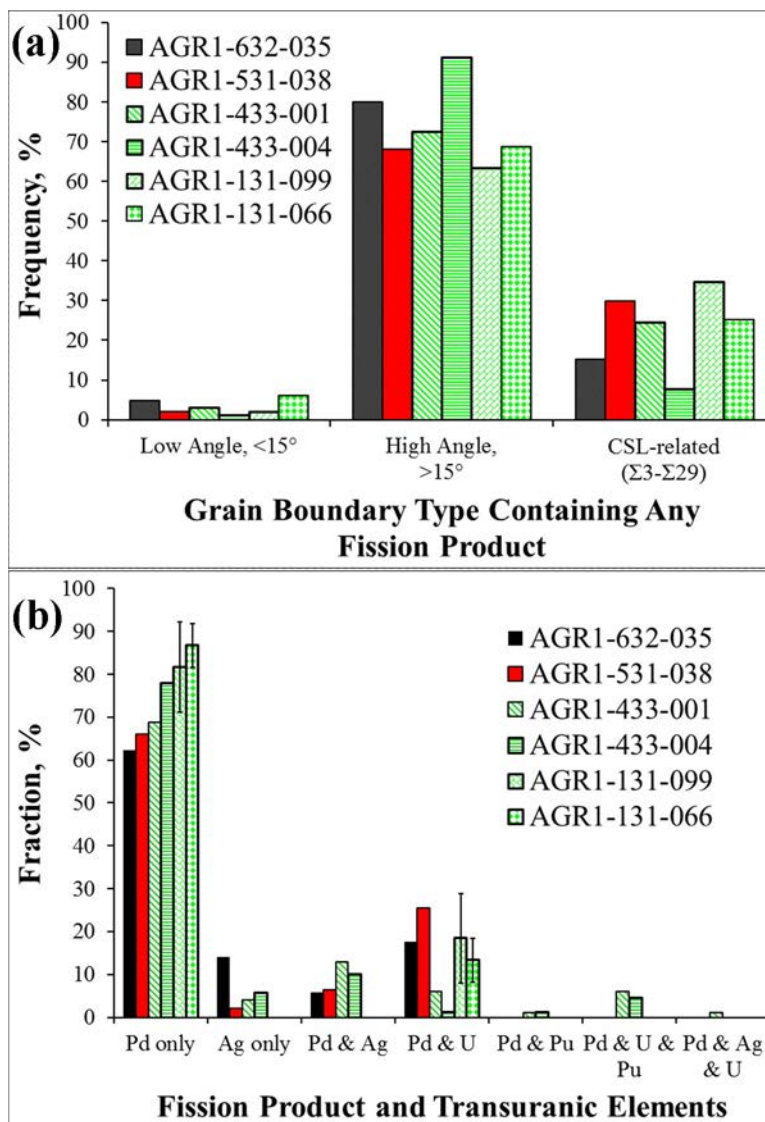


Figure 258. (a) Plot showing the types of grain boundaries on which fission product precipitates were found and (b) the distribution of fission product elements in the grain boundary precipitates. Variants are in different colors (i.e., Baseline in black, Variant 1 in red, and Variant 3 in green).

## 4.5 Fission Product Transport

Although numerous mechanisms for Ag transport were derived from reactor experimentation release data, out-of-pile experimentation under simulated conditions, and empirical studies over the past four decades, no definitive conclusion on the mechanism(s) responsible for Ag transport in an irradiated TRISO particle's SiC layer under very high-temperature reactor conditions has been reached. The experimental samples and test conditions have varied significantly and individual results have supported a variety of possible Ag transport mechanisms. Various Ag-110m transport mechanisms (such as grain boundary diffusion, surface diffusion, or vapor transport) through interconnected nano-pores or nano-cracks and Pd-assisted transport alongside grain boundaries have been identified in these out-of-pile experiments and also must be considered as potentially viable Ag-110m transport mechanisms in the SiC layer of TRISO fuel under neutron irradiation. To evaluate the applicability and significance of these out-of-pile transport mechanisms and transport mechanisms unique to neutron irradiation (such as enhanced bulk diffusion due to neutron irradiation-induced defects), characterization of microstructural and composition information, and the identification of Ag in the SiC layer of actual irradiated TRISO-coated particles is needed for irradiated TRISO fuel.

The work reported here has a direct impact on the knowledge of Ag transport and other fission product movement studies. Although transport mechanisms for each fission product are not discussed and explored in this section, a brief summary is provided listing the main findings predominantly impacting Ag transport mechanisms (it should be noted that this section is not meant to be a comprehensive scientific report on fission product transport mechanisms; instead this section only reports brief observations with immediate linkages to transport mechanisms based on the authors' knowledge):

- Ag transport is predominantly along grain boundaries with the rare two instances where Ag is identified within the SiC grain. This is in contrast with Pd, which is found both intra and intergranularly and separately and in combination of most other fission products identified during this study.
- From the complex nature of the precipitates seen from the varying phases and multiple element combinations in precipitates, it seems multiple mechanisms may be at play here.
- Because Ag, Pd, and U-only precipitates also were identified, a chemical-assisted transport mechanism is not necessarily present. (It is possible that other elements may be still present in these single element precipitates, but were below the limits of detection. A chemical-assisted transport may still be a viable transport mechanism for even these seemingly single element precipitates).
- Based on results from AGR-1 PIE advanced microscopy, Ag transport is not driven by kernel morphology.
- The changing grain boundary distribution from the inner to outer regions for the Variant 1 and Baseline particles (AGR1-531-038, AGR1-531-031, and AGR1-632-035) appears to have created a region (i.e., the center region) that controls the retention of Ag-110m. This was only found by analyzing inner, center and outer regions separately as no strong correlations were found when the data from all three of these regions was combined. (Additional analyses of irradiated Variant 1 and Baseline particles with similar irradiation histories also are needed to verify the trend and correlation found in this work.)
- Strong grain boundary characteristic correlations were found to exist in the center regions of the SiC layer for Variant 1 and Baseline particles (i.e., the center region exhibited):

- Negative correlation between Ag-110m retention and random, high-angle grain boundary fraction
- Positive correlation between Ag-110m retention and CSL-related grain boundary fraction
- Positive correlation between Ag-110m retention and twin boundary fraction
- Positive correlation between Ag-110m retention and the low-angle grain boundary fraction.
- The Variant 3 particles (AGR1-131-066, AGR1-131-099, AGR1-433-001, and AGR1-433-004) do not seem to exhibit a consistent change in the various grain boundary fractions from the inner to outer regions.
- The structure of grain boundary precipitates in Compact 4-3-3 particles are all cubic and, because a gradient in chemistries and multiple elements exist within a single fission product precipitate, substitutional cation swapping of Pd and Ag may occur. All diffraction patterns of micron-sized precipitates examined could be indexed as  $\text{UPd}_2\text{Si}_2$  (tetragonal, space group  $I4/mmm$ ). Because the chemical composition did not support stoichiometry, it was hypothesized that Ag could exchange with Pd.
- Neutron damage and its effect on fission product transport were not examined during PIE activities due to prioritization on fission product distribution, chemical composition, and grain boundary characteristics. However, this is a very important microstructural effect that needs to be considered in transport mechanistic studies. The alignment of voids on grain boundaries in the vicinity of Pd-containing precipitates within the SiC grains and at the triple-point precipitates on actual irradiated AGR-1 TRISO-coated Particle AGR1-632-035 shows a potential effect on transport mechanisms. This is further demonstrated with out-of-pile research conducted recently. It is recommended that further work is performed on irradiated TRISO particles from the AGR-1 and AGR-2 experiments on this topic.

## 4.6 Maturity Level of Techniques and Method Development

Significant progress was made on enhancing the knowledge of the behavior of TRISO-coated particles after neutron irradiation using advanced microscopic analysis. As can be seen from the previous sections in this detailed report, some techniques and measurements are more developed than others. The information provided in Table 114 provides a snapshot of the maturity level at this time.

Table 114. Maturity level and applicability for future AGR advanced microscopy and micro-analytical techniques. Only the techniques identified to be further explored or applied are indicated in this table. (The grading system used is as follows: “Good” means acceptable for PIE application, “Medium-Good” means it is successfully demonstrated, but it still needs optimization, and “Low” means low maturity and cannot be applied without significant effort and development).

Technique	Facility Readiness		Technique Maturity	
	NRC <sup>1</sup> /DOE <sup>2</sup> Licensed	Approved Controls	Equipment	Parameters Optimization
FIB	Yes: MFC-EML <sup>2</sup> Yes: MFC-IMCL <sup>2</sup>	Yes Yes, but not at the moment operational	Good Good	Good, have not received lamellae fabricated at IMCL; however, the parameters are known and developed by Jim Madden at MFC-EML-FIB; therefore, only the training of the operator will be necessary.
APT	Yes: CAES <sup>1</sup>	Yes	Good	Medium-Good, need validation and FIB-tip fabrication needs optimization.
EPMA	Yes: MFC-IMCL <sup>2</sup>	Yes: Currently not operational until Spring 2017 and then limited due to priority of other programs	Good	Process and standards established with work described in this report.
STEM	Yes: MFC-EML Yes: MFC-IMCL <sup>2</sup> Yes: CAES <sup>1</sup>	Yes	Good	Good, availability over the summer months challenging.
EELS EFTEM	Yes: CAES <sup>1</sup>	Yes	Good	Low, because this technique was not prioritized due to funding. However, now that a good baseline was established, quantification will need to receive higher priority and development of the EELS technique for irradiated SiC. The challenges is in having the sample preparation techniques produce thin enough lamellae for optimized EELS measurements without fracture due to the brittle nature of irradiated SiC.
HRTEM <sup>a</sup>	Yes: NMMU LANL	Yes	Good (NMMU) Medium-Good (LANL)	Good, recommended to explore other HRTEM equipment in U. S. with similar specifications as those of NMMU. Additionally, the instrument and researcher’s availability still remains a challenge for obtaining timely and relevant results and will be explored for the AGR-2 experiment samples.
PED	Yes: CAES	Yes	Good	Good, highly successful and time-consuming. Of great relevance to TRISO performance evaluation.
a. No equipment available at INL or close to INL at this moment.				

## 4.7 Publications and Scientific Achievements

The advanced microscopy and micro-analytical examination on AGR-1 experiment particles yielded a large pool of knowledge, which was transferred to the wider Advanced Reactor Technologies and high-temperature reactor community by means of more than 40 publications (reports, journal papers, and conference papers) and more than 30 presentations at conferences and workshops. Program meetings and NSUF scientific review board and users annual meetings (Appendix B).

Collaboration with universities (Idaho State University, NMMU, University of Wisconsin-Milwaukee, and Boise State University), other national laboratories (LANL and ORNL), and commercial entities (Bruker-Nano) were key in achieving successes.

The INL Award for Outstanding Scientific Paper for 2014 was presented on February 27, 2015, to Isabella van Rooyen and Thomas Lillo for “Identification of Silver and Palladium in Irradiated TRISO Coated Particles,” that was published in the *Journal of Nuclear Materials*, Vol. 446, pp. 178–186.

## 5. CONCLUSIONS SUMMARY

A significant evaluation and development of methods and operational strategies took place for advanced electron microscopy and micro-analysis techniques that resulted in significant successes. Techniques and methodologies are identified that will be applied to AGR-2 particle PIE and future AGR experiments. As an example, the STEM, TEM, HRTEM, EBSD, TKD, APT, PED, and EELS results are first-of-a-kind results on the irradiated SiC layer of TRISO-coated particles reported in open literature. Specifically, the STEM examination provided the first-of-a-kind results, indicating the presence of Ag in nano-sized precipitates at triple points and grain boundaries. This provides significant knowledge for Ag transport mechanistic studies that have been the topic of international research for the past 40 years. HRTEM analysis in 2013 provided the first image to the atomic level of Ag and Pd atoms on the grain boundaries of irradiated SiC. This also provided insight into the co-existing nature of Pd and Ag in the same grain boundary. Innovative nano-crystallographic measurements were pioneered on neutron irradiated SiC through successful demonstration of the first application of PED in conjunction with fission products in irradiated fuels. APT provided the first quantification of a grain boundary precipitate composition in addition to a 3D reconstruction of the precipitate. The NSUF-RTE funding was crucial in development and optimization of the advanced techniques described in this report and the AGR-1 PIE campaign.

The AGR-1 advanced microscopy and micro-analysis workscope focused on identification and distribution of fission products to obtain comparative information on composition and location. Predominantly, work focused on distribution within the SiC layer as the main fission product barrier. Ag was found both intra- and intergranularly, although predominantly in grain boundaries and triple points. Pd dominated most of the fission product precipitates examined, is often found separately, and was found throughout the SiC layer. Qualitatively, the Pd composition is generally greater than the Ag content, although no specific trend with regards to distribution in the SiC layer could be determined. It was further found that the Pd to Ag ratios were not constant and no specific trend in this ratio could be observed for the different SiC areas. U and Ag were only found as a combination in the low Ag retention safety-tested Particle AGR1-433-001. U was only found alone in precipitates from Compact 1-3-1—a Variant 3 fuel compact. Precipitates from the safety-tested Variant 3 particles from Compact 4-3-3 do not contain U separately.

It was found that the combinations of elements in precipitates are complex and varying in nature and often other elements (e.g., Eu, Ce, Pu, and Cs) can be present in precipitates that contain predominantly Pd, Si, Ag, and U; this complicates the interpretation to determine possible trends with fuel type, Ag retention, and SiC layer location. Generally, more element combinations exist for precipitates from low-Ag-retention particles compared to the high-retention particles irrespective of fuel type. Comparing the precipitate elemental combinations of the three fuel variants, no significant conclusions could be reached



other than that the SiC layer of all fuel types contains Cs and the Variant 3 particles from Compact 3-1-1 contain no Eu in the SiC layer. Cs is mostly identified in areas of the SiC layer near the IPyC/SiC interface and only found in areas of the SiC layers away from the IPyC/SiC interface in the low-Ag-retention safety-tested particle (AGR1-433-001).

More combinations of elements are identified for the safety-tested particles (Compact 4-3-3) compared to the particles only exposed to irradiation at anticipated operating temperatures. Additionally, it is observed that the low Ag retention particle (AGR1-433-001) exhibits the most element combinations and also contains up to six different elements in a single precipitate.

The presence of Ag predominantly on grain boundaries suggests that the grain boundary transport mechanism may be prominent. It appears the changing grain boundary distribution from the inner to outer regions for the Variant 1 and Baseline particles (i.e., AGR1-531-038, AGR1-531-031, and AGR1-632-035) has created a region (i.e., the SiC layer center region) that controls or, at least, correlates well with the retention of Ag-110m. (Additional analyses of irradiated Variant 1 and Baseline particles with similar irradiation histories also are needed to verify trends and correlations found in this work). If the following observations can be validated across a significant population of irradiated particles, the TRISO fabrication parameters potentially could be optimized to produce SiC layers with a minimal fraction of random, high angle grain boundaries, thereby improving Ag-110m retention: (1) a negative correlation between Ag-110m retention and random, high-angle grain boundary fraction, (2) a positive correlation between Ag-110m retention and CSL-related grain boundary fraction, and (3) a positive correlation between Ag-110m retention, twin-related boundary fraction, and (4) a positive correlation between Ag-110m retention and the low-angle grain boundary fraction. The Variant 3 particles (AGR1-131-066, AGR1-131-099, AGR1-433-001, and AGR1-433-004) do not seem to exhibit a consistent change in the various grain boundary fractions from the inner to outer regions.

Although this work was not predominantly focused on fission product mechanistic studies, most of the results and observations contributed toward knowledge of transport mechanisms. From this work, no single mechanism hypothesis can be reported. The complexity of mechanisms is further highlighted by the multiple variations of elemental combinations found in the fission product precipitations. This may indicate that various transport mechanisms are present, depending on specific irradiation conditions. In addition, it seems that movement of Ag is not assisted by a specific element in all cases due to the fact that various element combinations were identified and Ag was also found separately from any other fission products or uranium. Therefore, it is not necessarily true that a chemical-assisted transport mechanism is dominant.

Neutron damage and its effect on fission product transport were not examined during PIE activities due to prioritization on fission product distribution, chemical composition, and grain boundary characteristics. However, this is a very important microstructural effect that needs to be considered in transport mechanistic studies. The alignment of voids on grain boundaries in the vicinity of Pd-containing precipitates within the SiC grains and at the triple-point precipitates on actual irradiated AGR-1 TRISO coated particle AGR1-632-035 shows a potential effect on transport mechanisms. Recently, this was further demonstrated in out-of-pile research. It is recommended that additional work be performed on irradiated TRISO particles from the AGR-1 and AGR-2 experiments on this topic.

In conclusion, the evidence provided in this report and associated references show significant new results describing the behavior of TRISO fuel particles during irradiation testing and information contributing toward understanding of fission transport mechanisms. Suitable techniques, facilities, and methods were identified and developed during the AGR-1 advanced microscopy and micro-analysis campaign that was necessitated to achieve the main objectives of the advanced microscopy and micro-analysis campaign. Fission product identification and distribution and SiC grain boundary characteristics were prioritized during the AGR-1 campaign.

## 6. REFERENCES

- Aguiar, J. A., O. Anderoglu, S. Choudhury, J. K. Baldwin, Y. Wang, A. Misra, and B. P. Uberuaga, 2015, "Nanoscale morphologies at alloyed and irradiated metal-oxide bilayers," *Journal of Materials Science*, Vol. 50, No. 7, pp. 2726–2734, 2015.
- Baba, K., U. Miyagawa, K. Watanabe, Y. Sakamoto, T. B. Flanagan, 1990, "Electrical resistivity changes due to interstitial hydrogen in palladium-rich substitutional alloys," *Journal of Materials Science*, Vol. 25, No. 9, pp. 3910–3916, 1990.
- Barrachin, M., R. Fubourg, S. de Groot, M. P. Kissane, K. Bakker, 2011, "Fission-product behavior in irradiated TRISO-coated particles: Results of the HFR-EU1bis experiment and their interpretation," *Journal of Nuclear Materials*, Vol. 415, pp. 104–116, 2011.
- Brandes, E. A. and G. B. Brook, eds. 1992, *Smithells Metals Reference Book, Seventh Edition*. Butterworth-Heinemann, Ltd.: Oxford, 1992.
- Bretscher, H., P. Grütter, G. Indlekofer, H. Jenny, R. Lapka, P. Oelhafen, R. Wiesendanger, T. Zingg, H. - J. Güntherodt, 1987, "Physical properties of icosahedral and glassy Pd–U–Si alloys," *Zeitschrift für Physik B Condensed Matter*, Vol. 68, No. 2, pp. 313–324, 1987.
- Bruemmer, S. M., E.P. Simonen, P.M. Scott, P.L. Andresen, G.S. Was, J.L. Nelson, 1999, "Radiation-induced material changes and susceptibility to intergranular failure of light-water-reactor core internals," *Journal of Nuclear Materials*, Vol. 274, No. 3, pp. 299–314, 1999.
- Buschow, K. H. J. and D. B. De Mooij, 1986, "Structural and magnetic characteristics of several ternary compounds of the type  $GdX_2Si_2$  and  $UX_2Si_2$  ( $X=3d, 4d, \text{ or } 5d$  metal)," *Philips Journal of Research*, Vol. 41, pp. 55–76, 1986.
- Coles, B. R., 1956, "The lattice spacings of Ni - Cu and Pd - Ag alloys," *Journal of Institute of Metals*, Vol. 84, pp. 346–348, 1956.
- Collins, B. P., 2012, *AGR-1 Irradiation Test Final As-Run Report*, Idaho National Laboratory, INL/EXT-10-18097, Rev. 1, 2012.
- Coulthard, I. and T. K. Sham, 1996, "Charge Redistribution in Pd-Ag Alloys from a Local Perspective. Physical Review Letters," Vol. 77, No. 23, pp. 4824–4827.
- Demkowicz, P. A., 2010, PLN-2828, "AGR-1 Post-Irradiation Examination Plan," Rev. 1, Idaho National Laboratory, March 2010.
- Demkowicz, P., J. Harp, P. Winston, and S. Ploger, 2012, *AGR 1 Fuel Compact 6-3-2 Post Irradiation Examination Results*, INL/EXT-12-27123, Idaho National Laboratory, 2012.
- Demkowicz, P. A., J. M. Harp, P. L. Winston, and S. A. Ploger, 2013, *Analysis of Fission Products on the AGR-1 Capsule Components*, Idaho National Laboratory, INL/EXT-13-28483, Rev. 0, 2013.
- Demkowicz, P. A., J. D. Hunn, S. A. Ploger, R. N. Morris, C. A. Baldwin, J. M. Harp, P. L. Winston, T. J. Gerczak, I. J. van Rooyen, F. C. Montgomery, and C. M. Silva, 2014, "Irradiation Performance of AGR-1 High Temperature Reactor Fuel," *Proceedings of the HTR 2014, Weihai, China, October 27–31, 2014, Paper HTR2014-31182, published also in Nucl Eng Des, 306, 2-13 (2016)*.
- Demkowicz, P. A., J. D. Hunn, R. N. Morris, C. A. Baldwin, J. M. Harp, P. L. Winston, S. A. Ploger, T. Gerczak, I. J. van Rooyen, F. C. Montgomery, C. M. Silva, 2015, "Irradiation performance of AGR-1 high temperature reactor fuel," *Nuclear Engineering and Design*, 306 (2016) 2-13 <http://dx.doi.org/10.1016/j.nucengdes.2015.09.011>.
- Demkowicz, P. A., J. D. Hunn, R. N. Morris, I. Van Rooyen, T. Gerczak, J. M. Harp, and S. A. Ploger, 2015a, *AGR-1 Post Irradiation, Examination Final Report*, Idaho National Laboratory,

- INL/EXT-15-36407, 2015. Demkowicz, P. A., P. L. Winston, J. M. Harp, and S. A. Ploger, 2016a, *AGR-1 Compact 5-3-1 Post Irradiation Examination Results*, INL/EXT-15-36354, Idaho National Laboratory, 2016.
- Demkowicz, P. A., S. A. Ploger, P. L. Winston, and J. M. Harp, 2016b, *AGR-1 Compact 1-3-1 Post Irradiation Examination Results*, INL/EXT-15-36365, Idaho National Laboratory, 2016.
- Demkowicz, P. A., J. M. Harp, P. L. Winston, S. A. Ploger and I. J. van Rooyen, 2016c, *AGR-1 Compact 4-1-1 Post Irradiation, Examination Results*, INL/EXT-15-36169, 2016.
- Demkowicz, P. A., S. A. Ploger, and P. L. Winston, 2016d, *AGR 1 Compact 4-3-3 Safety Testing and Post Test Examination Results*, INL/EXT-16-38287, Idaho National Laboratory, 2016.
- Deng, J., H. Ko, P. Demkowicz, D. Morgan, and I. Szlufarska, 2015, “Grain boundary diffusion of Ag through polycrystalline SiC in TRISO fuel particles,” *Journal of Nuclear Materials*, Vol. 467, pp. 332–340, 2015.
- Engelhard, J., K. Krüger, H. Gottaut, 1975, “Investigations of the Impurities and Fission Products in the AVR Coolant at an Average Hot Temperature of 950°C,” *Nuclear Engineering Design*, Vol. 34, p. 85, 1975.
- Farthing, I. R. and C. T. Walker, 1990, *Heinrichs Mass Absorption Coefficients (For the K, L, and M X-ray Lines)*, JRC-ITU-TN-1990/K 0290140, Commission of the European Communities Joint Research Centre, Institute for Transuranium Elements, 1990.
- Foiles, S. M., M. I. Baskes, and M. S. Daw, 1986, “Embedded-atom-method functions for the FCC metals Cu, Ag, Au, Ni, Pd, Pt, and their alloys,” *Physical Review B*, Vol. 33, No. 12, pp. 7983–7991, 1986.
- Foiles, S. M., M. I. Baskes, and M. S. Daw, 1988, “Erratum: Embedded-atom-method functions for the FCC metals Cu, Ag, Au, Ni, Pd, Pt, and their alloys,” *Physical Review B*, Vol. 37, No. 17, pp. 10378–10378, 1988.
- Friedland, E., J. B. Malherbe, N. G. Van der Berg, H. Hlatshwayo, A. J. Botha, E. Wendler, and W. Wesch, 2009, “Study of Silver Diffusion in Silicon Carbide,” *Journal of Nuclear Materials*, Vol. 389, No. 2, pp. 326–331, 2009.
- Gerczak, T. J., B. Leng, K. Sridharan, J. L. Hunter Jr, A. J. Giordani, T. R. Allen, 2015, “Observation of Ag diffusion in ion implanted SiC,” *Journal of Nuclear Materials*, Vol. 461, pp. 314–324, June 2015.
- Goodhew, P. J., 1979, “Annealing twin formation by boundary dissociation,” *Met. Sci*, Vol. 13, pp. 108–112, 1979.
- Grover, S. B., D. A. Petti, and J. T. Maki, 2010, “Completion of the First NGNP Advanced Gas Reactor Fuel Irradiation Experiment, AGR 1, in the Advanced Test Reactor,” Paper 104, *Proceedings of HTR-2010, Prague, Czech Republic, October 18–20, 2010*.
- Harp, J. M., 2014, “Analysis of Individual Compact fission Product Inventory and Burnup for the AGR-1 TRISO Experiment Using Gamma Spectrometry,” ECAR-1682, Rev. 3, Idaho National Laboratory.
- Hassam, S., 2006, *Ag-Si Phase Diagram*, ASM Alloy Phase Diagrams Center, P. Villars, editor-in-chief; H. Okamoto and K. Cenzual, section editors; <http://www1.asminternational.org/AsmEnterprise/APD>, ASM International, Materials Park, Ohio, 2006.
- Hawkes, G. L., AGR-1 Daily As-run Thermal Analyses,” Idaho National Laboratory, ECAR-968, Revision 4, INL/MIS-11-23668, 2014.
- Herrmann, G. H. Gleiter, and G. Baro, 1976, “Investigation of low energy grain boundaries in metals by a sintering technique,” *Acta Metall.*, Vol. 24, pp. 353–359, 1976.

- Hick, H., H. Nabielek, J. York, 1970, *Evaluation of Gamma-Spectrometric Fission Product Release Measurements on Second Charge Centre Rods*, D.P. Report 733, OCED Dragon Project, 1970.
- Hunn, J. D. and R. A. Lowden, 2006a, *Data Compilation for AGR-1 Baseline Coated Particle Composite LEU01-46T*, ORNL/TM-2006/019, Revision 1, April 2006.
- Hunn, J. D. and R. A. Lowden, 2006b, *Data Compilation for AGR-1 Variant 1 Coated Particle Composite LEU01-47T*, ORNL/TM-2006/020, Revision 1, April 2006.
- Hunn, J. D. and R. A. Lowden, 2006c, *Data Compilation for AGR-1 Variant 3 Coated Particle Composite LEU01-49T*, ORNL/TM-2006/022, Revision 0, May 2006.
- Hunn, J. D., G. E. Jellison Jr., and R. A. Lowden, 2008, "Increase in Pyrolytic Carbon Optical Anisotropy and Density During Processing of Coated Particle Fuel Due to Heat Treatment," *Journal of Nuclear Materials*, Vol. 374, pp. 445–452, 2007.
- Hunn, J. D., C. A. Baldwin, T. J. Gerczak, F. C. Montgomery, R. N. Morris, and C. M. Silva, 2014, *AGR-1 Irradiated Compacts 5-2-3 and 5-2-1 PIE Report: Evaluation of As Irradiated Fuel Performance with Leach Burn Leach, IMGA, Materialography, and X-ray Tomography*, ORNL/TM-2014/171, Oak Ridge National Laboratory, Oak Ridge, Tennessee, 2014.
- Hunn, J. D., R. N. Morris, C. A. Baldwin, F. C. Montgomery, C. M. Silva, and T. J. Gerczak, 2015, *AGR-1 Irradiated Compact 4-4-2 PIE Report: Evaluation of As-Irradiated Fuel Performance with Leach Burn Leach, IMGA, Materialography, and X-ray Tomography*, ORNL/TM-2013/2362015.
- Hunn, J. D., C. A. Baldwin, T. J. Gerczak, F. C. Montgomery, R. N. Morris, C. M. Silva, P. A. Demkowicz, J. M. Harp, and S. A. Ploger, 2015, "Detection and Analysis of Particles with Failed SiC in AGR-1 Fuel Compacts," *Nuclear Engineering and Design*, In Press, April 6, 2016.
- IAEA-TECDOC-CD-1674, 2012, *Advances in High Temperature Gas Cooled Reactor Fuel Technology* International Atomic Energy Agency Vienna, 2012.
- Jain, A., Jain, S. Ping Ong, G. Hautier, W. Chen, W. Richards, S. Dacek, S. Cholia, D. Gunter, D. Skinner, G. Ceder, K. A. Persson, 2013, "Commentary: The Materials Project: A materials genome approach to accelerating materials innovation," *APL Mater.*, Vol. 1, No. 1, pp. 011002, 2013.
- Jain, A., G. Hautier, S. Ping Ong, C. J. Moore, C. C. Fischer, K. A. Persson, G. Ceder, 2011, "Formation enthalpies by mixing GGA and GGA + U calculations," *Physical Review B*, Vol. 84, No. 4, p. 045115, 2011.
- Khalil, S., N. Swaminathan, D. Schrader, A. J. Heim, D. D. Morgan, I. Szlufarska, 2011, "Diffusion of Ag along  $\Sigma$  3 boundaries in 3C-SiC," *Phys. Rev. B*, Vol. 84, pp. 214104, December 2011.
- Kim, D. H., H. You Kim, J. Hoon Ryu and H. Mo Lee, 2009, "Phase diagram of Ag-Pd bimetallic nanoclusters by molecular dynamics simulations: solid-to-liquid transition and size-dependent behavior," *Physical Chemistry Chemical Physics*, Vol. 11, No. 25, pp. 5079–5085, 2009.
- Kirchhofer, R., J. D. Hunn, P. A. Demkowicz, J. I. Cole, and B. P. Gorman, 2013, "Microstructure of TRISO coated particles from the AGR-1 experiment: SiC grain size and grain boundary character," *J. Nucl. Mater.*, Vol. 432, pp. 127–134, 2013.
- Kleykamp, H., 1975, *Mikrosondenuntersuchungen zum Verhalten der Spaltprodukte in hoch abgebrannten HTR-brennstoffen*, Kernforschungszentrum Karlsruhe, Report KfK 2213, 1975.
- Kleykamp, H. and S. G. Kang, 1996, "Pd-U Phase Diagram," *ASM Alloy Phase Diagrams Center*, P. Villars, editor-in-chief and H. Okamoto and K. Cenzual, section editors, <http://www1.asminternational.org/AsmEnterprise/APD>, ASM International, Materials Park, Ohio, 1996.

- Kofalt, D. D., D. D. Kofalt, I. A. Morrison, T. Egami, S. Preische, S. J. Poon, and P. J. Steinhardt, 1987, "Quasicrystallinity of icosahedral Pd<sub>58.8</sub>U<sub>20.6</sub>Si<sub>20.6</sub>," *Physical Review B*, Vol. 35, No. 9, pp. 4489–4492, 1987.
- Kondo, S., Y. Katoh, and L.L. Snead, 2008, "Unidirectional formation of tetrahedral voids in irradiated silicon carbide," *Appl. Phys. Letters*, Vol. 93, pp. 163110, 2008.
- Leciejewicz, J., H. Ptasiwicz-Bak, and A. Zygmunt, 1979, "Magnetic phase transitions in UPd<sub>2</sub>Si<sub>2</sub>," *Phys. Stat. Sol. (a)*, Vol. 51, pp. K71-K73, 1979.
- Leng, B., I. J. Van Rooyen, Y. Wu, I. Szlufarska, and K. Sridharan, 2016, "STEM/EDS Analysis of Fission Products in Irradiated TRISO Coated Particles of the AGR-1 Experiment," *Journal of Nuclear Materials*, Vol. 475, pp. 62–70, 2016.
- Li, Q., L. Song, L. Pan, Y. Chen, M. Ling, X. Zhuang, X. Zhang, 2014, "Density functional theory studies of electronic properties of PdAg/Pd surface alloys," *Applied Surface Science*, Vol. 288, pp. 69–75, 2014.
- Lillo, T. M. and I. J. van Rooyen, 2014, "Spatial Distribution of Pd, Ag & U in the SiC Layer of an Irradiated TRISO Fuel Particle," *Proceedings of the Microscopy & Microanalysis 2014 Meeting, Hartford, Connecticut, August 3–7, 2014*.
- Lillo, T. M. and I. J. van Rooyen, 2015, "Associations of Pd, U and Ag in the SiC Layer of Neutron-Irradiated TRISO Fuel," *Journal of Nuclear Materials*, Vol. 460, pp. 97–106, 2015.
- Lillo, T. M. and I. J. van Rooyen, 2016, "Influence of SiC Grain Boundary Character on Fission Product Transport in Irradiated TRISO Fuel," *Journal of Nuclear Materials*, Vol. 47, pp. 83–92, 2016.
- Lillo, T. M., I. J. van Rooyen, Y. Q. Wu, 2016, "Precession electron diffraction for SiC grain boundary characterization in unirradiated TRISO Fuel," *Nuclear Engineering and Design*, <http://dx.doi.org/10.1016/j.nucengdes.2016.05.027>, Vol. 305, pp. 277–283, August 15, 2016.
- Lillo, T. M., I. J. van Rooyen, H. Wen, J.A. Aguiar, 2017, *Supplemental PED Advanced Microscopy Data From Microstructural Analyses of AGR-1 TRISO Particles*, INL/LTD-16-39740, Idaho National Laboratory.
- Lojkowski, W., H. Gleiter, and R. Maurer, 1988, "Low energy grain boundaries in silver and copper close to the melting point," *Acta Metall.*, Vol. 36, pp. 69–79, 1988.
- López-Honorato, E., D. Yang, J. Tan, P. J. Meadows, and P. Xiao, 2010, "Silver Diffusion in Coated Fuel Particles," *J. Am. Ceram. Soc.*, Vol. 93, pp. 3076–3079, 2010.
- López-Honorato, E., H. Zhang, D. Yang and P. Xiao, 2011, "Silver diffusion in silicon carbide coatings," *J. Am. Ceram. Soc.*, Vol. 94, pp. 3064–3071.
- Lu, Z. W., S. H. Wei, and A. Zunger, 1991, "Electronic structure of random Ag<sub>0.5</sub>Pd<sub>0.5</sub> and Au<sub>0.5</sub>Al<sub>0.5</sub> alloys," *Physical Review B*, 1991, Vol. 44, No. 19, pp. 10470–10484.
- Lugg, N. R., G. Kothleitner, N. Shibata, Y. Ikuhara, 2015, "On the quantitiveness of EDS STEM," *Ultramicroscopy*, Vol. 151, pp. 150–159, 2015.
- Maki, J. T., 2009, *AGR-1 Irradiation Experiment Test Plan*, INL/EXT-05-00593, Rev. 3, October 2009.
- Malherbe, J. B., 2013, "Diffusion of fission products and radiation damage in SiC," *J. Phys.D.: Appl. Phys.*, Vol. 46, pp. 473001, 2013.
- Marazza, R., R. Ferro, G. Rambaldi, G. Zanichchi, 1977, "Some phases in ternary alloys of thorium and uranium with the Al<sub>4</sub>Ba-ThCu<sub>2</sub>Si<sub>2</sub>-type structure," *Journal of the Less-Common Metals*, Vol. 53, p. 193–197, 1977.

- Minato, K., T. Ogawa, K. Fukuda, M. Shimizu, Y. Tayama, I. Takahashi, 1994, "Fission product behavior in TRISO-coated  $\text{UO}_2$  fuel particles," *Journal of Nuclear Materials*, Vol. 208, pp. 266–281, 1994.
- Morioka, S. and Hasebe, M., 1990, "Ag-Pd Phase Diagram," *ASM Alloy Phase Diagrams Center*, P. Villars, editor-in-chief and H. Okamoto and K. Cenzual, section editors, <http://www1.asminternational.org/AsmEnterprise/APD>, ASM International, Materials Park, Ohio.
- Nabielek, H., P. E. Brown, P. Offerman, 1977, "Silver Release from Coated Particle Fuel," *Nuclear Technology*, Vol. 35, pp. 483, 1977.
- Neethling, J. H., J. H. O'Connell, and E. J. Olivier, 2012, "Palladium assisted silver transport in polycrystalline SiC," *Nucl. Eng. and Design*, Vol. 251, pp. 230–234, 2012.
- O'Connell, J. H. and J. H. Neethling, "Ag transport in high temperature neutron irradiated 3C-SiC," *Journal of Nuclear Materials*, Vol. 455, pp. 20–25, 2014.
- Olivier, E. J. and J. H. Neethling, 2013, "The role of Pd in the transport of Ag in SiC," *Journal of Nuclear Materials*, Vol. 432, pp. 252–260, 2013.
- Peterson, N. L., 1983, "Grain-boundary diffusion in metals," *Int. Met. Rev.*, Vol. 28, pp. 65–91, 1983.
- Poon, S. J., A. J. Drehman, and K. R. Lawless, 1985, "Glassy to Icosahedral Phase Transformation in Pd-U-Si Alloys," *Physical Review Letters*, Vol. 55, No. 21, pp. 2324–2327, 1985.
- Pouchou, J. and F. Pichoir, 1991, "Quantitative Analysis of Homogeneous or Stratified Microvolumes Applying the Model, "PAP," *Electron Probe Quantitation*, D. E. Newbury and K. F. J. Heinrich, eds., Plenum Press, New York, 1991.
- Price, P. J., 1973, "Neutron irradiation-induced voids in  $\beta$ -silicon carbide," *Journal of Nuclear Materials*, Vol. 48, No. 1., pp. 47–57, 1973.
- Priester, L., 1989, "Geometrical specialty and special properties of grain boundaries," *Rev. Phys. Appl.*, Vol. 24, pp. 419–438, 1989.
- Ptasiewicz-Bak, H., J. Leciejewicz, and A. Zygmunt, 1981, "Neutron diffraction study of magnetic ordering in  $\text{UPd}_2\text{Si}_2$ ,  $\text{UPd}_2\text{Ge}_2$ ,  $\text{URh}_2\text{Si}_2$ , and  $\text{URh}_2\text{Ge}_2$ ," *J. Phys. F: Metal Phys.*, Vol. 11, pp. 1225–1235, 1981.
- Rabone, J. and E. López-Honorato, 2015, "Density Functional Theory Metadynamics of Silver, Cesium and Palladium diffusion at  $\beta$ -SiC Grain Boundaries," *Journal of Nuclear Materials*, Vol. 458, pp. 56–63, March 2015.
- Ralls, K. M., T. H. Courtney, and J. Wulff, 1976, "Introduction to Materials Science and Engineering," John Wiley & Sons, New York, 374.
- Randle, V., 1993, *The Measurement of Grain Boundary Geometry*, Institute of Physics Publishing, Philadelphia, 1993.
- Randle, V., 1998, "Overview No. 127 The role of the grain boundary plane in cubic polycrystals," *Acta Mater.*, Vol. 46, pp. 1459–1480, 1997.
- Randle, V., 2004, "Twinning-related grain boundary engineering," *Acta mater.*, Vol. 52, pp. 4067–4081, 2004.
- Reed-Hill, R. E., *Physical Metallurgy Principles*, 2nd Edition, PWS Publishers, Boston, Massachusetts, 1973.
- Schrader, D., S. M. Khalil, T. Gerzcek, T. R. Allen, A. J. Heim, I. Szlufarska, D. Morgan, 2011, "Ag diffusion in cubic silicon carbide," *Journal of Nuclear Materials*, Vol. 408, pp. 257–271, 2011.

- Schwartz, G. P., 1978, "Segregation studies in Pd-Ag. Surface Science," Vol. 76, No. 1, pp. 113–129, 1978.
- Shemirani, B., H. Lin, M.F. Collins, C. V. Stager, J.D. Garrett, W. J. Buyers, 1993, "Magnetic structure of UPd<sub>2</sub>Si<sub>2</sub>," *Physical Review B*, Vol. 47, No. 13, 1993.
- Shen, Y., S. Poon, and G. Shiflet, 1986, "Crystallization of icosahedral phase from glassy Pd-U-Si alloys," *Physical Review B*, Vol. 34, No. 5, pp. 3516, 1986.
- Shewmon, P. G., 1969, *Transformations in Metals*, McGraw-Hill Book Co., New York, p. 63, 1969.
- Sterbentz, J. W. and H. D. Gougar, "Comparison of Fission Product Buildup in Candidate NGNP Fuel and the AGR-1 TRISO-Particle Irradiation Test," Idaho National Laboratory, Technical Evaluation Study, TEV-1301, 2011.
- Sterbentz, J. W., "JMOCUP As-Run Daily Depletion Calculation for the AGR-1 Experiment in ATR B-10 Position," Idaho National Laboratory, ECAR-958, Revision 2, INL/MIS-11-23655, 2013.
- Szlufarska, I., D. D. Morgan, S. Khalil, D. Shrader, and A. J. Heim, 2010, "Modeling of Ag diffusion in TRISO coated fuel particles," *ANS Trans.*, Vol. 102, pp. 751–752, 2010.
- Tan, L., T. R. Allen, J. D. Hunn, and J. H. Miller, 2008, "EBSD for microstructure and property characterization of the SiC-coating in TRISO fuel particles," *Journal of Nuclear Materials*, Vol. 372, pp. 400-404, 2008.
- Tiegs, T. N., 1982, Fission Product Pd-SiC Interaction in Irradiated Coated Particle Fuels, *Nucl. Technol*, Vol. 57, pp. 389–398, 1982.
- van Rooyen, I. J., D. E. Janney, B. D. Miller, J. L. Riesterer, P. A. Demkowicz, 2012, "Electron microscopic evaluation and fission product identification of irradiated TRISO coated particles from the AGR-1 experiment: A preliminary review," HTR2012-3-023, *Proceedings of HTR-2012, Tokyo, Japan, October 28–November 1, 2012*.
- van Rooyen, I. J., M. L. Dunzik, P. M. van Rooyen, and T. Trowbridge, 2012a, "On Techniques to Characterize and Correlate Grain Size, Grain Boundary Orientation and the Strength of the SiC Layer of TRISO Coated Particles - A Preliminary Study," Paper HTR2012 3 024, *Proceedings of the HTR 2012, Tokyo, Japan, October 28–November 1, 2012*.
- van Rooyen, I. J., B. D. Miller, D. E. Janney, J. Riesterer, P. A. Demkowicz, and J. Harp, 2012b, *Electron Microscopic Examination of Irradiated TRISO Coated Particles of Compact 6-3-2 of AGR-1 Experiment*, INL/EXT-11-23911, 2012.
- van Rooyen, I. J., 2013, "Summary report on Advanced microscopy performed on Irradiated AGR-1 Specimens," INL Interoffice Memorandum, CCN231379, September 2013.
- van Rooyen, I. J., Y. Q. Wu, T. M. Lillo, T. L. Trowbridge, J. M. Madden, and D. Goran, 2013, "Advanced Electron Microscopic Techniques Applied to the Characterization of Irradiation Effects and Fission Product Identification of Irradiated TRISO Coated Particles from the AGR-1 Experiment," *Proceedings of GLOBAL 2013, Salt Lake City, Utah, USA, September 29–October 3, 2013*.
- van Rooyen, I. J., E. J. Olivier, J. H. Neethling, 2014a, "Investigation of the Fission products silver, palladium and cadmium in neutron irradiated SiC using a Cs-corrected HRTEM," Paper HTR2014-31255, *Proceedings of the HTR2014, Weihai, China, October 27–31, 2014*.
- van Rooyen, I. J., Y. Q. Wu, and T. M. Lillo, 2014b, "Identification of Silver and Palladium in Irradiated TRISO Coated Particles of the AGR1 Experiment," *Journal of Nuclear Materials*, Vol. 446, pp. 178–186, 2014.



- van Rooyen, I. J., D. E. Janney, B. D. Miller, P. A. Demkowicz, and J. Riesterer, 2014c, “Electron microscopic evaluation and fission product identification of irradiated TRISO coated particles from the AGR-1 experiment, A Preliminary Review,” *Nuclear Engineering and Design*, Vol. 271, 2014, pp. 114–122.
- van Rooyen, I. J., E. J. Olivier, and J. H. Neethling, 2016, “Investigation of the Fission Products Silver, Palladium and Cadmium in Neutron Irradiated SiC using a Cs Corrected HRTEM,” *Journal of Nuclear Materials*, Vol. 476, pp. 93–101, 2016.
- van Rooyen, I. J., C. Hill, H. Wen, T. Trowbridge, 2017, *Scanning Electron Microscopic Examination of Irradiated TRISO Coated Particles of Compacts 4-1-1, 5-3-1, 1-3-1 and Safety Tested Compact 4-3-3 of AGR-1 Experiment*, INL external report in preparation, INL/EXT-15-36278, 2017.
- Was, G., *Fundamentals of Radiation Materials Science: Metals and Alloys*, Chapter: Radiation-Induced Segregation, pp. 255–299, New York, New York, Springer New York, 2017.
- Wen, H. and I. J. van Rooyen, 2016, “Fission products palladium, silver and cesium distribution in the uncorroded areas of the SiC layer of a neutron irradiated TRISO fuel particle,” submitted to *Journal of the European Ceramic Society*, November 2016.
- Wen, H., I. J. van Rooyen, J. D. Hunn, T. J. Gerczak, C. A. Baldwin, and F. C. Montgomery, 2015, “Advanced electron microscopy study of fission product distribution in the failed SiC layer of a neutron irradiated TRISO coated particle,” *Microscopy and Microanalysis 2015 (M&M2015)*, Portland, Oregon, August 2–7, 2015.
- Wen, H., I. J. van Rooyen, C. Hill, T. Trowbridge, B. Coryell, 2015a, “Fission product distribution in TRISO coated particles neutron irradiated to  $3.22 \times 10^{25}$  n/m<sup>2</sup> fast fluence at 1092°C,” *ASME Power and Energy 2015*, San Diego, California, June 28–July 2, 2015.
- Wen, H., I. J. van Rooyen, J. D. Hunn, T. J. Gerczak, 2016, “Advanced electron microscopy study of fission products Pd, Ag and Cs in carbon areas in the locally corroded SiC layer in a neutron irradiated TRISO fuel particle,” submitted to the *Journal of Nuclear Materials*, April 2016.
- Wolf, D., 1989, “Correlation between energy and volume expansion for grain boundaries in FCC metals,” *Scripta Met.*, Vol. 23, pp. 1913–1918, 1989.
- Wolf, D., 1990, “Structure-energy correlation for grain boundaries in f.c.c. metals – IV. Asymmetrical twist (general) boundaries,” *Acta Metall. Mater.*, Vol. 38, pp. 791–798, 1990.
- Wright, K. E. and I. van Rooyen, 2016, “Electron Probe Microanalysis of Irradiated and 1600°C Safety Tested AGR-1 TRISO Fuel Particles with Low and High Retained 110mAg,” *HTR2016*, Las Vegas, Nevada, November 2016, Paper 18570.
- Wu, Y. Q., I. J. Van Rooyen, J. W. Madden, J. Burns and H. M. Wen, 2016, “Atom Probe Tomography Characterization on TRISO fuels,” Journal article in preparation, 2016.
- Xiao, H. X., Y. Zhang, L. L. Snead, V. Shutthanandan, H. Z. Xue, and W. J. Weber, 2012, “Near surface and bulk behaviour of Ag in SiC,” *Journal of Nuclear Materials*, Vol. 420, pp. 123–130, 2012.

## **Appendix A**

### **Leverage of Additional Funding**

## Appendix A

### Leverage of Additional Funding

Advanced characterization work was further leveraged by using NSUF rapid turnaround funds for strategic projects to increase the fundamental scientific background on topics to enhance our knowledge on fission product transport, fission product distribution, and quantification. Specifically two projects contributed significantly to the progress in Advanced Gas Reactor (AGR)1-PIE:

1. Atom probe tomography (APT) for the first quantification of a nano-sized precipitate located in a grain boundary.
2. Innovative nano-crystallographic measurements (PED) were pioneered on neutron irradiated SiC through successful demonstration of the first application of PED in conjunction with fission products in irradiated fuels.

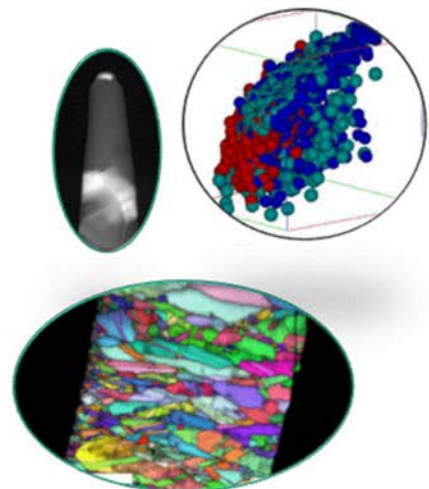
It should be noted that information provided in this appendix is only for information and not as a full Nuclear Science User Facility (NSUF) report. See more detail of the various NSUF-Rapid Turnaround Experiment (RTE) projects that contributed to the knowledgebase of the AGR advanced microscopy team in the presentation below.

### ***NSUF Rapid Turnaround Experiments “Leapfrog” our Understanding of Fission Product Transport Mechanisms in TRISO Coated Particles***

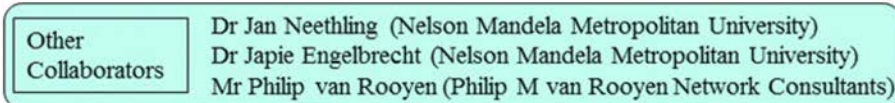
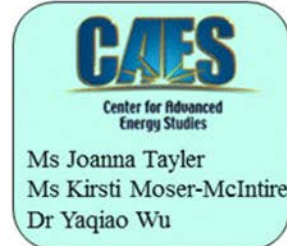
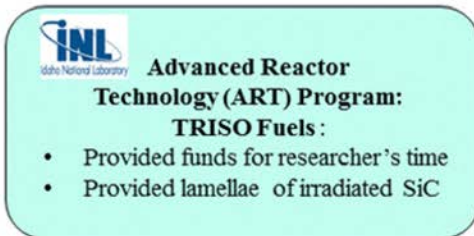
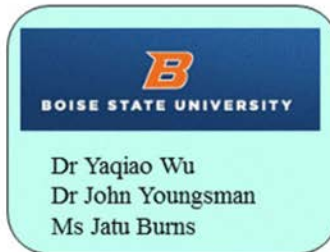
Isabella J van Rooyen  
August 16-17, 2016  
Idaho Falls



INL/CON-16-38976



## Acknowledgements



NSUF Science Review Board, Idaho Falls, August 16-17, 2016

## Fission Product Chemical Composition, Location & Structure

### STEM/EDS/EELS

UWM, INL

RTE-13-412

- First identification of Ag **INSIDE** SiC grain, previously only on grain boundaries or stacking faults
- U sub-grains found close to micron sized FP precipitate (ppt), possible intragranular path for U transport in SiC, may be related to voids and dislocation networks
- Publications:
  - 1 Journal article published
  - Multiple presentations (program, NSUF user's week)

ISU, INL

RTE-15-581

- IN PROGRESS, Eu & I found in nano ppt
- Publications: Presentation planned for NU-MAT2016

### Atom Probe Tomography

RTE-13-412

UWM INL, BSU

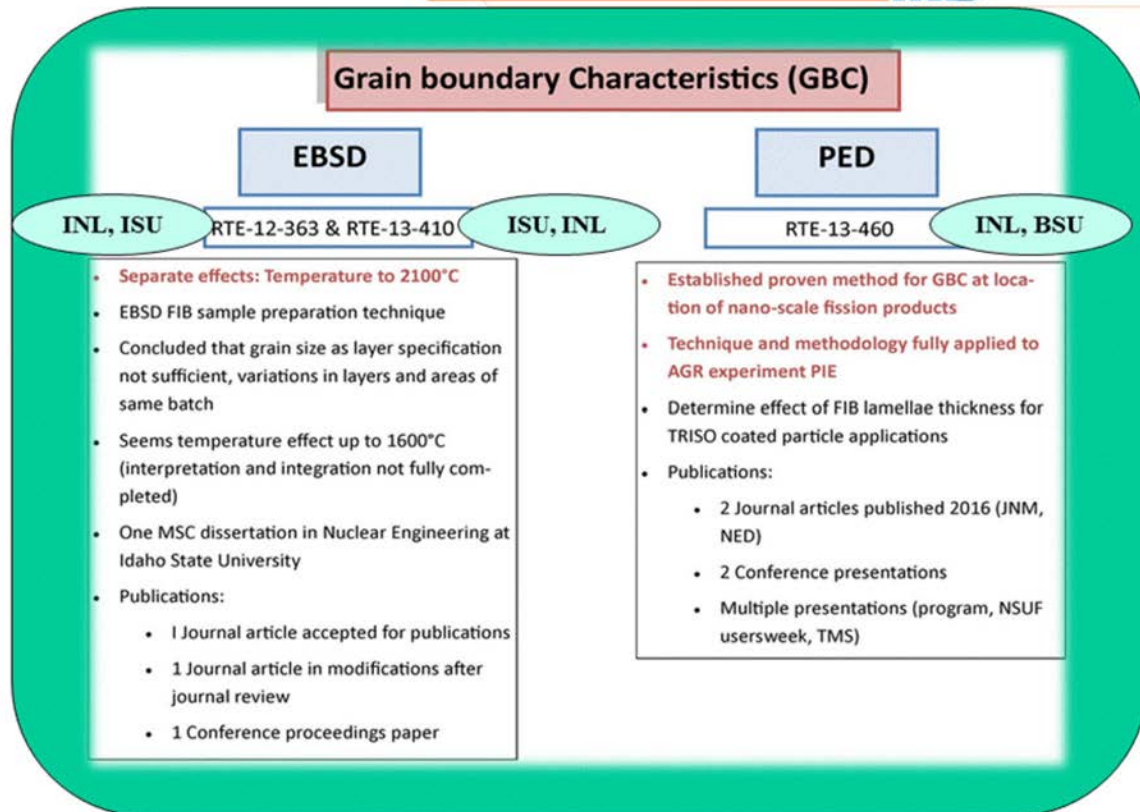
- Initially not successful locating FP ppt in top tAPT tip
- No FP identified due to Fractured tips from neutron irradiated SiC
- Tip fabrication (form, shape) successfully achieved
- Publications: Multiple program/NSUF presentations

RTE-14-541

BSU, INL

- Successful identification of nano sized Ag
- APT tip fabrication parameters for location established
- Laser parameters established for unirradiated and neutron irradiated SiC
- Publications:
  - 2 Journal presentation (TMS2016)

NSUF Science Review Board, Idaho Falls, August 16-17, 2016



NSUF Science Review Board, Idaho Falls, August 16-17, 2016

3



## Impact on AGR-1 PIE and science base

Technique	SEM/EDS/WDS	EELS/ EFTEM	STEM	EPMA	First Ag quantification non-homogenous distribution of atoms		
Compact 6-3-2 (Baseline)							
AGR1-632-030 (Low (21% ) Ag retention)	X	—	—	—	—	X NSUF 2015/2016	—
AGR1-632-034 (High (65%) Ag retention)	—	—	X	—	—	X NSUF 2014	—
AGR1-632-035 (High (79%) Ag retention)	X	X NSUF 2014/2015 NSUF 2016	X NSUF 2014	—	X NSUF 2013	X NSUF 2014	—
Compact 5-3-1 (Variant 1)							
AGR1-531-038 (Low (< 19%) Ag retention)	—	—	X	—	X	—	—
AGR1-531-031 (High (105%) Ag retention)	—	—	X	—	X	—	—
Compact 5-2-3 (Variant 1)							
AGR-523-SP01 (16% Ag retention)	—	—	—	—	X	—	—
AGR1-131-099 (Low (<6%) Ag retention)	—	—	—	—	X	—	X
AGR1-131-066 (High (39%) Ag retention)	—	—	—	—	X	—	X
Compact 4-1-1 (Variant 3)							
AGR-411-030 (Average (90%) Ag retention)	X	—	—	—	—	—	X
Compact 4-3-3 (Variant 3; 1600°C safety tested)							
AGR1-433-003 (Low (< 22%) Ag retention)	—	—	—	—	—	—	—
AGR1-433-007 (High (100%) Ag retention)	—	—	—	—	—	—	—
AGR1-433-001 (Low (66%) Ag retention)	—	—	—	—	X	—	X
AGR1-433-004 (High (98%) Ag retention)	—	—	—	—	X	—	X

• First Ag in SiC grains

• Confirmation of Ag finding in grain boundary and triple point

• Correlation strength with EBSD  
• EBSD sample preparation technique for irradiated fuel

Applied to AGR-1 coated particles  
• Correlation in center area and Ag retention  
• Variant 3 fuel inhibits Ag transport, not Pd and U

NSUF Science Review Board, Idaho Falls, August 16-17, 2016

5



## **Appendix B**

### **AGR-1 Advanced Microscopy and Micro-Analysis Publications and Presentations**

## Appendix B

### AGR-1 Advanced Microscopy and Micro-Analysis Publications and Presentations

Table B-1. AGR-1 advanced microscopy and micro-analysis publications and presentations.

Technique	Reports, Papers, Presentations
Advanced Microscopy Techniques	<p>Demkowicz, P. A., J. D. Hunn, R. N. Morris, I. Van Rooyen, T. Gerczak, J. M. Harp, and S. A. Ploger, <i>AGR-1 Post Irradiation, Examination Final Report</i>, Idaho National Laboratory, INL/EXT-15-36407, 2015.</p> <p>van Rooyen, I. J., 2013, "Summary report on Advanced microscopy performed on Irradiated AGR-1 Specimens," INL Interoffice Memorandum, CCN231379, September 2013.</p> <p>van Rooyen, I. J., Y. Q. Wu, T. M. Lillo, T. L. Trowbridge, J. M. Madden, and D. Goran, "Advanced Electron Microscopic Techniques Applied to the Characterization of Irradiation Effects and Fission Product Identification of Irradiated TRISO Coated Particles from the AGR-1 Experiment," <i>Proceedings of GLOBAL 2013, Salt Lake City, Utah, USA, September 29–October 3, 2013</i>.</p> <p>van Rooyen I.J., T. Lillo, H. Wen, K. Wright, J. Madden, J. Aguiar, <i>Advanced Electron Microscopy and Micro analytical technique development and application for Irradiated TRISO Coated Particles from the AGR 1 Experiment</i>, INL/EXT-15-36281, 2017.</p>
Basic SEM and TEM	<p>Demkowicz, P. A., J. M. Harp, P. L. Winston, S. A. Ploger and I. J. van Rooyen, AGR 1 Compact 4-1-1 Post Irradiation, Examination Results, INL/EXT-15-36169, 2016.</p> <p>van Rooyen, I. J., D. E. Janney, B. D. Miller, J. L. Riesterer, P. A. Demkowicz, 2012, "Electron microscopic evaluation and fission product identification of irradiated TRISO coated particles from the AGR-1 experiment: A preliminary review," HTR2012-3-023, <i>Proceedings of HTR-2012, Tokyo, Japan, October 28–November 1, 2012</i>.</p> <p>van Rooyen, I. J., B. D. Miller, D. E. Janney, J. Riesterer, P. A. Demkowicz, and J. Harp, <i>Electron Microscopic Examination of Irradiated TRISO Coated Particles of Compact 6-3-2 of AGR-1 Experiment</i>, INL/EXT-11-23911, 2012.</p> <p>van Rooyen, I. J., D. E. Janney, B. D. Miller, P. A. Demkowicz, and J. Riesterer, "Electron microscopic evaluation and fission product identification of irradiated TRISO coated particles from the AGR-1 experiment, A Preliminary Review," <i>Nuclear Engineering and Design</i>, Vol. 271, 2014, pp. 114–122.</p> <p>van Rooyen, I. J., C. Hill, H. Wen, T. Trowbridge, <i>Scanning Electron Microscopic Examination of Irradiated TRISO Coated Particles of Compacts 4-1-1, 5-3-1, 1-3-1 and Safety Tested Compact 4-3-3 of AGR-1 Experiment</i>, INL external report in preparation, INL/EXT-15-36278, 2017.</p> <p>van Rooyen, I. J., D. Janney, B. Miller, P. Demkowicz, J. Riesterer, "Electron microscopic evaluation and fission product identification in irradiated TRISO coated particles from the AGR-1 experiment: A preliminary review," <i>Nuclear Engineering and Design</i>, 271 (2014) 114-122 (Also presented at the <i>HTR2012 Tokyo</i>, October 28–November 1, 2012, paper HTR2012-3-023).</p>
EPMA	<p>Wright, K. E. and I. van Rooyen, 2016, "Electron Probe Microanalysis of Irradiated and 1600°C Safety Tested AGR 1 TRISO Fuel Particles with Low and High Retained 110mAg," <i>HTR2016, Las Vegas, Nevada, November 2016</i>, Paper 18570.</p>

Table B-1. (continued).

Technique	Reports, Papers, Presentations
	Wright, K.E., Van Rooyen, I. J., 2016, Fission Product Distribution in Irradiated TRISO Fuel, <i>Microscopy and Microanalysis</i> , Vol. 22, No. S3, pp. 1490–1491.
STEM	<p>Demkowicz, P. A., J. D. Hunn, R. N. Morris, C. A. Baldwin, J. M. Harp, P. L. Winston, S. A. Ploger, T. Gerczak, I. J. van Rooyen, F. C. Montgomery, C. M. Silva, “Irradiation performance of AGR-1 high temperature reactor fuel,” In Press, <i>Nuclear Engineering and Design</i>, <a href="http://dx.doi.org/10.1016/j.nucengdes.2015.09.011">http://dx.doi.org/10.1016/j.nucengdes.2015.09.011</a>, October 2015</p> <p>Leng, B., I. J. Van Rooyen, Y. Wu, I. Szlufarska, and K. Sridharan, “STEM/EDS Analysis of Fission Products in Irradiated TRISO Coated Particles of the AGR-1 Experiment,” <i>J. of Nucl. Mater.</i>, Vol. 475, pp. 62–70, 2016.</p> <p>Lillo, T. M. and I. J. van Rooyen, “Spatial Distribution of Pd, Ag &amp; U in the SiC Layer of an Irradiated TRISO Fuel Particle,” <i>Proceedings of the Microscopy &amp; Microanalysis 2014 Meeting</i>, Hartford, Connecticut, August 3–7, 2014.</p> <p>Lillo, T.M., I. J. van Rooyen, “Spatial Distribution of Pd, Ag &amp; U in the SiC Layer of an Irradiated TRISO Fuel Particle,” <i>Proceedings of the Microscopy &amp; Microanalysis 2014 Meeting</i>, Hartford, Connecticut, August 3–7, 2014.</p> <p>Lillo, T. M., and I. J. van Rooyen, “Associations of Pd, U and Ag in the SiC Layer of Neutron-Irradiated TRISO Fuel,” <i>J. Nuc. Matls.</i>, Vol. 460, pp. 97–106, 2015.</p> <p>van Rooyen, I. J., Y. Q. Wu, and T. M. Lillo, “Identification of Silver and Palladium in Irradiated TRISO Coated Particles of the AGR1 Experiment,” <i>Journal of Nuclear Materials</i>, Vol. 446, pp. 178–186, 2014.</p> <p>van Rooyen, I. J., T.M. Lillo, H. Wen, C.M. Hill, Terry Holesinger, Y.Q. Wu and J.A. Aguiar, “Micro-Nano-structural examination and fission product identification in neutron irradiated AGR-1 TRISO fuel particles using advanced micro-analytical and electron microscopic techniques,” <i>Proceedings of HTR2016, Las Vegas, Nevada, November 2016</i>, paper submitted</p> <p>van Rooyen, I. J., T. M. Lillo, Y.Q. Wu, “First-of-a-kind advanced electron microscopy characterization applied to identify silver- and palladium-containing fission products in irradiated TRISO coated particles of the AGR-1 experiment,” <i>INL Nuclear Fuels and Materials Spotlight</i>, Vol. 4, July 2013.</p> <p>van Rooyen, I. J. “Identification of Silver in Irradiated TRISO Coated Particles of the AGR-1 Experiment Using Advanced Electron Microscopic Techniques,” <i>Presentation at the INL Nuclear Science and Technology Peer Review, Idaho Falls, Idaho, June 3, 2013</i>.</p> <p>Wen, H. and I. J. van Rooyen, “Fission products palladium, silver and cesium distribution in the un-corroded areas of the locally corroded SiC layer of a neutron irradiated TRISO fuel particle,” to be submitted to <i>Journal of the European Ceramic Society</i>, October 2016.</p> <p>Wen, H., I. J. van Rooyen, J. D. Hunn, T. J. Gerczak, C. A. Baldwin, and F. C. Montgomery, “Advanced electron microscopy study of fission product distribution in the failed SiC layer of a neutron irradiated TRISO coated particle,” <i>Microscopy and Microanalysis 2015 (M&amp;M2015)</i>, Portland, Oregon, August 2–7, 2015.</p> <p>Wen, H., I. J. van Rooyen, C. Hill, T. Trowbridge, B. Coryell, 2015a, “Fission product distribution in TRISO coated particles neutron irradiated to <math>3.22 \times 10^{25}</math> n/m<sup>2</sup> fast fluence at 1092°C,” <i>ASME Power and Energy 2015, San Diego, California, June 28–July 2, 2015</i>.</p> <p>Wen, H., I. J. van Rooyen, J. D. Hunn, T. J. Gerczak, “Advanced electron microscopy study of fission products Pd, Ag and Cs in carbon areas in the locally corroded SiC layer in a neutron irradiated TRISO fuel particle,” submitted to the <i>Journal of Nuclear Materials</i>, April 2016.</p>

Table B-1. (continued).

Technique	Reports, Papers, Presentations
EELS, EFTEM	van Rooyen, I. J., Y. Q. Wu, T. M. Lillo, T. L. Trowbridge, J. M. Madden, and D. Goran, “Advanced Electron Microscopic Techniques Applied to the Characterization of Irradiation Effects and Fission Product Identification of Irradiated TRISO Coated Particles from the AGR-1 Experiment,” <i>Proceedings of GLOBAL 2013, Salt Lake City, Utah, USA, September 29–October 3, 2013</i> .
APT	Wu, Y. Q., I. J. Van Rooyen, J. W. Madden, J. Burns and H. M. Wen, 2016, “Atom Probe Tomography Characterization on TRISO fuels,” Journal article in preparation, 2016
HRTEM	<p>van Rooyen, I. J., E. J. Olivier, J. H. Neethling, 2014a, “Investigation of the Fission products silver, palladium and cadmium in neutron irradiated SiC using a Cs-corrected HRTEM,” Paper HTR2014-31255, <i>Proceedings of the HTR2014, Weihai, China, October 27–31, 2014</i>.</p> <p>van Rooyen, I. J., E. J. Olivier, and J. H. Neethling, 2016a, “Investigation of the Fission Products Silver, Palladium and Cadmium in Neutron Irradiated SiC using a Cs Corrected HRTEM,” <i>Journal of Nuclear Materials</i>, Vol. 476, pp. 93–101, 2016.</p>
EBSD and TKD	<p>Dunzik-Gougar, M. L., I. J. van Rooyen, P. M. van Rooyen, C. M. Hill, “Effect of CVD Production Parameters and Annealing on the Grain Characteristics of a Thin Silicon Carbide Layer,” submitted to <i>Journal of Nuclear Materials</i>, September 2015, revision in progress.</p> <p>van Rooyen, I. J., Y. Q. Wu, T. M. Lillo, T. L. Trowbridge, J. M. Madden, and D. Goran, “Advanced Electron Microscopic Techniques Applied to the Characterization of Irradiation Effects and Fission Product Identification of Irradiated TRISO Coated Particles from the AGR-1 Experiment,” <i>Proceedings of GLOBAL 2013, Salt Lake City, Utah, USA, September 29–October 3, 2013</i>.</p> <p>van Rooyen, I. J., M. L. Dunzik, P. M. van Rooyen, and T. Trowbridge, “On Techniques to Characterize and Correlate Grain Size, Grain Boundary Orientation and the Strength of the SiC Layer of TRISO Coated Particles - A Preliminary Study,” Paper HTR2012 -3-024, <i>Proceedings of the HTR 2012, Tokyo, Japan, October 28–November 1, 2012</i>.</p> <p>van Rooyen, I. J., P.M. van Rooyen and M.L. Dunzik-Gougar, “The Effect of High Temperature Annealing on the Grain Characteristics of a Thin Chemical Vapor Deposition Silicon Carbide Layer,” <i>Microscopy and Microanalysis</i>, Vol. 19 (Suppl. 2), pp 1948-1949, doi:10.1017/S1431927613011732, published online: 09 October 2013 (also presented at the <i>Microscopy &amp; Microanalysis Conference</i>, Indianapolis, August 4–8, 2013)</p>
PED	<p>Lillo, Thomas M., Isabella J. van Rooyen, Yaqiao Wu, 2015c, “Grain boundary character and fission product precipitation in SiC,” <i>Proceedings of the 2015 ANS Annual Meeting, June 7–11, 2015, San Antonio, Texas</i>.</p> <p>Lillo, T. M., and I. J. van Rooyen, 2016, “Influence of SiC Grain Boundary Character on Fission Product Transport in Irradiated TRISO Fuel,” <i>Journal of Nuclear Materials</i>, Vol. 47, pp. 83–92, 2016.</p> <p>Lillo, T. M., I. J. van Rooyen, Y. Q. Wu, 2016, “Precession electron diffraction for SiC grain boundary characterization in unirradiated TRISO Fuel,” <i>Nuclear Engineering and Design</i>, <a href="http://dx.doi.org/10.1016/j.nucengdes.2016.05.027">http://dx.doi.org/10.1016/j.nucengdes.2016.05.027</a>, Vol. 305, pp. 277–283, 2016.</p> <p>Lillo, T. M., I. J. van Rooyen, H. Wen, J. A. Aguiar, 2017, “Supplemental PED Advanced Microscopy Data From Microstructural Analyses of AGR-1 TRISO Particles,” Idaho National Laboratory, INL/LTD-16-39740, 2017.</p>

Table B-1. (continued).

Technique	Reports, Papers, Presentations
PED (continued)	<p>Lillo, T. M., I. J. van Rooyen, and J. A. Aguiar, "SiC grain boundary distributions, irradiation conditions and silver retention in irradiated AGR-1 TRISO fuel particles," <i>Proceedings of HTR2016, Las Vegas, Nevada, November 2016</i>, paper submitted.</p> <p>van Rooyen I. J. and T. M. Lillo, "SiC Grain Boundary Character and Fission Product Transport in irradiated TRISO coated particles," <i>INL Nuclear Fuels and Materials Spotlight</i>, Vol. 5, publication, in press July 2016.</p>
Transport Mechanisms and other SiC	<p>van Rooyen, I. J., M. L. Dunzik-Gougar, P. M. van Rooyen, "Silver (Ag) transport mechanisms in SiC layer of TRISO coated particles: A critical review," <i>Nuclear Engineering and Design</i>, Vol. 271, May 2014, p. 180-188, (Also presented at the <i>HTR2012 Tokyo 28 October-1-November 2012</i>, Paper HTR-3-040).</p> <p>van Rooyen, I. J., H. Nabielek, J. H. Neethling, M. J. Kania, and D. A. Petti, "Progress in solving the elusive Ag transport mechanism in TRISO coated particles: What's new?," <i>HTR2014-3-1261, Proceedings of the 7th International Topical Meeting on High Temperature Reactor Technology (HTR2014)</i>, Weiha, China, October 27–31, 2014.</p> <p>van Rooyen, I. J., M. L. Dunzik-Gougar, P. M. van Rooyen, "Silver (Ag) transport mechanisms in SiC layer of TRISO coated particles: A critical review," Paper HTR-3-040, <i>Proceedings of the HTR2012, Tokyo, Japan, October 28 –November 1, 2012</i>.</p> <p><u>* Continuation of previous work</u></p> <p>*Engelbrecht, J. A. A., G. Deyzel, E. G. Minnaar, W. E. Goosen, I. J. van Rooyen, "Assessment of neutron irradiated 3C-SiC implanted at 800C," <i>Journal of Applied Optics</i>, Vol. 36, No. 6, pp. 937–941, November 2015.</p> <p>*Engelbrecht, J. A. A., I. J. van Rooyen, A. Henry, E. Janzén, and B. Sephton, "Notes on the plasma resonance peak employed to determine doping in SiC," Accepted by <i>Infrared Physics &amp; Technology</i>, July 12, 2015, INFPHY-D-15-00093R1.</p> <p>*Engelbrecht, J. A. A., E. Jansen, I. J. van Rooyen, "Impact of dielectric parameters on the reflectivity of 3C-SiC wafers with a rough surface morphology in the reststrahlen region," <i>Physica B</i>, Vol. 439, pp. 115–118, 2014.(Also presented at the <i>South African Institute of Physics (SAIP), Kariega, 2013</i>.)</p> <p>*Engelbrecht, J. A. A., G. Deyzel, E. Minnaar, W. E. Goosen, I. J. van Rooyen, "The influence of neutron-irradiation at low temperatures on the dielectrical parameters of 3C-SiC," <i>Physica B</i>, Vol. 439, pp. 169–172, 2014.</p> <p>*Van Rooyen, I. J., J. J. A. Engelbrecht, A. Henry, E. Janzén, J. H. Neethling, P. M. van Rooyen, "The Influence of grain size and phosphorous-doping of polycrystalline 3C-SiC on Infrared Reflectance Spectra," <i>Journal of Nuclear Materials</i>, Vol. 422, No.1–3, pp. 103–108, 2012.</p> <p>*Van Rooyen, I. J., J. H. Neethling, A. Henry, E. Janzen, S. M. Mokoduwe, A. Janse van Vuuren, E. Olivier, "Effects of Phosphorous-doping and High Temperature Annealing on CVD grown 3C SiC," <i>Nuclear Engineering and Design</i>, Vol. 251, pp. 191–202, 2012.</p> <p>*Engelbrecht, J. A. A., I. J. van Rooyen, A. Henry, E. Janzén, and E. J. Olivier, "The origin of a peak in the reststrahlen region of SiC," <i>Physica B: Condensed Matter</i>, 407, pp. 1525–1528, 2012.</p> <p>*van Rooyen, I. J., J. H. Neethling, A. Henry, E. Janzen, S. M. Mokoduwe, A. Janse van Vuuren, E. Olivier, "Effects of Phosphorous-doping and High Temperature Annealing on CVD grown 3C SiC," <i>Nuclear Engineering and Design</i>, Vol. 251, pp. 191–202, 2012.</p>

Table B-1. (continued).

Technique	Reports, Papers, Presentations
	*Engelbrecht, J. A. A., I. J. van Rooyen, A. Henry, E. Janzén and E. J. Olivier, “The origin of a peak in the reststrahlen region of SiC,” <i>Physica B: Condensed Matter</i> , Vol. 407, pp. 1525–1528, 2012.
Presentations Only (Conferences)	<p>Demkowicz, P., S. Ploger, I. van Rooyen, J. Riesterer, “Microanalysis of irradiated coated particle fuel from the AGR-1 irradiation experiment,” <i>TMS 2012, March 2012</i>.</p> <p>Holesinger, T. G., I. J. van Rooyen, and W. Zhong, “Post-irradiation HRTEM examination of UCO Fuel Kernels from TRISO coated particles,” <i>TMS2017 Conference</i>, to be held in San Diego, California, February 26–March 2, 2017.</p> <p>van Rooyen, I., T. Holesinger, H. Wen, “High resolution electron microscopy examination of fission product precipitates in TRISO coated particles,” <i>TMS2016, 145th Annual Meeting &amp; Exhibition, Nashville Tennessee, USA, February 14–18, 2016</i>.</p> <p>van Rooyen, I. J. (Invited), “Identification of Silver in Irradiated TRISO Coated Particles of the AGR-1 Experiment Using Advanced Electron Microscopic Techniques,” <i>Presentation at the INL Nuclear Science and Technology Peer Review, June 3, 2013</i>.</p> <p>van Rooyen, I. J. (Invited), T. M. Lillo, K. Wright, J. A. Aguiar, and T. Holesinger, “Neutron irradiated SiC Advanced Analyses to understand Fission product Transport: Safety tested TRISO coated particle,” <i>TMS2017 Conference</i>, to be held in San Diego, California, February 26–March 2, 2017.</p> <p>van Rooyen, I. J., C. Hill, and T. Trowbridge, “Fission product distribution patterns as a comparative characterization tool for TRISO fuel performance,” <i>TMS2015 144th Annual meeting, Walt Disney World Orlando, Florida, USA, March 15–19, 2015</i>, An abstract was submitted and accepted for oral presentation.</p> <p>van Rooyen, I. J., (Invited), Y. Q. Wu, T. M. Lillo, J. Youngsman, and J. H. Neethling, “Approach and Micro-analysis techniques applied to study fission product transport mechanisms in neutron irradiated SiC layers,” <i>XXIII IMRC, Cancun, Mexico, August 17–22, 2014</i>.</p> <p>van Rooyen, I., M. L. Dunzik Gougar, P. van Rooyen, “Effect of Grain Characteristics on Mechanical properties of thin CVD SiC layers: A preliminary study,” <i>XXIII IMRC, Cancun, Mexico, August 17–22, 2014</i>.</p> <p>van Rooyen, I., B. Leng, Y. Wu, T. Lillo, I. Szlufarska, K. Sridharan, T. Gerczak, J. Madden, “Products in irradiated SiC using Scanning Transmission Electron Microscopy and Atom Probe Tomography RTE 13-412,” <i>ATR NSUF User’s week 2014, Idaho Falls, Idaho, June 4-6, 2014</i>.</p> <p>van Rooyen, I. J., T. M. Lillo and Y.Q. Wu, “Advanced Electron Microscopic Examination for the Identification of Silver and Palladium in Irradiated SiC,” <i>TMS 2014 Conference, San Diego, California, February 2014</i>.</p> <p>van Rooyen, I., M. L. Dunzik Gougar, P. van Rooyen, “The Application of EBSD measurements to determine the effect of Grain Characteristics on Mechanical Properties on thin CVD SiC Layers,” <i>ATR NSUF User’s week 2013, Idaho Falls, Idaho, June 10–14, 2013</i>.</p> <p>van Rooyen, I. J., T. L. Trowbridge, T. Lillo, “EBSD applications to predict nuclear fuel performance,” <i>EBSD2012 Conference, Pittsburgh, Pennsylvania, June 19–21, 2012</i>.</p>

Table B-1. (continued).

Technique	Reports, Papers, Presentations
Presentations Only (Conferences) (continued)	<p>Wen, H., I. J. van Rooyen, "Correlation of fission product transport to grain boundary character in neutron irradiated tristructural isotropic coated nuclear fuel particles," <i>TMS2016, 145th Annual Meeting &amp; Exhibition, Nashville Tennessee, USA, February 14–18, 2016.</i></p> <p>Wu, Y. Q., I. J. van Rooyen, J. Burns, J. W. Madden, and H. M. Wen, "Identification of Ag-phase in TRISO fuels by Atom Probe Tomography," <i>Materials Science &amp; Technology 2016, Salt Lake City, Utah, USA, October 23–27, 2016.</i></p> <p>Wu, Y. Q., I. J. van Rooyen, H. M. Wen, J. Burns, and J. W. Madden, "Microstructure Characterization of TRISO fuels by Atom Probe Tomography," <i>TMS2016, 145th Annual Meeting &amp; Exhibition, Nashville Tennessee, USA, February 14–18, 2016.</i></p> <p>Wu, Y. Q., I. J. van Rooyen, T. M. Lillo, and J. W. Madden, "Advances in Structural and Chemical Imaging," <i>ASCI 2014 Conference, Seattle, Washington, May 28, 2014.</i></p>
Workshop Presentations	<p>van Rooyen, I. J., T. M. Lillo, Y. Q. Wu, T. Trowbridge, H. Wen and C. Hill, "Development and Application of Advanced Characterization Techniques to understand Irradiated TRISO Fuel Behavior," <i>The 3rd Workshop on HTGR SiC Material Properties, September 30–October 1, 2014, Jeju Island, South Korea.</i></p> <p>van Rooyen, I. J., J. Youngsman, T. M. Lillo, Y. Q. Wu, D. Goran, M. E. Lee, W. E. Goosen, J. H. Neethling, T. L. Trowbridge and J. W. Madden, "Methods for identification of crystallographic parameters of irradiated SiC to understand fission product transport," <i>The 3rd Workshop on HTGR SiC Material Properties, Jeju Island, South Korea, September 30–October 1, 2014.</i></p> <p>van Rooyen, I. J., "Preliminary findings: Relationship between Grain size, grain boundary orientation and strength for the SiC layer of TRISO coated particles," <i>2nd Workshop on "HTGR SiC Materials properties," in conjunction with GIF VHTR Fuel/Fuel Cycle PMB meeting, Idaho Falls USA. January 19–20, 2012.</i></p> <p>van Rooyen, I. J., "The effect of irradiation and temperature on the Restrahlens shape of 3C-SiC reflectance infrared measurement: A preliminary study," <i>2nd Workshop on "HTGR SiC Materials properties, in conjunction with GIF VHTR Fuel/Fuel Cycle PMB meeting, Idaho Falls, Idaho, USA, January 19–20, 2012.</i></p> <p>van Rooyen, I. J., J. Riesterer, B. Miller, D. J. P. Demkowicz, "Preliminary findings: Microscopic examination and fission product precipitate identification in irradiated TRISO coated particles from the AGR-1 experiment," <i>2nd Workshop on "HTGR SiC Materials properties, in conjunction with GIF VHTR Fuel/Fuel Cycle PMB meeting, Idaho Falls, Idaho, USA, January 19–20, 2012.</i></p>



Table B-1. (continued).

Technique	Reports, Papers, Presentations
ART Program Review Presentations (2011–2016) and NSUF Users Week and Scientific Review Board	<p><u>AGR Fuels program review, yearly presentations 2011–2016</u></p> <p>van Rooyen, I. J., D. E. Janney, B. D. Miller, J. L. Riesterer, K. E. Wright, P. A. Demkowicz, “Electron Microscopic Characterization of TRISO Coated Particles of the AGR-1 Experiment at INL,” Salt Lake City, Utah, May 22–24, 2012.</p> <p>van Rooyen, I. J., “Electron Microscopic Characterization of AGR-1 TRISO Coated Particles,” Idaho Falls, Idaho, May 7–9, 2013.</p> <p>van Rooyen, I. J., “Advanced Microscopy and Micro-Analysis Results Summary,” Idaho Falls, Idaho, July 30, 2014.</p> <p>van Rooyen, I. J., T. M. Lillo, H. Wen, “AGR-1 Advanced Electron Microscopy Progress,” Idaho Falls, Idaho, July 15–16, 2015.</p> <p>van Rooyen, I. J., “AGR-1 and AGR-2 Advanced Microscopy and Micro-Analysis Progress,” Washington, D.C., June 7, 2016.</p> <p>NSUF users week presentations: yearly 2013–2016.</p> <p>NSUF scientific review board: 2016.</p>

## **Appendix C**

### **Diffraction Spot Differences**

## Appendix C

### Diffraction Spot Differences

Diffraction spot distances for Pd and Pd-Ag showing the d-spacings and for Pd and Pd-Ag as a comparison showing the close proximity, which complicated the differentiation between these compounds using this method only.

Diffraction Spots for Pd					Diffraction Spots for Pd-Ag				
H	k	l	s[sin( $\theta$ )/ $\lambda$ ]	d[Å]	h	k	l	s[sin( $\theta$ )/ $\lambda$ ]	d[Å]
1	1	1	0.218142	2.292081	1	1	1	0.216995	2.304205
0	0	2	0.251889	1.985	0	0	2	0.250564	1.9955
0	2	2	0.356225	1.403607	0	2	2	0.354351	1.411032
1	1	3	0.417711	1.197	1	1	3	0.415513	1.203332
2	2	2	0.436285	1.14604	2	2	2	0.433989	1.152102
0	0	4	0.503778	0.9925	0	0	4	0.501128	0.99775
1	3	3	0.54898	0.91078	1	3	3	0.546091	0.915598
0	2	4	0.563241	0.887719	0	2	4	0.560278	0.892415
2	2	4	0.617	0.810373	2	2	4	0.613753	0.814659
1	1	5	0.654427	0.764027	1	1	5	0.650984	0.768068
3	3	3	0.654427	0.764027	3	3	3	0.650984	0.768068
0	4	4	0.71245	0.701803	0	4	4	0.708701	0.705516
1	3	5	0.745098	0.671052	1	3	5	0.741178	0.674602
2	4	4	0.755668	0.661667	2	4	4	0.751691	0.665167
0	0	6	0.755668	0.661667	0	0	6	0.751691	0.665167
0	2	6	0.796543	0.627712	0	2	6	0.792352	0.631032
3	3	5	0.825874	0.605419	3	3	5	0.821528	0.608622
2	2	6	0.835422	0.5985	2	2	6	0.831026	0.601666
4	4	4	0.87257	0.57302	4	4	4	0.867978	0.576051
1	5	5	0.899424	0.555911	1	5	5	0.894692	0.558852
1	1	7	0.899424	0.555911	1	1	7	0.894692	0.558852
0	4	6	0.908199	0.55054	0	4	6	0.903421	0.553452
2	4	6	0.942483	0.530514	2	4	6	0.937524	0.53332
1	3	7	0.967399	0.51685	1	3	7	0.962308	0.519584
3	5	5	0.967399	0.51685	3	5	5	0.962308	0.519584